
THE QUASAR MAIN SEQUENCE AT EARLY COSMIC EPOCHS



ALICE DECONTO MACHADO

SUPERVISORS:

DR. ASCENSIÓN DEL OLMO OROZCO

DR. PAOLA MARZIANI

INSTITUTO DE ASTROFÍSICA DE ANDALUCÍA
CONSEJO SUPERIOR DE INVESTIGACIONES CIENTÍFICAS

UNIVERSIDAD DE GRANADA
PROGRAMA DE DOCTORADO EN FÍSICA Y MATEMÁTICAS

A thesis submitted for the degree of
Doctor of Philosophy

30th October 2024

Dedico esta tese a todas as pessoas que iluminaram meu caminho até aqui.

Em especial aos meus amados pais, Vânia Maria e Luiz Solomar,
por sempre me facilitarem o acesso a uma educação de qualidade, apesar das muitas dificuldades;
por me ensinarem a ver a vida ao meu redor com sensibilidade e a respeitar as diversas diferenças;
e, principalmente, por me ensinarem que a maior riqueza que posso ter reside nas pessoas que amo.

E aos meus avós, Eva Marina (*in memoriam*) e Ataíde (*in memoriam*),
por todas as noites que ficamos conversando e observando o céu estrelado em Camobi.
Mal sabia aquela jovem Alice que as suas duas estrelas favoritas ainda não estavam ali.

Obrigada por tudo.

E por tanto.

ACKNOWLEDGEMENTS

Uma das minhas músicas favoritas diz que *“é tão bonito quando a gente entende que a gente é tanta gente onde quer que a gente vá; e é tão bonito quando a gente sente que nunca está sozinho por mais que pense estar”*. Com essa frase gostaria de começar meus agradecimentos.

Sou muito grata a toda minha família pelo apoio que recebi durante estes anos, mesmo estando bastante longe de casa. A distância foi, e ainda é, um dos maiores desafios que enfrentei, e a saudade que carrego comigo é constante. Estar longe, especialmente nos momentos mais importantes, tornou tudo mais difícil, mas ao mesmo tempo me ensinou a valorizar ainda mais cada segundo que passamos juntos.

E quando me refiro a família, não me refiro somente à de sangue, mas também a que fui construindo ao largo destes anos e que foi se espalhando pelo globo. Tive a sorte de conhecer pessoas incríveis, com histórias interessantíssimas, que admiro muito. E, o que acho mais sorte ainda, posso dizer que a distância não limitou as amizades que levo comigo desde muitos mais anos atrás. Agradeço a cada uma destas pessoas queridas pelo carinho com o qual sempre me tratam e pela leveza que trazem à minha vida.

Quiero expresar mis agradecimientos a mis directoras de tesis Ascensión del Olmo y Paola Marziani por el soporte y las enseñanzas que me han transmitido en el desarrollo de esta tesis. He aprendido mucho con vosotras y llevaré lo que aprendí siempre conmigo. También me gustaría agradecer a Paola y al Observatorio Astronómico de Padova por las gratas estancias que tuve la oportunidad de disfrutar allí. No podría dejar de agradecer a Jaime, por toda la ayuda a lo largo de estos años, y a los demás miembros de nuestro grupo, en particular Isabel, Pepa, Sara, Laura, y Marta. I would like to also thank all the people from the IAA, and especially Kieu Ny, Estefania, and Carol, for their kindness, support, and friendship.

Este trabajo ha sido posible gracias a la financiación procedente de la beca INPhINIT de la fundación “la Caixa” (ID 100010434) y de los proyectos ID2019–106027GB–C41, PID2022-140871NB-C21 by “ERDF A way of making Europe”, y el proyecto Severo Ochoa CEX2021- 515001131-S del IAA financiada por MCIN/AEI/10.13039/501100011033, del Gobierno de España.

ABSTRACT

The Main Sequence (MS) of quasars emerged, in the early 2000s, as a powerful tool to contextualise and organise the observed spectroscopic diversity of the quasars on different spectral types according to key observational (in optical, UV, and X-rays) and physical parameters that are systematically changing along it and mainly driven by the accretion rate on to the central black hole. However, the work on the MS has been restricted mainly to low redshift ($z < 1$), where it is well established. Little is known about the MS at earlier cosmic epochs and high luminosity, because the most widely used parameters for its definition are shifted into the infrared domain, where spectroscopy of large samples is more difficult. This thesis aims to evaluate for the first time the behaviour of the MS at high redshift, focusing on the interplay between feedback mechanisms and the radio-loudness effect in the accretion processes of Active Galactic Nuclei (AGN).

Feedback from AGN is seen as one of the main contributors to the evolutionary process of galaxies, although their impact on host galaxies are still pending on detailed analysis. Specially at high and intermediate redshift, many sources seem to harbour a powerful central mechanism that allows for strong jets in radio and/or winds observed in the optical and UV ranges of their spectra. The analysis of the spectroscopic properties of these objects may be helpful to better understand the behaviour of these processes. By decomposing the broad emission line profiles into 3 or more components and analysing the blueshifted component, we are able to estimate the feedback contribution. Usually, high-ionisation lines such as C IV λ 1549 tend to present a more significant blueward asymmetry, while in H β for instance the contribution is not that strong (although present, in some cases). A good indicator of feedback in the optical range is often [O III] λ 5007, while in the UV notable blueshifted components can be seen in the many blends of the UV region.

Another important factor to be considered within the domain of AGN is the role of radio emission. In the context of the quasar MS at low redshifts, it is observed that radio-loud sources are primarily associated with Population B sources, which are characterised by quasars where minimal to no outflow motions are detected. The comparison between the strong C IV λ 1549 high-ionisation line and H β in terms of line widths and shifts with respect to rest-frame leads to an evaluation of the role of radiative forces in driving an accretion disk wind. While for non-jetted quasars the wind properties have been more extensively characterised as a function of luminosity and other physical parameters, the situation is by far less clear for jetted sources. The overarching issue is the effect of the relativistic jet on the wind, and on the structure of the emitting region in general.

In the redshift range that we are considering, the high-ionisation lines in the UV in the quasar rest-frame are redshifted into the optical domain, while the H β + [O III] spectral region is shifted into

the near-infrared. Observations covering the $H\beta$ spectral region were collected with the infrared spectrometer ISAAC at ESO-VLT. They make it possible to obtain an accurate measurement of the quasar rest-frame and to set the location of a quasar along the MS. In addition, the knowledge of the rest-frame allows for a quantitative comparison between low- and high-ionisation lines. Regarding the UV, the study is performed using mainly the archival data from the Sloan Digital Sky Survey (SDSS). The radio data analysed in this thesis were collected mainly from the 1.4-GHz NRAO VLA Sky Survey (NVSS) and the VLA FIRST Survey.

Along this thesis, an interline comparison has been performed with the aim to highlight the similarities found between the optical and UV ranges. In Part I, we are finding significant outflows not only in $[O\ III]\lambda 5007$ but also in lines with broader profiles such as $H\beta$ and $C\ IV\lambda 1549$, hinting at an association with the Broad Line Region emission. We are finding extremely broad $[O\ III]\lambda 5007$ emission, comparable to the width of the $H\beta$ broad profile in some highly accreting quasars. Additionally, emission lines like $[O\ III]\lambda\lambda 4959, 5007$ and $C\ IV\lambda 1549$ appear to follow very similar trends. Both $[O\ III]\lambda 5007$ and $C\ IV\lambda 1549$ outflows show very high amplitudes and a high degree of correlation, which may indicate a possible physical connection between the inner and outer outflows. This result mirrors the behaviour observed at low redshift for sources whose high-ionisation lines are dominated by an outflow component. At variance to the low- z samples, more than 60% of our high- z objects show $[O\ III]\lambda 5007$ blueshift larger than 250 km s^{-1} . The main factor governing the outflows in both $[O\ III]\lambda\lambda 4959, 5007$ and $C\ IV\lambda 1549$ is most likely the Eddington ratio, with a non-negligible role of luminosity affecting shift amplitudes.

In Part II, we discuss the radio dichotomy and the relation between radio and optical/UV properties. High-ionisation lines especially in radio-quiet sources usually present a significant asymmetry towards the blue that is strong evidence of outflow motions. In contrast, radio-loud quasars commonly display relatively modest outflowing components. The strongest radio emitters are also found with the more symmetric profiles in both UV and optical ranges. Our analysis suggest that the radio emission seems to somehow contribute to smaller outflows, and that the strongest outflows in both $[O\ III]\lambda 5007$ and $C\ IV\lambda 1549$ are caused mainly by accretion.

The Part III of this thesis explores how intermediate ionisation emission lines in the UV can be suitable to serve as virial broadening estimators for black hole mass computation at high and low redshift. We derive scaling laws using the $Al\ III\lambda 1860$ doublet and the $C\ III]\lambda 1909$ emission lines, since the line width of these lines are highly correlated with the one of $H\beta$, and consequently can be considered as equivalent for the majority of Population A quasars (usually high accretors) over five orders of magnitude in luminosity. Last, in Part IV we have analysed a small sample of radio-loud and radio-quiet quasars, and a preliminary analysis reveals that RL show sub-solar chemical abundances, lower compared to RQ. Additionally, our findings suggest that there is a gradient of metallicity across Pop. A and Pop. B, shedding light on their evolutionary paths.

RESUMEN

La Secuencia Principal (MS, del inglés *Main Sequence*) de los cuásares surgió a principios de los años 2000 como una herramienta poderosa para contextualizar y organizar la diversidad espectroscópica observada en los cuásares, distinguiendo diferentes tipos espectrales que respondían a parámetros observacionales clave e independientes (en óptico, UV y rayos X) y cuyos parámetros físicos asociados mostraban variaciones sistemáticas a lo largo de la secuencia, impulsados principalmente por la tasa de acreción sobre el agujero negro supermasivo central. Sin embargo, desde el establecimiento de la MS, su estudio ha estado limitado principalmente a cuásares a bajo corrimiento al rojo (*redshift*, $z < 1$), donde fue inicialmente establecida. Poco se conoce sobre la MS en épocas cósmicas más tempranas y en objetos de alta luminosidad, debido en parte a que los parámetros más utilizados para su caracterización se desplazan hacia el dominio infrarrojo, donde la espectroscopia en grandes muestras es más difícil. Esta tesis tiene entre sus objetivos evaluar, por la primera vez, el comportamiento de la MS a altos corrimientos al rojo, centrándose también en la interacción entre los mecanismos de retroalimentación entre el agujero negro supermasivo central y la galaxia anfitriona (en adelante *feedback*) y los efectos de la emisión en radio frecuencias sobre los procesos de acreción de los Núcleos Activos de Galaxias (AGN).

El *feedback* de los AGN se considera uno de los principales contribuyentes al proceso evolutivo de las galaxias, aunque su impacto sobre las galaxias anfitrionas aún requiere un mayor desarrollo y análisis detallado. Especialmente en corrimientos al rojo intermedios y altos, muchas fuentes parecen albergar un mecanismo central potente que permite la presencia de jets intensos en radio y vientos (*outflows*) que se observan en los rangos óptico y UV de sus espectros. El análisis de las propiedades espectroscópicas de estos objetos puede ser clave para comprender mejor el comportamiento de estos procesos. Al descomponer los perfiles de las líneas de emisión anchas en todas sus componentes, en general en tres o incluso más componentes, e identificar y analizar la componente desplazada hacia el azul, es posible estimar la contribución del *feedback*. Generalmente, las líneas de alta ionización, como C IV $\lambda 1549$, tienden a mostrar una asimetría significativa hacia el azul, mientras que en líneas anchas de baja ionización como H β , por ejemplo, la contribución es mucho menor (aunque está presente en algunos casos). Un buen indicador de *feedback* en el rango óptico es frecuentemente [O III] $\lambda 5007$, mientras que en el UV se pueden observar componentes desplazados al azul en muchas de las líneas anchas de emisión y *blends* presentes en esa región espectral.

Otro factor importante a considerar en el ámbito de los AGN es el papel de la emisión en radio frecuencias. En el contexto de la Secuencia Principal de los cuásares a bajo corrimiento al rojo, se observa que las fuentes intensas emisoras en radio (RL) están asociadas principalmente con los objetos de Población B, caracterizados por cuásares en los que se detectan mínimos o nulos despla-

mientos hacia el azul (también llamados de *outflows* e identificados con la presencia de vientos). La comparación entre la línea de alta ionización de C IV $\lambda 1549$ y H β (de baja ionización) en términos de anchura de las líneas y desplazamientos respecto a la velocidad de referencia del cuásar (en adelante *rest-frame*) permite evaluar el papel de las fuerzas radiativas en la generación de vientos intensos en el disco de acreción. Mientras que para los cuásares sin jets relativistas (RQ) en radio las propiedades del viento han sido más extensamente caracterizadas en función de la luminosidad y otros parámetros físicos, la situación es mucho menos clara para las fuentes con jets relativistas y emisión intensa en radio. Una cuestión importante a dilucidar en este tema es el efecto del jet relativista sobre el viento (y los correspondientes *outflows*), así como sobre la propia estructura de la región emisora en general.

En el rango de corrimiento al rojo que estamos considerando, las líneas de alta ionización en el UV en el *rest-frame* de los cuásares se desplazan al omino óptico, mientras que la región espectral de H β + [O III] se desplaza hacia el infrarrojo cercano. Las observaciones de la región espectral de H β se realizaron con el espectrómetro infrarrojo ISAAC en el telescopio VLT de la ESO (Chile). Estas observaciones nos permiten obtener una medida precisa del *rest-frame* de cada cuásar y situarlo en la Secuencia Principal, identificando su tipo espectral. Además, el conocimiento del *rest-frame* posibilita una comparación cuantitativa entre las líneas de baja y alta ionización. En cuanto al UV, para el estudio realizado se han utilizado principalmente datos del archivo espectroscópico del Sloan Digital Sky Survey (SDSS). Los datos en radio analizados en esta tesis provienen principalmente de los mapeos a 1.4 GHz del NRAO VLA Sky Survey (NVSS) y del VLA FIRST Survey.

A lo largo de esta tesis, se ha realizado una comparación entre líneas con el objetivo de resaltar las similitudes entre los rangos óptico y UV. En los estudios presentados en la Parte I, se han detectado *outflows* significativos no solo en [O III] $\lambda 5007$, sino también en líneas con perfiles anchos, como H β y C IV $\lambda 1549$, lo que sugiere una asociación con la emisión proveniente de la región de líneas anchas (BLR, del inglés *broad line region*). Se muestra la existencia de una emisión extremadamente ancha en [O III] $\lambda 5007$, comparable con la anchura del perfil de H β en cuásares con alta tasa de acreción. Además, líneas de emisión como [O III] $\lambda\lambda 4959, 5007$ y C IV $\lambda 1549$ parecen seguir tendencias muy similares. Tanto los *outflows* de [O III] $\lambda 5007$ como los de C IV $\lambda 1549$ muestran amplitudes muy altas y un alto grado de correlación, lo que podría indicar una posible conexión física entre los *outflows* producidos en la parte más interna y los producidos en la parte más externa del AGN. Este resultado parece reproducir el comportamiento observado en la población (minoritaria) de cuásares a bajo corrimiento al rojo en los que líneas de alta ionización como [O III] $\lambda 5007$ están dominadas por una componente de *outflow*. Sin embargo, a diferencia de las muestras a bajo z , más del 60% de nuestros objetos a alto z muestran un desplazamiento al azul de [O III] $\lambda 5007$ mayor que 250 km s^{-1} . Encontramos que el principal factor que gobierna los *outflows* de [O III] $\lambda\lambda 4959, 5007$ y C IV $\lambda 1549$ es la relación de Eddington (tasa de acreción), con un efecto de segundo orden, no despreciable, de la luminosidad del AGN asobre la amplitud de los desplazamientos al azul.

En la Parte II de la tesis, se aborda la dicotomía de los cuásares en radio (*radio-loud* y *radio-*

quiet, RL/RQ) y la relación entre las propiedades en radio y las propiedades ópticas/UV. Las líneas de alta ionización, especialmente en fuentes con emisión débil en radio (RQ), suelen presentar una asimetría significativa hacia el azul, lo que constituye una fuerte evidencia de flujos de materia hacia fuera, *outflows*. En cambio, los cuásares con emisión intensa en radio (RL) exhiben componentes de *outflow* relativamente moderados. De manera que, los cuásares con las emisiones en radio más potentes muestran los perfiles de las líneas más simétricos tanto en el rango UV como en el óptico. Nuestro análisis sugiere que la emisión en radio parece contribuir, de alguna manera, a *outflows* menores, y que los *outflows* más intensos, en ambas líneas de [O III] λ 5007 y C IV λ 1549, son debidos principalmente a la acreción.

La Parte III de esta tesis explora cómo líneas anchas de emisión de ionización intermedia en el UV son apropiadas como estimadores del ensanchamiento virial de las líneas y, en consecuencia, para la estimación de la masa del agujero negro a altos (y bajos) corrimientos al rojo. Se derivan las correspondientes leyes de escala utilizando las líneas anchas del doblete de Al III λ 1860 y de C III λ 1909, dado que encontramos que la anchura de estas líneas del UV está altamente correlacionada con la de H β y, en consecuencia, pueden considerarse equivalentes para la mayoría de los cuásares de Población A (generalmente de alta acreción). Relaciones que se verifican con una muestra de cuásares cubriendo cinco órdenes de magnitud en luminosidad. Finalmente, en la Parte IV, hemos analizado una muestra pequeña de cuásares *radio-loud* y *radio-quiet*, y el análisis preliminar revela que los cuásares *radio-loud* presentan metalicidades sub-solares/solares, más bajas que en el caso de los objetos *radio-quiet*. Además, nuestros resultados sugieren que existe un gradiente de metalicidad entre la Pop. A y la Pop. B en la MS, lo que podría arrojar luz sobre sus trayectorias evolutivas.

TABLE OF CONTENTS

List of figures	xviii
List of tables	xxiv
List of publications	2
1 Introduction	5
1.1 Active Galactic Nuclei	6
1.1.1 The unified scheme	8
1.1.2 The main historical classes of AGN	11
1.2 Type-I Quasars	12
1.2.1 Spectral energy distribution	13
1.2.2 Accretion rate	15
1.2.3 Radio emission and the RL/RQ dichotomy	16
1.2.4 The feedback mechanism and the outflows	17
1.2.5 Metallicity	20
1.3 The Eigenvector 1 and the quasar Main Sequence	21
1.3.1 The 4D Eigenvector 1	22
1.3.2 The quasar Main Sequence	23
1.4 Motivation of the thesis	28
1.4.1 Observational data and analysis methods	30
1.4.2 Outline	32
I Trends of high-redshift quasars along the Main Sequence	35
2 High-redshift quasars along the main sequence	36
2.1 Introduction	38
2.2 The sample	41
2.3 Observations and data	43
2.4 Spectral analysis	46
2.5 Results	50
2.6 Discussion	66
2.7 Conclusions	76

3	Isolating an outflow component in single-epoch spectra of quasars	78
3.1	Introduction	79
3.2	Data	81
3.3	Analysis	82
3.4	Results	83
3.5	Discussion	86
3.6	Summary and conclusion	89
II	The roles of AGN feedback and radio emission	92
4	Optical and UV properties of a RL and a RQ Pop. A at high z	93
4.1	Introduction	95
4.2	Sample & Observational Data	96
4.3	Spectral Analysis	98
4.4	Results	100
4.5	Discussion: Is there any relation between $H\beta+[O III]\lambda 5007$ and $CIV\lambda 1549$?	103
4.6	Conclusions	104
5	Exploring the links between quasar winds and radio emission along the MS at high z	105
5.1	Introduction	107
5.2	Samples	108
5.3	Observations and data analysis	112
5.4	Results	119
5.5	Discussion	128
5.6	Conclusions	137
III	Black hole mass estimation for quasars at high and low redshift	142
6	The intermediate-ionisation lines as virial broadening estimators for Pop. A quasars	143
6.1	Introduction	144
6.2	Sample	147
6.3	Data analysis	149
6.4	Results	154
6.5	Discussion	167
6.6	Summary and conclusion	173
IV	Metallicity along the quasar Main Sequence	176
7	Metal content in RL and RQ quasars in the main sequence context	177

7.1	Introduction	178
7.2	Composite spectra for spectral type B1 quasars	179
7.3	Analysis	180
7.4	Results	182
7.5	Discussion: metal enrichment along the quasar Main Sequence	188
7.6	Conclusions	189
8	From sub-solar to super-solar chemical abundances along the quasar main sequence	190
8.1	Introduction: A Main Sequence and the Eigenvector 1 for Quasars	191
8.2	Observations	193
8.3	Methodology and Data analysis	194
8.4	Case studies	199
8.5	Results	202
8.6	Discussion	207
8.7	Conclusion	208
	General conclusions of the thesis	210
	Future perspectives	217
	References	219
	Appendix A The ISAAC sample – Multicomponent fits and individual notes	237
A.1	ISAAC1	238
A.2	ISAAC2	256
	Appendix B Additional material from Chapter 5	264
B.1	Radio properties of the samples	265
B.2	Details on the estimations of the outflow parameters	269
	Appendix C Additional material from Chapter 6	275
C.1	Estimation of uncertainties	276
C.2	H β and 1900 blend paired comparison	279
C.3	Notes on individual objects	286

LIST OF FIGURES

1.1	Typical optical spectra of Type I and Type II AGN.	7
1.2	Scheme of the unified model of AGN.	8
1.3	Composite quasar spectrum from ~ 2000 SDSS quasars.	12
1.4	Density evolution of luminous quasars.	13
1.5	An illustrative scheme of an AGN broadband continuum spectral energy distribution.	14
1.6	Example of the line decomposition including the outflowing component.	19
1.7	Relations between the correlates of the 4DE1 for a low-redshift sample. Solid symbols represent radio-quiet sources. Yellow squares are Population A quasars. Plot from (Sulentic et al. 2007b).	22
1.8	The quasar MS at low redshift, represented by the sample of Zamfir et al. (2010).	24
1.9	Potential evolutionary interpretation of the quasar Main Sequence. Plot from Fraix-Burnet et al. (2017b).	25
1.10	Simplified scheme of the distinct structures that characterize Pop. A and Pop. B quasars.	27
1.11	Schematic representation of the quasar MS displacement in high redshift samples.	28
1.12	VLT telescopes, the ISAAC spectrograph, and its optical layout of the instrument.	32
2.1	Location of the complete sample in the Hubble diagram.	42
2.2	Sketch of the approach followed for broad profile fittings.	47
2.3	Location of our sources through the optical plane of the 4DE1.	51
2.4	Comparison between the different properties of the $H\beta$ emission line profile.	55
2.5	$W([\text{O III}]\lambda 5007)$ versus $c(9/10)$	58
2.6	FWHM of the full profile of $[\text{O III}]\lambda 5007$ versus centroid at 1/2 flux intensity ($c(1/2)$) for the $[\text{O III}]\lambda 5007$ emission line.	58
2.7	Comparison between the different properties of the C IV emission line profile.	64
2.8	Centroid velocity at 1/2 flux intensity, $c(1/2)$, for the C IV emission line versus the FWHM of the full profile of C IV.	64
2.9	Relation between $H\beta$ and $[\text{O III}]\lambda 5007$ emission lines.	67
2.10	Centroid velocity at 1/2 flux intensity ($c(1/2)$) of C IV $\lambda 1549$ vs $c(1/2)$ of $[\text{O III}]\lambda 5007$	67
2.11	$\text{FWHM}(H\beta_{\text{BC}})$ vs $\text{FWHM}(C\text{ IV}_{\text{full}})$ and $\text{FWHM}(H\beta_{\text{full}})$ vs $\text{FWHM}(C\text{ IV}_{\text{full}})$	68
2.12	$C\text{ IV}_{\text{full}}$ relation with Al III.	69
2.13	$\text{FWHM}(\text{Al III})$ vs $\text{FWHM}(H\beta_{\text{BC}})$ and $\text{FWHM}(\text{Al III})$ vs $\text{FWHM}(H\beta_{\text{full}})$	70
2.14	$M_{\text{BH}}(H\beta)$ compared to $M_{\text{BH}}(C\text{ IV})$ and to $M_{\text{BH}}(\text{Al III})$	71
2.15	$[\text{O III}]\lambda 5007$ dependence on physical parameters.	73
2.16	Dependence of C IV on different parameters.	74
2.17	Distribution of the different spectral types in a luminosity and Eddington ratio context.	75

3.1	Analysis of the $H\beta + [O III]\lambda\lambda 4959,5007$ region for the S02, M13, and M09 B1 composite spectra.	83
3.2	Analysis of the $H\beta + [O III]\lambda\lambda 4959,5007$ region for two high-luminosity, high- z quasars belonging to the B1 spectral type, HE0001-234 and [HB89] 0029+073.	85
3.3	Analysis of the $H\beta + [O III]\lambda\lambda 4959,5007$ region for the RQ composite spectrum of M13, and for the CD and FR-II composite spectra.	85
4.1	Optical spectra obtained with VLT/ISAAC for Q1410+036 and PKS2000-330.	96
4.2	Location of Q1410+036 and PKS2000-330 in the Hubble diagram.	96
4.3	Spectra of the UV region of Q1410+096 and PKS2000-330.	98
4.4	Fittings and residuals for the optical and UV region of Q1410+096 and PKS2000-330	99
4.5	Location of Q1410+096 and PKS2000-330 on the optical plane of the 4DE1.	102
5.1	Distributions of z and M_i for FOS, HEMS, ISAACI from Paper I, and the new ISAAC2 data.	110
5.2	Example of an ISAAC spectrum and of the decomposition analysis of the emission lines.	115
5.3	Location on the MS of the ten new sources from this work together with those from Paper I and the HEMS sample.	122
5.4	Velocity centroid $c(1/4)$ versus L/L_{Edd} for $[O III]\lambda 5007$ and $C IV\lambda 1549$	123
5.5	Comparison between the relative intensities of the blueshifted component for both $[O III]\lambda 5007$ and $C IV\lambda 1549$	124
5.6	Centroid velocities at one-quarter intensity ($c(1/4)$) cumulative distributions of the samples separated by radio-loudness and redshift range for $[O III]\lambda 5007$ and $C IV\lambda 1549$	124
5.7	Relation between radio-loudness R_K and R_{FeII} for low and high- z ranges.	126
5.8	Relation between radio-loudness and velocity centroid at one-quarter intensity of the $[O III]\lambda 5007$ emission line for low- and high- z ranges.	127
5.9	Relation between radio-loudness and the velocity centroid at one-quarter intensity of the $C IV\lambda 1549$ emission line for low- and high- z ranges.	128
5.10	Centroid velocity at at half flux intensity ($c(1/2)$) of $C IV\lambda 1549$ vs. $c(1/2)$ of $[O III]\lambda 5007$ for the full and outflow profiles of the high- z sample.	129
5.11	Relation between the outflow radio in kiloparsecs and the luminosity of the $[O III]\lambda 5007$ emission line for the five plotted samples.	130
5.12	Kinetic power \dot{E}_{kin} and thrust vs. bolometric luminosity for the $[O III]\lambda 5007$ outflow.	130
5.13	Kinetic power \dot{E}_{kin} and thrust vs. bolometric luminosity for the $C IV\lambda 1549$ emission line.	134
5.14	Comparison between the kinetic power \dot{E}_{kin} and thrust of $[O III]\lambda 5007$ and $C IV\lambda 1549$ outflows, for high- and low- z sources.	136
6.1	Distribution of redshift and of luminosity at 1700 \AA for the different subsamples considered in Marziani et al. (2022c).	148

6.2	FWHM(Al III) vs. FWHM(H β) (full profiles) and ratio r of FWHM Al III over FWHM H β for the joint sample, according to the sub-sample.	156
6.3	FWHM(Al III) vs. FWHM(H β) (full profiles) and FWHM ratio between Al III and H β for the joint sample, according to the spectral type.	157
6.4	FWHM(Al III) vs. FWHM(H β_{BC}) and FWHM ratio between Al III and H β_{BC} , $1/\xi_{AlIII}$, for the joint sample, according to the spectral type.	157
6.5	Behaviour of shift s^* of Al III and of the ratio FWHM Al III over FWHM H β with respect to rest frame as a function of the spectral type and parameter δ (Al III) as a function of spectral type.	160
6.6	FWHM(Al III) vs. FWHM(H β) and FWHM ratio of Al III and H β for the joint sample, according to luminosity at 1700Å.	161
6.7	H β and Al III profile parameter comparison as a function of luminosity.	161
6.8	Parameter δ (Al III) as a function of luminosity.	162
6.9	FWHM(CIII]) vs. FWHM(H β) for the joint sample and FWHM ratio of CIII] and H β , according to spectral types, according to spectral types and CIII] intensity.	163
6.10	H β and CIII] profile parameter comparison as a function of luminosity.	164
6.11	Decimal logarithm of black hole mass in units of solar masses computed from the relation of Vestergaard & Peterson (2006) based on FWHM H β vs. the one computed from the Al III FWHM following Eq. 6.5.	165
6.12	Decimal logarithm of black hole mass in units of solar masses computed from the relation of Vestergaard & Peterson (2006) based on the H β spectral range vs. the one computed from CIII] data following Eq. 6.7.	166
6.13	Decimal logarithm of black hole mass in units of solar masses computed from the scaling law based on FWHM CIII] (Eq. 6.7) vs. the one computed from the Al III FWHM following Eq. 6.5.	167
6.14	Decimal logarithm of black hole mass in units of solar masses computed from the CIV λ 1549-based scaling law of M19 vs. the ones computed from the relation of Vestergaard & Peterson (2006) based on FWHM H β and from the Al III FWHM following Eq. 6.5.	168
6.15	Shift s of Al III vs shift of CIV λ 1549 with respect to rest frame.	169
6.16	Analysis of the 1900 Å blend for the extreme Population A sources with excess emission on the blue side of Al III.	171
6.17	The distribution of the parameter \mathcal{A} , as defined in Sect. 6.5.3, for three groups of quasars: spectral types A1+A2, A3+A4, and the 6 quasars with a blue shifted excess fit to the 1900 Å blend (Fig. 6.16).	172
6.18	The distribution of xA sources in the plane defined by the intensity ratios CIII]/SiIII] vs Al III/SiIII].	172
7.1	Sketch of the optical plane of the MS, FWHM H β vs. R_{FeII}	180
7.2	The RQ and RL composite spectra covering the optical and the UV domain.	182

7.3	Analysis of prominent blends helpful for metallicity diagnostics.	183
7.4	Projections of the 3D parameter space n_H , U , Z	184
7.5	The spectrum of PKS 0226-038 in the optical and the UV domain.	187
8.1	Interpretation of the line profiles of low- and high-ionisation lines along the MS for isolating major spectroscopically resolved components.	196
8.2	Fits of the emission line spectrum of Fairall 9, the prototypical Population B source.	202
8.3	Projections of the 3D parameter space (U , n_H , Z) onto the (U , Z) (left) and (n_H , Z) planes, for the prototypical Pop. B source Fairall 9.	204
8.4	Projections of the 3D parameter space (U , n_H , Z) onto the (U , Z) and (n_H , Z) planes, for the Pop. A sources - Mark 335, Mark 478, and PHL 1092.	205
8.5	Sketch of the quasar main sequence at low redshift.	206
8.6	Sketch depicting the evolutionary interpretation of the quasar main sequence.	208
A.1.1	HE 0001-2340.	238
A.1.2	[HB89] 0029+073.	239
A.1.3	CTQ 0408.	239
A.1.4	SDSSJ005700.18+143737.7.	240
A.1.5	H 0055-2659.	241
A.1.6	SDSSJ1144358.52+052444.9.	241
A.1.7	SDSSJ115954.33+201921.1.	242
A.1.8	SDSSJ120147.90+120630.2.	243
A.1.9	SDSSJ132012.33+142037.1.	244
A.1.10	SDSSJ135831.78+050522.8.	245
A.1.11	Q 1410+096.	246
A.1.12	SDSSJ141546.24+112943.4.	247
A.1.13	B1422+231.	248
A.1.14	SDSSJ153830.55+085517.0.	249
A.1.15	SDSSJ161458.33+144836.9	250
A.1.16	PKS 1937-101.	250
A.1.17	PKS 2000-330.	251
A.1.18	SDSSJ210524.49+000407.3.	252
A.1.19	SDSSJ210831.56-063022.5.	253
A.1.20	SDSSJ212329.46-005052.9.	254
A.1.21	PKS 2126-15.	254
A.1.22	SDSSJ235808.54+012507.2.	255
A.2.1	PKS0226-038	256
A.2.2	PKS0237-23	257
A.2.3	BZQJ0544-2241	258
A.2.4	PKS0858-279	259

A.2.5	CTSJ01.03	260
A.2.6	WB J0948+0855	261
A.2.7	CTSJ03.14	262
A.2.8	PKS1448-232	262
A.2.9	[HB89] 1559+088	263
A.2.10	FBQS J2149-0811	263
B.1	Relation between W C IV λ 1549 and intensity ratio C IV λ 1549/H β with the ionisation parameter U for three density values $\log n_{\text{H}} = 9, 9.5, 10 \text{ cm}^{-3}$, column density $N_{\text{c}} = 10^{22} \text{ cm}^{-2}$, and 5 times solar metallicity.	272
B.2	Behaviour of ionisation parameter, electron temperature, C IV λ 1549 luminosity, and ionic fraction as a function of radius for density value $\log n_{\text{H}} = 9.5 \text{ cm}^{-3}$, and for the two adopted SEDs for the low- and high- z samples	273
C.1	Distribution of the log of parameter Q parameter for Al III and H β and distribution of $\log Q$ differences between H β and Al III for the joint sample.	278
C.2	Relation between the fractional uncertainty $\delta\text{FWHM}/\text{FWHM}$ and the logarithm of parameter Q	278
C.3	Analysis of the H β spectral range and of the 1900 Å blend for the sources of the <i>FOS*</i> subsample.	280
C.3	Analysis of H β and of the 1900 Å blend for the <i>FOS*</i> subsample (cont.).	281
C.3	Analysis of H β and of the 1900 Å blend for the <i>FOS*</i> subsample (cont.).	282
C.4	Analysis of the 1900 Å blend, for 10 Pop. A sources of the HE sub-sample.	283
C.5	Analysis of H β and of the 1900 Å blend for Pop. A sources of the ISAAC sample.	284
C.6	Analysis of H β and of the 1900 Å blend for Pop. A sources of the WISSH sample.	285

LIST OF TABLES

2.1	Source identification.	41
2.2	Log of optical observations with VLT/ISAAC.	44
2.3	UV spectra information.	45
2.4	Spectrophotometric measurements on $H\beta$	52
2.5	Results from <code>SPECFIT</code> analysis on $H\beta$	53
2.6	Measurements on the $[O\ III]\lambda 5007$ full line profile.	56
2.7	Linear relations ($y = a + b * x$) between different emission line properties.	59
2.8	Spectrophotometric measurements on the UV region.	59
2.9	Measurements on the 1900\AA blend.	60
2.10	Measurements on the $C\ IV\lambda 1549+He\ II\lambda 1640$ full line profiles and <code>SPECFIT</code> analysis.	62
2.11	Measurements on the full profiles of $Si\ IV\lambda 1397+O\ IV]\lambda 1402$	65
2.12	Linear relations between the different M_{BH} estimates using orthogonal and bisector methods.	72
2.13	Weighted averaged masses, luminosity at 5100\AA , and Eddington ratio (L/L_{Edd}), in logarithmic scale.	72
3.1	Physical parameters	81
3.2	Broad-line properties measurements	84
3.3	$H\beta$ profile properties measurements	84
3.4	Narrow line measurements	87
3.5	$[O\ III]\lambda 5007$ profile measurements	87
4.1	Main properties of PKS2000-330 and Q1410+096.	95
4.2	Flux intensities of the $H\beta$ and $C\ IV\lambda 1549$ emission lines.	100
4.3	Measurements for the optical range.	102
4.4	Measurements for the $C\ IV\lambda 1549$	102
5.1	Source identification of the ISAAC2 sample.	109
5.2	Log of optical observations with VLT/ISAAC.	110
5.3	UV spectra information.	113
5.4	Measurements on the $H\beta$ full broad line profile and derived properties of the $H\beta$ region.	114
5.5	Results from <code>specfit</code> analysis on the broad and narrow profiles of $H\beta$	114
5.6	Measurements on the $[O\ III]\lambda 5007$ line profile.	116
5.7	Measurements on the $C\ IV\lambda 1549$ full broad profile.	117
5.8	Results from our <code>specfit</code> analysis of $C\ IV\lambda 1549$ and $He\ II\lambda 1640$	117
5.9	Measurements on the $Si\ IV\lambda 1397+O\ IV]\lambda 1402$ broad lines.	117

5.10	Results from our <code>specfit</code> analysis of the 1900Å blend.	118
5.11	Radio properties of the full ISAAC sample.	118
5.12	Summary of assumed scaling relations and parameter values for wind dynamics. . .	132
5.14	Least-squares linear relations ($y = a + b * x$) between different outflow properties and the bolometric luminosity.	133
5.15	Average values and standard deviations of the [O III]λ5007 and C IVλ1549 outflow parameters for the different samples.	134
5.13	Properties of the [O III] and C IV outflows.	139
6.1	Sample properties	150
6.2	Observed spectrophotometric quantities and main sequence classification	158
7.1	Normalised emission line intensities	185
7.2	Derived values of U , Z , n_{H} and 1σ ranges ^a	187
7.3	Diagnostic line ratios measured on the PKS 0226-038 spectrum ^a	188
8.1	Diagnostic intensity ratios.	198
8.2	Object properties	201
8.3	Metallicity estimates along the quasar MS	205
B.1	Identification and radio properties of HEMS and FOS samples.	265
C.1	Relation between fractional uncertainties and Q	277

LIST OF PUBLICATIONS

Published and accepted articles included in this thesis

- *Optical and UV properties of a radio-loud and a radio-quiet Population A quasar at high redshift.*

Authors: **A. Deconto-Machado**, A. del Olmo, P. Marziani, G. Stirpe, and J. Perea.

Published in *Astronomische Nachrichten*, Volume 343, 1-2, e210084, 9 pages, January 2022.

DOI: 10.1002/asna.20210084.

- *High-redshift quasars along the Main Sequence.*

Authors: **A. Deconto-Machado**, A. del Olmo, P. Marziani, G. Stirpe, and J. Perea.

Published in *Astronomy and Astrophysics*. Volume 669, A83, 42 pages, January 2023.

DOI: 10.1051/0004-6361/202243801.

- *Exploring the links between quasar winds and radio emission along the Main Sequence at high redshift.*

Authors: **A. Deconto-Machado**, A. del Olmo, P. Marziani.

Accepted for publication at *Astronomy and Astrophysics*.

DOI: 10.1051/0004-6361/202449976.

- *Isolating an outflow component in single-epoch spectra of quasars.*

Authors: P. Marziani, **A. Deconto-Machado**, A. del Olmo.

Published in *Galaxies*, Volume 10, 54, 18 pages, March 2022.

DOI: 10.3390/galaxies10020054.

- *Metal content in relativistically jetted and radio-quiet quasars in the main sequence context.*

Authors: P. Marziani, S. Panda, **A. Deconto-Machado**, and A. del Olmo

Published in *Galaxies*, Volume 11, 52, 13 pages, March 2023.

DOI: 10.3390/galaxies11020052

- *From sub-solar to super-solar chemical abundances along the quasar main sequence.*

Authors: P. Marziani, A. Floris, **A. Deconto-Machado**, S. Panda, M. Sniegowska, K. Garnica, D. Dultzin, M. D'Onofrio, A. del Olmo, E. Bon, N. Bon.

Published in *Physics*, Volume 6, 1, 216-236, February 2024.

DOI: 10.3390/physics6010016

- *The intermediate-ionization lines as virial broadening estimators for Population A quasars.*

Authors: P. Marziani, A. del Olmo, C. Alenka Negrete, D. Dultzin, E. Piconcelli, G. Vietri, M. L. Martínez-Aldama, Mauro D’Onofrio, E. Bon, N. Bon, **A. Deconto-Machado**, G. M. Stirpe, T. M. Buendia Rios.

Published in the *Astrophysical Journal Supplement Series*, Volume 261, 2, 29 pages, July 2022.

DOI: 10.3847/1538-4365/ac6fd6.

Other published articles (not included in this volume)

In addition to the work presented in this thesis, I have also worked on the following publications during the period of my PhD:

- Related with the theme of the thesis

- *The main sequence view of quasars accreting at high rates: influence of star formation.*

Authors: P. Marziani, M. Śniegowska, S. Panda, B. Czerny, C. Alenka Negrete, D. Dultzin, K. Garnica, M. L. Martínez-Aldama, A. del Olmo, M. D’Onofrio, **A. Deconto-Machado**, V. Ganci, and the Extreme team.

Published in the *Research Notes of the American Astronomical Society*, Volume 5, p. 2, 25, 4 pages, February 2021.

DOI: 10.3847/2515-5172/abe46a.

- *The main sequence of quasars: the taming of the extremes.*

Authors: P. Marziani, E. Bon, N. Bon, M. D’Onofrio, B. Punsly, M. Śniegowska, B. Czerny, S. Panda, M. L. Martínez-Aldama, A. del Olmo, **A. Deconto-Machado**, C. Alenka Negrete, D. Dultzin, T. Buendia, K. Garnica.

Published in *Astronomische Nachrichten*, Volume 343, 1-2, e210082, 9 pages, January 2022.

DOI: 10.1002/asna.20210082.

- *The quasar 3C 47: extreme Population B jetted source with double-peaked profile.*

Authors: S. Terefe Mengistue, P. Marziani, A. del Olmo, M. Pović, J. Perea, **A. Deconto-Machado**.

Published in *Astronomy and Astrophysics*, Volume 685, A116, May 2024.

DOI: 10.1051/0004-6361/202348800.

- Indirectly related to the theme of the thesis

- *Ionised gas kinematics in MaNGA AGN. Extents of the narrow line and kinematically disturbed regions.*

Authors: **A. Deconto-Machado**, R. A. Riffel, G. S. Ilha, S. B. Rembold, T. Storchi-Bergmann, R. Riffel, J. S. Schimoia, D. P. Schneider, D. Bizyaev, S. Fend, D. Wylezalek, L. N. da Costa, J. C. do Nascimento, M. A. G. Maia.

Published in the *Astronomy and Astrophysics*, Volume 659, A131, March 2022.

DOI: 10.1051/0004-6361/202140613.

- *Gas phase metallicity determinations in nearby AGNs with SDSS-IV MaNGA: evidence of metal poor accretion.*

Authors: J. C. Nascimento, O. L. Dors, T. Storchi-Bergmann, N. D. Mallman, R. Riffel, G. S. Ilha, R. A. Riffel, S. B. Rembold, **A. Deconto-Machado**, L. N. Costa, M. Armah.

Published in the *Monthly Notices of the Astronomical Society*, Volume 535, 1, 807-821, June 2022.

DOI: 10.1093/mnras/stac771.

INTRODUCTION

1

1.1 Active Galactic Nuclei

Quasars are renowned as one of the most energetic objects in the Universe, outshining entire galaxies. Their history began in 1963, when radio astronomers from Cambridge detected for the first time remarkably bright radio sources that appear to present an optical counterpart (e.g., [Matthews & Sandage 1963](#); [Schmidt 1963](#); [Greenstein 1963](#)). While conducting observations of radio sources with the 200-inch telescope at Palomar Observatory, [Schmidt \(1963\)](#) stumbled upon an unusual object: 3C 273. Initially catalogued as a radio source, the optical spectrum of this source revealed a very high redshift for the epoch ($z \sim 0.16$), indicating that 3C 273 is actually located at a very significant distance from the Earth ([Schmidt 1963](#)). This measurement revealed that the object was not a star as initially expected but instead a distant and incredibly bright point-like source of energy. This discovery gave birth to the term “quasi-stellar” objects (QSOs), or quasars.

Further observations and studies along the years revealed that quasars are a class of active galactic nuclei (AGN). It is known nowadays that these objects are located in the central region of galaxies and present a spectral emission that can not be attributed only to the stars. It is expected that this emission is due to the presence of a supermassive black hole (SMBH) located in the galactic core, that is actively accreting the surrounding matter. This accretion process converts gravitational potential energy into kinetic energy and electromagnetic radiation (see Section 1.1.1). With an estimated duration of 10^7 a 10^9 years ([Martini & Weinberg 2001](#); [Marconi et al. 2004](#)), the nuclear activity is currently considered an important stage in the evolutionary path of galaxies. Throughout this phase, the AGN are a powerful source of energy and may produce an important impact in the formation and evolution of galaxies.

The first studies of AGN trace back to the beginning of the 20th century, when astronomers observed peculiar objects emitting intense radiation at the centers of “spiral nebulae” (that later on were recognised as galaxies). At that time, there was a debate about whether these objects were relatively nearby gaseous objects, like the Orion nebulae for instance, or distant unresolved stars. Trying to solve this question, [Fath \(1909\)](#) conducted observations at the Lick Observatory and captured optical spectra for some of these sources. Most of them showed a typical stellar spectra with absorption lines, suggesting that they consist of unresolved stars. However, NGC 1068 (also known

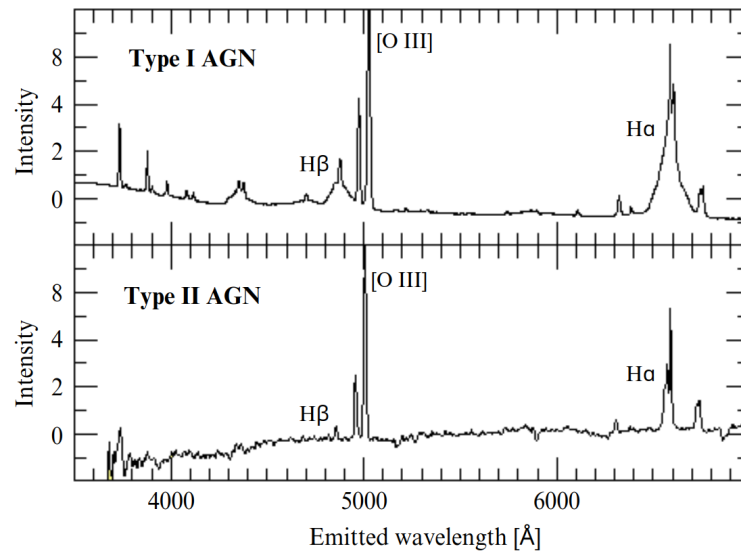


Fig. 1.1: Typical optical spectra of Type I (*top*) and Type II (*bottom*) AGN. Image edited from Bill Keel ([Bill Keel's Collection](#)).

as M 77) exhibited a composite spectrum that resembles the one of a gaseous nebulae, presenting unexpected strong emission lines. This was the first AGN to be discovered.

Through the following years, many astronomers reported the presence of nuclear emission lines in the spectral of spiral nebulae ([Slipher 1917](#); [Hubble 1926](#)) as the one found in NGC 1068. The pioneering work of [Seyfert \(1943\)](#) was one of the first systematic studies of such objects, taking into account six spirals: NGC 1068, NGC 1275, NGC 3516, NGC 4051, NGC 4151, and NGC 7469. The author found that the brightest sources of the sample, namely NGC 1068 and NGC 4151, were the ones that presented the strongest emission lines. These galaxies become to be known as *Seyfert galaxies*. Another important outcome of this work, which significantly contributed to the advance of our understanding of AGN, is the identification of two distinct spectral patterns: in NGC 1068, both forbidden and permitted lines exhibited similar profiles with widths around $\sim 3000 \text{ km s}^{-1}$; conversely, NGC 4151 displayed narrower forbidden lines and corresponding narrow cores of permitted lines, with only the Balmer lines presenting remarkably broad widths ($\sim 7500 \text{ km s}^{-1}$), absent in the forbidden lines. These results lead to the definition of two classes of spectra with emission lines ([Khachikyan & Weedman 1971](#), see Fig. 1.1):

- ★ *Type I*: present permitted emission lines (e.g. lines from the Balmer series, $H\alpha$ and $H\beta$) that are significantly broader than the forbidden emission lines;
- ★ *Type II*: the permitted and forbidden emission lines share similar widths.

Over the years, astronomers have made significant progress in understanding the nature and behaviour of AGN. They have discovered various types of AGN, including not only Seyfert galaxies but also LINERs, blazars, radio galaxies, and the quasars, each of these classes exhibiting unique observational features. Especially after the discovery of the quasars in the 1960s and new observations across different wavelengths, it became increasingly clear that there were underlying connections

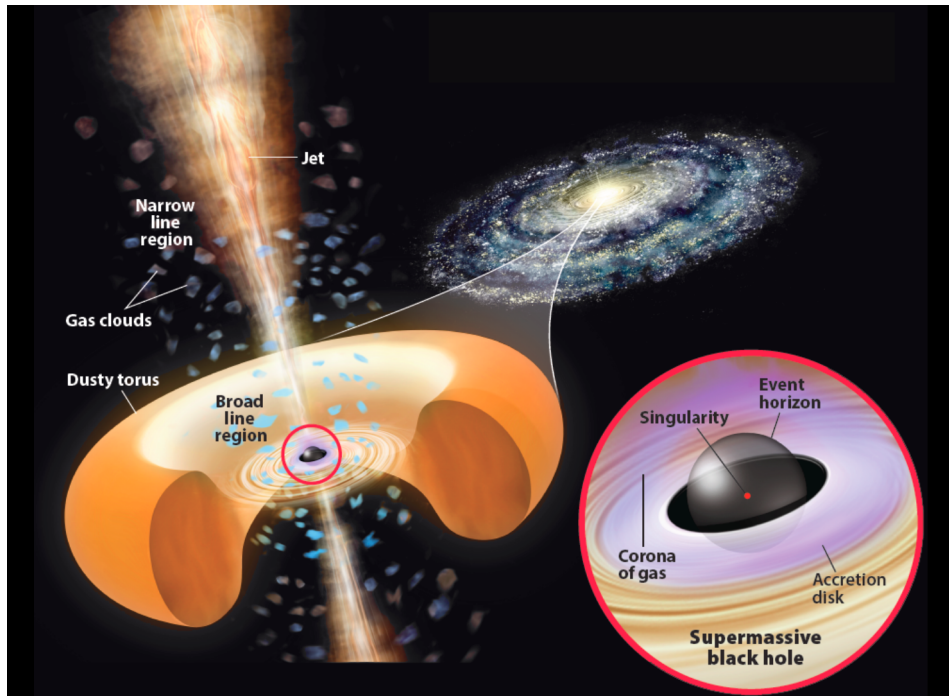


Fig. 1.2: Scheme of the unified model of AGN, as initially proposed by [Urry & Padovani \(1995\)](#). Credit: Roen Kelly, [Astronomy Magazine](#).

between the diverse classes of AGN. This highlighted the need to establish a standard model that could describe the physical phenomena behind such peculiar spectra.

1.1.1 The unified scheme

Many attempts to explain the diversity of AGN spectra were developed by the scientific community throughout the years. The most accepted framework that combines the majority of the similarities and differences observed in the spectra of AGN within the same scenario is the so-called “Unified Model of AGN” ([Antonucci 1993](#); [Urry & Padovani 1995](#)). A schematic representation of the Unified Model is presented in Fig. 1.2. This model delineates the structure of an AGN encompassing the following components:

- **Supermassive black hole (SMBH):** with masses typically larger than 10^5 - $10^6 M_{\odot}$ ([Kormendy & Richstone 1995](#)) and located at the galactic core, the SMBH accretes the nearby matter. Recent studies as [Choi et al. \(2024\)](#) suggest that $\sim 40\%$ of the total SMBH accretion is attributed to recycled gas, which is produced from stellar losses with a secondary substantial contribution coming from an external origin (e.g., through mergers), accounting for about 32% on average.
- **Accretion disk (AD):** consists of a swirling disk of gas surrounding the SMBH. This material undergoes gravitational attraction towards the central SMBH, shedding gravitational energy in the process which is then converted into electromagnetic radiation. This radiation can span ultraviolet, optical, and soft to hard X-rays spectral ranges. The AD can exhibit different sizes,

thicknesses, and column densities, as discussed in [Netzer \(2013\)](#). Typically, they are considered optically thick and geometrically thin disks, although these assumptions may vary based on the physical properties of the AGN, particularly the accretion rate, the black hole mass, and the spin. This type of disks is known to present cooling-dominated flows, characterised by highly efficient cooling mechanisms. This efficiency comes from a balance between the loss of angular momentum and the increase in kinetic energy due to the local viscosity. AD serves as an efficient mechanism for dissipating the angular momentum of the accreting matter and is considered an essential element in the formation of the relativistic jets observed in a fraction of the AGN.

- **Relativistic jets:** the accretion of matter by the central SMBH may produce energy from the very intense magnetic fields generated by the plasma forming the accretion disk. These fields have a high rotational velocity, which can collimate the flow of particles from the nucleus and, thus, give rise to jets of synchrotron radiation. The intensity of the jets in the radio frequencies may allow to distinct radio-quiet objects (weak radio emission) from radio-loud ones (high radio emission with relativistic jets), as further discussed in Sect. 1.2.3.
- **Broad Line Region (BLR):** located within the inner part of the torus (pc or sub-pc from the SMBH), this region is responsible to produce the broad emission lines observed in the spectra. This broadening effect arises from the Doppler shift induced by the high-velocity (with typical values going from $\sim 1000 - 20000 \text{ km s}^{-1}$, [Netzer 2015](#)) rotation of gas clouds surrounding the SMBH. Apart from the high velocity, it is estimated that these gas clouds also present high densities ($\gtrsim 10^8 \text{ cm}^{-3}$, [Osterbrock & Ferland 2006](#)). Forbidden emission lines, as wide as the permitted ones, are not observed in the BLR, indicating that only the permitted emission lines are produced in this region[†]. Indeed, forbidden transitions are only observable in rarefied conditions with low atomic density. Due to the ionisation of the gas, some variations in the continuous spectrum generated by the accretion disk occur quite frequently. These changes are likely to influence the BLR. By monitoring the spectrum and the time interval that the lines coming from the BLR take to show some variation in response, it is possible to obtain information about the structure of this region. This is one of the main forms of analysing the BLR, as this region lacks spatial resolution and, therefore, the use of techniques that involve imaging are, many times, infeasible. The BLR likely comprises two distinct emitting regions (especially in radio-quiet AGNs, [Collin-Souffrin & Lasota 1988](#); [Marziani et al. 1996](#)):

1) *Low-ionisation line (LIL) emitting region*, in which the Balmer lines and Fe II_{opt} are expected to be produced;

2) *High-ionisation line (HIL) emitting region*, associated with the production of lines like $\text{He II}\lambda 4686$, $\text{He II}\lambda 1640$, and $\text{C IV}\lambda 1549$.

[†]While it is true that forbidden lines typically exhibit narrower FWHM compared to permitted lines, exceptions exist where forbidden lines may have broader or similar FWHM. This can occur, for example, when the forbidden line profile is predominantly influenced by outflows (see e.g, Chapters 3, 2, and 5).

- **Torus:** surrounding the accretion disk there is a dusty torus (Urry & Padovani 1995). This is a region with a size ~ 0.1 -10 parsecs (Netzer 2015), characterised by low densities ($\sim 10^{3-6} \text{ cm}^{-3}$) and exceedingly high column densities ($\sim 10^{25} \text{ cm}^{-2}$). Different models have been proposed to represent the torus. First ones outline it as having a uniform dust distribution (e.g. Nenkova et al. 2008, and references therein). In line with the observations, it is nowadays expected that it has a “cumply” nature (see Ramos Almeida & Ricci 2017, and references therein). Moreover, a study by Ramos Almeida et al. (2011) suggests that the intrinsic properties of the torus may significantly influence the Type-I/Type-II classification of AGN. According to the authors, tori in Type-II AGN tend to be broader and clumpier, with lower optical depths compared to those in Type-I AGN. Additionally, observational evidence suggests that the dusty torus in very low luminosity AGN ($\lesssim 10^{42} \text{ erg s}^{-1}$) can even disappear in some cases (González-Martín et al. 2015).
- **Narrow Line Region (NLR):** The NLR comprehends a region much larger than the BLR, with sizes varying from tens of parsecs to kilo-parsecs. This fact allows the NLR to be spatially resolved in many of the observed sources, and the kinematics of this region extensively studied (e.g. Carniani et al. 2015; Fiore et al. 2017; Vietri et al. 2020, and references therein). The narrow emission lines observed in the spectra of AGNs typically have Full Width at Half Maximum (FWHM) values between 300 and 1000 $\text{km s}^{-1\dagger}$ (Netzer 2015). As forbidden emission lines only exhibit narrow components, it is inferred that they are likely produced in the NLR. This implies that the NLR has lower density compared to the BLR. Generally, densities of NLR range between 10^2 and 10^4 cm^{-3} , similar to the values found in planetary nebulae and in HII regions (Netzer 2013).

According to this unified model, all AGN classes contain the structural components described above, however observed at different line-of-sight and/or inclination. When viewed face-on, all the AGN components are observable, resulting in a type-I AGN (explained in Section 1.1). Conversely, when observed edge-on, the dusty torus obscures the UV and optical light emitted by the accretion disk and the broad line region. This obscuration may also affect the visibility of X-rays to some extent and may lead to the classification of a type-II object.

There are, however, challenges to the unified model of AGN. One of them arises from the observation of the so-called *true* type-II AGN. These are narrow-line AGN that apparently do not have a BLR as no broad lines are detected in either polarised light or near-IR spectroscopy (Tran 2001; Panessa & Bassani 2002; Tran 2003; Laor 2003). This observation could indicate that they are indeed genuine type-II AGNs without an obscured BLR. Alternatively, it could be due to a dense column of obscuring material toward the nucleus combined with the absence of a properly positioned unobscured scattering medium. X-ray spectroscopy has revealed the presence of an obscuring material along the line-of-sight to the nucleus of type-II AGNs. However, it is unclear whether this material also obscures the broad-line region (BLR), as some type-I AGNs exhibit strong X-ray absorption but

[†]There are some exceptions. Some high-ionization lines like [O III] λ 5007 that usually present narrow profiles can be broadened by the presence of outflowing components (see e.g., Chapters 2 and 5).

weaker absorption of the BLR (see e.g., [Laor 2003](#)). These results raise questions about the inner structure of these sources compared to other AGNs.

1.1.2 The main historical classes of AGN

Due to their wide range of characteristics and peculiarities, AGN can be classified into different types based on their observational properties and the underlying physical processes. These characteristics, which include the width and relative intensity of spectral emission lines, nuclear luminosity, radio emissions, among others, may vary across different AGN classes. The main historical classes of AGN are:

- **LINERs:** this class together with the Seyfert galaxies are currently known as Low-Luminosity AGN (LLAGN). The LINERs are known by their tendency to exhibit more intense low-ionisation emission lines compared to high-ionisation ones, in contrast to the emission profiles of more luminous AGN ([Heckman 1980](#)).
- **Seyfert galaxies:** its name has a historical origin, differing from quasars in their bolometric luminosity, so that they are called Seyfert galaxies when $M \gtrsim -22.2$ ($L_{\text{bol}} \lesssim 10^{44} \text{ erg s}^{-1}$). This type of AGN represent the most common type of AGN in the local Universe and are characterised by relatively low luminosity compared to other AGN classes. The optical spectra of these sources present intense high- and low-ionisation emission lines.
- **Radio galaxies:** they often exhibit extended radio jets and lobes, which result from the interaction of energetic particles with magnetic fields in the intergalactic medium. Radio galaxies can be further categorised into two main types: Fanaroff-Riley Type I (FR I) and Fanaroff-Riley Type II (FR II), based on the morphology of their radio emission.
- **Blazars:** characterised by their intense and variable emission across the electromagnetic spectrum, from radio waves to gamma rays. They are associated with relativistic jets pointing directly towards the observer, resulting in strong Doppler boosting of the emitted radiation. Blazars can be further classified into two main categories: the BL Lacertae objects (BL Lacs), which presents a spectrum with no emission lines, and the flat-spectrum radio quasars (FSRQs).
- **Quasars:** these sources are among the most luminous objects in the Universe, with luminosities exceeding that of the entire host galaxy. They appear as point-like sources of light and therefore their name comes from “quasi-stellar” objects. Quasars are thought to represent the high-luminosity end of the AGN population and are believed to be powered by intense accretion onto massive black holes in the centres of distant galaxies. They are the main topic of this thesis and will be further discussed in details on Sect. 1.2.

Advancements in technology have expanded our understanding of AGN, revealing a wide diversity of objects with unique characteristics that challenge the traditional AGN classification reported above. Among these discoveries are the *changing-look* AGN, characterised by significant variability in their

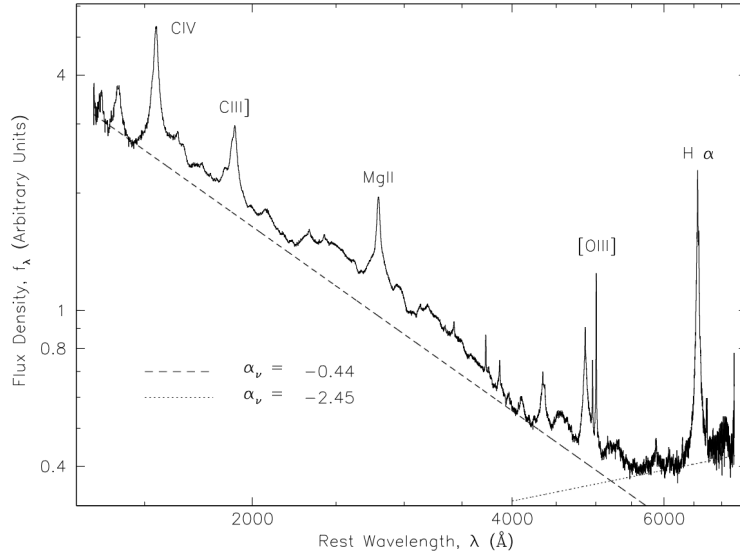


Fig. 1.3: Composite quasar spectrum from ~ 2000 SDSS quasars. Credits: [Vanden Berk et al. \(2001\)](#).

spectral properties over relatively short timescales, leading to changes in their classification (for instance going from type-I to type-II and vice-versa, [Matt et al. 2003](#); [Bianchi et al. 2005](#)). Another example are the *Red Geysers*, that have been identified as a class of AGN exhibiting powerful radio emission and large-scale outflows of ionised gas, often observed in red and quiescent galaxies (see e.g., [Roy et al. 2018](#); [Riffel et al. 2019](#)). In more recent observations facilitated by the James Webb Space Telescope (JWST), a potentially new class of faint “baby” AGN at high redshift (~ 5) has been detected, referred to as *little red dots* (LRD, [Matthee et al. 2024](#)).

1.2 Type-I Quasars

As said previously, the first quasar to be discovered was 3C 273 ([Schmidt 1963](#)), which remains one of the most well-studied objects in Astronomy. The analysis of 3C 273 provided invaluable insights into the nature of quasars and the behaviour of supermassive black holes. Nowadays, it is known that the quasars are the most luminous objects in the Universe, with bolometric luminosities $L_{\text{bol}} \gtrsim 10^{45}$ erg s^{-1} . Also many of these sources present strong high-energy emission in UV, X-ray, and γ -ray bands, as well as very significant relativistic jets.

Fig. 1.3 shows a composite optical/UV quasar spectrum from [Vanden Berk et al. \(2001\)](#), that includes more than 2000 spectra of quasars from the SDSS. This spectrum is a typical representative of the optical/UV emission from quasars, as it includes the more frequent emission lines in this wavelength range, including C IV $\lambda 1549$, the lines from the 1900Å blend, and the $\text{H}\beta + [\text{O III}] \lambda 5007$ region, but without taking into account the diversity observed in type-I quasars. The strong emission lines in the optical and UV regions are often very broad, high-excitation lines, which suggests rapid velocities in both NLR and BLR. The shape of the continuum in quasars is also unique in comparison with the other classes of AGN, as it is characterised by a power-law shape with a steep slope in the ultraviolet region.

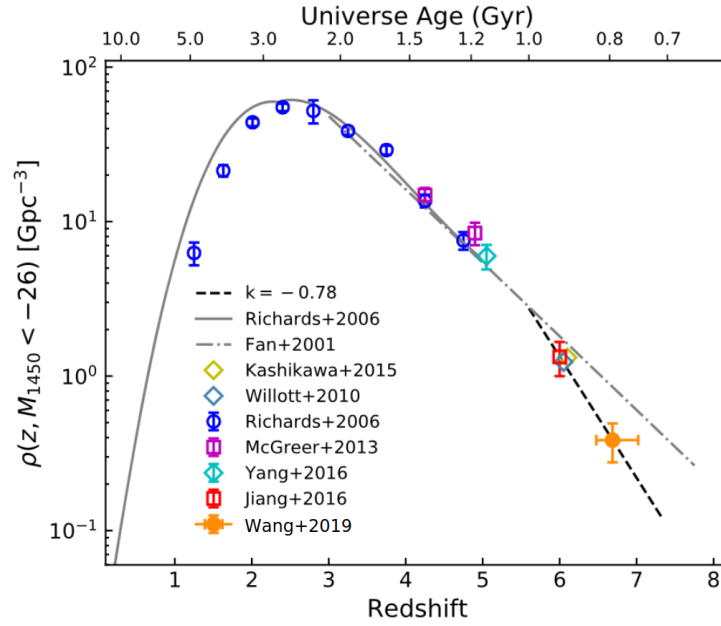


Fig. 1.4: Density evolution of luminous quasars. Credit: Wang et al. (2019), with small modifications.

Over time, an increasing number of sources with properties similar to 3C 273 have been identified and, as technology has advanced, quasars with progressively higher redshift were being discovered (see e.g., Sulentic et al. 2014b, for an overall historical view). It is nowadays known that quasars can be seen over cosmic epochs spanning 90% of the age of the Universe. Fig. 1.4 shows the estimated density of quasars in a large range of redshift, with the peak located around $z \sim 2-3$. These objects are observable from $z \sim 7$ to lower redshift (including $z < 1$), which corresponds to ages of the Universe from ~ 0.8 Gyr up to the present local Universe. More than sixty years after their discovery we have a generally accepted idea about their nature, although a fundamental empirical understanding is still lacking (see e.g., Marziani et al. 2018, and references therein). In the next sections, I will briefly discuss the main properties of type-I quasars that are related to the aims of this thesis.

1.2.1 Spectral energy distribution

Type-I AGN in general exhibit distinctive spectral energy distribution (SED) due to the sum of several contributions, arising from different regions, and that provide significant insights into their physical properties and mechanisms driving their emission across the electromagnetic spectrum. Fig. 1.5 shows a schematic overview of an AGN SED spanning from radio frequencies to hard X-rays. The illustration highlights the diverse physical components that collectively compose the observed SEDs of AGN. Depending on the type of AGN, the relative contribution of these components can present a very significant variation.

In the optical and ultraviolet spectral ranges, the SED of type-I quasar is characterised by a prominent continuum (thermal) emission originating from a geometrically thin, optically thick accretion disk around the SMBH. This prominence is the well-known “big blue bump” (blue line of Fig. 1.5; Malkan & Sargent 1982; Malkan 1983; Mathews & Ferland 1987). Additionally to this

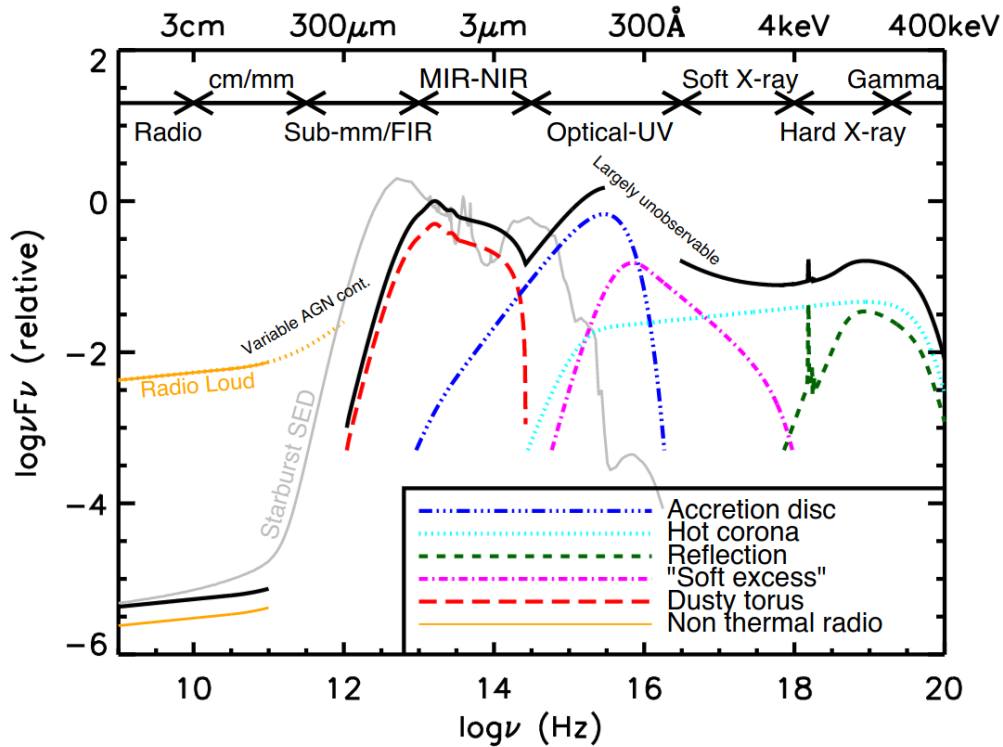


Fig. 1.5: An illustrative scheme of an AGN broadband continuum spectral energy distribution. Credit: [Harrison \(2014\)](#).

continuum, broad emission lines, such as the Balmer lines, are also often observed. Such lines arise from the reprocessing of UV radiation by gas clouds in the BLR surrounding the black hole.

As the energy from the accretion disk interacts with the surrounding gas and dust, it can also produce infrared (IR) emission (red line in Fig. 1.5). The IR component of the SED allows for understanding the properties of the torus, which absorbs and re-emits the intense radiation emitted by the accretion disk. The IR signatures in quasar SED may vary depending on the source and many studies attempt to characterise these SED in the near-to-mid-IR domain (see e.g., [Alonso-Herrero et al. 2003](#), and references therein).

Quasars can also exhibit strong X-ray emission originating from the innermost regions of the accretion disk and the surrounding corona. This emission can be seen in magenta (soft excess) and green (hard X-rays) traces in the SED of Fig. 1.5. X-ray observations help on the understanding of the high-energy processes occurring close to the black hole (e.g., thermal Comptonisation and the reflection of X-rays off the accretion disk).

The radio emission (yellow line in Fig. 1.5) often exhibits a characteristic double-lobed or jet-like structure, indicative of collimated outflows of plasma accelerated to relativistic velocities by the central black hole. These radio jets can extend over vast distances, spanning thousands to millions of light-years, and could play a crucial role in the feedback mechanisms that regulate star formation and galaxy evolution.

The AGN SED constitutes a key input to study the physics of the BLR through photoionisation models. There are many studies related to the SEDs and their dependence on different parameters as

the luminosity or the Eddington ratio (see e.g., [Ferland et al. 2020](#), and references therein). Typical SEDs have been obtained from large samples of nearby quasars representing average properties, but high-redshift, high-luminosity quasars usually with high accretion rates show differences compared to the less luminous nearby sources in such a way that the peak of the disk emission can be displaced towards lower frequencies ([Duras et al. 2017, 2020](#)). Along this thesis, I have considered the SED of [Krawczyk et al. \(2013\)](#) as a good approach for our sample at high redshift and the SED of [Mathews & Ferland \(1987\)](#) for sources at low redshift. These SEDs were used, for instance, in the photoionisation modelling that allows for using the most appropriate metallicity and other AGN properties when estimating outflow parameters. The complete description of the photoionisation modelling performed as well as the description of the approach used in the estimation of the outflow parameters are provided in Appendix B.2. The main results are presented in Chapter 5.

1.2.2 Accretion rate

Accretion rate in AGN represents an important tool to understand the energetic processes that govern these powerful objects. As mentioned in Section 1.1.1, AGN are powered by the gravitational energy released as matter falls onto a supermassive black hole at the galactic centre. The rate at which this matter accretes on the black hole influences the luminosity and behaviour of the AGN and can vary widely among the different classes of AGN and at different cosmic epochs.

Usually, the accretion rates are quantified through the Eddington accretion rate (or *Eddington ratio*), which is based on the luminosity of the accretion disk. The Eddington accretion rate is the maximum rate at which material can be accreted onto a black hole without the radiation pressure from the accretion disk exceeding the gravitational force assuming the accretion to be spherical ([Peterson 1997](#)). The Eddington ratio is defined as the ratio

$$\lambda_{\text{Edd}} = L_{\text{bol}}/L_{\text{Edd}}, \quad (1.1)$$

in which L_{bol} is the bolometric luminosity, defined as the luminosity of the source integrated across the whole electromagnetic spectrum, and L_{Edd} is the Eddington luminosity, which can be defined as:

$$L_{\text{Edd}} = 1.5 \times 10^{38} \frac{M_{\text{BH}}}{M_{\odot}} [\text{erg/s}], \quad (1.2)$$

where M_{BH} is the black hole mass and M_{\odot} is the mass of the Sun. Since the L_{Edd} is directly proportional to M_{BH} , one can write $L_{\text{bol}}/L_{\text{Edd}} \propto L_{\text{bol}}/M_{\text{BH}}$.

The power emitted by an AGN when converting mass into energy can be described as:

$$L_{\text{bol}} = \eta \dot{M} c^2, \quad (1.3)$$

where η is the radiative efficiency for accretion, $\dot{M} = dM/dt$ is the mass accretion rate, and c is the velocity of the light in vacuum. In the case in which the matter is confined in an accretion disk, η depends on the the geometry and radiative properties of the disk, which in turn may vary with \dot{M}

(Marziani et al. 2006, and references therein). Eq. 1.3 allows us to define an Eddington accretion rate given by $\dot{M}_{\text{Edd}} = L_{\text{Edd}}/\eta c^2$, and consequently, a dimensionless accretion rate $\dot{m} = \dot{M}/\dot{M}_{\text{Edd}}$.

The accretion rate \dot{m} together with the opacity of the accreting material are key factors when determining the fundamental structure of the accretion disk (Peterson 1997). When the accretion rate is low (i.e., $\dot{m} \lesssim 1$), the disk adopts a thin structure and emits radiation with a high efficiency, typically $\eta \sim 0.1$. However, at high accretion rates ($\dot{m} \gg 1$), as the radiation moves upward, it becomes partially confined by the accreting material, leading to the expansion of the disk into a thick structure. Conversely, under very low accretion rates ($\dot{m} \lesssim 0.1$), the disk becomes optically thin.

The Eddington accretion rate is a fundamental parameter when studying quasars. Many authors have shown the Eddington ratio seems to correlate with spectral properties of quasars, suggesting that these spectral properties are closely linked to the SMBH accretion rate (e.g., Sulentic et al. 2017). In this thesis, I aim to investigate what is the role of the accretion rate in the high-redshift quasar Main Sequence. Throughout this work, I consider *high accretors* the sources that present $\log \lambda_{\text{Edd}} \gtrsim 0.3$.

1.2.3 Radio emission and the RL/RQ dichotomy

One of the more important and much debated problems involving quasars is the fact that only about 10% of them are strong emitters in radio (radio-loud, RL; Kellermann et al. 1989; Wilson & Colbert 1995). These sources are usually characterised by powerful radio jets that extend from fractions of a parsec to kiloparsecs in extension, reaching extragalactic scales in extreme cases (e.g., Rawlings & Saunders 1991).

The radio emission is typically estimated through the radio-loudness parameter initially proposed by Kellermann et al. (1989). According to these authors, the rest-frame radio-loudness parameter R_{K} is defined as the ratio

$$R_{\text{K}} = f_{\nu, \text{radio}}/f_{\nu, \text{optical}} \quad (1.4)$$

between the specific flux at 5 GHz and the optical *B*-band flux. These authors propose that sources with ratios $R_{\text{K}} \gtrsim 10$ are considered to be RL, while $R_{\text{K}} < 10$ are representative of radio-quiet (RQ) sources. Over time, however, modified versions of R_{K} were proposed. All along this thesis, I will follow the R_{K} defined by Ganci et al. (2019), that uses the rest-frame specific flux at 1.4 GHz and the optical *g*-band.

The distinction between RL and RQ is not exactly easy, as it may be dependent of factors like the orientation of the source, internal extinction or the optical luminosity, and there exists the possibility of a real intrinsic dichotomy between RL and RQ quasars (Zamfir et al. 2008). It is known that a significant fraction of RQ and RL share similar spectroscopic properties (Zamfir et al. 2008; Sulentic et al. 2000a). Additionally, not only RL but also the RQ quasars can present radio jets (Blundell & Beasley 1998; Ulvestad et al. 2005). However, the main difference between RL and RQ sources seems to be that while the RQ present more moderate radio jets, the RL present very powerful, relativistic jets (Padovani 2016; Padovani et al. 2017). In this way, RL and RQ are assumed to have “jetted” and “non-jetted” radio emission, respectively (Padovani et al. 2017).

Some authors proposed the existence of an intermediate class of radio emitters, known as *radio-intermediate* (RI) sources, which may work as a bridge between the RL and RQ sources, as it exhibit characteristics that are neither purely RL nor RQ (see e.g., Falcke et al. 1996; Lacy et al. 2001, and references therein). The existence of this class, however, is a fact of issue nowadays, as some authors argue that their radio emission is not exclusively due to the AGN engine, but instead due to a combination of AGN and star-forming activity or even exclusively due to star-formation processes (Kellermann et al. 2016).

A powerful tool that allows for discerning whether the radio emission is due to the AGN or due to processes of star formation is the radio power (see e.g., Marziani et al. 2021b). Shankar et al. (2008) defines the radio power as:

$$P_{1.4\text{GHz}} = \frac{10^{-26} f_{\text{int}}}{(1+z)^{1-\alpha}} 4\pi d_L^2, \quad (1.5)$$

where f_{int} is the integrated flux intensity at 1.4 GHz in mJy, α is the spectral index at that frequency, and d_L is the luminosity distance in Mpc.

Many authors assume that a source is RL when $\log P_{1.4\text{GHz}} \gtrsim 31.6$ [$\text{erg s}^{-1} \text{Hz}^{-1}$] and $R_K \gtrsim 70$ (Sulentic et al. 2003; Zamfir et al. 2008; Ganci et al. 2019). These values are the ones found for the weakest Fanaroff Riley-II (FR-II, strong radio sources with prominent emitting lobes, see Fanaroff & Riley 1974) structures, as this class is found to be the prototypical RL (Barthel 1989; Jackson & Wall 1999; Sulentic et al. 2003). Nowadays, $R_K \gtrsim 70$ and $\log P \gtrsim 31.6 \text{ erg s}^{-1} \text{Hz}^{-1}$ are considered a reliable threshold for distinguishing truly jetted sources (see e.g., Ganci et al. 2019; Mengistue et al. 2023, and references therein). In this context, sources with $10 \lesssim R_K \lesssim 70$ are considered RI.

The radio classification based on the R_K and P parameters may be, however, affected also by the resolution of the radio data and the real morphology of the source. When considering kiloparsec scales, where features like radio lobes can be present, having a resolution power high enough to identify whether a source is *core-dominated* (CD, when radio emission is restricted to the core or dominated by it), *core+lobe* (CL, when there is a bright core and at least one lobe is visible), or *lobe-dominated* (LD, when the lobes are visible without a clearly-detected core or when the radio emission is predominantly from the lobes) can be a very tricky task. It is true especially in the case of the sources that I will analyse in this thesis, which have been detected mainly by the NRAO VLA Sky Survey (NVSS, Condon et al. 1998), the VLA Faint Images of the Radio Sky at Twenty-Centimeters (FIRST, Gregg et al. 1996; Becker et al. 1995), and the Sidney University Molonglo Sky Survey (Mauch et al. 2003) catalogues.

1.2.4 The feedback mechanism and the outflows

The process of matter accretion onto the SMBH in the center of a galaxy may lead to very energetic processes that are expected to play a very important role in the growth and evolution of galaxies over cosmic times. These processes are known as *AGN feedback* and represent one of the main topics studied in the field of extragalactic astronomy nowadays. The energy injected by the AGN can provide

a mechanism to prevent the cooling of gas or to expel gas from the galaxy (Fabian 2012). In some cases, it may influence the star formation in the host galaxy, either by triggering or suppressing it (see e.g., Mulcahey et al. 2022, and references therein). The AGN feedback can also affect the kinematics of the host galaxy by driving outflows and winds (Harrison et al. 2018). These outflows and winds can expel gas from the galaxy, thereby regulating the fuelling of the nuclear activity and its duty cycle (Morganti 2017; Harrison et al. 2018).

According to current literature, the feedback in AGN may occur in two modes, depending on the luminosity of the AGN:

- ★ **Kinetic (*radio*) mode:** in this case the luminosity is much lower than the Eddington luminosity (L_{Edd}), which is the maximum luminosity in which the dynamic equilibrium of the system is maintained. Feedback occurs mainly due to jets of relativistic particles, which prevent the cooling of the gas located in the galactic halo, making it difficult for stars to form in the galaxy (Fabian 2012). This mode is often observed in very massive galaxies and/or in the centres of galaxy clusters;
- ★ **Radiative (*quasar*) mode:** occurs when the AGN luminosity is high, close to the Eddington limit ($L \sim L_{\text{Edd}}$). Therefore, sources that are producing feedback in this mode are accreting in relatively high accretion rates (Harrison 2017). It is mainly driven by the radiation pressure on the ionised gas located in both BLR and NLR. This pressure makes the nucleus reach its accretion limit and consequently intense winds of gas (outflows) are expelled (Fabian 2012; Cielo et al. 2018). The quasar mode is particularly relevant at high redshift, where it is considered the primary mode of AGN feedback.

The feedback of AGN can be detected in various forms. One of them are the jets of relativistic particles (see Padovani 2016, for a review). In this case, the gas located in the inner region of the torus is accelerated, due to the combination of very intense gravitational fields produced by the black hole and the magnetic fields generated by the plasma that forms the accretion disk. These jets are in general collimated and perpendicular to the disk. As a result of the interaction of the accretion disk plasma and strong magnetic fields, synchrotron radiation and inverse Compton scattering occur. While the former is observed at radio wavelengths, the latter is found at shorter wavelengths such as X-rays and γ -rays (see e.g., Croton et al. 2006). This interaction is also responsible for the high velocities of the jets, which can reach up to a few tenths of the speed of light in a vacuum, and for the great distances reached by the ejections. Often, the size of the jet exceeds the limit of the host galaxy, which can affect its kinematics (Nesvadba et al. 2017; Mukherjee et al. 2016).

There is also feedback through the outflows, which consists of gas (ionised or molecular) flows away from the galactic centre. These outflows are in general produced through the interaction between the winds from the outer parts of the accretion disk and the circumnuclear gas of the galaxy. This gas presents different properties depending on the temperature and their different phases can be detected in a wide range of wavelengths in both emission and absorption lines through spectroscopic observations (see e.g., Ciccone et al. 2014; Harrison 2017; Fluetsch et al. 2021, and references therein).

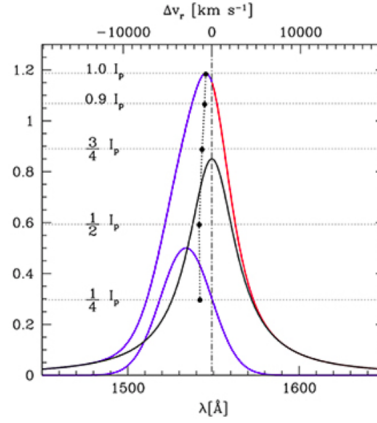


Fig. 1.6: Example of the line decomposition including the outflowing component (in blue). The different fractional intensities are shown in terms of the peak intensity of the full profile (I_p). Credits: [Marziani et al. \(2018\)](#).

This thesis focuses on ionised gas outflows, that typically are the ones that present the most chaotic kinematics. These outflows typically produce asymmetric line profiles in the AGN spectra, with an excess of flux in the blue wing of the emission line, which indicates the presence of gas moving in the direction of the observer. The detection of such peculiarities in the line profiles may help to understand the dynamics and orientation of the outflowing gas. A good approach to identify such outflow contributions is through the profile decomposition of high-ionisation lines such as [O III] λ 5007 and C IV λ 1549. Here, I will center the analysis into these two emission lines.

There are different approaches to measure the outflow velocities in the literature. One of them consists of determining the centroid shift of the line profile in different fractional intensities as initially established by [Marziani et al. \(1996\)](#). For relative intensities $x = \frac{1}{4}, \frac{1}{2}, \frac{3}{4}, \frac{9}{10}$, the centroid shift c can be written as:

$$c(x) = \frac{v_{r,R}(x) + v_{r,B}(x)}{2}, \quad (1.6)$$

in which $v_{r,R}$ and $v_{r,B}$ are the velocity shift on the red and blue sides of the profile, respectively, relative to the rest-frame of the source. Fig. 1.6 shows how the centroids shifts at different fractional intensities are sensitive to the outflowing component. In this thesis, I assume $x = \frac{9}{10}$ a good approach for the “peak” of the profile (i.e. the quasar rest-frame).

[O III] λ 5007

The forbidden [O III] λ 5007 emission line is a prominent emission line in the spectra of many AGN, as it is easily detected in the spectra of the majority of the AGN, and it is found to be a very good tracers of AGN-driven outflows (see e.g., [Mullaney et al. 2013](#); [Fischer 2013](#); [Fischer et al. 2018](#); [Storchi-Bergmann et al. 2018](#)). [O III] λ 5007 is also considered a reliable estimator of the kinematics of the ionised gas ([Fiore et al. 2017](#), and references therein). At high redshift, [Coatman et al. \(2019\)](#) found that the [O III] λ 5007 outflow kinematics are related to the Eddington ratio, with the outflow

kinematics being stronger in quasars with higher Eddington ratios. This finding is consistent with previous studies, such as [Coatman et al. \(2016, 2017\)](#), which found that the [O III] λ 5007 outflow kinematics are related to the quasar Eddington ratios in low-redshift quasars. Many works in both high- and low-redshift ranges revealed that the ionised gas [O III] λ 5007 mass outflow rate is positively correlated with the bolometric luminosity of the AGN, indicating that more luminous AGN have more powerful outflows (see e.g., [Fiore et al. 2017](#); [Vietri et al. 2018, 2020](#); [Deconto-Machado et al. 2023, 2024](#)). Additionally, [Zakamska et al. \(2016\)](#) analysed quasars at $z \sim 2.5$ and found [O III] λ 5007 outflows with extremely high velocities, suggesting that it cannot be confined by any realistic galaxy potential and is likely to escape from the galaxy, indicating a possible "blow-out" phase of quasar feedback observed during the peak epoch of galaxy formation.

C IV λ 1549

C IV λ 1549 outflows in type-I quasars have been previously studied in the literature (see e.g., [Bachev et al. 2004](#); [Sulentic et al. 2007a](#); [Richards et al. 2011](#); [Coatman et al. 2016, 2017](#); [Sulentic et al. 2017](#); [Marziani et al. 2019](#); [Vietri et al. 2020](#); [Deconto-Machado et al. 2023, 2024](#)). The outflows produced by the C IV λ 1549 can exhibit a very wide range of velocities, reaching in some cases a few thousands of km s^{-1} (e.g., [Vietri et al. 2020](#)). The profile of C IV λ 1549 usually present a significant asymmetry due to the excess of emission in the blue part of the line profile. It is also known that, similarly to [O III] λ 5007, the most luminous quasars are the ones that present the major contribution of the outflowing component to the full line profile, suggesting that a nuclear outflow provided from the BLR could be responsible for galactic-scale feedback effects ([Marziani et al. 2016a](#); [Deconto-Machado et al. 2024](#)).

In Parts I and II of this thesis, I dedicate a significant fraction of the discussion to the analysis of the outflows in redshift ranges between ~ 2 and 4. During this period, known as the cosmic noon, luminous quasars were relatively common. To understand the feedback effects driving galaxy evolution, it is necessary to focus on quasars from this epoch, as they exhibit the most extreme outflow parameters. Outflows observed at later cosmic epochs, at redshift ~ 0.1 - 0.2 , show some similarities to those observed during the peak of the quasar population, but they are less powerful. In Chapters 2 and 5, I estimate outflow parameters such as outflow mass rate and kinetic power for both [O III] λ 5007 and C IV λ 1549 emission lines. Details on these estimations can be also found in the Appendix B.2.

1.2.5 Metallicity

Another important topic to be considered within the framework of quasars is the role of the metallicity (Z) in the BLR. Studies have shown that the gas-phase metallicity of AGN in general may vary, impacting star formation rates, feedback mechanisms, and the galaxy evolution (see e.g., [Maiolino & Mannucci 2019](#), and references therein). Observations have revealed diverse BLR metallicities across different AGN types and environments ([Du et al. 2014](#); [Wang et al. 2022](#)). In particular, studies of high-redshift ($z \gtrsim 2$) and high-accreting quasars have shown highly metal-enriched BLR, with

metallicities several times greater than the solar value, suggesting a significant enrichment of the BLR environment at early cosmic epochs (e.g., Śniegowska et al. 2021; Garnica et al. 2022).

The high values of Z in the BLR may influence density and ionisation parameters (Murray et al. 1995). In order to evaluate the connection between these parameters, one can use tools like the CLOUDY code (Ferland et al. 2017), which employs line ratio diagnostics, mainly from the UV range and allows for determining the BLR metallicity itself. This technique has been applied in Chapters 8 and 7, where I present two pilot works that address the need to evaluate the trends of the metallicity under the context of the quasar Main Sequence.

1.3 The Eigenvector 1 and the quasar Main Sequence

The diversity in the spectra of quasars has long been a topic of active discussion among astronomers and many attempts to identify any systematic trends within this diversity were performed. One of the pioneering attempts in this direction was made by Boroson & Green (1992), which uses for the first time the principal component analysis (PCA) approach to unify the diverse group of AGN under the context of the Eigenvector 1 (E1). The E1 consists of a set of correlations detected in the optical and radio spectral ranges and is dominated by an anti-correlation between the strength of the optical Fe II blend and the peak intensity of the [O III] λ 5007 emission line. Boroson & Green (1992) also found a connection between the width of the broad H β emission associated with the E1.

These authors focused on the low-redshift range ($z < 0.5$) and analysed 87 sources from the Bright Quasar Survey (Schmidt & Green 1983). These objects, meeting the quasar classification based on their B-magnitude ($M_B > -22.2$), were studied across various energy ranges, including radio, infrared and X-rays. The low redshift of the sources allowed to concentrate the analysis on the region around H β that also includes [O III] λ 5007, He II λ 4686, and the Fe II blends present on both the blue and the red sides of H β . From their analysis, they have concluded that the E1 may be influenced by several physical parameters, such as the mass accretion rate, the black hole mass, the covering factor and velocity distribution of the BLR clouds, the orientation of the source to the observer, and the ionisation parameter (Boroson & Green 1992).

Similar correlations to that found by Boroson & Green (1992) in the optical range have been identified by many other authors (see e.g., Gaskell 1985b; Zheng & O'Brien 1990; Zheng & Keel 1991, and references therein). These trends, however, appear to extend beyond the optical domain: correlations between optical and X-ray ranges, for instance, have also been identified (Wilkes et al. 1987; Corbin 1993; Laor et al. 1994, 1997; Lawrence et al. 1997), leading to the possibility that the E1 may be influenced by soft X-ray emissions as well (see Wang et al. 1996).

Further studies have revealed correlations between the optical and UV spectroscopic properties (Wills et al. 1999; Kuraszkiewicz et al. 2000). Marziani et al. (1996) found a significant correlation in radio-quiet sources between the C IV EW and the C IV shift/asymmetry with the strength of the optical Fe II. Specifically, they found that C IV profiles with large blueshift/asymmetry exhibit lower EW and stronger Fe II emission. Additionally, Sulentic et al. (1995) has shown that while radio-quiet

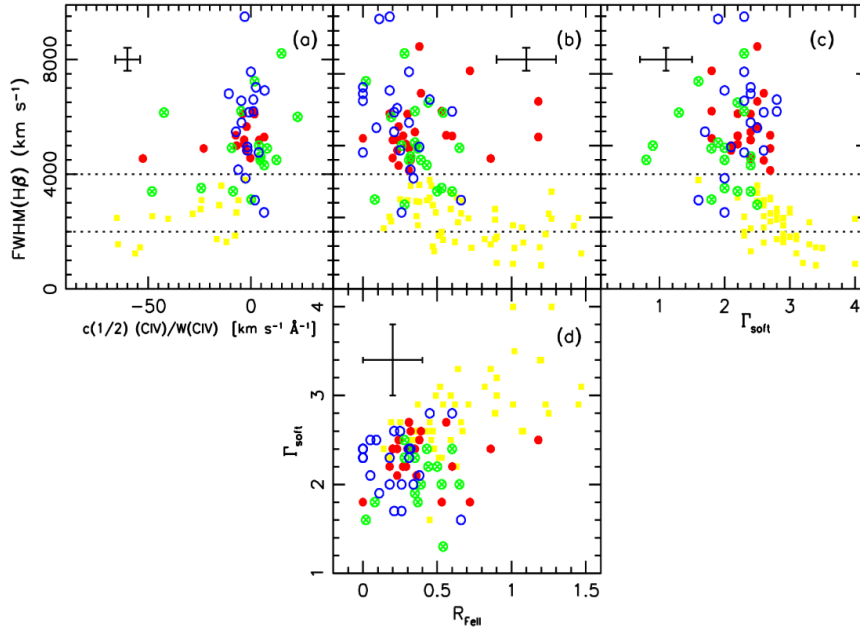


Fig. 1.7: Relations between the correlates of the 4DE1 for a low-redshift sample. Solid symbols represent radio-quiet sources. Yellow squares are Population A quasars. Plot from (Sulentic et al. 2007b).

quasars present extreme C iv blueshifts, radio-loud quasars are found to present extreme H β redshift and practically no C iv blueshifts. These findings suggest that the optical and UV properties of quasars are closely linked and that the radio-loud and radio-quiet populations exhibit distinct spectral characteristics.

The discovery of these cross-correlations across the different spectral ranges suggests that the E1 holds a significant potential for providing a more comprehensive understanding of the underlying physical drivers of quasar diversity. Over the years, these correlations have been confirmed with the exploration of SDSS-based samples (Wang et al. 2006; Zamfir et al. 2008; Kruczek et al. 2011; Richards et al. 2011; Shen & Ho 2014; Brotherton et al. 2015; Sun & Shen 2015) and the Eigenvector 1 set of correlations represents nowadays a very robust approach to study the physics of quasars.

1.3.1 The 4D Eigenvector 1

A more overarching version of the E1 formalism was introduced by Sulentic et al. (2000c). The authors take into consideration the samples from Boroson & Green (1992) and Marziani et al. (1996) as well as 24 sources from HST UV archival and optical ground-based spectra and establish a version of the E1, the *fourth-dimensional Eigenvector 1* (4DE1), that is based in four “orthogonal” observational parameters that respond to different physical processes:

1. **Full width of Half Maximum (FWHM) of the H β broad component**, thought to be a measure of virialised motions in the accretion disc and thus crucial for black hole mass estimations. As

it gives the width of the broad $H\beta$ emission line, it can provide information about the dynamics of the gas in the BLR. It was first identified as a E1 correlate by [Boroson & Green \(1992\)](#);

2. **Ratio between the intensities of the Fe II blend at 4570Å and $H\beta$** ($R_{\text{Fe II}} = I(\text{Fe II } \lambda 4570)/I(H\beta)$), sensitive to the ionisation state, the electron density, and column density of the BLR. It also helps to understand the relative strengths of these emission lines and their connection to the physical properties of the quasar (see e.g., [Panda et al. 2018](#); [Panda et al. 2019](#)). Initially, it was defined by [Boroson & Green \(1992\)](#) as $R_{\text{Fe II}} = W(\text{Fe II } \lambda 4570)/W(H\beta)$. Fe II emission is measured between 4434 and 4684Å;
3. **Blueshift of high-ionisation lines (HIL), such as C IV $\lambda 1549\text{Å}$** . It represents a strong diagnostic of winds/outflows in the higher ionisation broad line gas. In [Sulentic et al. \(2000c\)](#), the authors suggest that it may be an important E1 correlate, as C IV correlates with $R_{\text{Fe II}}$ and Γ_{soft} . It was later confirmed by [Sulentic et al. \(2007a\)](#) and references therein;
4. **Soft X-ray photon index (Γ_{soft})**, characterises the shape of the X-ray spectrum emitted by the quasar in the soft X-ray range. It helps to understand the physical processes occurring in the accretion disk and the accretion state of the black hole ([Mineshige et al. 2000](#); [Done et al. 2012](#)). $\Gamma_{\text{soft}} > 2$ are primarily observed in sources with $\text{FWHM}(H\beta_{\text{BC}}) < 4000 \text{ km s}^{-1}$ ([Boller et al. 1996](#); [Wang et al. 1996](#); [Sulentic et al. 2000a](#); [Grupe 2004](#), [García-Soto et al. \(in preparation\)](#)).

Fig. 1.7 shows 2D projections of the 4DE1. The intrinsic dispersion observed in these projections indicates that now all broad-line emitting AGN are alike, as there is a wide range of parameter values observed that goes beyond the measurement errors. Additionally, RL AGN exhibit a very restricted domain of occupation that is displaced from the majority of RQ sources (yellow symbols). Only about 25% of RQ sources are co-spatial with the RL domain, while the remaining RQ sources occupy a distinct, almost pure-RQ zone. This disparity suggests fundamental differences in the physics between RQ and RL sources. There is evidence for 4DE1 correlations mainly among the radio-quiet objects.

By considering the main four parameters, the 4DE1 framework has effectively synthesised and structured the varied spectral characteristics of type-I AGN, unveiling systematic trends and correlations that were previously concealed by apparent randomness. It also allowed for establishing connections between the 4DE1 parameters and quasar physical properties (M_{BH} , λ_{Edd} , etc.). In this thesis, my focus will be on the first three parameters of the 4DE1 ($\text{FWHM}(H\beta_{\text{BC}})$, $R_{\text{Fe II}}$, and the HIL blueshifts), as they may provide relevant information about the BLR structures. Special attention will be given to the 4DE1 optical plane, which works as a ‘‘Hertzsprung-Russel diagram for quasars’’, often referred to as the Main Sequence of quasars.

1.3.2 The quasar Main Sequence

The optical plane of the 4DE1, defined by the $\text{FWHM}(H\beta)$ vs. $R_{\text{Fe II}}$, is the so-called Main Sequence (MS) of quasars ([Marziani et al. 2001](#)). The MS was extensively studied for quasars with luminosities $\log L \lesssim 47 \text{ [erg s}^{-1}\text{]}$ and redshift lower than 0.8 (e.g., [Marziani et al. 2003b](#); [Sulentic et al. 2003](#);

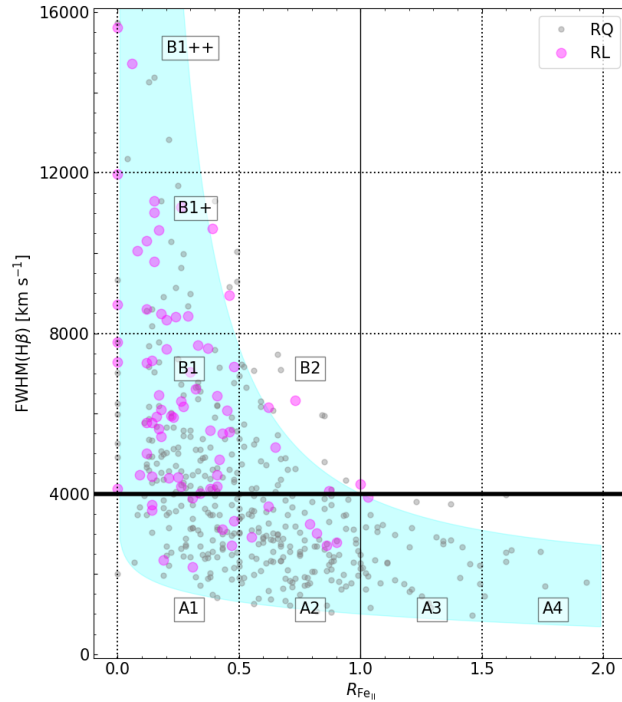


Fig. 1.8: The quasar MS at low redshift (blue-shaded area), represented by the sample of Zamfir et al. (2010). Grey and magenta circles indicate radio-quiet and radio-loud sources, respectively.

Bachev et al. 2004, and references therein). One of the largest low-redshift samples studied under the light of the MS is the one analysed by Zamfir et al. (2008) and Zamfir et al. (2010). The authors analysed ≈ 470 quasars with $z \lesssim 0.7$ that present high signal-to-noise ratio ($S/N \approx 29$) optical spectra observed with the Sloan Digital Sky Survey data release 5 (DR 5, Adelman-McCarthy et al. 2007). The sample covers a broad range of luminosity going from $\log L_{\text{bol}} = 10^{43}$ to 10^{47} [erg s^{-1}] and includes both radio-quiet and radio-loud sources.

At least at low-redshift ranges, the radio emission seems to play an important role within the 4DE1 context. Strong radio emitters (RL) exhibit a tendency towards weak Fe II emission, large FWHM of H β broad component, and a lack of soft X-ray excess (Sulentic et al. 2000a). Conversely, radio-quiet sources appear to span a wider variety across these parameters, including a broad range of Fe II emission strengths and varying FWHM values of the H β broad component (Marziani et al. 2001; Sulentic et al. 2002; Marziani et al. 2003c). It gave rise to the concept of two populations of quasars (including RL and RQ sources) at low redshift that present important spectroscopic differences:

- ★ **Population A (Pop. A):** with $\text{FWHM}(\text{H}\beta) \lesssim 4000 \text{ km s}^{-1}$ and a broad range of $R_{\text{Fe II}} < 0.5$. They tend to have significant blueshifts in high ionisation lines and show soft X-ray excess. Their Balmer line profiles are Lorentzian-like, and usually symmetric and unshifted. It was initially defined as an almost “pure” radio-quiet population (Sulentic et al. 2000a).
- ★ **Population B (Pop. B):** with a very wide range of $\text{FWHM}(\text{H}\beta)$, always $> 4000 \text{ km s}^{-1}$, and with very weak Fe II, $R_{\text{Fe II}} < 0.5$. They do not show in general important blueshifts in high-ionisation lines and neither X-rays excess. The Balmer lines in this case are usually well

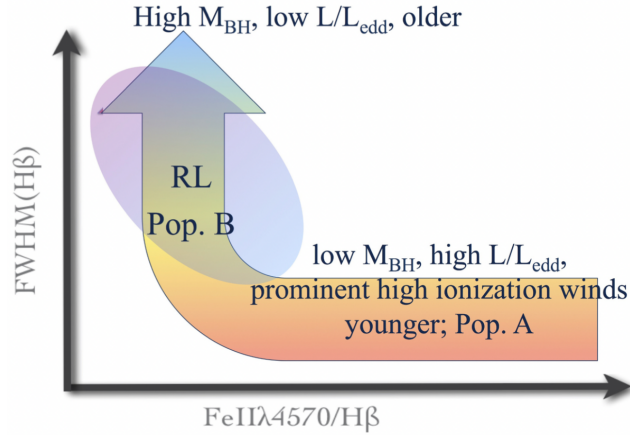


Fig. 1.9: Potential evolutionary interpretation of the quasar Main Sequence. Plot from [Fraix-Burnet et al. \(2017b\)](#).

represented by a double Gaussian (*broad + very broad* component), and are most often redward asymmetric. Its domain is expected to be occupied by both radio-loud and radio-quiet sources.

As more and more data are becoming available, it is now known that RL and RQ sources can be found within both Population A and Population B domains ([Ganci et al. 2019](#); [del Olmo et al. 2021](#)), although the RL show a clear preference of occupying predominantly the Pop. B region. It can be seen in Fig. 1.8, which shows the distribution of the sample defined by [Zamfir et al. \(2010\)](#) in the Main Sequence of quasars at redshift $z \lesssim 0.8$.

In addition to the two populations, the exploration of the distribution of low-redshift sources in the MS allows for its division into specific spectral types (ST) based on the $\text{FWHM}(\text{H}\beta)$ and Fe II emission strength, as defined by [Sulentic et al. \(2002\)](#). For Pop. A sources (typically with $\text{FWHM}(\text{H}\beta_{\text{BC}}) \lesssim 4000 \text{ km s}^{-1}$), the ST are defined by increasing $R_{\text{Fe II}}$ with intervals $\Delta R_{\text{Fe II}} = 0.5$, going from A1 with $R_{\text{Fe II}} \lesssim 0.5$ to A4 with $R_{\text{Fe II}} \gtrsim 1.5$. ST A3 and A4 correspond to extreme accreting quasars radiating near the Eddington limit. For Pop. B quasars ($\text{FWHM}(\text{H}\beta) > 4000 \text{ km s}^{-1}$ and $R_{\text{Fe II}} \lesssim 0.5$), the ST are defined in terms of increasing $\text{FWHM}(\text{H}\beta)$ with intervals $\Delta \text{FWHM}(\text{H}\beta) = 4000 \text{ km s}^{-1}$ in such a way that e.g. B1 corresponds to objects with $4000 < \text{FWHM}(\text{H}\beta) < 8000 \text{ km s}^{-1}$ or B1++ with $\text{FWHM}(\text{H}\beta) \gtrsim 12000 \text{ km s}^{-1}$ (see Fig. 1.8). It is already known that the sources within the same spectral type typically demonstrate similar spectroscopic features, such as line profiles and flux ratios, even though systematic changes may not be discarded, especially because the MS seems also to be affected by major physical properties.

One of these changes may be observed in the UV spectral domain: moving from B1++ to A4 spectral types is associated with an increase in the $\text{Al III} \lambda 1860 / \text{Si III} \lambda 1892$ rate and a decrease in $\text{C III} \lambda 1909 / \text{Si III} \lambda 1892$, as well as a decrease in the equivalent width of C IV, $W(\text{C IV})$. These variations suggest higher densities and metallicities and lower ionisation parameters of the low-ionisation lines emitting region of the BLR as we move towards higher values of the $R_{\text{Fe II}}$ parameter in the MS ([Baldwin et al. 1996](#); [Bachev et al. 2004](#); [Negrete et al. 2013](#)). Furthermore, in many low-redshift extreme Population A (xA) quasars, characterised by spectral types A3 and A4, the

outflow component dominates the C IV emission line profiles, while in some Population B quasars, it may be entirely absent (Sulentic et al. 2007a). Similarly, we observe a similar trend in [O III] outflows, with the average blueshift amplitude increasing towards the high R_{FeII} end of the MS (Zamanov et al. 2002; Marziani et al. 2003c; Cracco et al. 2016).

Additionally, despite some similarities such as asymmetries in emission line profiles, the scarcity of low- z radio-loud Population A sources may indicate distinct Eddington ratio and black hole mass distributions when compared to matched redshift and luminosity radio-quiet ones, as the RQ sources typically exhibit smaller masses and higher Eddington ratios (Woo & Urry 2002; Marziani et al. 2003c; Fraix-Burnet et al. 2017b). Several physical parameters may be associated with the MS correlations (see e.g., Marziani et al. 2018). The behaviour of some of these physical parameters within the MS context is shown in Fig. 1.9, which also illustrates a potential evolutionary progression from Pop. A to Pop. B, transitioning from the “wind-dominated” extreme of Pop. A quasars, characterised by intense Fe II emission and high accretion rates, to the more massive, low-accreting “disc-dominated” Pop. B sources.

The two main physical drivers of the MS are likely (Marziani et al. 2001, 2003c):

- ★ *Orientation:* The angle θ is defined as the inclination between the hypothetical axis of symmetry of the accretion disk and the line of sight at which the galaxy is observed. Given that the H β emission lines are probably emitted by flattened systems, the FWHM(H β) could be influenced by the inclination of the source, going from broader profiles when θ is high and narrower profiles for lower θ . Some studies also indicate that the orientation may influence also the [O III] λ 5007 shifts and W (Risaliti et al. 2011).
- ★ *Accretion rate:* Low values of Eddington ratio (given by L/L_{Edd} , usually $\lesssim 0.2-0.3$) are typically found in Pop. B quasars, while the extreme cases (the high accretors, $L/L_{\text{Edd}} \gtrsim 1$) are found mainly under the Pop. A domain.

The latter parameter, the accretion rate, seems to be the more important parameter within this context, as it potentially indicates a real physical dichotomy between Pop. A and Pop. B (Sulentic & Marziani 2015; Marziani et al. 2018). Fig. 1.10 elucidates the different structures that likely characterise the two populations of quasars. There is also the possibility that the observed Pop. A and Pop. B physical properties are interconnected by a gradual transition in accretion mode, rather than representing a strict dichotomy. This remains an open question in the current days.

The quasar Main Sequence at higher redshift

The MS is expected to be displaced towards higher FWHM(H β) with increasing luminosities and redshift, as indicated in Fig. 1.11. This expectation arises from the assumption that the motion within the low-ionization line emitting region of the BLR is primarily virial, and that the size of the BLR scales proportionally with luminosity. Consequently, it is expected that the FWHM of spectral lines originating from this region would exhibit a correlation with luminosity (see Marziani et al. 2018).

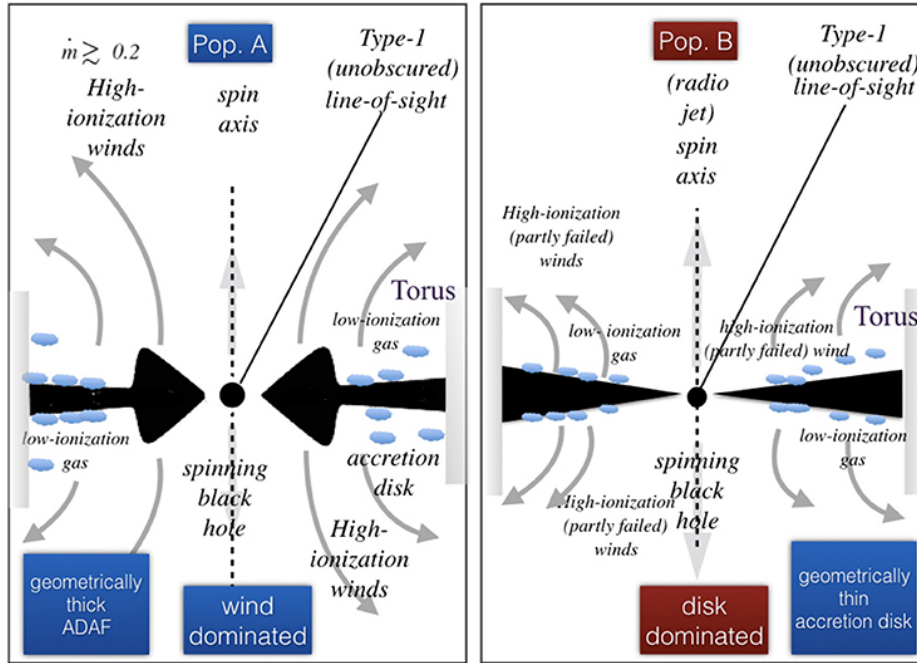


Fig. 1.10: Simplified scheme of the distinct structures that characterize Pop. A (left) and Pop. B (right), featuring a thick and a thin disk, respectively. Credits: [Marziani et al. \(2018\)](#).

However, research on the quasar Main Sequence has been primarily restricted to low redshift, corresponding to cosmic ages where the Universe was around 7-10 Gyr old. Until recently, our understanding of the MS at earlier cosmic epochs and higher luminosity was limited, mainly because it would imply observing the $H\beta$ spectral range using IR spectrometers, as it is displaced towards larger wavelengths due to the redshift of the source.

Presently, high-redshift quasar samples with near-infrared observations of the $H\beta$ spectral ranges are still relatively limited in number ([Capellupo et al. 2015](#); [Coatman et al. 2016](#); [Bischetti et al. 2017](#); [Vietri et al. 2020](#); [Matthews et al. 2021](#)). One of the first samples at high redshift to be studied under the context of the quasar MS is the VLT/ISAAC sample from [Sulentic et al. \(2004\)](#), [Sulentic et al. \(2006b\)](#), and [Marziani et al. \(2009\)](#). In [Marziani et al. \(2009\)](#), the authors analysed the optical spectra of 52 sources within a redshift range $z \approx 0.9-3.0$ and their results confirm the prediction of a systematic increase in minimum $\text{FWHM}(H\beta)$ with luminosity. They also found a systematic decrease in $W([\text{O III}])$ with increasing bolometric luminosity.

Twenty-eight of the sources from the VLT/ISAAC sample of [Marziani et al. \(2009\)](#) had additional UV spectra obtained, with the results of the analysis reported by [Sulentic et al. \(2017\)](#). The findings of these works combined suggested that both Pop. A and Pop. B quasars exhibit significant outflows at high redshift, whereas at lower redshift only Pop. A sources tend to show a contribution of outflowing gas. Additionally, extreme Pop. A within a redshift range of $z \approx 2.0-2.9$ were analysed in the UV region by [Martínez-Aldama et al. \(2018\)](#) using GTC spectra. Their findings indicate that xA sources at high redshift share similar characteristics with those at lower redshift, albeit with higher outflow velocities ($\sim 4000 \text{ km s}^{-1}$).

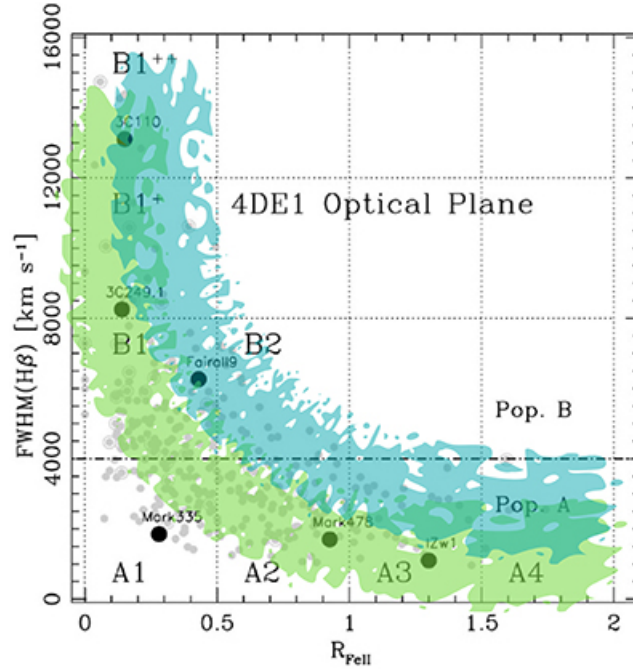


Fig. 1.11: Schematic representation of the quasar MS displacement in high redshift samples. The dark green shaded area indicates the expected location of a high luminosity ($\log L \gtrsim 47$) sample.

In the study of [Sulentic et al. \(2014a\)](#), GTC data were used to analyse 22 sources with a redshift $z \sim 2.35$. The authors found that the median properties of Pop. A and Pop. B, as well as their differences, are consistent at both high and low redshift. Furthermore, they also provide evidence for an excess of low metallicity quasars from this high-redshift sample. Dedicated analyses of the metal content in extreme Pop. A at high redshift have been later performed by [Śniegowska et al. \(2021\)](#) and [Garnica et al. \(2022\)](#), however with very restrict samples.

While these studies provide some insights into the behaviour of the quasar MS at high redshift, the current literature lacks a dedicated investigation on this topic. A more comprehensive analysis of the MS correlations, along with their relationships with primary physical properties of quasars, is needed. Questions such as whether all the MS correlations observed at low redshift remain valid at higher redshift and whether the Eddington ratio, for instance, continues to play a significant role in the MS dynamics need to be addressed. Answering these questions represents the primary objective of this thesis.

1.4 Motivation of the thesis

In this thesis, I perform the analysis of a sample of high-redshift quasars (described in Section 1.4.1) under the context of the 4DE1 scheme. One of the main objectives of this thesis is to advance our understanding of quasar physics through spectroscopic exploration of UV and optical (shifted in the optical and infrared domain due to the quasar redshift) emission line diagnostics, with a particular focus on the broad lines because such measures provide the most direct clues about the kinematics

and geometry of the central BLR in these sources. The analysis will be addressed to answer the main critical questions about the phenomenology and physics of quasar in the context of the 4DE1 parameter space, as can be:

1. **What is the behaviour of the quasar Main Sequence at high redshift?** As previously discussed, the quasar Main Sequence is well established at low redshift through the analysis of numerous samples in the existing literature. However, exploration of the quasar Main Sequence at high redshift has been relatively limited until now. The primary objective of this thesis is to advance the understanding of the 4DE1 and its Main Sequence of quasars at high redshift, aiming to see if the trends observed at low redshift remain consistent at high redshift. It will be performed following the most luminous high-redshift quasars ($\log L_{\text{bol}} = 47 - 48$) through the IR windows to access the optical spectra within this redshift range, as well as exploiting the UV spectral region observable at optical wavelengths.
2. **Does the feedback mechanism at high redshift follow the same 4DE1 trends observed in the low-redshift context?** Outflows observed at $z \sim 0.1 - 1$ display certain self-similarity, albeit notably less powerful compared to those observed during the peak of the luminous quasar population. I aim to investigate quasars at redshift between 1.5 and 4, where the physical conditions are most extreme, in order to confirm or not the presence of these trends at earlier cosmic epochs.
3. **Do RQ and RL have different physical properties?** Is there any evidence for a physical dichotomy between RL and RQ QSOs? One of our goals is to quantify what are the spectroscopic differences between radio-quiet, radio-intermediate, and radio-loud quasars based on the observed spectrum and its location in the 4DE1 main sequence. I also aim to connect the spectroscopic properties of these objects to their physical properties.

The specific objectives of this PhD thesis are:

- **To achieve information on the kinematics, dynamics, and geometry of the BLR** through the spectroscopic analysis in the UV and optical spectral ranges, shifted to the optical and IR domains because of the quasar redshift, of the broad emission lines of a sample of high-redshift quasars (z between 1.5 and 4), that includes both radio-loud and radio-quiet sources.
- **Study the properties of the radio emission**, as well as its relationship with optical and UV properties of the sample, and explore potential factors that may influence these relations.
- **Analyse the spectroscopic differences between RL and RQ** at high redshift and its relation with the two populations of QSO (A and B) and compare with the data available for low-redshift ($z < 1$) quasars.
- **Estimate the physical properties** for the observed sample, as black hole mass (M_{BH}), Eddington ratio (L/L_{Edd}), and metallicity of the gas in the BLR.

- **Study the presence of winds and outflows** in both RL and RQ, and their relationship with the populations A and B of quasar. Additionally, I aim to analyse the dynamical parameters of these outflows and their impact on feedback mechanisms within the host galaxy.

1.4.1 Observational data and analysis methods

The ISAAC sample

The collection of articles presented in this thesis emerged from a exhaustive spectroscopic analysis of a sample of high-redshift quasars in both optical and UV rest-frame spectral ranges. Referred to as the *ISAAC sample*, this dataset consists of 32 high-redshift ($1.5 \lesssim z \lesssim 3.7$) and high-luminosity ($47 \lesssim \log L_{\text{bol}} \lesssim 48$ [erg s^{-1}]) type-I quasars. Details about the ISAAC sample can be found mainly in Chapters 2 and 5. Spectral observations of the $\text{H}\beta + [\text{O III}]\lambda 5007$ region (shifted to the near-infrared due to the redshift) were conducted using the ISAAC spectrograph at ESO-VLT, under the programs 083.B-0273(A), 085.B-0162(A), and 086.B-0774(A).

The ISAAC spectrograph covered the infrared range of the electromagnetic spectrum, in the range $1 - 5 \mu\text{m}$, and was mounted on the Nasmyth A focus of Unit Telescope 3 (UT3). The VLT telescopes, the ISAAC spectrograph, and the optical layout of the instrument are shown in Fig. 1.12. Although ISAAC was equipped with two gratings, one for low resolution (LR) and another for medium resolution (MR), only the SW LR grating had been utilised in our observations. As we focus on the $\text{H}\beta + [\text{O III}]\lambda 5007$ spectral region and considering the redshift of our sources (between $\sim 2 - 4$) we used LR orders 4, 3, and 2, which corresponded to spectral ranges of $1.1 - 1.4$, $1.42 - 1.82$, and $1.82 - 2.5 \mu\text{m}$, respectively. All observations were conducted using a $0.6''$ slit, resulting in resolutions of 860, 840, and 750, respectively.

The spectroscopic reduction of the observations was performed in a standard way using the routines of the astronomical package IRAF. Once the data is reduced, it is possible to obtain an accurate measurement of the quasar rest-frame and determine its redshift by using emission lines such as $\text{H}\beta$ and $[\text{O III}]\lambda 5007$. The knowledge of the quasar rest-frame allows for a quantitative comparison between low- and high-ionisation lines from the optical/UV spectra. A more detailed explanation about the data reduction and the redshift estimation can be found in Chapters 2 and 5.

For the UV spectral range (observed in the optical domain at the redshift of the sample), that includes high ionisation lines as $\text{C IV}\lambda 1549$, He II , $\text{Si IV}\lambda 1397 + [\text{O IV}]\lambda 1402$, and the 1900\AA blend, I use archive spectra mainly from the Sloan Digital Sky Survey (SDSS) and in some cases digitised spectra from older literature.

Fluxes at radio frequencies and the study of radio morphologies of the sources were mainly collected from both the Faint Images of the Radio Sky at Twenty-Centimeters (FIRST, Becker et al. 1995; Gregg et al. 1996) and from the NRAO VLA Sky Survey (NVSS, Condon et al. 1998).

Other samples considered in this thesis

- Hamburg-ESO (HEMS):** represents the previous studies of the MS at relatively high redshift and consists of 52 high-luminosity quasars selected from the Hamburg-ESO survey (Wisotzki et al. 2000). The sources are extremely luminous, with bolometric luminosities between 10^{47} and 10^{48} erg s⁻¹ and are located in a redshift range between 0.9 and 3.1. The H β + [O III] λ 5007 region of these 52 sources were obtained with the same instrumentation that the present work and analysed by Sulentic et al. (2004), Sulentic et al. (2006b), and Marziani et al. (2009), focusing mainly on the H β emission line. 28 out of the 52 sources have a redshift $z \gtrsim 1.4$, which allows for the coverage of the C IV λ 1549, redshifted to the optical spectral region. The UV spectra of these 28 quasars were presented in Sulentic et al. (2017), which also performed a multicomponent fitting of these data and reanalysed the H β region of these 28 sources using the IRAF task `specfit`. Although both H β and [O III] λ 5007 were fitted in the optical region, the discussion was centred only on H β , and the [O III] λ 5007 data resulting from the fittings remain unpublished. In this thesis, I utilised the C IV λ 1549 and [O III] λ 5007 fittings performed by Sulentic et al. (2017). In some cases, I conducted a reanalysis when the original fitting did not align with the methodology followed in the fittings of the ISAAC data. To include these sources in the analysis presented here, I also estimated the Eddington ratio, black hole mass, radio-loudness, and other physical parameters following the same approach used for the ISAAC sample.
- Faint Object Spectrograph-HST (FOS):** the low-redshift ($\lesssim 0.5$) and low-luminosity ($\log L_{\text{bol}} \sim 45.6$ [erg s⁻¹]) FOS comparison sample was initially selected from Sulentic et al. (2007a). In this study, the parameters of the C IV λ 1549 emission line were analysed for 130 objects with Hubble spectra from the archive. However, the methodology used in Sulentic et al. (2007a) differs significantly from ours, as it only considered the full profile of C IV λ 1549 rather than employing a multicomponent fitting approach. Therefore, to include this sample in our analysis, I performed a reanalysis of the C IV λ 1549 emission line profiles using the same methodology applied to the ISAAC sample. Optical spectra for 84 of these sources are available in recent literature, and a spectral decomposition similar to the one applied to the other samples has been performed by Dr. Paola Marziani, focusing on both H β and [O III] λ 5007 emission lines. This sample serves as a comparison at low luminosity for both optical and UV spectral ranges. Similar to the HEMS sample, I have estimated the main physical parameters for the FOS sample discussed throughout this thesis using the same methodology applied to the ISAAC sample.

The spectroscopic analysis

Emission lines are characterised both through a parametrisation of the line profiles by measuring centroid velocities and widths at different fractional intensity, and by using multicomponent non-linear fitting routines as the `specfit` tool in IRAF (Kriss 1994), in which I include a power law to account

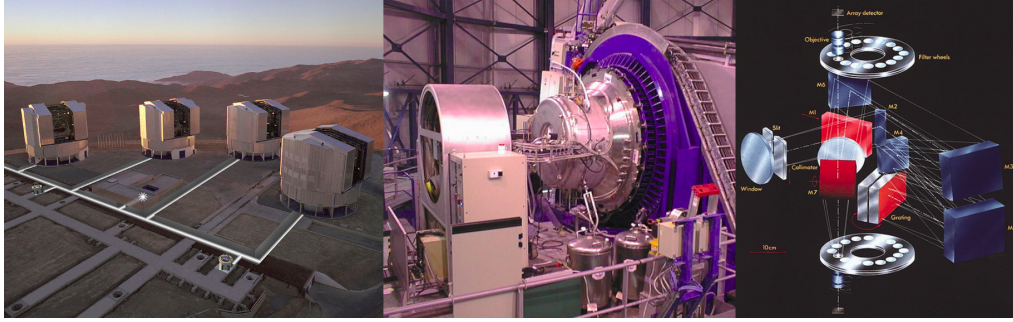


Fig. 1.12: From left to right: VLT telescopes, the ISAAC spectrograph, and the optical layout of the instrument.

for the source continuum, Fe II and/or Fe III semi-empirical templates as well as the emission line components.

In the models, I have considered three main components for the broad emission lines: (1) a *broad* (BC), (2) a *blueshifted* (BLUE), and (3) a *very broad* component (VBC). In addition, I have included a *narrower* component (NC) superimposed to the broad emission line profile. Narrow emission lines are usually well-fitted with only an NC, unless the line (e.g., [O III]) exhibits a blueward asymmetry, case in which we include a *semi-broad* component to account for this blueshift (outflowing component). A complete description of each of these components, the fitting procedures, and the analysis can be found especially in Chapter 2.

1.4.2 Outline

The overarching goal of this thesis is to investigate the interplay between AGN feedback, radio-loudness, and their combined effect on the quasar Main Sequence, particularly in a high-redshift context where the outflow properties are expected to exhibit their most extreme effects. To achieve this, a study focused on feedback mechanisms originating from both the BLR and NLR utilising optical and UV high-ionisation lines as tracers has been performed and a comprehensive analysis of the differences between RL and RQ sources has been conducted across a wide range of redshift, including a comparison sample at relatively low redshift. The thesis is divided into four parts, including different chapters, as follows.

Part I of this thesis is primarily focused on the study of the optical and UV spectral ranges of 22 high-redshift and high-luminosity quasars under the framework of the 4DE1 and its Main Sequence. In Chapter 2, I explore the many trends found in the Main Sequence of quasars at high redshift. I present new observations from the ESO-VLT ISAAC instrument for 22 sources and combine it with previous spectra from the literature to cover the optical and UV spectral ranges. Quantitative parametrisation and decomposition of emission line profiles are conducted using multicomponent fitting routines, taking into consideration emission lines such as $H\beta + [O III]\lambda 5007$, $Si IV\lambda 1397 + O IV]\lambda 1402$, $C IV\lambda 1549 + He II\lambda 1640$, and the 1900 Å blend. A detailed analysis of outflows provided from the BLR and NLR has been conducted focusing mainly in the emission of C IV and [O III]. Chapter 3 is centred on how to properly identify an outflow component not only in

[O III] but also in $H\beta$ in spectra of quasars with moderate accretion. Both Chapters 2 and 3 describe the spectroscopic analysis methodology followed throughout this thesis.

In Part II, the discussion is dedicated mainly to the effect of radio emission and AGN feedback processes in the quasar Main Sequence. Chapter 4 performs a comparison between one RQ and one RL quasar from the ISAAC sample that present the same Population classification in the quasar MS but present some differences in both optical and UV spectral ranges. In Chapter 5, I introduce 10 new sources that complete the ISAAC sample. The discussion about the optical and UV spectroscopic differences between RQ and RL sources is therefore expanded to the complete sample. Additionally, I also compare our high-redshift sample (ISAAC+HEMS) with the low-redshift data from the FOS sample and discuss the roles of the accretion rate and feedback on the spectra of quasars. An estimate of the main outflow parameters (i.e, outflow mass rate, kinetic power, and thrust) has also been performed for the [O III] and C IV outflows in both high- and low- z contexts.

Part III of this thesis investigates the potential use of intermediate ionisation UV broad emission lines as reliable virial broadening estimators, which is essential to derive black hole masses for high redshift quasars, when $H\beta$ is not observed in the optical. Specifically, we focus on deriving scaling laws using the C III] λ 1909 line and the Al III] λ 1860 doublet across a wide range of redshift. These particular lines are chosen because they are not affected by the strong outflows, often observed in the C IV] λ 1549 broad line, and their widths exhibit a significant correlation with the width of the $H\beta$ line, which is a well-established broadening estimator at low redshift. This approach is particularly applicable to Population A quasars, which are typically characterised by intermediate and high-accretion rates.

In the final section, Part IV, we conducted an analysis of the metallicity and physical conditions of the BLR in quasars along the Main Sequence, by comparing photoionisation models with sensitive diagnostic ratios of measured emission lines. Our study suggests a gradient of metallicity across different quasar populations, going from Pop. B with sub-solar values to Pop. A presenting super-solar metallicities in the most extreme cases. By examining these metallicity gradients, we gain a better understanding of the underlying mechanisms driving quasar evolution and the diverse pathways they may follow from their formation to their current state.

Parts III and IV present additional works related to the main topic of the thesis. The study about the chemical abundances and physical conditions of the BLR and the region where outflows originate, presented in Chapters 7 and 8 of Part IV, are the first preliminary results that we plan to study and apply in more detail for the ISAAC and HEMS samples in future works. Additional materials from the chapters are presented in the Appendix of this thesis.

Part I

Trends of high-redshift quasars along the Main Sequence

Over the years, many trends were observed in the quasar Main Sequence at low redshift, particularly in the optical and UV spectral ranges. As we gather more and more data from earlier epochs of the Universe, a key question arises: do the patterns noticed in the low-redshift objects also apply for those at higher redshift? This first part of the thesis aims to address this question through the study presented in two published papers.

The first paper focuses on the analysis of the initial 22 sources from the ISAAC sample within the context of the quasar Main Sequence. Specifically, interline comparisons are performed with the goal of highlight spectral similarities and discrepancies found between the optical and UV ranges at high redshift. This study also serves as a guide light to the quasar spectral decomposition applied throughout this thesis, as it establishes the methodology followed in the subsequent chapters.

The second paper is also related to the spectroscopic analysis, particularly focusing on the challenges associated with identifying outflow signatures within the spectra of quasars.

HIGH-REDSHIFT QUASARS ALONG THE MAIN SEQUENCE

2

Chapter based on the article published in *Astronomy & Astrophysics* by A. Deconto-Machado et al., volume 669, id. A83, 42 pages, January 2023. DOI: 10.1051/0004-6361/202243801

Abstract

The 4D Eigenvector 1 empirical formalism (4DE1) and its main sequence (MS) for quasars has emerged as a powerful tool for organising the diversity among quasar populations, as several key observational measures and physical parameters are systematically changing along it. Trends revealed by 4DE1 are very well established to explain all the diverse characteristics seen in low-redshift quasar samples. Nevertheless, the situation is far less clear when dealing with high-luminosity and high-redshift sources. Here, we aim to evaluate the behaviour of our sample of 22 quasars at high redshift ($2.2 \leq z \leq 3.7$) and high luminosity ($47.39 \leq L_{\text{bol}} \leq 48.36$) in the context of the 4DE1. Our approach involves studying quasar physics through a spectroscopic exploration of UV and optical emission line diagnostics. We used new observations from the ISAAC instrument at ESO-VLT and primarily from the SDSS to cover the optical and the UV rest-frames, respectively. The emission lines were characterised both via a quantitative parametrisation of the line profiles and a decomposition of the emission line profiles using multicomponent fitting routines. We provide spectrophotometric properties and line profile measurements for $\text{H}\beta + [\text{O III}]\lambda 5007$, as well as $\text{Si IV}\lambda 1397 + \text{O IV}]\lambda 1402$, $\text{C IV}\lambda 1549 + \text{He II}\lambda 1640$, and the 1900 \AA blend (including Al III , $\text{Si III}]\lambda 1892$, and $\text{C III}]\lambda 1909$). For six out of the 22 objects, a significantly blueshifted component on the $\text{H}\beta$ profile is present. In 14 out of 22 cases, an $\text{H}\beta$ outflowing component associated with $[\text{O III}]\lambda 5007$ is detected. The majority of $[\text{O III}]\lambda 5007$ emission line profiles show blueshifted velocities higher than 250 km s^{-1} . We find extremely broad $[\text{O III}]\lambda 5007$ emission that is comparable to the width of $\text{H}\beta$ broad profile in some highly accreting quasars. The $[\text{O III}]\lambda 5007$ and $\text{C IV}\lambda 1549$ blueshifts show very high amplitudes and a high degree of correlation. The line widths and shifts are correlated for both $[\text{O III}]\lambda 5007$ and $\text{C IV}\lambda 1549$, suggesting that emission from outflowing gas is providing a substantial broadening effect to both lines. Otherwise, the links between $\text{C IV}\lambda 1549$ centroid velocity at half intensity ($c(1/2)$), Eddington ratio (L/L_{Edd}), and bolometric luminosity are found to be in agreement with previous

studies of high-luminosity quasars. Our analysis suggests that the behaviour of quasars of very high luminosity all along the main sequence is strongly affected by powerful outflows involving a broad range of spatial scales. The main sequence correlations remain valid at high redshift and high luminosity even if a systematic increase in line width is observed. Scaling laws based on UV Al III λ 1860 and H β emission lines are equally reliable estimators of M_{BH} .

2.1 Introduction

The nature of the many differences seen in quasar spectra has been a key topic of interest in recent years and it continues to be a topic of active discussion. One of the first successful attempts to define the systematic trends of quasar spectra was carried out by Boroson & Green (1992). These authors organised the relations between the optical and radio spectral ranges into an Eigenvector 1 scheme based on studies of the 80 quasars from the Palomar-Green sample (Schmidt & Green 1983) and using a principal component analysis (PCA). This scheme primarily considers the anti-correlation seen between the optical Fe II strength and peak intensity of the [O III] λ 5007 emission line as well as the full width at half maximum (FWHM) of the broad component of H β (H β_{BC} , typically $\gtrsim 4000 \text{ km s}^{-1}$). A more overarching possibility for the arrangement of the individual characteristics found in the quasar spectra has been suggested by Sulentic et al. (2000a), taking into account several observational measures in the optical, UV, and X-ray spectral ranges as well as physical parameters such as outflow relevance and accretion mode. According to those authors, it is possible to organise the quasar diversity into a fourth dimensional (4D) correlation space known as Eigenvector 1 (4DE1).

One of the four key parameters considered by the 4DE1 is the FWHM of the Hydrogen H β broad component. Since the emission of Balmer lines like H β are thought to be arising from the quasar broad line region (BLR), this parameter can be used to measure black hole mass assuming gas to be virialised (Collin-Souffrin & Lasota 1988; Small & Blandford 1992; Marziani et al. 1996; McLure & Jarvis 2002; McLure & Dunlop 2004; Sulentic et al. 2006b; Assef et al. 2011; Shen 2013; Gaskell & Harrington 2018, and references therein). In addition, 4DE1 also considers the ratio between the intensities of the blend of Fe II emission lines at 4570Å and H β ($R_{\text{FeII}} = I(\text{Fe II } \lambda 4570)/I(\text{H}\beta)$), which can be used for the estimation of physical properties of the BLR such as the ionisation state, the electron density, and the column density of the ionised gas (Ferland et al. 2009; Panda et al. 2020).

The other parameters of the 4DE1 are the blueshifts of high-ionisation lines (HILs) with respect to the quasar systemic redshift and the soft X-ray photon index (Γ_{soft}). Examples of HILs include the C IV λ 1549 emission line and they are considered a strong diagnostic of outflows; there is also some evidence that the optical and UV properties are related (Bachev et al. 2004; Du et al. 2016b; Śniegowska et al. 2020). Similarly, the equivalent width of the optical Fe II contribution is seen as a measure of the thermal emission from the accretion disc (Singh et al. 1985; Walter & Fink 1993). The R_{FeII} , soft X-ray photon index, and the line width of H β are also significantly correlated among themselves (Wang et al. 1996; Boller et al. 1996; Sulentic et al. 2000c).

Explorations of the distribution of low-redshift ($z \lesssim 0.8$) quasars in the optical plane of the 4DE1 – defined by $\text{FWHM}(\text{H}\beta_{\text{BC}})$ versus R_{FeII} and referred to as the main sequence (MS) of quasars – have given rise to the identification of two main populations with very significant differences among their spectra (Zamfir et al. 2010). Population A quasars show low FWHM (usually $\leq 4000 \text{ km s}^{-1}$) and a wide range of R_{FeII} , while Population B sources present a very wide range of $\text{FWHM}(\text{H}\beta_{\text{BC}})$ but usually small R_{FeII} (≤ 1). Marziani et al. (2018) summarised more than 15 years of discussion on the empirical parametrisation of the quasar properties and their trends as well as the ways physical parameters are related to the accretion rate and feedback seem to be changing along the MS, going from quasars with low Fe II emission and high black hole mass ($\gtrsim 10^9 M_{\odot}$, Pop. B) to the extreme Pop. A, xA (Martínez-Aldama et al. 2018), with strong Fe II emission ($R_{\text{FeII}} > 1$) and strong blueshifts in HILs such as $\text{CIV}\lambda 1549$, indicating strong wind effects on the quasars (i.e. ‘wind-dominated’ sources, Richards et al. 2011).

The Eddington ratio as well as the orientation effect are seen as key properties in the MS context (Sulentic et al. 2000a; Marziani et al. 2001; Boroson 2002; Shen & Ho 2014; Sun & Shen 2015). The R_{FeII} parameter along with the $\text{H}\beta_{\text{BC}}$ FWHM can be associated with L/L_{Edd} (Marziani et al. 2001; Panda et al. 2019). Low values of the L/L_{Edd} (typically $\lesssim 0.2$) are usually found in Pop. B sources, while Pop. A sources are found to be high accretors (in extreme cases reaching $L/L_{\text{Edd}} \gtrsim 1$). Consequently, sources with the highest R_{FeII} are thought to be the ones with the highest Eddington ratios. Consistent results were also reported by Du et al. (2016b), denoting the strong correlation found between the Eddington ratio, shape of the broad profile of the $\text{H}\beta$ emission line, and the flux ratio $I(\text{H}\beta)/I(\text{Fe II})$ as the fundamental plane of accreting black holes. According to these authors, the shape of both Lorentzian and Gaussian profiles may reveal details on the BLR dynamic and may be different depending on the Eddington ratio (c.f. Collin et al. 2006; Kollatschny & Zetzl 2011). Regarding the width of the emission line profiles, the broadest sources that are more Gaussian-like due to a redward asymmetry can be seen as the sum of two Gaussians (usually a BC and a very broad component, VBC) and the sources that present a VBC, usually with $\text{FWHM} > 7000 \text{ km s}^{-1}$, are the ones displaying lower Eddington ratios (Marziani et al. 2003b, 2019). However, the line width is believed to be highly influenced by source orientation and the Eddington ratio (Marziani et al. 2001; McLure & Jarvis 2002; Zamfir et al. 2008; Panda et al. 2019). Since it is likely that $\text{H}\beta$ lines are emitted by flattened systems, orientation may affect the $\text{FWHM}(\text{H}\beta)$, going from broader (bigger θ , with θ indicating the inclination of the source with respect to the line-of-sight) to narrower (smaller θ) profiles.

Of special relevance is also the issue of sources that are radio-loud. Only about 10% of quasars are strong emitters in radio. Zamfir et al. (2010) analysed ~ 470 low-redshift ($z < 0.8$) quasars from the SDSS DR5 (Adelman-McCarthy et al. 2007) and found that in general the radio-loud sources are located in the Pop. B domain of the MS, while the radio-quiet are found in both populations. The location of the radio-loud (RL) quasars seems to indicate different properties with respect to a large fraction of the radio-quiet (RQ) sources. However, the fact that the RQs are distributed in both populations (A and B) complicates the interpretation. For instance, radio-loud and a large fraction of radio-quiet quasars both present strong asymmetries towards red wavelengths in the emission line

profiles (Marziani et al. 1996; Punsly 2010). The paucity of radio-loud Pop. A sources at low- z implies that the Eddington ratio and the black hole mass distributions are different for radio-quiet and radio-loud sources matched in redshift and luminosity (Woo & Urry 2002; Marziani et al. 2003b; Fraix-Burnet et al. 2017b). In the two cases, the radio-quiet quasars are the ones that usually present smaller masses and larger Eddington ratio. This is not necessarily true for sources at high redshift (Sikora et al. 2007; Marinello et al. 2020a; Diana et al. 2022).

The 4DE1 formalism and especially the MS represent the most effective way to distinguish quasars according to their BLR structural and kinematic differences. It has been extensively analysed in samples at $z < 0.8$ (e.g. Zamfir et al. 2010; Negrete et al. 2018). Trends among the optical plane of the 4DE1 and the L/L_{Edd} (e.g. sources with strong L/L_{Edd} are usually found to have strong R_{FeII}) are also seen in high-luminosity high- and intermediate-redshift sources ($z \gtrsim 2$ and $L \gtrsim 47$, Yuan & Wills 2003; Netzer et al. 2004; Sulentic et al. 2004). However, high- z quasar samples that have been studied including NIR observations of the $H\beta$ spectral range are relatively few (e.g. McIntosh et al. 1999; Capellupo et al. 2015; Coatman et al. 2016; Bischetti et al. 2017; Vietri et al. 2018, 2020; Matthews et al. 2021). One of the studies of high- z quasars under this context was performed by Marziani et al. (2009, hereafter M09). These authors analysed the optical region of 53 Hamburg-ESO sources in a redshift range of $z \approx 0.9 - 3.0$ using VLT ISAAC spectra (Sulentic et al. 2004, 2006b, M09). Additional UV spectra were obtained for some of these sources and the results are reported by Sulentic et al. (2017, hereafter S17). The authors found that both Pop. A and Pop. B quasars present evidences of significant outflows at high redshift while at low z only Pop. A sources tend to show strong contribution of outflowing gas. Extreme Pop. A quasars (xA) in a redshift range of $z = 2.0 - 2.9$ and with an averaged bolometric luminosity of $\log L \sim 47$ [erg s^{-1}] have been analysed in details on the UV region by Martínez-Aldama et al. (2018) using GTC spectra. These authors found that the xA sources at high z share the same characteristics of the sources at low redshift, albeit with the higher outflow velocities (reaching values of $\sim 4000 \text{ km s}^{-1}$).

In this chapter, we report new observations from VLT/ISAAC for 22 high-redshift and high-luminosity quasars, along with a data analysis of the UV and optical regions along the main sequence and discussion. Our goal is to improve the sampling of the MS and the understanding of high- z , high-luminosity quasars. To do so, we take advantage of previous high- and low- z samples and perform a comparison between the different data under the 4DE1 context. Details on the sample and on the observations are presented in §2.2 and §2.3. The procedures and the approach followed during the line decomposition are presented in detail on §2.4. Results on the complete analysis of both optical ($H\beta + [\text{O III}]\lambda 5007$) and UV ($\text{Si IV}\lambda 1392$, $\text{C IV}\lambda 1549$, and the 1900 \AA blend) regions are reported in §2.5. Additional discussions are provided in §2.6. In §2.7, we list the main conclusions of our work.

Table 2.1: Source identification.

Source (1)	RA (J2000) (2)	DEC (J2000) (3)	z (4)	δz (5)	$m^{(b)}$ (6)	Band (7)	M_i (8)	m_{VCV10} (9)	$f_{\text{Radio}} \text{ (mJy)}^{(h)}$ (10)	Survey (11)	Radio Class. (12)
HE 0001-2340	00 03 44.95	-23 23 54.7	2.2651 ^(a)	0.0036	14.78	H	-29.68	16.70 ^(c)	< 2.70	NVSS	RQ
[HB89] 0029+073	00 32 18.37	+07 38 32.4	3.2798 ^(a)	0.0055	15.12	K	-29.26	17.44 ^(d)	< 0.86	FIRST	RQ
CTQ 0408	00 41 31.49	-49 36 12.4	3.2540	0.0048	14.02	K	-29.86	16.10 ^(d)	7.26	SUMSS	RI
SDSSJ005700.18+143737.7	00 57 00.19	+14 37 37.7	2.6638	0.0023	15.70	H	-29.06	17.96 ^(e)	< 2.70	NVSS	RQ
H 0055-2659	00 57 57.92	-26 43 14.1	3.6599	0.0062	15.50	K	-30.74	17.47 ^(f)	< 2.70	NVSS	RQ
SDSSJ114358.52+052444.9	11 43 58.52	+05 24 44.9	2.5703	0.0038	15.54	H	-29.47	17.27 ^(e)	< 0.96	FIRST	RQ
SDSSJ115954.33+201921.1	11 59 54.33	+20 19 21.1	3.4277	0.0068	15.13	K	-29.92	17.92 ^(e)	< 0.97	FIRST	RQ
SDSSJ120147.90+120630.2	12 01 47.91	+12 06 30.2	3.5136	0.0063	14.60	K	-29.76	18.16 ^(e)	< 0.98	FIRST	RQ
SDSSJ132012.33+142037.1	13 20 12.34	+14 20 37.1	2.5356	0.0023	15.52	H	-28.87	17.82 ^(e)	< 0.98	FIRST	RQ
SDSSJ135831.78+050522.8	13 58 31.79	+05 05 22.7	2.4627	0.0020	15.40	H	-29.21	17.33 ^(e)	< 0.94	FIRST	RQ
Q 1410+096	14 13 21.05	+09 22 04.8	3.3240	0.0029	14.83	K	-29.44	17.80 ^(g)	< 0.99	FIRST	RQ
SDSSJ141546.24+112943.4	14 15 46.23	+11 29 43.4	2.5531	0.0043	14.53	H	-29.40	17.23 ^(e)	7.80	NVSS	RI
B1422+231	14 24 38.10	+22 56 01.0	3.6287	0.0031	12.66	K	-29.85	15.84 ^(e)	273.42	FIRST	RL
SDSSJ153830.55+085517.0	15 38 30.55	+08 55 17.1	3.5554	0.0060	14.72	K	-30.07	17.98 ^(e)	< 1.02	FIRST	RQ
SDSSJ161458.33+144836.9	16 14 58.34	+14 48 36.9	2.5698	0.0022	15.23	H	-29.41	17.43 ^(e)	< 0.94	FIRST	RQ
PKS 1937-101	19 39 57.30	-10 02 41.0	3.7908	0.0032	13.81	K	-30.40	17.00 ^(g)	838.30	NVSS	RL
PKS 2000-330	20 02 24.00	-32 51 47.0	3.7899	0.0033	15.15	K	-30.99	17.30 ^(g)	446.00	NVSS	RL
SDSSJ210524.49+000407.3	21 05 24.47	+00 04 07.3	2.3445	0.0020	14.59	H	-29.96	16.98 ^(e)	3.20	NVSS	RI
SDSSJ210831.56-063022.5	21 08 31.56	-06 30 22.6	2.3759 ^(a)	0.0016	15.77	H	-29.11	17.41 ^(e)	< 1.18	FIRST	RQ
SDSSJ212329.46-005052.9	21 23 29.46	-00 50 52.9	2.2800	0.0017	14.61	H	-29.76	16.62 ^(e)	< 0.96	FIRST	RQ
PKS 2126-15	21 29 12.10	-15 38 42.0	3.2987	0.0042	14.22	K	-29.88	17.00 ^(g)	589.70	NVSS	RL
SDSSJ235808.54+012507.2	23 58 08.62	+01 24 34.8	3.4009	0.0029	14.84	K	-29.58	17.50 ^(d)	< 0.96	FIRST	RQ

Notes. ^(a) Redshift estimation based on the [O III] λ 5007. ^(b) 2MASS magnitude. ^(c) m_{O} . ^(d) m_{R} . ^(e) m_{B} . ^(f) Photographic m_{B} . ^(g) m_{V} . ^(h) Values with < are the upper limits.

2.2 The sample

Our sample consists of 22 quasars with high redshift, going from $z = 2.2$ to $z = 3.7$, and with high luminosity ($47.39 \leq \log L_{\text{bol}} \leq 48.36$ [erg s⁻¹]), including both radio-loud and radio-quiet sources that were observed under the ESO programmes 083.B-0273(A) and 085.B-0162(A). These sources were selected from the Hamburg-ESO survey (HE, [Wisotzki et al. 2000](#)), which consists of a flux-limited ($m_{\text{B}} \approx 17.5$), colour-selected survey with a redshift range $0 \lesssim z \lesssim 3.2$. Our sample covers a redshift that allows for the detection and observation of the H β + [O III] λ 5007 region through the transparent window in the near-infrared with the ISAAC spectrograph at VLT ([Sulentic et al. 2006b, 2017](#)). There is also a cut in δ at +25 degrees due to the geographic location of the telescope. Table 2.1 presents the main properties of our sample, reporting the source identification according to the different catalogues (col. 1); right ascension and declination at J2000 coordinates (cols. 2 and 3, respectively); redshift estimated as explained in §2.2.1 (col. 4); redshift uncertainties (col. 5); the H - or K -band (depending on the range of the spectrum) apparent magnitude m_{H} or m_{K} from the 2-MASS catalogue (col. 6); the respective band (H or K, col. 7); the i -band absolute magnitude M_i (col. 8) estimated for our data; the apparent magnitude from [Véron-Cetty & Véron \(2010\)](#) (col. 9); the radio flux in mJy (col. 10) in the frequency of the survey listed in col. 11; radio classification according [Ganci et al. \(2019\)](#) is shown in col. 12 and explained in §2.3.3. The k -correction used is the one available on [Richards et al. \(2006\)](#) for sources with similar redshift and the galactic extinction were collected from the DR16 catalogue ([Lyke et al. 2020](#)). The luminosity distance was computed from the redshift using the approximation of [Sulentic et al. \(2006b\)](#), valid for $\Omega_{\text{M}} = 0.3$, $\Omega_{\Lambda} = 0.7$, and $H_0 = 70$ km s⁻¹ Mpc⁻¹.

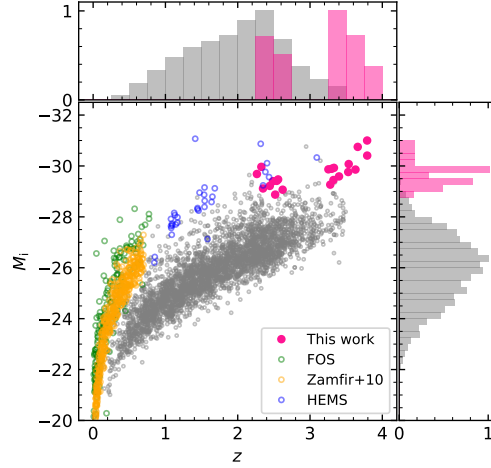


Fig. 2.1: Location of the complete sample in the Hubble diagram (pink spots). Gray dots represent a random subsample of the DR16 catalogue from Lyke et al. (2020) and green, yellow, and blue dots represent the comparison samples defined in §2.2.2.

For all sources, we have computed synthetic magnitudes H or K from our flux-calibrated spectra, and we have compared them with the 2MASS H - and K -band apparent magnitudes. In cases in which the difference between our m synthetic magnitudes and the 2MASS catalogue magnitudes is higher than 0.5 mag we use the m from 2MASS (these sources are identified in Table 2.1). Also, in one very special source (B1422+231) a magnification correction is applied lowering the flux by a factor of 6.6, which leads to a change in the magnitude, since this source is a gravitationally lensed quasar with four images (Patnaik et al. (1992); Assef et al. (2011); see Appendix A.1 for notes on individual objects). Apart from the well-known lensed quasar B1422+231, our sample includes other quasars known or suspected to undergo micro-lensing: SDSSJ141546.24+112943.4 (Sluse et al. 2012; Takahashi & Inoue 2014) and some candidates, as [HB89] 0029+073 (Jaunsen et al. 1995), but we did not apply any magnitude correction for lensing on these sources.

2.2.1 Redshift estimations and sample location in the Hubble diagram

Redshift measurements were based on the $H\beta$ emission line profile and were obtained from the observed wavelength of the $H\beta$ narrow component ($\text{FWHM} \lesssim 1000 \text{ km s}^{-1}$). The values are reported in Table 2.1. In the case of HE 0001-2340 and SDSSJ210831.56-063022.5 the redshift was estimated through the $[\text{O III}]\lambda 5007$ emission line, due to the difficulty of isolating a narrow component of $H\beta$. Before performing the spectral analysis, as described in §2.4, both optical and UV spectra are set at rest-frame using the IRAF task dopcor.

Figure 2.1 shows the location of the objects of the sample (pink spots) in the i -band absolute magnitude M_i versus redshift plane. Our sample as well as the comparison samples (defined in §2.2.2) are located at the high end of the luminosity distribution when compared with the SDSS DR16 data (grey spots, Lyke et al. 2020). Moreover, some of our sources are well located within the region with the highest values of the SDSS redshift distribution for quasars.

2.2.2 Comparison samples

We chose comparison samples that include high and low redshifts, as well as high- and low-luminosity sources that have been studied in the recent literature, as follows:

Low- z SDSS sources: Zamfir et al. (2008) and Zamfir et al. (2010) analysed ~ 470 low-redshift ($z \leq 0.7$) quasars with high signal-to-noise ($S/N \sim 29$) ratio optical spectra observed with the Sloan Digital Sky Survey data release (DR) 5 (Adelman-McCarthy et al. 2007), including both radio-loud and radio-quiet sources. This sample covers a wide range of bolometric luminosity, going from $\log L_{\text{bol}} = 10^{43}$ to $\log L_{\text{bol}} = 10^{47}$ erg s $^{-1}$.

High-luminosity Hamburg-ESO sample (hereafter, HEMS): Sulentic et al. (2004, 2006b) and M09 obtained, using the VLT-ISAAC camera, $H\beta$ region measurements for a sample of 53 high-redshift high-luminosity objects, selected from the Hamburg-ESO survey. The sources are extremely luminous ($47 \lesssim L_{\text{bol}} \lesssim 48$) and are located in a redshift range of $0.9 \lesssim z \lesssim 3.1$. We use these data as comparison sample at high L , for both $H\beta$ and [O III] lines. For the UV region we use the results provided by S17, who studied 28 quasars of the previous sample, and from which they obtained C IV $\lambda 1549$ observations with the VLT and TNG telescopes. The redshift range of the HEMS is $1.4 \leq z \leq 3.1$ and a typical bolometric luminosity is $L_{\text{bol}} \gtrsim 10^{47.5}$ erg s $^{-1}$. The location of the HEMS in the Hubble diagram is similar to the one of our data (Fig. 2.1) in terms of absolute magnitudes, although a large fraction of HE sources displays $1 \lesssim z \lesssim 2$.

Low-luminosity FOS data: The low-luminosity Faint Object Spectrograph (FOS) comparison sample was selected from Sulentic et al. (2007a, S07 from now on), where the authors analysed the C IV line parameters. Marziani et al. (2003b, hereafter M03) provide measurements on the $H\beta$ emission line for most sources in this sample. The typical bolometric luminosity of this sample is $\log L_{\text{bol}} \sim 45.6$ [erg s $^{-1}$] and a redshift range $z \leq 0.5$.

2.3 Observations and data

2.3.1 Near-infrared observations and data reduction

Spectra were taken in service mode in 2009 and 2010, with the infrared spectrometer ISAAC, mounted at the Nasmyth B focus of VLT-U1 (Antu) until August 2009, and later at the Nasmyth A focus of VLT-U3 (Melipal) at the ESO Paranal Observatory. Table 2.2 summarises the NIR observations, listing the date of observation (col. 2), used grating (col. 3), individual detector integration time (DIT) in seconds (col. 4), number of exposures with single exposure time equal to DIT (col. 5), range of air mass of the observations (col. 6), and the averaged seeing (col. 7). When the source was observed more than once (HE 0001-2340, [HB89] 0029+073, CTQ 0408, SDSSJ161458.33+144836.9, SDSSJ212329.46-005052.9, and PKS 2126-15), we combine the individual spectra to obtain a median weighted final spectrum for the analysis. Spectral resolutions are $\text{FWHM} = 16 \text{ \AA}$ in the H band and $\text{FWHM} = 22 \text{ \AA}$ in the K band.

Table 2.2: Log of optical observations with VLT/ISAAC.

Source	Date obs. (start)	Band	DIT (s)	N _{exp}	Airmass start-end	Averaged seeing
(1)	(2)	(3)	(4)	(5)	(6)	(7)
HE 0001-2340	2010-07-06	sH	180	12	1.05-1.02	1.03
	2010-07-24	sH	180	12	1.03-1.01	0.55
	2010-08-04	sH	180	12	1.06-1.12	1.44
[HB89] 0029+073	2009-09-03	sK	180	20	1.43-1.25	1.08
	2010-07-08	sK	180	20	1.25-1.19	0.49
	2010-08-04	sK	180	20	1.19-1.18	1.31
CTQ 0408	2009-07-09	sK	180	8	1.11-1.12	0.51
	2009-08-31	sK	180	8	1.11-1.12	3.05
SDSSJ005700.18+143737.7	2009-09-04	sH	180	28	1.44-1.98	1.99
H 0055-2659	2009-09-02	sK	180	40	1.01-1.23	1.25
SDSSJ114358.52+052444.9	2009-07-08	sH	180	20	1.34-1.67	0.83
SDSSJ115954.33+201921.1	2010-04-05	sK	175	24	2.35-1.69	1.08
SDSSJ120147.90+120630.2	2010-04-15	sK	180	20	1.92-1.49	1.23
SDSSJ132012.33+142037.1	2009-05-04	sH	180	24	1.36-1.28	1.37
SDSSJ135831.78+050522.8	2010-04-18	sH	180	20	1.23-1.18	0.73
Q 1410+096	2010-04-20	sK	180	28	1.45-1.23	0.83
SDSSJ141546.24+112943.4	2009-05-04	sH	180	20	1.24-1.26	0.50
B1422+231	2009-04-13	sK	180	12	1.50-1.48	0.98
SDSSJ153830.55+085517.0	2010-04-05	sK	180	20	1.20-1.24	1.14
SDSSJ161458.33+144836.9	2009-07-08	sH	180	20	1.33-1.30	1.35
	2009-09-22	sH	180	20	1.73-2.05	2.24
PKS 1937-101	2009-09-03	sK	180	12	1.13-1.23	1.07
PKS 2000-330	2009-08-31	sK	180	20	1.43-1.89	2.03
SDSSJ210524.49+000407.3	2010-07-23	sH	180	12	1.29-1.45	1.80
SDSSJ210831.56-063022.5	2010-06-19	sH	175	24	1.07-1.18	0.93
SDSSJ212329.46-005052.9	2010-07-08	sH	180	12	1.12-1.18	0.48
	2010-07-24	sH	180	12	1.41-1.27	0.90
PKS 2126-15	2009-09-01	sK	180	12	1.84-2.36	1.41
	2010-06-09	sK	180	16	1.26-1.12	1.07
SDSSJ235808.54+012507.2	2010-06-21	sK	180	20	1.25-1.13	1.01

Reductions were performed using standard IRAF routines. Several spectra for each source were taken, nodding the telescope between two positions (nodding amplitude = 20"). Each obtained frame was divided by the flat field provided by the ESO automated reduction pipeline. The 1D spectra were extracted using the IRAF program 'apall'. Cosmic ray hits were eliminated by interpolation using a median filter, comparing the affected spectrum with the other spectra of the same source.

For each position along the slit, a 1D xenon/argon arc spectrum was extracted from the calibration lamp frame, using the same extraction parameters as the corresponding target spectrum. The wavelength calibration was well modeled by 3rd order Chebyshev polynomial fits to the positions of 15-30 lines, with rms residuals of 0.3 Å in sH and 0.6 Å in sK. The wavelength calibration is usually affected by a small 0-order offset caused by grism and telescope movement, because the arc lamp frames were obtained in the daytime. A correction for these shifts was obtained by measuring the centroids of 2–3 OH sky against the arc calibration and calculating the average difference, which reached at most 2-3 pixels in either direction. Once matched with the corresponding arc calibrations, the individual spectra of each source were rebinned to a common linear wavelength scale and stacked.

The spectra of the atmospheric standard stars were extracted and wavelength-calibrated in the same way. All clearly identifiable stellar features (H and He I absorption lines) were eliminated

Table 2.3: UV spectra information.

Source	UV Spect.	Comments
(1)	(2)	(3)
SDSSJ005700.18+143737.7	BOSS	
SDSSJ114358.52+052444.9	BOSS	
SDSSJ115954.33+201921.1	SDSS	
SDSSJ120147.90+120630.2	BOSS	
SDSSJ132012.33+142037.1	BOSS	
SDSSJ135831.78+050522.8	BOSS	
Q 1410+096	SDSS	BAL
SDSSJ141546.24+112943.4	SDSS	BAL
SDSSJ153830.55+085517.0	BOSS	BAL ^(a)
SDSSJ161458.33+144836.9	BOSS	
PKS 2000-330	Barthel et al. (1990)	
SDSSJ210524.49+000407.3	SDSS	BAL
SDSSJ210831.56-063022.5	SDSS	
SDSSJ212329.46-005052.9	BOSS	
SDSSJ235808.54+012507.2	BOSS	

Notes. ^(a) In this case, there is only a small but significant absorption close to Si IV λ 1397 and do not affect the other UV emission lines that we are considering in the fittings.

from the stellar spectra by spline interpolation of the surrounding continuum intervals. Each target spectrum was then divided by its corresponding standard star spectrum in order to correct for the atmospheric absorption features. This was achieved with the IRAF routine ‘telluric’, which allows to optimise the correction with slight adjustments in shift and scaling of the standard spectrum. The correct flux calibration of each spectrum was achieved by scaling it according to the magnitude of the standard star and to the ratio of the respective DITs. Because the seeing often exceeded the width of the slit, significant light loss occurred and, therefore, the absolute flux scale of the spectra is not to be considered as accurate. However, in this long-wavelength range we consider the light losses to be independent of wavelength (i.e. we assume that differential atmospheric refraction is negligible) and thus they are not expected to affect the relative calibration of the spectra. We carried out an a posteriori evaluation of the absolute flux calibration uncertainty performing a comparison between the H/K -band magnitudes estimated by convolving the H/K filter with the observed spectrum and the H/K magnitudes in NED. The differences are smaller than 0.5 mag, except for SDSSJ132012.33+142037.1, SDSSJ141546.24+112943.4, and SDSSJ153830.55+085517.0, where a correction factor $\sim 0.880 \pm 0.176$ mag was applied.

2.3.2 UV

We found useful UV spectra (i.e. those including at least one of the three UV regions of our interest) for the 15/22 sources that are listed in Table 2.3, where we also list in col. 2 the database and reference from which each spectrum was obtained and then the broad absorption line (BAL) quasars in col. 3. We report the BAL sources as the analysis of the region in which the broad absorptions are located should be taken with care, once it demands the addition of absorption components in the fitting routine. The other seven quasars do not have useful UV spectra, either because they are old spectra that are

not digitally available and have low S/N not suitable for accurate profile fitting, or because they do not include any of the three UV regions we want to analyse (Si IV λ 1397+O IV λ 1402, CIV λ 1549+He II λ 1640, and the 1900 Å blend). For the UV spectral range (observed in the optical domain at the redshift of this sample), the spectra were collected mainly from the SDSS DR16 database (Ahumada et al. 2020, and references therein). For one source (PKS 2000-330), the UV spectrum was digitalised from Barthel et al. (1990). Four out of the 22 quasars (Q 1410+096, SDSSJ141546.24+112943.4, SDSSJ153830.55+085517.0, and SDSSJ210524.49+000407.3) are classified as BAL quasars, due to strong absorption lines (Gibson et al. 2009; Scaringi et al. 2009; Allen et al. 2011; Welling et al. 2014; Bruni et al. 2019; Yi et al. 2020).

2.3.3 Radio data

The radio fluxes presented in Table 2.1 were collected from the 1.4-GHz NRAO VLA Sky Survey (NVSS, Condon et al. (1998)) and from the VLA FIRST Survey (Gregg et al. 1996; Becker et al. 1995). The flux in radio is reported for seven of our sources and in the case the object is not detected we provide an upper limit to the flux, which corresponds to the detection limit (≈ 5 times the rms in both FIRST and NVSS catalogue) at the position of the source. In the case of CTQ 0408, there is no coverage either in the FIRST survey or in the NVSS survey. The radio flux for this source is obtained at 408MHz from the Sidney University Molonglo Sky Survey catalogue (Mauch et al. 2003). The radio classification is shown in col. 12 of Table 2.1 and was determined following Ganci et al. (2019) via the estimation of a modified rest-frame radio loudness parameter $R_K = f_{\nu,\text{radio}}/f_{\nu,\text{optical}}$ (Kellermann et al. 1989), defined as the ratio between the specific flux at 1.4 GHz and in the g -band. Accordingly, our sample is separated into three different ranges: radio-quiet (RQ; $R_K < 10$), radio-intermediate (RI; $10 \leq R_K < 70$), and radio-loud (RL; $R_K \geq 70$). Of the seven sources with radio detection, three of them (CTQ 0408, SDSSJ141546.24+112943.4, and SDSSJ210524.49+000407.3) are classified as radio-intermediate. The radio-loud sources from our sample are B1422+231, PKS 1937-101, PKS 2000-330, and PKS 2126-15, about 20% of the sources of this sample. We plan to carry out a similar spectroscopic study focused on RL quasars to supplement those listed in Table 2.1 in a forthcoming chapter.

2.4 Spectral analysis

2.4.1 Optical range: Multicomponent fitting

H β

The multicomponent fits were performed, after the spectra were set at rest-frame, using the SPECFIT routine from IRAF (Kriss 1994). This routine allows for simultaneous minimum- χ^2 fit of the continuum approximated by a power-law and the spectral line components yielding FWHM, peak

Empirical decomposition of broad profiles

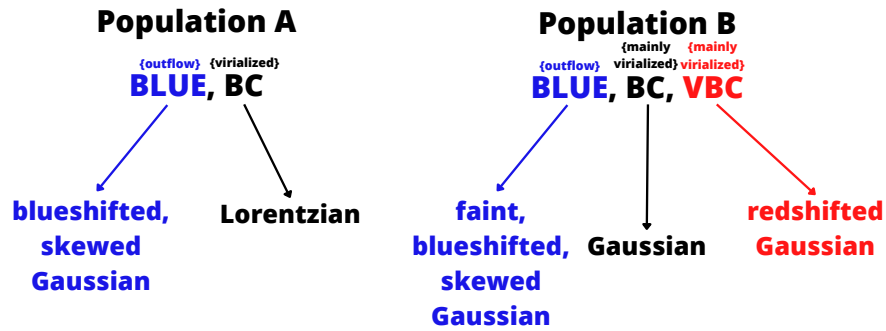


Fig. 2.2: Sketch of the approach followed for broad profile fittings.

wavelength, and intensity of all line components. In the optical range, we fit the $H\beta$ profile as well as the $[O\ III]\lambda\lambda 4959, 5007$ emission lines and the Fe II multiplets for the 22 objects.

Our approach includes the continuum (a power law), a semi-empirical scalable Fe II emission template and the emission line components to fit the $H\beta + [O\ III]\lambda\lambda 4959, 5007$ region. The Fe II template used is almost identical to the one of [Boroson & Green \(1992\)](#). The specfit routine allows for the scaling, broadening, and shifting of the Fe II template to model the observed features ([Marziani et al. 2003b](#)). A sketch illustrating the decomposition approach performed on the fits of the broad profiles for the is presented in Fig. 2.2. The fit of the $H\beta$ full profile takes into account three main components:

Broad component (BC): this component is kept symmetric, set almost always at rest-frame, and presents a FWHM range that goes from $\gtrsim 3000\text{ km s}^{-1}$ for some Pop. A and $\lesssim 6000\text{ km s}^{-1}$ for Pop. B quasars. The profile changes depending on the quasar population, presenting a Lorentzian-like shape for Pop. A and a Gaussian-like one for Pop. B sources ([Sulentic et al. 2002](#); [Marziani et al. 2003b](#); [Zamfir et al. 2010](#); [Cracco et al. 2016](#));

Blueshifted component (BLUE): our first assumption is to model this component by only a blue-shifted Gaussian (symmetric or skewed) profile with FWHM and shift similar to the $[O\ III]\lambda 5007$ semi-broad component (SBC, explained in §2.4.1). When the $H\beta$ profile does not correspond to the blueshifted SBC of $[O\ III]\lambda 5007$ profile, it is included in the fitting an additional Gaussian blue-shifted component that may not belong to NLR emission (BLUE). Unlike the SBC, BLUE is believed to be associated with emission of outflowing gas from within the BLR ([Negrete et al. 2018](#));

Very broad component (VBC): this is clearly observed in Population B sources ([Sulentic et al. 2017](#); [Wolf et al. 2020](#)). It is always represented by a redshifted Gaussian profile and it is thought to be related with the high-ionisation virialised region closest to the continuum source ([Peterson & Ferland 1986](#); [Snedden & Gaskell 2007](#); [Wang & Li 2011](#)). This component can easily achieve $\text{FWHM} \gtrsim 10000\text{ km s}^{-1}$.

In addition, we include a narrow component (NC) superimposed to the broad emission line profile and it is fitted as an unshifted Gaussian. The population classification depends on the FWHM of the full profile. Depending on the population assignment, different components are included and they assume different line shapes. An exhaustive analysis of the fittings were performed and in borderline cases (i.e. with line width close to the boundary between Pop. A and B), the final conclusion on the population of the source is based on the χ^2 of the fitting (i.e. the fittings with the minimum χ^2 are selected).

[O III] λ 5007

An approach similar to the one used for H β is also followed for the [O III] $\lambda\lambda$ 4959, 5007 emission line profiles. The [O III] $\lambda\lambda$ 4959, 5007 full profile is assumed to be well represented by a Gaussian narrow (FWHM $\lesssim 1200$ km s $^{-1}$) component set at rest-frame or shifted to the blue and a semi-broad component (SBC, FWHM typically $\lesssim 3000$ km s $^{-1}$) that usually appears more shifted to the blue (~ 1000 km/s, Zhang et al. 2011; Marziani et al. 2016b, 2022b). The NC is modelled as a Gaussian profile for the two populations and in a first approach the NC of both H β and [O III] λ 5007 share the same line width. The blueshifted contributions can be modelled by one or more Gaussian profiles and in some cases the Gaussian needs to be asymmetric towards the blue to account for the line shape, namely, to be a 'skewed' Gaussian. The use of a skewed Gaussian has a physical motivation, as it might be associated with bipolar outflow emission in which the receding side of the outflow is obscured. Apart from that, both [O III] λ 4959 and [O III] λ 5007 emission line profiles are assumed to have the same FWHM and shifts, and the intensity ratio between the two lines is kept fixed at 1:3 (Dimitrijević et al. 2007).

2.4.2 UV range: Multicomponent fitting

Fits were performed for three different regions centred on Si IV λ 1397+O IV] λ 1402, C IV λ 1549+He II λ 1640, and the 1900 Å blend that includes the Al III λ 1860 doublet, Si III] λ 1892, Si II λ 1816, and C III] λ 1909. The UV fittings are presented for 15 sources. The fits were not carried out in cases where the emission lines are strongly affected by BALs. The fittings of the absorption lines are performed in sources in which the presence of these lines allows to clearly see the emission line profile (as in the case of mini-BALs; Sulentic et al. 2006a). The UV blends are fit following the population assignments from the H β spectral range. The only exception is SDSSJ153830.55+085517.0, where its UV spectrum cannot be fitted in agreement with its classification as Pop. B in the H β region, as highlighted in the Appendix A.1.

1900 Å blend

In the UV region corresponding to the 1900 Å blend, the fittings are performed considering the Al III λ 1860 doublet, Si III] λ 1892, Si II λ 1816, and C III] λ 1909 emission line profiles. Here, Fe III is especially relevant on the red side of the 1900 Å blend and its modelling was performed using the

Vestergaard & Wilkes (2001) empirical template, and following the same approach as for the optical Fe II. Broad line components of the 1900 Å blend in Pop. A sources are fitted by Lorentzian profiles while in Pop. B by Gaussian functions (as is the case of H β in the optical spectral range), keeping the same (or at least a comparable) FWHM to the broad component of H β .

In several Pop. A and more frequently in xA quasars, the Fe III template and the C III] λ 1909 broad component do not adequately reproduce the shape of the red side of the 1900 Å blend. A better model of the C III] λ 1909 region is achieved assuming an additional contribution mostly likely due to the Fe III line at 1914 Å. The same approach was employed in Martínez-Aldama et al. (2018).

Regarding the Pop. B sources, the C III] λ 1909 emission line is well represented by the same combination applied for Pop. B H β : VBC+BC+NC. The VBC FWHM is expected to be ≥ 4000 km s $^{-1}$, and the NC FWHM ~ 1000 km s $^{-1}$ (there is only one source that shows a significant NC in C III]). Differently from C III] λ 1909, lines such as the Al III λ 1860 doublet, Si III] λ 1892, and Si II λ 1816 are assumed not to present a very broad component (Buendía-Rios et al. 2023). They are fit by only one BC.

C IV λ 1549+He II λ 1640

In order to fit the C IV λ 1549+He II λ 1640 blend and contaminant lines within it, we use the approach followed by S17. As in the previous fits, we represent Pop. A profiles of C IV λ 1549 and He II λ 1640 by a broad and a blueshifted component. Pop. B are represented by the combination VBC+BC+BLUE. The broad components of C IV λ 1549 and He II λ 1640 are fixed at rest-frame and the other components are left free to vary in wavelength. Nevertheless, the FWHM and shapes of He II λ 1640 BC and BLUE are restricted to be equal (or comparable) to the corresponding ones of C IV λ 1549. These constraints are physically motivated since both C IV λ 1549 and He II λ 1640 are expected to be emitted from the same regions, because of the similar ionisation potential of the parent ionic species. An additional condition is that the broad component (BC) of C IV λ 1549 and He II λ 1640 FWHM should be equal or larger to the one of H β , following previous works (e.g. Sulentic et al. 2017, and references therein).

Si IV λ 1397+O IV] λ 1402

For the Si IV λ 1397+O IV] λ 1402 emission lines region, we follow the same steps as in the C IV+He II blend. The Si IV λ 1397+O IV] λ 1402 feature profile is similar to the one of C IV λ 1549, and is therefore expected to present BC and blueshifted component similar to those of C IV λ 1549. The broad component in this case is also kept at rest-frame and any other necessary component is free to change in all the parameters.

2.4.3 Analysis of the full profile parameters for the optical and UV regions

Apart from the multicomponent analysis, the H β and [O III] emission line profiles are also characterised through the parametrisation of the full profile by measuring centroids and widths at different fractional intensities (1/4, 1/2, 3/4, and 9/10), as well as asymmetry and kurtosis indexes in order to

provide a quantitative description independent of the `SPECFIT` modelling. In the case of $H\beta$, the full profile ($H\beta_{\text{full}}$) for Pop. B quasars is represented by BC+VBC plus BLUE when detected. For Pop. A quasars, full $H\beta$ profile consists of BC plus BLUE if an additional blue component is present. For [O III] we consider NC and one (or more, if needed) blueshifted SBC. Full profile parameters for the UV region are provided for the $C\text{IV}\lambda 1549$ broad emission line, excluding NC.

2.4.4 Error estimates

Uncertainties in the multicomponent fits were estimated by running Markov Chain Monte Carlo (MCMC) simulations, following the approach described in [Marziani et al. \(2022c\)](#) for both optical and UV spectral ranges. Observed spectra were modeled using the components employed in the best fit, with a Markov Chain to sample the domain around the minimum χ^2 . The dispersion in the posterior distribution of a parameter was assumed to be its 1σ confidence interval. For the optical range, the errors are around the order of 10% for the FWHM of the $H\beta_{\text{BC}}$ and $[\text{O III}]_{\text{SBC}}$. Larger uncertainties ($\sim 30\%$) are found for the narrow components of both lines and for the blueshifted component of $H\beta$. Flux uncertainties for strong or sharp emission lines are $\sim 10\%$, while typical errors for the continuum and Fe II are $\sim 5\%$ and $\sim 15\%$ respectively, if Fe II is reasonably strong. For the UV, the FWHM uncertainties are between 10% and 15% and errors on intensity measurements are usually $\lesssim 10\%$ for the strongest emission line components.

2.5 Results

2.5.1 Location in the optical plane of main sequence

After performing the multicomponent fitting, we can locate the sample in the MS optical plane, using the $\text{FWHM}(H\beta_{\text{full}})$ as well as the flux ratio of $\text{Fe II}\lambda 4570$ and $H\beta$, R_{FeII} . Figure 2.3 shows the location of the sources and a comparison between our sample and low- and high- z samples. The grey- and green-shaded areas in the plot indicate the location of low-redshift quasars on the MS, with the xA sources situated on the green shadow.

Our sample shows a slight displacement in the direction of increasing $\text{FWHM}(H\beta)$, if compared to low- z samples (e.g. [Zamfir et al. 2010](#), and the shaded area in Fig. 2.3). There are some Pop. A sources that present a $\text{FWHM}(H\beta_{\text{full}}) \sim 5000 \text{ km s}^{-1}$. The Pop. A-B boundary at $\text{FWHM}(H\beta) = 4000 \text{ km s}^{-1}$ is reasonable when considering low redshift and, consequently, lower luminosity ranges than those of high- z quasars ([Sulentic et al. 2004](#)). However, at high luminosity there is a significant effect on the $H\beta$ profile width that may shift the boundary between Pop. A and B by more than 1000 km s^{-1} (M09). Up and bottom purple shadows in Fig. 2.3 indicate, respectively, the Pop. A-B boundary and the minimum $\text{FWHM}(H\beta)$ found in a $47 \leq \log L_{\text{bol}} \leq 48$ range that are representative of our sample. Both boundaries were determined following M09.

Of the 22 sources of our sample, 12 are classified as Pop. A and 10 as Pop. B quasars. We found three sources to belong to spectral type (ST) A1; six Pop. A2; three Pop. A3 (extreme A); eight to be

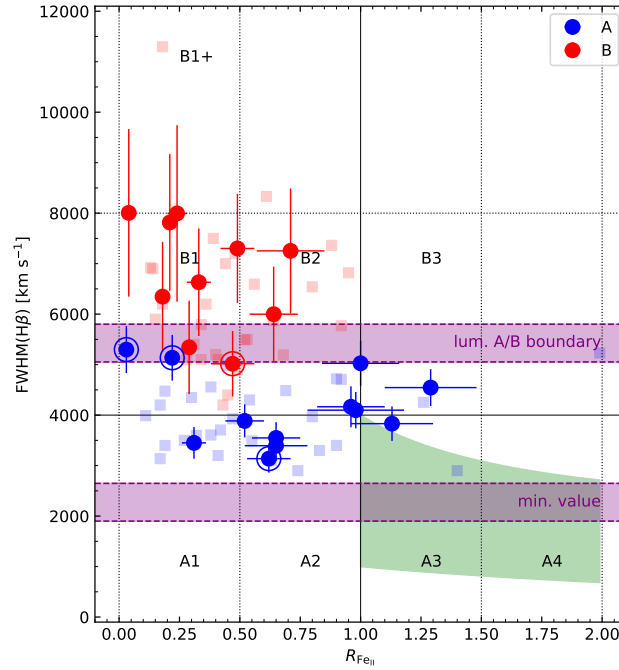


Fig. 2.3: Location of our sources through the optical plane of the 4DE1. Pop. A quasars are represented by blue circles and Pop. B by red circles. The radio-loud sources from the sample are surrounded by a circle in the plot. Grey and green regions indicate the distribution of the main sequence of quasars across the 4DE1 optical plane in a low- z context (Marziani et al. 2018). Spectral types (ST) of the MS are labelled according to Sulentic et al. (2002). Blue and red squares indicate high-redshift Pop. A and Pop. B quasars from M09, respectively. Purple-shaded areas show the luminosity-dependent boundary between Pops. A and B and the minimum FWHM value for sources with $47 \leq L_{\text{bol}} \leq 48$ and assuming $\alpha = 0.67$ (Marziani et al. 2009).

Pop. B1; and two Pop B2. The four radio-loud objects (B1422+231, PKS 1937-101, PKS 2000-330, and PKS 2126-15) are identified in Figure 2.3 by the blue and red symbols surrounded by an open circle. Three of them are classified as Pop. A and only PKS 2126-15 is a Pop. B quasar. Of the three radio-intermediate, two (SDSSJ141546.24+112943.4, ST B2; SDSSJ210524.49+000407.3, A3) show significant Fe II and an overall spectrum associated with high accretion rates (Ganci et al. 2019; del Olmo et al. 2021; Marziani et al. 2022a). Only CTQ 0408 is classified as B1, with an optical spectrum resembling the powerful jetted sources at low z . The orientation may strongly affect the classification of the sources, especially in the cases when the $\text{FWHM}(\text{H}\beta)$ is at the border line of the A-B boundary. Orientation effects could be particularly important in the case of core-dominated RL sources, as the pole-on orientation may imply a narrowing of low-ionisation emission line widths (Wills & Browne 1986; Marziani et al. 2001; Sulentic et al. 2003; Rokaki et al. 2003; Zamfir et al. 2008; Bisogni et al. 2017).

There is just one case of a blatant disagreement between the classification deduced from the optical and UV spectra of the same source: SDSSJ153830.55+085517.0, which is optically classified as Pop. B but presents clearly Pop. A-like profiles in the UV spectrum (see §A.1.14 and Fig. A.1.14 in the Appendix A.1). In this case, it was necessary to fit the optical as Pop. B and the UV as Pop. A.

Table 2.4: Spectrophotometric measurements on H β .

Source	Spectral Type	$f_{\lambda,5100}^{(a)}$	$W(\text{H}\beta)$	$W([\text{O III}])$ [\AA]	$R_{\text{Fe II}}$
(1)	(2)	(3)	(4)	(5)	(6)
Population A					
SDSSJ005700.18+143737.7	A3	2.5 ± 0.3	53 ± 6	4.5 ± 0.5	1.13 ± 0.17
SDSSJ132012.33+142037.1	A1	1.2 ± 0.1	74 ± 9	19.8 ± 2.4	0.31 ± 0.05
SDSSJ135831.78+050522.8	A2	2.2 ± 0.3	68 ± 8	16.3 ± 2.0	0.65 ± 0.10
Q 1410+096	A2	3.0 ± 0.4	57 ± 7	13.7 ± 1.6	0.65 ± 0.13
B1422+231	A1	4.0 ± 0.5	78 ± 9	9.3 ± 1.1	0.22 ± 0.03
SDSSJ161458.33+144836.9	A2	2.3 ± 0.3	83 ± 9	16.8 ± 2.0	0.52 ± 0.08
PKS 1937-101	A1	7.6 ± 0.9	62 ± 7	13.5 ± 1.6	0.03 ± 0.01
PKS 2000-330	A2	2.8 ± 0.3	59 ± 7	15.1 ± 1.8	0.62 ± 0.09
SDSSJ210524.49+000407.3	A3	3.9 ± 0.5	31 ± 4	0.4 ± 3.0	1.00 ± 0.16
SDSSJ210831.56-063022.5	A3	1.4 ± 0.2	44 ± 6	4.7 ± 0.6	1.29 ± 0.19
SDSSJ212329.46-005052.9	A2	4.4 ± 0.5	34 ± 5	5.5 ± 0.7	0.96 ± 0.14
SDSSJ235808.54+012507.2	A2	4.7 ± 0.6	63 ± 8	10.7 ± 1.3	0.98 ± 0.20
Population B					
HE 0001-2340	B1	1.6 ± 0.2	77 ± 9	10.6 ± 1.3	0.33 ± 0.05
[HB89] 0029+073	B1	2.4 ± 0.3	62 ± 7	7.8 ± 0.9	0.18 ± 0.02
CTQ 408	B1	6.9 ± 0.8	53 ± 6	2.5 ± 4.0	0.49 ± 0.07
H 0055-2659	B1	1.9 ± 0.2	92 ± 11	40.6 ± 4.9	0.29 ± 0.03
SDSSJ114358.52+052444.9	B2	1.1 ± 0.1	82 ± 10	5.4 ± 0.6	0.64 ± 0.10
SDSSJ115954.33+201921.1	B1	2.5 ± 0.3	78 ± 9	15.2 ± 1.8	0.04 ± 0.01
SDSSJ120147.90+120630.2	B1	4.3 ± 0.5	117 ± 14	21.0 ± 2.5	0.24 ± 0.04
SDSSJ141546.24+112943.4	B2	2.1 ± 0.3	108 ± 13	33.9 ± 4.1	0.71 ± 0.14
SDSSJ153830.55+085517.0	B1	1.1 ± 0.1	94 ± 11	5.5 ± 0.7	0.21 ± 0.03
PKS 2126-15	B1	4.8 ± 0.6	93 ± 11	10.0 ± 1.2	0.47 ± 0.09

Notes. ^(a) In units of $10^{-15} \text{ erg s}^{-1} \text{ cm}^{-2} \text{ \AA}^{-1}$.

Table 2.5: Results from SPECFIT analysis on H β .

Source (1)	H β full broad profile								Full broad profile (BLUE+BC+VBC)									Narrow profile (SBC+NC)						
	FWHM [km s $^{-1}$] (2)	A. I. (3)	Kurt. (4)	c(\downarrow) [km s $^{-1}$] (5)	c(\downarrow) [km s $^{-1}$] (6)	c(\downarrow) [km s $^{-1}$] (7)	c($\frac{\circ}{\circ}$) [km s $^{-1}$] (8)	$f_{tot}^{(b)}$ (9)	BLUE $^{(a)}$			BC			VBC			$f_{tot}^{(c)}$ (19)	SBC			NC		
									I/I_{tot} (10)	FWHM [km s $^{-1}$] (11)	Shift [km s $^{-1}$] (12)	I/I_{tot} (13)	FWHM [km s $^{-1}$] (14)	Shift [km s $^{-1}$] (15)	I/I_{tot} (16)	FWHM [km s $^{-1}$] (17)	Shift [km s $^{-1}$] (18)		I/I_{tot} (20)	FWHM [km s $^{-1}$] (21)	Shift [km s $^{-1}$] (22)	I/I_{tot} (23)	FWHM [km s $^{-1}$] (24)	Shift [km s $^{-1}$] (25)
Population A																								
SDSSJ005700.18+143737.7	3830 ± 342	-0.09 ± 0.01	0.33 ± 0.01	-359 ± 237	-326 ± 83	-137 ± 107	-82 ± 118	1.66 ± 0.20	0.08 ± 0.03	2562 ± 359	-2154 ± 548	0.92 ± 0.06	3255 ± 346	0 ± 10	1.89 ± 0.23	0.00	1.00 ± 0.32	873 ± 93	0 ± 10
SDSSJ132012.33+142037.1	3450 ± 314	-0.11 ± 0.03	0.31 ± 0.01	-476 ± 323	-215 ± 72	-138 ± 93	-125 ± 110	0.91 ± 0.11	0.12 ± 0.05	7519 ± 1053	-1745 ± 584	0.88 ± 0.05	3224 ± 343	-41 ± 14	1.13 ± 0.14	0.00	1.00 ± 0.32	623 ± 66	-22 ± 17
SDSSJ135831.78+050522.8	3548 ± 314	0.00 ± 0.12	0.33 ± 0.01	-1 ± 297	0 ± 60	0 ± 97	0 ± 120	1.58 ± 0.19	0.00	0.92 ± 0.06	3548 ± 377	0 ± 10	1.49 ± 0.18	1.00 ± 0.32	5497 ± 770	-1712 ± 572	0.00
Q 1410+096	3394 ± 299	0.00 ± 0.08	0.33 ± 0.01	54 ± 279	54 ± 58	54 ± 92	54 ± 112	1.79 ± 0.21	0.00	1.00 ± 0.06	3394 ± 361	54 ± 58	0.37 ± 0.04	1.00 ± 0.32	4581 ± 320	-3144 ± 1051	0.00
B1422+231	5136 ± 452	0.00 ± 0.06	0.33 ± 0.01	-1 ± 422	-1 ± 89	0 ± 139	0 ± 169	3.20 ± 0.38	0.00	1.00 ± 0.06	5135 ± 546	0 ± 10	0.57 ± 0.07	0.00	1.00 ± 0.32	1113 ± 118	0 ± 10
SDSSJ161458.33+144836.9	3885 ± 349	-0.06 ± 0.11	0.33 ± 0.01	-241 ± 327	-98 ± 73	-51 ± 106	-38 ± 130	1.89 ± 0.21	0.09 ± 0.03	7224 ± 506	-1713 ± 571	0.91 ± 0.06	3721 ± 396	0 ± 10	0.54 ± 0.06	0.70 ± 0.25	2445 ± 170	-1709 ± 569	0.30 ± 0.09	439 ± 47	0 ± 10
PKS 1937-101	5298 ± 466	0.00 ± 0.07	0.33 ± 0.01	56 ± 434	56 ± 92	56 ± 144	56 ± 174	5.15 ± 0.62	0.00	1.00 ± 0.06	5296 ± 563	56 ± 92	1.57 ± 0.19	0.29 ± 0.09	2618 ± 183	-555 ± 183	0.71 ± 0.22	852 ± 91	-47 ± -77
PKS 2000-330	3230 ± 294	-0.06 ± 0.07	0.32 ± 0.01	-175 ± 306	-30 ± 61	1 ± 89	9 ± 108	1.92 ± 0.22	0.05 ± 0.01	5499 ± 385	-3127 ± 1031	0.95 ± 0.06	3138 ± 334	28 ± 54	2.31 ± 0.28	0.36 ± 0.11	1499 ± 105	-599 ± 197	0.63 ± 0.20	1082 ± 115	-46 ± -89
SDSSJ210524.49+000407.3	5026 ± 446	0.00 ± 0.06	0.33 ± 0.01	-1 ± 420	0 ± 85	0 ± 137	0 ± 169	1.28 ± 0.15	0.00	1.00 ± 0.6	5026 ± 534	0 ± 10	0.40 ± 0.05	0.00	1.00 ± 0.32	1407 ± 150	0 ± 10
SDSSJ210831.56+063022.5	4545 ± 200	0.00 ± 0.04	0.33 ± 0.01	93 ± 372	93 ± 79	93 ± 124	93 ± 149	0.60 ± 0.08	0.00	0.91 ± 0.06	4543 ± 483	93 ± 16	0.68 ± 0.08	0.89 ± 0.28	2597 ± 364	-2018 ± 347	0.11 ± 0.03	1403 ± 149	0 ± 10
SDSSJ212329.46+005052.9	4165 ± 366	0.00 ± 0.03	0.33 ± 0.01	-1 ± 342	-1 ± 72	0 ± 200	-1 ± 231	1.60 ± 0.22	0.00	0.89 ± 0.05	4164 ± 443	0 ± 10	2.40 ± 0.29	0.86 ± 0.27	4969 ± 696	-1844 ± 323	0.14 ± 0.04	1188 ± 126	0 ± 10
SDSSJ235808.54+012507.2	4098 ± 360	0.03 ± 0.06	0.35 ± 0.01	0 ± 336	0 ± 70	0 ± 111	-1 ± 136	2.88 ± 0.35	0.00	1.00 ± 0.06	4098 ± 436	0 ± 10	3.76 ± 0.45	0.38 ± 0.12	2463 ± 172	-1030 ± 340	0.61 ± 0.19	954 ± 101	0 ± 10
Median	3991 ± 1141	0.00 ± 0.06	0.33 ± 0.01	-1 ± 205	-0.5 ± 61	0 ± 27	0 ± 51	1.72 ± 0.65	0.08 ± 0.02	6362 ± 2533	-1949 ± 660	0.93 ± 0.09	3909 ± 1305	0 ± 34	1.31 ± 1.43	0.78 ± 0.54	2607 ± 2219	-1710 ± 965	0.67 ± 0.62	1018 ± 312	0 ± 16
Population B																								
HE 0001-2340	6632 ± 1065	0.16 ± 0.22	0.37 ± 0.01	1757 ± 873	1134 ± 153	960 ± 354	909 ± 471	1.30 ± 0.16	0.00	0.42 ± 0.06	5063 ± 366	681 ± 92	0.58 ± 0.06	10982 ± 1955	2538 ± 342	0.33 ± 0.04	0.34 ± 0.11	3772 ± 264	-414 ± 136	0.65 ± 0.21	1067 ± 77	0 ± 10 $^{(d)}$
[HB89] 0029+073	6347 ± 1085	0.18 ± 0.05	0.37 ± 0.01	932 ± 757	292 ± 138	51 ± 339	-19 ± 442	1.54 ± 0.18	0.07 ± 0.01	4995 ± 837	-1216 ± 575	0.33 ± 0.05	4508 ± 326	-310 ± 147	0.60 ± 0.06	9609 ± 1710	1430 ± 193	1.54 ± 0.18	0.00	1.00 ± 0.32	1024 ± 74	0 ± 10
CTQ 408	7301 ± 1081	0.10 ± 0.09	0.40 ± 0.02	724 ± 910	306 ± 179	197 ± 390	164 ± 528	3.90 ± 0.47	0.00	0.52 ± 0.08	6050 ± 437	0 ± 10	0.48 ± 0.05	13243 ± 2357	1963 ± 264	2.54 ± 0.30	0.00	1.00 ± 0.32	1500 ± 108	0 ± 10
H 0055-2659	5342 ± 925	0.36 ± 0.13	0.30 ± 0.03	2249 ± 1085	580 ± 101	380 ± 283	329 ± 377	1.85 ± 0.22	0.00	0.27 ± 0.04	4609 ± 333	-224 ± 39	0.73 ± 0.07	13355 ± 2377	2527 ± 340	0.82 ± 0.10	0.00	1.00 ± 0.32	1500 ± 108	0 ± 10
SDSSJ143558.52+052444.9	5999 ± 942	0.24 ± 0.15	0.34 ± 0.05	1485 ± 1408	354 ± 133	210 ± 319	170 ± 431	1.00 ± 0.12	0.00	0.52 ± 0.08	5007 ± 362	0 ± 10	0.48 ± 0.05	13341 ± 2375	4095 ± 552	0.34 ± 0.04	0.47 ± 0.15	1830 ± 128	-1277 ± 421	0.53 ± 0.17	1304 ± 94	0 ± 10 $^{(d)}$
SDSSJ115954.33+201921.1	8006 ± 1659	0.29 ± 0.10	0.33 ± 0.01	2389 ± 1025	950 ± 133	469 ± 422	359 ± 536	2.05 ± 0.25	0.00	0.36 ± 0.05	5458 ± 395	-35 ± 15	0.64 ± 0.06	12924 ± 2300	3287 ± 443	0.42 ± 0.05	0.72 ± 0.23	2660 ± 186	-1215 ± 401	0.27 ± 0.08	995 ± 72	-101 ± 14
SDSSJ120147.90+120630.2	7995 ± 1748	0.28 ± 0.11	0.33 ± 0.01	2331 ± 947	1124 ± 140	540 ± 421	414 ± 519	4.31 ± 0.52	0.00	0.30 ± 0.0	4986 ± 360	9 ± 10	0.70 ± 0.07	12190 ± 2170	2850 ± 384	6.33 ± 0.76	0.05 ± 0.01	1879 ± 131	-246 ± 81	0.95 ± 0.30	1879 ± 136	-1 ± 10
SDSSJ141546.24+112943.4	7253 ± 1237	0.23 ± 0.11	0.36 ± 0.02	1769 ± 952	736 ± 145	447 ± 387	367 ± 510	1.59 ± 0.19	0.00	0.45 ± 0.07	5544 ± 401	14 ± 13	0.55 ± 0.05	11523 ± 2051	3144 ± 423	1.31 ± 0.16	0.29 ± 0.09	1000 ± 70	-784 ± 258	0.71 ± 0.22	1162 ± 84	14 ± 13
SDSSJ153830.55+085517.0	7816 ± 1354	0.25 ± 0.11	0.35 ± 0.02	2090 ± 1081	800 ± 152	478 ± 415	390 ± 548	1.16 ± 0.14	0.00	0.47 ± 0.07	6038 ± 437	9 ± 12	0.53 ± 0.05	12642 ± 2250	3869 ± 521	0.50 ± 0.06	0.00	1.00 ± 0.32	1000 ± 72	-1 ± 10
PKS 2126-15 $^{(e)}$	5018 ± 648	0.50 ± 0.09	0.22 ± 0.01	2104 ± 414	81 ± 51	-303 ± 168	-713 ± 90	4.28 ± 0.51	0.09 ± 0.02	4662 ± 781	-4717 ± 2970	0.35 ± 0.05	4074 ± 295	-589 ± 371	0.56 ± 0.05	9992 ± 1779	3583 ± 483	3.34 ± 0.40	0.17 ± 0.05	1345 ± 94	-426 ± 140	0.83 ± 0.26	922 ± 67	0 ± 10
Median	6942 ± 1601	0.24 ± 0.09	0.34 ± 0.03	1929 ± 659	658 ± 594	413 ± 275	344 ± 218	1.72 ± 2.07	0.08 ± 0.01	4828 ± 166	-2966 ± 1750	0.39 ± 0.13	5035 ± 819	0 ± 186	0.57 ± 0.09	12416 ± 2046	2997 ± 980	1.06 ± 1.85	0.31 ± 0.23	1854 ± 998	-605 ± 690	0.89 ± 0.33	1114 ± 445	0 ± 1

Notes. $^{(a)}$ In these columns, we report additional blueshifted components that were included in the H β profile. $^{(b)}$ In units of 10^{-13} erg s $^{-1}$ cm $^{-2}$. $^{(c)}$ In units of 10^{-14} erg s $^{-1}$ cm $^{-2}$. $^{(d)}$ There is an additional contribution due to small blueshifted components associated with narrow line emission. $^{(e)}$ Full profile centroid velocities and the presence of a BLUE H β component in this case are affected by the location of the continuum.

2.5.2 Optical

H β

Appendix A.1 shows the full VLT-ISAAC optical spectra and their respective H β + [O III] $\lambda\lambda$ 4959, 5007 fittings. Spectrophotometric measurements on H β are presented in Table 2.4. The ST of each source is listed in col. 2; the specific continuum flux at 5100Å (in rest-frame) is in col. 3; equivalent width (EW) of the H β and [O III] λ 5007 full profiles in cols. 4 and 5, respectively; and the Fe II prominence parameter (R_{FeII}) is listed in col. 7.

Table 2.5 reports measurements on the H β profile. First we present the parameters obtained through the analysis of the H β full broad profile, including FWHM(H β_{full}) (col. 2), asymmetry index (col. 3), kurtosis (col. 4), and the centroid velocity shifts at $\frac{1}{4}$, $\frac{1}{2}$, $\frac{3}{4}$, and $\frac{9}{10}$ fractional intensity (cols. 5, 6, 7, and 8, respectively). In col. 9, we list the full H β line flux (i.e., the flux for all broad line components, BC and VBC and BLUE, whenever appropriate). For each broad component isolated with the SPECFIT analysis we report, from cols. 10 to 18, flux normalised by the total flux (I/I_{tot}), FWHM, and velocity shift. Then, col. 19 shows the total flux of the narrow profile (SBC+NC) and from cols. 20 to 25 we report I/I_{tot} , FWHM, and shift for these components. Additionally, we provide, in the last row of Pop. A and B, respectively, the median values of the measurements, together with the interquartile range.

The centroid velocities are close to the rest-frame wavelength for the majority of Pop. A and only two of the Pop. A quasars present $c(1/2)$ strongly shifted towards the blue with an averaged value of $\approx -271 \text{ km s}^{-1}$. These sources are SDSSJ005700-18+14737.7 (ST A3) and SDSSJ132012.33+142037.1 (A1), both of them presenting a clear blueshifted contribution in H β profile. In the case of Pop. B quasars, the centroid velocities are significantly shifted towards the red wing of the profile in every fractional intensity for the majority of the sources, with an averaged $c(1/2)$ value of $\sim 640 \text{ km s}^{-1}$. Even higher values are found for $c(1/4)$: Pop. B present an averaged value of $\approx 1780 \text{ km s}^{-1}$ while Pop. A have $c(1/4) \approx -149 \text{ km s}^{-1}$.

Overall, Pop. B sources show FWHM(H β_{full}) values that are much larger than those of Pop. A, usually $\sim 6000 \text{ km s}^{-1}$. This difference is a direct consequence of the definition of Pop. A and B. The Pop. B asymmetry index is positive and very significantly different from 0, since the contribution of the VBC – that reaches FWHM values $\gtrsim 10000 \text{ km s}^{-1}$ – in all cases represents $\gtrsim 50\%$ of the full emission line profile. In other words, differently from Pop. A sources (in which only a symmetric BC is enough to represent the full profile in the majority of the cases), a second redshifted component is always needed to reproduce the strong red wing of the observed H β profile.

Semi-broad H β blueshifts could be mainly associated with the [O III] λ 5007 SBC. However, in some cases, an additional BLUE H β component is needed (see Table 2.5). In particular, PKS 2126-15 presents a huge BLUE blueshift of $\approx -4700 \text{ km s}^{-1}$, associated with a boxy termination of the H β blue wing. A second peculiarity of this source is that the H β BC is significantly shifted to the blue, down to half maximum, which is at variance with all other Pop. B sources.

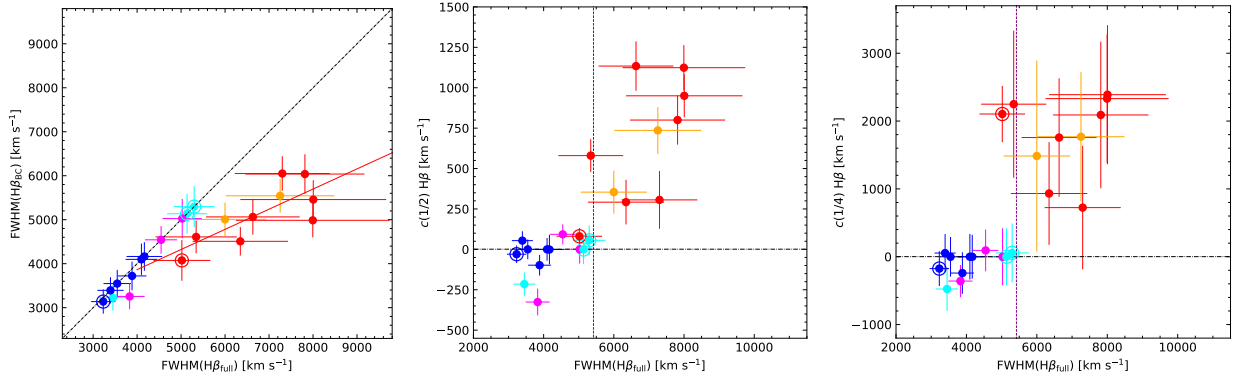


Fig. 2.4: Comparison between the different properties of the $H\beta$ emission line profile. *Left panel:* $\text{FWHM}(H\beta_{BC})$ vs FWHM of the full $H\beta$ profile. *Central panel:* velocity centroid at 1/2 intensity $c(1/2)$ vs $\text{FWHM}(H\beta_{full})$. *Right panel:* velocity centroid at 1/4 flux intensity $c(1/4)$ vs $\text{FWHM}(H\beta_{full})$. Symbols surrounded by open circles show the radio-loud sources and filled circles represent the radio-quiet from the sample. Red line represent the linear regression performed for Pop. B. Horizontal dashed lines in the central and right panels indicate $c(1/4) = 0$ and $c(1/2) = 0$ for $H\beta$, respectively. Purple vertical dashed lines shows the boundary between Pop. A and Pop. B. The many MS spectral type (ST) are represented in different colours: A1 (●); A2 (●); A3 (●); B1 (●); and B2 (●).

The $H\beta$ NC is weak especially in Pop. A ($\lesssim 0.02$ of the $H\beta$ line flux), although it is observed in all cases save two Pop. A2 sources (SDSSJ132012.33+142037.1 and Q 1410+096). In Pop. B, the narrow component is somewhat stronger but always $\lesssim 0.05$ of the line flux. Given its weakness, the NC is therefore not significantly affecting the flux of any broad component measured in this chapter.

Relation between $\text{FWHM}(H\beta_{full})$ and $\text{FWHM}(H\beta_{BC})$. This work confirms previous studies (e.g. Sulentic et al. 2006b; Marziani et al. 2009, and references therein) that showed that the full $H\beta$ profile of Pop. A can be accounted for mostly by the BC, and that a redshifted VBC seems to be absent in Population A but present in Pop. B sources: Table 2.5 lists centroid and asymmetry index values for Pop. B sources of $1000 \lesssim c(\frac{1}{4}) \lesssim 2000 \text{ km s}^{-1}$ and ≈ 0.2 , respectively. For Pop. A these values are $\lesssim 0 \text{ km s}^{-1}$ and 0.

The left plot of Fig. 2.4 shows the relation between the FWHM of the BC and the FWHM of the full profile of $H\beta$ for the two populations. Pop. A and Pop. B sources follow different trends for the ratio $\xi(H\beta) = \text{FWHM}(H\beta_{BC})/\text{FWHM}(H\beta_{full})$. For Pop. A quasars, we obtain $\xi(H\beta) = 1.00$ for all sources but four (SDSSJ005700.18+143737.7, SDSSJ132012.33+142037.1, SDSSJ161458.33+144836.9, and PKS2000-330, with $\xi(H\beta) \approx 0.9$ due to the presence of a blueshifted component). The $\xi(H\beta)$ ratio for Pop. B is only ≈ 0.76 , indicating that the Pop. B $H\beta$ full profile is less representative of the BC than the Pop. A sources. Similar results were also shown by Marziani et al. (2013a): they obtain $\xi(H\beta) = 1.00$ for Pop. A and ~ 0.78 for Pop. B quasars. In our sample Pop. B sources usually present a very strong and wide VBC component that accounts for ≈ 0.57 of the profile, with a mean FWHM of 11240 km s^{-1} . Meanwhile, as mentioned, the Pop. A sources in general are well represented by only a BC. This also seems to be true for the radio-loud Pop. A sources from the sample.

Table 2.6: Measurements on the [O III] λ 5007 full line profile.

Source (1)	[O III] λ 5007 full profile					SBC			NC		
	FWHM [km s ⁻¹] (2)	A. I. (3)	Kurtosis (4)	$c(1/2)$ [km s ⁻¹] (5)	$c(9/10)$ [km s ⁻¹] (6)	I/I_{tot} (7)	FWHM [km s ⁻¹] (8)	Shift [km s ⁻¹] (9)	I/I_{tot} (10)	FWHM [km s ⁻¹] (11)	Shift [km s ⁻¹] (12)
Population A											
SDSSJ005700.18+143737.7 ^(a)	764::	-0.01::	0.45::	-89::	-88::	0.27::	1214::	-1856::	0.732::	761::	-87::
SDSSJ132012.33+142037.1	2124 ± 147	-0.54 ± 0.01	0.23 ± 0.01	-770 ± 62	-221 ± 36	0.64 ± 0.06	2275 ± 235	-1429 ± 115	0.357 ± 0.114	895 ± 95	-149 ± 22
SDSSJ135831.78+050522.8	4320 ± 297	-0.43 ± 0.05	0.19 ± 0.10	-1895 ± 91	-630 ± 59	0.90 ± 0.08	5422 ± 561	-2080 ± 100	0.096 ± 0.031	1000 ± 106	-534 ± 80
Q 1410+096	3363 ± 283	-0.52 ± 0.01	0.28 ± 0.01	-1404 ± 107	-656 ± 72	0.73 ± 0.07	5573 ± 577	-1255 ± 96	0.267 ± 0.085	1379 ± 147	-260 ± 39
B1422+231	1535 ± 99	-0.18 ± 0.01	0.43 ± 0.01	-217 ± 26	-88 ± 47	0.32 ± 0.03	1128 ± 117	-850 ± 102	0.680 ± 0.218	1117 ± 119	27 ± 4
SDSSJ161458.33+144836.9	2616 ± 160	-0.49 ± 0.01	0.28 ± 0.02	-1452 ± 54	-800 ± 50	0.75 ± 0.07	2759 ± 286	-1875 ± 70	0.245 ± 0.078	1006 ± 107	-667 ± 100
PKS 1937-101	1046 ± 79	-0.15 ± 0.09	0.35 ± 0.02	-155 ± 17	-135 ± 31	0.57 ± 0.05	2657 ± 275	-484 ± 53	0.432 ± 0.138	832 ± 88	-120 ± 18
PKS 2000-330	1314 ± 89	-0.13 ± 0.01	0.42 ± 0.01	-425 ± 22	-371 ± 41	0.42 ± 0.04	1500 ± 155	-827 ± 43	0.578 ± 0.185	1082 ± 115	-263 ± 39
SDSSJ210524.49+000407.3	1365::	0.00::	0.45::	201::	202::	1.00::	1361::	203::	0.000
SDSSJ210831.56-063022.5	3665::	0.00::	0.46::	-1243::	-1242::	1.00::	3679::	-1244::	0.000
SDSSJ212329.46-005052.9	3656 ± 247	-0.04 ± 0.04	0.39 ± 0.02	-2885 ± 58	-2584 ± 119	0.88 ± 0.08	4719 ± 488	-2376 ± 48	0.115::	2043::	174::
SDSSJ235808.54+012507.2	1870 ± 224	0.00 ± 0.03	0.46 ± 0.01	-943 ± 78	-500 ± 49	1.00 ± 0.09	2464 ± 255	-1053 ± 87	0.000
Median	1997 ± 2045	-0.14 ± 0.42	0.40 ± 0.17	-856 ± 1214	-500 ± 707	0.68 ± 0.49	2560 ± 2032	-1249 ± 1016	0.312 ± 0.493	1082 ± 427	-120 ± 288
Population B											
HE 0001-2340	1029 ± 145	-0.07 ± 0.10	0.40 ± 0.02	-24 ± 30	-12 ± 64	0.43 ± 0.03	2768 ± 90	-443 ± 554	0.565 ± 0.202	894 ± 65	-1 ± 10
[HB89] 0029+073	1866 ± 271	-0.47 ± 0.01	0.38 ± 0.01	-922 ± 97	-562 ± 114	1.00 ± 0.06	3431 ± 168	-397 ± 42	0.000
CTQ 408	1497 ± 190	0.00 ± 0.01	0.46 ± 0.01	-524 ± 37	-524 ± 97	1.00 ± 0.09	1500 ± 401	-524 ± 37	0.000
H 0055-2659	1405 ± 325	-0.47 ± 0.06	0.25 ± 0.01	-198 ± 103	-91 ± 81	0.50 ± 0.07	3204 ± 412	-599 ± 312	0.496 ± 0.177	912 ± 66	69 ± 10
SDSSJ114358.52+052444.9	2577 ± 251	0.05 ± 0.03	0.54 ± 0.02	-968 ± 52	-1079 ± 186	0.78 ± 0.03	1982 ± 83	-1295 ± 70	0.220 ± 0.078	1304 ± 94	-1 ± 10
SDSSJ115954.33+201921.1	1233 ± 186	-0.20 ± 0.10	0.37 ± 0.03	-347 ± 46	-302 ± 76	0.55 ± 0.07	2684 ± 204	-499 ± 66	0.448 ± 0.160	995 ± 72	-261 ± 39
SDSSJ120147.90+120630.2	2584 ± 200	-0.10 ± 0.01	0.61 ± 0.01	-594 ± 49	-504 ± 126	0.72 ± 0.05	1879 ± 196	-978 ± 81	0.280 ± 0.100	1129 ± 82	244 ± 37
SDSSJ141546.24+112943.4	1193 ± 204	-0.37 ± 0.01	0.38 ± 0.01	-116 ± 70	55 ± 75	0.47 ± 0.04	1499 ± 111	-415 ± 250	0.526 ± 0.188	700 ± 51	151 ± 23
SDSSJ153830.55+085517.0	1520 ± 192	0.00 ± 0.01	0.46 ± 0.01	-545 ± 38	-545 ± 97	1.00 ± 0.09	1523 ± 101	-545 ± 38	0.000
PKS 2126-15	1212 ± 167	-0.22 ± 0.03	0.41 ± 0.01	-441 ± 44	-355 ± 75	0.30 ± 0.09	1332 ± 272	-988 ± 99	0.702 ± 0.250	937 ± 68	-285 ± 43
Median	1451 ± 562	-0.15 ± 0.31	0.40 ± 0.08	-482 ± 346	-429 ± 396	0.52 ± 0.32	1930 ± 1241	-534 ± 426	0.364 ± 0.463	937 ± 159	-1 ± 241

Notes. ^a [O III] λ 5007 location is not clear for this source since it is placed at the red end of the observed spectrum. In this case, the measurements were performed with [O III] λ 4959.

Clear distinctions between Pop. A and Pop. B are also seen in the center and left panels of Fig. 2.4, which present the $c(1/2)$ and $c(1/4)$ vs FWHM($H\beta_{\text{full}}$) relations, respectively. Pop. A sources show in general no shift, within the uncertainties, or a negative value of velocity centroids in the case of the 4 sources with a BLUE component (with average centroid values at 1/2 and 1/4 of -167 and -312 km s⁻¹, respectively). On the other hand, Pop. B sources always present positive velocities for $c(1/2)$ and $c(1/4)$, with a mean value of 658 and 1929 km s⁻¹, respectively, as a consequence of a very strong VBC. The VBC individually has a median velocity shift of ~ 3000 km s⁻¹, in a range from -1500 to 4000 km s⁻¹. These results are in complete agreement with previous results (e.g. Wolf et al. 2020, and references therein).

[O III] λ 4959, 5007

High-ionisation lines like [O III] λ 5007 are seen as one of the main detectors of outflowing gas in radio-quiet sources (Zamanov et al. 2002; Komossa et al. 2008; Zhang et al. 2011; Marziani et al. 2016b). In the case of radio-loud sources, narrow-line outflowing gas has been associated with jets through the blueshifted line components (Capetti et al. 1996; Axon et al. 2000; Bicknell 2002; Kauffmann et al. 2008; Best & Heckman 2012; Reynaldi & Feinstein 2013; Jarvis et al. 2019; Berton & Järvelä 2021). Outflows are also detected in $H\beta$. Usually, the blueshifted components on the $H\beta$ profile are related to those found for the [O III] λ 5007 lines (Carniani et al. 2015; Cresci et al. 2015; Brusa et al. 2015; Marziani et al. 2022b). The results obtained for [O III] λ 5007 full profile and individual components are reported in Table 2.6. We present FWHM (col. 2), asymmetry (col. 3),

kurtosis (col. 4), and the centroid velocities at 1/2 and 9/10 intensities (cols. 5 and 6, respectively) for the full profile. Relative intensities, FWHM, and shifts are reported for the [O III] λ 5007 blueshifted components (cols. 7 to 9) and for the narrow components (cols. 10 to 12) of each quasar. It is difficult to distinguish the relative contribution of the two components in the majority of the cases. One of the main reasons for this is that in many sources the full [O III] λ 5007 emission is shifted to the blue, implying a shift of [O III] λ 5007 NC with respect to the rest-frame. Some sources like SDSSJ135831.78+050522.8 and SDSSJ161458.33+144836.9 present a NC strongly shifted to the blue, reaching shifts of ≈ -530 and -670 km s $^{-1}$ respectively, comparable to the shifts found for the semi-broad component (see e.g. Figs. A.1.10 and A.1.15 in the Appendix A.1). This is consistent with outflowing gas dominating the [O III] λ 5007 luminosity in luminous quasars (Shen & Ho 2014; Bischetti et al. 2017; Zakamska et al. 2016).

The remarkable feature of the [O III] λ 5007 profiles is a very intense and blueshifted SBC, such as the one of SDSSJ135831.78+050522.8 (Fig. A.1.10), which presents a blueshifted SBC that accounts for the full [O III] λ 5007 profile with a FWHM ≈ 5422 km s $^{-1}$ and a shift of ≈ -2080 km s $^{-1}$. In this case, the blueshifted SBC corresponds to 90% of the full profile and can be interpreted as a strong indicative of outflowing gas. SDSSJ135831.78+050522.8, along with Q 1410+096 (Fig. A.1.11 in the Appendix A.1), which shows a very similar profile, requires a strong and broad [O III] λ 5007 to account for the flux on the red side of H β . In our high luminosity sample, for 15/22 objects ($\sim 70\%$) the blueshifted SBC accounts for more than 50% of the total intensity of the [O III] profile. In fact, in six of these sources, the [O III] consists of exclusively a blueshifted SBC.

Very small blueshifted components are found in low-redshift [O III] λ 5007 profiles of Pop. B AGN (Zamfir et al. 2008; Sulentic et al. 2004) and even in Population A, shifts at peak above 250 km s $^{-1}$ are very rare (the so-called ‘blue-outliers’; Zamanov et al. 2002). At high-redshift, Pop. B [O III] λ 5007 profiles do present significant blueshifted SBC components but they still present different properties when compared to Pop. A sources: in our sample, the full profiles of Pop. A present a [O III] FWHM ≈ 2000 km s $^{-1}$ while Pop. B profiles have FWHM ≈ 1450 km s $^{-1}$. The more remarkable difference is seen in the shifts at 9/10 and 1/2 intensities of the full profile ($c(1/2) \approx -850$ km s $^{-1}$ for Pop. A and ≈ -480 km s $^{-1}$ for Pop. B). However, the A.I. of the two populations are almost the same, indicating that the lines present similar profile shapes. The [O III] λ 5007 emission of both Pop. A and Pop. B appears to be strongly affected (if not dominated) by outflowing gas.

An important consequence for redshift estimates is that the [O III] λ 5007 lines should be avoided when considering high- z quasars. In addition, three Pop. A (SDSSJ210524.49+000407.3, SDSSJ210831.56-063022.5, and SDSSJ235808.54+012507.2) and three Pop. B sources ([HB89] 0029+073, CTQ 0408, and SDSSJ153830.55+085517.0) present [O III] λ 5007 full profiles that can be well represented only by the blueshifted component (see the respective spectra in Figs. A.1.22, A.1.2, A.1.3, and A.1.14 in the Appendix A.1).

Figure 2.5 shows the relation between $W([O III])$ and $|c(9/10)|$ of [O III] λ 5007. For our sample, the $W([O III])$ ranges from $\approx 50\text{\AA}$ for some Pop. B sources to $< 1\text{\AA}$ for xAs, reaching the detection limit. It shares the same location as the high-redshift HE data. No clear difference between the location of Pop. A and Pop. B is confirmed by the median values of equivalent widths, 12\AA vs 10\AA

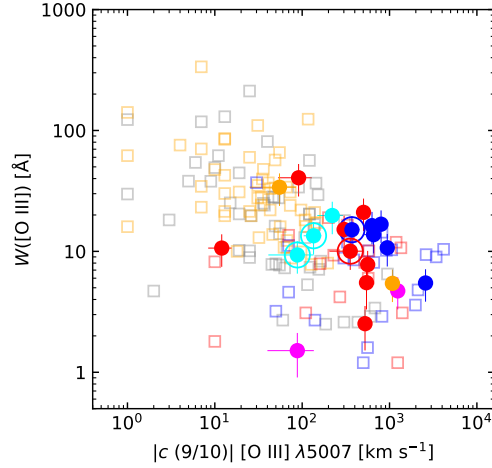


Fig. 2.5: $W([\text{O III}]\lambda 5007)$ versus $c(9/10)$. Blue and red squares indicate high-redshift Pop. A and Pop. B quasars from M09 while grey and orange open squares represent low- z sources from Marziani et al. (2003b), respectively. Colour scheme for our sample as the same as in Fig. 2.4. Error bars refer to 1σ level of confidence and were estimated only for our sample.

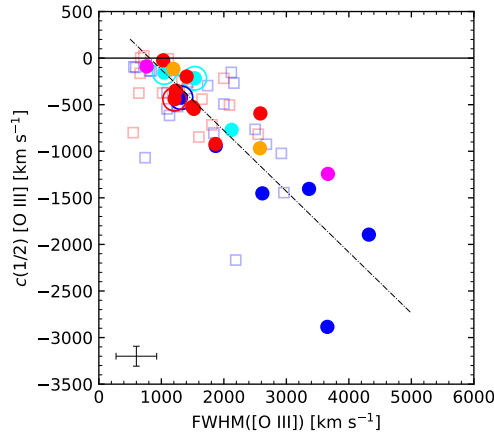


Fig. 2.6: FWHM of the full profile of $[\text{O III}]\lambda 5007$ versus centroid at 1/2 flux intensity ($c(1/2)$) for the $[\text{O III}]\lambda 5007$ emission line. Blue and red squares indicate high-redshift sources from M09. Dashed line represents a linear regression. Colour scheme is the same as in Fig. 2.4. Error bars refer to 1σ level of confidence and were estimated only for our sample.

for Pop. A and B, respectively (the average W is affected by the two A3 extremely faint sources with $W([\text{O III}]) \lesssim 1\text{Å}$). At low z (and low luminosity), sources have considerably larger W values but lower velocity centroids than the high- z sample. Our sample is located at the low end of the $W([\text{O III}])$ distribution of low- z sources as expected for luminous quasars (Shen & Ho 2014), and in a shift range that at low z is the exclusive domain of the rare, namesake ‘blue outliers’ (Marziani et al. 2016a). Figure 2.5 also shows that the radio-loud quasars from our sample are very tightly grouped together with moderate blueshifts for high- L quasars ($\lesssim 500\text{ km s}^{-1}$ at 0.9 fractional intensity).

A comparison between $c(1/2)$ and FWHM of the $[\text{O III}]\lambda 5007$ profiles is shown in Fig. 2.6. There is a strong correlation between the blueshift of $[\text{O III}]$, parameterised by the centroid at 1/2 intensity,

Table 2.7: Linear relations ($y = a + b * x$) between different emission line properties.

y (1)	x (2)	Method (3)	$a \pm \delta a$ (4)	$b \pm \delta b$ (5)	RMSE (6)	CC (7)	ρ -value (8)
$c(1/2)_{[\text{O III}]}$	FWHM($[\text{O III}]$)	Least squares	530 ± 205	-0.65 ± 0.08	402	-0.86	4.1×10^{-7}
$c(1/2)_{\text{C IV}}$	FWHM(CIV)	Least squares	$2000 \pm 737^{(a)}$	$-0.68 \pm 0.10^{(a)}$	429	-0.90 ^(a)	1.1×10^{-4} ^(a)
$\log W(\text{CIV})$	$\log [c(1/2)]_{\text{C IV}}$	Bisector	$3.21 \pm 0.17^{(a)}$	$-0.58 \pm 0.05^{(a)}$	0.28	-0.64 ^(a)	2.1×10^{-12} ^(a)
$\log W(\text{CIV})$	$\log \text{FWHM}(\text{CIV})$	Bisector	$8.31 \pm 0.71^{(a)}$	$-1.84 \pm 0.19^{(a)}$	0.31	-0.49 ^(a)	2.5×10^{-7} ^(a)
$c(1/2)_{\text{C IV}}$	$c(1/2)_{[\text{O III}]}$	Orthogonal	-1239 ± 276	1.50 ± 0.31	1086	0.45	4×10^{-3}

Notes. ^(a) Only for Pop. A.

Table 2.8: Spectrophotometric measurements on the UV region.

Source (1)	$f_{\lambda 1750}^{(a)}$ (2)	$f(\text{Si IV}+\text{O IV})^{(b)}$ (3)	$W(\text{Si IV}+\text{O IV})$ [Å] (4)	$f(\text{C IV})^{(b)}$ (5)	$W(\text{C IV})$ [Å] (6)	$f(\text{He II})^{(b)}$ (7)	$W(\text{He II})$ [Å] (8)	$f(\text{Al III})^{(b)}$ (9)	$W(\text{Al III})$ [Å] (10)	$f(\text{C III})^{(b)}$ (11)	$W(\text{C III})$ [Å] (12)	$f(\text{Si III})^{(b)}$ (13)	$W(\text{Si III})$ [Å] (14)
Population A													
SDSSJ005700.18+143737.7 ^(c)	5.9 ± 0.9	1.29 ± 0.19	16 ± 2	1.58 ± 0.24	22 ± 3	0.33 ± 0.05	5 ± 1	0.41 ± 0.06	8 ± 1	0.23 ± 0.03	5 ± 1	0.42 ± 0.06	8 ± 1
SDSSJ132012.33+142037.1	7.9 ± 1.2	1.77 ± 0.27	18 ± 2	3.66 ± 0.55	40 ± 5	0.81 ± 0.12	10 ± 1	0.31 ± 0.05	4 ± 1	0.57 ± 0.09	8 ± 1	0.75 ± 0.11	11 ± 1
SDSSJ135831.78+050522.8	13.6 ± 2.0	3.78 ± 0.57	20 ± 2	5.43 ± 0.81	34 ± 4	1.31 ± 0.20	9 ± 1	0.89 ± 0.13	7 ± 1	1.01 ± 0.15	9 ± 1	1.52 ± 0.23	13 ± 2
Q 1410+096	14.1 ± 2.1	2.45 ± 0.37	15 ± 2	3.50 ± 0.53	23 ± 3	1.50 ± 0.23	10 ± 1	0.96 ± 0.14	7 ± 1	1.17 ± 0.18	9 ± 1	1.18 ± 0.18	9 ± 1
SDSSJ161458.33+144836.9	15.4 ± 2.3	2.90 ± 0.44	14 ± 2	5.74 ± 0.86	31 ± 4	0.94 ± 0.14	6 ± 1	0.57 ± 0.09	4 ± 1	1.41 ± 0.21	11 ± 1	1.32 ± 0.20	10 ± 1
PKS 2000-330 ^(c)	-	3.20 ± 0.48	4 ± 2	4.50 ± 0.68	19 ± 2	-	-	-	-	-	-	-	-
SDSSJ210524.47+000407.3 ^{(d)(e)}	21.8 ± 3.3	-	-	1.50 ± 0.23	6 ± 1	0.75 ± 0.11	3 ± 1	2.19 ± 0.33	10 ± 1	0.51 ± 0.08	2 ± 1	1.97 ± 0.30	9 ± 1
SDSSJ210831.56-063022.5 ^(e)	14.3 ± 2.1	2.47 ± 0.37	14 ± 2	2.25 ± 0.34	13 ± 2	0.14 ± 0.02	1 ± 1	1.01 ± 0.15	7 ± 1	0.31 ± 0.05	2 ± 1	0.94 ± 0.14	7 ± 1
SDSSJ212329.46-005052.9	23.9 ± 3.6	3.58 ± 0.54	9 ± 1	6.09 ± 0.91	19 ± 2	0.85 ± 0.13	3 ± 1	1.77 ± 0.27	9 ± 1	0.59 ± 0.09	3 ± 1	1.89 ± 0.28	10 ± 1
SDSSJ235808.54+012507.2	7.5 ± 1.1	1.52 ± 0.23	12 ± 1	2.55 ± 0.38	25 ± 3	0.71 ± 0.11	8 ± 1	1.91 ± 0.29	5 ± 1	0.47 ± 0.07	8 ± 1	0.61 ± 0.09	10 ± 1
Population B													
SDSSJ114358.52+052444.9	20.2 ± 3.0	2.28 ± 0.34	8 ± 1	5.86 ± 0.88	24 ± 3	1.42 ± 0.21	6 ± 1	0.71 ± 0.11	4 ± 1	1.30 ± 0.20	7 ± 1	0.98 ± 0.15	5 ± 1
SDSSJ115954.33+201921.1	24.3 ± 3.6	3.64 ± 0.55	12 ± 1	5.55 ± 0.83	20 ± 2	0.92 ± 0.14	4 ± 1	1.14 ± 0.17	5 ± 1	1.94 ± 0.29	9 ± 1	0.62 ± 0.09	3 ± 1
SDSSJ120147.90+120630.2	16.3 ± 2.4	3.44 ± 0.52	15 ± 2	7.57 ± 1.14	37 ± 4	1.63 ± 0.24	9 ± 1	0.67 ± 0.10	5 ± 1	3.00 ± 0.45	22 ± 3	1.13 ± 0.17	8 ± 1
SDSSJ141546.24+112943.4 ^(d)	16.8 ± 2.5	-	-	-	-	-	-	1.59 ± 0.24	7 ± 1	5.10 ± 0.77	23 ± 3	2.83 ± 0.42	13 ± 2
SDSSJ153830.55+085517.0 ^(f)	17.4 ± 2.6	4.92 ± 0.74	19 ± 2	5.34 ± 0.80	24 ± 3	0.64 ± 0.10	3 ± 1	1.91 ± 0.29	12 ± 1	0.94 ± 0.14	6 ± 1	1.27 ± 0.19	8 ± 1

Notes. ^(a) In units of $10^{-15} \text{ erg s}^{-1} \text{ cm}^{-2} \text{ \AA}^{-1}$. ^(b) In units of $10^{-13} \text{ erg s}^{-1} \text{ cm}^{-2}$. ^(c) The UV spectrum does not cover the 1900 Å blend. ^(d) Presents broad absorption lines in the regions of C IV $\lambda 1549$ +He II $\lambda 1640$ and Si IV $\lambda 1397$ +O IV $\lambda 1402$. ^(e) We consider BLUE+BC when estimating fluxes and equivalent widths of Al III and Si III $\lambda 1892$. ^(f) This source is optically classified as Pop. B, but the UV spectrum fits perfectly with the one of a Pop. A quasar.

and the FWHM. The dashed line in the plot traces the linear regression between both parameters, derived from an unweighted least squares fit:

$$c(1/2)_{[\text{O III}]} \approx (-0.65 \pm 0.08) \text{FWHM}([\text{O III}]) + (530 \pm 205). \quad (2.1)$$

Table 2.7 lists this linear relation, along with the other that relates to C IV. We report the fitted parameters (cols. 1 and 2), the method used (col. 3), the linear correlation coefficients (cols. 4 and 5), the rms (col. 6), the Pearson r score (col. 7), and its associated null hypothesis probability value (col. 8). Equation 2.1 confirms several previous works (Komossa et al. 2008; Marziani et al. 2016b) and justifies the interpretation of the [O III] $\lambda 5007$ profile in terms of a blueshifted semibroad component and of a narrow component (Zhang et al. 2011).

Table 2.9: Measurements on the 1900Å blend.

Source	Al III λ 1860 BLUE			Al III λ 1860 BC			Si III λ 1892 BLUE			Si III λ 1892 BC			C III λ 1909 BC			C III λ 1909 VBC			C III λ 1909 NC			Fe III λ 1914			
	I/I_{tot}	FWHM [km s $^{-1}$]	Shift [km s $^{-1}$]	I/I_{tot}	FWHM [km s $^{-1}$]	Shift [km s $^{-1}$]	I/I_{tot}	FWHM [km s $^{-1}$]	Shift [km s $^{-1}$]	I/I_{tot}	FWHM [km s $^{-1}$]	Shift [km s $^{-1}$]	I/I_{tot}	FWHM [km s $^{-1}$]	Shift [km s $^{-1}$]	I/I_{tot}	FWHM [km s $^{-1}$]	Shift [km s $^{-1}$]	I/I_{tot}	FWHM [km s $^{-1}$]	Shift [km s $^{-1}$]	I/I_{tot}	FWHM [km s $^{-1}$]	Shift [km s $^{-1}$]	
(1)	(2)	(3)	(4)	(5)	(6)	(7)	(8)	(9)	(10)	(11)	(12)	(13)	(14)	(15)	(16)	(17)	(18)	(19)	(20)	(21)	(22)	(23)	(24)	(25)	
Population A																									
SDSSJ005700.18+143737.7	0.47 ± 0.04	3268 ± 396	-1686 ± 202	0.53 ± 0.04	2792 ± 283	0 ± 10	0.36 ± 0.07	3268 ± 392	-1686 ± -202	0.64 ± 0.13	2792 ± 335	-3 ± 11	1.00 ± 0.18	2400 ± 288	0 ± 10
SDSSJ132012.33+142037.1	0.27 ± 0.02	1731 ± 210	-967 ± 116	0.72 ± 0.06	2029 ± 206	0 ± 10	0.00	0.08 ± 0.02	3030 ± 364	0 ± 10	0.92 ± 0.17	3030 ± 364	0 ± 10
SDSSJ135831.78+050522.8	0.00	1.00 ± 0.08	4225 ± 428	0 ± 10	0.00	1.00 ± 0.21	4225 ± 507	0 ± 10	1.00 ± 0.18	2720 ± 326	0 ± 10
Q 1410+096	0.00	1.00 ± 0.08	2604 ± 264	279 ± 33	0.00	1.00 ± 0.21	2604 ± 312	279 ± 33	1.00 ± 0.18	2604 ± 312	278 ± 58
SDSSJ161458.33+144836.9	0.00	1.00 ± 0.08	3374 ± 342	0 ± 10	0.00	1.00 ± 0.21	3374 ± 405	0 ± 10	1.00 ± 0.18	3319 ± 398	0 ± 10
SDSSJ210524.49+000407.3	0.61 ± 0.05	4365 ± 529	-2003 ± 240	0.39 ± 0.03	3672 ± 372	0 ± 10	0.23 ± 0.04	3415 ± 410	-2002 ± -240	0.77 ± 0.16	4169 ± 500	0 ± 10	1.00 ± 0.18	2577 ± 309	0 ± 10
SDSSJ210831.56-063022.5	0.36 ± 0.03	3181 ± 386	-1951 ± 234	0.64 ± 0.05	4173 ± 423	0 ± 10	0.21 ± 0.04	3187 ± 382	-1951 ± -234	0.79 ± 0.17	4173 ± 501	0 ± 10	1.00 ± 0.18	3156 ± 379	0 ± 10
SDSSJ212329.46-005052.9	0.00	1.00 ± 0.08	5122 ± 519	0 ± 10	0.00	1.00 ± 0.21	5122 ± 615	0 ± 10	1.00 ± 0.18	3125 ± 375	0 ± 10
SDSSJ235808.54+012507.2	0.00	1.00 ± 0.08	3243 ± 329	0 ± 10	0.00	1.00 ± 0.21	3243 ± 389	0 ± 10	1.00 ± 0.18	3243 ± 389	0 ± 10
Median	0.00 ± 0.36	3224 ± 723	-1818 ± 457	1.00 ± 0.36	3374 ± 1381	...	0.23 ± 0.07	3268 ± 114	-1951 ± 158	...	3374 ± 1381	2760 ± 552
Population B																									
SDSSJ114358.52+052444.9	0.00	1.00 ± 0.08	3967 ± 402	0 ± 10	0.00	1.00 ± 0.18	3967 ± 476	-3 ± 11	0.50 ± 0.10	3967 ± 476	0 ± 10	0.50 ± 0.05	7038 ± 1253	2842 ± 369	0.02 ± 0.01	1000 ± 178	0 ± 10	0.00
SDSSJ115954.33+201921.1	0.00	1.00 ± 0.08	4999 ± 506	0 ± 10	0.00	1.00 ± 0.18	4999 ± 600	0 ± 10	0.64 ± 0.13	4999 ± 600	0 ± 10	0.36 ± 0.03	6563 ± 1168	1998 ± 260	0.01 ± 0.01	733 ± 130	0 ± 10	0.00
SDSSJ120147.90+120630.2	0.00	1.00 ± 0.08	3999 ± 405	0 ± 10	0.00	1.00 ± 0.18	3999 ± 480	0 ± 10	0.70 ± 0.14	3999 ± 480	0 ± 10	0.30 ± 0.03	7046 ± 1254	2207 ± 287	0.01 ± 0.01	999 ± 178	0 ± 10	0.00
SDSSJ141546.24+112943.4	0.00	1.00 ± 0.08	5105 ± 517	0 ± 10	0.00	1.00 ± 0.18	5105 ± 613	0 ± 10	0.64 ± 0.13	4101 ± 492	0 ± 10	0.36 ± 0.03	7365 ± 1311	3134 ± 407	0.10 ± 0.01	1062 ± 189	0 ± 10	0.00
SDSSJ153830.55+085517.0 ^(a)	0.00	1.00 ± 0.08	3085 ± 313	0 ± 10	0.00	1.00 ± 0.18	3085 ± 370	0 ± 10	1.00 ± 0.20	3104 ± 372	28 ± 16	0.00	1.00 ± 0.12	3141 ± 377	783 ± 94	
Median	3999 ± 1032	3999 ± 1032	...	0.64 ± 0.06	3999 ± 134	...	0.36 ± 0.05	7042 ± 206	2524 ± 760	...	999 ± 83	

Notes. ^(a) UV line profiles of this source were fitted with Lorentzian shapes. See note in the Appendix A.1 (Fig. A.1.14)

2.5.3 UV

The fits for the UV emission lines are shown in Appendix A.1, along with the full UV spectra of the 15 available sources (10 Pop. A and 5 Pop. B). Spectrophotometric measurements in the UV region are reported in Table 2.8 and concern the 1900 Å blend, C IV λ 1549+He II λ 1640, as well as flux intensity and equivalent width of Si IV+O IV (cols. 3-4), C IV (cols. 5-6), He II (cols. 7-8), Al III (cols. 9-10), C III] (cols. 11-12), and Si III (cols 13-14).

1900 Å blend

Table 2.9 presents the measurements resulting from the `specfit` analysis of the 1900 Å blend. Intensities, FWHM, and shifts are shown for the emission line profiles and their components, whenever the profile presents more than just one component. In cols. 2 to 4, we list the relative intensity, FWHM, and shift of the blueshifted component of Al III λ 1860; cols. 5 to 7 show the broad component of Al III λ 1860; cols. 8 to 10 for Si III] λ 1892 BLUE; cols. 11 to 13 for Si III] λ 1892 BC; cols. 14 to 16, the BC of C III] λ 1909; cols. 17 to 19, the VBC of C III] λ 1909; cols. 20 to 22, the NC of C III] λ 1909; and, finally, cols. 23 to 25 for a Fe III] λ 1914 emission line component.

The Al III λ 1860 contribution can be well fitted assuming only a BC for all Pop. A sources but four: SDSSJ005700.18+143737.7, SDSSJ210524.49+000407.3, SDSSJ210831.56-063022.5, and SDSSJ132012.33+142037.1. These same three sources are the ones that are located in the A3 region of the quasar MS. In these cases, we need to add a BLUE component with $3000 \leq \text{FWHM} \leq 4500 \text{ km s}^{-1}$ in the Al III λ 1860 doublet and in the Si III] λ 1892 emission line profile. We have imposed the same FWHM for both components.

The Pop. A C III] λ 1909 profile can be well reproduced by a strong BC at rest-frame in combination with a component that accounts for the Fe III] λ 1914 contributions in its red wing. The motivation to include the Fe III] λ 1914 line resides in the selective enhancement due to Lyman α fluorescence that is well-known to affect the UV Fe II emission and Fe III emission as well (Sigut & Pradhan 1998; Sigut et al. 2004). Of the Fe II features the UV multiplet 191 at λ 1785 is known to be enhanced by Ly α fluorescence: a strong Fe II UV multiplet 191 may suggest a strong Fe III] λ 1914 line. There is an overall consistency between the presence of the Fe III] λ 1914 line and the detection of the Fe II feature (8 out of 10 Pop. A sources with UV suitable data have both). However, the relative contribution of the C III] λ 1909 and Fe III] λ 1914 remains difficult to ascertain because the two lines are severely blended together and some Fe III] λ 1914 emission is already included in the Fe III template.

For Pop. B sources, Al III and Si III] λ 1892 are well represented by only one component and in the five cases these emission lines share the same FWHM and are centred at the respective rest-frame wavelength. However, the C III] λ 1909 VBC is systematically less broad than the H β VBC: average FWHM is $\approx 7000 \text{ km s}^{-1}$ for C III] versus $\approx 12000 \text{ km s}^{-1}$ for H β .

Table 2.10: Measurements on the CIV λ 1549+He II λ 1640 full line profiles and SPECFIT analysis.

Source (1)	CIV λ 1549 full profile								CIV λ 1549									He II λ 1640													
	FWHM [km s ⁻¹] (2)	A. L. (3)	Kurt. (4)	c($\frac{1}{2}$) [km s ⁻¹] (5) (6)		c($\frac{3}{4}$) [km s ⁻¹] (7) (8)		BLUE			BC			VBC			BLUE			BC			VBC								
				I/I_{tot}	FWHM [km s ⁻¹] (10)	Shift [km s ⁻¹] (11)	I/I_{tot}	FWHM [km s ⁻¹] (12)	Shift [km s ⁻¹] (13)	I/I_{tot}	FWHM [km s ⁻¹] (14)	Shift [km s ⁻¹] (15)	I/I_{tot}	FWHM [km s ⁻¹] (16)	Shift [km s ⁻¹] (17)	I/I_{tot}	FWHM [km s ⁻¹] (18)	Shift [km s ⁻¹] (19)	I/I_{tot}	FWHM [km s ⁻¹] (20)	Shift [km s ⁻¹] (21)	I/I_{tot}	FWHM [km s ⁻¹] (22)	Shift [km s ⁻¹] (23)	I/I_{tot}	FWHM [km s ⁻¹] (24)	Shift [km s ⁻¹] (25)	I/I_{tot}	FWHM [km s ⁻¹] (26)		
Population A																															
SDSSJ005700.18+143737.7	8648 ± 562	-0.38 ± 0.01	0.40 ± 0.01	-4951 ± 334	-3994 ± 181	-3272 ± 272	-2604 ± 326	0.81 ± 0.05	13187 ± 1846	-2318 ± 278	0.19 ± 0.05	2808 ± 298	0 ± 10	0.67 ± 0.04	13187 ± 1846	-4249 ± 510	0.33 ± 0.02	2808 ± 298	0 ± 10
SDSSJ132012.33+142037.1	5549 ± 399	-0.36 ± 0.01	0.37 ± 0.01	-2956 ± 263	-2407 ± 124	-1830 ± 177	-1419 ± 190	0.72 ± 0.04	8739 ± 1223	-1446 ± 174	0.28 ± 0.03	3278 ± 348	0 ± 10	0.60 ± 0.04	9837 ± 1377	-3388 ± 407	0.40 ± 0.02	3278 ± 348	0 ± 10
SDSSJ153831.78+050522.8	7365 ± 655	-0.27 ± 0.03	0.30 ± 0.01	-3188 ± 416	-2460 ± 190	-1808 ± 256	-1556 ± 187	0.52 ± 0.03	11983 ± 1678	-1909 ± 229	0.48 ± 0.02	4404 ± 468	0 ± 10	0.55 ± 0.03	11983 ± 1678	-3386 ± 406	0.45 ± 0.03	4404 ± 468	0 ± 10
Q 1410+096	6311 ± 552	-0.18 ± 0.05	0.33 ± 0.01	-2604 ± 374	-1746 ± 179	-1052 ± 172	-1691 ± 90	0.41 ± 0.03	10881 ± 1523	-1526 ± 183	0.59 ± 0.01	3293 ± 350	0 ± 10	0.53 ± 0.03	9369 ± 1312	-7880 ± 946	0.47 ± 0.03	3292 ± 350	0 ± 10
SDSSJ161458.33+144836.9	5790 ± 554	-0.27 ± 0.03	0.30 ± 0.02	-2779 ± 327	-2394 ± 139	-1894 ± 190	-1519 ± 168	0.59 ± 0.04	9333 ± 1307	-1609 ± 193	0.41 ± 0.01	3816 ± 406	0 ± 10	0.66 ± 0.04	9556 ± 1338	-5483 ± 658	0.34 ± 0.02	3816 ± 406	0 ± 10
PKS 2000-330	4950 ± 346	-0.33 ± 0.01	0.39 ± 0.01	-2373 ± 226	-1923 ± 104	-1465 ± 154	-1155 ± 169	0.70 ± 0.04	7340 ± 1028	-1300 ± 156	0.30 ± 0.02	3142 ± 334	0 ± 10
SDSSJ210524.49+000407.3	8443 ± 592	-0.15 ± 0.01	0.43 ± 0.01	-5060 ± 297	-4695 ± 134	-4452 ± 228	-4175 ± 279	0.89 ± 0.05	10418 ± 1459	-3926 ± 471	0.11 ± 0.02	3504 ± 372	-82 ± 20	0.55 ± 0.03	10418 ± 1459	-8749 ± 1050	0.45 ± 0.03	3504 ± 372	-81 ± 20
SDSSJ210831.56-063022.5	9389 ± 619	-0.30 ± 0.01	0.42 ± 0.01	-5744 ± 365	-4982 ± 177	-4284 ± 264	-3709 ± 334	0.87 ± 0.05	13618 ± 1907	-3250 ± 390	0.13 ± 0.01	4340 ± 461	0 ± 10	0.70 ± 0.04	13618 ± 1907	-3250 ± 390	0.30 ± 0.02	4340 ± 461	0 ± 10
SDSSJ212329.46-005052.9	7978 ± 524	-0.21 ± 0.01	0.42 ± 0.01	-3752 ± 332	-3311 ± 139	-2876 ± 231	-2551 ± 277	0.72 ± 0.04	10217 ± 1430	-2694 ± 323	0.28 ± 0.01	5457 ± 580	0 ± 10	0.63 ± 0.04	10217 ± 1430	-4233 ± 508	0.37 ± 0.02	5457 ± 580	0 ± 10
SDSSJ235808.54+012507.2	6504 ± 398	-0.25 ± 0.01	0.44 ± 0.01	-3197 ± 245	-2727 ± 114	-2312 ± 186	-2029 ± 235	0.80 ± 0.05	8302 ± 1162	-2163 ± 260	0.20 ± 0.01	3468 ± 369	0 ± 10	0.49 ± 0.03	9231 ± 1292	-5323 ± 639	0.51 ± 0.03	3468 ± 369	0 ± 10
Median	6934 ± 2406	-0.27 ± 0.10	0.39 ± 0.08	-3192 ± 1828	-2593 ± 1426	-2103 ± 1359	-1860 ± 1062	0.72 ± 0.19	10317 ± 2820	-2036 ± 1053	0.28 ± 0.19	3486 ± 927	0.60 ± 0.11	10217 ± 2427	-4249 ± 2095	0.4 ± 0.11	3504 ± 1048
Population B																															
SDSSJ114358.52+052444.9	7078 ± 766	-0.30 ± 0.05	0.27 ± 0.01	-3049 ± 511	-2059 ± 230	-1375 ± 204	-1147 ± 185	0.60 ± 0.06	14345 ± 1037	-1497 ± 180	0.24 ± 0.04	5055 ± 365	0 ± 10	0.16 ± 0.02	11848 ± 2109	3822 ± 515	0.57 ± 0.06	14345 ± 1037	-3216 ± 433	0.17 ± 0.02	5055 ± 365	0 ± 10	0.26 ± 0.03	11848 ± 2109	2540 ± 342	
SDSSJ115954.33+201921.1	5741 ± 585	-0.08 ± 0.05	0.29 ± 0.01	-1671 ± 444	-1851 ± 122	-1516 ± 166	-1253 ± 174	0.54 ± 0.05	9933 ± 718	-1307 ± 157	0.32 ± 0.05	5716 ± 413	0 ± 10	0.14 ± 0.01	8458 ± 1506	4397 ± 592	0.36 ± 0.04	9933 ± 718	-1307 ± 176	0.07 ± 0.01	5716 ± 413	0 ± 10	0.58 ± 0.06	8458 ± 1506	4397 ± 592	
SDSSJ120147.90+120630.2	4995 ± 475	-0.08 ± 0.04	0.32 ± 0.01	-1354 ± 284	-1133 ± 104	-1061 ± 148	-1015 ± 152	0.50 ± 0.05	7464 ± 540	-1454 ± 174	0.35 ± 0.05	3945 ± 285	0 ± 10	0.15 ± 0.01	6710 ± 1194	1508 ± 203	0.44 ± 0.04	7464 ± 540	-4676 ± 630	0.09 ± 0.01	3945 ± 285	0 ± 10	0.47 ± 0.05	6710 ± 1194	1508 ± 203	
SDSSJ153830.55+085517.0	5819 ± 448	-0.41 ± 0.02	0.35 ± 0.02	-2841 ± 303	-2108 ± 147	-1381 ± 187	-961 ± 185	0.68 ± 0.07	10024 ± 725	-992 ± 119	0.32 ± 0.05	4313 ± 312	0 ± 10	0.48 ± 0.05	10024 ± 725	-992 ± 134	0.52 ± 0.08	4313 ± 312	0 ± 10	
Median	5780 ± 1474	-0.17 ± 0.21	0.30 ± 0.06	-2256 ± 1563	-1955 ± 783	-1378 ± 342	-1081 ± 252	0.57 ± 0.15	9978 ± 2162	-1380 ± 415	0.30 ± 0.07	4129 ± 1268	...	0.15 ± 0.01	8458 ± 2569	3822 ± 1444	0.46 ± 0.16	9978 ± 2087	-2261 ± 2920	0.14 ± 0.24	4129 ± 1255	...	0.47 ± 0.16	8458 ± 2569	2540 ± 1444	

C IV λ 1549+He II λ 1640

Measurements related to the C IV λ 1549+He II λ 1640 blend are reported in Table 2.10. As for H β , we list FWHM (col. 2), A.I. (col. 3), kurtosis (col. 4), and centroids $c(1/4)$, $c(1/2)$, $c(3/4)$ and $c(9/10)$ in cols. 5 to 8 for the C IV λ 1549 full line profile. Information on individual components is also given for both C IV λ 1549 and He II λ 1640. Columns 9-11 give the relative intensity I/I_{tot} , FWHM, and shift for C IV λ 1549 BLUE; cols. 12-14 for C IV λ 1549 BC; cols. 15-17 for C IV λ 1549 VBC; cols. 18-20 for He II λ 1640 BLUE; cols. 21-23 for He II λ 1640 BC; and cols. 24-26 for He II λ 1640 VBC.

We have 10 out of 12 Pop. A sources and four out of 10 Pop. B quasars with C IV covered for analysis. The fits are remarkably good and allow for the ‘plateau’ found as an extension of the red wing of C IV λ 1549 close to 1575 Å, which can usually be well reproduced by fitting C IV λ 1549 and He II λ 1640 with the same FWHM for blueshifted, broad, and very broad components (Fine et al. 2010; Marziani et al. 2010). In general, Pop. A objects present a larger FWHM of the full profile, always $\geq 4900 \text{ km s}^{-1}$, with respect to Pop. B. Pop. A are also those that in general present higher asymmetries and shifts towards the blue. Apart from SDSSJ212329.46-005052.9, all Pop. A sources present a $\text{FWHM}(\text{C IV}_{\text{BC}}) \leq 4500 \text{ km s}^{-1}$. The Pop. A3 SDSSJ210831.56-063022.5 is the source with the strongest blueshift, reaching $c(1/2) \approx -4980 \text{ km s}^{-1}$ and with similar values of fractional intensities along the profile (as can be seen in the top plot of Fig. 2.7).

In the case of Pop. B sources, we have found that the VBC accounts for only $\sim 15\%$ of the full profile. The widest VBC FWHM is seen in SDSSJ114358.52+052444.9, which reaches 11848 km s^{-1} with a shift of 3822 km s^{-1} . This same source is the one that also presents the broadest FWHM of the BLUE (14345 km s^{-1}) and larger shift (-1497 km s^{-1}). In all Pop. B cases, the BLUE component accounts for at least 50% of the C IV full profile, but still a fraction that is lower than in Pop. A ($\sim 70\%$). Correspondingly, the Pop. A C IV λ 1549 profiles in general present higher blueshifts and asymmetry indexes than the ones measured in Pop. B.

The top and bottom panels from Fig. 2.7 show the relation between the rest-frame equivalent widths of C IV λ 1549 and the centroid velocities at 1/2 peak intensity ($c(1/2)$) and FWHM respectively). We also include in the figure the bright, high- z xA sample of Martínez-Aldama et al. (2018) as well as the high- z data from S17 and the FOS low- z data from S07. Our data are in good agreement with the ones of Martínez-Aldama et al. (2018) and S17. Our sample, together with the high- L comparison samples, presents smaller values of C IV λ 1549 equivalent width when compared with the FOS data. Additionally, the high- z , high- L sources are those that present the most blueshifted C IV λ 1549 profiles among all quasars (Shen et al. 2011; Rankine et al. 2020; Vietri et al. 2018, 2020). The Pearson correlation coefficient between W and $c(1/2)$ of C IV λ 1549 for the Pop. A sources is -0.64 (with $\rho = 2.1 \times 10^{-12}$) and their relation is given in Table 2.7. There is also a correlation between W and FWHM C IV λ 1549 with $r \approx -0.49$, if we restrict the samples to only Pop. A objects (Table 2.7).

Figure 2.8 presents the strong correlation between FWHM and $c(1/2)$ of the C IV line, with a Pearson $r \approx -0.90$ for high- z Pop. A sources:

$$c(1/2)_{\text{CIV}} = (-0.68 \pm 0.10)\text{FWHM}(\text{C IV}) + (2000 \pm 737). \quad (2.2)$$

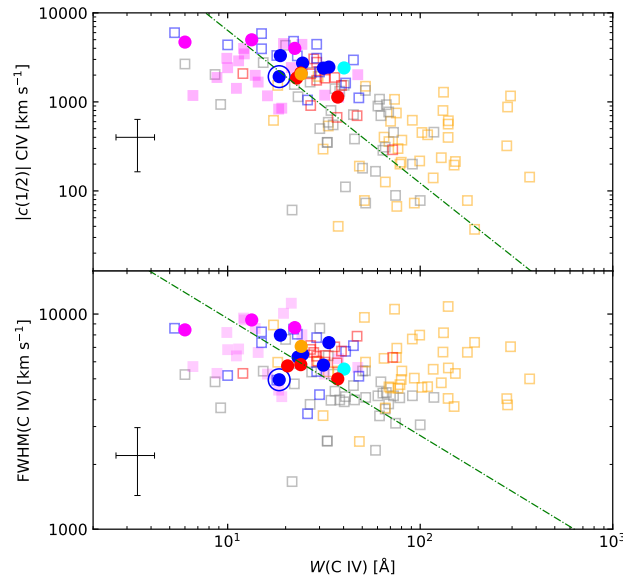


Fig. 2.7: Comparison between the different properties of the CIV emission line profile. *Top*: Relation between centroid velocity at 1/2 intensity ($c(1/2)$) and rest-frame equivalent width of CIV λ 1549. *Bottom*: FWHM of CIV λ 1549 versus $W(\text{CIV})$. Colour scheme for our sample is the same as in Fig. 2.4. Filled magenta squares indicate data from Martínez-Aldama et al. (2018). Blue and red open squares represent Pop. A and Pop. B HE sources from S17. Low- z FOS data from S07 are represented by grey (Pop. A) and orange (Pop. B) squares. Green point-dashed lines indicate the linear regression obtained through the bisector method including only the Pop. A sources from the four samples. Error bars refer to 1σ level of confidence and were estimated only for our sample.

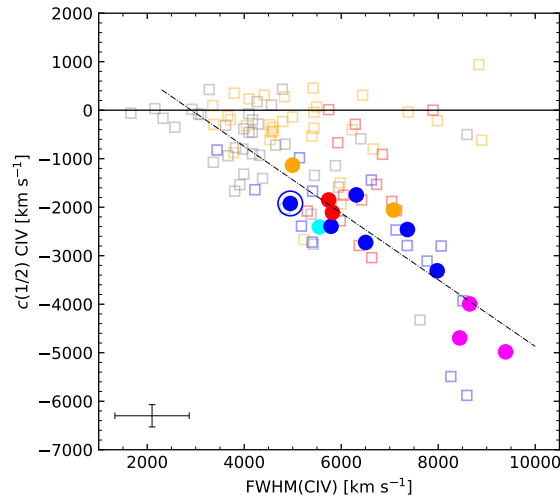


Fig. 2.8: Centroid velocity at 1/2 flux intensity, $c(1/2)$, for the CIV emission line versus the FWHM of the full profile of CIV. Filled circles represent our sample and the colour scheme is the same as in Fig. 2.4. Blue and red open squares are high-redshift sources from S17. Low- z Pop. A and Pop. B are represented by grey and orange open squares, respectively. Dashed line represents the least squares linear regression presented in Eq. 2.2, including only Pop. A sources. Error bars refer to 1σ level of confidence for our sample.

Table 2.11: Measurements on the full profiles of Si IV λ 1397+OIV] λ 1402.

Source	FWHM [km s ⁻¹]	A.I.	Kurtosis	$c(1/2)$ [km s ⁻¹]	$c(9/10)$ [km s ⁻¹]
(1)	(2)	(3)	(4)	(5)	(6)
Population A					
SDSSJ005700.18+143737.7	8659 ± 1202	-0.34 ± 0.02	0.36 ± 0.03	-2110 ± 377	-858 ± 443
SDSSJ132012.33+142037.1	5128 ± 859	-0.26 ± 0.05	0.34 ± 0.01	-376 ± 249	131 ± 293
SDSSJ135831.78+050522.8	7438 ± 1658	-0.27 ± 0.07	0.31 ± 0.01	-150 ± 534	499 ± 395
Q 1410+096	5430 ± 790	0.00 ± 0.09	0.40 ± 0.01	750 ± 157	666 ± 335
SDSSJ161458.33+144836.9	7370 ± 860	-0.26 ± 0.06	0.48 ± 0.01	-392 ± 227	680 ± 844
PKS 2000-330	3494 ± 329	0.32 ± 0.13	0.55 ± 0.02	888 ± 63	54 ± 112
SDSSJ210831.56-063022.5	9253 ± 1880	-0.24 ± 0.05	0.28 ± 0.03	-2613 ± 481	-1618 ± 452
SDSSJ212329.46-005052.9	6157 ± 892	-0.06 ± 0.05	0.40 ± 0.01	-868 ± 190	-635 ± 396
SDSSJ235808.54+012507.2	7135 ± 974	-0.14 ± 0.03	0.40 ± 0.01	-533 ± 252	-55 ± 443
Median	7135 ± 1888	-0.14 ± 0.20	0.40 ± 0.04	-392 ± 718	-55 ± 1134
Population B					
SDSSJ114358.52+052444.9	7070 ± 1027	-0.11 ± 0.05	0.40 ± 0.01	184 ± 242	394 ± 439
SDSSJ115954.33+201921.1	6813 ± 1372	-0.12 ± 0.07	0.34 ± 0.01	257 ± 396	644 ± 378
SDSSJ120147.90+120630.2	5000 ± 717	-0.18 ± 0.20	0.34 ± 0.04	667 ± 156	609 ± 315
SDSSJ153830.55+085517.0	5906 ± 1222	-0.18 ± 0.02	0.36 ± 0.01	159 ± 416	504 ± 413
Median	6359 ± 1197	-0.15 ± 0.06	0.35 ± 0.03	220 ± 181	556 ± 141

This relation is in good agreement with previous results (e.g. [Coatman et al. 2016](#); [Marziani et al. 2016a](#); [Sulentic et al. 2017](#); [Sun et al. 2018](#); [Vietri et al. 2018](#), and references therein). As the blueshift of C IV increases, FWHM(C IV) is likely to increase as well. Both C IV FWHM and blueshift parameterised by $c(1/2)$ show a clear increase from spectral types A1 to A3, the latter being those with the highest blueshifts (median value ≈ -4500 km s⁻¹) and the widest FWHM (median ≈ 9000 km s⁻¹).

In the case of C IV λ 1549 in Pop. B sources, the shifts at 1/2 flux intensities are also displaced towards blue wavelengths with average value of $c(1/2) = -1681$ km s⁻¹ and mean FWHM ≈ 5940 km s⁻¹, somewhat smaller than for Pop. A. However, the $c(1/2)$ values for the Pop. B sources from our sample are still higher than the majority of the low-luminosity and low-redshift quasars, which usually present a $c(1/2) \leq 200$ km s⁻¹. Low-luminosity Pop. B spectra show a sort of dichotomy in the C IV λ 1549 shift distribution: a fraction of sources remains unshifted or with modest shifts to the blue (the orange and grey “cloud” of points in Fig. 2.8). The FOS low-luminosity and low-redshift sources tend to present smaller $c(1/2)$ in the C IV λ 1549 emission line when compared with our data. This indicates that the C IV λ 1549 blueshifted components seen in higher-luminosity sources are more prominent than the ones observed in quasars of lower luminosities.

Si IV λ 1397+OIV] λ 1402

Table 2.11 presents the measurements on the full profile of Si IV λ 1397+OIV] λ 1402. We report values of FWHM (col. 2), A.I. (col. 3), kurtosis (col. 4), $c(1/2)$ (col. 5), and $c(9/10)$ (col. 6). Si IV λ 1397+OIV] λ 1402 BC is set at rest-frame and our initial guess for this component takes into account the results obtained for the C IV_{BC} after fitting the C IV λ 1549+He II λ 1640 region. SDSSJ141546.24+112943.4 has very strong and wide absorption lines in this region of the UV spectra, which makes it difficult to perform a reliable fitting (see Fig. A.1.12 in the Appendix A.1).

Regarding the BLUE of Si IV λ 1397+O IV λ 1402, they are very wide (even if they are apparently not as wide as in C IV λ 1549+He II λ 1640), reaching more than 6000 km s⁻¹ in all cases, and representing a significant percentage of the full emission line profile. The shifts towards shorter wavelength are also smaller than for C IV λ 1549, but they are still very high, going from 800 to 2700 km s⁻¹, with the extreme amplitude of SDSSJ135831.78+050522.8 that reaches \approx 4400 km s⁻¹.

The fluxes of C IV λ 1549 and Si IV λ 1397 presented in Table 2.8 indicate that on average Pop. A presents higher values of the C IV λ 1549/Si IV λ 1397 ratio (\approx 0.69) than Pop. B (\approx 0.49). This discrepancy may be linked to differences in chemical abundances with Pop. A sources being systematically more metal rich (c.f. [Śniegowska et al. 2021](#); [Punsly et al. 2020](#)). However, the issue goes beyond the scope of the present work and will be discussed elsewhere.

2.6 Discussion

In the previous section, we show that Pop. A and Pop. B sources may reflect different contributions of line emitting gas that produces prominent blueshifted features and is most likely associated with an outflow. To shed further light on the role of outflows, we now report an interline comparison in both the optical and UV spectral regions. We highlight the effect of the outflowing components on the estimate of physical parameters such as black hole mass and Eddington ratio.

2.6.1 Defining the outflow

H β and [O III] λ 5007

The relation between the FWHM of the full profiles of H β and [O III] λ 5007 is shown in Fig. 2.9. In general, the two populations present a FWHM(H β _{full}) higher than FWHM([O III]_{full}), as expected from previous observations ([Sulentic et al. 2004, 2007a](#); [Zamfir et al. 2010, M09](#)). At low- z , only in the case of the ‘blue-outliers’ the [O III] λ 5007 profiles appear to be very boxy-shaped and with the FWHM $>$ 1000 km s⁻¹. Some of these sources are NLSy1s and the [O III] λ 5007 FWHM is becoming comparable to the one of the broad H β profile sources ([Zamanov et al. 2002](#); [Komossa et al. 2008](#); [Cracco et al. 2016](#); [Komossa et al. 2018](#); [Berton & Järvelä 2021](#)). At high z and high luminosity the [O III] λ 5007 profiles often appear much broader, as do also the H β broad profiles ([Carniani et al. 2015](#); [Fiore et al. 2017](#); [Villar Martín et al. 2020](#)). Two cases in point, taken from previous works, are 2QZJ002830.4-281706 at $z = 2$. ([Cano-Díaz et al. 2012](#); [Carniani et al. 2015](#)) and HE0940-1050 at $z = 3.1$ ([Marziani et al. 2017a](#)). We have four sources that present [O III] λ 5007 FWHM above 3000 km s⁻¹, comparable to the H β FWHM, with one extraordinary case in which FWHM(H β _{full}) is smaller than FWHM([O III]_{full}) (SDSSJ135831.78+050522.8, Pop. A1), with FWHM(H β _{full}) \approx 3550 km s⁻¹ and FWHM([O III]_{full}) \approx 4320 km s⁻¹ (see Fig. A.1.10). Although FWHM of [O III] λ 5007 \gtrsim 2000 km s⁻¹ are frequently observed at high luminosity, some extreme values should be taken with care because the [O III] λ 5007 profiles are weak and broad: it is difficult to properly define the [O III] λ 5007 profiles especially when the broad H β red wing is strong.

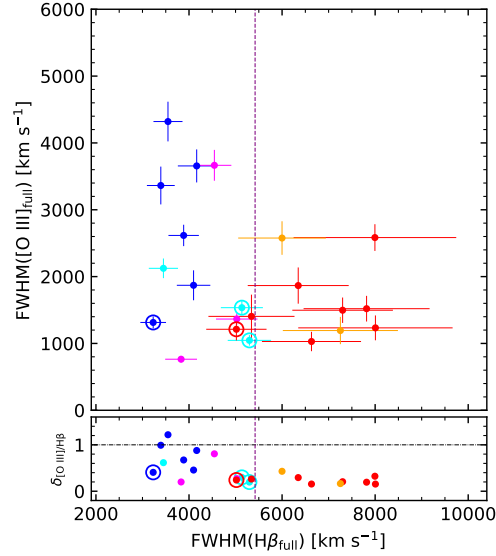


Fig. 2.9: Relation between $H\beta$ and $[O\text{ III}]\lambda 5007$ emission lines. *Top panel:* FWHM of the full profile of $[O\text{ III}]\lambda 5007$ vs FWHM of the full profile of $H\beta$. *Bottom panel:* Ratio $\delta_{[O\text{ III}]/H\beta} = \text{FWHM}([O\text{ III}]_{\text{full}})/\text{FWHM}(H\beta_{\text{full}})$ vs FWHM of the full profile of $H\beta$. As in Fig. 2.4, each colour represent one different spectral type, and symbols surrounded by open circles indicate the radio-loud quasars.

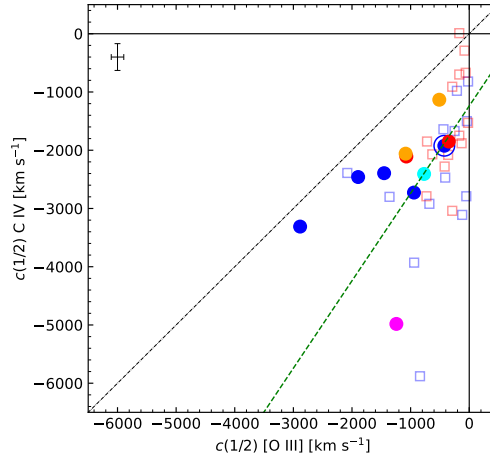


Fig. 2.10: Centroid velocity at 1/2 flux intensity ($c(1/2)$) of $C\text{ IV}\lambda 1549$ vs $c(1/2)$ of $[O\text{ III}]\lambda 5007$. Blue and red open squares show the HE Pop. A and Pop. B sources studied by M09 and S17. Colour scheme is the same as in Fig. 2.4. The green line indicates the linear regression between $c(1/2)$ of $C\text{ IV}\lambda 1549$ and $[O\text{ III}]\lambda 5007$ obtained through the orthogonal least square method. The error bars refer to 1σ level of confidence for our sample.

$[O\text{ III}]\lambda 5007$ versus $C\text{ IV}\lambda 1549$

Figure 2.10 shows the relation between $c(1/2)$ for $[O\text{ III}]\lambda 5007$ and $C\text{ IV}\lambda 1549$. The HE comparison sample analysed in M09 and S17 is included. The sources that present strong shifts in the $[O\text{ III}]\lambda 5007$ emission line profiles will also present it in $C\text{ IV}\lambda 1549$, in agreement with the HE data. Both lines show a correlation between their widths and shifts (Fig. 2.6 for $[O\text{ III}]\lambda 5007$ and Fig. 2.8 for

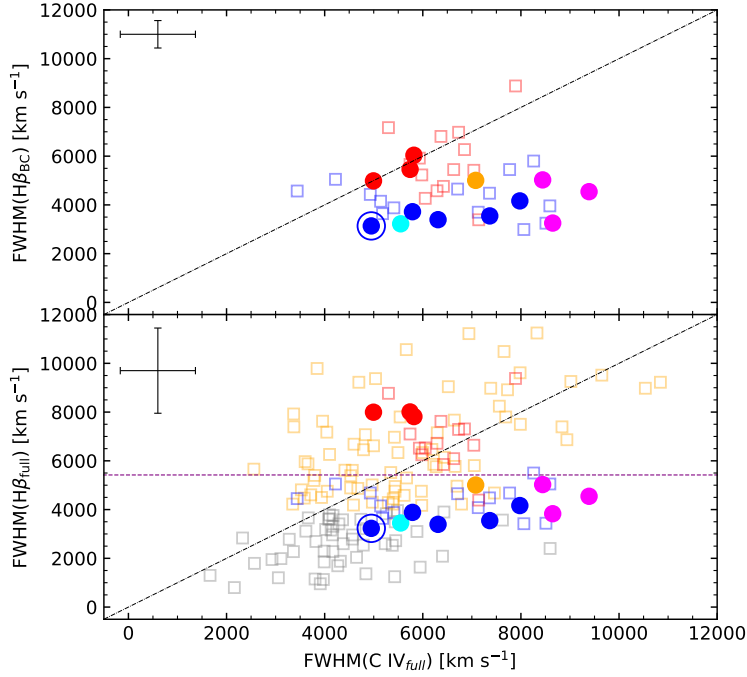


Fig. 2.11: $\text{FWHM}(\text{H}\beta_{\text{BC}})$ vs $\text{FWHM}(\text{C IV}_{\text{full}})$ and $\text{FWHM}(\text{H}\beta_{\text{full}})$ vs $\text{FWHM}(\text{C IV}_{\text{full}})$. Sources are identified according to the different bins of spectral types following colour scheme from Fig. 2.4. Blue and red open squares represent Pop. A and Pop. B sources from S17 and grey and orange open squares indicate Pop. A and Pop. B from S07, respectively. Horizontal purple line indicates the A-B boundary and the error bars on the top left of the plots refer to 1σ level of confidence for our sample.

$\text{C IV}\lambda 1549$) indicating that the broadening is mainly associated with a blueshifted component that is increasing in prominence with increasing shift. The least-squares linear regression of Fig. 2.10 (considering both HEMS and our sample) is given by:

$$c(1/2)_{\text{CIV}} = (1.50 \pm 0.31) c(1/2)_{[\text{O III}]}\lambda 5007 + (-1239 \pm 276), \quad (2.3)$$

in a good agreement with the study of Coatman et al. (2019). The trend (actually, a weak, marginally significant correlation at a 3σ confidence level) of Fig. 2.10 raises the issue of the relation between $[\text{O III}]\lambda 5007$ and $\text{C IV}\lambda 1549$ outflows. There is evidence suggesting that the semi-broad component of $[\text{O III}]\lambda 5007$ W remains almost constant with luminosity (Marziani et al. 2016b, §4.3), overwhelming the narrow, core component. The narrow component is however mainly associated with the NLR that may extend up to tens of kpc (Bennert et al. 2002, 2006). The dispersion in the relation with more sources around 0 shift in $[\text{O III}]\lambda 5007$ might be explained by a narrow component whose strength may depend on the past AGN evolution (Storchi-Bergmann et al. 2018). It is therefore not surprising that, even if a large $\text{C IV}\lambda 1549$ shift is measured, the $[\text{O III}]\lambda 5007$ profile may be unshifted or show only a modest blueshift. However, the presence of a shift correlation and the relatively large $[\text{O III}]\lambda 5007/\text{C IV}\lambda 1549$ FWHM ratio support a physical connection between an inner outflow on scales of a few hundreds gravitational radii where the BLUE $\text{C IV}\lambda 1549$ component is emitted, and an outflow at the outer edge of the BLR, beyond $10^4 - 10^5$ gravitational radii (Zamanov et al. 2002),

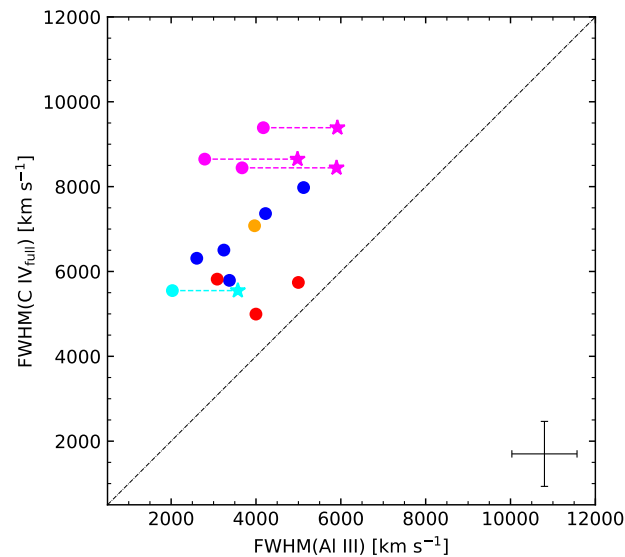


Fig. 2.12: C IV_{full} relation with Al III. Colour scheme is the same as in Fig. 2.4. Data points joined by a dashed line are those for which a significant blueshifted emission component has been isolated. The data points to the left refer to the Al III BC only and the right ones (star symbol) to the full profile FWHM (BC+BLUE). Error bars refer to 1σ level of confidence.

where the [O III] λ 5007 semibroad component likely originates. The nature of this connection remains unclear. It is beyond the scope of the present chapter and might be investigated elsewhere.

C IV λ 1549 versus H β

The top panel of Fig. 2.11 represents the relation between FWHM(H β _{BC}) and FWHM(C IV_{full}), including the S17 sample. Our data is in agreement with this comparison sample in terms of a clear A-B separation. The Pop. A sources seem to present a trend from A1 to A3 in the FWHM(C IV_{full}) where the A3 sources show the largest values. The FWHM(C IV_{full}) is larger than the FWHM(H β _{BC}), and the widths of the two lines are not correlated. There is a degeneracy between C IV λ 1549 and H β : to a single value of H β FWHM corresponds a wide range of C IV λ 1549 FWHM (c.f. S07, Capellupo et al. 2015; Mejía-Restrepo et al. 2016; Coatman et al. 2017). The systematically broader profile can be interpreted as a consequence of the dominance of the outflow component in the C IV λ 1549 line profile (Marziani et al. 2019).

The bottom panel of Fig. 2.11 shows the FWHM(C IV_{full}) vs FWHM(H β _{full}) where, apart from including S17 data, we also display the low- z sample from S07 for comparison. In this plot, the separation between Pop. A and Pop. B is even clearer: Pop. A sources show broader C IV λ 1549, while those of Pop. B have values consistent with, or narrower, than H β .

C IV λ 1549 versus Al III

Figure 2.12 shows FWHM of the full profiles of C IV λ 1549 versus FWHM of Al III. The FWHM(C IV_{full}) presents significantly higher values than FWHM(Al III). This indicates that the relation between

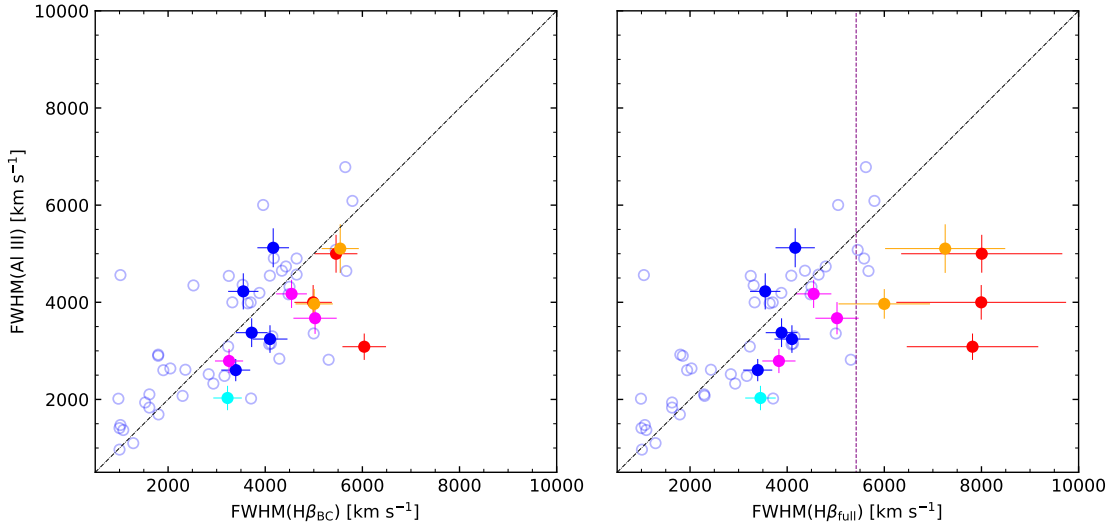


Fig. 2.13: $\text{FWHM}(\text{Al III})$ vs $\text{FWHM}(\text{H}\beta_{\text{BC}})$ (left panel) and $\text{FWHM}(\text{Al III})$ vs $\text{FWHM}(\text{H}\beta_{\text{full}})$ (right panel). Sources are identified according to the different bins of spectral types following colour scheme from Fig. 2.4. Blue open circles show the data from M22 Pop. A sources for a comparison. Vertical purple line indicates the A/B boundary for our sample.

$\text{CIV}\lambda 1549$ and Al III is similar to the one of $\text{CIV}\lambda 1549$ and $\text{H}\beta$. In both cases, the $\text{CIV}\lambda 1549$ FWHM tends to be larger: in particular, always significantly so for Pop. A and larger or consistent for Pop. B. The cyan and magenta dashed lines connect the FWHM estimated from the Al III BC with and without a BLUE component: without the BLUE (stars), the Al III FWHM becomes closer to, but remains significantly smaller than the FWHM of the $\text{CIV}\lambda 1549$ full profile.

2.6.2 Virial black hole mass estimates

A comparison between the FWHM of $\text{Al III}\lambda 1860$ and $\text{H}\beta$ (BC and full) profiles is shown in Fig. 2.13. The figure includes the data from Marziani et al. (2022c, hereafter M22) that involve exclusively Pop. A sources. The FWHM of $\text{H}\beta_{\text{BC}}$ is consistent with the FWHM of $\text{Al III}\lambda 1860$ for Pop. A: their average ratio (FWHM Al III over $\text{FWHM H}\beta$) in our sample is $\approx 0.87 \pm 0.18$. The right panel of Fig. 2.13 shows a comparison between $\text{FWHM}(\text{Al III})$ vs FWHM of full $\text{H}\beta$. The purple dotted vertical line indicates the A/B boundary as in Fig. 2.3. The location of our Pop. A objects remains in agreement with the results from M22, and with those for $\text{H}\beta_{\text{BC}}$. There is a clear deviation from the 1:1 line in the location of Pop. B sources: for the 5 Population B sources of our sample the average ratio is just 0.57 ± 0.12 (c.f. Marziani et al. 2017c). These results provide evidence that Pop. B Al III is systematically narrower than $\text{H}\beta$ full profile, most likely because of the strong VBC contribution. The ratio FWHM Al III over $\text{H}\beta_{\text{BC}}$ is in fair agreement $\approx 0.79 \pm 0.16$ for Pop. B, and therefore the $\text{H}\beta$ VBC should not be included on the black hole mass estimation. The 20 % difference between the $\text{FWHM H}\beta_{\text{BC}}$ and FWHM Al III for Pop. B sources is marginally significant and should be confirmed by larger samples.

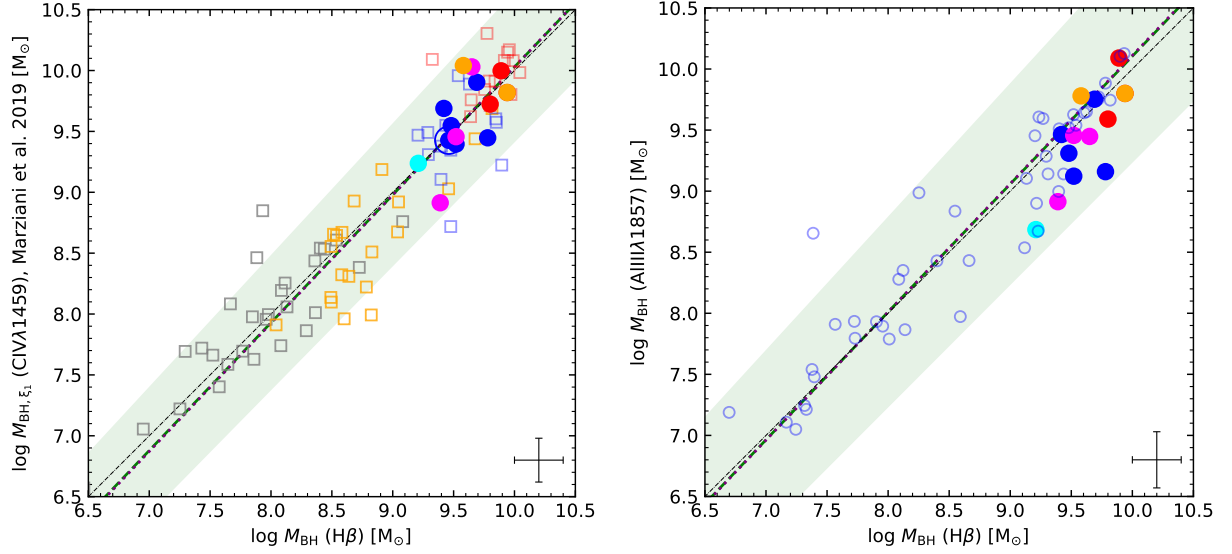


Fig. 2.14: $M_{\text{BH}}(\text{H}\beta)$ compared to $M_{\text{BH}}(\text{C IV})$ (left panel) and to $M_{\text{BH}}(\text{Al III})$ (right panel). Open squares on the left plot represent the low- and high-redshift sources analysed by Marziani et al. (2019) (blue and red for high- z and grey and orange for low- z Pop. A and Pop. B, respectively). Blue dots on the right panel are for the M22 data. Green and purple dashed lines indicate the linear regressions using bisector and orthogonal methods, respectively. Colour scheme is the same as in Fig. 2.4.

The black hole masses are estimated through different scaling relations using emission lines such as those based on the FWHM of $\text{H}\beta$, $\text{Al III}\lambda 1860$, and $\text{C IV}\lambda 1549$. The scaling law of Vestergaard & Peterson (2006) was used to estimate the mass M_{BH} with FWHM $\text{H}\beta_{\text{BC}}$. We used Equation (18) from Marziani et al. (2019, $\sigma = 0.33$) to estimate M_{BH} with the $\text{C IV}\lambda 1549$ FWHM. The left panel of Fig. 2.14 presents a comparison between the M_{BH} estimates using the scaling law for $\text{C IV}\lambda 1549$ from Marziani et al. (2019) and the $\text{H}\beta$ scaling law of Vestergaard & Peterson (2006). The open squares in this plot indicate the data from Marziani et al. (2019), which include high- and low- z sources. Our sample agrees with the previous estimates and corresponds to the extreme cases, with the largest M_{BH} reaching $10^{10} M_{\odot}$.

The plot of $M_{\text{BH, Al III}}$ versus $M_{\text{BH, H}\beta}$ (right panel of Fig. 2.14) relies on the M_{BH} scaling law from M22. The $M_{\text{BH, H}\beta}$ and $M_{\text{BH, Al III}}$ values obtained for our sources are compatible within the confidence interval of the M22 scaling law for Al III. We caution that the relation given in this equation has been derived for Pop. A sources and, consequently, it may lead to larger uncertainties for Pop. B quasars. For these sources we apply a correction $\xi = \text{FWHM}_{\text{H}\beta, \text{BC}} / \text{FWHM}_{\text{Al III}} = 1.35 \pm 0.10$ to the $\text{FWHM}(\text{Al III})$ (Marziani et al. 2017a, who assumed $\text{FWHM}_{\text{H}\beta, \text{BC}}$ as the reference virial broadening estimator).

The equations that describe the relations between M_{BH} estimations using ξ -corrected $\text{C IV}\lambda 1549$ and Al III are listed in Table 2.12. Column 1 lists the method used for the linear regression (orthogonal and bisector); cols. 2 and 3 present the linear and angular coefficients, along with the respective standard deviations; rms error and Pearson correlation coefficient r are reported in cols. 4 and 5, respectively.

Table 2.12: Linear relations between the different M_{BH} estimates using orthogonal and bisector methods.

Method	$a \pm \delta a$	$b \pm \delta b$	RMS	CC
(1)	(2)	(3)	(4)	(5)
$M_{\text{BH,CIV,M19}} = a + b * M_{\text{BH,H}\beta,\text{VP06}}$				
Orthogonal	-0.495 ± 0.306	1.053 ± 0.034	0.315	0.949
Bisector	-0.471 ± 0.289	1.050 ± 0.032		
$M_{\text{BH,AIII,M22}} = a + b * M_{\text{BH,H}\beta,\text{VP06}}$				
Orthogonal	-0.389 ± 0.431	1.050 ± 0.047	0.320	0.948
Bisector	-0.366 ± 0.411	1.047 ± 0.045		

Table 2.13: Weighted averaged masses, luminosity at 5100Å, and Eddington ratio (L/L_{Edd}), in logarithmic scale.

Source	$M_{\text{BH,H}\beta}$	M_{BH}	$L(1450\text{Å})$	$L(5100\text{Å})$	L/L_{Edd}
(1)	(2)	(3)	(4)	(5)	(6)
Population A					
SDSSJ005700.18+143737.7	9.39 ± 1.41	9.37 ± 0.27	46.65 ± 5.60	46.41 ± 5.57	0.10 ± 0.01
SDSSJ132012.33+142037.1	9.21 ± 1.38	9.19 ± 0.14	46.74 ± 5.61	46.42 ± 5.57	0.03 ± 0.01
SDSSJ135831.78+050522.8	9.42 ± 1.41	9.56 ± 0.11	46.97 ± 5.64	46.67 ± 5.60	0.07 ± 0.01
Q 1410+096	9.52 ± 1.43	9.42 ± 0.20	47.11 ± 5.65	46.92 ± 5.63	0.32 ± 0.04
B1422+231 ^(a)	9.96 ± 1.49	-	-	47.07 ± 5.65	-0.07 ± 0.01
SDSSJ161458.33+144836.9	9.48 ± 1.42	9.49 ± 0.10	47.05 ± 5.65	46.69 ± 5.60	0.04 ± 0.01
PKS 1937-101 ^(a)	10.14 ± 1.52	-	-	47.36 ± 5.68	0.05 ± 0.01
PKS 2000-330	9.46 ± 1.42	9.21 ± 0.04 ^(c)	46.58::	46.94 ± 5.63	0.30 ± 0.04
SDSSJ210524.47+000407.3	9.84 ± 1.48	9.83 ± 0.28 ^(b)	47.16 ± 5.66	46.89 ± 5.63	-0.13 ± 0.02
SDSSJ210831.56-063022.5	9.52 ± 1.43	9.63 ± 0.12	46.98 ± 5.64	46.43 ± 5.57	-0.26 ± 0.03
SDSSJ212329.46-005052.9	9.69 ± 1.45	9.77 ± 0.08	47.19 ± 5.66	46.92 ± 5.63	0.05 ± 0.01
SDSSJ235808.54+012507.2	9.78 ± 1.47	9.57 ± 0.31	46.85 ± 5.62	47.11 ± 5.65	0.15 ± 0.02
Population B					
HE 0001-2340 ^(a)	9.63 ± 1.44	-	-	46.48 ± 5.58	-0.33 ± 0.04
[HB89] 0029+073 ^(a)	9.71 ± 1.46	-	-	46.81 ± 5.62	-0.07 ± 0.01
CTQ 0408 ^(a)	10.20 ± 1.53	-	-	47.26 ± 5.67	-0.12 ± 0.01
H 0055-2659 ^(a)	9.69 ± 1.45	-	-	46.75 ± 5.61	-0.12 ± 0.01
SDSSJ114358.52+052444.9	9.58 ± 1.44	9.75 ± 0.25	47.16 ± 5.66	46.39 ± 5.57	-0.05 ± 0.01
SDSSJ115954.33+201921.1	9.89 ± 1.48	9.90 ± 0.05	47.36 ± 5.68	46.84 ± 5.62	-0.23 ± 0.03
SDSSJ120147.90+120630.2	9.94 ± 1.49	9.89 ± 0.2	47.19 ± 5.66	47.09 ± 5.65	0.03 ± 0.01
SDSSJ141546.24+112943.4	9.80 ± 1.47	9.78 ± 0.07 ^(b)	47.08 ± 5.65	46.64 ± 5.60	-0.33 ± 0.04
SDSSJ153830.55+085517.0	9.80 ± 1.47	9.76 ± 0.24	47.23 ± 5.67	46.50 ± 5.58	-0.47 ± 0.06
PKS 2126-15 ^(a)	9.78 ± 1.47	-	-	47.11 ± 5.65	0.16 ± 0.02

Notes. ^(a) The CIV λ 1549 and the 1900 Å blend regions were not fitted in these cases. ^(b) We compute the weighted averaged mass between the H β and Al III estimates only. ^(c) We compute the weighted averaged mass between the H β and CIV λ 1549 estimates only.

The original CIV λ 1549 VP06 relation lacks a correction because of the bias introduced by non-virial broadening (i.e. by the blueshifted component; Brotherton et al. 2015; Coatman et al. 2017; Marziani et al. 2019). If M_{BH} estimated with the uncorrected VP06 relations are used, there is a significant deviation in the 1:1 relation between H β and CIV λ 1549 M_{BH} estimates and a large scatter (rms ≈ 0.42). We therefore utilise the scaling laws based on Al III and ξ -corrected CIV λ 1549 that may provide less biased estimators with respect to H β -based M_{BH} scaling law.

Table 2.13 lists the individual values of H β black hole masses (col. 2), the weighted averages of M_{BH} (col. 3), the luminosity at 1450Å and 5100Å (cols. 4 and 5, respectively), as well as the Eddington ratio of each source (col.6). We have considered the mass estimates using H β , Al III, and

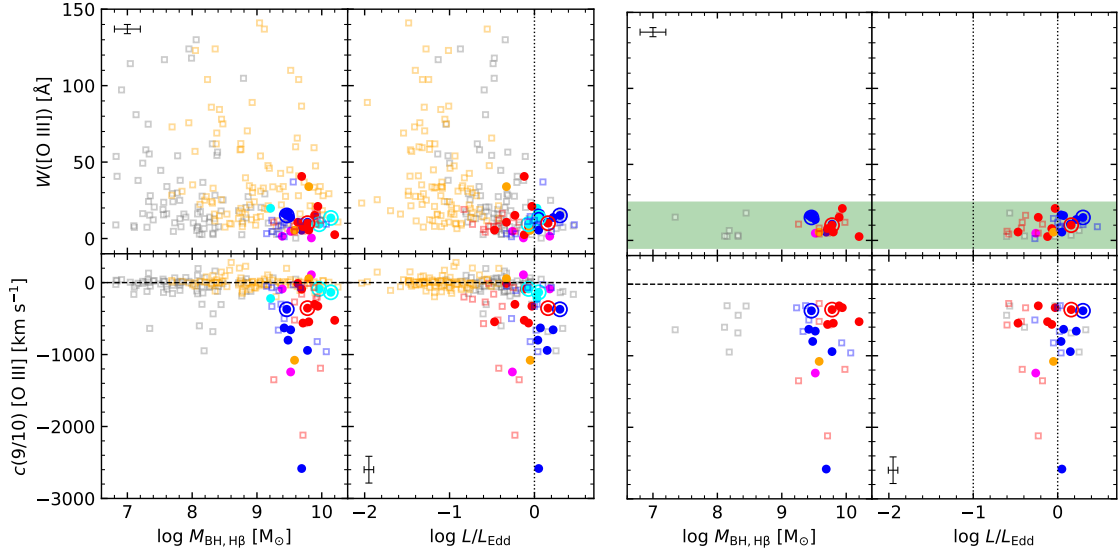


Fig. 2.15: [O III] λ 5007 dependence on physical parameters. *Left panel:* Our full sample in comparison with the full M03 (grey for Pop. A and orange for Pop. B) and HE (blue for Pop. A and red for Pop. B) samples. *Right panel:* Only sources with $c(9/10) < -250 \text{ km s}^{-1}$. Our data follow the same colour scheme as in Fig. 2.4.

C IV λ 1549 to determine the weighted average of M_{BH} and used the FWHM errors as weights. In addition, H β M_{BH} are reported since they are available for all sources of our sample and needed to compare our data to previous samples. We adopted a bolometric correction of 10 for the optical range in accordance with the value assumed in the previous works we consider for comparison (e.g. Richards et al. 2006; S07; S17; M19), although lower bolometric corrections are expected in the $L_{\text{bol}} > 10^{47} \text{ erg s}^{-1}$ luminosity range (Marconi et al. 2004; Netzer 2019), which may introduce a bias towards higher accretion rates. The bolometric correction adopted in the UV range is 3.5 (Elvis et al. 1994).

2.6.3 Dependence on accretion parameters

[O III] λ 5007

Figure 2.15 shows the dependence of $W([\text{O III}])$ and $c(9/10) [\text{O III}]$ on $M_{\text{BH,H}\beta}$ and L/L_{Edd} . Our sample presents $W([\text{O III}]) < 25 \text{ \AA}$ in the majority of the cases, with only two outliers (SDSSJ141546.24+112943.4 with $\approx 34 \text{ \AA}$ and H 0055-2659 with $\approx 41 \text{ \AA}$). The $W([\text{O III}])$ of our sample is relatively small when compared with low- z sources. However, our data more frequently show blueshifts in $c(9/10)$.

The right panels of Fig. 2.15 consider only sources that present $c(9/10) < -250 \text{ km s}^{-1}$. In this case, all the sources fit within $W([\text{O III}]) \lesssim 25 \text{ \AA}$ and are found in a wide range of M_{BH} as for the distribution of the full samples. Sources with $c(9/10) < -250 \text{ km s}^{-1}$ have an average Eddington ratio of -0.09: at high Eddington ratios, the [O III] λ 5007 profiles tend to be strongly affected or dominated by the blueshifted SBC. In addition, the [O III] λ 5007 W remains roughly constant over a wide range of masses (and luminosity), indicating that the luminosity of the blueshifted SBC is proportional to

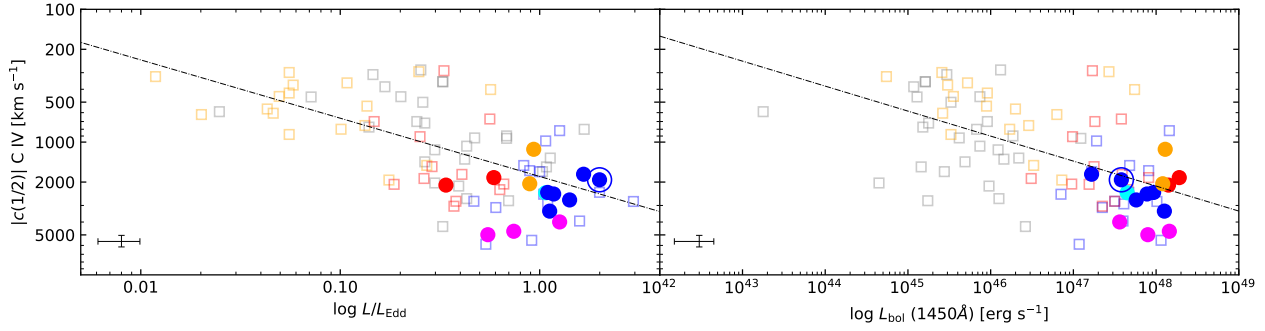


Fig. 2.16: Dependence of CIV on different parameters. *Left panel:* Relation between CIV $c(1/2)$ and L/L_{Edd} . *Right panel:* CIV $c(1/2)$ vs $L_{\text{bol}}(1450\text{\AA})$. Grey and orange squares represent low- z Pop. A and Pop. B quasars respectively, while blue and red open squares indicate HE Pop. A and Pop. B sources from S17. Colour scheme is the same as in Fig. 2.4. Linear regressions are shown by the dashed lines. The errors refer only to our sample.

the continuum luminosity. This result provides evidence that the outflow traced by the blueshifted $[\text{O III}]\lambda 5007$ is directly related to the active nucleus, as proportionality between line and continuum luminosity is a classical proof of photoionisation (Osterbrock & Shuder 1982).

CIV $\lambda 1549$

In Fig. 2.16, we provide an analysis of the dependence of CIV $\lambda 1549$ shift measured by $c(1/2)$ on luminosity and L/L_{Edd} . We include the data analysed by Marziani et al. (2019), along with the present sample data. The same trend appears to be followed by both ours and Marziani et al. (2019) samples. Sources that present the largest values of CIV $\lambda 1549$ $c(1/2)$ are Population A, with two xAs (SDSSJ210524.47+000407.3 and SDSSJ210831.56-063022.5), reaching $c(1/2) \approx -5000$ km s $^{-1}$.

As in S17, the left plot of Fig. 2.16 indicate a clear relation (with a Pearson correlation coefficient of 0.59) between $c(1/2)$ of CIV $\lambda 1549$ and L/L_{Edd} , given by the following equation for the absolute value of the centroid shift at 1/2:

$$\log |c(1/2)|_{\text{CIV}} = (0.43 \pm 0.06) \log L/L_{\text{Edd}} + (3.25 \pm 0.04). \quad (2.4)$$

A similar relation can also be derived between the absolute value of CIV $\lambda 1549$ $c(1/2)$ and $L_{\text{bol}}(1450\text{\AA})$ (right panel of Fig. 2.16):

$$\log |c(1/2)|_{\text{CIV}} = (0.18 \pm 0.03) \log L_{\text{bol}} + (-5.70 \pm 1.46). \quad (2.5)$$

The Pearson correlation coefficient in this case is 0.54. These relations are consistent with those of S17 who found slope ≈ 0.5 and ≈ 0.2 for the dependence on Eddington ratio and luminosity, respectively. Since the S17 data were included in the linear regression, we can say that the new data confirm the slope difference that suggests a major role of the L/L_{Edd} for governing the shift amplitude and a secondary effect of luminosity.

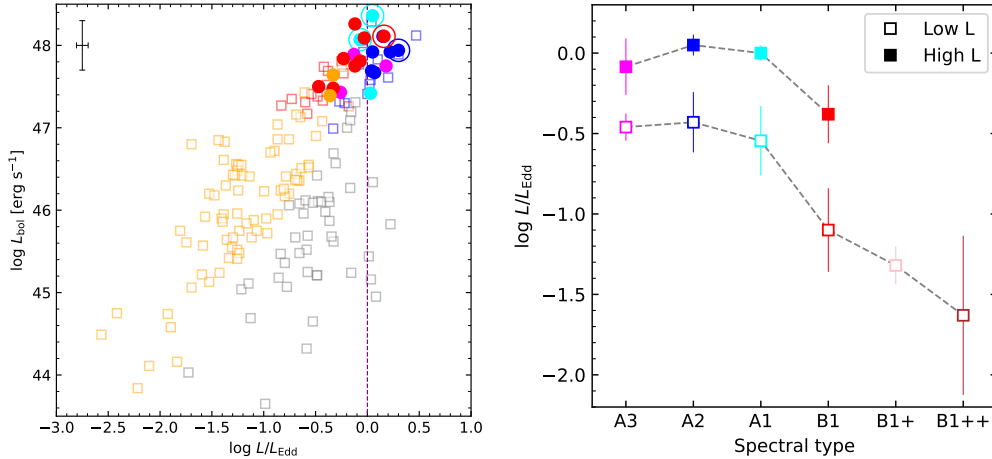


Fig. 2.17: Distribution of the different spectral types in a luminosity and Eddington ratio (L/L_{Edd}) context. *Left plot:* Bolometric luminosity L_{bol} vs L/L_{Edd} . Squared symbols identify the samples of S07 (low- z) and of S17 (high- z sources). Vertical purple line indicates $L/L_{\text{Edd}} = 1$. Colour scheme is the same as in Fig. 2.4. *Right plot:* Median values of the Eddington ratio separated into high-luminosity ($\log L > 47 \text{ erg s}^{-1}$) and low luminosity for each spectral type. We have included our own sources, along with the comparison samples. Error bars indicate the semi-interquartile range.

2.6.4 Redefining optical properties of high- z sources

Figure 2.17 shows the relation between the Eddington ratio and the bolometric luminosity. The distinction between Pop. A and Pop. B is very clear in both low- and high-redshift samples including our sample as well as the data analysed by S07 and S17. The systematically higher Eddington ratio of the high-luminosity samples may be in part the result of a Malmquist type bias (Sulentic et al. 2014a) on the assumption of a constant bolometric correction over a wide range in luminosity, orientation effects, and intrinsic evolution of the Eddington ratio (e.g. Cavaliere & Vittorini 2000; Volonteri et al. 2003; Shankar et al. 2009). For instance, the radio-loud sources from our sample seem to be the more extreme cases of their respective population, reaching $L/L_{\text{Edd}} \sim 1$. They are core-dominated and presumably beamed in the direction of the observer. The line profiles appear composite, in the sense that they show a narrower core superimposed on a VBC. The width of the narrower core may be lowered if the emitting regions are constrained within a flattened geometry that is seen pole-on. This effect blurs the distinction between Pop. A and B, letting sources that are intrinsically Pop. B enter into the domain of Pop. A in the MS optical plane (Fig. 2.3; Marziani et al. 2001; Zamfir et al. 2008).

The right panel of Fig. 2.17 presents the median values of the Eddington ratio for each individual spectral type, distinguishing between higher ($L > 10^{47} \text{ erg s}^{-1}$) and lower ($L < 10^{47} \text{ erg s}^{-1}$) luminosity sources (S07; M09; S17, together with our sample). The Eddington ratio is consistently higher in Pop. A sources rather than in Pop. B sources for both cases of luminosity and redshift separation. Low-redshift, low-luminosity sources present very small L/L_{Edd} values for Pop. B. The more extreme case is for low-redshift Pop. B1++, with a $L/L_{\text{Edd}} \approx -1.65$. On the converse Pop. A sources have more similar values at low and high luminosity. There is no notable difference between high and low-luminosity and high and low-redshift distribution on the spectral type and $\log L/L_{\text{Edd}}$ plane,

which may indicate that the more luminous sources present the highest Eddington ratios because of a Malmquist-type bias (Sulentic et al. 2014a) rather than evolutionary effects on L/L_{Edd} .

Of the four quasars that are radio-loud, B1422+231, PKS 1937-101, and PKS 2000-330 are classified as Pop. A, while PKS 2126-15 is a Pop. B source. From four sources we can only make some preliminary considerations that will be properly discussed in a companion paper involving mainly radio-loud objects. The basic result is that the four RLs do not have outstanding properties with respect to the RQ samples considered in this chapter. They share the trends between $H\beta$ and [O III] λ 5007 RQ profile parameters. A remarkable aspect is that the four RL AGN studied in this chapter show high Eddington ratio, a fact that is never observed in powerful RL sources at low- z (Sikora et al. 2007; Zamfir et al. 2008) that are more frequently classified as population B sources. At low- z , low-power, ‘jetted’ sources for which high Eddington ratio has been estimated to be ~ 1 are known to exist (the so-called RL NLSy1s; Komossa et al. 2006; Berton et al. 2015; Foschini et al. 2015). Even if L/L_{Edd} might be overestimated, the implication is that there is apparently no empirical inconsistency between powerful jetted emission and high accretion rate.

2.7 Conclusions

We presented a sample of 22 high-redshift and high-luminosity quasars (12 Pop. A; 10 Pop. B) observed with the VLT/ISAAC spectrograph to cover the $H\beta$ spectral range shifted into the near infrared. A dedicated analysis has been performed on the most prominent emission features in the new optical spectra ($H\beta$, [O III] λ 5007, Fe II), as well as in survey or published UV spectra (Al III, CIII], C IV λ 1549, Si IV λ 1397, Fe II, Fe III) to measure several parameters related to the emitting gas physical conditions and dynamics. Our main conclusions are as follows.

1. We confirm that the full profile of $H\beta$ may be generally well represented by solely a Lorentzian BC for Pop. A quasars, while two Gaussians (BC and VBC) provide a satisfactory fit for those of Pop. B, with the broader, redshifted VBC accounting for $\approx 50\%$ of the emission line. Also, some Pop. A $H\beta$ profiles from our sample present outflowing components that seem to be related to those observed in the [O III] λ 5007 lines.
2. Compared to low- z and low-luminosity samples, our data presents a displacement in the MS in the direction of higher values of FWHM of the $H\beta$ full profile and R_{FeII} . The relation between profile parameters and the M_{BH} and L/L_{Edd} differences between Pop. A and B are also confirmed, in the form seen in previous high-luminosity samples.
3. The [O III] λ 5007 profile is broad and not reproducible with a simple Gaussian. All [O III] λ 5007 profiles of our sample are blueshifted by more than 250 km s^{-1} . Differently from the low z range, high- z Pop. B [O III] λ 5007 profiles present significant contribution of blueshifted semi-broad components, even though they are still less strong than the ones found in Pop. A sources. Nevertheless, both population seem to share similar asymmetry indexes, which indicates that their profiles present comparable shapes.

4. In some cases, the [O III] λ 5007 FWHM reach values comparable to those of H β . This effect is found, in particular, for sources with high L/L_{Edd} , and may be compared with the case of highly-accreting NLSy1s at low z . Line widths appear extraordinarily large (thousands km s^{-1}) because of the high black hole mass values involved. [O III] λ 5007 correlations between FWHM and shift, and also between W and shift mirror the correlations seen in C IV λ 1549.
5. The [O III] λ 5007 lines should be avoided for accurate redshift estimates in high- L , high- z quasars, as in most of sources the [O III] lines are dominated by a blueshifted SBC and no rest-frame narrow component could be clearly identified. The average shift of the [O III] profile peak is $\sim -520 \text{ km s}^{-1}$, which may lead to a considerable systematic blueshift of $\delta z \sim 0.0017$ on the redshift estimation.
6. Several C IV λ 1549 correlations (most notably the one between shift and width) and the C IV λ 1549 parameters' dependence on Eddington ratio and mass (or luminosity) are confirmed (including the ones of S17). Outflow-dominated profiles tend to have low- W , large FWHM, and shifts. The three parameters are definitely related.
7. We exploit the VP06 scaling law as reference for M_{BH} estimates, and we verified that the scaling law based on Al III is a reliable estimator with respect to black hole masses derived from H β . The C IV λ 1549 scaling law requires a FWHM correction.
8. [O III] λ 5007 and C IV λ 1549 seem to follow a very similar, strong correlation between FWHM and shift, as measured by the $c(1/2)$. The [O III] λ 5007 and C IV λ 1549 outflow velocities are related, as suggested by the correlation between their shift amplitudes shown in Fig. 2.10.
9. The radio loud sources in the high- z range seem to be radiating at high values of Eddington ratio (with $L/L_{\text{Edd}} \sim 1$), which is at variance with low- z values, where the most powerful jetted sources belong to Population B and radiate at a modest Eddington ratio.

The sample studied in this chapter is the first part of a sample involving roughly an equal number of RQ and of RI and RL sources. The data in this chapter provide a RQ comparison sample for the ISAAC spectra of RL sources that will be presented in a future paper.

ISOLATING AN OUTFLOW COMPONENT IN SINGLE-EPOCH SPECTRA OF QUASARS

3

Chapter based on the article published in *Galaxies* by P. Marziani, A. Deconto-Machado, and A. del Olmo, volume 10, 54, 18 pages, March 2022. DOI: 10.3390/galaxies10020054

Abstract

Gaseous outflows appear to be a universal property of type-1 and type-2 active galactic nuclei (AGN). The main diagnostic is provided by emission features shifted to higher frequency via the Doppler effect, implying that the emitting gas is moving toward the observer. However, beyond the presence of blueshift, the observational signatures of the outflows are often unclear, and no established criteria exist to isolate the outflow contribution in the integrated, single-epoch spectra of type-1 AGN. The emission spectrum collected with the typical apertures of long-slit spectroscopy or of fibre optics sample contributions over a broad range of spatial scales, making it difficult to analyse the line profiles in terms of different kinematic components. Nevertheless, hundred of thousands of quasars spectra collected at moderate resolution demand a proper analysis of the line profiles for proper dynamical modelling of the emitting regions. In this small contribution we shall analyse several profiles of the H γ Balmer line H β from composite and individual optical spectra of sources radiating at moderate Eddington ratio (Population B following [Sulentic et al. \(2000a\)](#)). Features and profile shapes that might be traced to outflow due to narrow-line region gas are detected over a wide range of luminosity.

3.1 Introduction

Type-1 active galactic nuclei (AGN) are characterised by the presence of broad and narrow optical and UV lines (for introductions see e.g., [Osterbrock & Mathews \(1986\)](#); [Netzer \(1990\)](#); [Peterson \(1997\)](#); [Sulentic et al. \(2000a\)](#); [Osterbrock & Ferland \(2006\)](#); [Marziani et al. \(2006\)](#)). Spectra show a mind-boggling variety of broad emission line profiles not only among different objects, but also among different lines in the spectrum of the same object. [Sulentic \(1989\)](#) carried out measurements of spectral shifts and asymmetries exhibited by the broad lines relative to the narrow ones, proposing an empirical classification scheme for the broad H γ Balmer line H β . Among the classes identified by

Sulentic (1989), two stand out: AR,R and AR,B, where AR means red-ward asymmetric, and the letter after the comma indicates either a shift of the line peak toward the red or the blue.

Fast forward more than 30 years, type-1 quasars are now being contextualised on the basis of the main sequence (MS) trends (e.g., Sulentic et al. 2000a; Shen & Ho 2014; Panda et al. 2018). Type-1 AGN have been grouped into two main populations, Population A and B, defined on the basis of the Balmer line widths (more specifically of $H\beta$: $\text{FWHM } H\beta \lesssim 4000 \text{ km s}^{-1}$ for Population A; $\text{FWHM } H\beta \gtrsim 4000 \text{ km s}^{-1}$ for Population B (Sulentic et al. 2000a, 2011) at low and moderate luminosity $\log L \lesssim 46$ [erg s^{-1}]). The classification of the quasar population along the MS has its main physical foundation on systematic differences in Eddington ratio (Marziani et al. 2003c): Population A sources typically have $L/L_{\text{Edd}} \gtrsim 0.2$, with extreme Population A sources reaching $L/L_{\text{Edd}} \gtrsim 1$ (Marziani & Sulentic 2014), values close to the expected theoretical limit for super-Eddington accretion rate (Abramowicz et al. 1988; Mineshige et al. 2000; Sadowski 2011). Usually Pop. B sources present lower values of Eddington ratio when compared with the ones of Pop. A. The governing parameter of the MS itself appears to be Eddington ratio convolved with the effect of orientation (e.g., Sun & Shen 2015; Panda et al. 2019).*

Sources showing prominent $H\beta$ red asymmetries (i.e., AR,R according to Sulentic (1989)) are classified as belonging to Population B (Marziani et al. 2003c; Sulentic et al. 2011). The red asymmetry itself can be considered as a defining feature of Population B sources, hinting at the presence of a “very broad component” (VBC) at the line base (Peterson & Ferland 1986; Marziani & Sulentic 1993; Sulentic et al. 2000c; Wang & Li 2011; Punsly 2013; Wolf et al. 2020). The physical properties of the region associated with the VBC are largely undetermined (e.g., Snedden & Gaskell 2007) but the general consensus is that the region is located at the innermost radii of the broad line region (BLR), closest to the central continuum source. This inference follows from the deduction of a velocity field dominated by virial motions, at least for several population B sources (Peterson & Wandel 1999; Peterson et al. 2004). The dynamical conditions of the “very broad line region” (VBLR) are subject of current debate (Punsly et al. 2020). Two main alternatives have been proposed: infall and obscuration (Wang et al. 2017), or gravitational and transverse redshift (Gaskell 1988; Corbin 1995; Popovic et al. 1995; Gavrilović et al. 2007; Bon et al. 2015; Punsly et al. 2020). Both mechanisms are however still consistent with a virial velocity field as the main broadening factor.

Gaseous outflows appear to be ubiquitous in type-1 AGN, although their traceability and their kinetic power varies greatly along the main sequence (Marziani & Sulentic 2012b; Marziani et al. 2016b). The signature of outflows in the optical and UV spectra is provided by the blueshift of emission lines with respect to the rest frame, under the assumption that the shift is due to Doppler effect on the wavelength of lines emitted by gas moving toward us, and that the receding side of the flow is mainly hidden from view (e.g., Leighly & Moore 2004). While there is unambiguous evidence of outflows from the emitting regions of quasars radiating at high Eddington ratio, the situation is by far less clear for Pop. B where the accretion rate is modest, as implied by the Eddington ratio $\lesssim 0.2$. High-resolution X-ray and ultraviolet (UV) observations of the prototypical Population B source

*In flux limited samples Pop. A and B may have similar luminosity distributions. If this is the case Pop. B sources are expected to host more massive black holes, considering the systematic differences in Eddington ratio.

Table 3.1: Physical parameters

Spectrum	z	$\log L$ [erg s ⁻¹]	$\log M_{\text{BH}}^a$ [M _⊙]	$\log L/L_{\text{Edd}}$
Composite spectra				
B1S02	0 – 0.7	45.63 ^b	8.52	-1.07
B1M13	0.4 – 0.7	46.31 ^b	9.19	-1.06
B1M09	0.9 – 2.6	47.29 ^c	9.63	-0.51
Individual, high- L quasars				
HE0001–2340	2.2651	47.09 ^c	9.78	-0.86
Q0029+079	3.2798	47.43 ^c	9.95	-0.70
Composite spectra, jetted				
B1M13CD	0.4 – 0.7	46.51 ^b	9.39	-1.05
B1M13FRII	0.4 – 0.7	46.62 ^b	9.44	-1.00

^a: Black hole mass computed from the H β scaling law provided by Vestergaard & Peterson (2006), using the H β full profile FWHM. Applying the average correction suggested for spectral type B1 would lower the mass by a factor 0.64, and increase the L/L_{Edd} ratio by the same factor. ^b Bolometric correction assumed a factor 10; ^c Bolometric correction assumed a factor 4, as appropriate for very high luminosity sources following Netzer (2019).

NGC 5548 reveal a persistent ionised outflow traced by UV and X-ray absorption and emission lines (Kaastra et al. 2014). However, the CIV λ 1549 emission line profile lacks strong evidence of such an outflow, also because of the prominent red line wing merging with He II λ 1640 (Fine et al. 2010).

In this short note, we address the very specific issue of the origin of sources showing a blueshift at the peak of the H β emission line i.e., of the AR,B classification. The focus is on the H β line because the line is a singlet, and its peak is isolated from other contaminants, offering a clear view of its broad and narrow components. The [O III] λ 4959,5007 lines recorded along with H β help to assess the nature of the H β line profile. In addition, the narrow, high-ionisation [O III] λ 5007 emission lines are known to be affected by outflows, as indicated by the frequent blueward asymmetries and even systematic shifts (Whittle 1985; Bennert et al. 2002; Komossa et al. 2008; Zamanov et al. 2002; Marziani et al. 2016a), Section 3.2 presents the data used in this work, a set of composite spectra covering a wide range in luminosity and redshift, for which the H β and the [O III] λ 4959,5007 emission has been covered with optical and IR spectroscopic observations. Details on how the spectral analysis was performed are shown in Section 3.3. The main results come from the profile comparison of the H β and [O III] λ 5007 (Section 3.4), and are briefly analysed in terms of the physical conditions of the line emitting gas, as well as of the dynamical parameters of the outflow (Section 3.5).

3.2 Data

The data analysed in this chapter refer to the most widely populated spectral type of Population B, B1, defined by FWHM H β in the range 4000 – 8000 km s⁻¹ (Sulentic et al. 2002). Median composite spectra covering the H β range were computed over the spectral type B1 sources belonging to two samples of low-to-moderate redshift and luminosity, (Sulentic et al. 2000a; Marziani et al. 2013a, hereafter S02 and M13), and one sample of intermediate z and high luminosity (Marziani et al. 2009, hereafter M09). The S02 composites are based on the individual observations of Marziani et al. (2003b) that involved 97 B1 spectra. The M13 composites are SDSS spectra in the redshift range

0.4 – 0.7, covering both MgII λ 2800 and H β . The radio-quiet B1 composite was computed over 179 spectra, while the CD and FR-II composites involved 16 and 23 spectra, respectively. The B1 composite of M09 included 22 high-luminosity, Hamburg ESO (HE) quasars. Median composites were constructed from continuum-normalised (at 5100 Å) spectra, after a determination of the heliocentric redshift based on [O II] λ 3727 or narrow component of H β , two low-ionisation narrow line that provide the best estimators of the systemic redshift of the host galaxy (Bon et al. 2020). The accurate redshift correction allowed for the preservation of the spectral resolution of the individual spectra. The M13 composites should therefore have a resolving power $\lambda/\delta\lambda \sim 2000$. The resolving power is only slightly lower for S02, $\lambda/\delta\lambda \sim 1000$. The HE ISAAC near-IR observations were all collected with a narrow slit (0.6 arcsec) that yielded $\lambda/\delta\lambda \sim 1000$, comparable to the spectra of the samples observed with optical spectrometers. Their main properties are summarised in Table 3.1, where the first column lists an identification code, and the following columns list the redshift range, and median values of bolometric luminosity, black hole mass M_{BH} , and Eddington ratio L/L_{Edd} . In addition to the composite spectra, the spectra of two quasars of extreme luminosity at intermediate redshift (Deconto-Machado et al. 2022, in preparation) provide examples of two opposite cases, one where a prominent outflow signature is detected (Q0029+079), and one in which there is no obvious evidence of outflow (HE0001-2340). The last two lines of Table 3.1 consider composites for core dominated (CD) and Fanaroff-Riley (FR) sources belonging to spectral type B1 from the M13 sample. These two composite were defined to address the somewhat controversial issue of the mild-ionised outflow presence among radio-loud, jetted AGN. † The data of Table 3.1 confirm that the empirical selection of spectral type B1 corresponds to the selection of modest L/L_{Edd} radiators. At the higher redshift and luminosity, the L/L_{Edd} appears somewhat higher ($L/L_{\text{Edd}} \approx 0.3$) because of the preferential selection of higher L/L_{Edd} for a fixed black hole mass in flux limited surveys (Sulentic et al. 2014a).

3.3 Analysis

The non-linear multicomponent fits were performed using the SPECFIT routine from IRAF (Kriss 1994). This routine allows for simultaneous minimum- χ^2 fit of the continuum approximated by a power-law and the spectral line components yielding FWHM, peak wavelength, and intensity of all line components. In the optical range we fit the H β profile as well as the [O III] λ 4959,5007 emission lines and the Fe II multiplets accounted for by a scaled and broadened template (Boroson & Green 1992). The details of the multi-component analysis has been given in several previous papers (e.g., Sulentic et al. 2017) and will not be repeated here. Suffice to say that the broad profiles of Pop. B sources can be successfully modelled with two Gaussians: (1) one narrower, unshifted or slightly shifted to the red; and (2) one broader, with FWHM $\sim 10000 \text{ km s}^{-1}$, and shifted by few thousands km s^{-1} to the red (Marziani et al. 2003a). This model accounts for the AR,R profile type. In addition to the model decomposition, we measured several parameters on the full broad profile

†We consider the attribute “radio-loud” as synonym of relativistically jetted (Padovani 2016, 2017).

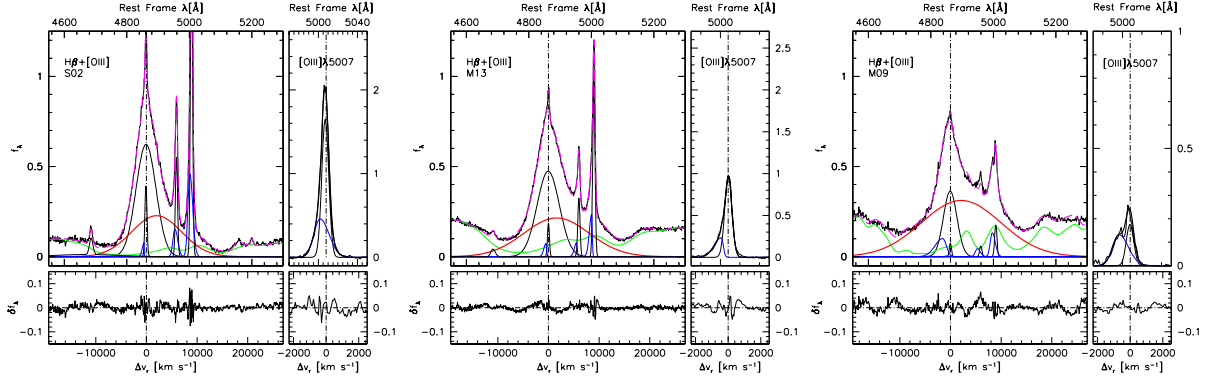


Fig. 3.1: Analysis of the $H\beta + [O\ III]\lambda\lambda 4959,5007$ region for the **S02** (left), **M13** (middle) and **M09** (right) B1 composite spectra. Continuum subtracted spectra are shown in the rest frame, over the range 4550 — 5300 Å (left panel), with an expansion around $[O\ III]\lambda 5007$ (right panels). Thin solid lines: continuum-subtracted spectrum; dashed magenta line: model spectrum; thick black line: $H\beta$ broad component; red thick line, $H\beta$ very broad component; thin smooth black lines: narrow components of $H\beta$ and $[O\ III]\lambda 5007$; blue lines: blue shifted components. Green lines trace the scaled and broadened Fe II emission template. The lower panel show the observed minus model residuals in radial velocity scale.

(Zamfir et al. 2010). The definitions of the centroids and of the asymmetry index $A.I.$ are reported below for convenience:

$$c\left(\frac{i}{4}\right) = \frac{v_{r,B}\left(\frac{i}{4}\right) + v_{r,R}\left(\frac{i}{4}\right)}{2}, \quad i = 1, 2, 3; \quad \frac{i}{4} = 0.9, \quad (3.1)$$

where c is the speed of light and the radial velocities are measured with respect to the rest frame at fractional intensities $\frac{i}{4}$ for each value of the index i on the blue and red side of the line with respect to the rest frame.

$$A.I.\left(\frac{1}{4}\right) = \frac{v_{r,B}\left(\frac{1}{4}\right) + v_{r,R}\left(\frac{1}{4}\right) - 2v_{r,P}}{v_{r,R}\left(\frac{1}{4}\right) - v_{r,B}\left(\frac{1}{4}\right)}. \quad (3.2)$$

Note that the $A.I.$, unlike the centroids, is defined as a shift with respect to the line peak radial velocity $v_{r,P}$ ($v_{r,P}$ is measured with respect to rest frame; a suitable proxy is provided by $c(0.9)$).

3.4 Results

Broad $H\beta$ Fig. 3.1 shows the continuum-subtracted spectra and their models for the three composite spectra or **S02**, **M13**, and **M09** (left, middle and right panel, respectively). The measurements of the broad $H\beta$ line parameters are reported in Table 3.2. For each spectrum, Table 3.2 lists the normalised flux F of the $H\beta$ full broad profile ($H\beta_{BC} + H\beta_{VBC} + H\beta_{BLUE}$), its equivalent width $W_{H\beta}$ in Å, and the normalised fluxes of the $H\beta_{BC}$ and $H\beta_{VBC}$ separately. The following columns report several parameters for the $H\beta$ blue shifted excess with respect to the standard Population B decomposition involving only $H\beta_{BC}$ and $H\beta_{VBC}$: normalised flux, equivalent width, peak shift, FWHM and skew.

Table 3.2: Broad-line properties measurements

Spectrum	$H\beta$		$H\beta_{BC}$	$H\beta_{VBC}$	$H\beta_{BLUE}$			FeII λ 4570		
	F	W ^a	F	F	F	Shift ^b	FWHM ^b	Skew ^c	F	W
Composite spectra										
B1S02	95.3	86.7	49.8	45.4	18.1	14.6
B1M13	122.3	126.5	52.5	69.8	47.8	43.0
B1M09	123.3	129.1	19.6	99.1	4.6	-1535	3611	0.5	39.2	34.1
Individual, high- L quasars										
HE0001	99.3	95.1	26.7	72.7	20.6	16.3
Q0029	69.8	66.4	13.9	32.2	23.7	-2097	4711	1.2	25.8	21.4
Composite spectra, jetted										
B1M13CD	113.8	118.5	42.9	70.9	35.6	32.7
B1M13FRII	129.8	131.1	57.5	72.3	24.6	21.9

^a in units of \AA ; ^b in units of km s^{-1} . ^c skew as reported by the `SPECTFIT` routine; it is equal to the conventional definition of the skew (Azzalini & Regoli 2012) + 1.

Table 3.3: $H\beta$ profile properties measurements

Spectrum	FWHM ^a	AI	$c(1/4)^a$	$c(1/2)^a$	$c(3/4)^a$	$c(0.9)^a$
Composite spectra						
B1S02	5560 \pm 170	0.12 \pm 0.03	680 \pm 230	250 \pm 80	160 \pm 70	130 \pm 50
B1M13	6540 \pm 210	0.12 \pm 0.06	740 \pm 340	150 \pm 110	50 \pm 90	40 \pm 60
B1M09	6010 \pm 450	0.28 \pm 0.06	2120 \pm 490	-50 \pm 220	-230 \pm 70	-270 \pm 50
Individual, high- L quasars						
HE0001	6510 \pm 690	0.29 \pm 0.09	2700 \pm 560	1310 \pm 340	900 \pm 170	830 \pm 110
Q0029	6200 \pm 380	0.18 \pm 0.10	430 \pm 500	-380 \pm 190	-500 \pm 160	-500 \pm 110
Composite spectra, jetted						
B1M13CD	6880 \pm 240	0.23 \pm 0.06	1520 \pm 380	270 \pm 120	70 \pm 90	20 \pm 60
B1M13FRII	6790 \pm 220	0.10 \pm 0.06	820 \pm 330	320 \pm 110	240 \pm 90	230 \pm 60

^a In units of km s^{-1} .

The last columns yield the normalised flux and the equivalent width of the FeII λ 4570 emission blend as defined by Boroson & Green (1992). The equivalent width values correspond roughly to the normalised flux, so that they are reported only for the main features. The normalised fluxes can be approximately converted into luminosities by multiplying them by the luminosity values reported in Table 3.1 divided by the bolometric correction and by 5100 i.e., by the wavelength in \AA at which the continuum was normalised. Table 3.3 reports the FWHM, A.I., and centroids as defined in §3.3 for the broad $H\beta$ profile ($H\beta_{BC} + H\beta_{VBC} + H\beta_{BLUE}$ i.e., without considering the narrow [$H\beta_{NC}$] and semi-broad [$H\beta_{SBC}$] components associated with narrow-line region emission). Only at the highest L blueshifted emission with broad profile ($H\beta_{BLUE}$) is detected in the $H\beta$ profile: in this case, the $H\beta_{BLUE}$ contribution is $\lesssim 5\%$ of the total line luminosity for the M09 and reaches about 1/3 of the total line luminosity in the admittedly extreme Q0029 case. In no case, however, the $H\beta_{BLUE}$ is able to create a significant shift to the blue close to the line base: the red asymmetry dominates, and even the Q0029 $H\beta$ broad profile is “symmetrised” toward the line base, with centroid at $\frac{1}{4}$ peak intensity close to 0 km s^{-1} .

[O III] λ 5007 and $H\beta$ narrow-line emission Table 3.4 summarises the measurements of the components associated with the narrow-line region (NLR) emission i.e., narrow and semi-broad components of $H\beta$ and [O III] λ 5007 ($H\beta_{NC}$, [O III] λ 5007_{NC}, and $H\beta_{SBC}$ and [O III] λ 5007_{SBC}), for which nor-

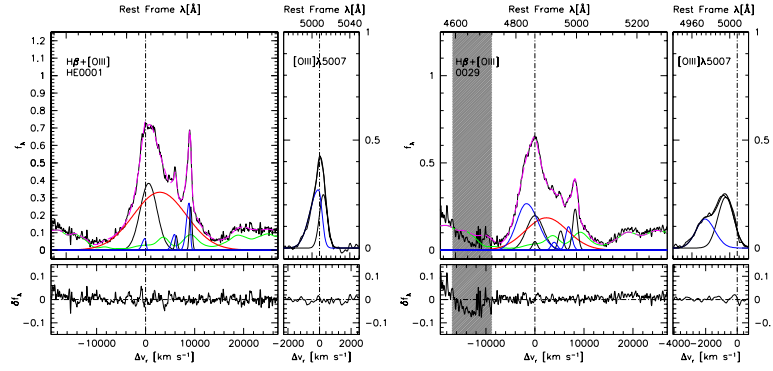


Fig. 3.2: Analysis of the $H\beta + [O\text{ III}]\lambda\lambda 4959, 5007$ region for two high-luminosity, high- z quasars belonging to the B1 spectral type. The left one, HE0001-234, shows no appreciable evidence of blueshift, while the right one [HB89] 0029+073 requires a stronger blue shifted excess for $[O\text{ III}]\lambda\lambda 4959, 5007$, and an even stronger and broader one to fit $H\beta$. Colour coding of the components is the same as in the previous Figure. The shaded area identifies a spectral region affected by atmospheric absorptions.

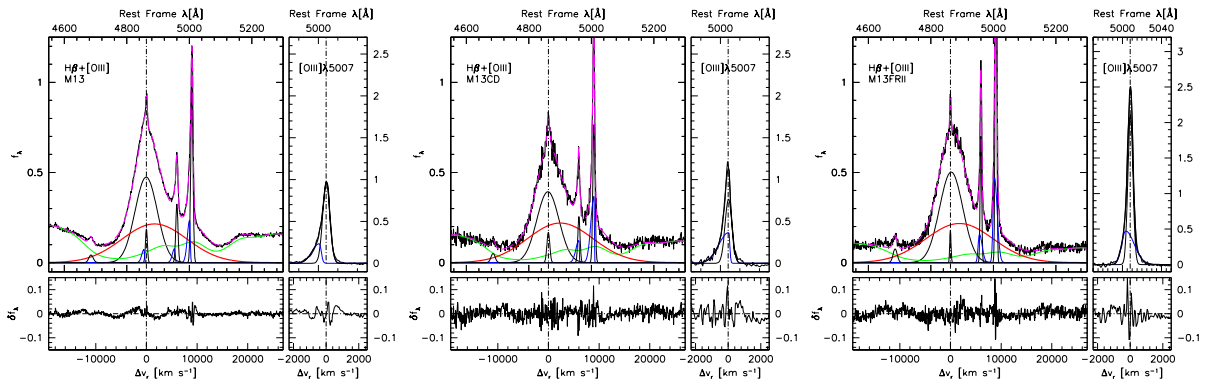


Fig. 3.3: Analysis of the $H\beta + [O\text{ III}]\lambda\lambda 4959, 5007$ region for the RQ composite spectrum of **M13** (left), and for the CD and FR-II composite spectra (middle and right respectively). Color coding of the components is the same as in the previous Figures.

malised flux, equivalent width, shift and FWHM are reported. The skew parameter is reported only for the semi-broad components, as the narrow components are assumed to be symmetric Gaussian, within a few tens km s^{-1} from the rest frame (Bon et al. 2020).

The **S02** composite shows a broad + narrow component profile very well represented by three Gaussians: the symmetric unshifted $H\beta_{\text{NC}}$, the unshifted $H\beta_{\text{BC}}$ and the $H\beta_{\text{VBC}}$ with a significant shift to the red. A small blue shifted excess appears at the interface between the $H\beta_{\text{NC}}$ and the $H\beta_{\text{BC}}$, and has been modelled by an additional Gaussian. Its intensity is so low that a very good fit with no significant worsening in the χ^2 can be achieved also without it. Most notably, the $[O\text{ III}]\lambda 5007$ profile (enlarged in the right panel) is also fairly symmetric: a small centroid blueshift $\sim -50 \text{ km s}^{-1}$ is detected only at $\frac{1}{4}$ peak intensity (Table 3.5, where the $[O\text{ III}]\lambda 5007$ full profile parameters are reported as in Table 3.3 for $H\beta$). The relatively large shift reported for $[O\text{ III}]\lambda 5007_{\text{SBC}}$ is compensated by a red-ward skew (Fig. 3.1, right panel on the left plot). In this case, the decomposition $[O\text{ III}]\lambda 5007_{\text{NC}}$

— $[\text{O III}]\lambda 5007_{\text{SBC}}$ is especially uncertain, and a more reliable measurement is provided by the centroid.

The **M13** composite spectrum appears as a “goiter” at the top of the $\text{H}\beta_{\text{BC}}$ broad profile. The $[\text{O III}]\lambda 5007$ profile is also fairly asymmetric, and can be modelled by a narrower, almost unshifted component and a skewed Gaussian displaced to the blue by $\approx -500 \text{ km s}^{-1}$. The top of the $\text{H}\beta$ profile is well-fit by assuming two components with the same shift, width and asymmetry of the model components $[\text{O III}]\lambda 5007$ line. The consistency between the model of $\text{H}\beta_{\text{SBC}}$ and $[\text{O III}]\lambda 5007_{\text{SBC}}$ provide evidence that the $\text{H}\beta$ blueshifted and skewed component is associated with a NLR outflow. The **M09** composite can be equally modelled with the same skewed and blueshifted component for $\text{H}\beta$ and $[\text{O III}]\lambda 5007$. However, this model would require an implausibly strong $[\text{O III}]\lambda\lambda 4959, 5007$ emission. The fit shown in the bottom panel of Fig. 3.1 assumes a broader component for the $\text{H}\beta$ emission.

At very high luminosity (Fig. 3.2) a prominent outflow is apparently absent in one Pop. B $\text{H}\beta$ profile (HE0001) but very prominent in another (Q0029). If the classification of Q0029 as a Population B source is correct, the model of the blue “goiter” at the side of the $\text{H}\beta$ profile implies a strong contribution of blueshifted emission with a broad profile. The $[\text{O III}]\lambda 5007$ profiles are also different: the equivalent width W is higher and the shift lower in the case of HE0001, where no significant $\text{H}\beta$ outflow is detected. By all means, the properties of Q0029 appear more extreme. We predict that this source will show extreme $\text{C IV}\lambda 1549$ blueshift, with amplitude of several thousands km s^{-1} .

The $[\text{O III}]\lambda 5007$ shift and the A.I. become more negative and the equivalent width decreases with increasing luminosity. This is a pure luminosity effect that goes in the same sense of the effect of increasing Eddington ratio in sample covering the full span of $L/L_{\text{Edd}} \sim 10^{-2} - 1$, and can be interpreted as due to NLR evolution with redshift (Marziani et al. 2016b).

Jetted sources The CD and FR-II composites from the sample of **M13** (Fig. 3.3) show the $[\text{O III}]\lambda 5007$ blueshifted and skewed component is not detected in $\text{H}\beta$, implying that for this component the intensity ratio $[\text{O III}]\lambda 5007/\text{H}\beta \gg 1$. In addition the $[\text{O III}]\lambda 5007$ profile for the FR-II composite spectrum is much more symmetric than that of the CD composite, whose A.I. and centroid shifts are more consistent with the RQ composite of same sample. This systematic difference may arise because of the different viewing angles expected for CD (seen almost pole on) and FR-II sources (seen at a viewing angle $\approx 40 - 60$ (Urry & Padovani 1995)).

3.5 Discussion

The analysis performed above has been focused on sources radiating at relatively modest L/L_{Edd} (Population B) but covering a wide range of redshifts ($0 \lesssim z \lesssim 3$) and luminosities. Significant outflow features have been detected in the NLR, as traced by the $\text{H}\beta_{\text{NC}}$ and $[\text{O III}]\lambda\lambda 4959, 5007$ blue shifted

Table 3.4: Narrow line measurements

Spectrum	$H\beta_{\text{NC}}$				$H\beta_{\text{SBC}}$				$[\text{O III}]\lambda 5007_{\text{NC}}$				$[\text{O III}]\lambda 5007_{\text{SBC}}$					
	F	W ^a	Shift ^b	FWHM ^b	F	W ^a	Shift ^b	FWHM ^b	Skew ^c	F	W ^a	Shift ^b	FWHM ^b	F	W ^a	Shift ^b	FWHM ^b	Skew ^c
Composite spectra																		
B1S02	3.33	3.00	-9	492	0.59	0.53	-349	881	...	14.6	14.0	12	499	8.86	8.45	-307	881	1.47
B1M13	1.45	1.45	-8	450	0.83	0.85	-480	1054	0.26	8.9	9.7	11	513	2.76	3.00	-417	1054	0.26
B1M09	0.65	0.70	-25	508	0.06	0.07	-752	932	1.46	1.6	1.8	-15	528	2.68	2.97	-688	932	1.46
Individual, high- <i>L</i> quasars																		
HE0001	0.11	0.10	-25	2202	1.05	0.99	-133	1301	0.41	2.6	2.7	239	592	4.39	4.43	-69	1301	0.41
Q0029	1.00	0.95	-6	1181	0.00	0.00	4.9	4.9	-728	1181	3.36	3.30	-2051	1340	1.12
Composite spectra, jetted																		
B1M13CD	1.92	1.96	-25	662	0.00	0.00	6.8	7.4	20	497	5.17	5.62	39	1439	0.10
B1M13FRII	0.94	0.98	-25	300	0.00	0.00	13.5	13.0	11	360	7.65	8.11	-279	585	2.12

^a: in units of Å; ^b: in units of km s⁻¹. ^c skew as reported by the SPECFIT routine; it is equal to the conventional definition of the skew (Azzalini & Regoli 2012) + 1.

Table 3.5: [O III]λ5007 profile measurements

Spectrum	FWHM ^a	AI	c(1/4) ^a	c(1/2) ^a	c(3/4) ^a	c(0.9) ^a
Composite spectra						
B1S02	580 ± 30	-0.10 ± 0.08	-40 ± 40	-10 ± 20	0 ± 20	0 ± 10
B1M13	560 ± 40	-0.23 ± 0.11	-80 ± 50	-20 ± 20	10 ± 10	30 ± 10
B1M09	1100 ± 120	-0.43 ± 0.05	-380 ± 40	-280 ± 60	-60 ± 20	-40 ± 10
Individual, high- <i>L</i> quasars						
HE0001	900 ± 70	-0.26 ± 0.07	-100 ± 40	0 ± 30	70 ± 30	80 ± 10
Q0029	2120 ± 140	-0.37 ± 0.04	-1360 ± 60	-1240 ± 70	-860 ± 50	-830 ± 30
Composite spectra, jetted						
B1M13CD	490 ± 40	-0.18 ± 0.12	-90 ± 50	-70 ± 20	-10 ± 20	-10 ± 10
B1M13FRII	440 ± 30	-0.10 ± 0.09	-20 ± 30	10 ± 10	10 ± 10	10 ± 10

^a: in units of km s⁻¹.

components. At high luminosity, significant blueshift are found not only in the [O III]λλ4959,5007 lines, but also with a broader profile, hinting at an association with the BLR emission.

3.5.1 How important is the outflow component?

The present analysis relies on the important assumption that the Population B profile at $H\beta$ low-*z* and luminosity is not significantly affected by any outflowing gas. Reverberation mapping campaigns in the early 2000s provided evidence that the main broadening mechanism is indeed provided by a virial velocity field of gas orbiting around a point-like mass. More recent works points toward a more complex situation (Denney et al. 2009; Du et al. 2018; U et al. 2022, Bao et al. 2022, in preparation), although the main inference from velocity-resolved reverberation mapping studies for the sources with the red $H\beta$ asymmetry is that the velocity field is predominantly virial, with the frequent detection of infall motions. The detection of infall is based on the shorter time delay of the red wing, not on the response of the line core.

3.5.2 Identifying an outflow component

The $H\beta$ profile of Population B presents a clear inflection between $H\beta_{BC}$ and $H\beta_{NC}$ that can be explained on the basis of the expected radial emissivity of $H\beta$ (Sulentic & Marziani 1999). The identification of an outflow component may be achieved by considering the following options:

- no significant centroid blueshift in the broad profile of $H\beta$ and symmetric appearance at the interface between $H\beta_{NC}$ and $H\beta_{BC}$, with the peak of the broad profile showing no shift or a slight redshift: no evidence of outflow.
- No significant centroid blueshift in the broad profile of $H\beta$ and “goiter” appearance at the interface between $H\beta_{NC}$ and $H\beta_{BC}$: If the $[O\ III]\lambda 5007$ line shows a significant blueward asymmetry, and a model of the $[O\ III]\lambda 5007$ line profile with a core and semi-broad component is applicable to the $H\beta$ profile, then it is likely that the outflow is mainly associated with the NLR emission.
- Even modest centroid blueshift in the broad profile of $H\beta$ at fractional intensity $\frac{3}{4}$ or 0.9, the outflow might involve BLR emission. In this case, the $H\beta_{BLUE}$ corresponds to the prominent blueshifted emission of the $C\ IV\lambda 1549$ line observed at high luminosity (Sulentic et al. 2017). The detection of $H\beta_{BLUE}$ is made more difficult by the $C\ IV\lambda 1549/H\beta$ ratio expected to be $\gg 1$.

3.5.3 Location and physical nature of the outflow

Even in case of modest accretion rate, the outflow can be radiatively driven (Netzer & Marziani 2010). The ratio between the radiation and gravitation force can be written as $a_{rad}/a_{grav} \approx 7.2 L/L_{Edd} N_{c,23}^{-1}$ where $N_{c,23}$ is the Hydrogen column density in units of 10^{23} cm^{-2} (e.g., Ferland et al. 2009). For $L/L_{Edd} \sim 0.1$, gas of moderate common density $N_{c,23} \sim 0.1$ could be accelerated to $a_{rad}/a_{grav} \sim 10$ (c.f. Eq. 6 of Netzer & Marziani (2010) Marziani et al. 2010). The first underlying assumption is that all of the photon momentum of the ionising continuum is transferred to the line emitting gas. The second assumption is that the gas is optically thick to the ionising continuum, and this condition is more easily verified if the ionisation parameter is low, implying that the low column density gas located farther out from the AGN continuum source might be preferentially accelerated. This might explain why we see a signature due to a semi-broad component in $H\beta$, $H\beta_{SBC}$, in turn associated with the $[O\ III]\lambda 5007$ semi-broad component, likely at the inner edge of the NLR, may be the main signature of outflow in low L/L_{Edd} sources.

Regarding the BLR, at low luminosity there is no signature of outflow, if our interpretation of the profile is correct. For Population B sources, however, the observed spectrum can be explained by the locally optimised cloud (LOC) scheme, in which a range of ionisation parameters, density and column density is assumed, and the emerging spectrum is set by the parameters at which lines are emitted most efficiently (Baldwin et al. 1995; Korista et al. 1997). This is to say that there might be always gas as “light” as needed for an outflow; however, that outflow may not produce a significant signature in the emission line spectrum. Powerful outflow at modest Eddington ratio may become

possible only at high luminosity (e.g., Murray & Chiang 1997; Proga et al. 1998; Laor & Brandt 2002), as predicted from wind theory, and confirmed by observations (Bischetti et al. 2017; Vietri 2017; Vietri et al. 2018; Sulentic et al. 2017).

3.5.4 The fate of the outflowing gas: no feedback effects at low L

The mass outflow rate at a distance r can be written as, if the flow is confined to a solid angle of Ω of volume $\frac{4}{3}\pi r^3 \frac{\Omega}{4\pi}$: $\dot{M}_0^{\text{ion}} = \rho \Omega r^2 v_0 = \frac{M_0^{\text{ion}}}{V} \Omega r^2 v_0 \propto L v_0 r^{-1}$ (Cano-Díaz et al. 2012), and implies $\dot{M}^{\text{ion}} \sim 30 L_{44} v_{0,1000} r_{1\text{kpc}}^{-1} \left(\frac{Z}{5Z_\odot}\right)^{-1} n_3^{-1}$, where the mass of ionised gas can be directly estimated from the line luminosity: $M_{\text{ion}} \sim 1 \cdot 10^7 L_{44} \left(\frac{Z}{5Z_\odot}\right)^{-1} n_3^{-1}$.[‡] The low-luminosity cases **S02** and **M13** imply that the outflow velocity is $v_{0,1000} \sim 1$ from the peak shift of [O III] $\lambda 5007_{\text{SBC}}$, and the [O III] $\lambda 5007_{\text{SBC}}$ luminosity is $\log L_{[\text{OIII}]} \sim 42$. Assuming $Z \approx 1Z_\odot$ as appropriate for Population B sources (Punsly et al. 2020), $M_{\text{ion}} \sim 5 \cdot 10^5 n_3^{-1}$, and $\dot{M}^{\text{ion}} \sim 0.15 r_{1\text{kpc}}^{-1} n_3^{-1}$. By the same token the thrust and kinetic power can be written as $\dot{M}v \sim 1.9 \cdot 10^{35} L_{44} v_{0,1000}^2 r_{1\text{kpc}}^{-1} \left(\frac{Z}{5Z_\odot}\right)^{-1} n_3^{-1}$ and $\dot{\epsilon} \sim 10^{43} L_{44} v_{0,1000}^3 r_{1\text{kpc}}^{-1} \left(\frac{Z}{5Z_\odot}\right)^{-1} n_3^{-1}$, which become $\dot{M}v \sim 1 \cdot 10^{34} r_{1\text{kpc}}^{-1} n_3^{-1}$ and $\dot{\epsilon} \sim 5 \cdot 10^{41} r_{1\text{kpc}}^{-1} n_3^{-1}$. Even assuming that we are observing a flow at $r \sim 10$ pc, the kinetic power is $\dot{\epsilon} \lesssim 10^{44}$ erg s⁻¹, a factor ≈ 100 below the bolometric luminosity and ≈ 1000 the Eddington luminosity of the **M13** case. The emitting gas might be beyond or at the limit of the black hole sphere of influence given by $r \approx GM/\sigma_\star^2 \approx 8 \cdot 10^{19} M_{9,\odot}/\sigma_{\star,400}^2$ cm, where the σ_\star is the velocity dispersion associated with the bulge of the host galaxy in units of 400 km s⁻¹. At this radius, the escape velocity is expected to be $v_{\text{esc}} \sim 500$ km s⁻¹ for a $10^9 M_\odot$ black hole. It is therefore doubtful whether the outflowing gas might be even able to escape from the sphere of influence of the black hole. Even less likely is that the outflowing gas might “wreak havoc” galaxy-wide in the bulge and disk of the host, due to the small amount of gas masses involved in the outflow, and due to the escape velocity that can be as high as $v_{\text{esc}} \gtrsim 1000$ km s⁻¹ in the inner regions of a massive spheroid or in a giant spiral such as the Milky Way (Monari et al. 2018).

The scenario might radically change at high luminosity: considering the **M09** composite, the velocity of [O III] $\lambda 5007_{\text{SBC}}$ is higher by a factor ≈ 2 , and the line luminosity by a factor ~ 10 , implying a 20-, 40-, ~ 100 -fold increase over the **M13** case in mass flow, thrust and kinetic power, respectively. In the **M09** case the kinetic power would be comparable to the Eddington luminosity. An even more powerful outflow is expected for Q0029.

3.6 Summary and conclusion

The analysis of outflow signatures carried out in the present chapter has been focused on three samples of type-1 AGN covering a wide range of luminosity.

[‡]Note that the filling factor is not appearing explicitly because by using the line luminosity we already are considering the volume of the line emitting gas. The fraction of volume that is actually occupied by the line emitting gas then depends on its density.

The detection of different kinematic components in single epoch profiles is a complicated issue. The apertures and slit widths used in ground-based observation add up the emission from AGN continuum, BLR, NLR, and host galaxy that are associated with widely different spatial scales. The case of Population B sources of spectral type B1 is especially well-suited to analyse the presence of an outflow component in the Balmer $H\beta$ line for sources that are radiating at modest Eddington ratio.

Generally speaking, the detection of significant systematic blueshifts in the centroid measurements can be taken as a signature of outflow. If the blueshift/blue asymmetry is confined at the top of the $H\beta$ line, and the $H\beta$ narrow emission can be modelled as $[O\ III]\lambda 5007$ assuming a semi-broad and a narrow component with a similar parameter, then the evidence of the outflow (the “goiter” in the line profile) remains confined to the NLR. However, if the $H\beta$ centroid at $\frac{3}{4}$ or at lower fractional intensity is also blue shifted, it is likely that a BLR outflow is being detected. Low column density gas can be driven into an outflow by radiation forces. Blueshifts in the line core can be therefore straightforwardly interpreted by an outflow component, without invoking binary BLR, in turn pointing toward sub-parsec binary black holes. Other spectral types along the MS have been identified as frequently involving binary black hole candidates (Ganci et al. 2019; del Olmo et al. 2021).

The estimates of mass flow, thrust and kinetic power are highly uncertain because of the lack of spatially-resolved data. This situation might be changing soon with the development of integral-field spectrographs. Nonetheless, even maximising the coarse estimates reported above, it is unlikely that the thrust and the kinetic power (just $\sim 10^{-2}$ the Eddington luminosity as derived for the S02 and M13 samples) might have a strong impact on the host galaxy evolution, not to mention the possibility of driving the black hole mass — bulge correlation (e.g., D’Onofrio et al. 2021, and references therein). Even if the $[O\ III]\lambda 5007$ samples only emission from mildly ionised gas, and the mass flow might be dominated by the higher-ionisation gas, for low luminosity AGN such as the prototypical Population B Seyfert-1 NGC 5548 the kinetic luminosity remains a very small fraction of the Eddington luminosity (Kaastra et al. 2014; Kriss 2017). The situation is expected to change at the “cosmic noon” at redshifts in the range 1 — 2, when the most luminous quasars are observed, and of which M09 provides a representative spectrum.

Part II

The roles of AGN feedback and radio emission

AGN outflows and winds in general seem to be an ubiquitous feature of the central regions of galaxies. Especially at high and intermediate redshift, many sources seem to harbour a powerful central mechanism that allows for strong winds observed in the optical and UV ranges of their spectra. Through the decomposition of the broad emission line profiles as explained in Part I of this thesis, we are able to find some hint of the real relevance of winds for the structure and dynamics of the broad line emitting regions. High ionisation lines such as C IV λ 1549 and [O III] λ 5007 usually present a significant asymmetry towards the blue side of the spectra especially in radio-quiet quasars, which is a strong evidence of outflow motions. This part of the thesis focuses on evaluating whether this pattern also still true for radio-loud sources.

The first paper, in Chapter 4, presents a spectroscopic comparative study of two Pop. A quasars, with the same MS spectral type, from our ISAAC sample, one radio-loud and the other radio-quiet. Although these two sources exhibit similar optical spectra, they diverge significantly in the UV domain. Chapter 5 contains a fundamental part of the thesis in which we present the 10 type-I quasars that complete the ISAAC sample at high redshift, which is complemented with a spectroscopic re-analysis in the UV and optical of the high- z HEMS sample and a sample of 84 quasars at redshift < 1 . We carried out a deep analysis of the outflows, as well as the estimation of the dynamical parameters of the detected outflows and their possible influence of feedback in the host galaxy, placing special emphasis on the radio-loudness and presence or absence of jets.

OPTICAL AND UV PROPERTIES OF A RADIO-LOUD AND A RADIO-QUIET POPULATION A QUASAR AT HIGH REDSHIFT

4

Chapter based on the article published in *Astronomische Nachrichten* by A. Deconto-Machado et al., volume 343, 1-2, e210084, 9 pages, January 2022. DOI: 10.1002/asna.20210084

Abstract

Different properties of quasars may be observed and analysed through the many ranges of the electromagnetic spectrum. Pioneering studies showed that an “H-R diagram” for quasars was needed to organise these data, and that more than two dimensions were necessary: a four dimensional Eigenvector (4DE1) parameter space was proposed. The 4DE1 makes use of independent observational properties obtained from the optical and UV emission lines, as well as from the soft-X rays. The 4DE1 “optical plane”, also known as the quasar Main Sequence (MS), identifies different spectral types in order to describe a consistent picture of QSOs. In this work we present a spectroscopic analysis focused on the comparison between two sources, one radio-loud (PKS2000-330, $z = 3.7899$) and one radio-quiet (Q1410+096, $z = 3.3240$), both showing Population A quasar spectral properties. Optical spectra were observed in the infrared with VLT/ESO, and the additional measures in UV were obtained through the fitting of archive spectra. The analysis was performed through a non-linear multi-component decomposition of the emission line profiles. Results are shown in order to highlight the effects of the radio-loudness on their emission line properties. The two quasars share similar optical spectroscopic properties and are very close on the MS classification while presenting significant differences on the UV data. Both sources show significant blueshifts in the UV lines but important differences in their UV general behaviour. While the radio-quiet source Q1410+096 shows a typical Pop A UV spectrum with similar intensities and shapes on both CIV λ 1549 and SiIV λ 1392, the UV spectrum of the strong radio-loud PKS2000-330 closely resembles the one of population B of quasars.

Table 4.1: Main properties of PKS2000-330 and Q1410+096.

Source	RA (J2000)	DEC (J2000)	z	M_i	m_H
(1)	(2)	(3)	(4)	(5)	(6)
Q1410+096	14 13 21.05	+09 22 04.8	3.3240	-29.44	15.62
PKS2000-330	20 02 24.00	-32 51 47.0	3.7899	-30.99	15.32

4.1 Introduction

In order to organise the spectroscopic diversity observed in low-redshift quasars, Sulentic et al. (2000a) introduced the fourth-dimensional Eigenvector 1 (4DE1), a correlation space that considers several key observational measures (including optical, UV, and X-ray) as well as physical parameters such as outflow prominence and accretion mode. One of the most important measures is the full width at half maximum (FWHM) of the $H\beta$ broad component, thought to be a measure of virialised motions in the accretion disc and thus crucial for black hole mass estimations. Also, another fundamental parameter is the ratio between the intensities of the Fe II blend at 4570Å and $H\beta$ ($R_{FeII} = I(\text{Fe II } \lambda 4570)/I(H\beta)$), that is related to the Eddington ratio (Marziani et al. 2001) and many of the optical and UV spectral line measures (Kovačević et al. 2010; Marziani et al. 2010; Shapovalova et al. 2012), and which could be used to estimate physical parameters of the Broad Line Region (BLR) as the ionisation state, the electron density or the column density (Panda et al. 2020; Ferland et al. 2009).

The optical plane of the 4DE1 (defined by the $\text{FWHM}(H\beta)$ vs. R_{FeII}) is the so-called Main Sequence (MS) of quasars and the physical parameters related with accretion rate and outflowing gas seem to be changing along it (Marziani et al. 2018). The MS gave rise to the concept of two populations of quasars, which present significant spectroscopic differences (Zamfir et al. 2010). Along the Main Sequence, the physical properties vary from sources with low Fe II emission and high black hole mass “disk-dominated” QSOs (Population B), to the extreme Population A with strong Fe II emission, narrower Lorentzian line profiles, lower ionisation spectra and evidence of strong outflows, “wind-dominated” quasars (Martínez-Aldama et al. 2018). The optical plane of the 4DE1 is driven by the Eddington ratio convolved with orientation effects, and a critical Eddington ratio of $L/L_{\text{Edd}} \approx 0.2$, associated with an accretion mode change, may play a key role in the observed MS (Marziani et al. 2019; Sulentic et al. 2017).

Only 10% of the known quasars are strong emitters in radio (radio-loud). Zamfir et al. (2010) analysed about 500 quasars observed with Sloan Digital Sky survey (SDSS) and found that radio-quiet sources are distributed equally in Pop. A and Pop. B. But this is not true for radio-loud sources. In the optical domain of the 4DE1, the radio-loud sources show a preference of having FWHM of $H\beta$ higher than 4000 km s^{-1} and a R_{FeII} lower than 0.5, which are the properties that characterise Pop. B quasars. However, recent results have found a relatively high fraction of intermediate radio-emitters in extreme Pop. A quasars (del Olmo et al. 2021; Ganci et al. 2019). These results may support a real dichotomy between radio-loud and radio-quiet QSOs. This work aims to contribute to that study by analysing the spectroscopic differences of two Population A quasars at high redshift, one radio-loud and one radio-quiet. Observational data and properties of the two quasars are described in Section

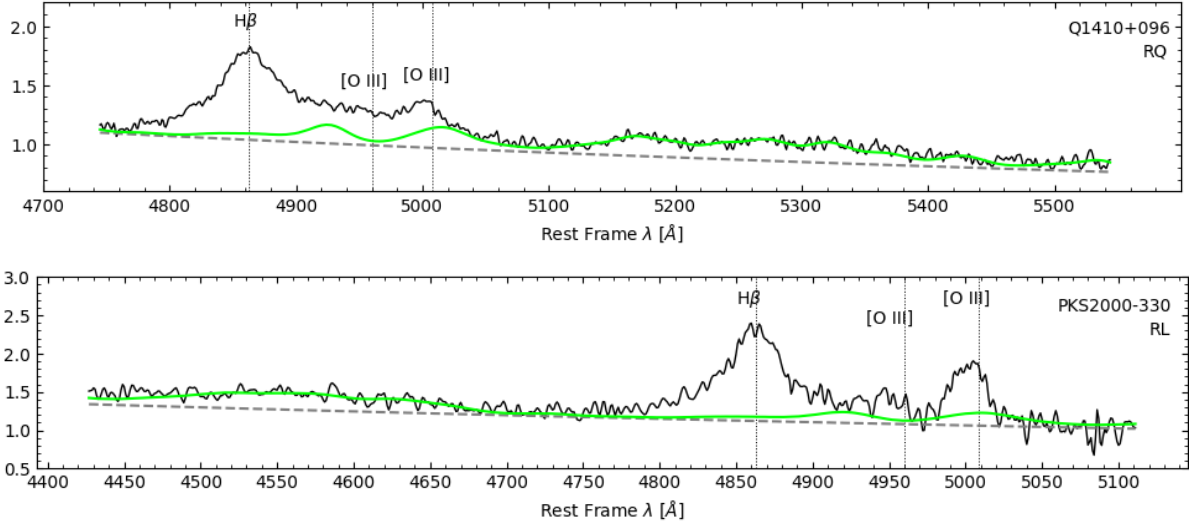


Fig. 4.1: Optical spectra obtained with VLT/ISAAC for Q1410+036 (top panel) and PKS2000-330 (bottom panel). Grey dashed line indicates the power-law obtained on the SPECFIT fitting to represent the continuum level. Green line shows the FeII contribution. Vertical dotted lines indicate the rest-frame of the main emission lines on the spectra.

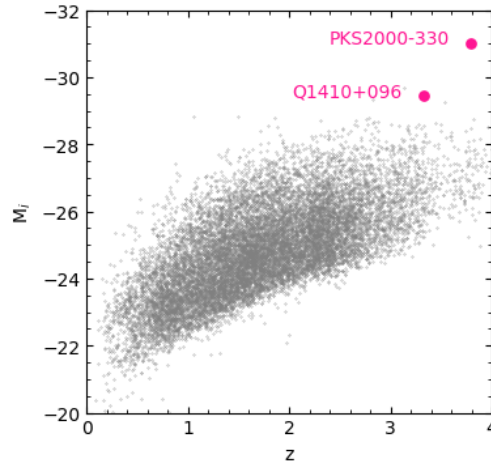


Fig. 4.2: Location of the two sources (in pink) in the Hubble diagram. Grey dots represent a random subsample of the SDSS DR-16 catalogue from Lyke et al. (2020). Galactic extinctions are obtained from Schlafly & Finkbeiner (2011) and K -correction through Richards et al. (2006).

2. The performed optical and UV spectral analysis are presented in Sec. 3, while the main results are detailed in Sec. 4. Comparison of the spectroscopic properties of both sources and the main conclusions are presented in sections 5 and 6 respectively.

4.2 Sample & Observational Data

In this work we present measured properties in the optical and UV spectral regions of two quasars, one radio-loud (PKS200-330) and one radio-quiet (Q1410+096), selected from our ongoing work of

a complete sample of 36 quasars at high redshift ($z = 2 - 4$), that will be presented in a forthcoming paper. The infrared observations were performed at the 8-meter VLT telescope, through the European Southern Observatory (ESO) programmes 083.B-0273(A) for PKS2000-330 and 085.B-0162(A) for the observations of Q1410+096. The ISAAC spectrograph was operated in service mode with a slit width of $0.6''$. The spectroscopic reduction of the new VLT observations were performed in the standard way using the routines of the astronomical package IRAF. Fig. 4.1 shows the obtained rest-frame optical spectra of the two quasars, with a S/N ratio of ≈ 55 in both spectra. Redshift estimation was performed based on the $H\beta$ emission line profile fitting, and then the same z was applied for both optical and UV spectra.

For the UV spectral range (observed in the optical domain at the redshift of the sample), which includes high ionisation lines as C IV $\lambda 1549$, He II $\lambda 1640$, Si IV+O IV] $\lambda 1500$, we use the archive from the Sloan Digital Sky Survey to obtain the spectrum of Q1410+096. In the case of PKS2000-330 (the radio-loud source) the UV spectrum was digitised from Barthel et al. (1990). Fluxes at radio frequencies and the study of radio data of the sources were collected from the Faint Images of the Radio Sky at Twenty-Centimeters (FIRST) survey archive, as well as from the NVSS survey.

The selected sources are among the objects with the highest redshift (z) in our sample. The motivation behind selecting these two QSOs is that they share a similar MS location and a similar optical spectrum, but are different in terms of radio emission and UV spectrum. Table 4.1 lists the coordinates (Col. 2 and 3), estimated redshift (z , Col. 4), i -band absolute magnitude (M_i , Col. 5), and H -band apparent magnitude (m_H , Col. 6) of these two sources. In Fig. 4.2 is shown the location of the two sources in the M_i vs. z plane, where we have also represented a random QSO subsample from the SDSS DR16 catalogue (Lyke et al. 2020) for a comparison with our data. The two sources present higher absolute magnitude M_i and larger redshift when compared with the SDSS data average.

- **Q1410+096:** this object has been identified as a Broad Absorption Line (BAL) QSO (Allen et al. 2011) with absorptions seen mainly on the region of the C IV $\lambda 1549$ and Si IV $\lambda 1397$ emission lines (see Fig. 4.3). The UV spectrum was obtained from the SDSS archive through the DR16 catalogue (Ahumada et al. 2020). The Q1410+096 redshift is reported in the SDSS database as 3.3405, which is significantly different (by $\delta z \sim 0.0165$) from our estimation in the optical spectrum, $z \approx 3.3240$. We have verified that there are no calibration problems in the optical spectrum. In addition, our determination of the redshift is based on the fitting of the $H\beta$ line, showing a peaked and well-defined profile (see Fig. 4.4 upper left) in which the uncertainty in the centroid of the $H\beta$ is about 100 km s^{-1} . We have also carried out a fitting of the 1900\AA blend in the UV SDSS spectrum and we have verified that (as can be seen in Fig. 4.3 upper, where rest-frame position of the emission lines of the 1900\AA blend are shown) the redshift determined through $H\beta$ is in very good agreement with the one we obtained from the main emission lines of the 1900\AA blend (Al III $\lambda 1857$ doublet, Si III] $\lambda 1892$ and C III] $\lambda 1908$). Probably the different redshift in the SDSS database could be due to some error in the redshift estimation of the SDSS DR8 automatic pipeline for this object.

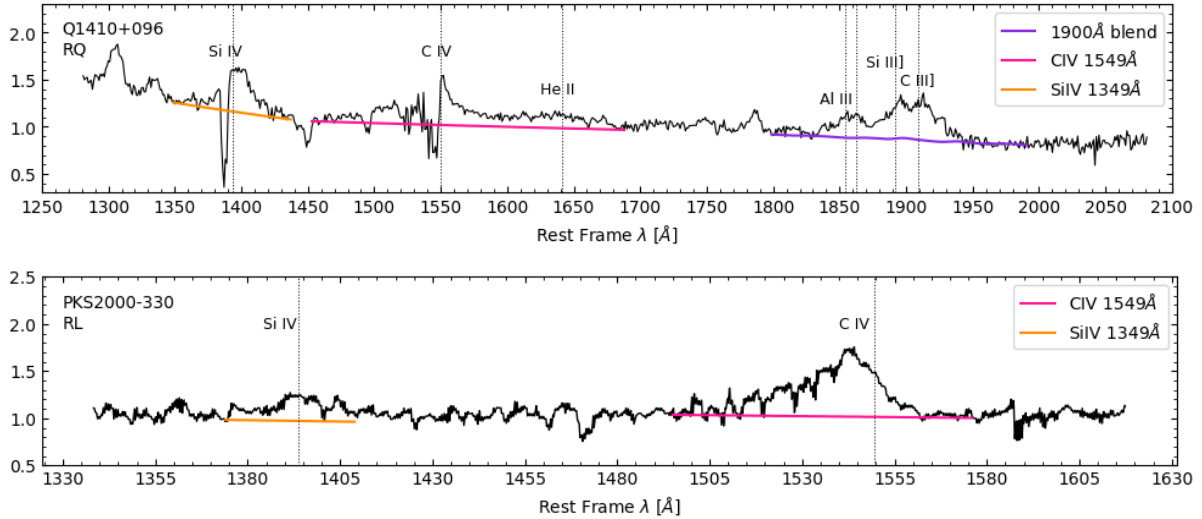


Fig. 4.3: Spectra for the UV region of Q1410+096 (top panel) and PKS2000-330 (bottom panel). Orange, pink, and purple lines identify the local fitted continuum by `specfit` on the corresponding UV regions. Vertical dotted lines show the rest-frame (obtained from the $H\beta$ fittings) of the main emission lines on the spectra.

- PKS2000-330:** This source is a very powerful radio-loud quasar, presenting a radio flux of 446.0 ± 15.7 mJy according to the NVSS catalogue (Condon et al. 1998), and a corresponding radio-loudness parameter $R_k = 4118$, computed following the approach introduced by Kellermann et al. (1989). No emission information is provided by the FIRST catalogue as the position of this source is not in the sky area covered by the FIRST survey. There is also no available spectrum for this object in the SDSS database. For doing the UV spectral analysis, we digitised the one provided by Barthel et al. (1990). This spectrum has a smaller wavelength range than the one of Q1410+096, and it does not cover 1900Å blend nor $HeII\lambda 1640$ emission line. We therefore analysed only $SiIV\lambda 1397$ and $CIV\lambda 1549$ regions. Regarding the optical region, PKS2000-330 present a very peaked and Lorentzian-like $H\beta$ profile, which also allows for a good estimation of the rest-frame.

4.3 Spectral Analysis

The spectral analysis was carried out through the `SPECFIT` routine of IRAF. By using this tool, we were able to perform simultaneously a minimum- χ^2 fit of the continuum, the FeII pseudo-continuum and the emission/absorption individual spectral line components. In the regions of interest, we have fit for the two sources the $H\beta + [O III]\lambda\lambda 4959, 5007\text{Å}$ lines in the optical range, and $SiIV\lambda 1397 + OIV\lambda 1402$ and $CIV\lambda 1549 + HeII\lambda 1640$ emissions (only C IV in the case of PKS2000-330 as its spectrum does not cover the He II line) in the UV spectra.

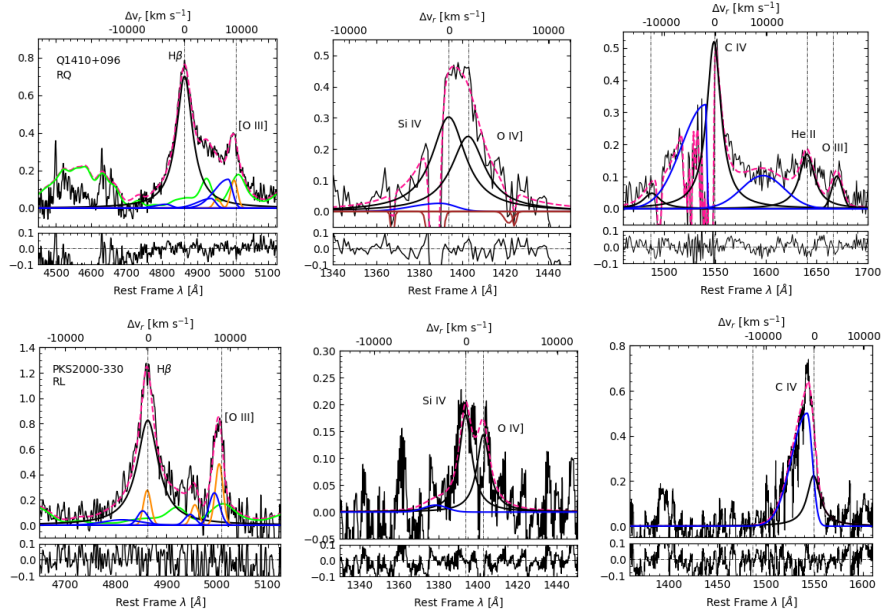


Fig. 4.4: Fittings and residuals for the optical and UV region of Q1410+096 (top panels) and PKS2000-330 (bottom panels). *From left to right*: $H\beta$ + $[O\ III]\lambda\lambda 4959,5007$, $Si\ IV\lambda 1392$, and $C\ IV\lambda 1549$ emission lines regions. Pink dashed lines show the final fitting. Broad components are represented by black lines, while blueshifted components are in blue. Orange and green lines represent narrow and Fe II components. Brown lines represent the absorptions seen in the spectra. Residuals are shown in the bottom of each plot.

4.3.1 Optical range

In the `SPECFIT` fits of the optical region we adopted a power law to describe the continuum. For the Fe II emission, located at both sides of $H\beta$, we used a scalable Fe II template as is explained in [Marziani et al. \(2009\)](#). Since Q1410+096 and PKS2000-330 are Population A quasars, the full broad profile of $H\beta$ of the two objects has been modelled including initially three components (see e.g. [Marziani et al. \(2018\)](#)): 1) a symmetric and unshifted Lorentzian-like profile broad component (BC, in order to account for the virialised subsystem of the BLR); 2) a blueshifted Gaussian component (BLUE), sometimes skewed, as is the case of Q1410+096. This component is mainly detected in Pop. A quasars and it is related with non-virial motions and/or outflowing gas. Usually, when its presence is needed, it is fitted with the same FWHM and shift of the ones observed in the $[O\ III]$ lines; and 3) a narrower Gaussian component (NC) consistently modelled with the narrow component of $[O\ III]$.

In the case of the $[O\ III]\lambda\lambda 4959,5007$ emission lines, each line of the doublet is fitted by a "narrow" symmetrical Gaussian component (NC), and an added semi-broad blueshifted Gaussian component (named BLUE) associated to the presence of outflows. We fitted the doublet considering a fixed ratio of theoretical intensities of 1:3 ([Dimitrijević et al. 2007](#)), the same FWHM, and same line shift. As in $H\beta$, the $[O\ III]\lambda\lambda 4959,5007$ BLUE component are allowed to be skewed to the blue, indicating the presence of an outflow contribution. Also, our initial guess is that the blueshifted components of $H\beta$ and $[O\ III]\lambda\lambda 4959,5007$ share the same shift, FWHM and asymmetry.

Table 4.2: Flux intensities of the $H\beta$ and C IV $\lambda 1549$ emission lines.

Source	$f(H\beta)$ [10^{-15} erg s $^{-1}$ cm $^{-2}$ Å $^{-1}$]	$f(C\ IV\ \lambda 1549)$ [10^{-15} erg s $^{-1}$ cm $^{-2}$ Å $^{-1}$]
(1)	(2)	(3)
Q1410+096	5.9	2.2
PKS2000-330	6.6	4.5

4.3.2 UV range

Regarding the fitting of the UV spectra, we divide the spectral range into two regions centred on the most important emission lines: one in which C IV $\lambda 1549$ dominates the emission, and the other centred in Si IV $\lambda 1397$ +O IV $\lambda 1402$ lines. In both cases the continuum was modelled locally by a power-law as it is shown in Fig. 4.3. Similarly to the $H\beta$ line, broad UV lines are fitted by using an unshifted Lorentzian profile (BC), kept fixed at the rest-frame determined with $H\beta$, plus one or more asymmetric Gaussians to model the blueward excess (BLUE).

In the case of Q1410+096 where both C IV and Si IV are contaminated by the presence of strong absorption features in the blue side, the fittings include absorption lines modelled as Gaussians, so that SPECIFY takes into account them to evaluate the broad emission lines parameters. Nevertheless, the contamination by strong absorption features in the blue side of both profiles make the fit less accurate and the fitted parameters affected by larger uncertainties. Since C IV $\lambda 1549$ and He II $\lambda 1640$ are expected to present a similar shape, the spectral analysis of the He II $\lambda 1640$ emission line in Q1410+096 is performed in a similar way of C IV $\lambda 1549$, sharing the same FWHM and shifts (Martínez-Aldama et al. 2018). In the same way, broad component of Si IV was modelled with the same emission components of C IV (BC+BLUE), with only the flux varying freely.

4.4 Results

4.4.1 $H\beta$ + $[O\ III]\lambda\lambda 4959, 5507$

Fig. 4.1 shows the VLT spectra used on the $H\beta$ + $[O\ III]\lambda\lambda 4959, 5507$. The two objects show very similar behaviour on the optical range, specially in terms of Fe II contribution (green lines) and $H\beta$ profile. Flux intensities of $H\beta$ are shown in Table 4.2. SPECIFY models for the optical data of the two sources are shown in the left plots of Fig. 4.4. The FWHM of the $H\beta$ broad component of Q1410+096 and PKS2000-330 are also very similar, however the shape of the profile at the rest-frame wavelength present a small difference making it necessary to include a very narrow component to account for the narrowed peak seen in the profile of PKS2000-330.

Table 4.3 lists the measurements we obtained after the SPECIFY fitting for the optical region. We present FWHM and centroid velocity at 1/2 intensity ($c(1/2)$) of the full profile for $H\beta$ and $[O$

III] $\lambda\lambda$ 4959,5007 as well as the relative intensity compared to the total flux (I/I_{tot}), and the FWHM and wavelength shift for the individual line components. There are no shifts for the broad line components of H β . Also, we do not include the blueshifted components of the H β profile on the full profile measures because they are too small to present a significant contribution to the full emission line or are clearly related with the [O III] $\lambda\lambda$ 4959,5007 blueshifted components (case in which it is possible that the components present the same physical origin). In the case of the [O III] $\lambda\lambda$ 4959,5007 emission lines, the blueshifted components are stronger and present a more skewed shape for Q1410+096 than for PKS2000-330.

After performing the multicomponent fitting, we can locate the two sources on the optical plane of the MS. Fig. 4.5 shows the location of Q1410+096 and PKS2000-300 on the Main Sequence (represented by the grey and green areas). The red dashed line indicates the A/B Population boundary for the FWHM in the Main Sequence corresponding to a quasar luminosity of about 10^{48} erg s $^{-1}$, representative of the luminosity of our sample, according to Marziani et al. (2009). As can be seen, the two sources are very similar in terms of FWHM(H β) and R_{FeII} and are classified as Pop. A2 quasars.

4.4.2 UV

UV spectra and fittings of the CIV λ 1549+He II λ 1640 and Si IV λ 1392 are shown in Figs. 4.3 and 4.4, respectively. Table 4.4 reports the FWHM and $c(1/2)$ of the C IV full profile as well as the intensities, FWHM, and shift of the individual components. The blueshifted component of the C IV λ 1549 is usually much stronger than the ones observed in the optical range, which can be seen as an indicative of wind activities surrounding the central region. This is also observed in the two sources, where the full profile of C IV is blueshifted by about 2000 km s $^{-1}$. In the case of the RQ BAL Q1410+096 the presence of strong absorption features could explain the lower blue-shift observed (parameterised by $c(1/2)$) in the C IV full profile when compared with the RL PKS2000-330. Previous studies had shown that smaller values of $c(1/2)$ in UV lines in BALs are due mainly to the presence of deep absorptions in the blue side of the profiles (Martínez-Aldama et al. 2018).

Also, when comparing the two sources in this region, it is clear that their spectral behaviour is different. While in Q1410+096 the ratio between the intensities of C IV λ 1594 and Si IV λ 1397 is ~ 0.96 (a value expected for Pop. A quasars), the situation is the opposite for PKS2000-330. In this case, there is a very small contribution of Si IV λ 1397, much smaller than the C IV λ 1549 profile, presenting a Pop. B-like UV spectrum with a C IV λ 1594/Si IV λ 1397 ~ 1.40 .

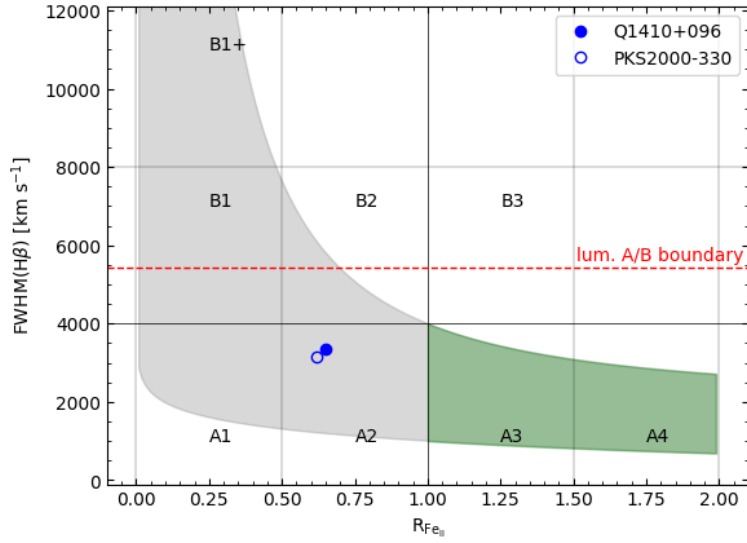


Fig. 4.5: Location of the two sources on the optical plane of the 4DE1. The radio-quiet quasar (Q1410+096) is represented by the filled circle, while the radio-loud quasar (PKS2000-330) is shown as an open circle. Grey and green regions indicate the distribution of the Main Sequence of quasars. Red horizontal line shows the Population A/B boundary for high luminosity quasars, following the $\text{FWHM}(\text{H}\beta)\text{-}M_i$ relation from [Sulentic et al. \(2004\)](#).

Table 4.3: Measurements for the optical range.

Source	Optical													
	$\text{H}\beta_{\text{full}}$		$\text{H}\beta_{\text{BC}}$		$\text{H}\beta_{\text{NC}}$		$[\text{O III}]_{\text{full}}$		$[\text{O III}]_{\text{BLUE}}$		$[\text{O III}]_{\text{NC}}$			
	FWHM [km s^{-1}]	$c(1/2)$ [km s^{-1}]	I/I_{tot}	FWHM [km s^{-1}]	I/I_{tot}	FWHM [km s^{-1}]	FWHM [km s^{-1}]	$c(1/2)$ [km s^{-1}]	I/I_{tot}	FWHM [km s^{-1}]	Shift [km s^{-1}]	I/I_{tot}	FWHM [km s^{-1}]	Shift [km s^{-1}]
(1)	(2)	(3)	(4)	(5)	(6)	(7)	(8)	(9)	(10)	(11)	(12)	(13)	(14)	(15)
Q1410+096	3394	54	1.0	3394	-	-	3363	-1404	0.73	5573	-1255	0.27	1379	-260
PKS2000-330	3138	28	0.93	3138	0.072	1082	1314	-425	0.42	1550	-827	0.58	1082	-263

Table 4.4: Measurements for the C IV $\lambda 1549$.

Source	UV							
	C IV _{full}		C IV _{BLUE}			C IV _{BC}		
	FWHM [km s^{-1}]	$c(1/2)$ [km s^{-1}]	I/I_{tot}	FWHM [km s^{-1}]	Shift [km s^{-1}]	I/I_{tot}	FWHM [km s^{-1}]	
(1)	(2)	(3)	(4)	(5)	(6)	(7)	(8)	
Q1410+096	6311	-1746	0.42	10882	-1525	0.58	3293	
PKS2000-330	4950	-1923	0.71	7339	-1219	0.29	3141	

4.5 Discussion: Is there any relation between $H\beta+[O III]\lambda 5007$ and $CIV\lambda 1549$?

By analysing Table 4.4, it is clear that the blueshift component plays an important role in the full profile of $CIV\lambda 1549$ in the two sources, with a comparable shift towards lower wavelengths ($\sim 2000 \text{ km s}^{-1}$). Q1410+096 (radio-quiet) shows a $CIV\lambda 1549$ BLUE with a $FWHM = 10882 \text{ km s}^{-1}$, while PKS2000-330 (radio-loud) have a CIV_{BLUE} that is somewhat narrower ($\sim 7300 \text{ km s}^{-1}$). The fact that radio-quiet sources show a preference of having wider $FWHM(CIV_{BLUE})$ than the radio-loud ones is already known by the recent literature and seems to be the normal behaviour in this type of sources. Apart from that, these results also may indicate that there is an important contribution of outflowing gas in the nuclear activity in the two sources, in agreement with previous results in other quasar samples (Marziani et al. 2017a; Sulentic et al. 2017).

Another point that we would like to highlight here is that the radio-quiet we analyse presents a slightly higher shift to blue wavelengths when compared to the radio-loud. However, this behaviour is not exclusively observed in $CIV\lambda 1549$. Actually, it is also seen in the blueshifted component of $[O III]\lambda\lambda 4959,5007$ (Ganci et al. 2019), although rare radio-loud NLSy1s do show significant shifts in $[O III]$ (Berton et al. 2016). In the two sources, $CIV\lambda 1549$ and $[O III]\lambda\lambda 4959,5007$ present similar shifts towards the blue. As a consequence, the full profiles of these two emission lines present a negative $c(1/2)$, indicating a strong contribution of the blueshifted components to the full profile. Also, the $FWHM(CIV_{full})$ is much wider for the radio-quiet source than for the radio-loud source, with a difference greater than 1000 km s^{-1} for $CIV\lambda 1549$ and $\sim 2000 \text{ km s}^{-1}$ for $[O III]\lambda\lambda 4959,5007$.

Both $[O III]\lambda\lambda 4959,5007$ and $CIV\lambda 1549$ blueshifted components represent a significant fraction of their respective full profiles. This is an expected behaviour especially at high/intermediate redshift (Sulentic et al. 2004, 2007a; Marziani et al. 2009). When compared to samples with lower redshift, sources such as Q1410+096 and PKS2000-330 (and in general sources at intermediate redshifts) tend to show components in lines like $[O III]\lambda\lambda 4959,5007$ and $CIV\lambda 1549$ that are wider and more blueshifted.

Sulentic et al. (2017), for instance, analyse samples with different redshifts and luminosities showing that the higher the luminosity, the stronger the CIV outflows tend to be. In the high- z context, the emission component related with the outflowing gas becomes the dominant constituent of the broad profile. Similar behaviour is observed in $[O III]$ emission lines, which present significant differences in the full profile when comparing high and low luminosity sources. Cano-Díaz et al. (2012) find a massive outflow on kpc scales in the $[O III]$ for 2QZJ002830.4-281706, which has a $z = 2.4$. Similar results were also found in Marziani et al. (2016b), for a Hamburg ESO sample with intermediate z and high luminosity. Zakamska et al. (2016) analyse four extremely red quasars with $z \sim 2.5$ and discover blueshifted components with very broad $FWHM$ and strongly shifted towards blue wavelengths.

The $FWHM$ of the broad components of $H\beta$ and $CIV\lambda 1549$ also indicate some correspondence between optical and UV regions. For Q1410+096, the $FWHM$ of the two lines differ by $\sim 100 \text{ km}$

s^{-1} . And in the case of PKS2000-330, this difference is smaller than 5 km s^{-1} . When considering the full profile, it can be well reproduced by almost only the BC component in the $\text{H}\beta$ profile. This is not true for $\text{C IV}\lambda 1549$, case in which the FWHM of the broad component represent only 58% for Q1410+096 and 29% for PKS2000-330.

4.6 Conclusions

We analysed a pair of Pop. A2 quasars, which are similar respect to the optical spectra and are very close on the MS classification but present significant differences on the UV data and also on the radio emission: one is a very powerful radio-loud QSO (PKS2000-330) and the other is a radio quiet (Q1410+096). The main conclusions are:

- The $\text{C IV}\lambda 1549$ and $[\text{O III}]\lambda\lambda 4959,5007$ emission line profiles present a similar behaviour in Q1410+096 and also in PKS2000-330, with a more significant shift towards lower wavelengths in the case of the radio-quiet quasar;
- The $[\text{O III}]\lambda\lambda 4959,5007$ emission lines in the two sources are different. In PKS2000-330, we observe a symmetric blueshifted component. On the other hand, in Q1410+096 it is necessary a very skewed blueshifted component (also in $\text{H}\beta$). This may be an indicative that the two objects probably have different behaviour in the observed winds;
- The general behaviour of the UV spectra is very different when comparing the two sources. In the case of the radio-quiet source (Q1410+096) $\text{C IV}\lambda 1549$ and $\text{Si IV}\lambda 1392$ are very similar in intensity and shape, which is a characteristic expected for Pop. A quasars. The same is not true for PKS2000-330, which is a radio-loud quasar and present a more Pop. B-like spectrum in the UV region.

However, a more detailed study is needed in order to perform a complete analysis of the clear behaviour of radio-quiet and radio-loud sources along the Main Sequence. The next step of this work will be to perform an analysis of the spectroscopic properties of our complete sample of 36 quasars and to study the differences between radio-loud and radio-quiet sources.

EXPLORING THE LINKS BETWEEN QUASAR WINDS AND RADIO EMISSION ALONG THE MAIN SEQUENCE AT HIGH REDSHIFT

5

Chapter based on the article accepted for publication at *Astronomy & Astrophysics* by A. Deconto-Machado, A. del Olmo, P. Marziani, 2024. DOI: 10.1051/0004-6361/202449976

Abstract

Despite the increasing prevalence of radio-loud (RL) sources at cosmic noon, our understanding of the underlying physics that governs the accretion disc outflows in these particular sources and its dissimilarity with radio-quiet (RQ) quasars remains somewhat limited. Disentangling the real impact of the radio-loudness and accretion on the outflow parameters remains a challenge to this day. We present ten new spectra of high-redshift and high-luminosity quasars and combine these with previous data at both high and low redshift with the aim being to evaluate the role of the feedback from RL and RQ AGN. The final high-redshift ($1.5 \lesssim z \lesssim 3.9$), high-luminosity ($47.1 \leq \log(L) \leq 48.5$) sample consists of a combination of 60 quasars from our ISAAC and the Hamburg-ESO surveys. The low-redshift ($z \leq 0.8$) sample has 84 quasars that have been analysed in the optical and with the Faint Object Spectrograph (FOS) data in the UV. We perform a multicomponent analysis of optical and UV emission line profiles along the quasar main sequence, and provide a relation that can be used to estimate the main outflow parameters (mass rate, thrust, and kinetic power) in both the BLR and NLR through the analysis of the [O III] λ 5007 and C IV λ 1549 emission lines. Spectrophotometric properties and line profile measurements are presented for H β + [O III] λ 5007, Si IV λ 1397+O IV] λ 1402, C IV λ 1549+He II λ 1640, and the 1900Å blend. High-ionisation lines, such as C IV λ 1549 and [O III] λ 5007, usually present a significant asymmetry toward the blue, especially in radio-quiet sources. This is strong evidence of outflow motions. In the ISAAC sample, 72% of the quasars where [O III] is clearly detected present significant outflows, with centroid velocity at half intensity blueshifted to values of greater than $\sim 250 \text{ km s}^{-1}$. Radio-loud quasars tend to present slightly more modest blueshifted components in both the UV and optical ranges. The behaviour of [O III] λ 5007 mirrors that of C IV λ 1549, with blueshift amplitudes between the two lines showing a

high degree of correlation, which appears unaffected by the presence of radio emission. In contrast to the situation at low redshift, both RL and RQ AGN outflow parameters at high luminosity appear in the range needed to provide feedback effects on their host galaxies. Both high- and low- z RL quasars exhibit smaller outflows compared to RQ quasars, suggesting a potential role of radio-loudness in mitigating outflow effects. Nevertheless, the radio-loudness effect on AGN feedback is much less significant than the effect of accretion, with this latter emerging as the main driver of nuclear outflows.

5.1 Introduction

It is now established that quasar spectra do not scatter randomly around an average, and that a systematic scheme is needed to organise their spectral diversity. One of the most successful tools to analyse such objects makes use of independent observational properties obtained from the optical and UV emission lines, as well as from soft X-rays (the 4D Eigenvector 1 (4DE1) correlation space; [Boroson & Green 1992](#); [Sulentic et al. 2000c](#)). As part of the 4DE1, it is possible to identify a sequence of quasars in the plane defined by two optical parameters: the full width at half maximum of the $H\beta$ emission line ($\text{FWHM}(H\beta)$) and the ratio between the intensities of the blend of Fe II emission lines at 4570\AA and $H\beta$ (R_{FeII}). This relation has come to be known as the main sequence of quasars (MS; [Sulentic et al. 2000a,c](#); [Marziani et al. 2001](#); [Shen & Ho 2014](#); [Marziani et al. 2018](#)). Several multi-frequency correlations associated with the MS are well established at low redshift and low luminosity (e.g., see the summary tables in [Sulentic et al. 2011](#); [Fraix-Burnet et al. 2017b](#)).

At low redshift, it appears that the jetted* (radio-loud, RL) sources show a preference for the Population B (Pop. B) domain in the MS, while the radio-quiet (RQ) sources are distributed equally between Population A (Pop. A) and Pop. B ([Zamfir et al. 2008](#)). This suggests potential differences in spectral and physical properties between RL and RQ sources. The phenomenology involves broader lines for RL than for RQ sources (as most RL sources are in Pop. B), and an optical spectrum showing lower Fe II and a higher ionisation degree with respect to full samples of RQ quasars in both the broad-line region (BLR) and the narrow-line region (NLR) ([Marziani et al. 2003c](#); [Zamfir et al. 2010](#); [Kovačević-Dojčinović & Popović 2015](#); [Coziol et al. 2017](#); [Ganci et al. 2019](#)). Consequently, the low- z RQ sources seem to follow different distributions of Eddington ratio and black hole mass than the RL ones ([Woo & Urry 2002](#); [Marziani et al. 2003b](#); [Sikora et al. 2007](#); [Fraix-Burnet et al. 2017b](#)). In general, at low- z , RQ sources are the ones that usually present smaller masses and larger Eddington ratios.

Outflows appear to be ubiquitous in both the BLR and NLR (e.g., [Coatman et al. 2019](#); [Vietri et al. 2020](#); [Marziani et al. 2022c](#), and references therein). However, at low z , mild-ionisation gas outflows observed in jetted sources appear to be weaker than in the RQ ones ([Marziani et al. 1996](#); [Bachev et al. 2004](#); [Punsly 2010](#); [Richards et al. 2011](#)). This may not be at odds with the higher ionisation degree revealed in RLs (e.g., [Buttiglione et al. 2010](#); [Mengistue et al. 2023](#)), although a

*Here we define “jetted” sources the ones that present a radio-loudness parameter $R_K \geq 1.8$ (also called here as “radio-loud”, [Ganci et al. 2019](#), see also §5.3.4).

full physical explanation is still missing, mainly because of the still-limited scope of detailed studies of accretion disk outflows in RL quasars. This difference between RQ and RL outflows is observed at both high and low redshift. A key distinction is however that at high redshift, the outflows appear significantly stronger compared to those at low redshift (Richards et al. 2011; Sulentic et al. 2017; Deconto-Machado et al. 2023). At low-redshift ranges, many authors have found ionised gas outflows on kiloparsec (kpc) scales; however their impact is only in the central region of the galaxies (e.g., Kim et al. 2023, and references therein).

An increasing number of RL sources are being discovered at cosmic noon (e.g., Patil et al. 2022; Breiding et al. 2023, and references therein). Their rest-frame optical properties remain poorly studied, as they require high-signal-to-noise-ratio (S/N) moderate-dispersion IR spectroscopy. For this reason, we obtained new IR spectroscopic observations for a further ten high-redshift ($z \sim 1.5 - 2.5$) and high-luminosity ($M_B \lesssim -27$) quasars. The targets are intended to cover the rest-frame $H\beta$ range, and include both RQ and jetted (or RL) objects, completing the sample reported in Deconto-Machado et al. (2023, hereafter Paper I). Our main aim is to clarify the origin of several phenomenological differences between RL and RQ and in particular the relation between accretion status, accretion disk outflows, and the presence of powerful relativistic ejections, exploiting the MS and its correlation with the $C\text{IV}\lambda 1549$ and $[\text{O III}]\lambda 5007$ emission.

In addition to the rest-frame optical data, we collected archival rest-frame UV data for the targets in the present chapter and in Paper I, and we defined comparison samples for which both rest-frame UV and optical data are available (Section 5.2). The data analysis includes a discussion about UV and optical regions for the two different quasar populations and the spectral types that have been defined along the quasar MS (Section 5.3). The measurements carried out in both the optical (Fe II, $H\beta$, $+\text{[O III]}\lambda 5007$) and UV ($\text{SiIV}\lambda 1397$, $\text{C IV}\lambda 1549$, and the 1900\AA blend) regions are reported in Section 5.4, and their interpretation in terms of the outflow dynamical parameters is presented in Section 5.5. We show that the RQ and RL populations are both associated with high Eddington ratios at high luminosity, and that BLR and NLR scale outflows are consistently powerful, albeit they are somewhat weaker in RL sources. This difference between RQ and RL outflows might be due to an apparently minor effect related to the propagation of the relativistic jet. In Section 5.6, we summarise our key findings and discuss some implications of our results.

5.2 Samples

5.2.1 The new ISAAC2 sample

New near-infrared (NIR) spectroscopic observations for ten quasars (hereafter ISAAC2 sample) were obtained to cover the high-redshift ($1.55 \leq z \leq 2.45$) and high-luminosity ($47.18 \leq \log L_{\text{bol}} \leq 48.14$ [erg s^{-1}]) ranges. The redshift range of this sample allows the detection and observation of the $H\beta+\text{[O III]}\lambda 5007$ region through the transparent window in the NIR with the ISAAC spectrograph at the VLT. These spectra, together with those from Paper I complete what we refer to from now on as the ISAAC sample (32 sources in total), which is described in more detail in §5.2.2.

Table 5.1: Source identification of the ISAAC2 sample.

Source (1)	RA (2)	DEC (3)	z (4)	δz (5)	m_H (6)	M_i (7)
PKS0226-038	02 28 53.26	-03 37 05.30	2.0692	0.0002	15.97	-28.55
PKS0237-23	02 40 08.17	-23 09 15.72	2.2298	0.0008	14.52	-29.79
BZQJ0544-2241	05 44 08.63	-22 40 37.10	1.5547	0.0003	14.90	-27.99
PKS0858-279	09 00 40.03	-28 08 20.35	2.1725	0.0007	13.65	-31.26
CTSJ01.03	09 39 51.10	-18 32 15.00	2.3754	0.0004	14.98	-30.07
WB J0948+0855	09 48 53.60	+08 55 14.45	1.9842	0.0016	15.17	-29.01
CTSJ03.14	10 18 21.75	-21 40 07.80	2.4493	0.0003	15.57	-28.51
PKS1448-232	14 51 02.50	-23 29 31.08	2.2264	0.0002	14.97	-29.13
[HB89]1559+088	16 02 22.73	+08 45 38.42	2.2837	0.0007	15.01	-29.02
FBQS J2149-0811	21 49 48.18	-08 10 16.60	2.1295	0.0002	15.74	-28.48

Notes. Column (1) Source identification according to the different catalogues. Columns (2) and (3) Right ascension (hh mm ss) and Declination (dd mm ss) respectively, at J2000 coordinates. (4) Redshift estimated as explained in Section 5.2.1. (5) Redshift uncertainty. (6) H -band apparent magnitude (m_H) from the 2-MASS catalogue. (7) i -band absolute magnitude M_i .

Table 5.1 lists the main properties of the ISAAC2 sample. The redshift was estimated using a similar approach to that used in Paper I. For five sources (PKS0226-038, PKS0858-279, CTSJ01.03, CTSJ03.14, and PKS1448-232), the redshift estimation relied on the observed wavelength of the narrow component (NC) of $H\beta$, which is also consistent with the central wavelength of the [O III] NC. For PKS0237-23, BZQJ0544-2241, [HB89]1559+088, and FBQS J2149-0811, the redshift was determined using the broad component (BC) of $H\beta$, whose peak wavelength agrees with the peak of a very faint $H\beta$ NC in all cases except PKS0237-23 and [HB89]1559+088, where the NC is only barely detected. In the case of WB J0948+0855, the presence of strong telluric bands, combined with the fact that the $H\beta$ region is at the edge of the spectrum, significantly affect the estimation of the $H\beta$ peak centroid, leading to large uncertainties. Therefore, we used the Mg II $\lambda\lambda 2796, 2803$ doublet from the SDSS UV spectrum to determine the redshift for this source (see spectral fitting in Fig. A.2.6). The luminosity distance was estimated from the redshift using the approximation reported in Sulentic et al. (2006b), which is valid for $\Omega_M = 0.3$, $\Omega_\Lambda = 0.7$, and $H_0 = 70 \text{ km s}^{-1} \text{ Mpc}^{-1}$.

5.2.2 The complete ISAAC sample

Our complete ISAAC sample comprises 32 quasars, consisting of 22 sources from Paper I, along with the ten new objects presented in this work. These quasars are characterised by high redshift values, ranging from $z = 1.55$ to $z = 3.80$, and high luminosity ($47.18 \lesssim \log L_{\text{bol}} \lesssim 48.36$ [erg s⁻¹]), including both RL (10) and RQ (22) sources. The ISAAC sample was selected from the catalogue of Véron-Cetty & Véron (2010, VCV), among the type 1 quasars observable from the Paranal Observatory, with declination $\delta \leq 25^\circ$, and with a redshift of between 1 and 4 according to VCV (from where the first estimation of the redshift was obtained), which would allow good coverage of the $H\beta$ and [O III] region through the NIR windows with the ISAAC spectrograph at the VLT. Figure 5.1 shows the distribution in z and M_i of the complete ISAAC sample, along with the other samples

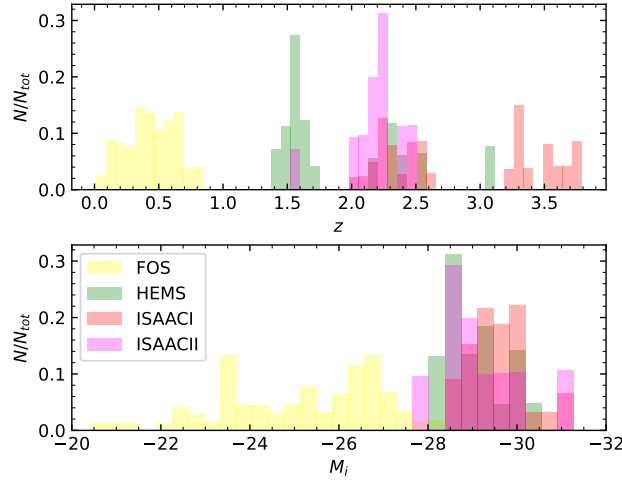


Fig. 5.1: Distributions of z and M_i for FOS, HEMS, ISAACI from Paper I, and the new ISAAC2 data. Each distribution was normalised separately.

Table 5.2: Log of optical observations with VLT/ISAAC.

Source	Date obs. (start)	Band	DIT (s)	N_{exp}	Airmass start-end
(1)	(2)	(3)	(4)	(5)	(6)
PKS0226-038	Jan 27, 2011	sH	160	16	1.50-1.87
PKS0237-23	Nov 17, 2010	sH	140	16	1.48-1.78
BZQJ0544-2241	Nov 24, 2010	J	145	24	1.01-1.04
PKS0858-279	Oct 13, 2010	sH	140	8	1.79-1.46
CTSJ01.03	Oct 27, 2010	sH	180	12	1.65-1.41
WB J0948+0855	Jan 26, 2011	sH	160	12	1.27-1.21
CTSJ03.14	Nov 23, 2010	sH	160	12	1.34-1.18
PKS1448-232	Jan 31, 2011	sH	160	16	2.01-1.58
[HB89]1559+088	Feb 01, 2011	sH	170	16	2.19-1.70
FBQS J2149-0811	Oct 26, 2010	sH	160	16	1.09-1.23

Notes. (1) Source identification. (2) Date of observation. (3) Grating used. (4) Individual Detector Integration Time (DIT). (5) Number of exposures with single exposure time equal to DIT. (6) Range of air mass of the observations.

considered in this work (described in §5.2.3). The ISAAC2 sample exhibits a very similar M_i range to ISAAC1, although ISAAC1 has a more extended distribution in the z context, with some cases reaching redshifts of as high as ~ 3.8 .

5.2.3 Other samples

This work includes two additional, previously published samples, at high and low redshift (including RL and RQ sources). Ultraviolet and optical spectra are available for both, and these were analysed using the same approach for the decomposition of the emission line profiles. These two additional samples are as follows:

High-redshift Hamburg-ESO sample (hereafter, HEMS): The HEMS sample consists of the 28 high-luminosity and high-redshift objects with measurements reported by Sulentic et al. (2017), where a detailed analysis (based on the same methodology as that used for our ISAAC sample) of the $H\beta$ and $C\text{IV}\lambda 1549$ broad emission lines is presented. This sample was selected for having additional UV spectra from the original 52 sources with ISAAC $H\beta$ observations of the Hamburg-ESO (HE) sample discussed in Sulentic et al. (2004, 2006b) and Marziani et al. (2009). These sources are extremely luminous ($47.5 \lesssim \log L_{\text{bol}} \lesssim 48$ [erg s⁻¹]) and are located in a redshift range of $1.4 \lesssim z \lesssim 3.1$. The radio properties of the HEMS sample are listed in Table B.1, together with the UV and optical full profile measured parameters for this sample and used in this chapter. From the 28 quasars, 24 are classified as RQ, while four are RL sources. We combine these data with our ISAAC1+ISAAC2 sources to build a high-luminosity sample to be analysed in the present work. As can be seen in Fig. 5.1, the HEMS sample shares similar *i*-band absolute magnitudes with the ISAAC sample.

Low-redshift FOS data: The low-luminosity sample was selected from Sulentic et al. (2007a), who analysed the $C\text{IV}\lambda 1549$ emission line parameters of 130 low-redshift sources observed with the Faint Object Spectrograph (FOS) on board HST. Of these 130 quasars, 84 have optical spectra available in the recent literature, and we reanalysed them following the same approach as that used for the ISAAC data. We use this sample as a comparison sample at low L for both optical and UV spectral ranges. Table B.1 also lists the radio properties and the UV and optical full profile parameters (velocity centroids at half ($c(1/2)$) and one-quarter ($c(1/4)$) of the intensity of $C\text{IV}$ and $[\text{O III}]$) of the FOS sample. This sample includes both RQ and RL (50 and 34 sources, respectively) and has a typical bolometric luminosity of ~ 45.6 [erg s⁻¹] and a redshift of $z \leq 0.8$, as shown in Fig. 5.1.

In the analysis carried out in Sections §5.4 and §5.5, our high- z high-luminosity sample (including RQ and RL sources) consists of the combination of the full ISAAC (ISAAC1+ISAAC2) and HEMS samples, as they share similar redshift and luminosity ranges. This high- z sample consists of 60 sources in total (32 from ISAAC and 28 from HEMS), of which 58 objects have an $[\text{O III}]$ detection. For the other 2, in the case of SDSSJ005700.18+143737.7, $[\text{O III}]$ is located very close to the edge of the spectrum, and for WB J0948+0855, the region is completely affected by absorption lines. From these 58 sources, 34 are identified as blue outliers in $[\text{O III}]$ (i.e., velocity shifts at half intensity $c(1/2)$ higher than -250 km s⁻¹; see §5.4.1), with 20 sources from ISAAC (representing $\sim 62\%$ of the sample) and 14 from HEMS ($\sim 50\%$ of the sample). Regarding $C\text{IV}$ at high z , data are available for 48 (20 from ISAAC and 28 from HEMS), wherein blueshifts are identified in all sources but HE2355-4621.

The low- z low-luminosity sample consists of the 84 reanalysed FOS sources, for which measurement data are available for both $[\text{O III}]$ and $C\text{IV}$. Among them, 11 sources in $[\text{O III}]$ and 21 in $C\text{IV}$ present a significant blueshifted component. For both emission lines, a source is classified as a blue outlier and consequently considered to have an outflow if its full profile exhibits a velocity centroid at half peak intensity $c(1/2) < -250$ km s⁻¹. Also for the FOS low- z sample, when the $[\text{O III}]$ full profile shows slightly smaller $c(1/2)$ blueshift, the object is identified with an outflow if its blueshifted

component (after the spectral fitting; see section 5.3.3) has a significant intensity ($\gtrsim 40\%$) relative to the full profile. The list of sources identified as outliers is reported in Table 5.13.

Throughout Sections 5.4 and 5.5, the sample size depends on the analysis done. We consider the complete samples (i.e., the 60 sources at high z and 84 ones at low z) when discussing the general behaviour of the profiles or, for example, of the effect of radio-loudness on the line profiles both in CIV and [O III]. However, when addressing outflows and their dynamical parameters, only the objects identified as exhibiting blueshifted components are taken into account.

5.3 Observations and data analysis

5.3.1 NIR observations and data reduction

The new spectra were taken in service mode in 2010 and 2011 under the ESO programme 086.B-0774(A), with the IR spectrometer ISAAC mounted at the Nasmyth A focus of VLT-U3 (Melipal) at the ESO Paranal Observatory. A summary of the observations is listed in Table 5.2.

Reductions were performed following a standard methodology in NIR observations, that is, using standard IRAF routines, and following the procedures described in Paper I. Pairs of spectra were taken by nodding the telescope between two positions, A and B, displaced on the CCD frame and following an ABBA cycle, as this allows a better subtraction of the sky. The wavelength calibration was achieved from xenon and argon arc spectra with rms residuals of 0.4\AA in J and 0.6\AA in sH. This wavelength calibration was corrected for small zero-order offsets by measuring the centroids of several OH sky lines against the arc calibration. The 2D wavelength-calibrated spectra (A and B) of each pair AB or BA were rebinned to a common linear wavelength scale. The sky background was then subtracted using the double-subtraction technique. For each rebinned wavelength 2D spectra, we computed a frame (A-B or B-A), so that the reduced image (AB or BA) consists of two spectra of the source, one positive and one negative, positioned as separated by the nod throw and in which the sky has been removed. We then extracted the 1D wavelength-calibrated spectra using the task `apsum`, creating one spectrum for each nodding position. The 1D -B (or -A) spectrum was subtracted again to obtain a final 1D A-(-B) = A+B spectrum for each observing AB and BA sequence of the ABBA cycle. Finally, all double-subtracted spectra were stacked together.

The absolute flux calibration was performed through observations of standard telluric stars, with the same setup as that used to obtain quasar spectra. The standard star spectral energy distributions (SEDs) were retrieved from the Library of Stellar Spectra for spectrophotometric calibration available at ESO[†]. The absolute flux scale for the standard star was provided by the Two Micron All Sky Survey (2MASS, [Skrutskie et al. 2006](#)) magnitudes. Each standard star SED spectrum was then divided by its corresponding spectrum in order to correct for the atmospheric absorption features (IRAF routine `telluric`). Spectra were also corrected for galactic extinction.

[†]https://www.eso.org/sci/observing/tools/standards/IR_spectral_library.html

Table 5.3: UV spectra information.

Source (1)	UV Spect. (2)
PKS0226-038	BOSS
PKS0237-23	Wilkes et al. (1983)
BZQJ0544-2241	Perlman et al. (1998)
PKS0858-279	Stickel et al. (1993)
CTSJ01.03	Tytler et al. (2004)
WB J0948+0855	BOSS
CTSJ03.14	6dFGS
PKS1448-232	...
[HB89]1559+088	SDSS
FBQS J2149-0811	...

Notes. (1) Source identification. (2) Database of reference from which the UV spectra were obtained.

As a final step, we evaluated the absolute flux calibration uncertainty on the quasar spectra by performing a comparison between the J/H -band magnitudes estimated by convolving the J/H 2MASS filter with the observed spectrum and the J/H magnitudes in the NASA/IPAC Extragalactic Database (NED). The average difference between 2MASS and our flux estimations is 0.026 mag, with the largest value of 0.091 ± 0.018 mag found for CTSJ01.03.

5.3.2 Optical data

Eight out of the ten new sources from the ISAAC2 sample have rest-frame UV spectra that cover at least one of the three regions of our interest (i.e., Si IV λ 1397+O IV] λ 1402, C IV λ 1549+He II λ 1402, and the 1900Å blend regions). Table 5.3 reports the database or reference from which each UV spectrum was obtained. For four quasars (PKS0237-23, BZQJ0544-2241, PKS0858-279, and CTSJ01.03) it was necessary to digitise the spectra from the respective references reported in Table 5.3. This process was performed using the WebPlotDigitizer facility [‡]. The only sources for which we could not find useful UV spectra are PKS1448-232 and FBQS J2149-0811. For these two quasars, the available UV spectra have an insufficient S/N to perform the fittings.

5.3.3 Data analysis

We carried out our spectral analysis in two complementary ways, following the methodology described in Paper I. After setting the spectra at rest-frame, we performed a multicomponent fit using the `specfit` (Kriss 1994) routine from the IRAF package. This routine allows a simultaneous minimum- χ^2 fit of the continuum approximated by a power law, a scalable Fe II (or Fe III) pseudo-continuum, and the spectral line components, yielding the full width at half maximum (FWHM), the peak wavelength, and the intensity of all line components (see Fig. 2 of Paper I for an illustration of the decomposition analysis of the broad lines). We also include absorption lines in the event that some emission profiles (usually those of C IV) are affected by them. In addition, we performed a study of

[‡]<https://automeris.io/>

Table 5.4: Measurements on the $H\beta$ full broad line profile and derived properties of the $H\beta$ region.

Source	$F_{5100\text{\AA}}$	F_{tot}	W [Å]	FWHM [km s ⁻¹]	A.I.	c(1/4) [km s ⁻¹]	c(1/2) [km s ⁻¹]	c(3/4) [km s ⁻¹]	c(9/10) [km s ⁻¹]	R_{FeII}	ST	$\log L_{\text{bol}}$ [erg s ⁻¹]	$\log M_{\text{BH}}$ [M_{\odot}]	$\log L/L_{\text{Edd}}$
(1)	(2)	(3)	(4)	(5)	(6)	(7)	(8)	(9)	(10)	(11)	(12)	(13)	(14)	(15)
Population A														
BZQJ0544-2241	4.53	2.52	51	5191 ± 458	-0.05 ± 0.09	-266 ± 402	-174 ± 93	-94 ± 141	-57 ± 170	0.69	A2	47.52	9.66	-0.31
WB J0948+0855 ^(a)	2.88	1.27	43	5580 ± 494	0.00 ± 0.11	-1 ± 456	-1 ± 92	0 ± 149	0 ± 184	0.89	A2	47.45	9.74	-0.46
CTSJ01.03	1.96	1.73	81	4551 ± 403	0.00 ± 0.20	320 ± 372	321 ± 75	321 ± 122	321 ± 150	0.21	A1	47.37	9.52	-0.33
FBQS J2149-0811	1.73	1.80	113	4992 ± 442	0.00 ± 0.11	0 ± 408	0 ± 82	-1 ± 133	-1 ± 165	0.23	A1	47.26	9.55	-0.46
Population B														
PKS0226-038	1.48	0.99	66	5280 ± 420	0.46 ± 0.05	2874 ± 646	109 ± 53	-45 ± 140	-86 ± 190	0.62	B2	47.18	9.44	-0.44
PKS0237-23	5.19	4.48	89	7986 ± 821	0.31 ± 0.11	2546 ± 389	1374 ± 65	730 ± 211	574 ± 262	0.42	B1	47.76	9.85	-0.27
PKS0858-279 ^(a)	12.9	7.84	56	5385 ± 402	0.15 ± 0.11	790 ± 388	299 ± 61	191 ± 141	159 ± 191	0.47	B1	48.14	9.91	0.05
CTSJ03.14 ^(a)	3.44	3.61	102	4056 ± 305	0.07 ± 0.09	271 ± 274	100 ± 52	62 ± 106	50 ± 143	0.38	B1	47.62	9.36	0.08
PKS1448-232	3.43	4.53	129	4397 ± 364	0.54 ± 0.09	3664 ± 745	263 ± 47	150 ± 114	122 ± 153	0.07	B1	47.58	9.43	-0.02
[HB89]1559+088	3.31	3.66	110	5802 ± 514	0.01 ± 0.18	71 ± 750	-314 ± 115	-39 ± 157	13 ± 184	0.29	B1	47.57	9.56	-0.16

Notes. (1) Source identification. (2) Flux of the continuum on the 5100Å wavelength, corrected for galactic extinction, in units of 10^{-15} erg s⁻¹ cm⁻² Å⁻¹. (3) Full $H\beta$ line flux (i.e., the flux for all broad line components, BC, and VBC, and BLUE whenever appropriate), in units of 10^{-13} erg s⁻¹ cm⁻². (4) $H\beta$ equivalent width W . (5) FWHM. (6) Asymmetry index (A.I.). (7), (8), (9), (10) Centroid velocity shifts at $\frac{1}{4}$, $\frac{1}{2}$, $\frac{3}{4}$, and $\frac{9}{10}$ fractional intensities. (11) Ratio R_{FeII} (see §5.4.2). (12) Spectral types according to the quasar main sequence. (13) Bolometric luminosity. (14) Black hole mass. (15) Eddington ratio. ^(a) $H\beta$ profile may be affected by the correction of the telluric absorptions present in the spectrum (see Appendix A.2).

 Table 5.5: Results from specific analysis on the broad and narrow profiles of $H\beta$.

Source	Full broad profile (BLUE+BC+VBC)									Full narrow profile (SBC+NC)						
	BLUE			BC			VBC			SBC				NC		
	F/F_{tot}	FWHM [km s ⁻¹]	Peak [km s ⁻¹]	F/F_{tot}	FWHM [km s ⁻¹]	Peak [km s ⁻¹]	F/F_{tot}	FWHM [km s ⁻¹]	Peak [km s ⁻¹]	F_{tot}	F/F_{tot}	FWHM [km s ⁻¹]	Peak [km s ⁻¹]	F/F_{tot}	FWHM [km s ⁻¹]	Peak [km s ⁻¹]
(1)	(2)	(3)	(4)	(5)	(6)	(7)	(8)	(9)	(10)	(11)	(12)	(13)	(14)	(15)	(16)	(17)
Population A																
BZQJ0544-2241	0.04	5580	-2461	0.96	4877	0	0.35	0.09	1618	-591	0.91	1187	0
WB J0948+0855	1.00	5579	0
CTSJ01.03 ^(a)	1.00	4546	321	1.00	0.18	1437	-1080	0.82	1388	0
FBQS J2149-0811 ^(b)	1.00	4992	0	0.24	0.33	1488	-1263	0.67	1258	0
Population B																
PKS0226-038	0.55	4620	-258	0.45	10495	6340	0.41	0.37	1169	-1051	0.63	901	0
PKS0237-23	0.41	5331	0	0.59	10304	3881	0.11	1.00	654:	230:
PKS0858-279	0.56	4571	6	0.44	10342	2640	6.85	0.55	1273	-1182	0.45	1168	0
CTSJ03.14	0.47	3268	0	0.53	7975	644	0.43	1.00	693	0
PKS1448-232	0.38	3615	16	0.62	14381	5824	1.31	0.61	1045	-724	0.39	1007	0
[HB89]1559+088	0.08	4702	-3110	0.33	3807	0	0.59	14817	1341	0.44	1.00	1581	-759

Notes. (1) Source identification. (2), (3), (4) Relative flux F/F_{tot} , FWHM, and velocity shift of the peak for the BLUE component. (5), (6), (7) Same for the BC. (8), (9), (10) Same for the VBC. (11) Total flux of the $H\beta$ narrow profile, in units of 10^{-14} erg s⁻¹ cm⁻². (12), (13), (14) Relative flux F/F_{tot} , FWHM, and velocity shift of the peak for the SBC component. (15), (16), (17) Same for the NC. ^(a) Very difficult to separate SBC and NC (see Fig. A.2.5). ^(b) SBC and NC very weak and uncertain (see Fig. A.2.10).

the full broad emission line profiles after subtracting the continuum power law, Fe II, and the narrow components.

$H\beta$ spectral region

In the $H\beta$ region fittings, apart from the power law and the scalable Fe II template, for the $H\beta$ BLR broad emission line, we include: (1) a broad component (BC), which is symmetric and typically set at the rest-frame wavelength (Lorentzian-like shape for Pop. A and Gaussian for Pop. B); a very broad component (VBC), representing the innermost part of the BLR, characterised by a Gaussian shape and only present in Pop. B; and (3) a blueshifted component (BLUE), if needed, represented by

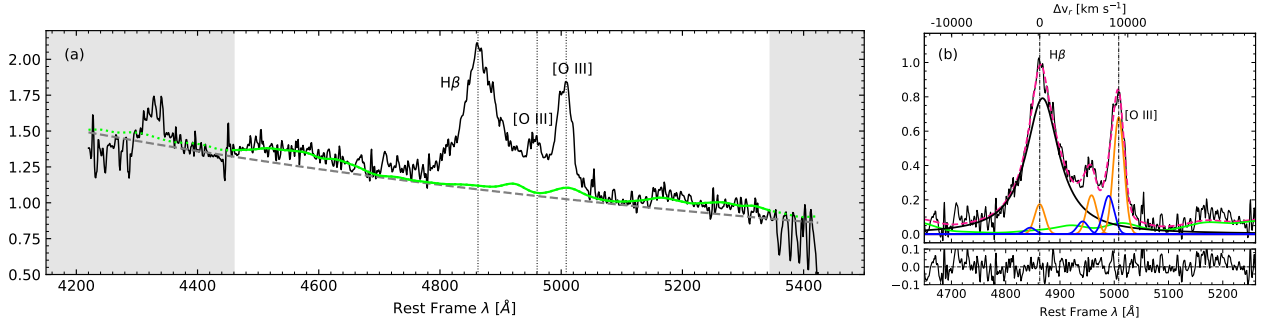


Fig. 5.2: Example of an ISAAC spectrum and of the decomposition analysis of the emission lines. (a) Rest-frame optical spectrum of CTSJ01.03. The white area shows the spectral region used in the fitting. The grey dashed line indicates the continuum level obtained with the `specfit` multicomponent fitting. Fe II contributions are represented by the green line. (b) Example of the H β + [O III] emission line decomposition (upper panel) and its respective residuals (bottom panel). Black, orange, and blue lines indicate the broad, the narrow, and the blueshifted components of the profile, respectively. The final fit is shown by the pink dashed line.

a Gaussian profile (with the option of being skewed). In addition, we include a narrow component superimposed on the broad H β that may include up to two components: the proper narrow component (NC), usually with $\text{FWHM} \leq 1200 \text{ km s}^{-1}$ and fitted as an unshifted Gaussian; and a semi-broad component (SBC), represented by a blueshifted (symmetric or skewed) Gaussian profile with FWHM and shift similar to the [O III] semi-broad component, if present (see below for [O III] components). A final fitting for each spectrum —based on the best-fit model with the minimum χ^2 — was obtained after performing a set of models both as Pop. A and Pop. B.

Figure 5.2 shows the multicomponent decomposition of the H β + [O III] spectral region for one of our sources. The fittings of the complete ISAAC2 sample are shown in the Appendix A.2, along with their respective VLT-ISAAC optical spectra. Measurements on the H β full broad profiles of the ISAAC2 sample are listed in Table 5.4, where properties derived from the H β region are also included. We calculated L_{bol} from the continuum flux at 5100 \AA and by applying the bolometric correction factor expected for the respective luminosity range as established by Netzer (2019). The black hole mass M_{BH} for each quasar was estimated using the H β scaling law of Vestergaard & Peterson (2006, Eq. (5)). We computed the Eddington ratio (L/L_{Edd}) using the bolometric luminosity and with $L_{\text{Edd}} = 1.5 \cdot 10^{38} M_{\text{BH}}$. The corresponding individual components obtained from the `specfit` decomposition of the broad H β profile are reported in Table 5.5.

The [O III] λ 5007 emission line profiles were modelled assuming that each line consists of a narrower, centred Gaussian component (NC) and one (or more) skewed blueshifted Gaussian semi-broad component (SBC) representing bipolar outflow emissions, where the recessing side of the outflow remains obscured (see e.g., Zamanov et al. 2002; Kim et al. 2023, and references therein). Similarly to H β , the results obtained for the full profile and the components of [O III] λ 5007 are reported in Table 5.6.

Table 5.6: Measurements on the [O III] λ 5007 line profile.

Source	F_{tot}	W [Å]	[O III] λ 5007 full profile				SBC			NC		
			FWHM [km s $^{-1}$]	A.I.	$c(1/2)$ [km s $^{-1}$]	$c(9/10)$ [km s $^{-1}$]	F/F_{tot}	FWHM [km s $^{-1}$]	Peak [km s $^{-1}$]	F/F_{tot}	FWHM [km s $^{-1}$]	Peak [km s $^{-1}$]
(1)	(2)	(3)	(4)	(5)	(6)	(7)	(8)	(9)	(10)	(11)	(12)	(13)
Population A												
BZQJ0544-2241 ^(a)	0.27	6	1374 \pm 360:	-0.07 \pm 0.04:	-369 \pm 40:	-339 \pm 88:	0.45	1618	-621	0.55	1187	-247
CTSJ01.03	0.44	22	1709 \pm 123	-0.18 \pm 0.02	-191 \pm 33	-88 \pm 553	0.25	1437	-1110	0.75	1388	0
FBQS J2149-0811 ^(a)	0.14	9	1477 \pm 440:	-0.20 \pm 0.10:	-319 \pm 58:	-248 \pm 92:	0.25	1488	-1292	0.75	1258	-187
Population B												
PKS0226-038	0.31	22	979 \pm 69	-0.27 \pm 0.16	-46 \pm 16	-18 \pm 31	0.24	1169	-1080	0.76	901	0
PKS0237-23	0.31	6	1602 \pm 109	0.09 \pm 0.01	-805 \pm 21	-922 \pm 42	0.83	1423	-899	0.17	654::	-34::
PKS0858-279	0.33	3	1506 \pm 234	-0.35 \pm 0.02	-114 \pm 80	27 \pm 42	0.31	1273	-1211	0.69	1168	65
CTSJ03.14	1.34	40	860 \pm 92	-0.29 \pm 0.13	-120 \pm 40	-38 \pm 21	0.27	1774	-504	0.73	693	-38
PKS1448-232	0.36	11	1154 \pm 74	-0.08 \pm 0.02	-271 \pm 17	-240 \pm 36	0.24	1045	-754	0.76	1007	-161
[HB89]1559+088	0.31	10	885 \pm 215	-0.51 \pm 0.03	-605 \pm 69	-538 \pm 52	0.54	1581	-1452	0.46	688	-498

Notes. (1) Source identification. (2) [O III] λ 5007 total flux, in units of 10^{-13} erg s $^{-1}$ cm $^{-2}$. (3) Equivalent width, W . (4), (5), (6), (7) FWHM, asymmetry index, and the centroid velocities at $\frac{1}{2}$ and $\frac{9}{10}$ intensities of the full profile. (8), (9), (10) Relative intensity, FWHM, and peak shift for the [O III] semi-broad (in general blueshifted) component. (11), (12), (13) Same for the [O III] narrow component. ^(a) [O III] λ 5007 may be affected by the correction of the telluric absorptions present in the spectrum (see the spectra available in the Appendix A.2).

UV spectral region

The UV spectral analysis is performed for three different regions: one centred in the Si IV λ 1397+O IV] λ 1402 lines, one in which the C IV λ 1549 dominates the emission together with a less strong He II λ 1640 line, and another region considering the emission lines from the 1900Å blend (consisting mainly of the Al III λ 1860 doublet, Si III] λ 1892, and C III] λ 1909). In the three spectral regions, the continuum was modelled locally by a power law, and the Fe III multiplets (e.g., the strong lines observed on the red side of the 1900Å blend) were modelled using the Vestergaard & Wilkes (2001) empirical template. For some Pop. A sources, an additional Fe III λ 1914 emission line is needed to fully represent the red side of C III] λ 1909 (see e.g., Martínez-Aldama et al. 2018). The broad UV lines (Si IV λ 1397, C IV λ 1549, He II λ 1640, and C III] λ 1909) are fitted by the same three model components employed for H β , varying their relative contribution to each line flux, as detailed in Paper I.

Table 5.7 provides measurements for the C IV λ 1549 full broad profile, and information on the C IV λ 1549 and He II λ 1640 individual components is given in Table 5.8. The FWHM and peak shift of the C IV λ 1549 and He II λ 1640 components were suitable for representing the profiles in all cases apart from CTSJ03.14, for which the He II λ 1640 BLUE is much narrower than the C IV λ 1549 component.

Table 5.9 shows the measurements on the full profile of Si IV λ 1397 and O IV] λ 1402. Similar to the approach taken in Paper I, we also set the Si IV λ 1397 BC at rest-frame and select a FWHM similar to that determined for C IV λ 1549 BC as an initial guess.

The measurements resulting from the `specfit` analysis of the 1900Å blend are presented in Table 5.10. As Si III] λ 1892 has the same peak rest-frame velocity and FWHM as Al III, we do not report these values for the Si III] line in the table.

Table 5.7: Measurements on the CIV λ 1549 full broad profile.

Source	W [Å]	FWHM [km s ⁻¹]	A.I.	c(1/4) [km s ⁻¹]	c(1/2) [km s ⁻¹]	c(3/4) [km s ⁻¹]	c(9/10) [km s ⁻¹]
(1)	(2)	(3)	(4)	(5)	(6)	(7)	(8)
Population A							
WB J0948+0855	4.99 ± 0.21	10363 ± 984	-0.52 ± 0.03	-6901 ± 642	-5334 ± 354	-3008 ± 366	-2207 ± 235
CTSJ01.03	19.35 ± 0.82	4381 ± 367	-0.38 ± 0.06	-2250 ± 421	-1660 ± 120	-1100 ± 126	-762 ± 147
Population B							
PKS0226-038	32.03 ± 1.36	4898 ± 508	-0.31 ± 0.06	-1878 ± 397	-1148 ± 153	-665 ± 139	-474 ± 141
PKS0237-23	25.47 ± 1.08	7269 ± 729	-0.01 ± 0.06	-1281 ± 646	-1461 ± 168	-1213 ± 217	-1199 ± 179
CTSJ03.14	30.04 ± 1.27	4087 ± 385	-0.30 ± 0.05	-1632 ± 369	-650 ± 105	-481 ± 113	-471 ± 113
[HB89]1559+088	27.87 ± 1.18	4922 ± 527	-0.06 ± 0.05	-1492 ± 340	-1601 ± 94	-1420 ± 144	-1241 ± 145

Notes. (1) Source identification. (2) Equivalent width. (3) FWHM. (4) Asymmetry index. (5), (6), (7) and (8) Velocity centroids at different fractional intensities in km s⁻¹.

Table 5.8: Results from our specfit analysis of CIV λ 1549 and He II λ 1640.

Source	CIV λ 1549									He II λ 1640								
	CIV λ 1549 BLUE				CIV λ 1549 BC		CIV λ 1549 VBC			He II λ 1640 BLUE		He II λ 1640 BC		He II λ 1640 VBC				
	F_{tot}	F/F_{tot}	FWHM [km s ⁻¹]	Peak [km s ⁻¹]	F/F_{tot}	FWHM [km s ⁻¹]	F/F_{tot}	FWHM [km s ⁻¹]	Peak [km s ⁻¹]	F_{tot}	F/F_{tot}	FWHM [km s ⁻¹]	Peak [km s ⁻¹]	F/F_{tot}	FWHM [km s ⁻¹]	Peak [km s ⁻¹]		
(1)	(2)	(3)	(4)	(5)	(6)	(7)	(8)	(9)	(10)	(11)	(12)	(13)	(14)	(15)	(16)	(17)	(18)	(19)
Population A																		
WB J0948+0855	0.75	0.82	22060	-2129	0.25	5558	0.15	0.72	22060	-2129	0.28	5558
CTSJ01.03	11.87	0.68	9263	-530	0.32	4562	1.82	0.62	9263	-530	0.38	4562
Population B																		
PKS0226-038	3.43	0.52	10535	-590	0.21	3525	0.28	10908	1842	0.77	0.58	10535	-3180	0.22	3535	0.20	10908	1842
PKS0237-23	16.85	0.44	10778	-1970	0.20	4209	0.36	10503	2624	3.08	0.40	10778	-1970	0.20	4209	0.40	10503	2624
CTSJ03.14	5.89	0.48	10299	-1103	0.40	3274	0.13	10500	2035	0.78	0.33	5500	-1025	0.07	3274	0.61	10500	2035
[HB89]1559+088	4.89	0.46	7129	-1394	0.25	4226	0.29	12931	2035	0.66	0.34	7129	-1394	0.13	4226	0.53	12931	2035

Notes. (1) Source identification. (2) CIV λ 1549 total flux, in units of 10^{-13} erg s⁻¹ cm⁻². (3), (4), (5) Relative intensity, FWHM, and peak shift for the CIV λ 1549 BLUE component. (6), (7) Relative intensity and FWHM of the CIV λ 1549 BC, which is centered in the respective rest-frame. (8), (9), (10) Relative intensity, FWHM, and peak shift of the CIV λ 1549 VBC. Columns (11)-(19) show the same, but for He II λ 1640.

Table 5.9: Measurements on the SiIV λ 1397+OIV λ 1402 broad lines.

Source	$F_{\text{tot}}^{(a)}$	FWHM [km s ⁻¹]	A.I.	c(1/2) [km s ⁻¹]	c(9/10) [km s ⁻¹]
(1)	(2)	(3)	(4)	(5)	(6)
Population A					
WB J0948+0855	0.92	9878 ± 1013	0.07 ± 0.03	-2257 ± 192	-2633 ± 411
Population B					
PKS0226-038	1.24	6387 ± 1005	-0.09 ± 0.12	465 ± 228	756 ± 415
PKS0237-23	2.42	5084 ± 666	0.06 ± 0.03	965 ± 119	881 ± 323
[HB89]1559+088	1.96	7661 ± 1114	0.00 ± 0.06	-566 ± 284	-752 ± 474

Notes. (1) Source identification. (2) Total flux, in units of 10^{-13} erg s⁻¹ cm⁻². (3) FWHM. (4) Asymmetry index. (5) and (6) Velocity centroids at $\frac{1}{2}$ and $\frac{9}{10}$ fractional intensities.

5.3.4 Radio data

The radio properties for the complete ISAAC sample are reported in Table 5.11. The radio fluxes used to estimate these parameters were obtained from the 1.4-GHz NRAO VLA Sky Survey (NVSS, Condon et al. 1998) and from the VLA Faint Images of the Radio Sky at Twenty-Centimeters survey (FIRST, Gregg et al. 1996; Becker et al. 1995) catalogues. In the case of CTQ 0408, which is not

Table 5.10: Results from our specfit analysis of the 1900Å blend.

Source (1)	Al III					Si III λ 1892				C III] λ 1909+Fe II λ 1914												
	Al III BLUE					Al III BC ^(b)				C III] λ 1909 BC ^(b)				C III] λ 1909 VBC			C III] λ 1909 NC ^(b)			Fe III λ 1914		
	F_{tot} [Å]	W [Å]	F/F_{tot}	FWHM [km s ⁻¹]	Peak [km s ⁻¹]	F/F_{tot}	FWHM [km s ⁻¹]	F_{tot}	W [Å]	F_{tot}	W [Å]	F/F_{tot}	FWHM [km s ⁻¹]	F/F_{tot}	FWHM [km s ⁻¹]	Peak [km s ⁻¹]	F/F_{tot}	FWHM [km s ⁻¹]	F_{tot}	FWHM [km s ⁻¹]	Peak [km s ⁻¹]	
Population A																						
BZQJ0544-2241	12.61	5.44	1.00	5559	9.17	4.03	1.23	5.46	1.00	5382	9.17	5105	3169	
WB J0948+0855	8.55	5.31	0.33	3184	-2011	0.67	5549	5.57	4.38	1.28	1.19	1.00	5549	1.46	5177	1618	
Population B																						
PKS0226-038	3.38	3.52	1.00	4722	5.26	5.60	0.87	9.97	0.65	4722	0.35	7018	2467	0.06	999	
PKS0858-279	32.88	2.96	1.00	4973	44.3	4.05	7.75	7.15	0.66	4973	0.34	8588	4908	
CTSJ03.14	2.12	1.64	1.00	3044	2.97	2.46	1.10	9.78	0.83	3044	0.17	6954	2948	0.03	970	
[HB89]1559+088	3.42	2.55	1.00	4226	9.15	7.02	0.96	7.65	0.42	4226	0.58	7338	2207	0.01	999	

Notes. (1) Source identification. (2) Al III total flux, in units of 10^{-14} erg s⁻¹ cm⁻². (3) Al III Equivalent width W . (4), (5) and (6) Relative intensity, FWHM, and peak shift respectively for the Al III BLUE component. (7) and (8) Relative intensity and FWHM for the Al III BC, centred in the respective rest-frame. (9) and (10) Si III λ 1892 total flux (in units of 10^{-14} erg s⁻¹ cm⁻²) and W . (11), (12) Same for C III] λ 1909. (13) and (14) Relative intensity and FWHM for C III] λ 1909 BC, centred in the respective rest-frame. (15), (16) and (17) Relative intensity, FWHM, and peak shift for the C III] λ 1909 VBC. (18) and (19) Relative intensity and FWHM for the C III] λ 1909 NC, centred in the respective rest-frame. (20), (21) and (22) Fe III λ 1914 total flux (in units of 10^{-14} erg s⁻¹ cm⁻²), FWHM and peak shift.

Table 5.11: Radio properties of the full ISAAC sample.

Source (1)	$f_{1.4\text{GHz}}$ [mJy] (2)	$P_{1.4\text{GHz}}$ (3)	$\log R_K$ (4)	Survey (5)	Radio Class. (6)
ISAAC1					
HE 0001-2340	< 0.90	< 0.15	< 0.48	NVSS	RQ
[HB89]0029+073	< 0.24	< 0.08	< -0.12	FIRST	RQ
CTQ 0408	< 2.49	< 0.85	< 0.43	SUMSS	RQ
SDSSJ005700.18+143737.7	< 0.90	< 0.21	< 0.35	NVSS	RQ
H 0055-2659	< 0.90	< 0.38	< 0.60	NVSS	RQ
SDSSJ114358.52+052444.9	< 0.28	< 0.06	< 0.17	FIRST	RQ
SDSSJ115954.33+201921.1	< 0.29	< 0.11	< -0.04	FIRST	RQ
SDSSJ120147.90+120630.2	< 0.29	< 0.11	< -0.26	FIRST	RQ
SDSSJ132012.33+142037.1	< 0.29	< 0.06	< 0.15	FIRST	RQ
SDSSJ135831.78+050522.8	< 0.28	< 0.06	< -0.15	FIRST	RQ
Q 1410+096	< 0.30	< 0.11	< -0.13	FIRST	RQ
SDSSJ141546.24+112943.4	6.50	1.41	1.27	NVSS	RI
B1422+231	284.67	119	2.78	FIRST	RL
SDSSJ153830.55+085517.0	< 0.31	< 0.12	< 0.36	FIRST	RQ
SDSSJ161458.33+144836.9	< 0.28	< 0.06	< -0.13	FIRST	RQ
PKS 1937-101	838	381	2.99	NVSS	RL
PKS 2000-330	446	202	3.14	NVSS	RL
SDSSJ210524.49+000407.3	2.50	0.46	0.54	NVSS	RQ
SDSSJ210831.56-063022.5	< 0.37	< 0.07	< 0.18	FIRST	RQ
SDSSJ212329.46-005052.9	< 0.29	< 0.05	< -0.45	FIRST	RQ
PKS 2126-15	589	207	2.97	NVSS	RL
SDSSJ235808.54+012507.2	< 0.28	< 0.11	< -0.32	FIRST	RQ
ISAAC2					
PKS0226-038	939	135	3.50	NVSS	RL
PKS0237-23	6256	1043	3.80	NVSS	RL
BZQJ0544-2241	133	10.78	2.06	NVSS	RL
PKS0858-279	1474	233	2.77	NVSS	RL
CTSJ01.03	2.90	0.55	0.92	NVSS	RQ
WB J0948+0855	36.50	4.88	1.78	NVSS	RI
CTSJ03.14	151	30.31	2.40	NVSS	RL
PKS1448-232	439	73.03	2.83	NVSS	RL
[HB89]1559+088	4.50	0.79	0.87	NVSS	RQ
FBQS J2149-0811	< 0.36	< 0.05	< 0.02	FIRST	RQ

Notes. (1) Source identification. (2) Radio flux at 1.4 GHz. (3) Radio power P at 1.4 GHz, in units of 10^{26} W Hz⁻¹. (4) Radio-loudness parameter. (5) Survey from which we obtain the radio data. (6) Radio classification.

covered by these two surveys, we estimated the upper limit for the flux from the SUMSS catalogue (Mauch et al. 2003). The R_K parameter is determined as the ratio between the rest-frame specific fluxes at 1.4 GHz and at the g -band effective wavelength (following Ganci et al. 2019). We then considered three different ranges of radio-loudness: radio-quiet (RQ; $R_K < 10$), radio-intermediate (RI; $10 \leq R_K \leq 70$), and radio-loud (RL; $R_K \geq 70$).

If the object is not detected (for the 50% of the sample: 16 sources, 15 from ISAAC1, and one from ISAAC2), an upper limit on the radio flux is set equal to a detection threshold (of ~ 2 times the rms in both FIRST and NVSS catalogues) at the position of the source. Our preference is to rely on the FIRST detection limit as its maps have a higher sensitivity than NVSS and allow for a better restrictive upper limit. However, in cases where the position of the object does not fall within the current coverage of the FIRST catalogue, we then use the NVSS detection limit. When considering the complete ISAAC sample, we have 10 RL, 2 RI, and 20 RQ sources.

For objects from both the HEMS and the FOS sample, we re-estimated the values of R_K using the same methodology as that employed for the ISAAC data. Of the 28 sources of the HEMS sample, 4 are RL and 24 RQ. As mentioned in section 5.2.3, in the low-luminosity FOS sample there are 34 RL and 50 RQ sources.

By default, we define that the sources initially classified as RI are considered together with the RQ objects, unless we have evidence that the source is jetted. The enhancement of the radio emission in RIs is possibly related to star formation (Condon et al. 2013; Bonzini et al. 2015; Caccianiga et al. 2015; Ganci et al. 2019), a powerful broad line region and extended ionised outflows (Panessa et al. 2019, and references therein), or intrinsic reddening in the optical fluxes.

5.4 Results

5.4.1 ISAAC1 and ISAAC2 basic results: Synopsis

The optical and UV main spectral properties of ISAAC1 and ISAAC2 are fully consistent.

$H\beta$ – The dichotomy between Pop. A and Pop. B is preserved in the complete ISAAC sample, with Pop. A quasars usually presenting lower values of $H\beta$ W and FWHM. However, it is noteworthy that the lowest FWHM($H\beta$) values in ISAAC2 are observed in two Pop. B quasars (CTSJ03.14 and PKS1448-232), both of which are blazar candidates, and therefore the FWHM may be strongly influenced by the source orientation. Among the ISAAC2 $H\beta$ Pop. A profiles, all are symmetric except for BZQJ0544-2241, which requires an additional (usually weak) BLUE component to fully represent the $H\beta$ line. In contrast, the $H\beta$ profiles in Pop. B sources are all redward asymmetric, with the exception of [HB89]1559+088, which is nearly symmetric and also requires a BLUE component. This additional component is added when the blueshift observed in the $H\beta$ profile does not correspond to the blueshifted SBC observed in [O III] λ 5007. The full ISAAC sample has eight quasars (five Pop. A and three Pop. B) with a BLUE component, whose contribution to the profile has an average value of $\approx 8\%$. The mean asymmetry index for the whole ISAAC sample Pop. B is 0.26 (same for only ISAAC2) and they have the full broad profile with an average velocity centroid $c(1/4)$ of

1740 km s⁻¹. This is attributed to the fact that, in Pop. B, the most prominent broad component is the VBC, which accounts for 54% of the H β profile in the ISAAC2 sample (57% for the whole ISAAC), with median FWHM and shift values of \approx 10420 and 3149 km s⁻¹, respectively. Consistent values are found for the full ISAAC sample, with a median FWHM and a shift of the VBC of 11760 and 3000 km s⁻¹, respectively, in good agreement with the values obtained in HEMS sources (e.g., [Marziani et al. 2009](#); [Sulentic et al. 2017](#), see also [Vietri et al. 2018, 2020](#); [Wolf et al. 2020](#) for extremely broad H β profiles).

[O III] λ 5007 – In the full ISAAC sample, both populations (A and B) exhibit significant blueshifts, with the most pronounced ones observed in Pop. A sources. In most of the full ISAAC sample, both the [O III] SBC and NC are often not in the rest-frame. Additionally, for 18 out of the 32 sources from the whole ISAAC sample (16 from ISAAC1 and two from ISAAC2), the SBC is the strongest component, accounting for \sim 64% of the flux in the case of Pop. A and \sim 52% of the flux for Pop. B. Consequently, the two populations A and B also differ in terms of FWHM, with the Pop. A on average showing slightly broader profiles due to the presence of a stronger SBC. Moreover, in contrast to the low- z scenario, where the majority of the [O III] λ 5007 profiles exhibit blueshift velocity centroids at half intensity, $c(1/2)$, of lower than 250 km s⁻¹ ([Zamanov et al. 2002](#); [Marziani et al. 2016a](#)), in our complete high- z ISAAC sample, 62% of the sources have blueshifts in [O III] of greater than 250 km s⁻¹ and are considered outliers. However, in ISAAC2, we do not observe the few very large [O III] profiles (FWHM \sim 4000 km s⁻¹) measured in ISAAC1. This may be a consequence of the fact that ISAAC1 is primarily composed of RQ sources (which typically exhibit broader [O III] λ 5007 profiles than RL ones; see §5.4.5), while a significant fraction of ISAAC2 sources are classified as RL. Significant [O III] outflows appear to be a common feature at high redshift and have also been observed in other samples (see e.g., [Kakkad et al. 2020](#)). As discussed in [Paper I](#), the [O III] profile almost always appears peculiar when compared to those of optically selected samples at low redshift ([Zamanov et al. 2002](#); [Marziani et al. 2003c](#); [Bian et al. 2005](#); [Zhang et al. 2011](#); [Cracco et al. 2016](#)), with higher shift amplitude and broader widths.

C IV λ 1549 – Consistent results with ISAAC1 are also observed for ISAAC2 C IV λ 1549 profiles. In general, the Pop. B sources from ISAAC2 tend to exhibit slightly larger values of W than Pop. A. This is also observed in the full ISAAC sample (median $W \sim 27$ Å for Pop. B vs. ~ 21 Å for Pop. A). Conversely, Pop. A sources tend to show greater FWHM, asymmetry, and centroid velocity, which is in agreement with the HEMS sample ([Sulentic et al. 2017](#)). The BLUE is the strongest component in the full ISAAC sample, and contributes to $\sim 72\%$ and $\sim 51\%$ of the full C IV λ 1549 flux for Pop. A and Pop. B, respectively. Consistently, the largest blueshifts are found for the BLUE components of Pop. A sources, which achieve a median value of $c(1/2)$ of the full C IV λ 1549 profile of $\sim -2590 \pm 1890$ km s⁻¹ for the entire ISAAC sample. In the case of Pop. B, this value is $\sim -1530 \pm 760$ km s⁻¹. Centroid shifts are comparable to those derived in recent works that followed a similar analysis strategy ([Coatman et al. 2016](#); [Vietri et al. 2018](#); [Temple et al. 2023](#), and especially [Sulentic et al. \(2017\)](#), who analyze the HEMS sample). Both [O III] λ 5007 and C IV λ 1549 suggest the presence of

extremely powerful winds in the NLR and BLR (Marziani et al. 2016b,a; Fiore et al. 2017; Bischetti et al. 2017). At variance with low- z , low-luminosity sources, the blueshifted emission associated with the winds is prominent in both Pop. A and B, as further discussed in §5.5.1 and §5.5.2.

1900Å blend – In the ISAAC2 sample, we have 1900Å blend data for six of the ten objects (two Pop. A and four Pop. B). The 1900Å blend properties observed in the ISAAC2 sample also appear consistent with the full ISAAC sample, as well as with the expectations from recent works involving intermediate-redshift sources (Temple et al. 2020; Marziani et al. 2022b; Buendía-Rios et al. 2023). Considering the whole ISAAC sample (11 Pop. A and 9 Pop. B quasars), we find that the BLUE component in Al III is detected in only 5 Pop. A sources, with an average blueshift of ~ -1720 km s $^{-1}$ and accounts for $\sim 40\%$ of the full profile. For Pop. B, all nine sources show Al III profiles well-represented by a single rest-frame BC with averaged FWHM ~ 4240 km s $^{-1}$. For Si III]λ1892, only three Pop. A exhibit a BLUE component, with an average shift of ~ -1880 km s $^{-1}$. Regarding the C III]λ1909 profiles, Pop. A sources are suitably represented by a rest-frame BC with FWHM ~ 3370 km s $^{-1}$. Of the 11 Pop. A sources, 9 required an additional Fe III component at ~ 1914 Å. The Pop. B C III]λ1909 profiles are fitted by the combination BC+VBC, where the VBC is weaker than that of Hβ, as it represents only 37% of the full profile, with an FWHM of ~ 7240 km s $^{-1}$.

5.4.2 The optical plane of the 4DE1 parameter space

The classification as population A or B on the quasar MS is based on two parameters that can only be measured from NIR spectra: the FWHM of the Hβ full broad profile and the strength of the Fe II blend at 4570Å, defined as the ratio between the intensities of the blue blend of Fe II at 4750Å and Hβ, $R_{\text{Fe II}}$. We set the Pop. A/Pop. B limit according to the luminosity-dependent FWHM value, as explained in Paper I. We measured the $R_{\text{Fe II}}$ parameter to assign a number from 1 to 4 to the spectral type (ST) covering the range $0 \leq R_{\text{Fe II}} \leq 2$ with a step of $\Delta R_{\text{Fe II}} = 0.5$ (Sulentic et al. 2002).

The location of the whole ISAAC sample on the MS optical plane is shown in Fig. 5.3, where the 28 sources belonging to the HEMS sample are also represented. As discussed in Paper I, the sources of high luminosity, such as the ten new quasars presented here, show a displacement in the direction of increasing FWHM(Hβ) by 1000 – 1500 km s $^{-1}$ with respect to the low-luminosity, low- z samples (see also Sulentic et al. 2017). Of the ten new sources, six are classified as Pop. B and four as Pop. A. CTSJ03.14 and PKS1448-232 (see the models in Figs. A.2.7 and A.2.8, respectively), two RLs classified as B1, are located below the Pop A/B boundary for their luminosity. Both sources are blazar candidates (see Massaro et al. (2014) for CTSJ03.14 and Massaro et al. (2015) for PKS1448-232), implying that the FWHM of Hβ may be significantly lowered by a pole-on orientation of the line-emitting region. In the complete sample considered in this work (ISAAC1+ISAAC2+HEMS), there are 30 sources classified as Pop. A (including 5 RL) and 30 classified as Pop. B (including 8 RL).

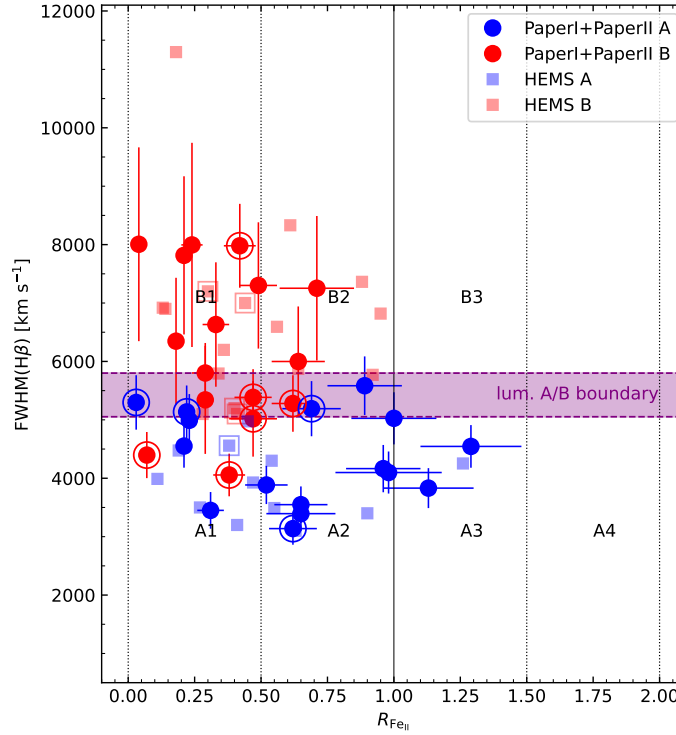


Fig. 5.3: Location on the MS of the ten new sources from this work together with those from [Paper I](#) (circles) and the HEMS sample (squares). Pop. A quasars are represented by blue symbols and Pop. B by red symbols. The RL sources are surrounded by an open circle or square in the plot. The grey region indicates the distribution of the MS of quasars at low z . The purple-shaded area shows the luminosity-dependent boundary between Pops. A and B for high-luminosity sources, as described in detail in [Paper I](#).

5.4.3 The role of physical parameters

In [Paper I](#), we show that while the bolometric luminosity, L_{bol} , and the black hole mass (M_{BH}) exhibit trends with the C IV blueshifts, the primary correlation is observed with the Eddington ratio, with the higher C IV blueshift in the higher accretion rate (see e.g., §6.3 of [Paper I](#), and references therein). These results are reconfirmed in the present work. By including the new data from ISAAC2 in the sample composed of both high- and low- z data, we find a relation between C IV $c(1/4)$ blueshift ($< -250 \text{ km s}^{-1}$) and L_{bol} with a slope of 0.21 ± 0.07 (with a Pearson correlation coefficient c.c. of 0.61, $\rho \sim 10^{-9}$). The slope 0.14 ± 0.06 , and Pearson c.c. ~ 0.48 ($\rho \sim 10^{-6}$) suggest an even weaker relation between C IV $c(1/4)$ and the black hole mass M_{BH} . Regarding the Eddington ratio, we find the following relation (with a Pearson c.c. ~ 0.66 and a ρ -value for the null hypothesis $\sim 10^{-11}$):

$$\log |c(1/4)_{\text{CIV}}| = (0.43 \pm 0.05) \log L/L_{\text{Edd}} + (3.39 \pm 0.04). \quad (5.1)$$

Similar results, albeit less significant, are observed for [O III]. When analysing the 45 sources (34 high- z and 11 low- z) that exhibit significant [O III] outflows, we find a slope of 0.12 ± 0.07 between [O III] $c(1/4)$ and L_{bol} (Pearson c.c. ~ 0.31 , $\rho \sim 10^{-2}$). Concerning L/L_{Edd} , we obtain (Pearson c.c.

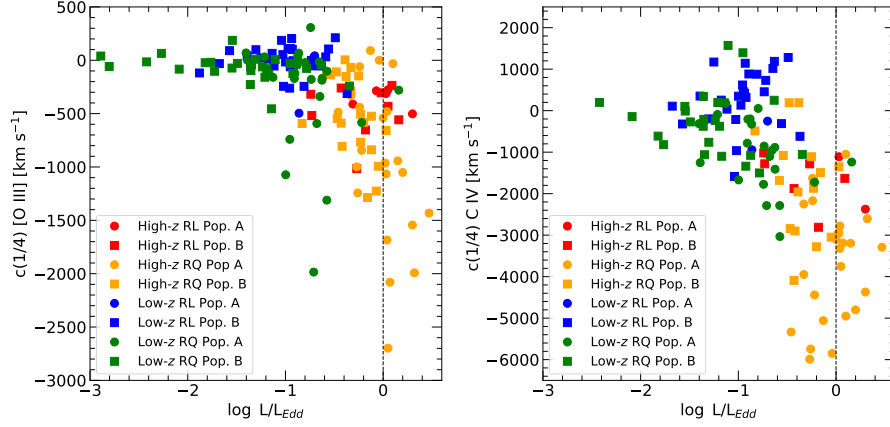


Fig. 5.4: Velocity centroid $c(1/4)$ versus L/L_{Edd} for $[\text{O III}]\lambda 5007$ (left) and $\text{C IV}\lambda 1549$ (right). Dark green and blue symbols correspond, respectively, to RQ and RL sources at low- z , while orange (RQ) and red (RL) symbols represent high- z quasars. Within each colour, filled squares represent Pop. B sources and the bullets Pop. A quasars.

~ 0.48 , $\rho \sim 10^{-4}$):

$$\log |c(1/4)_{[\text{O III}]}| = (0.33 \pm 0.09) \log L/L_{\text{Edd}} + (2.91 \pm 0.04). \quad (5.2)$$

In close agreement with these relations, Fig. 5.4 shows the dependence of $c(1/4)$ on L/L_{Edd} for the $[\text{O III}]\lambda 5007$ and $\text{C IV}\lambda 1549$ emission lines, where we include all the measurements of $c(1/4)$ velocity centroids of both lines (blueshifted or not) and for both low- and high- z samples. For the two emission lines, strong outflows (i.e., $\gtrsim 500 \text{ km s}^{-1}$ for $[\text{O III}]\lambda 5007$ and $\gtrsim 2000 \text{ km s}^{-1}$ for $\text{C IV}\lambda 1549$) are found at Eddington ratios of $\log L/L_{\text{Edd}} \gtrsim -0.8$ ($L/L_{\text{Edd}} \sim 0.2$), consistent with previous results (see e.g., Marziani et al. 2003c; Bian et al. 2005; Komossa et al. 2008; Marziani et al. 2016b; Cracco et al. 2016; Coatman et al. 2016; Wang et al. 2018; Ayubinia et al. 2023).

The effect of high Eddington ratio is strengthened at high luminosity. The high z to low z comparison is consistent with the weaker luminosity effect (outflow velocity $\propto L^{\frac{1}{4}}$) on both the RL and RQ samples, which is expected for radiation-driven winds and becomes appreciable when considering samples spread over a wide range of luminosities (Laor & Brandt 2002, c.f. Sulentic et al. 2017).

The radio-loudness appears to play a role in reducing the outflow velocities in both $[\text{O III}]\lambda 5007$ and $\text{C IV}\lambda 1549$. The sources that present the most significant blueshifts in both $[\text{O III}]$ and C IV in Fig. 5.4 are all RQ. Conversely, the RL sources (blue and red symbols) exhibit lower outflow velocities. This result is in good agreement with previous findings (e.g., Marziani et al. 2003c; Laor 2018) and is discussed in more detail in §5.4.4 and 5.4.5.

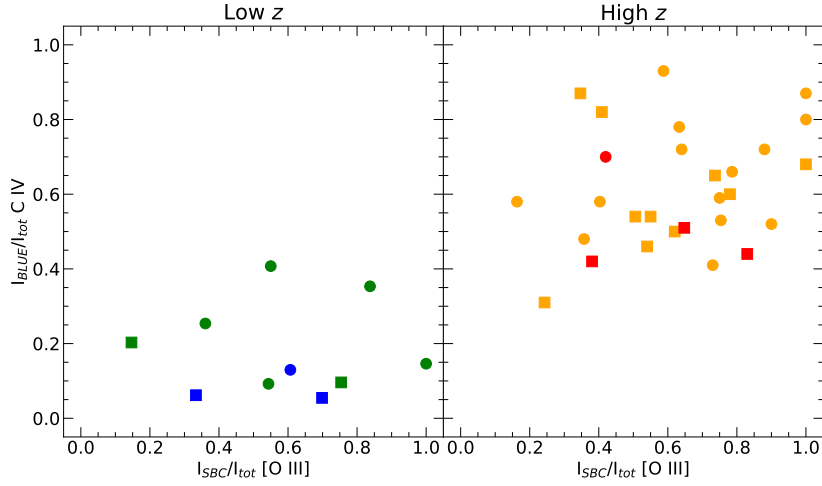


Fig. 5.5: Comparison between the relative intensities of the blueshifted component for both $[O III]\lambda 5007$ and $C IV\lambda 1549$. Low- z and high- z sources are represented in the *left* and *right* panels, respectively.

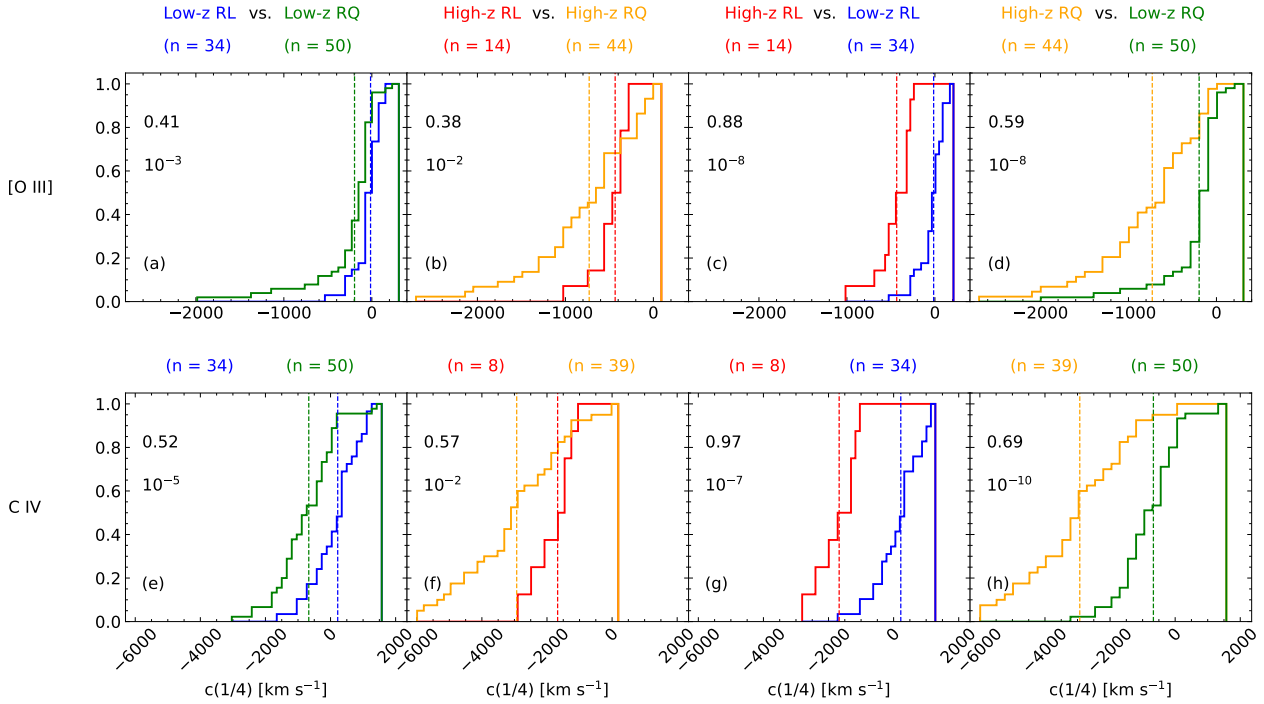


Fig. 5.6: Centroid velocities at one-quarter intensity ($c(1/4)$) cumulative distributions of the samples separated by radio-loudness and redshift range for $[O III]\lambda 5007$ (*top* panels) and $C IV\lambda 1549$ (*bottom* panels). Kolmogórov-Smirnov tests were performed comparing different subsamples identified at the top of the panels. KS statistics for each comparison are shown in the top left corner of each plot together with the respective ρ -value. Vertical lines indicate the mean value for each subsample.

5.4.4 Inter-comparison between RL and RQ sources at low and high z : $[O III]\lambda 5007$ versus $C IV\lambda 1549$

Figure 5.5 presents a comparison between $[O III]$ and $C IV$ in terms of the relative intensity of the outflowing component (SBC for $[O III]\lambda 5007$ and BLUE for $C IV\lambda 1549$) with respect to the full

profiles, $I_{\text{BLUE}}/I_{\text{tot}}$. In this case, we exclusively consider sources that are identified as blue outliers in [O III] and which also present blueshifts in C IV. Therefore, the sample shown in Fig. 5.5 has 28 high- z sources (14 from ISAAC and 14 from HEMS) and 9 low- z sources from the FOS sample. In addition, in the FOS sample, there are seven objects in which only a blueshifted SBC [O III] component (with no clear NC) is detected, which nevertheless present shifts in the $c(1/2)$ of lower than -250 . Clearly identifying any outflow in these cases would require higher resolution and an improved S/N compared to the data available in the present work.

At low redshift, the behaviour of the BLUE component appears to be different in [O III] and C IV in terms of relative intensity: while the [O III] outflowing component can achieve a $I_{\text{SBC}}/I_{\text{tot}}$ of up to nearly $\sim 100\%$ of the total intensity of the full profile, the C IV outflowing component never surpasses $\sim 40\%$ of the entire profile, with the lower values found for the RL sources.

The right panel of Fig. 5.5 shows the same analysis but for the high-redshift range. At variance with the low- z sample, the [O III] $\lambda 5007$ and C IV $\lambda 1549$ emission lines exhibit very similar behaviour with respect to their outflowing component, and their ratio $I_{\text{BLUE}}/I_{\text{tot}}$ can vary from $\sim 20\%$ to 100% of the full profile, with the largest contributions found in RQ sources. The RL–RQ difference at high redshift is consistent with that found at low redshift, with the RL sources presenting clearly fainter [O III] $\lambda 5007$ SBC and C IV $\lambda 1549$ BLUE.

We analysed the RL and RQ blueshift distributions in an attempt to characterise other parameters affected by radio-loudness. Figure 5.6 shows the cumulative distribution functions of centroid velocities at one-quarter flux intensity ($c(1/4)$) of both [O III] $\lambda 5007$ and C IV $\lambda 1549$ emission lines for the samples by separating them according to the radio classification and the redshift range. All sources with [O III] or C IV spectral information have been taken into account regardless of the shift. Panel (a) shows a comparison between RL and RQ at low redshift for the [O III] $\lambda 5007$ $c(1/4)$. In this case, the Kolmogórov-Smirnov (KS) test reveals that the RL and RQ subsamples are statistically indistinguishable, although the RQ sources, in general, present larger values of $c(1/4)$ towards the blue, which indicates stronger outflows than for RL sources. A similar result is found when comparing RL and RQ $c(1/4)$ at high z (panel (b) of Fig. 5.6).

Panel (c) of Fig. 5.6 compares the RL sources at high- and low- z ranges. The KS test indicates that the distributions are significantly different (~ 0.88 , $\rho \sim 10^{-8}$), with the RL sources at high redshift presenting higher outflow velocities (mean value $\sim -420 \text{ km s}^{-1}$) than the ones at lower redshifts ($\sim -40 \text{ km s}^{-1}$). The same is found when comparing RQ sources at high and low redshift (panel (d)). The difference in this case is still significant due to a more prominent outflow at high z , with $c(1/4)$ mean values ≈ -740 and $\approx -200 \text{ km s}^{-1}$ for high and low z , respectively.

The bottom panels of Fig. 5.6 show the results for the C IV $\lambda 1549$ emission line. In general, the $c(1/4)$ of this line follows the same behaviour as [O III], albeit with stronger outflows. In both RQs and RLs, there is a statistically very significant difference between the distributions of C IV $c(1/4)$ at high and low redshift. The more extreme difference is found between RL sources at high and low z , where the distributions are completely different (KS coefficient of 0.97, and a probability of coming from the same distribution $\rho \sim 10^{-7}$). The significance is extremely high, even if the RL subsample in the case of C IV $\lambda 1549$ at high z contains only seven sources.

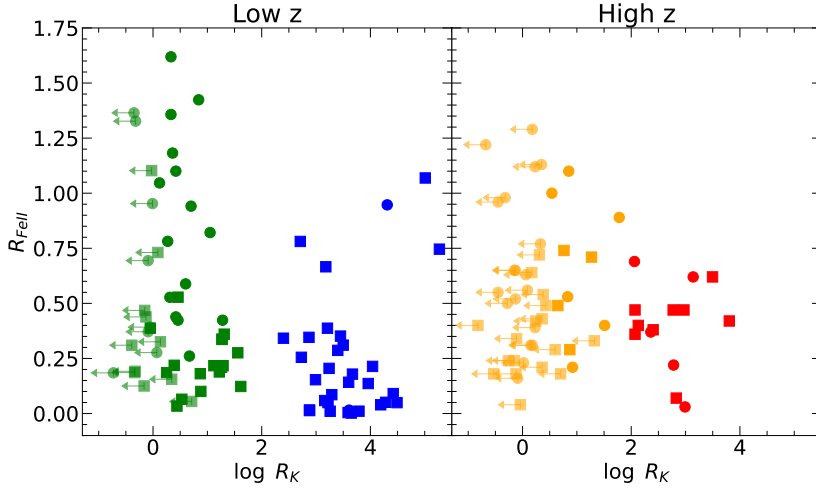


Fig. 5.7: Relation between radio-loudness R_K and $R_{\text{Fe II}}$ for low- z (*left*) and high- z (*right*) ranges. R_K upper limits are indicated by arrows alongside the symbol. The colour scheme is the same as that in Fig. 5.4.

The cumulative distributions of both [O III] and C IV centroid shifts demonstrate that the main difference between samples is when they widely differ in luminosity, not radio-loudness. In the two redshift domains considered (corresponding on average to a difference in luminosity of a factor ≈ 60), Fig. 5.4 and Fig. 5.6 show that there is second-order effect related to radio-loudness in both C IV $\lambda 1549$ and [O III] $\lambda 5007$. The effect is more significant at low- z (with a $\rho \sim 10^{-5}$), although a similar difference in shift amplitude is detected also at high redshift. In the latter case, the small number of sources means that our results regarding this effect are not statistically significant. In summary, the effect of radio-loudness is consistent in the low- z and high- z samples, with lower blueshifted velocities and outflows in the RLs, albeit weaker than the effects of luminosity and accretion rate (see section 5.4.3).

5.4.5 Trends with radio-loudness

Fe II

The relation between the $R_{\text{Fe II}}$ with the radio-loudness parameter R_K is shown in Fig. 5.7. In both low- and high- z ranges, the RQ sources are the ones that can present $R_{\text{Fe II}}$ values from ~ 0 up to more than 1, with the most extreme cases found for the low-redshift RQ Pop. A quasars. With the exception of these extreme sources, the RQ sources at high and low z present a very similar distribution, with a mean $R_{\text{Fe II}}$ value for low- z RQ sources of ~ 0.52 , while for high- z RQ sources this value is ~ 0.55 .

The RL quasars tend to present lower values of $R_{\text{Fe II}}$, which rarely exceeds the threshold of $R_{\text{Fe II}} = 1$. The fact that the RL sources are weaker Fe II emitters than the RQ ones has already been observed in previous studies (e.g., Yuan & Wills 2003; Netzer et al. 2004; Sulentic et al. 2004). In general, the sources that present strong Fe II emission are found to also present very high Eddington ratios, which are more frequently found in RQ sources of Pop. A. Hence, this difference in $R_{\text{Fe II}}$

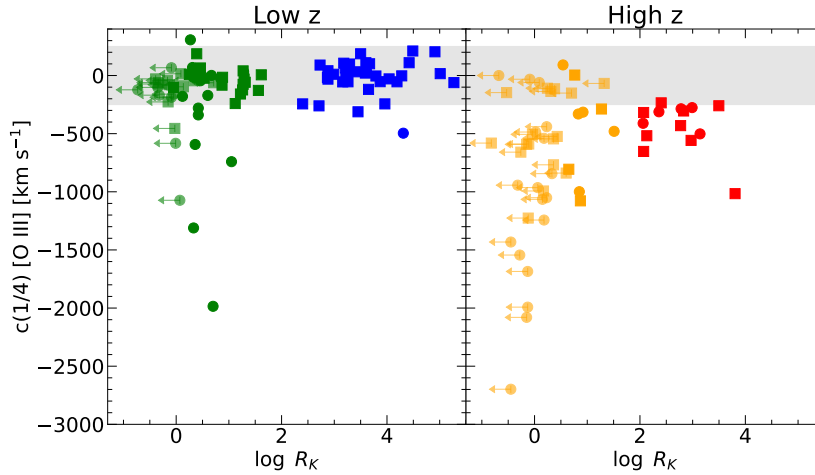


Fig. 5.8: Relation between radio-loudness and velocity centroid at one-quarter intensity of the [O III] λ 5007 emission line for low- z (*left*) and high- z (*right*) ranges. Gray shaded areas in both plots indicate the $c(1/4)$ range between 250 and -250 km s^{-1} . R_K upper limits are indicated by arrows alongside the symbol. The colour scheme is the same as that in Fig. 5.4.

between RL and RQ sources may also be linked to the accretion rate, which somehow can contribute to enhancing the Fe II emission in strong accretors.

The mean $R_{\text{Fe II}}$ values of low- and high-redshift RL sources are ~ 0.25 and ~ 0.40 , respectively. This result is intriguing, although it could simply be related to differences in the Eddington ratios of the samples at high and low z , with missing high- z sources at the lowest Eddington ratios because they are too faint to be detected in major surveys such as the SDSS (Sulentic et al. 2014a).

[O III] λ 5007

Figure 5.8 shows the relation between R_K and $c(1/4)$ of [O III] λ 5007 for low- and high- z ranges separately. In both ranges, RQ sources exhibit larger outflow velocities compared to RL sources, with the RQ sources achieving values of ~ -2000 at low z and $\sim -2700 \text{ km s}^{-1}$ at high z . This difference in outflow velocity between RQ and RL quasars has previously been reported (e.g., Marziani et al. 2003c, 2016a; Ganci et al. 2019, and references therein) and may be a consequence of the presence of relativistic jets in RL sources, which can potentially reduce the impact of the outflows on the optical emission. In contrast, RQ sources lack such strong radio jets, allowing the outflows to have a more significant influence on the optical emission (e.g., Padovani 2016).

At low redshifts, the majority of the sources (including both RQ and RL) do not exhibit [O III] λ 5007 $c(1/4)$ values that exceed 250 km s^{-1} , and therefore do not present significant [O III] λ 5007 outflows. Only eight objects (seven RQ and one RL) within this redshift range in our FOS sample present relevant [O III] $c(1/4)$ blueshifts of $\sim -500 \text{ km s}^{-1}$.

The right panel of Fig. 5.8 shows the same analysis, but this time focuses on high- z sources. In this redshift range, $\sim 75\%$ of the RQ sources present blueshifts of greater than 250 km s^{-1} , and in some cases can achieve very strong velocities, as is the case of SDSS J212329.46-005052.9 (\sim

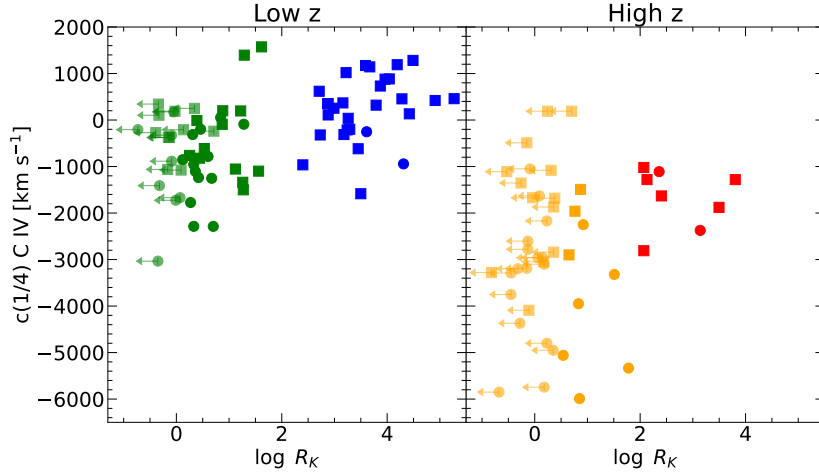


Fig. 5.9: Relation between radio-loudness and the velocity centroid at one-quarter intensity of the $\text{C IV } \lambda 1549$ emission line for low- z (*left*) and high- z (*right*) ranges. R_K upper limits are indicated by arrows alongside the symbol. The colour scheme is the same as in Fig. 5.4.

2700 km s^{-1}). All the high-redshift RL sources from our sample present significant blueshifts, with a $[\text{O III}] \lambda 5007$ $c(1/4)$ range of between ~ 230 and 1000 km s^{-1} .

$\text{C IV } \lambda 1549$

It has long since been known that $[\text{O III}] \lambda 5007$ and $\text{C IV } \lambda 1549$ show similarities in their phenomenology (e.g., Zamanov et al. 2002; Coatman et al. 2019; Deconto-Machado et al. 2023). In Fig. 5.9 we repeat the $[\text{O III}] \lambda 5007$ analysis described in §5.4.5 for $\text{C IV } \lambda 1549$. As for $[\text{O III}] \lambda 5007$, the majority of RQ sources at low z present negative values of $\text{C IV } \lambda 1549$ $c(1/4)$, while the vast majority of RL sources show positive values or values very close to 0 - 500 km s^{-1} to the blue. Regarding the high- z range, it is already known that the largest shifts are also found in RQ sources (see e.g., Richards et al. 2011, 2021, and references therein). This is no different in our high- z sample, where almost all sources (including both RQ and RL) present very significant outflow velocities. The average $\text{C IV } c(1/4)$ blueshift for RL sources is $\sim 1900 \text{ km s}^{-1}$. The relation between the $[\text{O III}] \lambda 5007$ and $\text{C IV } \lambda 1549$ emission lines does not seem to be affected by the radio emission; however, the comparison between RQ and RL at high z for the $\text{C IV } \lambda 1549$ emission line is limited by the fact that we have a very small sample of RL sources in this redshift range (only seven objects, two Pop. A and five Pop. B) and more data are definitely required.

5.5 Discussion

5.5.1 Dominance of outflows

$\text{C IV } \lambda 1549$ somehow seems to be a magnified version of $[\text{O III}] \lambda 5007$, presenting very similar trends but with higher outflow velocities. The left plot of Fig. 5.10 shows the relation between the centroid

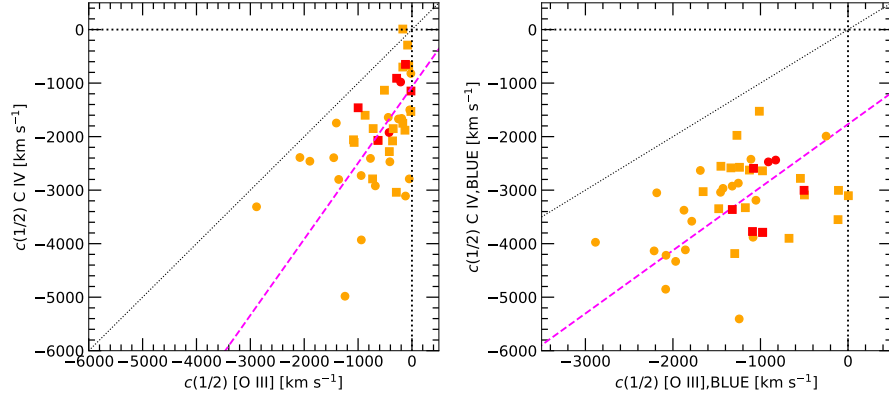


Fig. 5.10: Centroid velocity at half flux intensity ($c(1/2)$) of C IV $\lambda 1549$ vs. $c(1/2)$ of [O III] $\lambda 5007$ for the full (*left*) and outflow (*right*) profiles of the high- z sample. The magenta lines indicate the linear regression between $c(1/2)$ of C IV and [O III] for both cases obtained through the bisector method. Dotted black lines represent the 1:1 relation. The colour scheme is the same as in Fig. 5.4.

velocity at half intensity ($c(1/2)$) for the full profiles of [O III] $\lambda 5007$ and C IV $\lambda 1549$ at high redshift, including the sources from HEMS, Paper I, and from the present paper. The result reported in Paper I is strengthened: ISAAC2 objects that present strong shifts in the [O III] $\lambda 5007$ emission line profiles do present them also in C IV $\lambda 1549$. The bisector linear relation after including all ISAAC data is

$$c(1/2)_{\text{C IV}} = (1.42 \pm 0.23) \times c(1/2)_{[\text{O III}]}} + (-1071 \pm 148), \quad (5.3)$$

with a correlation coefficient ≈ 0.51 . This trend is consistent with the results reported by Coatman et al. (2019) and Vietri et al. (2020) at high redshift.

In both [O III] and C IV, the largest blueshifts are found in Pop. A sources (represented by orange bullets in the figures), which usually present the largest accretion rates. Figure 5.10 also shows that the largest outflow velocities in [O III] and in C IV are found in RQ sources, indicating that the accretion may be the main driver of these outflows (Nesvadba et al. 2007; Kukreti et al. 2023). A similar relation is found when considering the $c(1/2)$ of only the outflowing (BLUE) components of both [O III] $\lambda 5007$ and C IV $\lambda 1549$ emission lines, as shown in the right plot of Fig. 5.10. In this case, the orthogonal linear relation (with a c.c. of 0.40) is given by

$$c(1/2)_{\text{C IV,BLUE}} = (1.27 \pm 0.99) \times c(1/2)_{[\text{O III],BLUE}} + (-1432 \pm 1323). \quad (5.4)$$

At high z , the outflows appear to be more prominent than at low z (see also Fig. 5.4), consolidating the idea that the accretion rate is the main driver of the outflows. The accretion rate in most of the sources at high z is higher ($-0.6 \lesssim \log L/L_{\text{Edd}} \lesssim 0.4$) than in the case of sources at low z ($-2 \lesssim \log L/L_{\text{Edd}} \lesssim 0$; see also e.g., Cavaliere & Vittorini 2000; Hopkins et al. 2006), even if the difference could be in part due to a selection effect, as mentioned in Section 5.4.5.

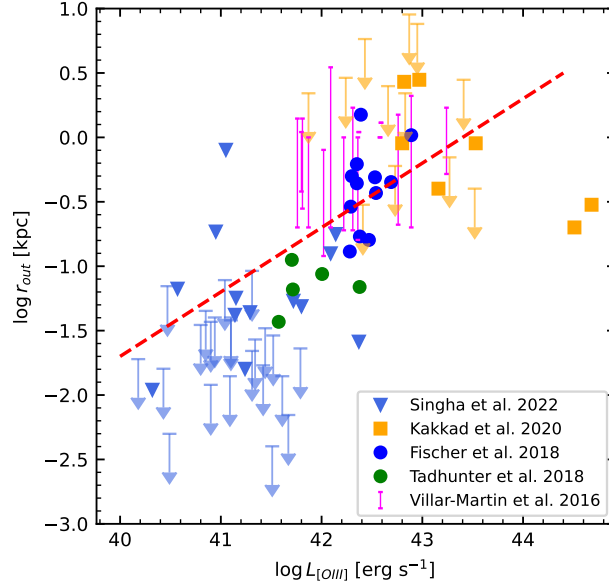


Fig. 5.11: Relation between the outflow radius in kiloparsecs and the luminosity of the [O III] λ 5007 emission line for the five plotted samples. The red dashed line represents the adopted least squares linear regression. Magenta vertical lines symbolise the minimum and maximum estimated radii in the Villar-Martin sample. Arrows correspond to upper limits.

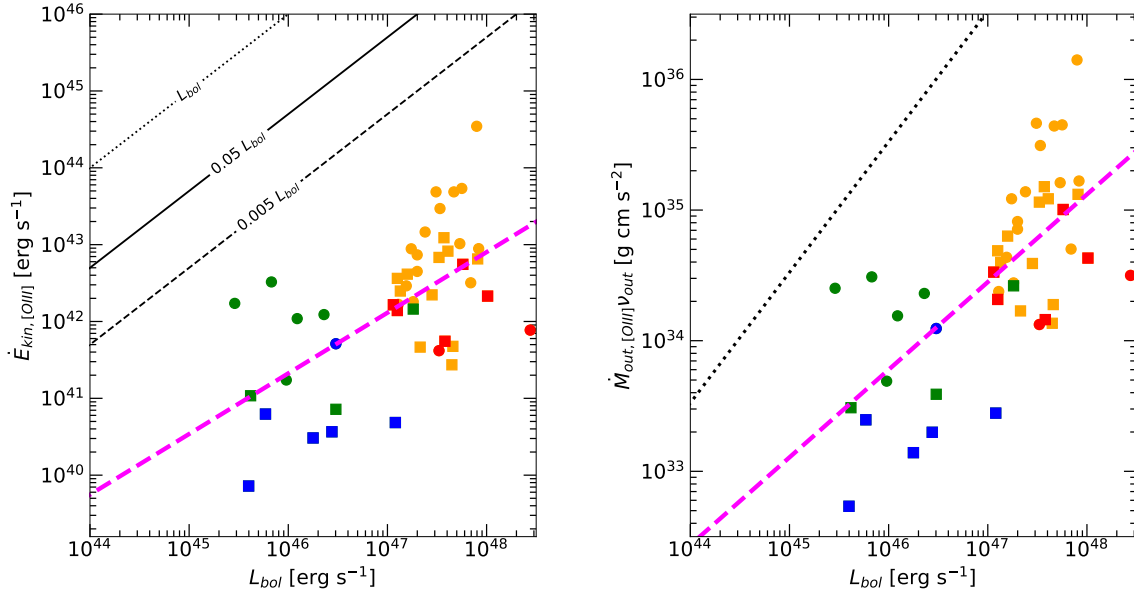


Fig. 5.12: Kinetic power \dot{E}_{kin} (left) and thrust (*right*) vs. bolometric luminosity for the [O III] λ 5007 outflow. The two outflow parameters were estimated by varying the outflow radius according to Eq. 5.9 and assuming $v_{\text{out}} = c(1/2)$. Magenta dashed lines indicate the least-squares linear regression. Black dotted, continuous, and dashed lines on the left plot show $\dot{E}_{\text{kin}} = L_{\text{bol}}$, $\dot{E}_{\text{kin}} = 0.05L_{\text{bol}}$, and $\dot{E}_{\text{kin}} = 0.005L_{\text{bol}}$, respectively. The dotted line in the right panel indicates $\dot{M}_{\text{out}}v_o = L_{\text{bol}}/c$. Typical uncertainties are displayed in the bottom-right corner of the plots. The colour scheme is the same as in Fig. 5.4.

5.5.2 Dynamical parameters of the outflows

We estimated the mass-outflow rate (\dot{M}), the kinetic power (\dot{E}_{kin}), and the thrust ($\dot{M} v_o$) adopting a simple biconical outflow, and using an analogous methodology to that of [Marziani et al. \(2016a, 2017a\)](#); our methodology is summarised in Appendix B.2. In this framework, the relations are formally identical for [O III] and C IV $\lambda 1549$, and namely:

$$M_{\text{ion}} \propto L^{\text{out}} Z^{-1} n_{\text{H}}^{-1}, \quad (5.5)$$

where L is the outflow-emitted line luminosity, n_{H} the electron density and Z the metallicity. The mass outflow rate ($\dot{M}_{\text{ion}}^{\text{out}}$) and the thrust ($\dot{M}_{\text{ion}}^{\text{out}} v_{\text{out}}$) at a radius r and with an outflow velocity v_{out} , might be written as:

$$\dot{M}_{\text{ion}}^{\text{out}} \propto L^{\text{out}} v_{\text{out}} r^{-1} Z^{-1} n_{\text{H}}^{-1}, \quad (5.6)$$

$$\dot{M}_{\text{ion}}^{\text{out}} v_{\text{out}} \propto L^{\text{out}} v_{\text{out}}^2 r^{-1} Z^{-1} n_{\text{H}}^{-1}. \quad (5.7)$$

The kinetic power, \dot{E}_{kin} , is then given by $\dot{E}_{\text{out}} \sim \frac{1}{2} \dot{M}_{\text{out}} v_{\text{out}}^2$, which leads to

$$\dot{E}_{\text{kin}} \propto L^{\text{out}} v_{\text{out}}^3 r^{-1} Z^{-1} n_{\text{H}}^{-1}. \quad (5.8)$$

The parameters entering the previous equations are estimated using different relations for [O III] and C IV, and are briefly discussed in following sections and in Appendix B.2. The adopted parameters and relevant scaling relations are summarised in Table 5.12.

When estimating wind parameters in quasars, such as mass-outflow rate, thrust, and kinetic power, several sources of error can affect the accuracy of these measurements. These errors arise from various observational and methodological issues, including the complexity of the line profiles, spatial resolution limitations, and the assumptions made in the models used for interpretation, where the last two are expected to be the dominating sources of uncertainty in the estimation of the wind parameters. For C IV $\lambda 1549$ in particular, the uncertainty in the conversion between line luminosity and ionised gas could be ~ 3 at a 3σ confidence level. We have considered a range of densities of 0.5 dex around $\log n_{\text{H}}$ radius of the emitting region; Z estimates in quasars suggest very high metallicity, and a range around $5Z_{\odot}$, where between 2 and 20 times solar seems possible both at high and low redshifts ([Hamann & Ferland 1993](#); [Garnica et al. 2022](#); [Floris et al. 2024](#)). The geometry of the outflow would contribute a factor 3 via the comparison between the spherically symmetric case and a flat layer. The 1σ uncertainty in the emitting radius is $\pm 30\%$ if ascribed only to the uncertainty of the scaling law parameter, while uncertainty on the outflow velocity is typically $\sim 30\%$. Propagating these uncertainties quadratically would result in a typical factor of ≈ 5 at 1σ confidence level.

Similar considerations were applied to [O III]: a factor of ≈ 3 at 1σ in density, a factor of ≈ 2 in Z and in the luminosity-to-ionised mass gas conversion, and a factor of ≈ 2 in the zero point of the radius–luminosity ($L([\text{O III}])$) relation. These factors contribute to a comparable uncertainty estimate, a factor of ≈ 5 at 1σ confidence level, and should be taken into account in the interpretation of the analysis that follows.

Table 5.12: Summary of assumed scaling relations and parameter values for wind dynamics.

Parameter	Low z		High z	
	C IV	[O III]	C IV	[O III]
M_{ion}	$\propto L_{\text{CIV}}^{\text{out}}$	$\propto L_{[\text{OIII}]}^{\text{out}}$	$\propto L_{\text{CIV}}^{\text{out}}$	$\propto L_{[\text{OIII}]}^{\text{out}}$
$Z [Z_{\odot}]$	5	5	5	2
$n_{\text{H}} [\text{cm}^{-3}]$	$10^{9.5}$	10^3	$10^{9.5}$	10^3
r [cm]	$\propto \lambda L_{\lambda}(1350)$	$\propto L([\text{O III}])$	$\propto \lambda L_{\lambda}(1350)$	$\propto L([\text{O III}])$
v [km s $^{-1}$]	$c(\frac{1}{2}) + 2\sigma$	$c(\frac{1}{2})$	$c(\frac{1}{2}) + 2\sigma$	$c(\frac{1}{2})$

[O III] λ 5007

We consider a situation where the outflow radius r is allowed to vary depending on the [O III] λ 5007 luminosity of each source. In the case of sources spanning four orders of magnitude in luminosity, it is nonphysical to assume that the size of the emitting region is constant, as there is evidence of compact emission at low- z (Zamanov et al. 2002), and of kiloparsec(kpc)-sized outflows at high luminosity (e.g., Harrison et al. 2014). Conventional scaling laws of narrow-line regions with luminosity are not expected to exclusively trace the outflowing [O III] component (Bennert et al. 2002, 2006).

Figure 5.11 shows the outflow radius as a function of the [O III] λ 5007 luminosity for the integral field spectroscopy (IFU) data analysed by Villar-Martín et al. (2016), Fischer et al. (2018), Tadhunter et al. (2018), Kakkad et al. (2020), and Singha et al. (2022), where we also show a least squares linear relation between these two quantities, imposing a slope of 0.5:

$$\log(r) = (0.5) \times \log(L_{[\text{O III}],\text{full}}) + (-21.7 \pm 0.1). \quad (5.9)$$

The slope 0.5, which gives a reasonable representation of the radius– $L_{[\text{O III}]}$ relation in Fig. 5.11, is imposed to ensure consistent ionisation conditions as a function of luminosity. This scaling relation was then applied to our sources, considering the luminosity of the entire [O III] emission line profile. Our low- z sample exhibits [O III] luminosities (full profile) ranging from approximately $10^{40.6}$ up to $10^{43.1}$ erg s $^{-1}$, while the high- z sources have luminosities of between $10^{43.4}$ and $10^{44.9}$ erg s $^{-1}$. Consequently, we find [O III] outflow radii r ranging from ~ 0.04 to 0.71 kpc at low- z , in agreement with recent values obtained for IFU resolved [O III] in low- z AGN (see e.g. Deconto-Machado et al. 2022b), and from 0.97 to 5.81 kpc at high- z .

The parameters used to estimate the outflow properties associated with the [O III] λ 5007 emission line are listed in Table 5.13. The estimated values of the mass rate \dot{M}_{out} derived from equation B.2 in the Appendix span from ~ 0.08 to 3.43 M_{\odot} yr $^{-1}$ for low luminosities ($\lesssim 10^{46}$ erg s $^{-1}$) and from ~ 6.2 to 114.0 M_{\odot} yr $^{-1}$ for higher luminosities.

The relations between the [O III] outflow kinetic power \dot{E}_{kin} and thrust $\dot{M}_{\text{out}}v_o$ with the bolometric luminosity L_{bol} are shown in Fig. 5.12. We assume a density of $n_{\text{H}} = 10^3$ cm $^{-3}$ for both high- and low- z contexts. For metallicity, we adopt $Z = 5Z_{\odot}$ for low- z , considering the compactness of the outflow, and $Z = 2Z_{\odot}$ for high- z , aligning with the typical values used in the computations for the NLR metallicity at high z (see e.g., Xu et al. 2018). Additionally, as detailed in Section B.2.1, we assume the outflow velocity to be $c(1/2)$ of the BLUE component. If instead we were to follow the

Table 5.14: Least-squares linear relations ($y = a + b * x$) between different outflow properties and the bolometric luminosity.

y (1)	x (2)	Sources (3)	$a \pm \delta a$ (4)	$b \pm \delta b$ (5)	RMSE (6)	CC (7)	ρ -value (8)
[O III] λ 5007							
$\log \dot{E}_{\text{kin},44}$	$\log L_{\text{bol},44}$	45	-4.09 ± 0.44	0.86 ± 0.14	0.009	0.69	1.7×10^{-6}
$\log \dot{M}_{\text{out}v_{0,34}}$	$\log L_{\text{bol},44}$	45	-1.62 ± 0.31	0.79 ± 0.09	0.017	0.78	2.7×10^{-10}
C IV λ 1549							
$\log \dot{E}_{\text{kin},44}$	$\log L_{\text{bol},44}$	68	-3.59 ± 0.25	1.24 ± 0.08	0.075	0.87	2.1×10^{-22}
$\log \dot{M}_{\text{out}v_{0,34}}$	$\log L_{\text{bol},44}$	68	-2.08 ± 0.22	1.19 ± 0.07	0.069	0.90	3.7×10^{-25}

Notes. (1), (2) Fitted parameters. (3) Number of sources. (4), (5) Linear correlation coefficients. (6) Root mean square error. (7), (8) Pearson r score and its associated null hypothesis probability value.

assumption of $c(1/2) + 2\sigma$ as done by [Fiore et al. \(2017\)](#), this would result in an ~ 2.5 larger outflow velocity in our estimates of the outflow parameters. Typical errors are represented in the error bars of Fig. 5.12. The results of the linear correlation analysis between these outflow parameters for [O III] λ 5007 and C IV λ 1549 are reported in Table 5.14. We find correlation coefficients of 0.66 and 0.74 (with ρ -value of $\sim 10^{-7}$ and $\sim 10^{-9}$, respectively) between the kinetic power and the thrust with the bolometric luminosity. Similar correlations have already been extensively discussed by other authors (e.g., [Carniani et al. 2015](#); [Feruglio et al. 2015](#); [Fiore et al. 2017](#), and references therein).

In our analysis of [O III] \dot{E}_{kin} with luminosity-dependent r , none of the sources display a ratio reaching at least 5% of the bolometric luminosity (filled line in Fig. 5.12), a threshold needed for a significant impact on the host galaxy dynamics, and to account for the black hole mass–velocity dispersion correlation and host-spheroid co-evolution (e.g., [Di Matteo et al. 2005](#)). Star formation quenching might be easier, if an AGN outflow induces a wind in the diffuse interstellar medium that in turn induces a flattening and shredding of molecular clouds ([Hopkins & Elvis 2010](#)). A threshold for this effect occurs when the kinetic efficiency is much lower than the 5% limit, $\dot{E}_{\text{kin}}/L_{\text{bol}} \sim 5 \times 10^{-3}$ (short dashed line in Fig. 5.12). Based on the criteria of both [Hopkins & Elvis \(2010\)](#) and [Di Matteo et al. \(2005\)](#), the [O III] λ 5007 outflow parameters do not provide an efficient feedback mechanism, at either low or high z (although see the discussion of Section 5). Similar results have recently been found at low redshift ([Kim et al. 2023](#), and references therein). These latter authors derived $\dot{E}_{\text{kin}} \lesssim 0.1\% L_{\text{bol}}$ for a sample of low- z type-1 AGN. It is likely that part of the [O III] emitting gas has already dissipated part of its energy and momentum, as the emitting regions can extend over several kpc. Along the same line of reasoning, the AGN outflows traced by the [O III] emission are likely to impact the central kiloparsecs scales, but their effects on galactic scales are more debatable.

The thrust ranges from $\sim 2.2 \times 10^{32}$ to 3.1×10^{34} g cm s $^{-2}$ in the case of the low-luminosity sample; at high luminosity, the thrust increases significantly to the larger outflow masses and higher velocities and the values are found between $\sim 3.3 \times 10^{34}$ and 3.5×10^{36} g cm s $^{-2}$. In all cases, however, the [O III] thrust is $\ll L/c$, in agreement with [Vietri et al. \(2020\)](#).

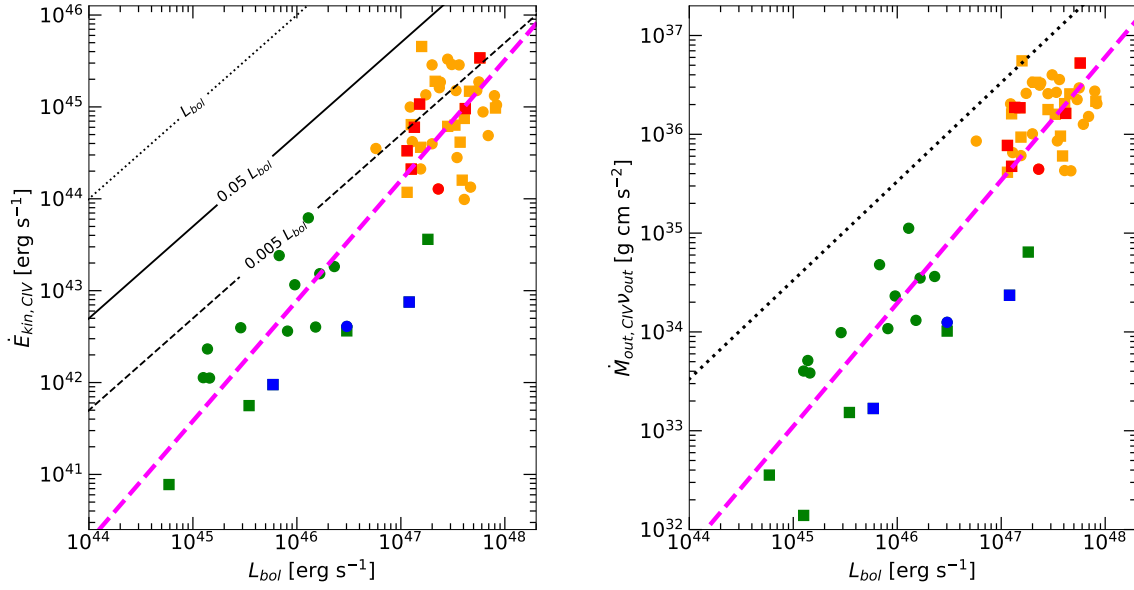


Fig. 5.13: Kinetic power \dot{E}_{kin} (*left plot*) and thrust (*right*) vs. bolometric luminosity for the CIV $\lambda 1549$ emission line. The two outflow parameters were estimated by varying the outflow radius depending on λL_{λ} as defined in Kaspi et al. (2021). Magenta dashed lines indicate the least squares linear regression. Black dotted, continuous, and dashed lines show $\dot{E}_{\text{kin}} = L_{\text{bol}}$, $\dot{E}_{\text{kin}} = 0.05 L_{\text{bol}}$, and $\dot{E}_{\text{kin}} = 0.005 L_{\text{bol}}$ respectively. The dotted line in the right panel indicates $\dot{M}_{\text{out}} v_o = L_{\text{bol}}/c$. Typical uncertainties are displayed in the bottom-right corner of the plots. The colour scheme is the same as that in Fig. 5.4.

Table 5.15: Average values and standard deviations of the [O III] $\lambda 5007$ and CIV $\lambda 1549$ outflow parameters for the different samples.

Sample	[O III] $\lambda 5007$			CIV $\lambda 1549$		
	\dot{M}_{out} [$M_{\odot} \text{ yr}^{-1}$]	$\dot{M}_{\text{out}} v_o$ [$10^{35} \text{ g cm s}^{-2}$]	\dot{E}_{kin} [$10^{43} \text{ erg s}^{-1}$]	\dot{M}_{out} [$M_{\odot} \text{ yr}^{-1}$]	$\dot{M}_{\text{out}} v_o$ [$10^{36} \text{ g cm s}^{-2}$]	\dot{E}_{kin} [$10^{45} \text{ erg s}^{-1}$]
(1)	(2)	(3)	(4)	(5)	(6)	(7)
ISAAC	34.35 ± 24.73	3.12 ± 3.48	3.50 ± 5.30	38.59 ± 20.25	3.05 ± 1.53	2.03 ± 1.16
HEMS	28.71 ± 30.01	4.07 ± 9.03	10.11 ± 29.33	24.32 ± 14.51	1.18 ± 0.87	0.48 ± 0.45
FOS	1.58 ± 1.12	0.11 ± 0.11	0.24 ± 0.34	0.37 ± 0.39	0.01 ± 0.01	0.01 ± 0.01

Notes. (1) Sample identification. (2), (3), (4) Outflow mass rate, thrust, and kinetic power of [O III] outflows. (5), (6), (7) Same for CIV outflows.

CIV $\lambda 1549$

The ionised gas mass producing the CIV $\lambda 1549$ line was estimated following the results obtained from CLOUDY photoionisation computations by using two different SEDs representing the two main samples of sources considered in this work: a SED from Mathews & Ferland (1987) for the low- z FOS sample, and the more appropriate SED from Krawczyk et al. (2013) for high-luminosity high- z ISAAC and HEMS samples, and taking also into account the constraints imposed by the measurements of the observed quantities in the spectra, such as the $W(\text{CIV})$ or the CIV $\lambda 1549/\text{H}\beta$ ratio. All the calculations and assumptions for the CIV outflow parameters are reported in Appendix B.2.2. For CIV $\lambda 1549$, we consider that (at variance with [O III]) the CIV outflow is accelerated to a final outflow velocity of $c(1/2) + 2\sigma$ of the blueshifted component.

As in [O III], we estimated the radius r independently for each source, and based on the luminosity at 1350\AA . In the case of C IV, we use the consolidated scaling relation of [Kaspi et al. \(2021\)](#):

$$\frac{r_{\text{BLR}}}{10 \text{ lt days}} = (0.34 \pm 0.11) \left(\frac{\lambda L_{\lambda}(1350\text{\AA})}{10^{43} \text{ erg s}^{-1}} \right)^{0.45 \pm 0.05}, \quad (5.10)$$

where r_{BLR} is the radius of the BLR.

For our sources, the specific luminosities at 1350\AA range from approximately $10^{44.5}$ up to $10^{46.5}$ erg s^{-1} at low z and from $10^{45.9}$ to $10^{47.6}$ erg s^{-1} at high z . With these luminosity values, we find C IV $\lambda 1549$ outflow radii varying from 0.06 to 0.37 pc at high z and 0.01 to 0.11 pc at low z .

Table 5.13 lists the properties of the C IV $\lambda 1549$ used in estimating the outflow parameters. The relations between the C IV outflow parameters and the bolometric luminosity are shown in Fig. 5.13 and the respective linear correlations are reported in Table 5.14. The outflow parameters considered in this work (kinetic power \dot{E}_{kin} and thrust $\dot{M}_{\text{out}} v_o$) show very good correlations with the bolometric luminosity (as expected), reaching correlation coefficients of ~ 0.9 and $P \ll 10^{-20}$ in both cases.

The left plot of Fig. 5.13 shows the kinetic power of C IV outflows. We find that 15 of the 42 high- z sources present a $\dot{E}_{\text{kin}}/L_{\text{bol}}$ ratio of $\gtrsim 5 \times 10^{-3}$, 8 of them show an $\dot{E}_{\text{kin}}/L_{\text{bol}}$ of around 0.01, and 3 sources exhibit a ratio of close to 0.05 (between 1 to 3%). The situation is different when we consider the low- z sample. In this case, only two sources, [HB89]1259+593 and [HB89]1543+489, have a $\dot{E}_{\text{kin}}/L_{\text{bol}}$ ratio of $\gtrsim 5 \times 10^{-3}$. This is hardly surprising considering that the luminosity of the BLUE component is highly correlated with 1350\AA luminosity with a slope $\approx 1.8 \gg 1$, and that outflow velocities are systematically higher at high L . At high L , the kinetic power reaches values for which a substantial feedback effect might be possible: a considerable fraction of sources present $\dot{E}_{\text{kin}} \gtrsim 0.005 L_{\text{bol}}$ and some of them are close to the limit $0.05 L_{\text{bol}}$, which is the minimum energetic requirement for feedback to lead to the black hole mass–host velocity dispersion relation according to [Di Matteo et al. \(2005\)](#).

The right panel of Fig. 5.13 shows the behaviour of the thrust in different luminosity ranges. Thrust values from $\sim 10^{35}$ to 10^{36} g cm s^{-2} at high luminosity and from $\sim 10^{32}$ to 10^{35} g cm^{-2} at low L . At high luminosity, the thrust values are slightly closer to their AGN L/c momentum rate than at low luminosity. It seems reasonable that the C IV-emitting gas in the inner BLR may not have yet suffered losses in energy and momentum (unlike [O III]), which would imply that, at least at high L , the outflow is somehow able to exploit the full luminosity of the continuum for its acceleration. Radiative acceleration is apparently less efficient at low z . The reason for the difference – at low luminosity, most sources remain substantially below the threshold lines at $0.005 L_{\text{bol}}$ and L_{bol}/c – is not entirely clear. A simple explanation is that the acceleration might involve a smaller fraction of the gas mass at low L . Lowering the gas density by an order of magnitude would reconcile the low- z values with the critical limits. A lower density (or a higher degree of ionisation, see Appendix B.2.2) would increase the gas mass needed to explain the observed line luminosity and thus increase the outflowing gas mass proportionally. Lower-density gas might be associated with lower-column-density gas, which can be more efficiently accelerated ([Netzer & Marziani 2010](#)).

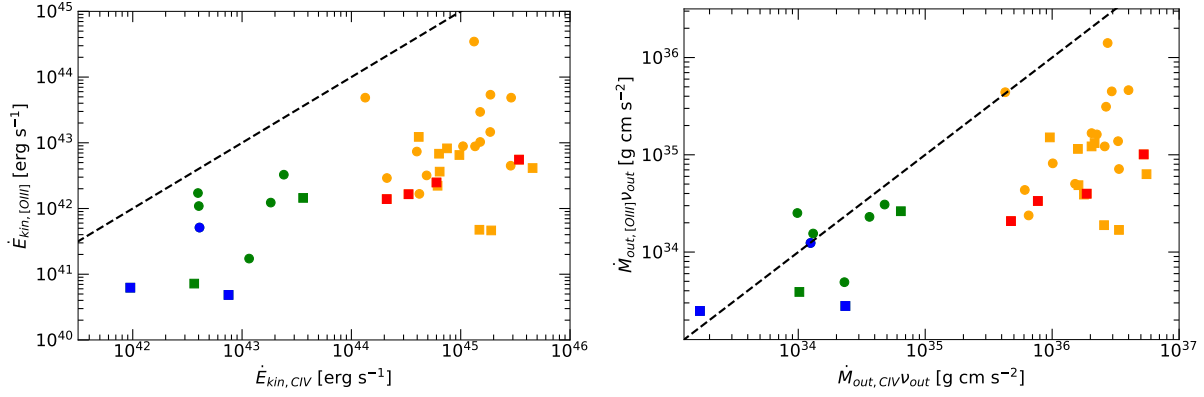


Fig. 5.14: Comparison between the kinetic power \dot{E}_{kin} (left) and thrust (right) of [O III] λ 5007 and CIV λ 1549 outflows, for high- z (orange and red symbols) and low- z (blue and green symbols) sources. Both parameters have been estimated by evaluating the outflow radius in each source according Eqs.5.9 and 5.10 for [O III] and CIV, respectively. Black dashed lines indicate the 1:1 relation. The colour scheme is the same as in Fig. 5.4.

We conclude that there is the possibility of a significant feedback effect due to the mildly ionised BLR outflow from the high-ionisation broad-line gas observed in luminous quasars at the cosmic noon, and that this possibility appears more remote for lower-luminosity, low- z quasars. This conclusion appears to be valid for both RQ and RL sources: the slightly lower velocities measured on the CIV λ 1549 profile of the RLs are not enough to significantly affect the outflow dynamical parameters with respect to the RQ population (Fig. 5.13).

Comparison between the outflow parameters of [O III] λ 5007 and CIV λ 1549

The average values and standard deviations of [O III] λ 5007 and CIV λ 1549 outflow parameters for the three analysed samples (ISAAC and HEMS at high- z , and FOS at low- z) are listed in Table 5.13. Figure 5.14 presents a comparison between the estimated kinetic power and thrust for the [O III] λ 5007 (left panel) and CIV λ 1549 (right panel) emission lines. From the results obtained independently for [O III] and CIV and at high- and low- z , in the previous sections, as well as from the comparison of the outflow parameters in the BLR and NLR through the analysis of both lines, we make the following inferences:

- The ISAAC and HEMS (high-redshift) samples share similar values for the outflow parameters, mass-outflow rate, thrust, and kinetic power. This is true for both [O III] and CIV, with the CIV emission line presenting consistently stronger wind parameters than those estimated from [O III]. The FOS (low-redshift) sample exhibits substantially lower values for all outflow parameters (\approx one and two orders of magnitude in [O III] and CIV, respectively).
- At high redshift, the CIV outflow parameters indicate a significant influence: 16 out of 42 have $\dot{E}_{kin} > 0.005L_{bol}$, and in some cases this value approaches $\sim 3\%$ of L_{bol} . Regarding [O III], our results suggest that although the outflowing gas at high redshift seems to be induced by the AGN, its impact is possibly restricted to the central kiloparsecs due to its low efficiency.

- In contrast to the outflows at low redshift, some of the C IV outflows at high redshift exhibit thrust values on the order of L_{bol}/c , suggesting that the outflowing gas in this scenario may be momentum-conserving. This characteristic is not observed in [O III] for either high- or low-redshift ranges.
- It is intriguing that, at low- z , C IV and [O III] have consistent thrust values, which is at variance with high-luminosity sources (Fig. 5.14), even if both of them fall short of the L/c line. If this is accurate, it might be a consequence of the compactness of the emitting regions in low- z quasars: $\dot{M}_{\text{out}}v_0$ is inversely proportional to the radius and in the case of the low-luminosity NLSy1s, the [O III]-emitting regions might be very compact ($\lesssim 10$ pc), therefore preserving a signature of the AGN radiative acceleration.

5.5.3 A tentative physical explanation for the RL/RQ difference in wind profiles

Observations of the C IV $\lambda 1549$ line in the ISAAC sample suggest systematically lower blueshifts for RL than for RQ quasars, in agreement with previous studies both at high and low- z (see e.g., Wills et al. 1995; Sulentic et al. 1995; Corbin & Boroson 1996; Marziani et al. 1996; Richards et al. 2011). According to Sulentic et al. (2015, and references therein), two phenomena might be relevant here.

First, the pressure exerted by the jet in its propagation surpasses the thermal pressure of the BLR gas and the hydrostatic pressure of the expected emitting gas for the blueshifted component attributed to the accretion disc wind. This suggests the existence of an “avoidance zone” near the radio axis that may be wider in the case of powerful relativistic jets, potentially suppressing emission along radial lines close to the jet axis. The second important phenomenon to be considered is the impact on the inner BLR due to the cocoon associated with the relativistic ejection. The wind might start farther from the central BH due to cocoon pressure, reaching a lower terminal velocity.

5.6 Conclusions

We present an additional sample of ten high-redshift, high-luminosity quasars observed with the VLT/ISAAC spectrograph, completing our ISAAC sample, discussed in Paper I. These data cover the $H\beta$ spectral range, shifted to the near-infrared due to its redshift, and are combined with rest-frame UV spectra observed in the optical and available in the literature. The analysis at high redshift involves 32 sources from our ISAAC sample and 28 sources from the HEMS survey, including both RL and RQ sources and with bolometric luminosities in the range from $\approx 10^{47}$ to $10^{48.5}$ [erg s $^{-1}$]. A comparison sample is made with 84 low-redshift, low-luminosity sources selected from the FOS data. We performed a spectroscopic exploration of UV and optical emission line diagnostics along the quasar main sequence, including a dedicated analysis of the differences between RL and RQ sources at both high and low redshifts. Additionally, we investigated the main feedback properties from both

the BLR and NLR using high-ionisation lines (C IV and [O III], respectively). Our main conclusions are as follows.

1. The shift in the main sequence toward broader $H\beta$ profiles and higher R_{FeII} observed at high redshift in Paper I is reconfirmed with the inclusion of the ten new sources. RL quasars from our high- z sample consistently exhibit a tendency toward lower R_{FeII} compared to the RQ ones.
2. High- z RL/RQ sources have stronger outflows than low- z RL/RQ sources as inferred from both [O III] λ 5007 and C IV λ 1549, which indicates that the accretion rate may be the primary driver of these outflows.
3. RL sources have smaller outflows compared to RQ sources in both high- and low- z ranges. This suggests that the radio-loudness has a second-order effect on the outflow. However, more data on high- z RL sources are needed.
4. Both RQ and RL outflows may induce a significant feedback effect at the high luminosities encountered in the high- z sample.
5. In the end, the outflow “power” is proportional to the AGN luminosity, via the line luminosity that enters linearly, and the increase in outflow velocity with luminosity that is expected to be weaker ($\propto L^{\frac{1}{4}}$ for a radiation driven wind). However, this increase becomes more significant if a luminosity range as large as $\sim 10^3 - 10^4$ is considered, as in the case of the samples presented in this chapter. Within limited luminosity ranges, the dominant effect is associated with the radiative output per unit mass (i.e., the Eddington ratio).
6. The C IV λ 1549 line follows the same trends as [O III] λ 5007, albeit with larger outflow velocities and stronger outflow parameters. The relations between these two emission lines does not seem to be affected by the radio emission.

Our findings suggest that, regardless of the influence of accretion and radio emission, the outflow is likely to significantly affect the host galaxy at high luminosity. Less clear is the role of outflows from the BLR and NLR at low- z due to the much lower luminosity and smaller outflow velocity.

Table 5.13: Properties of the [O III] and C IV outflows.

Source	[O III]						C IV				
	L_{bol} [erg s ⁻¹] (2)	L_{full} [erg s ⁻¹] (3)	L_{SBC} [erg s ⁻¹] (4)	r_{out} [kpc] (5)	$I_{\text{SBC}}/I_{\text{tot}}c(1/2)_{\text{SBC}}$ [km s ⁻¹] (6)	L_{BLUE} [erg s ⁻¹] (7)	$L(1350\text{\AA})$ [erg s ⁻¹] (8)	$r_{\text{out}}c(1/2)_{\text{BLUE}}$ [pc] (9)	$c(1/2)_{\text{BLUE}}$ [km s ⁻¹] (10)	$\text{FWHM}_{\text{BLUE}}$ [km s ⁻¹] (11)	
ISAAC1+ISAAC2											
[HB89] 0029+073	47.65	44.02	43.97	2.03	1.00	-396		no C IV spectrum available			
SDSSJ005700.18+143737.7	47.56	[O III] not covered by the spectrum				44.74	46.73	0.14	-4765	13187	
PKS0226-038	47.18	full [O III] $c(1/2) > -250$ km s ⁻¹				44.77	46.81	0.15	-2593	10535	
PKS0237-23	47.76	44.06	43.98	2.13	0.83	-1091	45.43	47.48	0.30	-3773	10778
BZQJ0544-2241	47.52	43.81	43.47	1.60	0.45	-620		C IV at the edge of the spectrum			
CTSJ01.03	47.37	full [O III] $c(1/2) > -250$ km s ⁻¹				45.49	47.68	0.37	-2423	9263	
WB J0948+0855	47.45	no [O III] outflow detected				44.29	46.97	0.17	-6917	22060	
CTSJ03.14	47.62	full [O III] $c(1/2) > -250$ km s ⁻¹				45.05	47.59	0.33	-3003	10299	
SDSSJ114358.52+052444.9	47.20	43.41	43.31	1.02	0.78	-1294	45.17	47.30	0.25	-4185	14345
SDSSJ115954.33+201921.1	47.66	44.32	44.06	2.89	0.55	-498	45.21	47.47	0.29	-3090	9933
SDSSJ120147.90+120630.2	47.91	44.65	44.49	4.20	0.62	-977	45.32	47.40	0.27	-2639	7464
SDSSJ132012.33+142037.1	47.24	43.98	43.79	1.95	0.64	-1428	45.04	46.87	0.16	-2967	8739
SDSSJ135831.78+050522.8	47.49	44.16	44.13	2.39	0.90	-2079	45.05	47.12	0.20	-4217	11983
Q1410+096	47.73	44.34	44.20	2.95	0.73	-1254	44.88	47.15	0.21	-4135	10881
PKS1448-232	47.58	44.11	43.49	2.27	0.24	-753		no C IV spectrum available			
SDSSJ153830.55+085517.0	47.33	43.56	43.56	1.20	1.00	-544	45.31	47.39	0.27	-2780	10024
[HB89] 1559+088	47.57	44.06	43.82	2.15	0.56	-1611	44.92	47.21	0.22	-2554	7129
SDSSJ161458.33+144836.9	47.53	44.18	44.06	2.45	0.75	-1874	45.15	47.26	0.24	-3375	9333
PKS1937-101	48.44	44.79	44.55	4.97	0.57	-483		no C IV spectrum available			
PKS2000-330	47.71	44.43	44.06	3.27	0.42	-826	45.27	46.50	0.11	-4325	7835
SDSSJ210524.49+000407.3	47.79	full [O III] $c(1/2) > -250$ km s ⁻¹				44.71	47.40	0.27	-5071	10418	
SDSSJ210831.56-063022.5	47.30	43.37	43.37	0.97	1.00	-1243	44.88	47.22	0.23	-5406	13618
SDSSJ212329.46-005052.9	47.75	43.95	43.90	1.88	0.88	-2376	45.21	47.51	0.31	-3974	10217
PKS2126-15	48.01	44.38	43.85	3.08	0.30	-988		no C IV spectrum available			
FBQJ2149-0811	47.26	43.68	43.08	1.38	0.25	-1291		no C IV spectrum available			
SDSSJ235808.54+012507.2	47.92	44.40	44.40	3.15	1.00	-1052	45.04	47.08	0.20	-3189	8302
HEMS											
HE0035-2853	47.19	full [O III] $c(1/2) > -250$ km s ⁻¹				44.79	46.73	0.14	-3028	5530	
HE0043-2300	47.36	full [O III] $c(1/2) > -250$ km s ⁻¹				44.73	46.75	0.14	-2472	3840	
HE0058-3231	47.49	full [O III] $c(1/2) > -250$ km s ⁻¹				44.63	46.70	0.13	-3004	5200	
HE0109-3518	47.61	full [O III] $c(1/2) > -250$ km s ⁻¹				45.31	47.63	0.35	-1991	3020	
HE0122-3759	47.38	43.65	43.35	1.34	0.63	-2083	45.17	47.08	0.20	-4851	7520
HE0203-4627	47.10	43.41	42.80	1.02	0.24	-1322	44.25	46.46	0.10	-3362	6450
HE0205-3756	47.85	46.84	43.56	1.73	0.48	-1456	45.14	47.11	0.20	-3040	4640
HE0248-3628	46.76	full [O III] $c(1/2) > -250$ km s ⁻¹				44.80	46.98	0.18	-3880	5140	
HE0251-5550	47.84	44.42	43.74	3.22	0.16	-1253	45.45	47.38	0.27	-2869	4170
HE0349-5249	47.89	full [O III] $c(1/2) > -250$ km s ⁻¹				45.07	47.06	0.19	-3104	5525	
HE0359-3959	47.11	[O III] region dominated by Fe II				44.11	46.54	0.11	-6042	7940	
HE0436-3709	47.48	full [O III] $c(1/2) > -250$ km s ⁻¹				44.05	45.97	0.06	-3551	5670	
HE0507-3236	47.19	43.82	43.32	1.61	0.36	-1323	44.68	46.69	0.13	-2925	4720
HE0512-3329	47.30	43.77	43.31	1.52	0.40	-1785	44.63	46.32	0.09	-3581	5000
HE0926-0201	47.61	44.31	44.01	2.84	0.41	-1338	45.36	47.13	0.21	-2584	5560
HE0940-1050	47.90	44.93	44.26	5.81	0.75	-4857	45.40	47.48	0.30	-4331	6270
HE1039-0724	47.06	full [O III] $c(1/2) > -250$ km s ⁻¹				44.70	46.73	0.14	-1976	4350	
HE1104-1805	47.54	full [O III] $c(1/2) > -250$ km s ⁻¹				45.08	47.15	0.21	-2632	4610	
HE1120+0154	47.59	full [O III] $c(1/2) > -250$ km s ⁻¹				45.08	47.06	0.19	-1526	4400	
HE1347-2457	48.17	[O III] region dominated by Fe II				45.54	47.53	0.31	-5538	7720	
HE1349+0007	47.10	43.42	43.08	1.03	0.35	-1477	45.06	46.85	0.16	-3347	5377
HE1409+0101	47.52	44.18	44.03	2.46	0.74	-1173	45.11	46.97	0.17	-3328	5390

Table 5.13: continued.

Source	[O III]					CIV					FWHM _{BLUE} [km s ⁻¹]
	L_{bol} [erg s ⁻¹]	L_{full} [erg s ⁻¹]	L_{SBC} [erg s ⁻¹]	r_{out} [kpc]	$I_{\text{SBC}}/I_{\text{tot}}$ c(1/2) _{SBC} [km s ⁻¹]	L_{BLUE} [erg s ⁻¹]	$L(1350\text{\AA})$ [erg s ⁻¹]	r_{out} c(1/2) _{BLUE} [pc]	$c(1/2)$ [km s ⁻¹]		
(1)	(2)	(3)	(4)	(5)	(6)	(7)	(8)	(9)	(10)	(11)	(12)
HE2147-3212	47.09	full [O III]	c(1/2) > -250 km s ⁻¹			44.96	46.82	0.15	-4116	6650	
HE2156-4020	47.45	43.66	43.34	1.35	0.51	-1126	45.46	47.38	0.27	-2625	5000
HE2202-2557	47.13	43.53	43.20	1.16	0.38	-1240	45.22	46.66	0.13	-2573	4490
HE2349-3800	47.06	43.69	43.41	1.40	0.65	-975	44.48	46.45	0.10	-3788	5710
HE2352-4010	47.67	44.25	44.11	2.67	0.79	-2185	44.82	47.14	0.21	-3050	3760
FOS											
PG 0044+030	46.48	43.05	43.00	0.66	0.75	-366	42.01	46.01	0.06	-3251	4580
Mrk 1502	45.46	41.14	40.73	0.07	0.55	-1352	41.25	44.58	0.01	-2270	6750
3C 057	46.48	43.10	42.84	0.71	0.61	-817	42.38	46.45	0.10	-3355	3697
3C 84	44.23	42.32	41.25	0.28	0.91	-437	CIV strongly affected by noise				
LEDA 75249	45.84	no [O III] outflow detected					42.01	45.53	0.04	-2206	6318
[HB89] 0850+440	46.18	42.37	42.10	0.31	0.54	-1396	42.12	45.71	0.05	-2926	3739
SDSS J100402.61+285535.3	46.36	42.88	42.77	0.55	0.70	-1058	42.18	45.81	0.05	-3198	8043
PG 1116+215	45.98	42.83	42.44	0.52	0.36	-700	41.93	45.68	0.05	-2882	8348
LBQS 1138+0204	45.69	no [O III] outflow detected					41.57	45.32	0.03	-2553	8122
3C 273	47.08	43.10	42.94	0.71	0.69	-344	42.62	46.35	0.09	-1645	5587
SBS 1259+593	46.11	no [O III] outflow detected					42.74	46.15	0.07	-3866	8394
FBQS J131217.7+351521	45.60	42.15	41.98	0.24	0.62	-264	full CIV c(1/2) > -250, strongly affected by absorption				
FBQS J1405+2555	45.14	no [O III] outflow detected					41.23	45.37	0.03	-3841	6074
[HB89] 1415+451	45.10	40.62	40.60	0.04	1.00	-593	41.21	44.65	0.02	-1472	4862
[HB89] 1425+267	45.54	no [O III] outflow detected					40.64	44.82	0.02	-4283	3543
Mrk 478	45.16	no [O III] outflow detected					41.26	44.89	0.02	-1526	5032
[HB89] 1444+407	45.91	no [O III] outflow detected					41.92	45.64	0.04	-3110	4232
[HB89] 1538+477	47.26	no [O III] outflow detected					42.64	46.49	0.11	-3492	9104
[HB89] 1543+489	45.83	41.89	41.81	0.18	0.84	-2105	42.30	45.81	0.05	-3301	7901
Mrk 509	45.10	no [O III] outflow detected					39.73	44.52	0.01	-2713	3069
PG 2112+059	46.22	no [O III] outflow detected					42.33	45.90	0.06	-3120	6573
MR 2251-178	44.77	no [O III] outflow detected					40.32	44.54	0.01	-2363	2334
[HB89] 2349-014	45.77	no [O III] outflow detected					40.17	44.53	0.01	-5746	6476

Notes. (1) Source identification. (2) Bolometric luminosity. (3) Luminosity of the [O III] full profile applied in the scaling law for estimating the outflow radius r_{out} (Eq. 5.9). (4) Luminosity of only the [O III] outflowing component, named AS SBC for [O III]. (5) [O III] outflow radius estimated using the Eq. 5.9. (6) [O III] SBC relative intensity. (7) Outflow velocity that we assume to be the centroid at $\frac{1}{2}$ intensity of the [O III] SBC component. (8) Luminosity of the CIV outflowing BLUE component. (9) Specific luminosity at 1350Å, entering in Eq. 5.10. (10) Estimated CIV outflow radius. (11) CIV outflow velocity. (12) FWHM of the CIV λ 1549 BLUE component.

Part III

Black hole mass estimation for quasars at high and low redshift

In the 1900s, astronomers began to explore the use of emission lines from gas surrounding black holes as a means of estimating their masses. These emission lines, produced by the interaction of the gas with the intense radiation emitted by the black hole, can be used to infer the velocity of the gas and hence the mass of the black hole. In recent years, advancements in technology and observational techniques have allowed for more precise and accurate black hole mass estimations.

Here, we use observational spectroscopic data covering a wide range of quasar luminosities to propose scaling laws and compare the black hole mass estimates derived from different emission lines. We discuss the relation between the black hole mass determined through the $H\beta$ emission line and through intermediate-ionisation emission lines, such as Al III and CIII] for a sample that includes both high- and low-redshift Population A quasars. In this study, we have demonstrated for the first time two scaling laws using intermediate ionisation UV broad emission lines. These laws enable the estimation of black hole masses in quasars observed in the optical range up to redshift $z \sim 4$ and in the NIR up to $z \sim 7$. These relations were applied to estimate black hole masses and, subsequently, the Eddington ratios in our sample using the available UV lines.

THE INTERMEDIATE-IONISATION LINES AS VIRIAL BROADENING ESTIMATORS FOR POPULATION A QUASARS

6

Chapter based on the article published in The Astrophysical Journal Supplement Series by P. Marziani et al. (A. Deconto-Machado included), volume 261, issue 2, id.30, 29 pages, August 2022. DOI: 10.3847/1538-4365/ac6fd6

Abstract

The identification of a virial broadening estimator in the quasar UV rest frame suitable for black hole mass computation at high redshift has become an important issue. We compare the HI Balmer $H\beta$ line width to the ones of two intermediate ionisation lines: the AlIII λ 1860 doublet and the CIII] λ 1909 line, over a wide interval of redshift and luminosity ($0 \lesssim z \lesssim 3.5$; $43 \lesssim \log L \lesssim 48.5$ [erg s⁻¹]), for 48 sources belonging to the quasar population characterised by mid-to-high values of the Eddington ratio (Population A following [Sulentic et al. 2000a](#)). The present analysis indicates that the line width of AlIII λ 1860 and $H\beta$ are highly correlated, and can be considered equivalent for most Population A quasars over five orders of magnitude in luminosity; for CIII] λ 1909, multiplication by a constant correction factor $\xi \approx 1.25$ is sufficient to bring the FWHM of CIII] in agreement with the one of $H\beta$. The statistical concordance between low-ionisation and intermediate-ionisation lines suggests that they predominantly arise from the same virialised part of the broad line region. However, blueshifts of modest amplitude (few hundred km s⁻¹) with respect to the quasar rest frame and an excess ($\lesssim 1.1$) Al III broadening with respect to $H\beta$ are found in a fraction of our sample. Scaling laws to estimate M_{BH} of high redshift quasar using the Al III and the CIII] line widths have rms scatter ≈ 0.3 dex. The Al III scaling law takes the form $\log M_{\text{BH}} \approx 0.58 \log L_{1700,44} + 2 \log \text{FWHM} + 0.49$ [M_{\odot}].

6.1 Introduction

The energetics of all accretion-related phenomena occurring in active galactic nuclei (AGN) can be tied down to the mass of the central black hole. The mass (M_{BH}) of the black holes at the origin of the

AGN phenomenon is now reputed a key parameter in the evolution of galaxies and in cosmology as well (e.g., [Kormendy & Ho 2013](#); [Vogelsberger et al. 2014](#); [Heckman & Best 2014](#)), and its estimation has become an important branch of extragalactic research. Black hole mass estimates on large type-1 AGN samples are carried out employing a deceptively-simple formulation of the virial theorem, under the assumption that all the mass of the system is concentrated in the centre of gravity provided by the black hole (see e.g., [Marziani & Sulentic 2012a](#); [Shen 2013](#); [Peterson 2014](#), for reviews): $M_{\text{BH}} = f_{\text{S}} r_{\text{BLR}} (\delta v)^2 / G$, where f_{S} is a structure factor (a.k.a. virial or form factor) dependent on the emitting region geometry and dynamics, the radius r_{BLR} the distance of the line emitting region from the continuum source, and δv a suitable measure of the line broadening (e.g., FWHM or dispersion σ , [Vestergaard & Peterson 2006](#); [Peterson et al. 2004](#)). The main underlying assumptions are that the broadening is due to Doppler effect because of the line emitting gas motion, and that the velocity field is such that the emitting gas remains gravitationally bound to the black hole.

Early UV and optical inter-line shift analysis provided evidence that not all the line emitting gas is bound to the black hole (e.g., [Gaskell 1982](#); [Tytler & Fan 1992](#); [Brotherton et al. 1994b](#); [Marziani et al. 1996](#); [Leighly & Moore 2004](#)). The scenario emerging from more recent studies is that outflows are ubiquitous in active galactic nuclei. They occur under a wide range of physical conditions, and are detected in almost every band of the electromagnetic spectrum and on a wide range of spatial scales, from a few gravitational radii to tens of kpc (e.g., [Capetti et al. 1996](#); [Colbert et al. 1998](#); [Everett 2007](#); [Carniani et al. 2015](#); [Bischetti et al. 2017](#); [Komossa et al. 2018](#); [Kakkad et al. 2020](#); [Vietri et al. 2020](#); [Laurenti et al. 2021](#)). At high luminosity, massive outflows provide feedback effects to the host galaxy (e.g., [Fabian 2012](#); [King & Pounds 2015](#); [King & Muldrew 2016](#); [Barai et al. 2018](#)), and are invoked to account for the M_{BH} -bulge velocity dispersion correlation (e.g., [Kormendy & Ho 2013](#), and references therein). For $z \gtrsim 4$, M_{BH} estimates rely on the C IV $\lambda 1549$ high-ionisation line, and the highest- z sources appear to be almost always high-accretors ([Bañados et al. 2018](#); [Nardini et al. 2019](#)). Two studies pointed out 20 years ago the similarity between X-ray and UV properties of high- z quasars and local quasars accreting at high rates (e.g., [Mathur 2000](#); [Sulentic et al. 2000a](#)). The source of concerns is that high-ionisation lines such as C IV $\lambda 1549$ are subject to a considerable broadening and blueshifts associated with outflow motions already at low redshift ([Coatman et al. 2016](#); [Sulentic et al. 2017](#); [Marinello et al. 2020a](#), see [Marinello et al. 2020b](#) for a detailed study of the prototypical source PHL 1092). Overestimates of the virial broadening by a factor as large as ≈ 5 ([Netzer et al. 2007](#); [Sulentic et al. 2007a](#); [Mejía-Restrepo et al. 2016](#); [Mejía-Restrepo et al. 2018b](#)) for supermassive black holes at high z may even pose a spurious challenge to concordance cosmology (e.g., [Trakhtenbrot et al. 2015](#)) and lead to erroneous inferences on the properties of the seed black holes believed to be fledgling precursors of massive black holes.

This chapter is focused on the measurement of the line width of the UV intermediate-ionisation lines at $\approx 1900 \text{ \AA}$ and on their use for black hole mass measurements for large quasar samples, over a wide interval of luminosity and of redshift. The blend at $\lambda 1900 \text{ \AA}$ is due, at least in part, to the Al III $\lambda 1860$ doublet and to the Si III] $\lambda 1892$ and C III] $\lambda 1909$ lines. Al III is a resonant doublet ($^2P_{\frac{3}{2}, \frac{1}{2}}^o \rightarrow ^2S_{\frac{1}{2}}$) while Si III] and C III] are due to inter-combination transitions ($^3P_1^o \rightarrow ^1S_0$) with widely

different critical densities ($\approx 2 \cdot 10^{11} \text{ cm}^{-3}$ and $\approx 3 \cdot 10^9 \text{ cm}^{-3}$, respectively; Zheng 1988; Negrete et al. 2012). The parent ionic species imply ionisation potentials $15 \lesssim \chi_i \lesssim 30 \text{ eV}$, intermediate between the ones of low-ionisation lines (LILs), and the ones of high-ionisation lines (HILs; $\chi_i \gtrsim 40 - 50 \text{ eV}$). The intermediate-ionisation lines (IILs) at 1900 \AA are well-placed to provide a high redshift estimator; they can be observed with optical spectrometers up to $z \sim 4$. Observations can be extended in the NIR ($13,500 \text{ \AA}$) up to $z \sim 5.7$ without solution of continuity, thereby sampling a redshift domain that is crucial for understanding the primordial growth of massive black holes and galaxy formation. In principle, observations could be extended to the H band to cover the as yet mostly uncharged range $6.5 \lesssim z \lesssim 8$, a feat that may well become possible with the advent of James Webb Space Telescope (Gardner et al. 2006), of the ESO Extremely Large Telescope (Gilmozzi & Spyromilio 2007), and of the next-generation large-aperture telescopes (see e.g., D’Onofrio & Marziani 2018, for a review of foreseeable technological developments).

The quasar main sequence provides much needed discerning abilities for the exploitation of the IILs (e.g., Sulentic et al. 2000a; Bachev et al. 2004; Marziani et al. 2001; Shen & Ho 2014; Panda et al. 2018), as line profiles and intensities of individual sources are not considered as isolated entities in the main sequence context, but interpreted as part of consolidated trends. Broad line measurements involving $H\beta$ line width and Fe II strength are not randomly distributed but instead define a sequence that has become known as the quasar “main sequence” (MS; e.g., Sulentic et al. 2000a; Shen & Ho 2014; Panda et al. 2019; Wildy et al. 2019). The Fe II strength is parameterised by the intensity ratio involving the Fe II blue blend at 4570 \AA and broad $H\beta$ i.e., $R_{\text{FeII}} = I(\text{FeII}\lambda 4570)/I(H\beta)$, and the Hydrogen $H\beta$ line width by its FWHM. MS sources with higher R_{FeII} show narrower broad $H\beta$ (Population A, $\text{FWHM}(H\beta) \lesssim 4000 \text{ km s}^{-1}$), and sources with broader $H\beta$ profiles tendentially show low R_{FeII} (Pop. B with $\text{FWHM}(H\beta) \gtrsim 4000 \text{ km s}^{-1}$, Sulentic et al. 2000a, 2011). It is also known that optical and UV observational properties are correlated (e.g., Sulentic et al. 2000b; Bachev et al. 2004; Sulentic et al. 2007a; Du et al. 2016b; Śniegowska et al. 2018). In this chapter, the attention is restricted to sources radiating at relatively high Eddington ratio ($L/L_{\text{Edd}} \gtrsim 0.1 - 0.2$) i.e., to Population A that accounts for the large majority of sources discovered at high z . In the course of our analysis we realised that sources radiating at lower Eddington ratio ($0.01 \lesssim L/L_{\text{Edd}} \lesssim 0.1 - 0.2$) show a different behaviour of the 1900 blend and will be considered elsewhere.

The coverage of the $H\beta$ spectral range greatly eases the determination of the redshift as well as the positional classification of sources along the MS. In addition, $\text{FWHM } H\beta$ has been employed as a virial broadening estimator of M_{BH} since the earliest single-epoch observations of large samples of quasars, and in more recent times as well (e.g., McLure & Jarvis 2002; McLure & Dunlop 2004; Vestergaard & Peterson 2006; Assef et al. 2011; Trakhtenbrot & Netzer 2012; Shen & Liu 2012). The $H\beta$ line is likely to be still the most widely used line for M_{BH} computations for low redshift quasars ($z \lesssim 1$). Our analysis relies on the availability of both $H\beta$ and the 1900 blend lines, as we will consider $\text{FWHM } H\beta$ as the reference “virial broadening estimator” (VBE).

Section 6.2 introduces the samples used in the present work, covering a wide range in redshift and luminosity, $0 \lesssim z \lesssim 3.5$; $44 \lesssim \log L \lesssim 48.5 [\text{erg s}^{-1}]$. The data were obtained with instruments operating in widely different spectral ranges (UV, optical, IR); as a consequence, S/N ratio values vary

widely and the uncertainty assessment requires a dedicated approach (Section 6.3, and Appendix C.1). The Section 8.5 introduces paired fits to H β and the 1900 blend (an atlas is provided in Appendix C.2), along with several line width measures, and the relation between H β and Al III measurements. A scaling law for M_{BH} determination equivalent to the one based on H β but based on the IIL broadening is discussed in Section 8.6.

6.2 Sample

Low-luminosity 1900 and H β data (FOS* sample) We considered a Faint Object Spectrograph (FOS) sample from Sulentic et al. (2007a, hereafter S07) as a low- L and low- z sample. For the sake of the present chapter, we restrict the S07 sample to 28 sources covering the 1900 blend spectral range and with previous measurements for the H β profile and R_{FeII} (FOS* sample). The spectra covering the H β spectral range come from Marziani et al. (2003b, hereafter M03), as well as from the SDSS (York et al. 2000) and the 6dF (Jones et al. 2004; Table 6.1 provides information on the provenience of individual spectra). The FOS high-resolution grisms yielded an inverse resolution $\lambda/\delta\lambda \sim 1000$, equivalent to typical resolution of the data of M03 and of the SDSS. The S/N is above $\gtrsim 20$ for both the optical and UV low-redshift data. The FOS* sample has a typical bolometric luminosity $\log L \sim 45.6$ [erg s $^{-1}$] and a redshift $z \lesssim 0.5$.

High-luminosity VLT and TNG data for Hamburg-ESO quasars (HE sample) The sample of high- L quasars includes 10 sources identified in the Hamburg-ESO survey (Wisotzki et al. 2000) in the redshift range $1.4 \lesssim z \lesssim 2.6$. All HE quasars satisfy the condition on the bolometric luminosity $\log L \gtrsim 10^{47.5}$ erg s $^{-1}$ and are discussed in detail by Sulentic et al. (2017, hereafter S17), where C IV $\lambda 1549$ and H β were analysed. The sample used in this chapter is restricted to the 9 Population A sources with VLT/FORS1 spectra and 1 TNG/DOLORES (HE1347-2457) spectrum that cover the 1900 Å blend. The spectral resolutions at FWHM are $\lesssim 300$ km s $^{-1}$ and $\lesssim 600$ km s $^{-1}$ for the spectrographs FORS1 and DOLORES, respectively. The resolution of the ISAAC spectra covering H β is ≈ 300 km s $^{-1}$ (Sulentic et al. 2004). Typical S/N values are $\gtrsim 50$.

Additional high-luminosity sources (ISAAC sample) Additional ISAAC spectra were obtained under programme 083.B-0273(A), for three targets SDSS J005700.18+143737.7, SDSS J132012.33+142037.1, SDSS J161458.33+144836.9. They have been reduced following the same procedures employed for the HE quasars. The data will be presented in a forthcoming paper (Deconto Machado et al., in preparation). Matching rest-frame UV spectra were collected from the SDSS and BOSS (Smees et al. 2013), with a resolving power $R = \lambda/\text{FWHM} \sim 2000$.

High-luminosity sources from the WISSH (WISSH sample) We included near-infrared (NIR) spectroscopic observations of 7 WISSH Population A quasars QSOs (Vietri et al. 2018), obtained with LUCI at the Large Binocular Telescope and in one case with SINFONI at VLT. Basic information

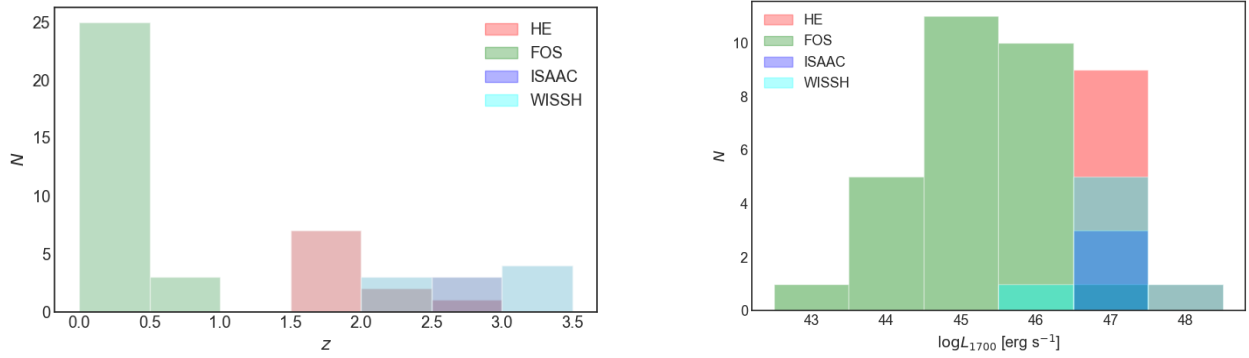


Fig. 6.1: Distribution of redshift (left) and of luminosity at 1700 Å (right) for the four sub-samples considered in this chapter.

on this sample is provided in Table 1 of [Vietri et al. \(2018\)](#). The matching rest-frame UV spectra are from the SDSS. The higher resolution implies a somewhat lower S/N with respect to the ISAAC spectra; we restrict our analysis to the spectra above a minimum S/N ≈ 15 . Redshifts measured for this chapter agree very well with the values reported by [Vietri et al. \(2018\)](#) if the H β profile is sharp; they are lower by 300-400 km s⁻¹ in four cases with relatively shallow profiles due to the different fitting techniques.

Joint sample Table 6.1 lists in the following order source identification, redshift, specific rest-frame flux in the UV at 1700 Å ($f_{\lambda,1700}$), S/N at 1700 Å reference to the origin of the spectrum, specific flux in the optical at 5100 Å ($f_{\lambda,5100}$), S/N at 5100 Å, and reference to the origin of the optical spectrum. Table footnotes list references to the flux scale origin, in case the spectrum had uncertain or no absolute spectrophotometric flux calibration. Notes include the radio loudness classification ([Zamfir et al. 2008](#); [Ganci et al. 2019](#)): radio-loud (RL), radio-intermediate (RI), and radio-quiet (RQ). Only two sources (HE 0043-2300 and 3C 57) are “jetted” in the sense of having a powerful relativistic jet ([Padovani 2017](#)). HE 0043-2300 is listed as a flat-spectrum radio quasar with dominant blazar characteristics in the Roma-BZCAT ([Massaro et al. 2009](#)), and 3C 57 is a compact-steep source (CSS; [O’Dea 1998](#), [Sulentic et al. 2015](#)). Two other sources qualify as radio-intermediate (HE 0132-4313 and HE0248-3628), and are briefly discussed in Appendix C.3.

6.3 Data analysis

6.3.1 The quasar main sequence as an interpretative aid

In the following the framework of the quasar MS to make assumptions on line shapes, both in the optical and in the UV spectral ranges. There are several papers that provide a description of the main trends associated with the MS. [Fraix-Burnet et al. \(2017a\)](#) reviews the main multi-frequency trends. [Sulentic et al. \(2000a, 2011\)](#) review the case for two different quasar Populations: Population A (at low z , $\text{FWHM H}\beta \lesssim 4000 \text{ km s}^{-1}$), and Population B ($\text{FWHM H}\beta \gtrsim 4000 \text{ km s}^{-1}$). The limit is luminosity-dependent ([S17](#)), and reaches $\text{FWHM} \gtrsim 5500 \text{ km s}^{-1}$ at high luminosity $\log L \sim 48$). In the optical plane of the MS defined by $\text{FWHM H}\beta$ vs R_{FeII} Population A has been subdivided into 4 spectral types (STs) according to Fe II prominence: A1, with $R_{\text{FeII}} \lesssim 0.5$; A2, with $0.5 \lesssim R_{\text{FeII}} \lesssim 1.0$; A3, with $1.0 \lesssim R_{\text{FeII}} \lesssim 1.5$; A4, with $1.5 \lesssim R_{\text{FeII}} \lesssim 2.0$ ([Sulentic et al. 2002](#), see also [Shen & Ho 2014](#) for an analogous approach). The condition $R_{\text{FeII}} \gtrsim 1.0$ restricts the MS to the tip of high R_{FeII} values, and encompasses 10% of objects (referred to as extreme Population A). At low- z they are mostly narrow-line Seyfert-1 (NLSy1s) driving the MS correlations ([Boroson & Green 1992](#); [Sulentic et al. 2000a](#); [Du et al. 2016b](#)). Sources with $R_{\text{FeII}} \gtrsim 2$ do exist ([Lipari et al. 1993](#); [Graham et al. 1996](#)) but they are exceedingly rare (less than 1%) in optically-selected samples ([Marziani et al. 2013a](#), hereafter [M13a](#)). We therefore group all sources with $R_{\text{FeII}} \gtrsim 1.5$ in A4.

6.3.2 Multicomponent χ^2 -minimisation

Resolution and S/N of the available spectra are adequate for a multicomponent nonlinear fitting analysis using the IRAF routine `specfit` ([Kriss 1994](#)), involving an accurate deconvolution of $\text{H}\beta$, $[\text{O III}]\lambda\lambda 4959, 5007$, Fe II, $\text{He II}\lambda 4686$ in the optical, and of Al III, C III] and Si III] in the UV. A χ^2 minimisation analysis is necessary in all cases, since the strongest lines are heavily blended together, and the blend involves also features extended over a broad wavelength range, due to Fe II (mainly optical, and UV to a lesser extent) and Fe III (UV only).

6.3.3 $\text{H}\beta$ line

The $\text{H}\beta$ Balmer emission line is a reliable estimator of the “virial” broadening in samples of moderate-to-high luminosity ([Wang et al. 2009](#); [Trakhtenbrot & Netzer 2012](#); [Shen & Liu 2012](#)). Typically, the $\text{H}\beta$ line profiles are fairly symmetric, and are thought to be dominated by a virialised component ([Peterson & Wandel 1999](#); [Peterson et al. 2004](#), [S17](#)). Several previous works noted that $\text{H}\beta$ shows a Lorentzian-like profile in sources belonging to Population A (e.g., [Véron-Cetty et al. 2001](#); [Sulentic et al. 2002](#); [Cracco et al. 2016](#), this is also seen in $\text{Mg II}\lambda 2800$, [Marziani et al. 2013b](#); [Popović et al. 2019](#)). However, the $\text{H}\beta$ profiles can be affected by slight asymmetries and small centroid shifts. In Population A they are mostly due to blueshifted excess, often modelled with a blueward asymmetric Gaussian component (BLUE), strongly affecting the $\text{C IV}\lambda 1549$ line profiles, and related to outflows

Table 6.1: Sample properties

IAU code	Common name	z	$f_{\lambda,1700}^a$	S/N_{1700}	Ref. ^b	$f_{\lambda,5100}^a$	S/N_{5100}	Ref. ^b	Notes
FOS* sample									
J00063+2012	MRK 0335	0.0252	60.8	15	S07	5.92	55	M03	
J00392-5117	[WPV85] 007	0.0290	2.5	15	S07	2.02 ^c	45	6dF	
J00535+1241	UGC 00545	0.0605	28.2	40	S07	5.77	70	M03	
J00573-2222	TON S180	0.0620	31.8	45	S07	14.6	55	M03	
J01342-4258	HE 0132-4313	0.2370	15.2	50	S07	1.44 ^d	15	6dF	RI
J02019-1132	3C 057	0.6713	17.7	25	S07	1.90	35	S15	CSS
J06300+6905	HS 0624+6907	0.3702	51.7	30	S07	5.04 ^e	40	M03	
J07086-4933	1H 0707-495	0.0408	22.2	20	S07	2.14 ^f	35	6dF	
J08535+4349	[HB89] 0850+440	0.5149	5.7	20	S07	0.50	15	M03	
J09199+5106	NGC 2841 UB3	0.5563	11.0	30	S07	1.25	40	SDSS	
J09568+4115	PG 0953+414	0.2347	17.1	30	S07	2.15	75	M03	
J10040+2855	PG 1001+291	0.3298	17.2	25	S07	1.92	45	M03	
J10043+0513	PG 1001+054	0.1611	4.9	10	S07	1.50	30	M03	
J11185+4025	PG 1115+407	0.1536	11.7	20	S07	0.46	30	M03	
J11191+2119	PG 1116+215	0.1765	41.3	40	S07	2.62	50	M03	
J12142+1403	PG 1211+143	0.0811	31.0	20	S07	5.45	40	M03	
J12217+7518	MRK 0205	0.0711	23.6	35	S07	1.73	55	M03	
J13012+5902	SBS 1259+593	0.4776	19.1	25	S07	0.59	50	M03	
J13238+6541	PG 1322+659	0.1674	9.5	40	S07	0.71	35	M03	
J14052+2555	PG 1402+262	0.1633	22.6	25	S07	1.54	45	M03	
J14063+2223	PG 1404+226	0.0973	5.8	15	S07	1.12	60	M03	
J14170+4456	PG 1415+451	0.1151	10.2	25	S07	0.86	35	M03	
J14297+4747	[HB89] 1427+480	0.2199	7.6	30	S07	0.30	55	M03	
J14421+3526	MRK 0478	0.0771	28.2	25	S07	2.04	55	M03	
J14467+4035	[HB89] 1444+407	0.2670	18.7	45	S07	1.02	20	M03	
J15591+3501	UGC 10120	0.0313	7.3	20	S07	2.29	55	SDSS	
J21148+0607	[HB89] 2112+059	0.4608	14.9	25	S07	0.81	50	M03	
J22426+2943	UGC 12163	0.0245	10.9	40	S07	0.67	25	M03	
HE sample									
J00456-2243	HE0043-2300	1.5402	15.5	115	S17	3.2	70	S17	RL
J01242-3744	HE0122-3759	2.2004	21.7	95	S17	2.2	30	S17	
J02509-3616	HE0248-3628	1.5355	24.2	200	S17	0.8	50	S17	RL, inv. radio sp.
J04012-3951	HE0359-3959	1.5209	12.1	105	S17	1.8	40	S17	
J05092-3232	HE0507-3236	1.5759	11.7	160	S17	2.1	25	S17	
J05141-3326	HE0512-3329	1.5862	7.7	40	S17	2.7	25	S17	
J11065-1821	HE1104-1805	2.3180	23.9	75	S17	3.0	15	S17	
J13506-2512	HE1347-2457	2.5986	48.0	75	S17	3.9	50	S17	
J21508-3158	HE2147-3212	1.5432	17.0	150	S17	1.7	20	S17	
J23555-3953	HE2352-4010	1.5799	35.5	85	S17	6.3	60	S17	
ISAAC sample									
J00570+1437	SDSSJ005700.18+143737.7	2.6635	14.0	55	SDSS	2.78	40	D22	normalized at 5000 Å
J13202+1420	SDSSJ132012.33+142037.1	2.5357	8.4	40	SDSS	1.32	25	D22	normalized at 5000 Å
J16149+1448	SDSSJ161458.33+144836.9	2.5703	15.3	50	SDSS	2.54	45	D22	normalized at 5000 Å
WISSH sample									
0801+5210	SDSS J080117.79+521034.5	3.2565	29.4	30	SDSS	4.12	20	V18	
1157+2724	SDSS J115747.99+272459.6	2.2133	4.2	15	SDSS	2.37	25	V18	HiBAL QSO
1201+0116	SDSS J120144.36+011611.6	3.2476	17.0	30	SDSS	3.31	20	V18	
1236+6554	SDSS J123641.45+655442.1	3.4170	22.9	45	SDSS	2.30	25	V18	
1421+4633	SDSS J142123.97+463318.0	3.4477	20.9	25	SDSS	3.28	15	V18	
1521+5202	SDSS J152156.48+520238.5	2.2189	59.8	80	SDSS	8.40	35	V18	
2123-0050	SDSS J212329.46-005052.9	2.2791	32.2	60	SDSS	5.75	45	V18	

Notes. RL: jetted, $\log R_K \geq 100$ following [Ganci et al. \(2019\)](#); RI: $10 \lesssim \log R_K \lesssim 100$; CSS: compact steep spectrum radio-source. ^a In units of $10^{-15} \text{ erg s}^{-1} \text{ cm}^{-2} \text{ \AA}^{-1}$, in rest frame, not corrected for Galactic extinction. ^b Reference to the origin of the spectra: S17; S07; M03; D22: Deconto Machado et al., in preparation; SDSS: SDSS and BOSS, [Smees et al. \(2013\)](#); 6dF: [Jones et al. \(2004\)](#). ^c Uncalibrated 6dF spectrum; flux scale set by a quick-look magnitude as in S07. [Grupe et al. \(1998\)](#) luminosity yields $f_{\lambda,5100} \approx 3.1 \cdot 10^{-15} \text{ erg s}^{-1} \text{ cm}^{-2} \text{ \AA}^{-1}$. Very low $f_{\lambda,1700}/f_{\lambda,5100} \approx 1$ ratio. The $f_{\lambda,1700}$ from the S07 HST/FOS spectrum corresponds to a deep minimum of the UV flux. Later observations show a more than 5-fold increase in the UV continuum ([Leighly et al. 2015](#)). ^d Uncalibrated 6dF spectrum; flux scale set by a quick-look magnitude as in S07. [Grupe et al. \(2010\)](#) V luminosity implies $f_{\lambda,5100} \approx 0.86 \cdot 10^{-15} \text{ erg s}^{-1} \text{ cm}^{-2} \text{ \AA}^{-1}$. ^e Uncalibrated spectrum; flux scale set by a quick-look magnitude as in S07. [Decarli et al. \(2010\)](#) yield $5.24 \cdot 10^{-15} \text{ erg s}^{-1} \text{ cm}^{-2} \text{ \AA}^{-1}$, in close agreement. ^f Uncalibrated 6dF spectrum; flux scale set by a quick-look magnitude as in S07. [Giannuzzo & Stirpe \(1996\)](#) yield $1.80 \cdot 10^{-15} \text{ erg s}^{-1} \text{ cm}^{-2} \text{ \AA}^{-1}$, in close agreement.

(e.g., S17, and references therein, Negrete et al. 2018). In $H\beta$, BLUE is detected as a faint excess on the blue side of the symmetric profile assumed as the virialised component of $H\beta$, almost only in extreme Population A (several examples are shown in the Figures of the atlas of Appendix C.2). Even when the BLUE component is detected, its influence on the $H\beta$ FWHM is modest, leading at most to an increase of the broadening $\approx 10\%$ over the FWHM of the symmetric broad profile (Negrete et al. 2018).

To extract a profile that excludes the blueshifted excess, we considered a model of the broad $H\beta$ line with the following components (based on the approach of Negrete et al. 2018):

- the $H\beta_{BC}$, modelled with an (almost) unshifted Lorentzian profile;
- a blueshifted excess (BLUE) modelled with a blueshifted Gaussian with free skew parameter (Azzalini & Regoli 2012). The skewed Gaussian function has no more outliers than the normal distribution, and retains the shape of the normal distribution on the skewed side. It is consistent with the suppression of the receding side of an optically thin flow obscured by an optically thick structure (i.e., the accretion disk);
- the $H\beta_{NC}$, modelled with a Gaussian, unshifted with respect to rest frame;
- Fe II emission, modelled with a scaled and broadened template (e.g., Boroson & Green 1992), as defined by Negrete et al. (2018);
- $[O\ III]\lambda\lambda 4959,5007$, modelled by a core-component (assumed Gaussian and symmetric) and a semi-broad component (assumed Gaussian but with the possibility of being skewed). This approach has been followed in several previous work (e.g., Zhang et al. 2011);
- HeII $\lambda 4686$, broad and narrow component. HeII $\lambda 4686$ is not always detected in the spectra, especially in the case of strong Fe II emission, but the line was included in the fits.

6.3.4 The 1900 blend

The range 1700 – 2000 is dominated by the 1900Å blend which includes Al III, Si III], C III], as well as Fe II and Fe III lines. On the blue side of the blend Si III] $\lambda 1816$ and N III] $\lambda 1750$ are also detected. The relative intensity of these lines (apart from N III] $\lambda 1750$ that is not affecting the blend and for which further observations are needed) is known to be a function of the location along the quasar main sequence (Bachev et al. 2004). The line profiles and relative intensities are systematically different not only between Population A and B, but also within Pop. A there is a systematic trend of increasing Al III and decreasing C III] prominence with increasing Fe II emission (Bachev et al. 2004).

Our interpretation of the 1900 blend for Population A sources closely follows previous analyses (Baldwin et al. 1996; Wills et al. 1999; Baldwin et al. 2004; Richards et al. 2011; Negrete et al. 2012; Martínez-Aldama et al. 2018). The fits include the following components (described in detail by Martínez-Aldama et al. 2018):

- Al III, SiIII], and CIII], modelled with a Lorentzian profile. We assume that the shapes of the strongest lines are consistent with the ones considered for the H β broad components (Lorentzian for Pop. A), and that FWHM Al III = FWHM SiIII] (Negrete et al. 2013). The fitting routine may introduce a systematic blueshift to minimise χ^2 , in the case the profile is significantly affected by an unresolved blue shifted component, as observed in the case of MgII λ 2800 (M13a);
- Fe III emission, very intense in extreme Population A spectra, modelled with an empirical template (Vestergaard & Wilkes 2001). Recent photoionisation calculations indicate a more significant contribution of Fe III emission in correspondence of SiIII] (Temple et al. 2020). However, the new Fe III model spectrum is consistent with the empirical template of Vestergaard & Wilkes (2001).

The Fe III template is usually included with the peak shift of CIII] free to vary in the interval 1908 – 1915 Å (see Martínez-Aldama et al. 2018). In the case the peak shift is around 1914 Å, the Fe III component may be representing more the λ 1914 line anomalously enhanced by Ly α fluorescence than CIII]. Considering the severe blending of these two lines, and the weakness of CIII] in Population A, the relative contribution of CIII] and Fe III λ 1914 cannot be measured properly. However, if the peak wavelength of the blend around CIII] is close to 1914 Å, the Fe III λ 1914 line was included in the fit;

- Si II λ 1816, usually fainter than Al III. This line is expected to be stronger in extreme Population A (Negrete et al. 2012);
- Fe II emission, modelled with a scaled and broadened theoretical template (Bruhweiler & Verner 2008; Martínez-Aldama et al. 2018). The Fe II_{UV} emission is never very strong around 1900 Å, and at any rate gives rise to an almost flat pseudo-continuum that is not affecting the relative intensity ratios of the Al III, SiIII], CIII] lines. A spiky feature around 1780 Å is identified with UV Fe II multiplet # 191 (Fe II λ 1785). In several extreme cases, attempting to scale the Fe II template to the Fe II λ 1785 intensity required large Fe II emission (Martínez-Aldama et al. 2018). In such cases the Fe II λ 1785 feature may have been selectively enhanced by Ly α fluorescence over the expectation of the Bruhweiler & Verner (2008) template. Considering the difficult assessment of the Fe II_{UV} emission, no measurements are reported in the present chapter.
- a blueshifted excess (BLUE) modelled with a blueshifted skew Gaussian. At high luminosity in the HE sample, there are 2 cases (HE0359-3959 and HE1347-2457) where a strong blueshifted component is obviously affecting the profile of the 1900 blend. Other cases are also detected in the WISSH sample (see §6.5.3 for the interpretation of the 1900 blend profiles involving a blue shifted excess). For two objects, the BLUE emission is overwhelming and masking the emission of the individual Al III, SiIII], CIII] broad components (Section 6.5.3). Otherwise, the appearance of the blend is not suggesting, even at the highest luminosity, the presence of

an outflow component spectroscopically resolved (i.e., of significant blueshifted emission as detected in CIV λ 1549). Small in Al III blueshifts do occur, but with amplitude \ll than their FWHM.

6.3.5 Full profile measurements

We assume that the symmetric and unshifted $H\beta_{BC}$ is the representative line components of the virialised part of the BLR. It is expedient to define a parameter ξ as follows:

$$\xi_{\text{line}} = \text{FWHM}_{\text{vir}}/\text{FWHM}, \quad (6.1)$$

where the FWHM_{vir} is the FWHM of the “virialised” component, in the following assumed to be $H\beta_{BC}$, and the FWHM is the FWHM measured on the full profile (i.e., without correction for asymmetry and shifts) of any line. In the case of $H\beta$, $\text{FWHM } H\beta \approx \text{FWHM } H\beta_{BC}$, and $\xi_{H\beta} \approx 1$ (Section 6.4.1). For the sake of this work, $H\beta$ and $H\beta_{BC}$ can be considered almost equivalent, so that we will rely on the $H\beta_{BC}$ — $H\beta$ decomposition obtained with `specfit` only in a few instances. The blue excess is usually faint with respect to $H\beta_{BC}$ and no empirical correction has been applied.

A goal of the present chapter is to derive ξ for Al III and CIII]. Similarly as for $H\beta$, the Al III lines are fit by symmetric functions. This approach has been applied in all cases and appears appropriate for the wide majority of spectra ($\approx 90\%$), where there is no evidence of a strong BLUE in Al III and the Al III peak position is left free to vary to account for small shifts that might be due to a spectroscopically-unresolved outflowing component. A few cases for which there is evidence of contamination by a strong blue shifted excess are discussed in Sect. 6.5.3.

6.3.6 Error estimates

The data used in this chapter come from an array of instruments yielding spectra with widely different S/N. In addition, the comparison is between two emission lines, one of which is relatively strong ($W(H\beta) \sim 100 \text{ \AA}$), and one faint ($W(\text{Al III}) \lesssim 10 \text{ \AA}$ in most cases). To make things worse, at low z the Al III line is also recorded on lower S/N spectra. These and other systematic differences have to be quantitatively taken into account in the error estimates. A quality parameter Q has been defined for Al III, $H\beta$, and CIII] as the ratio between the line equivalent width and its FWHM multiplied by the S/N ratio measured on the continuum. The Q values can be computed using the parameters reported in Tables 6.1 and 6.2. The systematic differences in the spectra covering Al III and $H\beta$ are reflected in the distribution of Q : $H\beta$ and Al III occupy two different domains (Figures in Appendix C.1). The corresponding fractional uncertainties in FWHM computed from dedicated Markov Chain Monte Carlo (MCMC) simulations or by defining a relation with the Q parameter as detailed in Appendix C.1 are significantly different for the two lines, being just a few percent in the FWHM of the narrowest sources with strong and sharp $H\beta$ and at worst $\approx 10\%$, but in the range $\approx 10\% — 50\%$ for Al III.

6.4 Results

6.4.1 Immediate results

The `specfit` analysis results are provided in form of an atlas (Appendix C.2) for the FOS^{*}, HE, ISAAC, and WISSH samples. The Al III and H β spectral range are shown after continuum subtraction, on a normalised flux scale (at 1700 and 5100 Å). The parameters measured with the `specfit` analysis or on the full profiles for H β , and Al III are reported in Table 6.2. Table 6.2 lists, in the following order: identification by IAU code name (Col. 1), rest-frame flux and equivalent width of the H β line (Cols. 2–3). The following columns (Cols. 4–6) report the H β profile parameters: FWHM H β , FWHM H β_{BC} , and shift. Here for shift s we intend the radial velocity of the line peak with respect to the rest frame as defined from the redshift measured in the H β spectral range; parameter R_{FeII} and spectral type (Cols. 7–8); rest-frame flux, equivalent width, FWHM and shift of the Al III line (Cols. 9–12). The FWHM refers to the individual component of the doublet, whereas flux and equivalent width W are measured over the full doublet; flux of Si III] (Col. 13); C III] flux and FWHM (Cols. 14–15). The Fe III flux measurement (Col. 16) was obtained by integrating the template over the range 1800 – 2150 Å. The upper limit of the wavelength range set at 2150 Å allows the inclusion of a broad feature peaking at $\approx 2050 - 2080$ Å and mostly ascribed to Fe III emission (Martínez-Aldama et al. 2018). Further information on the reported parameters are given in the Table footnotes. Errors on line widths have been computed from the numerical simulations described in Appendix C.1 or from the data listed in Tables 6.1 and 6.2 that yield Q . The same approach has been followed for errors on line intensities and line shifts.

The values of the H β FWHM for the WISSH quasars are fully consistent with those reported by Vietri et al. (2018) for all but two targets, namely SDSS J152156.48+520238.5 and SDSS J115747.99+272459.6, for which a discrepancy can be explained in terms of a different fitting technique. Intensity ratios computed between lines in the UV and the optical should be viewed with extreme care. The observations are not synoptical and were not collected with the aim of photometric accuracy.

6.4.2 FWHM H β vs. FWHM Al III

Fig. 6.2 shows the FWHM Al III vs FWHM H β full profile. The overall consistency in the FWHM of the two lines is rather obvious from the plot. In the case of Al III and H β , the Pearson's correlation coefficient is ≈ 0.785 ($P \sim 5 \cdot 10^{-8}$ of a chance correlation). A best fit with the ordinary least-squares (OLS) bisector yields

$$\text{FWHM Al III} \approx (273 \pm 216) + (0.933 \pm 0.059)\text{FWHM H}\beta. \quad (6.2)$$

The two lines are, on average, unbiased estimators of each other, with a 0 point offset that reflects the tendency of the Al III lines to be somewhat broader than H β but is not statistically significant (the offset by 250 km s⁻¹ is at less than 1 σ confidence level). An orthogonal LSQ fit yields slope and

offset consistent with the OLS. The normalised $\chi_v^2 \approx 1$ also indicates that the ratio between the FWHM of the two lines is 1 within the uncertainties. The maximum FWHM $\approx 6000 \text{ km s}^{-1}$ is observed for the sources of the highest luminosity (Section 6.4.4) and is below the luminosity-dependent FWHM limit of Population A.

Fig. 6.2 should be compared to Fig. 3 of Marziani et al. (2019, hereafter M19), where one can see that there is no obvious relation between the FWHM of C IV $\lambda 1549$ and the FWHM of H β . For the Pop. A sources C IV $\lambda 1549$ is systematically broader than H β , apart from in two cases in the HE sample, and FWHM(C IV $\lambda 1549$) shows a broad range of values for similar FWHM H β i.e., FWHM(C IV $\lambda 1549$) is almost degenerate with respect to H β . The C IV $\lambda 1549$ line FWHM values are so much larger than the ones of H β making it possible that the M_{BH} derived from FWHM C IV $\lambda 1549$ might be higher by even more than one order of magnitude than the one derived from the H β FWHM, as pointed out in several past works (Sulentic et al. 2007a; Netzer et al. 2007; Marziani & Sulentic 2012a; Mejía-Restrepo et al. 2016). We remark again that the Al III line may show a blueshifted excess in 6 sources in our sample, with convincing evidence in only two cases (Sect. 6.5.3) but that the line profile is otherwise well represented by a symmetric Lorentzian. In the case of a blueshifted excess, the good agreement between FWHM Al III and FWHM H β is in part due to the Si II $\lambda 1816$ emission that, if no blueshifted Al III emission is allowed, becomes very strong in the fit of the 6 sources, and compensate for the blueshifted excess. Si II $\lambda 1816$ is expected to be enhanced in the physical conditions of extreme sources (Negrete et al. 2012, Section 6.5.3). At the same time, including the Si II $\lambda 1816$ line in the fits allows for a standard procedure that does not require identification and a screening for the sources with a strong blueshifted excess, which apparently follow the correlation between Al III and H β full profile in Fig. 6.3.

6.4.3 Dependence on spectral type and R_{FeII}

FWHM

In Fig. 6.2 the data points are colour coded according to their original subsamples. Fig. 6.3 shows the joint sample FWHM Al III vs FWHM H β full profile colour-coded according to ST. There are systematic differences between the various STs, in the sense that A1 sources have Al III narrower than H β (at the relatively high confidence level of 2σ), and Al III and H β FWHM are almost equal for ST A2. The Al III and H β FWHM ratio is reversed, in the sense that H β is narrower than Al III, for STs A3 and A4 grouped together. The difference between STs is reinforced if only the BC of H β is considered (Fig. 6.4), since the FWHM H β_{BC} is slightly lower than the FWHM H β of the full H β broad profile, with $\xi_{\text{H}\beta} \approx 0.97 \pm 0.05$ on average, but $\xi_{\text{H}\beta} \approx 0.79$ for the spectral types A3 and A4. If we define $\xi_{\text{AlIII}} = \text{FWHM}(\text{H}\beta_{\text{BC}})/\text{FWHM}(\text{Al III})$, we have the following median values (\pm semi-interquartile range):

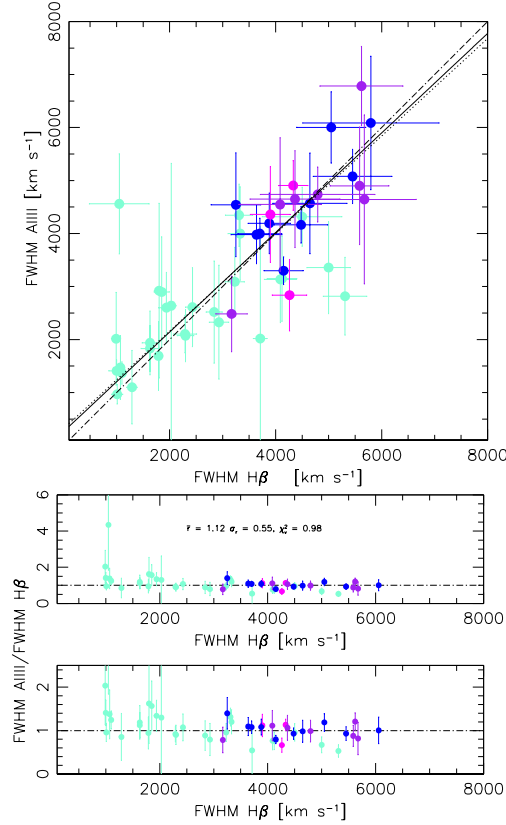


Fig. 6.2: Top panel: FWHM(AI III) vs. FWHM(H β) (full profiles) for the joint sample. Data points are colour-coded according to sub-sample: FOS * - aquamarine (\bullet), HE - blue (\bullet), ISAAC - magenta (\bullet), WISSH - purple (\bullet). Dot-dashed line: 1:1 relation; filled line: best fit obtained using the bisector technique; dotted line: best fit using the least orthogonal distance method (Press et al. 1992). Middle panel: ratio r of FWHM AI III over FWHM H β . The average ratio \bar{r} , the standard deviation σ_r and the normalised χ^2_v are reported. Bottom: same as the middle panel, with an expanded scale along the y axis.

ST	$\mu_{\frac{1}{2}}(1/\xi_{\text{AIII}}) \pm \text{SIQR}$
A3-A4	1.267 ± 0.223
A2	1.093 ± 0.176
A1	0.796 ± 0.158

A2 is the highest-prevalence ST in Population A, with $\xi \approx 1$. However, across Population A there is a significant trend that implies differences of $\pm 20 - 25\%$ with respect to unity. The A3-A4 result is after all not surprising, considering that quasars belonging to these spectral types with the strongest Fe II emission are the sources most affected by the high-ionisation outflows detected in the C IV $\lambda 1549$ line. The A1 result i.e., AI III lines narrower than H β by $\approx 20\%$ comes more as a surprise, and it is intriguing that it is consistent that also for the B Population AI III is narrower than H β (del Olmo et al., in preparation; Marziani et al. 2017b). This result may hint at a small but systematic extra broadening not associated with virial motions in A2.

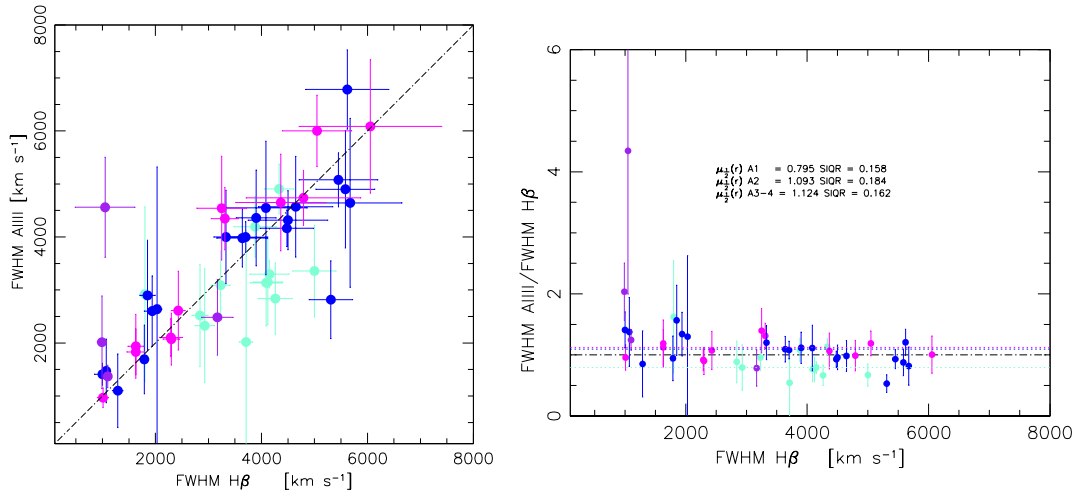


Fig. 6.3: Left panel: FWHM(AI III) vs. FWHM(H β) (full profiles) for the joint sample. Data points are colour-coded according to spectral type: A1 - aquamarine (\bullet), A2 - blue (\bullet), A3 - magenta (\bullet), A4 - purple (\bullet). Right: FWHM ratio between AI III and H β . The median ratio $\mu_{\frac{1}{2}}(r)$ =FWHM AI III/FWHM H β , and SIQR are reported for spectral types A1 and A2, and the union of A3 and A4.

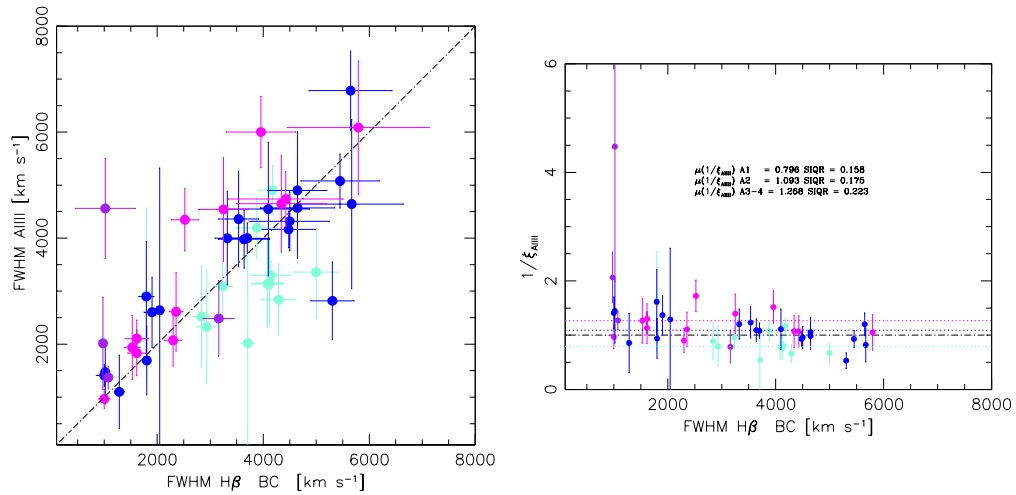


Fig. 6.4: Left panel: FWHM(AI III) vs. FWHM(H β_{BC}) for the joint sample. Data points are colour-coded according to spectral type as in Fig. 6.3. Right panel: FWHM ratio between AI III and H β_{BC} , $1/\xi_{AIII}$. The median ratio $\mu_{\frac{1}{2}}(1/\xi_{AIII})$ and the SIQR are reported for spectral types A1 and A2, and for the union of A3 and A4, as in Fig. 6.3.

Table 6.2: Observed spectrophotometric quantities and main sequence classification

IAU code	$H\beta$					R_{FeII}	SpT	Al III				SiIII]	CIII]		Fe III
	F	W	FWHM	FWHM BC	Shift			F	W	FWHM	Shift		F	FWHM	
(1)	(2)	(3)	(4)	(5)	(6)	(7)	(8)	(9)	(10)	(11)	(12)	(13)	(14)	(15)	(16)
FOS sample															
J00063+2012	544 ± 14	99	1790 ± 82	1802	-130 ± 20	0.527 ± 0.07	A2	92.5 ± 36.2	1.7	1691 ± 650	110 ± 200	316.8 ± 50.6	345.0 ± 29.0	800 ± 77	1579.8 ± 328.9
J00392-5117	103 ± 6	50	1290 ± 100	1283	-10 ± 20	0.842 ± 0.09	A2	8.9 ± 3.0	4.6	1100 ± 693	-90 ± 230	21.3 ± 5.1	50.9 ± 7.2	1634 ± 268	90.1 ± 12.3
J00535+1241	294 ± 12	45	1100 ± 64	1077	-30 ± 20	1.619 ± 0.06	A4	184.4 ± 17.2	7.2	1370 ± 212	-300 ± 160	321.5 ± 32.5	277.7 ± 102.3	1225 ± 324	857.8 ± 148.8
J00573-2222	741 ± 23	47	1070 ± 30	1019	0 ± 10	0.737 ± 0.06	A2	50.2 ± 9.0	1.6	1473 ± 602	-270 ± 240	125.8 ± 21.3	289.7 ± 46.3	1672 ± 224	184.9 ± 27.3
J01342-4258	35 ± 5	25	1050 ± 565	1019	40 ± 130	2.054 ± 0.25	A4	71.7 ± 16.6	5.2	4560 ± 945	-520 ± 570	48.6 ± 22.8	11.7 ± 3.0	5456 ± 959	250.6 ± 35.9
J02019-1132	122 ± 14	66	4500 ± 751	4500	30 ± 140	0.947 ± 0.15	A2	41.5 ± 5.5	2.4	4318 ± 558	250 ± 450	110.4 ± 40.5	173.3 ± 28.3	4318 ± 965	25.3 ± 4.6
J06300+6905	167 ± 6	140	5000 ± 410	4998	90 ± 80	0.281 ± 0.11	A1	137.1 ± 32.4	2.9	3358 ± 869	-480 ± 620	261.6 ± 126.6	1119.4 ± 182.0	2962 ± 504	225.0 ± 37.5
J07086-4933	74 ± 5	33	990 ± 86	980	40 ± 30	1.717 ± 0.11	A4	48.9 ± 17.3	2.2	2015 ± 874	-140 ± 620	120.0 ± 43.6	39.4 ± 10.4	2188 ± 432	429.1 ± 50.6
J08535+4349	73 ± 6	125	4090 ± 304	4080	230 ± 80	0.277 ± 0.13	A1	18.3 ± 3.6	3.5	3135 ± 816	500 ± 260	50.4 ± 18.5	59.2 ± 13.7	1889 ± 342	63.4 ± 12.7
J09199+5106	162 ± 9	106	5310 ± 411	5310	270 ± 80	0.878 ± 0.08	A2	23.6 ± 6.2	2.2	2817 ± 733	200 ± 630	55.3 ± 12.9	103.3 ± 26.7	3626 ± 507	135.4 ± 39.1
J09568+4115	393 ± 6	154	3710 ± 129	3710	180 ± 30	1.185 ± 0.08	A1	30.6 ± 10.7	1.9	2019 ± 2111	160 ± 430	50.1 ± 19.8	188.8 ± 31.2	1922 ± 354	157.2 ± 23.8
J10040+2855	135 ± 7	63	1940 ± 151	1900	-40 ± 40	0.953 ± 0.09	A2	84.3 ± 26.9	5.7	2602 ± 666	-70 ± 430	141.7 ± 32.2	140.7 ± 37.2	1943 ± 361	101.0 ± 16.6
J10043+0513	136 ± 7	90	1850 ± 143	1800	-110 ± 40	0.694 ± 0.08	A2	25.6 ± 9.6	6.2	2898 ± 1041	-60 ± 480	72.7 ± 19.3	73.7 ± 21.6	1828 ± 344	117.0 ± 20.5
J11185+4025	39 ± 1	83	2030 ± 95	2050	50 ± 20	0.588 ± 0.07	A2	36.7 ± 12.0	3.3	2638 ± 2688	230 ± 390	55.7 ± 21.8	95.5 ± 22.4	1963 ± 464	190.9 ± 24.6
J11191+2119	406 ± 17	147	3230 ± 179	3230	40 ± 20	0.439 ± 0.07	A1	180.9 ± 50.0	5.3	3089 ± 651	120 ± 390	413.7 ± 73.8	510.3 ± 92.2	2450 ± 437	883.6 ± 138.3
J12142+1403	644 ± 25	111	1800 ± 92	1800	80 ± 20	0.424 ± 0.06	A1	80.9 ± 34.7	2.9	2922 ± 1649	-160 ± 530	117.4 ± 39.1	349.3 ± 72.9	1609 ± 291	420.3 ± 77.8
J12217+7518	224 ± 11	135	4120 ± 280	4120	300 ± 30	0.255 ± 0.07	A1	69.1 ± 22.0	3.2	3149 ± 804	-310 ± 430	217.9 ± 45.6	226.4 ± 58.5	2246 ± 416	178.7 ± 29.4
J13012+5902	37 ± 2	57	3310 ± 257	2520	130 ± 60	1.365 ± 0.09	A3	136.0 ± 25.0	8.8	4347 ± 590	-160 ± 630	141.8 ± 42.1	74.0 ± 30.9	5215 ± 519	487.2 ± 95.7
J13238+6541	69 ± 4	94	2930 ± 182	2930	-80 ± 80	0.497 ± 0.07	A1	12.7 ± 6.9	1.4	2326 ± 1075	-320 ± 770	57.3 ± 19.0	160.5 ± 30.0	2076 ± 399	42.2 ± 6.9
J14052+2555	73 ± 4	91	2300 ± 158	2300	-90 ± 30	1.15 ± 0.08	A3	93.3 ± 28.3	4.8	2073 ± 491	480 ± 410	184.2 ± 38.2	42.7 ± 14.7	801 ± 155	559.7 ± 90.4
J14063+2223	70 ± 6	59	1630 ± 151	1530	-10 ± 30	1.1 ± 0.11	A3	33.1 ± 5.1	6.8	1937 ± 604	-180 ± 410	62.2 ± 12.1	31.2 ± 14.6	1703 ± 496	121.8 ± 26.8
J14170+4456	51 ± 6	63	2290 ± 217	1620	0 ± 70	1.182 ± 0.13	A3	57.6 ± 4.1	6.4	2104 ± 353	-80 ± 250	119.4 ± 20.4	121.7 ± 22.5	2010 ± 234	161.2 ± 22.0
J14297+4747	48 ± 2	151	2840 ± 153	2840	300 ± 30	0.392 ± 0.05	A1	14.7 ± 5.7	2.1	2519 ± 965	280 ± 490	29.5 ± 8.3	92.4 ± 19.5	1795 ± 325	79.2 ± 14.0
J14421+3526	114 ± 7	55	1630 ± 169	1610	-140 ± 20	1.357 ± 0.09	A3	105.8 ± 32.1	4.0	1832 ± 433	-260 ± 410	229.5 ± 46.9	448.2 ± 101.3	2007 ± 366	559.7 ± 90.4
J14467+4035	77 ± 3	74	2430 ± 131	2360	30 ± 30	1.327 ± 0.06	A3	62.4 ± 6.6	3.6	2611 ± 745	120 ± 360	142.6 ± 33.3	106.5 ± 27.7	2059 ± 435	373.6 ± 51.4
J15591+3501	121 ± 7	44	1010 ± 105	1000	100 ± 20	1.424 ± 0.10	A3	21.1 ± 2.7	3.3	967 ± 185	180 ± 340	64.3 ± 8.5	152.4 ± 20.2	1534 ± 239	150.4 ± 17.9
J21148+0607	86 ± 4	119	3330 ± 298	3320	0 ± 30	0.781 ± 0.08	A2	119.0 ± 34.2	9.3	3999 ± 883	10 ± 400	295.2 ± 55.0	297.1 ± 54.4	2995 ± 535	131.9 ± 20.9
J22426+2943	29 ± 2	47	1000 ± 149	1000	-20 ± 40	0.821 ± 0.15	A2	18.2 ± 2.5	1.7	1410 ± 207	-290 ± 370	52.3 ± 4.8	108.1 ± 28.9	1507 ± 344	75.2 ± 10.3
HE sample															
J00456-2243	229 ± 9	68	4150 ± 370	4146	190 ± 60	0.37 ± 0.10	A1	54.0 ± 4.7	4.1	3299 ± 261	10 ± 190	93.0 ± 16.0	230.0 ± 63.7	3295 ± 474	82.0 ± 15.1
J01242-3744	111 ± 10	48	3250 ± 469	3250	0 ± 100	1.155 ± 0.14	A3	102.0 ± 28.8	5.3	4543 ± 981	10 ± 390	94.0 ± 20.5	0.0	...	146.0 ± 23.0
J02509-3616	39 ± 3	44	4480 ± 504	4480	-20 ± 120	0.531 ± 0.13	A2	69.0 ± 4.9	3.1	4164 ± 345	20 ± 130	122.0 ± 13.8	18.0 ± 2.3	3990 ± 537	0.0
J04012-3951	88 ± 9	50	5049 ± 652	3957	-20 ± 80	1.103 ± 0.14	A3	70.0 ± 8.6	6.2	6003 ± 673	-150 ± 380	39.0 ± 9.9	17.0 ± 8.8	2052 ± 356	122.0 ± 16.9
J05092-3232	149 ± 8	67	3880 ± 403	3880	-130 ± 80	0.311 ± 0.10	A1	48.0 ± 6.8	4.3	4193 ± 574	-50 ± 450	96.0 ± 32.3	56.0 ± 15.4	2500 ± 467	34.0 ± 6.2
J05141-3326	228 ± 15	82	3702 ± 415	3700	0 ± 80	0.656 ± 0.07	A2	57.0 ± 5.6	7.5	3998 ± 291	20 ± 550	129.0 ± 39.0	67.0 ± 17.2	2255 ± 435	81.0 ± 15.4
J11065-1821	366 ± 35	121	4647 ± 702	4646	-50 ± 110	0.557 ± 0.11	A2	108.0 ± 29.6	4.9	4570 ± 951	0 ± 390	205.0 ± 37.1	113.0 ± 30.8	3138 ± 576	95.0 ± 14.8
J13506-2512	162 ± 29	37	6087 ± 1346	5795	0 ± 180	1.266 ± 0.23	A3	404.0 ± 101.9	9.5	6087 ± 1259	-1480 ± 620	269.0 ± 52.5	17.0 ± 9.6	2190 ± 652	543.0 ± 67.0
J21508-3158	120 ± 9	66	5452 ± 741	5450	0 ± 130	0.816 ± 0.10	A2	104.0 ± 13.1	7.0	5078 ± 513	-360 ± 190	139.0 ± 43.3	66.0 ± 19.0	4095 ± 696	75.0 ± 10.2
J23555-3953	318 ± 21	46	3639 ± 481	3640	0 ± 100	0.549 ± 0.08	A2	99.0 ± 8.9	3.2	3979 ± 547	0 ± 270	150.0 ± 27.0	0.0	...	370.0 ± 70.2
ISAAC sample															
J00570+1437	219 ± 15	86.3	3901 ± 377	3535	-20 ± 70	0.838 ± 0.10	A2	120.0 ± 32.7	10.2	4360 ± 904	-510 ± 380	99.0 ± 21.2	56.0 ± 16.7	3370 ± 637	57.9 ± 9.0
J13202+1420	122 ± 7	97.0	4262 ± 325	4290	-150 ± 80	0.282 ± 0.05	A1	45.0 ± 5.3	6.5	2838 ± 674	-710 ± 280	78.0 ± 23.9	96.0 ± 25.5	3282 ± 523	48.0 ± 7.8
J16149+1448	231 ± 21	91.5	4332 ± 277	4177	-80 ± 40	0.423 ± 0.10	A1	51.0 ± 4.5	4.1	4906 ± 470	30 ± 310	169.0 ± 21.9	128.0 ± 32.6	3499 ± 712	0.3 ± 0.04
WISSH sample															
J0801+5210	294 ± 36	71	5620 ± 784	5648	-128 ± 140	0.55 ± 0.15	A2	269.8 ± 22.6	10.7	6783 ± 747	-270 ± 400	285.3 ± 33.8	171.6 ± 47.0	4576 ± 934	49.3 ± 9.7
J1157+2724	87 ± 7	37	3169 ± 298	3161	-128 ± 100	1.68 ± 0.17	A4	26.4 ± 3.1	6.7	2484 ± 715	-560 ± 590	95.2 ± 11.4	66.6 ± 15.9	2913 ± 512	1.6 ± 0.2
J1201+0116	211 ± 23	59	4085 ± 779	4095	-134 ± 140	0.60 ± 0.15	A2	126.1 ± 16.6	9.0	4548 ± 814	-710 ± 620	141.0 ± 21.8	94.4 ± 23.8	3100 ± 770	2.4 ± 0.4
J1236+6554	141 ± 15	60	5674 ± 976	5669	225 ± 130	0.52 ± 0.12	A1	106.4 ± 35.2	5.3	4644 ± 1262	-520 ± 440	163.5 ± 39.5	3.5 ± 2.7	4317 ± 998	0.0
J1421+4633	214 ± 27	66	5584 ± 556	4646	-21 ± 140	0.99 ± 0.20	A2	174.5 ± 63.2	10.0	4901 ± 1594	-1030 ± 470	151.6 ± 44.5	0.0	...	251.0 ± 43.3
J1521+5202	188 ± 23	21	4366 ± 851	4343	81 ± 150	1.15 ± 0.18	A3	212.6 ± 27.9	4.1	4650 ± 914	-510 ± 760	271.8 ± 26.0	1.8 ± 0.5	1248 ± 385	251.7 ± 47.8
J2123-0050	296 ± 24	51	4793 ± 1082	4426	-61 ± 80	1.12 ± 0.11	A3	179.3 ± 20.6	6.6	4737 ± 518	-610 ± 340	218.6 ± 35.3	226.1 ± 53.0	4519 ± 703	23.7 ± 3.8

Notes.(1) JCODE identification of the object; (2) total flux of $H\beta$ (sum of all broad line components); (3) equivalent width of the full $H\beta$ profile, in Å; (4) FWHM $H\beta$ measured on the full profile, in km s^{-1} ; (5) FWHM $H\beta$ measured on the broad component ($H\beta_{BC}$), in km s^{-1} ; (6) peak shift of the $H\beta$ broad profile; (7) R_{FeII} parameter; (8) spectral type SpT following Sulentic et al. (2002); (9) total flux of the Al III doublet; (10) Al III equivalent width in Å; (11) FWHM of the individual line components of the Al III doublet; (12) shift of Al III, in units of km s^{-1} ; (13) flux of SiIII]; (14) flux of CIII]; (15) CIII] FWHM; (16) flux of Fe III computed over the range between 1800 – 2150 Å. All measurements are in the quasar rest frame and line fluxes are all in units of $10^{-15} \text{ erg s}^{-1} \text{ cm}^{-2}$.

Shifts

In addition to shifts with respect to the rest frame, we consider also the shift s^* defined as the radial velocity difference between the peak position of the Lorentzian function describing the individual components of the Al III doublet with respect to the quasars rest frame and the peak position of H β and (reported in Table 6.2) i.e., $s^*(\text{AlIII}) = s(\text{AlIII}) - s(\text{H}\beta)$. We adopt this definition because the spectral resolution and the intrinsic line width make it difficult to resolve the outflow in the Al III profile. In the C IV $\lambda 1549$ and H β profiles, and even in the ones of Mg II $\lambda 2800$, it is possible to isolate a blue-shifted excess that contributes most of the C IV $\lambda 1549$ flux in several cases, superimposed to a symmetric profile originating in the low ionisation part of the BLR. In the case of Al III, this approach is more difficult, in part because of the low S/N (a blueshifted contribution as faint as the one of H β would be undetectable for Al III, especially in the FOS spectra), in part because of the intrinsic rarity of sources with a strong blue-shifted excess. In addition, the H β_{NC} is often overwhelmed by the H β_{BC} , making it difficult to accurately measure its width and shift. The shifts of H β broad profile with respect to the rest frame set by the H β_{NC} are usually modest, and the median is consistent with 0, $\mu(s(\text{H}\beta)) \approx 0 \pm 65 \text{ km s}^{-1}$. The shift estimators s^* and s therefore yield results that are in close agreement.

Fig. 6.5 shows that the s^* amplitude is relatively modest for spectral type A3. ST A4 shows a larger shift, associated with an increase in the FWHM Al III with respect to H β , although with a large scatter. This is due to an outstanding case, HE0132-4313, a NLSy1 with FWHM Al III / FWHM H $\beta \approx 5$, a behaviour frequent for the C IV $\lambda 1549$ in strong Fe II emitters but apparently rarer for Al III.

Taken together, the FWHM and shift data suggest that major discrepancies are more likely for the relatively rare, stronger Fe II emitters, ST A3 and A4. The left panel of Fig. 6.5 shows that only A4 has a median shift that is significantly different from 0. A4 sources are relatively rare sources (4 in our sample, and $\approx 3\%$ in M13a). In addition to the shift amplitude in km s^{-1} , the line shift normalised by line width may be a better description of the “dynamical relevance” of the outflowing component (Marziani et al. 2013b). The parameters $\delta(\frac{i}{4}) = c(\frac{i}{4}) / \text{FWHM}(\frac{i}{4})$, $i = 1, 2, 3$, yield the centroids $c(\frac{i}{4})$ at fractional peak intensity $\frac{i}{4}$ normalised by the full width at the same fractional peak intensity $\text{FWHM}(\frac{i}{4})$. In the case of the Al III shifts as defined above, δ can be approximated as $\delta(\text{AlIII}) \approx s(\text{AlIII}) / \text{FWHM}(\text{AlIII})$. The values of the $|\delta \text{ Al III}|$ are $\lesssim 0.05$ (right panel of Fig. 6.5) save in the case of spectral type A4 where $\delta \approx -0.1$.

6.4.4 Dependence on luminosity

FWHM

An important clue to the interpretation of the Al III broadening is provided by the trends with luminosity. Fig. 6.6 shows FWHM Al III vs. FWHM H β with data points colour-coded according to luminosity. There is no significant deviation from equality for the FWHM of H β and Al III. At higher luminosity, both the Al III and the H β line become broader, and the largest line widths are measured on the ESO, ISAAC and WISSH samples. The ratio $r = \text{FWHM Al III} / \text{FWHM H}\beta \approx 1/\xi$ also does

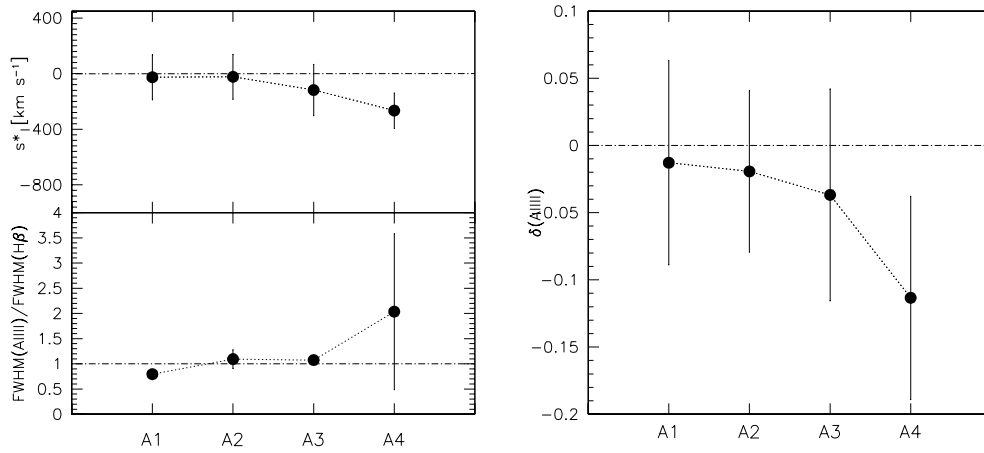


Fig. 6.5: Left, upper panel: behaviour of shift s^* of Al III with respect to rest frame as a function of the spectral type. Reported values are sample medians and error bars are SIQR. Left bottom panel: same, for the ratio FWHM Al III over FWHM H β . Right: parameter $\delta(\text{Al III})$ as a function of spectral type.

not depend on luminosity: dividing the sample by about one half at $\log L_{1700} = 46$ [erg s⁻¹] yields median r values for the subsamples above and below this limit that are very close to 1 (left panel of Fig. 6.6).

The statistical equality between FWHM H β and FWHM Al III is not breaking down at any luminosity, at least within the limit sets by our sample and data quality. The explanation resides in the fact that both line FWHM increase in the same way with luminosity, as shown by the left, top panel of Fig. 6.7. The trends for H β , Al III, and CIII] alike (CIII] is discussed in Section 6.4.5) can be explained if the broadening of the line is basically set by the virial velocity at the luminosity-dependent radius of the emitting region, $r_{\text{BLR}} \propto L^{\frac{1}{2}}$. Under the standard virial assumption, we expect that $\text{FWHM}(\text{H}\beta) \propto M_{\text{BH}}^{\frac{1}{4}} (L/L_{\text{Edd}})^{-\frac{1}{4}} f_{\text{S}}(\theta)^{-\frac{1}{2}}$, with f_{S} assumed to be mainly dependent of the angle θ between the accretion disk axis and the line of sight (Mejía-Restrepo et al. 2018a). Equivalently, $\text{FWHM}(\text{H}\beta) \propto L^{\frac{1}{4}} (L/L_{\text{Edd}})^{-\frac{1}{2}} f_{\text{S}}(\theta)^{-\frac{1}{2}}$. While L/L_{Edd} is changing in a narrow range (0.2 — 1) and f_{S} is also changing by a factor a few, M_{BH} is instead spanning around 4 orders of magnitude. Over such a broad ranges of masses or, alternatively, luminosity, we might expect that the dominant effect in the FWHM increase is associated right with mass or luminosity. In Fig. 6.7 the trend expected for $\text{FWHM}(\text{H}\beta) \propto L^{\frac{1}{4}}$ is overlaid to the data points, and is consistent with the data in the luminosity range $44.5 \lesssim \log L_{1700} \lesssim 47.5$ [erg s⁻¹], where a five-fold increase of the FWHM of both H β and Al III is seen.

Shift

The blueshifts involve radial velocities that are relatively modest (right panel of Fig. 6.7). Al III shifts exceed 1000 km s⁻¹ only in two cases of extreme luminosity. Even if we see some increase toward higher s values in the highest luminosity range, several high-luminosity sources remain unshifted within the uncertainties. If we consider the dependence of shifts on luminosity, at high L there is an

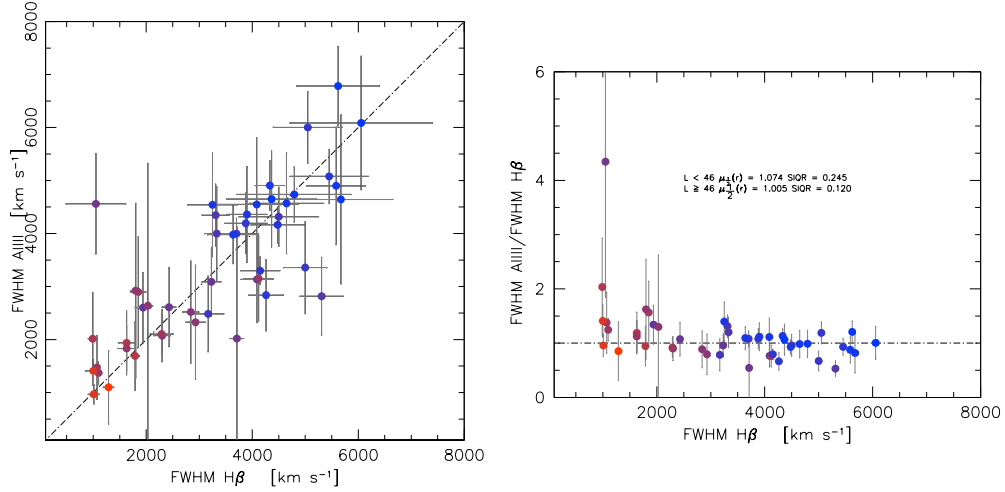


Fig. 6.6: Left panel: FWHM(Al III) vs. FWHM(H β) for the joint sample. Data points are colour-coded according to luminosity at 1700 Å, from red (lowest; $\log L_{1700} \sim 44$) to blue (highest; $\log L_{1700} \sim 47$). Right panel: FWHM ratio of Al III and H β . The median ratios $\mu_{1/2} r$ and the SIQR r are reported for more luminous ($\log L \geq 46$ [erg/s]) and less luminous ($\log L < 46$) quasars.

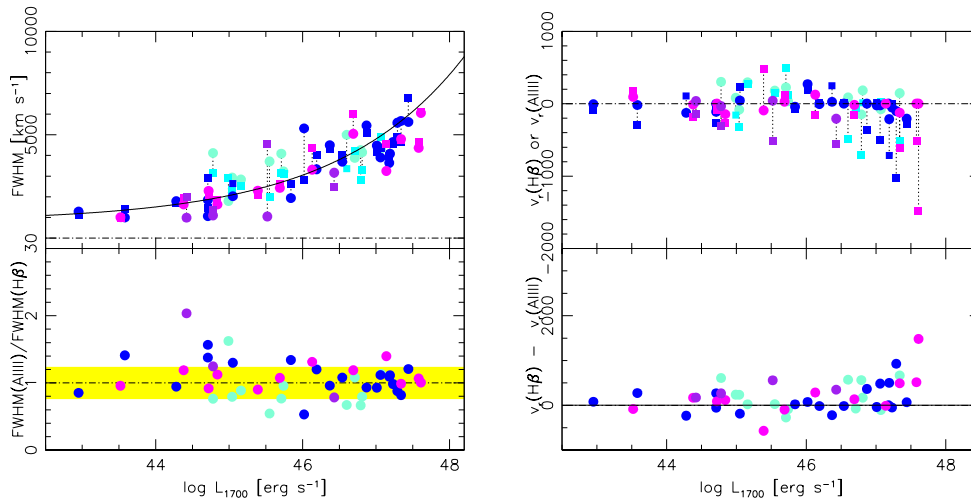


Fig. 6.7: H β and Al III profile parameter comparison as a function of luminosity. Left panel: behaviour of FWHM Al III and H β (upper half) and of the ratio FWHM(Al III)/FWHM(H β) as a function of $\log L$ at 1700 Å. The filled line traces the expected increase of the FWHM in a virialised system with $L^{\frac{1}{4}}$. The data point are identified on the basis of spectral type as in Fig. 6.3. The yellow band marks the region where FWHM(Al III)/FWHM(H β)=1 within the errors: the median value of the uncertainty of the ratios, $\approx \pm 25\%$. Right panels: shifts of H β and Al III (upper half), and their difference s^* as a function of $\log L(1700)$ (lower half). The vertical dotted lines join H β and Al III parameters for the same object (e.g., they are not error bars).

increase in the range of blueshifts involving values that are relatively large (several hundred km s^{-1} ; Fig. 6.7). The parameter δ as a function of L has a more erratic behaviour (Fig. 6.8), but only at the highest L $\delta \approx -0.1$, and the effect of the line shift is at a 10% level. Fig. 6.8 is consistent with Al III blueshifts becoming more frequent and of increasing amplitude with luminosity.

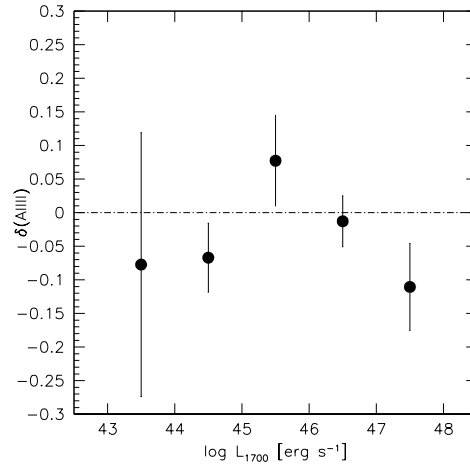


Fig. 6.8: Parameter $\delta(\text{Al III})$ as a function of luminosity. Median values are plotted for 1 dex luminosity intervals. Error bars are sample SIQR.

6.4.5 FWHM $\text{H}\beta$ and FWHM C III]

The C III] line has been considered as a possible virial broadening estimator, and has been a target of reverberation mapping monitoring (Trevese et al. 2007, 2014; Lira et al. 2018; Kaspi et al. 2021). The problem in Population A is that C III] shows a strong gradient in its intensity. In spectral type A1, C III] is by far the strongest line in the 1900 Å blend, but its prominence decreases with increasing $R_{\text{Fe II}}$, i.e., going toward spectral type A3 (Bachev et al. 2004). In spectral types A3 and A4 C III] is affected by the severe blending with Si III] and Fe III emission (much more severe than for Al III), and may become so weak to the point of being barely detectable or even undetectable (Vestergaard & Wilkes 2001; Negrete et al. 2014; Temple et al. 2020; Bachev et al. 2004; Martínez-Aldama et al. 2018). In addition, the C III] line has a rather low critical density, and its intensity is exposed to the vagaries of density and ionisation fluctuations much more than Al III , whose emission is highly efficient in dense gas over a broad range of ionisation levels (Marziani et al. 2020, and Sect. 6.5.3). The measurements of the C III] width might be inaccurate in extreme Population A if Fe III contamination is strong. It is therefore legitimate to expect a greater dispersion in the width relation of C III] with $\text{H}\beta$.

The FWHM of C III] is shown against the FWHM of $\text{H}\beta$ full profile in Fig. 6.9, left panel. Error bars show uncertainties computed following the prescription of Appendix C.1. Not surprisingly, the scatter in the FWHM ratio between C III] and $\text{H}\beta$ is larger than in the case of Al III . The right and left (top) panels of Fig. 6.9 show that there is a significant deviation from unity, although for relatively narrow profiles around 2000 km s^{-1} the FWHM C III] is close to the 1:1 line. The χ^2_ν is much higher than 1. The bottom panel shows the ratio between FWHM C III] and FWHM $\text{H}\beta$ colour-coded according to C III] strength. The limit was set at normalised intensity (roughly equal to equivalent width) $I = 10$. The trend for sources above this limit implies $\text{FWHM C III]} = \xi_{\text{C III]}} \text{FWHM H}\beta \approx 0.77 \text{ FWHM H}\beta$.

We did not detect any strong difference in the trend with luminosity of $\text{H}\beta$ and C III] FWHM, as it has been the case for $\text{H}\beta$ and Al III . The two lines follow a similar trend with luminosity at 1700 Å

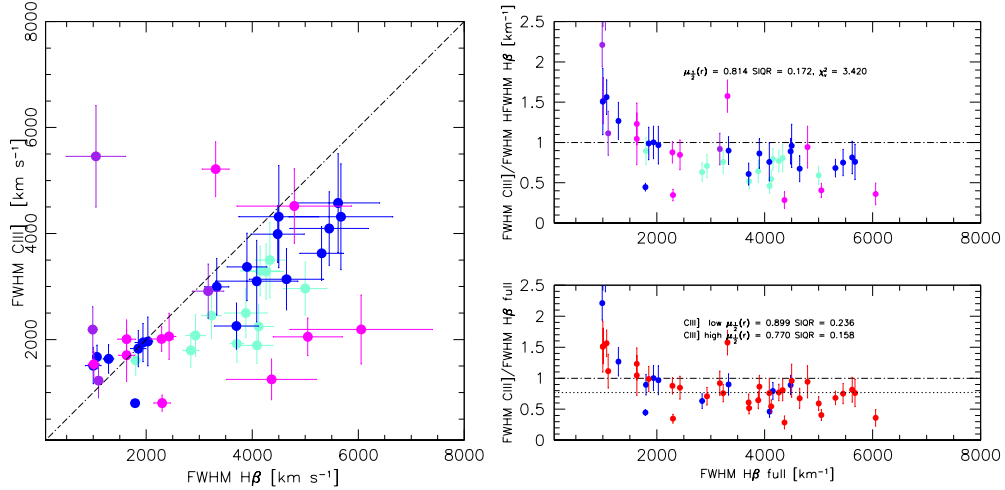


Fig. 6.9: Left panel: FWHM(CIII)] vs. FWHM(H β) for the joint sample. Data points are colour-coded according to spectral types, as for Fig. 6.3. Right, top panel: FWHM ratio of CIII] and H β , The median ratio $\mu_{\frac{1}{2}}(r)$, with $r = \text{FWHM CIII]}/\text{FWHM H}\beta$, and the SIQR are reported. Right, bottom panel: same ratio with the data colour-coded according to CIII] intensity: normalised intensity > 10 (red) and ≤ 10 (blue). Values of $\mu_{\frac{1}{2}}(r)$ and SIQR are reported for stronger and weaker CIII] emitters.

(Fig. 6.10). No shift analysis was carried out for CIII] due to the severe blending with SiIII] and Fe III.

The narrower profile of CIII] indicates a higher distance from the central continuum source than the one obtained from H β , if the velocity field is predominantly virial (Peterson & Wandel 2000). This result is also consistent with the findings of Negrete et al. (2013) who, using CIII] intensity ratios in a photoionisation estimate of the emitting region radius, obtained much larger radii than the ones obtained from reverberation mappings of H β .

6.4.6 A M_{BH} scaling law based on Al III

The goal is to obtain an M_{BH} estimator based on Al III that is consistent with the scaling law derived for H β . In this context, the process is much simpler than in the case of C IV $\lambda 1549$, where large blueshifts introduced a significant correction and a second-order dependence on luminosity of FWHM C IV $\lambda 1549$ could not be bypassed. The H β and Al III widths of the two lines grow in a similar trend with L (Fig. 6.7). The M_{BH} scaling law can be derived in the form $\log M_{\text{BH}} = \alpha \cdot \log L + 2 \cdot \log \text{FWHM} + \gamma$ by minimising the scatter and any systematic deviation of M_{BH} estimated from Al III with respect to the H β -derived masses from the Vestergaard & Peterson (2006) scaling law:

$$\log M_{\text{BH}}(\text{H}\beta) \approx 0.5 \log L_{5100,44} + 2 \log(\text{FWHM}(\text{H}\beta)) + 0.91, \quad (6.3)$$

where $L_{5100,44}$ is the rest frame luminosity λL_{λ} at 5100 Å in units of $10^{44} \text{ erg s}^{-1}$, and the FWHM H β is in km s^{-1} , considering that no correction is needed to FWHM Al III (i.e., $\xi_{\text{Al III}} \approx 1$). The

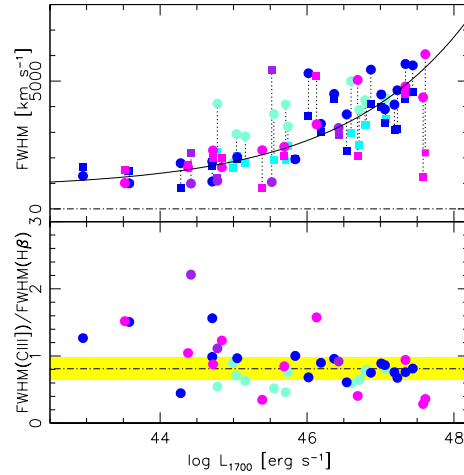


Fig. 6.10: $H\beta$ and CIII] profile parameter comparison as a function of luminosity. Top panel: Behaviour of FWHM CIII] and $H\beta$ (upper half) and of the ratio $\text{FWHM}(\text{CIII]})/\text{FWHM}(\text{H}\beta)$ as a function of $\log L$ at 1700 \AA . The data point are colour-coded on the basis of spectral type. As in Fig. 6.7, the filled line traces the expected increase of the FWHM in a virialised system with $L^{\frac{1}{4}}$. The yellow band marks the region where $\text{FWHM}(\text{C IV } \lambda 1549)/\text{FWHM}(\text{H}\beta) \approx 0.8$ within the errors. The width of the band has been set by the median value of the uncertainty of the ratios, ± 0.17 . The vertical dotted lines join $H\beta$ and Al III parameters for the same object.

Vestergaard & Peterson (2006) scaling law is a landmark that has been applied in hundreds of quasar studies. However, the Vestergaard & Peterson (2006) $H\beta$ scaling law provides individual estimates with large error bars in relative estimates (≈ 0.5 dex at 1σ , see the discussion in their chapter). This is a limit to the precision of any scaling law based on the match with the one based on $H\beta$. The large error bars of individual mass estimates can be mainly explained on the basis of orientation effects (M19) and of trends along the spectral types of the main sequence (Du & Wang 2019).

If this condition is enforced, the relation between M_{BH} from Al III and from $H\beta$ (Fig. 6.11) can be written as:

$$\log M_{\text{BH}}(\text{AlIII}) \approx (1.000 \pm 0.043) \log M_{\text{BH}}(\text{H}\beta) - (0.001 \pm 0.367). \quad (6.4)$$

The Al III scaling law takes the form, with the FWHM in km s^{-1} :

$$\log M_{\text{BH}}(\text{AlIII}) \approx (0.579^{+0.031}_{-0.029}) \log L_{1700,44} + 2 \log (\text{FWHM}(\text{AlIII})) + (0.490^{+0.110}_{-0.060}), \quad (6.5)$$

with an rms scatter $\sigma \approx 0.29$. Figure 6.11 suggests the presence of a well-behaved distribution with a few outlying points. The relation of Eq. 6.5 considers the FWHM of 47 sources. One data point has been excluded applying a σ clipping algorithm (the one A4 outlier, HE0132-4313). This selective procedure is justified by the fact that only some of the most extreme sources of Population A (not all of them) show large blueshifts and only one (HE0132-4313) a FWHM in excess to $H\beta$ by a large factor, deviating at more than 3 times the sample rms. Removal of HE0132-4313 provides however only a minor, not significant change in the fitting parameters. The scaling law parameter

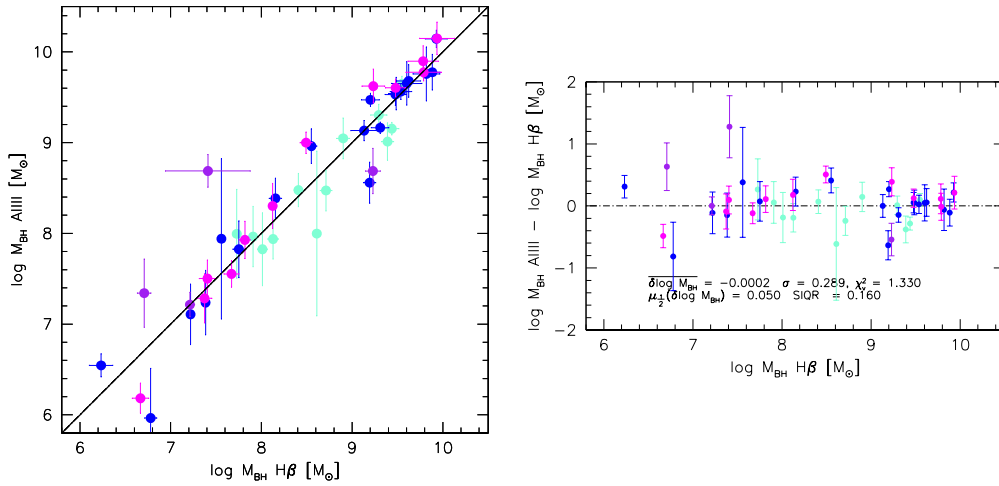


Fig. 6.11: Decimal logarithm of black hole mass in units of solar masses computed from the relation of Vestergaard & Peterson (2006) based on FWHM H β vs. the one computed from the Al III FWHM following Eq. 6.5, with sub-samples identified by colour according to their spectral types. The filled line traces Eq. 6.4, while the dot-dashed line is the equality line. The right panel shows the residuals as a function of the M_{BH} derived from H β . Average values of the $\log M_{\text{BH}}$ differences, standard deviation and normalised χ^2_{ν} are reported for the joint sample minus one outlier with $\delta > 1$ (top row). The bottom rows yields the median and the SIQR.

uncertainties have been estimated computing the coefficients α and γ over a wide range of values and defining the interval where agreement between M_{BH} from H β and Al III (Eq. 6.4) is satisfied within $1.00 \pm 1\sigma$ for the best-fitting slope and $0.00 \pm 1\sigma$ for the intercepts (respectively ≈ 0.043 and ≈ 0.367 , as per Eq. 6.4). Due to some scatter in FWHM relation at FWHM H $\beta_{\text{BC}} \sim 1000 \text{ km s}^{-1}$ and the possibility of predominantly face-on orientation (Mejía-Restrepo et al. 2018a) the M_{BH} estimates at $M_{\text{BH}} \lesssim 10^7 M_{\odot}$ should be viewed with care due to the paucity of data points.

It is important to remark that this result, unlike the one on CIV $\lambda 1549$ M_{BH} estimates, is obtained without any correction on the measured FWHM. The Al III and H β relation should be considered equivalent with respect to M_{BH} estimates in large samples of Population A sources. No scaling law $r_{\text{BLR}} - L$ has been ever derived from reverberation mapping on the Al III lines. However, it is reassuring that the luminosity exponent ($\approx 0.579^{+0.031}_{-0.029}$) deviates by about 1σ from the one entering the scaling law $r_{\text{BLR}} - L$ derived by Bentz et al. (2013) for H β .

6.4.7 A M_{BH} scaling law based on CIII]

An approach analogous to the one adopted for Al III was also applied to CIII]. The goal is to obtain an M_{BH} estimator based on CIII] that is consistent with the scaling law derived for H β . The process is again much simpler than in the case of CIV $\lambda 1549$, where large blueshift introduced a significant correction and a second-order dependence on luminosity of FWHM CIV $\lambda 1549$ could not be bypassed. Considering that only a very simple correction is needed to FWHM CIII], $\xi_{\text{CIII]}} \approx 1.25$, the M_{BH} scaling law can be derived in the form $\log M_{\text{BH}} = \alpha \cdot \log L + 2 \cdot \log \xi_{\text{CIII]}} \text{FWHM} + \gamma$ by minimising

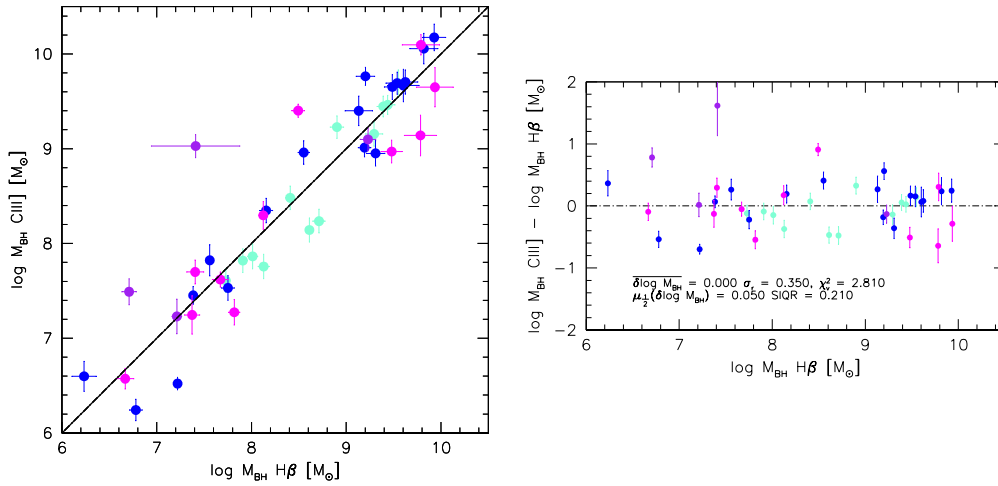


Fig. 6.12: Decimal logarithm of black hole mass in units of solar masses computed from the relation of Vestergaard & Peterson (2006) based on the $H\beta$ spectral range vs. the one computed from the CIII] data following Eq. 6.7, with spectral types colour-coded as in Fig. 6.3. As for Fig. 6.11, the filled line traces Eq. 6.6, while the dot-dashed line is the equality line. The right panel shows residuals as a function of M_{BH} derived from $H\beta$. Average, standard deviation, and χ^2_ν of the $\log M_{\text{BH}}$ difference are reported on the top-row of the inside caption; the bottom row reports median and SIQR.

the scatter and any systematic deviation of M_{BH} estimated from CIII] with respect to the $H\beta$ -derived masses. Figure 6.12 suggests the presence of a well-behaved distribution with a few outlying points. The condition

$$M_{\text{BH}}(\text{CIII])} \approx (1.000 \pm 0.053)M_{\text{BH}}(H\beta) + (0.000 \pm 0.454) \quad (6.6)$$

is satisfied if the CIII] scaling law takes the form:

$$\log M_{\text{BH}} \text{ CIII]} \approx (0.6765 \pm 0.0450) \log L_{1700,44} + 2 \log (\xi_{\text{CIII]} \text{FWHM}(\text{CIII]))} + (0.332 \pm 0.120), \quad (6.7)$$

with an rms scatter $\sigma \approx 0.35$ (excluding 1 outlier, for 44 objects). The scaling law parameter uncertainties have been estimated varying the coefficients α and γ as for the Al III case.

The M_{BH} CIII] scaling law is derived with a simple correction on the measured FWHM CIII]. The CIII] and $H\beta$ relation should be considered equivalent with respect to M_{BH} estimates in large samples of Population A sources. Care should however be taken to consider sources in which CIII] can be measured ($W \gtrsim 10\text{\AA}$) and to identify extreme objects, as discussed in Section 6.5.3. In addition, the heterogeneity of the sample and the possibility of different trends in different FWHM domains ($\text{FWHM}(\text{CIII])} \approx \text{FWHM}(H\beta)$ if $\text{FWHM} \lesssim 3000 \text{ km s}^{-1}$) makes the scaling law with Al III more reliable.

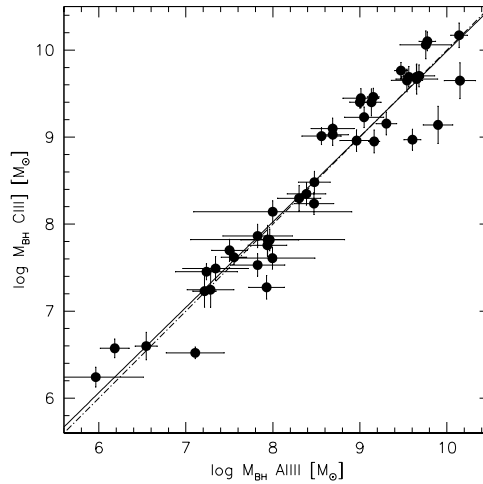


Fig. 6.13: Decimal logarithm of black hole mass in units of solar masses computed from the scaling law based on FWHM CIII] (Eq. 6.7) vs. the one computed from the Al III FWHM following Eq. 6.5. The filled line traces an unweighted least square fit; the dot-dashed line is the equality line.

6.5 Discussion

In the following we first compare the scaling laws obtained for Al III and CIII] (Sect. 6.5.1). The present work detects systematic shifts of Al III toward the blue. Even if they are on average slightly above the uncertainties, it is interesting to analyse them in the context of systematic shifts affecting the prominent high and low-ionisation lines of C IV λ 1549 and Mg II λ 2800 (Section 6.5.2), and to consider more in detail sources in the spectral type where Al III are broader than the H β ones (Section 6.5.3).

6.5.1 Consistency of scaling laws

The scaling laws derived for Al III and CIII] are mutually consistent. Black hole mass estimates are shown in Fig. 6.13. An unweighted lsq fit yields slope 0.975 ± 0.043 , consistent with unity, and intercept 0.246 ± 0.371 , with an rms scatter ≈ 0.302 . The median difference of the mass values obtained with the two scaling laws is $\mu(\log M_{\text{BH}}(\text{CIII]}) - \log M_{\text{BH}}(\text{AlIII})) \approx 0.06 \pm 0.20$ (SIQR).

The $r_{\text{BLR}} - L$ implicit in Eq. 6.6 is consistent with the $r_{\text{BLR}} - L$ relation derived for C IV λ 1549 in a previous study (Trevese et al. 2014), and only slightly higher than the one derived in the early study of Kaspi et al. (2007, $\alpha \approx 0.52 - 0.55$, c.f. Kaspi et al. 2021). More high S/N spectroscopic observations, including monitoring, should be carried out to explore the full potential of the 1900 Å blend lines and especially of CIII] as VBEs.

The scaling law derived from the Al III line is consistent with the C IV λ 1549-based scaling law (M19): Fig. 6.14 indicates only a slight bias (less than the SIQR ≈ 0.2 dex, and the rms ≈ 0.3 dex), as the C IV λ 1549 scaling law apparently overestimates the M_{BH} by $\approx 20\%$ and $\approx 40\%$ with respect to the M_{BH} estimates based on Al III and H β , respectively. Considering that the C IV λ 1549-based scaling law requires a large correction (ξ_{CIV} can be as low as ≈ 0.2) to the C IV λ 1549 FWHM dependent on

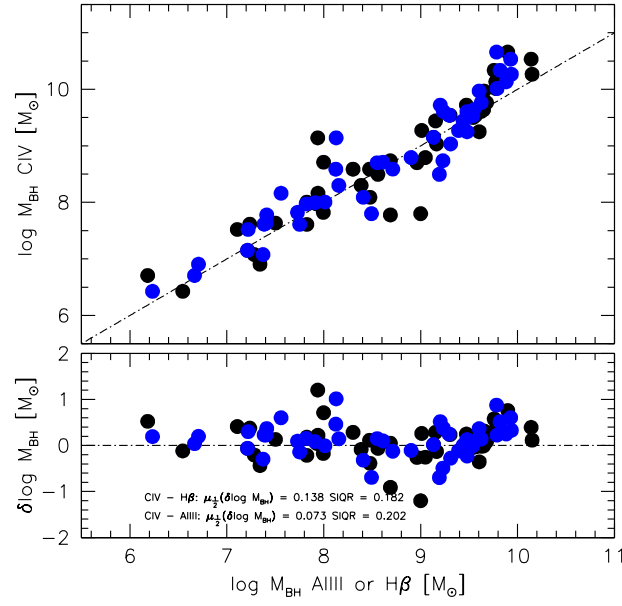


Fig. 6.14: Decimal logarithm of black hole mass in units of solar masses computed from the CIV λ 1549-based scaling law of M19 vs the ones computed from the relation of Vestergaard & Peterson (2006) based on FWHM H β (blue) and from the Al III FWHM following Eq. 6.5 (black). The dot-dashed is the equality line. The bottom panel shows the residuals as a function of M_{BH} . Median and SIQR of the $\log M_{\text{BH}}$ differences $\delta \log M_{\text{BH}} = \log M_{\text{BH}} \text{ CIV} - \log M_{\text{BH}} \text{ Al III}$ and $\delta \log M_{\text{BH}} = \log M_{\text{BH}} \text{ CIV} - \log M_{\text{BH}} \text{ H}\beta$ are reported in the inside caption.

both line shift and luminosity, the Al III scaling law should be preferred in case observations of both CIV λ 1549 and Al III are available.

6.5.2 Shifts of Al III vs shifts of CIV λ 1549 and MgII λ 2800

Fig 6.15 shows the Al III peak shifts reported in Table 6.2 vs. the centroid at half maximum of CIV λ 1549 from S07, S17, Deconto-Machado et al. (2022, in preparation), and the “peak” shift given by Vietri et al. (2018) for the four subsamples of the present work. The Al III shift is usually very modest, and a factor of ~ 10 lower than the shift measured for CIV λ 1549. The Al III and CIV λ 1549 shifts are however significantly correlated (Pearson’s correlation coefficient ≈ 0.54 , with a significance $P \approx 1. - 2 \cdot 10^{-3}$):

$$s(\text{AlIII}) \approx (0.114 \pm 0.026)c\left(\frac{1}{2}\right)(\text{CIV}) + (50.0 \pm 68.5)\text{km s}^{-1}. \quad (6.8)$$

The slope is shallow, but the correlation indicates that the shifts in Al III and CIV λ 1549 are likely to be due to the same physical effect. If we ascribe the small displacements observed in the peak shift s of Al III to the effect of outflows, the outflow prominence is much lower than in the case of CIV λ 1549, both in terms of radial velocity values and of δ .

As mentioned, CIV λ 1549 shifts and FWHM are correlated, implying that the broader the line, the higher the shift amplitude becomes (Coatman et al. 2016; Sulentic et al. 2017). The Al III shows a

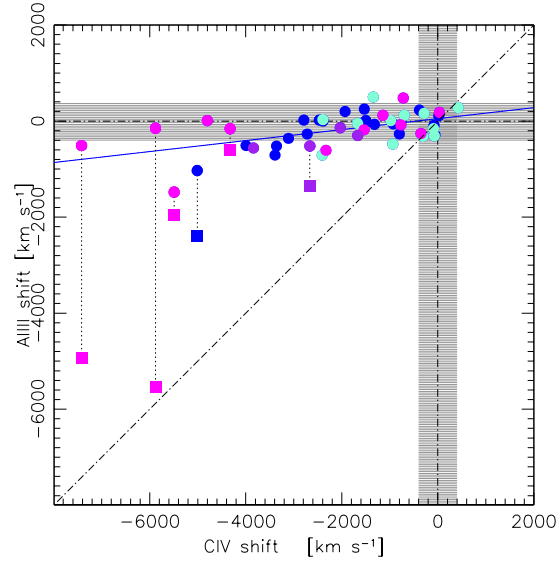


Fig. 6.15: Shift s of Al III vs shift of CIV $\lambda 1549$ with respect to rest frame. Data points are identified according to the spectral type, with the same color code of Fig. 6.3. The filled and dot-dashed lines trace an unweighted least square fit and the equality line, respectively. The grey bands identify uncertainties ranges in radial velocity $\pm 400 \text{ km s}^{-1}$ where the lines are not significantly shifted. Squares refer to the $c(\frac{1}{2})$ Al III in the case the excess emission on the blue side of Al III has been ascribed to Al III. See Section 6.5.3.

consistent behavior, but apparently masked by the much lower shift amplitudes; the presence of Al III blueshifts appears to be statistically significant at very high luminosity, and for spectral type A3 and A4. When CIV $\lambda 1549$ shows large blueshifts i.e., for high R_{FeII} or very high luminosity, the Al III line becomes broader than $\text{H}\beta$ (even if the two lines remain in fair agreement). We see a relation between Al III line shift and widths: in ST A3 and A4, where shifts are larger, the Al III FWHM exceeds the one of $\text{H}\beta$ (Figure 6.5).

The Al III and CIV $\lambda 1549$ results on line shifts are also consistent with the ones obtained for MgII $\lambda 2800$. Small amplitude blueshifts of a few hundreds km s^{-1} were measured on the full line profile of MgII $\lambda 2800$ (Marziani et al. 2013b). For MgII $\lambda 2800$ the separation of a BLUE component and a symmetric Lorentzian has been possible on median composite spectra because of the high S/N and of the peaky line core of the MgII $\lambda 2800$ line. The same operation is not feasible for individual Al III profiles that are often significantly affected by noise, and in some cases even barely above noise. The Al III, CIV $\lambda 1549$ and MgII $\lambda 2800$ are all resonance lines that may be subject to selective line-driven acceleration (Murray & Chiang 1997; Proga 2007; Risaliti & Elvis 2010). The different velocity amplitudes most likely reflect the difference in the line emitting region distance from the continuum source and in physical properties, such as ionisation parameter, density and column density.

Rare sources with large shift amplitudes in Al III are expected to be intrinsically infrequent even at the redshift where luminous quasars were fairly common ($z \approx 1.5 - 2$) and, even if over-represented because of a Malmquist-type bias, they are outstanding and pretty easily recognisable, especially in large samples of AGN (Sect. 6.5.3). The most striking case directly resembling CIV $\lambda 1549$ is the one

of HE0132-4313 which is an object of fairly low luminosity and an outlier in the plots FWHM Al III vs FWHM H β . Sources with large shift amplitude may be excluded or flagged if black hole mass estimates are being carried out.

6.5.3 xA quasars

There are 16 sources meeting the criterion $R_{\text{FeII}} \geq 1$ in the joint sample. The wide majority of these sources shows Al III blueshift with respect to H β . The average shift is rather modest, ≈ -250 although for 7 of them, $s \lesssim -250 \text{ km s}^{-1}$. Six objects show evidence of a strong excess on the blue side of the 1900 blend. Fits to the 1900 blend of these sources following the standard approach are shown in Appendix C.2. The fits have been repeated by allowing for an extra BLUE in the 1900 blend, represented as a skewed Gaussian (Fig. 6.16). The blueshifted excess in some cases cannot be distinguished from strong Si II $\lambda 1816$ emission. The Si II $\lambda 1816$ emission line can be of strength comparable to Al III in the condition of low ionisation and high density derived for the virialised component (Negrete et al. 2012).

In two cases (e.g., HE0359-3959, and SDSS J152156.48+520238.5) the blueshifted excess is so overwhelming that Si II $\lambda 1816$ emission cannot account for the excess unless the Si II $\lambda 1816$ line itself is significantly blueshifted. These are perhaps the best cases supporting the evidence for a significant BLUE in Al III. It is reasonable to assume that the blueshifted excess is mainly due to Al III, being Al III a resonant line for which BALs are also observed. Broad absorption components are observed in the Al III profile, even if rarely, and with terminal radial velocity of the absorption through much lower than the one of C IV $\lambda 1549$ (Gibson et al. 2009).

The Eddington ratio values derived from the continuum luminosity at 1700 Å (after Galactic extinction correction) multiplied by a bolometric correction factor $k_{\text{bol}} \approx 3.5$, and from the M_{BH} estimated from Eq. 6.5 range between $L/L_{\text{Edd}} \approx 0.2$ and $L/L_{\text{Edd}} \approx 1.5$. If the luminosity-dependent k_{bol} is applied to the 1700 Å continuum, $0.2 \lesssim L/L_{\text{Edd}} \lesssim 1.1$. Both estimates confirm that all quasars of the presented sample are within the range expected for Pop. A sources. The xA sources are at the high end of the L/L_{Edd} distribution, with $\mu(\log L/L_{\text{Edd}}) \approx -0.18$, and the Al III BLUE sources are even more extreme with $\mu(\log L/L_{\text{Edd}}) \approx -0.105$. Extreme radiation forces may make it possible to blow out rather dense/high column density gas from the virialised region associated with the emission of the low- and intermediate ionisation lines (Netzer & Marziani 2010). Sources showing a strong BLUE in Al III could be the most extreme accretors, perhaps in a particular “blow-out” phase of the quasar evolution (D’Onofrio & Marziani 2018).

A related issue is whether sources with a strong blue-shifted component in Al III can be empirically distinguished from the rest of Pop. A quasars, without resorting to the knowledge of the rest frame. The FWHM of the whole blend (i.e., of the sum of all lines after continuum subtraction) is clearly affected by spectral type: going from A1 to A4 we see an overall decrease of prominence in CIII], and an increase in Al III with respect to the other line. The blue-shifted excess should further increase the FWHM of the blend. The parameter

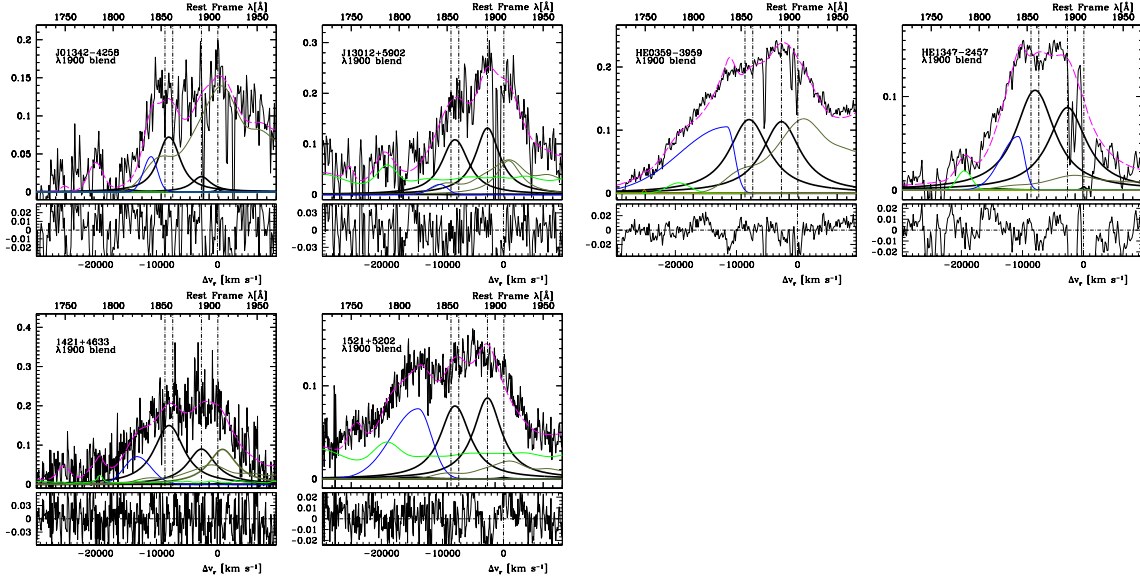


Fig. 6.16: Analysis of the 1900 Å blend for the extreme Population A sources with excess emission on the blue side of Al III. Abscissa scales are rest-frame wavelength in Å and radial velocity from rest frame wavelength of CIII]. Ordinate scale is normalized specific flux by the value at 1700 Å. The black lines identify Al III, SiIII]. The blueshifted excess BLUE is traced by a thick blue line. Green lines trace the adopted Fe II (pale) and Fe III (dark) templates. Note that CIII] emission is almost absent, as all of the emission on the red side of SiIII] can be ascribed to Fe III.

$$\mathcal{A} = \frac{\text{FWHM}_{1900}}{(10^{\log(\lambda L_{\lambda})_{1700} - 44})^{0.25}} \quad (6.9)$$

normalises the FWHM of the whole blend FWHM_{1900} (i.e., the sum of all line components) because of the increase of the line width with luminosity by a factor $L^{\frac{1}{4}}$. Fig. 6.17 shows the distribution of the \mathcal{A} for the sources of ST A1 and A2, A3 and A4, and the 6 quasars for which the 1900 blend was fit with the addition of a blue-shifted excess. The distributions of A1+A2 and A3+A4 are significantly different at a 3σ confidence level according to a K-S test. However, there is considerable overlap around $\mathcal{A} \approx 3000 \text{ km s}^{-1}$, making it difficult to unambiguously distinguishing between xAs, xAs with blue-shifted excess and other sources.

Consistency of UV and optical classification for extreme Population A

Extreme quasars can be identified by employing selection criteria in the optical and UV (MS14). The consistency of the selection criteria is however little tested, since observations covering both the 1900 Å range and the H β one are still rare. In the joint sample most sources with $R_{\text{FeII}} \gtrsim 1$ also satisfy the UV intensity-ratio conditions Al III/SiIII] > 0.5, and SiIII] > CIII]. Figure 6.18 shows the location of the data points identified according to spectral type (defined by ranges of the optical parameter R_{FeII} ; A3 and A4 satisfy the condition $R_{\text{FeII}} \gtrsim 1$ by definition) in the plane defined by the UV ratios CIII]/SiIII] vs. Al III/SiIII]. There are several borderline cases, but only one in which the criteria are not satisfied: J15591+3501 with intensity ratios CIII]/SiIII] $\approx 2.38 \pm 0.45$, and Al III/SiIII] $\approx 0.33 \pm 0.06$.

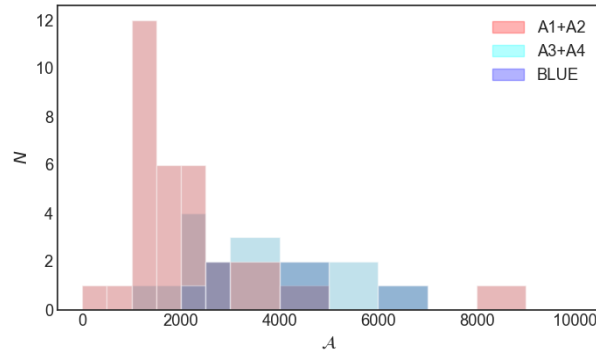


Fig. 6.17: The distribution of the parameter \mathcal{A} , as defined in Sect. 6.5.3, for three groups of quasars: spectral types A1+A2, A3+A4, and the 6 quasars with a blue shifted excess fit to the 1900 Å blend (Fig. 6.16).

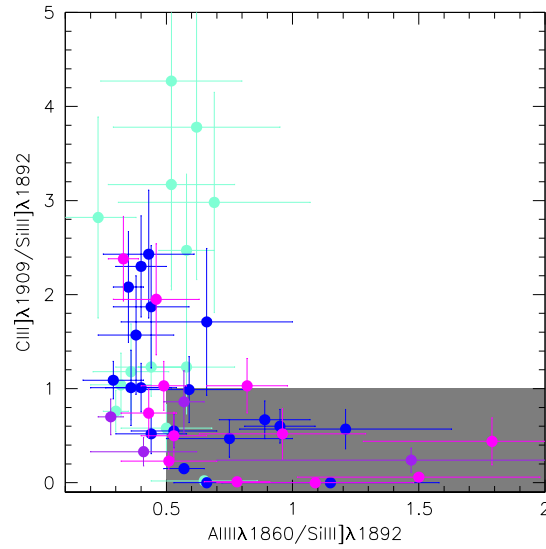


Fig. 6.18: The distribution of xA sources in the plane defined by the intensity ratios CIII]/SiIII] vs AlIII]/SiIII]. The area associated with xA sources is the lower-left shaded box. Sources are colour coded according to spectral type as in the previous Figures.

For J14421+3526, the feature at ≈ 1910 Å is most likely a blend of Fe III and CIII]. In this case, only an upper limit can be assigned to the CIII] intensity, and the UV selection criteria may not have been violated. The reason of the discordance for J15591+3501 is not clear. The majority of objects ($\approx 80\%$) in Figure 6.18 supports the equivalence between the two xA selection criteria suggested by MS14. Apart from borderline cases, five A2 sources (4 if we exclude J1421+4633 with $R_{\text{FeII}} \approx 0.99$) out of 19 enter the domain of the xA (the grey shaded area of Figure 6.18). These sources appear to be genuine xA in terms of the UV intensity ratios, but have lower than expected R_{FeII} ($0.5 \lesssim R_{\text{FeII}} \lesssim 1$). It is intriguing that the four sources all belong to the high- z samples. The possibility of systematic differences as a function of redshift in the relative abundance of iron with respect to carbon and α elements should be further investigated (e.g., Martínez-Aldama et al. 2021, and references therein).

6.6 Summary and conclusion

The present investigation has shown a substantial equivalence of $H\beta$ and Al III and CIII] as virial broadening estimators for Population A quasars, thereby providing a tool suitable for M_{BH} estimates up to $z \lesssim 4$ from observations obtained with optical spectrometers. More in detail, the salient results of the present investigation can be summarised as follows:

- the Al III and $H\beta$ FWHM are highly correlated and, in the joint sample of 48 Population A sources, can be considered statistically equivalent over 4 orders of magnitude in luminosity (Sections 6.4.1 and 6.4.2).
- The FWHM ratio between Al III and $H\beta$ increases with increasing R_{FeII} or, equivalently, from spectral type A1 to A4 (Sect. 6.4.3). Extreme Pop. A sources appear to be 20% broader than the sample average, while spectral type A1 20 % narrower than spectral type A2.
- Systematic blueshifts are revealed in Al III; however, in most cases the amplitude of the blueshifts is modest or smaller than the uncertainties, reaching a sample median for spectral types A3 and A4 of just $\approx -160 \text{ km s}^{-1}$ (Sections 6.4.3 and 6.4.4).
- The line FWHM of $H\beta$, Al III and CIII] increases with luminosity as a function of $L^{\frac{1}{4}}$, as expected for a virial velocity field of the line emitting gas (Sect. 6.4.5).
- The following scaling law between M_{BH} and luminosity and FWHM Al III: $\log M_{\text{BH}}(\text{AlIII}) \approx (0.579^{+0.031}_{-0.029}) \log L_{1700,44} + 2 \log (\text{FWHM}(\text{AlIII})) + (0.490^{+0.110}_{-0.060})$ (Eq. 6.5 in Sect. 6.4.6) provides an estimate of M_{BH} with an rms scatter of ≈ 0.3 dex with respect to the $H\beta$ -derived masses, for $M_{\text{BH}} \gtrsim 10^7 M_{\odot}$.
- An analogous scaling law has been defined also for CIII] (Eq. 6.7 in Sect. 6.4.7). The measurement of the CIII] FWHM is however more strongly affected by the severe blending and by the CIII] weakness in sources with high R_{FeII} . The CIII] scaling law requires a constant correction factor to the FWHM of CIII], $\xi_{\text{CIII]]} \approx 1.25$. The scaling laws derived from Al III and CIII] line width are mutually consistent (Sect. 6.5.1).
- Although Al III shift amplitudes are $\approx \frac{1}{10}$ the shifts of C IV $\lambda 1549$ (Section 6.5.2), it is unclear whether Al III can be exploited as a virial luminosity estimator for extreme Population A sources (Section 6.5.3): the Al III profile is strongly affected by a blueshifted excess in several extreme Pop. A sources (Sect. 6.5.3). The majority of quasars show consistency between FWHM Al III and $H\beta$, and a minority of sources that show $\text{FWHM Al III} \gg \text{FWHM } H\beta$ might be easy to recognise in large samples. The extent of systematic effects should however be analysed by a thorough study of a very large sample of xA sources with full coverage of the optical and UV rest-frame ranges from 1000 to 5500 Å.

These results show that the Al III line is a good UV substitute of $H\beta$ and can be used for black hole mass estimations with the advantage to be at the rest-frame of the source. The results on FWHM Al III should be compared with the ones obtained for C IV $\lambda 1549$ (M19), where the equivalence was obtained at the expense of corrections that were dependent on the accurate knowledge of the quasar rest frame, and therefore not fully achievable without additional measurements in spectral ranges distinct from the one of C IV $\lambda 1549$: the [O II] $\lambda 3727$ line is the narrow low ionisation line closest in wavelength to C IV $\lambda 1549$ and offers a reliable rest frame estimator (Bon et al. 2020), but is very rarely covered along with C IV $\lambda 1549$.

Part IV

Metallicity along the quasar Main Sequence

There is a growing interest to assess the physical conditions of the line emitting gas in the BLR, partly motivated by the over-solar abundances found in luminous quasars and its possible relation with intense star formation. In addition, estimation of the metallicity in the BLR can provide fundamental information about the feedback with the host galaxy and the co-evolution between the galaxies and their central SMBH. Here we present two pilot works focused on the evaluation of the metallicity and physical conditions of the BLR in quasar along the Main Sequence, by comparing photoionisation models with sensitive diagnostic ratios of measured emission lines. Our analysis also emphasises the need to isolate the components that are spectroscopically resolved, and may correspond to emitting regions (outflows, broad region, very broad region) in different physical conditions.

The first paper focuses on the analysis of the chemical composition of low- z radio-loud and radio-quiet quasars under the 4DE1 context, while the second one investigates the metal content especially in the BLR of AGN across the Main Sequence and reveals a possible gradient of metallicity across the different quasar populations. Both of these works represent a initial step in this topic and further research is needed to fully understand the relationship between metallicity and the evolutionary paths of quasars, as well as their influence on their host galaxies.

METAL CONTENT IN RELATIVISTICALLY JETTED AND RADIO-QUIET QUASARS IN THE MAIN SEQUENCE CONTEXT

7

Chapter based on the article published in *Galaxies Journal* by P. Marziani, S. Panda, A. Decontomachado, A. del Olmo, volume 11, issue 2, id.52, 13 pages, March 2023. DOI: 10.3390/galaxies11020052

Abstract

Optical and UV properties of radio-quiet (RQ) and radio-loud (RL, relativistically "jetted") active galactic nuclei (AGN) are known to differ markedly; however, it is still unclear what is due to a sample selection and what is associated with intrinsic differences in the inner workings of their emitting regions. Chemical composition is an important parameter related to the trends of the quasar main sequence. Recent works suggest that in addition to physical properties such as density, column density, and ionisation level, strong Fe II emitters require very high metal content. Little is known, however, about the chemical composition of jetted radio-loud sources. In this short note, we present a pilot analysis of the chemical composition of low- z radio-loud and radio-quiet quasars. Optical and UV spectra from ground and space were combined to allow for precise measurements of metallicity-sensitive diagnostic ratios. The comparison between radio-quiet and radio-loud was carried out for sources in the same domain of the Eigenvector 1/main sequence parameter space. Arrays of dedicated photoionisation simulations with the input of appropriate spectral energy distributions indicate that metallicity is slightly sub-solar for both RQ and RL AGN, with a lower value for RLs. The metal content of the broad line emitting region likely reflects a similar enrichment story for both classes of AGN not involving recent circumnuclear or nuclear starbursts.

7.1 Introduction

Type-1 active galactic nuclei (AGN) are characterised by the presence of broad and narrow optical and UV lines (for an introduction, see e.g., [Netzer \(1990\)](#); [Peterson \(1997\)](#); [Osterbrock & Ferland \(2006\)](#)).

AGN spectra show a mind-boggling variety of broad emission line profiles not only among different objects but also among different lines in the spectrum of the same object. For stars, the identification of optical spectral types and luminosity classes allows for the knowledge of the most relevant physical parameters, including the star's evolutionary status (Kaler 1997). This feat is not as yet possible for AGN. Although, progress in the empirical classification has yielded a coarse contextualisation of the main accretion properties, such as black hole mass, Eddington ratio, outflow prominence, spectral energy distributions, emitting region size, the metal content of the line emitting gas, etc. (e.g., Peterson 2014; Du et al. 2016b; Marziani et al. 2016b; Panda et al. 2018; Panda et al. 2019; Ferland et al. 2020; Panda 2021a). The main set of correlations was derived from a principal component analysis (PCA) on a sample of several tens of quasars (Boroson & Green 1992). The importance of the Eigenvector 1 derived from the PCA has revealed itself over the years (Sulentic & Marziani 2015), leading to the definition of what has become known as the main sequence of quasars (Sulentic et al. 2000a; Shen & Ho 2014). The optical plane of this main sequence is identified by the line width of the HI Balmer line $H\beta$ (FWHM $H\beta$) and the prominence of a singly-ionised emission, defined as the flux ratio between the Fe II blends centred at $\lambda 4570$ and $H\beta$ itself (hereafter R_{FeII}). The distribution of type 1, unobscured AGN takes the form of an elbow-shaped sequence in the optical plane (see e.g., Figure 7.1). The ranges of R_{FeII} and FWHM $H\beta$ define spectral types (Sulentic et al. 2002; Shen & Ho 2014), and different classes may show different occupations in the plane (Figure 7.1). A case in point is provided by RQ and RL (Zamfir et al. 2008): most powerful, relativistically jetted sources cluster in Population B - with moderate Fe II emission and relatively broad $H\beta$ line profiles ($4000 \text{ km s}^{-1} \lesssim \text{FWHM}(H\beta) \lesssim 8000 \text{ km s}^{-1}$). The broader spectral type shows higher fractions of RL; however, these spectral bins have a low prevalence, and a sizeable fraction of all type 1 AGN falls only in bin B1. This spectral type is, therefore, well suited for an inter-comparison between RQ and RL properties. In the following, we will build composite spectra for jetted and non-jetted sources of spectral type B1 (§ 7.2). The analysis takes advantage of the main sequence (MS) correlations concerning line profiles in the spectral type B1 (§ 7.3). It's focused on the measurements of intensity ratios intended to be diagnostics of the metal content of the line emitting gas. Intensity ratios are interpreted using arrays of photoionisation simulations covering a broad range in metallicity. Results (§ 8.5) suggest slightly sub-solar or solar metallicity and provide evidence of significant diversity in terms of chemical enrichment and evolutionary status along the main sequence (§ 7.5).

7.2 Composite spectra for spectral type B1 quasars

To obtain spectral data of good quality covering the full spectral ranges from 1000 \AA to $\approx 6000 \text{ \AA}$ (i.e., from $\text{Ly}\alpha$ to $H\beta$ included) for the same object is still a non-trivial feat for low- z quasars, as the UV coverage demands space-based observations. Here, we consider one sample of 20 RL and one sample of 16 RQ sources, all belonging to spectral type B1, in the redshift range $\approx 0.002 - 0.5$ and $\approx 0.25 - 0.65$, for RQ and RL respectively. The absolute magnitudes derived from the quick look magnitudes in the NASA Extragalactic Database (NED), and the range is between -21

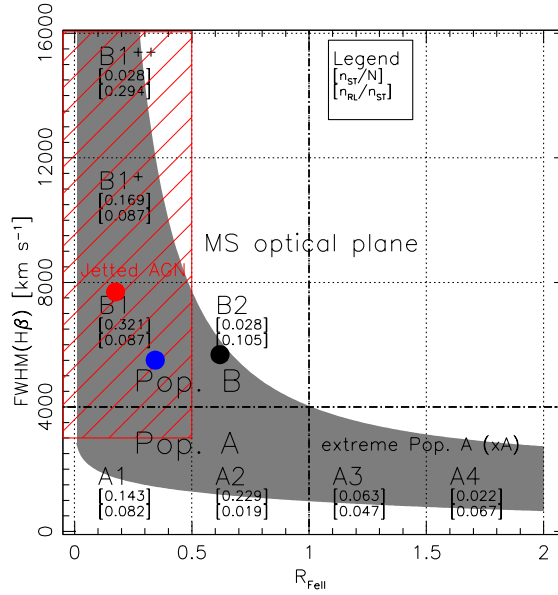


Fig. 7.1: Sketch of the optical plane of the MS, FWHM $H\beta$ vs. R_{FeII} . Numbers in square brackets provide, from top to bottom, the complete sample fractional occupation, the fraction of jetted (core-dominated + Fanaroff-Riley II) sources in each spectral bin. The shaded area identifies the region along the sequence with a high prevalence of jetted sources (c.f. Ref. (Marziani et al. 2021a)). The original sample is described in Ref. Marziani et al. (2003b). Points mark the location of the composite spectra (red: RL; blue: RQ) and of PKS 0226-038 (black).

and -27 (RQ), and between -23.5 and -26.5 (RL), which correspond to bolometric luminosities in the range $\log L \sim 45 - 47$ [erg s^{-1}]. The UV data are HST/FOS observations analysed in Ref. Sulentic et al. (2007a), and the optical spectra were obtained from Ref. Marziani et al. (2003b). The spectral similarity ensures consistency of black hole mass and Eddington ratio. We built median and average composites for the RQ and RL classes that look consistent. As the median combination is not improving the S/N, the fitting analysis was performed only on the averages. The average S/N is high with $S/N \approx 90$ for the RQ composites, and ≈ 130 and ≈ 55 for the visual and UV ranges in the RL composite, respectively. The composite spectra are shown in Figure 7.2.

7.3 Analysis

7.3.1 Line profiles

Pop. B $H\beta$ profiles show a redward asymmetry modelled with a broader redshifted ($\text{FWHM} \sim 10000$ km s^{-1} , shift at line base $\sim 1000 - 2000$ km s^{-1}) and a narrower Gaussian (Sulentic et al. 2002; Marziani et al. 2009). The very broad Gaussian component is meant to represent the innermost part of the broad line region (BLR), providing a simple representation of the radial stratification of the BLR in Pop. B suggested by reverberation mapping (Snedden & Gaskell 2007). This component (hereafter the very broad component, VBC) has been associated with a physical region of high-ionisation

virialised gas and closest to the continuum source - the very broad line region, VBLR (Peterson & Ferland 1986; Brotherton et al. 1994a; Sulentic et al. 2000c; Wang & Li 2011). While the physical properties of the VBLR line emitting gas are not well known, a decomposition of the full H β profile into a symmetric, unshifted H β component (H β_{BC}) and a H β_{VBC} provide an excellent fit to most H β Pop. B profiles (Sulentic et al. 2002; Zamfir et al. 2010).

The multicomponent fits were performed using the SPECFIT routine from IRAF (Kriss 1994). This routine allows for the simultaneous minimum- χ^2 fit of the continuum approximated by a power law and the spectral line components yielding FWHM, peak wavelength, and intensity for all line components. In the optical range, we fit the H β profile and the [O III] $\lambda\lambda$ 4959,5007 emission lines, and the Fe II multiplets for the composite objects.

7.3.2 Diagnostics of Metallicity and photo-ionisation modelling

Diagnostics from the rest-frame UV spectrum take advantage of the observations of strong resonance lines that are collisionally excited Negrete et al. (2012, 2013) and at least constrain density n_H , ionisation parameter U , and chemical abundance Z . For instance, C IV λ 1549/Ly α , C IV λ 1549/(Si IV + O IV) λ 1400, C IV λ 1549/He II λ 1640, N V λ 1240/He II λ 1640 are sensitive to metallicity; and Al III λ 1860/Si III λ 1892, Si III λ 1892/C III λ 1909 are sensitive to density, since inter-combination lines have a well defined critical density (Negrete et al. 2012; Marziani et al. 2015). Ratios of lines involving different ionic stages of the same element are obviously sensitive to the ionisation parameter. The lines emitted from ionic species of Silicon and Aluminium deserve special attention - they are two elements greatly enhanced in Supernova ejecta (Chieffi & Limongi 2013). This approach has yielded tight constraints, especially for sources radiating at high Eddington ratio (Negrete et al. 2012; Śniegowska et al. 2021; Garnica et al. 2022), where physical properties are consequently well-constrained because they converge toward an extreme.

The photo-ionisation code Cloudy Ferland et al. (2017) models the ionisation, chemical, and thermal state of gas exposed to a radiation field and predicts its emission spectra and physical parameters. Cloudy simulations require inputs in terms of n_H , U , Z , quasar spectral energy distribution (SED), and column density N_c . The ionisation parameter $U = Q(H)/4\pi r_{BLR}^2 cn_H$, where $Q(H) = \int_{\nu_0}^{\infty} L_{\nu}/h\nu$ is the number of ionising photons, provides the ratio between photon and hydrogen number density and is dependent on the spectral energy distribution of the ionising continuum. The simulations were carried out assuming the RL and RQ SEDs from Laor et al. Laor et al. (1997) representative of the SED of B1 objects (work in preparation). The geometry was assumed open, plane-parallel, meaning that a slab of emitting gas is exposed to a radiation field only on one side. Arrays of Cloudy photo-ionisation models* for a given metallicity Z and column density N_c , constant density n and ionisation parameter U were evaluated at steps of 0.25 dex covering the ranges $7 \leq \log n_H \leq 13$ [cm^{-3}], $-3 \leq \log U \leq 1$. The single-value metallicity arrays were computed for $\log Z$ at -3.0, -2.7, -2.3, -2.0, -1.7, -1.3, -1.0, -0.7, -0.3, 0, 0.3., 0.7, 1.0, and 1.3 in solar units, i.e. from 0.001 Z_{\odot}

* $N(n_H) \times N(U) = 425$. The overall number of models includes 14 values of metallicity, and for RL and RQ SEDs, is 6,358.

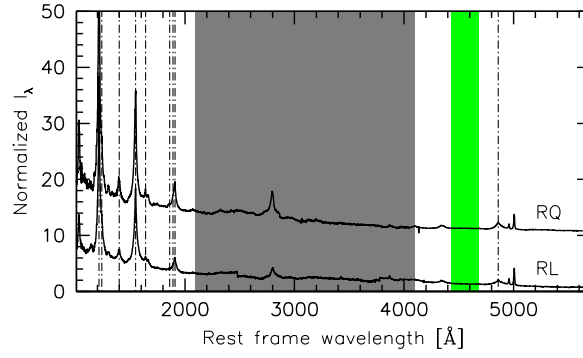


Fig. 7.2: The RQ and RL composite spectra covering the optical and the UV domain. The green shaded area marks the range used to measure the Fe II $\lambda 4570$ blend. The grey-shaded region has not been considered in the analysis due to the limited number of available spectra in this region. The RL spectrum has been vertically shifted for clarity. The dot-dashed lines identify the main emission feature included in the non-linear χ^2 fitting procedures.

to $20 Z_{\odot}$. No dust and no micro-turbulence broadening were included in the calculations. The Z calculations are based on a single zone assumption for the BLR. The lowest values of the density may bias the solutions toward cases where significant [O III] $\lambda\lambda 4959, 5007$ is expected; all cases with [O III] $\lambda 5007 / H\beta > 0.1$ were excluded, as no broad [O III] $\lambda\lambda 4959, 5007$ is observed. A more refined analysis in the framework of the locally optimised emitting cloud model (Baldwin et al. 1995; Korista et al. 1997; Guo et al. 2020) is deferred to an eventual work.

7.4 Results

7.4.1 Composite spectra

The composite average spectra are shown in Figure 7.2. The spectral similarity between the two classes already evident in Figure 7.2 is confirmed by the profile comparison of Fig. 7.3. Both spectra are Fe II weak; show weak NV $\lambda 1240$; Al III is weak while the C III] line is by far the most prominent in the 1900 Å blend encompassing Si III] and C III] along with Al III. All lines can be successfully decomposed into a BC and a VBC. Apparently, there is no VBC in the Al III and Si III] lines and in Fe II. No prominent BC is observed in the He II optical and UV lines, at variance with $H\beta$, $Ly\alpha$, CIV $\lambda 1549$, and the other lines. The absence of a prominent BC in Helium lines is typical (Marziani & Sulentic 1993), albeit the implications for the BLR structure are not obvious even on a qualitative basis. Table 7.1 reports the line fluxes normalised to $H\beta$. In view of the heuristic decomposition approach, fluxes are reported for the BC, VBC, and sum of the two components, i.e., for the full broad profile (total flux). Each value in this table has been normalised by the corresponding component of $H\beta$. Error analysis has been performed empirically or on the basis of previous analyses ($H\beta$ and Fe II: Refs. Marziani et al. (2003b, 2022c); CIV $\lambda 1549$: (Sulentic et al. 2017); blend at 1900 Å: Refs. Garnica et al. (2022); Marziani et al. (2022c); NV $\lambda 1240$: Ref. Śniegowska et al. (2021)). The undetected He II BC was considered in the models as $He II / H\beta \lesssim 0.1$. A more refined treatment of uncertainties is deferred to future work.

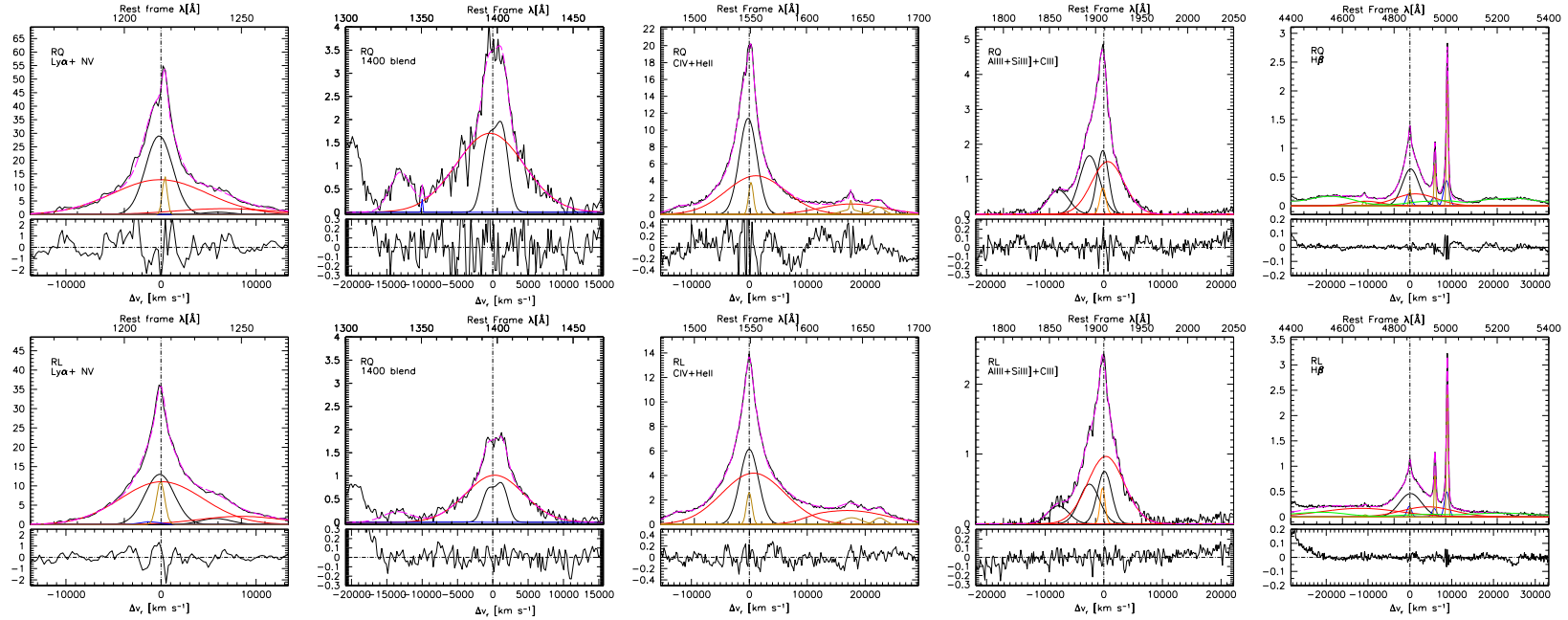


Fig. 7.3: Analysis of prominent blends helpful for metallicity diagnostics. Continuum subtracted spectra are shown in the rest frame, with the blend ordered with an increasing wavelength from left to right: the $\text{Ly}\alpha + \text{NV}\lambda 1240$ blend, $\text{SiIV}\lambda 1397 + \text{OIV]}\lambda 1402$; $\text{CIV}\lambda 1549 + \text{He II}$; the 1900\AA blend made up mainly of Al III , SiIII , CIII ; the $\text{H}\beta + [\text{O III}]\lambda\lambda 4959, 5007$ region. Dashed magenta line: model spectrum; thick solid line: broad components; red thick line: very broad components; thin orange lines: narrow components of $\text{H}\beta$ and $[\text{O III}]\lambda 5007$; blue lines: blue-shifted components. Green lines trace the scaled and broadened Fe II emission template. The lower panels show the observed minus model residuals in the radial velocity scale.

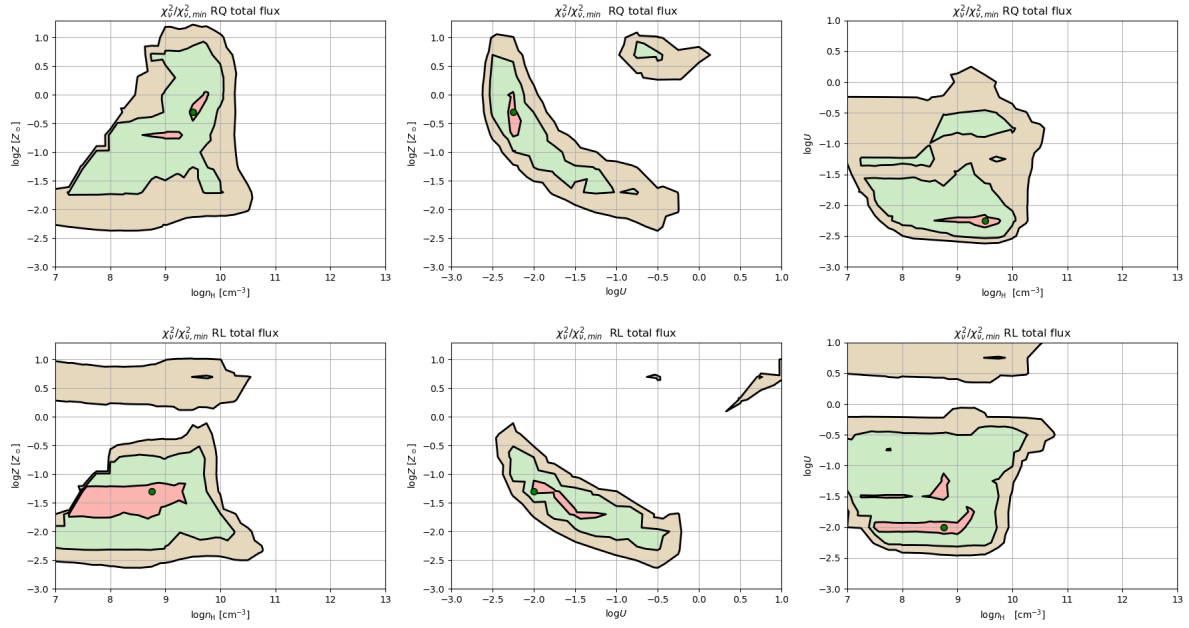


Fig. 7.4: Projections of the 3D parameter space n_H , U , Z . Isophotal contour traces the 1,2,3 σ confidence levels; the green spot identifies the values of n_H , U , Z yielding the minimum χ^2_{ν} . The upper panels are for RQ, lower panels are for RL. Regions of the parameter space where $[\text{O III}]\lambda 5007/\text{H}\beta > 0.1$ have been assigned a very high χ^2_{ν} .

Spectral differences between the two classes are not striking on a qualitative basis. We note a stronger redward asymmetry in RL sources. This is, however, a result known for a long time (Marziani et al. 2003c; Punsly 2010). The optical Fe II emission is twice as strong in RQ than in RL; this is also consistent with previous results Marziani et al. (2021a). The intensity ratios most commonly used in Z estimates are marginally higher for RQ than for RL. $\text{SiIV}\lambda 1397 + \text{OIV}]\lambda 1402/\text{CIV}\lambda 1549$, ≈ 0.24 vs 0.15 for RQ and RL, respectively. Similarly, $\text{Al III}/\text{CIII}] \approx 0.2$ vs 0.12; $\text{NV}\lambda 1240/\text{H}\beta \approx 1.32$ vs 1.05, if total fluxes are considered.

We computed the normalised χ^2_{ν} in the following form, to constrain the value of the metallicity from the values of the diagnostic ratios. For each spectrum k , and for each component c , we can write (following Ref. Śniegowska et al. (2021)):

$$\chi^2_{\nu, \text{kc}}(n_H, U, Z) = \frac{1}{n_f} \sum_i \left(\frac{R_{\text{kci}} - R_{\text{kci, mod}}(n_H, U, Z)}{\delta R_{\text{kci}}} \right)^2 \quad (7.1)$$

where the summation is made over the available diagnostic ratios. The number of degrees of freedom n_f is 8 for the composites and 7 for the case of PKS 0226-038 presented in § 7.4.2. The χ^2_{ν} is computed to the results of the Cloudy simulations as a function of U , n_H , and Z (subscript ‘mod’). The following independent intensity ratios were considered in the summation: $\text{NV}\lambda 1240/\text{CIV}\lambda 1549$, $\text{CIV}\lambda 1549/\text{He II}\lambda 1640$, $\text{CIV}\lambda 1549/\text{H}\beta$, $\text{SiIV}\lambda 1397 + \text{OIV}]\lambda 1402/\text{CIV}\lambda 1549$, $\text{Al III}/\text{CIV}\lambda 1549$, $\text{Al III}/\text{Si III}]$, $\text{Al III}/\text{CIII}]$, $\text{He II}/\text{H}\beta$, $\text{Fe II}\lambda 4570/\text{H}\beta$. The ratios were computed for BC, VBC, and total line intensity. Non-detections were treated as upper limits.

Table 7.1: Normalised emission line intensities

Line Id.	Comp.	$I/I_{H\beta}$	$I/I_{H\beta}$
		RQ	RL
NV λ 1240	BC	0.257 ± 0.081	0.450 ± 0.142
	VBC	2.604 ± 0.701	1.646 ± 0.792
	Total	1.323 ± 0.402	1.053 ± 0.320
SiIV λ 1397+ OIV] λ 1402	BC	0.667 ± 0.149	0.294 ± 0.053
	VBC	2.237 ± 0.403	0.961 ± 0.173
	Total	1.380 ± 0.218	0.630 ± 0.100
CIV λ 1549	BC	4.382 ± 0.620	2.545 ± 0.360
	VBC	7.158 ± 1.012	5.840 ± 0.826
	Total	5.643 ± 0.399	4.207 ± 0.297
He II λ 1640	BC	0.228 ± 0.072	0.238 ± 0.075
	VBC	2.099 ± 0.469	1.817 ± 0.406
	Total	1.078 ± 0.222	1.034 ± 0.213
Al III	BC	0.388 ± 0.123	0.150 ± 0.046
	Total	0.485 ± 0.100	0.156 ± 0.063
CIII]	BC	0.556 ± 0.124	0.291 ± 0.064
	VBC	1.548 ± 0.346	0.951 ± 0.213
	Total	1.007 ± 0.113	0.624 ± 0.070
FeII λ 4570	Total	0.344 ± 0.088	0.175 ± 0.088
He II	BC	$\lesssim 0.1$	$\lesssim 0.1$
	VBC	0.299 ± 0.152	$\lesssim 1.299$
	Total	0.136 ± 0.068	$\lesssim 0.655$

Fig. 7.4 shows the projections of the 3D space U , n_{H} , Z . Each contour in the plane braces elements of the grid of Cloudy parameter space that is consistent with the minimum χ^2_{v} within the uncertainties at 1σ , 2σ , and 3σ confidence levels.

The distribution of the data points is constrained in a range of U , n_{H} , Z , at very low density, relatively high ionisation, and low metallicity. Within the limit in U , and n_{H} , the distribution of Z is slightly sub-solar for the RQ ($Z \approx 0.5Z_{\odot}$), and even more sub-solar for the radio loud, ($Z \approx 0.1Z_{\odot}$). There is a relatively broad range of density and ionisation parameters and metallicities that are consistent within 2σ confidence level from the minimum χ^2 . This is probably a reflection of the stratified nature of the emitting region in Population B and the intrinsic heterogeneity of the composites.

The values reported in Table 7.2 for the sub-regions confirm the validity of the virial scenario, with U increasing by a factor $\gtrsim 10$ between BLR and VBLR. The derived density is not changing strongly, as implied by the strong CIII] VBC. Since the distance from the centre of gravity scales with the inverse of the velocity dispersion squared (i.e., $r \propto \text{FWHM}^{-2}$, we might expect that $U/U_{\text{BLR}} \sim \text{FWHM}_{\text{VBLR}}^4/\text{FWHM}_{\text{BLR}}^4 \sim (2.32 - 2.55)^4 \sim 29 - 42$. The U values reported in Table 7.2 indicate ratios between 1 – 2 orders of magnitudes, consistent with the ones expected from a virial velocity field.

The Z values all fall in ranges that are consistent. The results for the sub-regions should be seen with some care, as the VBC measurements are difficult for He II, He II λ 1640, NV λ 1240. The fairly high metallicity value for RQ VBLR is due to several line ratios being consistently higher than for the RL case: C IV λ 1549/H β , (SiIV λ 1397+OIV] λ 1402)/C IV λ 1549, (SiIV λ 1397+OIV] λ 1402)/He II λ 1640, and NV λ 1240/He II λ 1640 are between 30% and a factor 2 higher for the VBLR of RQ than of RL. This epitomises the need for very accurate measurements on the line profiles.

These results can be compared with the ones derived from the analysis of the Sloan composite spectrum (Vanden Berk et al. 2004). Values of the intensity ratios reported in their Table 2, and the assumption of typical 10% uncertainties for most ratios, do not provide any constraint on Z , and loose constraints on density ($\log n_{\text{H}} \sim 9.5^{+1.5}_{-2.5}$) and ionisation ($\log U \sim -1.75 - -0.5$). Averaging the full dataset of a large colour-based spectroscopic survey presents major hindrances. Spectral bins are likely to be associated with intrinsic differences in Z . Building a composite combines all survey spectra with a weight proportional to the relative prevalence of each spectral type (e.g., Sulentic & Marziani 2015). Since the most populated spectral bins along the sequence is B1, with A2 the second most populated (Marziani et al. 2013a; Shen & Ho 2014), the appearance of the composite spectrum is resembling the Pop. B RQ composite is some key features, and A2 in others. For example, the moderate Fe II/H β and SiIV λ 1397+OIV] λ 1402)/C IV λ 1549 values are consistent with solar or super-solar Z . The composite is yielding line ratios that reflect a combination of physical properties from individual spectra; on the other hand, it does not reflect the spectral diversity of a large population of type-1 AGN, as extreme sources are just a minority ($\lesssim 5\%$; Fig. 7.1).

Table 7.2: Derived values of U , Z , n_{H} and 1σ ranges^a

Class	Region	$\log U$	$\Delta \log U$	$\log Z$	$\Delta \log Z$	$\log n_{\text{H}}$	$\Delta \log n_{\text{H}}$
RQ	Tot.	-2.25	-2.25 – -2.25	-0.30	-0.70 – 0.00	9.50	8.50 – 9.75
RQ	BLR	-2.25	-2.25 – -1.75	0.30	-0.70 – 1.00	10.25	9.25 – 10.75
RQ	VBLR	0.00	0.00 – 0.00	0.70	0.70 – 0.70	9.50	9.50 – 9.75
RL	Tot.	-2.00	-2.00 – -0.75	-1.30	-2.00 – -1.30	8.75	7.00 – 9.75
RL	BLR	-1.50	-2.00 – -0.75	-1.70	-2.00 – -1.00	10.25	8.75 – 10.50
RL	VBLR	-0.75	-1.25 – -0.25	-2.00	-2.00 – -1.70	7.75	7.00 – 10.25

^a: ionisation parameter U , abundance Z in solar units, and Hydrogen particle density n_{H} in units of cm^{-3} . The ranges are defined by the limiting elements of the model grid that are compatible with the minimum χ^2_{ν} within 1σ confidence level.

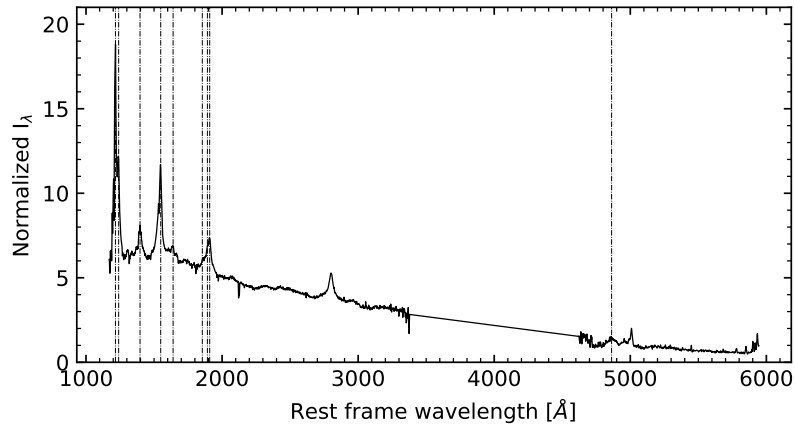


Fig. 7.5: The spectrum of PKS 0226-038 in the optical and the UV domain. The dot-dashed lines identify the main emission features included in the non-linear χ^2 fitting procedures. The straight line traces a range where data are unavailable for this source.

7.4.2 A typical RL source at high z

PKS 0226–038 is a luminous jetted source at the cosmic noon ($z \approx 2.06922$; $M_{\text{B}} \approx -28.0$, and Kellermann’s radio loudness parameter Kellermann et al. (1989), $R_{\text{K}} \sim 10^3$). Its optical and UV spectrum is markedly different from the Population B composite at low z : CIII] is weaker, Fe II stronger, and Al III is almost as strong as C IV $\lambda 1549$ (Fig. 7.5). No diagnostic based on NV $\lambda 1240$ and He II is available in this case. The measured diagnostic ratios are reported in Table 7.3. The uncertainties were assumed to be $\approx 10\%$ for the intensities normalised to H β save for C IV $\lambda 1549$ /H β that is affected by a re-scaling ($\approx 20\%$) and for Fe II $\lambda 4570$ for which $\delta R_{\text{FeII}} = 0.1$ was assumed. In this case, the Fe II $\lambda 4570$ (Fig. 7.5) is partly missing because of a telluric absorption. The Fe II optical emission is well-represented by a "solid" template with fixed multiplet ratios.

The derived values of the metallicity are well constrained with minimum χ^2 obtained for $\log Z/Z_{\odot} \approx 1$, with 1σ uncertainty equal to 0.3 dex. The ionisation parameter $\log U \approx -2.75$ and density $\log n_{\text{H}} \sim 11.75$ [cm^{-3}] are significantly lower and higher with respect to the values at low- z . The three parameters reflect the moderate R_{FeII} , high Al III/C IV $\lambda 1549$ (yielding low ionisation and high Z), and low CIII]/SiIII] (implying a high density).

Table 7.3: Diagnostic line ratios measured on the PKS 0226-038 spectrum^a

Ratio Id.	Value
C IV λ 1549/He II λ 1640	4.436 \pm 0.627
(Si IV λ 1397+ O IV] λ 1402)/C IV λ 1549	0.361 \pm 0.051
(Si IV λ 1397+ O IV] λ 1402)/He II λ 1640	1.603 \pm 0.227
C IV λ 1549/H β	3.460 \pm 0.720
Al III/C IV λ 1549	0.986 \pm 0.139
Al III/Si III]	0.642 \pm 0.091
Si III]/C III]	6.034 \pm 0.853
R_{FeII}	0.62 \pm 0.10

^aLine ratios refer to the total flux of the full broad line profiles.

7.5 Discussion: metal enrichment along the quasar Main Sequence

Several basic results emerge from the present analysis:

1. RQ Pop. B sources show slightly sub-solar or solar metallicities;
2. in the same spectral bin along the MS, RL sources show definitely sub-solar chemical abundances, lower with respect to RQ. The difference is not marginal and is supported by several diagnostic indicators consistently observed to be lower in RL sources. It is also consistent with the location of the RL template in the MS, displaced toward broader H β and lower R_{FeII} with respect to the RQ one.
3. there is an important difference in properties at the extremes of the E1 MS: Here, we focused only on the low- R_{FeII} extreme deriving sub-solar metallicity. However, highly-super-solar Z estimates were derived at the other end of the MS, with $R_{\text{FeII}} \gtrsim 1$ (Śniegowska et al. 2021; Garnica et al. 2022);

The first result is not completely unexpected, since a similar analysis yielded slightly sub-solar abundances for NGC 1275 (Punsly et al. 2018) and Pop. B sources are known to have similar intensity ratios (Marziani et al. 2010).

The origin of the RQ and RL Z difference is likely associated with a difference in sample/host galaxy evolutionary history. At the modest accretion rates required to sustain the low Eddington ratio of B1 sources, there is no need to invoke "cataclysmic" events such as recent, major wet mergers to explain the AGN luminosity via super-Eddington accretion rates (D'Onofrio & Marziani 2018), and accretion material could be provided via stellar mass loss in early-type galaxies (Padovani & Matteucci 1993). The general impression of low- z Population B is that of fairly evolved systems, past their prime of accretion events (Fraix-Burnet et al. 2017b). This impression, is further reinforced in

the case of radio-loud sources, where sub-parsec binary black holes at the stable end of their in-spiral phase are relatively frequent (Krause et al. 2019).

The gradient in chemical composition is also no surprise. While it is possible to account for an increase in Fe II along the sequence only based on ionisation degree and density Marziani et al. (2001), a thorough quantitative assessment requires also a change in chemical composition Panda et al. (2019). We pass from sources where singly ionised iron emission is barely detected to sources where it dominates the thermal balance of the emitting regions, overwhelming the entire Balmer line emission.

The case of the high- z RL source PKS 0226–038 signifies the co-existence of powerful relativistic ejections and BLR physical conditions typical of sources radiating at $L/L_{\text{Edd}} \gtrsim 0.1 - 0.2$ (Population A according to Ref. Sulentic et al. (2000a)). It is known for a long time that the radio-loud fraction among AGN increases with redshift Padovani et al. (1993); La Franca et al. (1994). However, the realisation of the high prevalence of unambiguously jetted AGN at $z \gtrsim 1$ radiating at high L/L_{Edd} is a recent result. The Eddington ratio of PKS 0226-038 is $\log L/L_{\text{Edd}} \approx -0.43$. It belongs to the spectral type B2, that include sources in the R_{FeII} range $0.5 - 1$, and with moderate accretion rate. Strong Fe II emission is a rather rare occurrence among RLs at low- z (especially in Fanaroff-Riley II sources, (Zamfir et al. 2008)), it is frequently found at high redshift (Ref. Deconto-Machado et al. (2023), and article in preparation), along with higher L/L_{Edd} . This is probably a consequence of the increase in average accretion rate at the epochs corresponding to the cosmic noon (Cavaliere & Vittorini 2000; Marconi et al. 2004; Hopkins et al. 2006), and much beyond. Indeed, highly accreting jetted sources are being discovered up to redshift ≈ 6 (Bañados et al. 2021; Ighina et al. 2023).

7.6 Conclusions

This pilot work revealed a population of quasars with slightly sub-solar abundances. We can infer a metallicity trend along the quasar MS on the basis of previous results and of the analysis presented in this paper, supporting the assumptions in the study of (Panda et al. 2019), although the MS-oriented analysis has been yet focused only on the spectral types, B1 and extreme Population A. Full analysis for individual spectral types isolated along the MS (Sulentic et al. 2002) is still needed. Special attention should also be devoted to high- z high- L sources. At high- z , sample selection effects could be even more important, excluding a population of sources on the basis of their low accretion rate (Sulentic et al. 2014a). At high luminosities, wind effects are expected to be maximised and may introduce another factor in the chemical enrichment of the broad-line emitting gas.

FROM SUB-SOLAR TO SUPER-SOLAR CHEMICAL ABUNDANCES ALONG THE QUASAR MAIN SEQUENCE

8

Chapter based on the article published in Physics Journal by P. Marziani, A. Floris, A. Deconto-Machado, et al., volume 6, no. 1, 20 pages, February 2024. DOI: 10.3390/physics6010016

Abstract

The 4D Eigenvector 1 sequence has proven to be a highly effective tool for organising observational and physical properties of type 1 active galactic nuclei (AGN). In this paper, we present multiple measurements of metallicity for the broad line region gas, from new or previously published data. We demonstrate a consistent trend along the optical plane of the E1 (also known as the quasar main sequence), defined by the line width of $H\beta$ and by a parameter measuring the prominence of singly-ionised iron emission. The trend involves an increase from sub-solar metallicity in correspondence with extreme Population B (weak Fe II emission, large $H\beta$ FWHM) to metallicity several tens the solar value in correspondence with extreme Population A (very strong Fe II optical emission, narrower $H\beta$ profiles). The data establish the metallicity as a correlate of the 4D E1/main sequence. If the very high metallicity ($Z \gtrsim 10Z_{\odot}$) gas is expelled from the sphere of influence of the central black hole, as indicated by the widespread evidence of nuclear outflows and disk wind in the case of sources radiating at high Eddington ratio, then it is possible that the outflows from quasars played a role in chemically enriching the host galaxy.

8.1 Introduction: A Main Sequence and the Eigenvector 1 for Quasars

The main sequence (MS) concept in quasar research draws parallels with stellar evolutionary sequences, but in this case, it is applied to quasar properties. A study on a sample of Palomar-Green quasars detected an interesting anti-correlation between the strength of the $FeII\lambda 4570$ emission line

and the Full Width at Half Maximum (FWHM) of the broad H β emission line of type-1 quasars with low redshifts ($z < 1$, Boroson & Green (1992)). This anti-correlation suggests that, as the FeII λ 4570 feature becomes stronger, the FWHM tends to decrease, and is one of the main correlations known as the Eigenvector 1 of quasars. This finding has been established through the analysis of samples of increasing size over the years (Gaskell 1985a; Sulentic et al. 2000c; Zamfir et al. 2010; Shen & Ho 2014), and has proved to be fundamental to organise type-1 AGN properties in a systematic way with predictive ability.

Quasars are categorised into different spectral types along the MS (e.g., Shen & Ho 2014), and two primary populations, referred to as Population A and Population B, have been identified (Sulentic et al. 2000c). These categories are based on specific properties such as the Eddington ratio (a measure of the accretion rate) and orientation (Shen & Ho 2014; Sun & Shen 2015; Panda et al. 2019). The "4DE1" classification, introduced by Sulentic et al. (2000c), further organises quasar properties according to the Eddington ratio and orientation, revealing a systematic pattern of variation across different types of AGN encompassing their outflow phenomenology and their accretion mode (Giustini & Proga 2019). The assignation of most quasar spectral types permitted the prediction of their UV, X-ray, radio, and FIR properties with a high degree of confidence.

The MS, much like the equivalent concept in stellar evolution, is used as an evolutionary framework for understanding quasars. This sequence spans from young and rejuvenated quasars, characterised by specific spectral properties (Extreme Population A), to older and more mature quasars with distinct characteristics (Population B). Differences in factors such as black hole mass, Eddington ratio, disk winds, or outflow properties, derived from the strengths and profiles of emission lines are used to define and distinguish these evolutionary stages (Du et al. 2016a; Fraix-Burnet et al. 2017b).

Currently, the available evidence regarding the correlation between metal content in the broad line emitting region (BLR) and the quasar main sequence (MS) remains partial and inconclusive (Panda et al. 2019; Panda 2021b). There is a long tradition of studies attempting to estimate the metallicity in the BLR of AGN over a broad range of redshift, from $z \approx 0$, up to $z \approx 6$ (e.g., Hamann & Ferland 1993; Nagao et al. 2006b; Juarez et al. 2009; Matsuoka et al. 2011; Shin et al. 2013; Sameshima et al. 2017; Wang et al. 2022). All these studies derive metallicity in the range from a few times solar to about 10 times solar, values that are significantly higher than the ones found even in most massive and metal-rich galaxies (Matteucci 2012; Xu et al. 2018). When considering the past metallicity estimates along the main sequence, an intriguing trend emerges: not all quasars are accreting matter with super-solar metal content (Marziani et al. 2023), and only at one end of the MS, the BLR gas may be enriched by a metal content even above ten times solar, possibly with pollution by supernova ejecta (Śniegowska et al. 2021).

In this contribution, we will use the results of a new analysis and of several recent papers to gather a view of the global trend along the MS. Section 8.2 summarises the new observations from ground- and space-based observatories. Section 8.3 elucidates the methodology applied to the metallicity estimates, stressing the need to isolate line components that are spectroscopically resolved, and may correspond to emitting regions in different physical conditions (§8.3.1). Results of several individual sources and composite spectra representative of entire spectral types (ST) introduced in §8.4 clearly

delineate a sequence of increasing metallicity from extreme Population B to extreme Population A (§8.5). As outflows from the AGN are of special relevance for galactic evolution (Di Matteo et al. 2005; Hopkins et al. 2006; Somerville & Davé 2015), it is important to isolate the corresponding line component, whenever possible (§8.5.3). The AGN outflows may provide enrichment of the nuclear and circumnuclear region of the host galaxies (§8.6), although ensuing chemical feedback is expected to be relevant only at high AGN luminosity. In § 8.6, we outline how the different metallicities inferred for the BLR of low- z AGN fit the evolutionary interpretation of the quasar MS.

8.2 Observations

The new spectral data employed in this study were acquired through a series of distinct observations. Specifically:

- For Mrk 335, Mrk 478, and Fairall 9, we utilised optical spectra sourced from Marziani et al. (2003b). Additionally, the UV spectra of Mrk 335 were obtained during observations conducted on the 4th and 7th of January 2013, utilising the Cosmic Origins Spectrograph (COS) aboard the Hubble Space Telescope (HST) with the G140L grism. The UV spectra of Mrk 478 were acquired on the 5th of December 1996, utilising the HST’s Faint Object Spectrograph (FOS) and employing the G130H and G190H grisms. For Fairall 9, UV spectra were collected on the 22nd of January 1993, utilising the HST’s FOS with the G190H and G270H grisms, and subsequently on the 18th of July 2012, employing the HST’s COS with the G130M and G160M grisms.
- For NGC 1275, the data were sourced from Punsly et al. (2018). Optical spectra encompassed various observations spanning the period from 1983 to 2017. Additionally, UV spectra were procured from the HST, with FOS observations in 1993 and COS observations in 2011.
- For PHL 1092, data were drawn from Marinello et al. (2020b). Optical spectra were captured using the Goodman spectrograph at the 4.1-meter telescope of the Southern Observatory for Astrophysical Research (SOAR) on the night of 12th December 2014. The UV spectra were obtained using the HST’s Space Telescope Imaging Spectrograph (STIS) on the night of 20th August 2003.

In addition, we considered:

- composite spectra for radio-loud (RL) and radio-quiet (RQ) Population B sources. The data on which the composites were based were described in a previous work Marziani et al. (2023);
- median results for two samples of xA sources at intermediate redshift ($z \approx 2$) Śniegowska et al. (2021); Garnica et al. (2022) lacking the rest-frame optical spectrum.

8.3 Methodology and Data analysis

8.3.1 Multicomponent analysis

A crucial technique in quasar studies is the multicomponent analysis, which involves dissecting complex emission line profiles into distinct components. This approach allows us to uncover details about different regions of emission, potentially revealing information about kinematics, velocities, and structures. Line ratios, such as those involving C IV $\lambda\lambda 1549, 1549$, He II $\lambda 1640$, Al III $\lambda 1860$, and Si IV $\lambda 1397 + \text{OIV}] \lambda 1402$, are used as diagnostic tools to infer physical conditions, such as ionisation and metallicity, within the quasar environments. In the spectra of quasars, both low-ionisation and high-ionisation optical and UV lines are observed (LILs and HILs, respectively), and they provide valuable insights into the physical conditions and structure of the quasar BLR. These lines are emitted, at least in part, in distinct regions with different characteristics (Collin-Souffrin et al. 1988; Elvis 2000).

We distinguish a broad component (BC) that is broadened by the Doppler effect due to the rapid motion of the gas in the BLR in a velocity field dominated by Keplerian motions (Peterson & Wandel 1999, 2000). Lines meeting this condition are also referred to as “virialised broad emission lines.” Low-ionisation lines like H β and Mg II $\lambda 2800$ are typically emitted in the virialised BLR, which may be characterised by high densities and column densities, but relatively low ionisation (ionisation parameter $\sim 10^{-2}$). High-ionisation lines like C IV $\lambda\lambda 1549, 1549$, He II $\lambda 1640$ and NV $\lambda\lambda 1240, 1240$ are also emitted in the virialised BLR. However, these lines trace the regions of the BLR that are exposed to the most intense and energetic radiation from the accretion disk (Collin-Souffrin et al. 1988; Elvis 2000). They are often broader than low-ionisation lines due to higher velocities in this part of the BLR, and show prominent blueshifts (Richards et al. 2011; Coatman et al. 2016).

In short, we subdivide all lines into three main components that can account for the diversity of line profiles, along the quasar MS, resulting from the balance between gravitation and radiation forces (Ferland et al. 2009).

Population A

Broad Component (BC) Represented by a Lorentzian function, symmetric and unshifted or slightly redshifted (Véron-Cetty et al. 2001; Zamfir et al. 2010).

Blueshifted Component (BLUE) It is defined as the excess of emission on the blue side of the BC. The shape can be irregular, but the profiles resemble “triangular” or “trapezoidal shapes” (Marziani et al. 2017a; Vietri et al. 2018) that are usually well modelled by asymmetric Gaussian (Marziani et al. 2017a; Deconto-Machado et al. 2023). The blueshifted component can be very prominent at high Eddington ratios and high luminosity, dominating the HIL emission (Leighly & Moore 2004; Mejía-Restrepo et al. 2016; Vietri et al. 2020). The BLUE is increasing in prominence in the HILs along the quasar main sequence and reaches its maximum at ST A3-A4, where R_{FeII} is also at a maximum.

The two components most likely represent coexisting regions (Wang et al. 2011), albeit in very different physical and dynamical conditions. While the BC is associated with a dense, low ionisation region, capable of emitting mainly (but not exclusively) LILs and maintaining a virialised velocity field (for which a large column density is needed (Marconi et al. 2009)), the outflowing gas should be of higher ionisation. The assumption that BLUE and BC refer to regions with the same metallicity has been questioned by models of the AGN involving nuclear star formation (Wang et al. 2006), and in the following, we will attempt independent metallicity estimates from BLUE and BC.

Population B

Broad Component (BC) Represented by a Gaussian function, symmetric and unshifted or slightly redshifted (Zamfir et al. 2010).

Very Broad Component (VBC) Represented by a Gaussian function, redshifted by about ~ 2000 km s⁻¹ (Zamfir et al. 2010; Wolf et al. 2020). Given the virial velocity field of the emitting regions, this component represents the innermost emission of the BLR. Several works have described the Population B Balmer profiles in terms of a BLR and a very broad line region (VBLR, Peterson & Ferland 1986; Snedden & Gaskell 2004). It is unclear whether the emitting gas might be so highly ionised to be optically thin to the Lyman continuum (Morris & Ward 1989). The origin of the redshift is the subject of current debate, and two main alternatives have been proposed: gravitational redshift (Netzer 1977; Corbin 1995; Popovic et al. 1995; Muñoz et al. 2003; Mediavilla et al. 2018; Fian et al. 2022), and infall (Wang et al. 2014). The data unambiguously support the gravitational redshift hypothesis only for $\log M_{\text{BH}} \gtrsim 8.7$ [M_{\odot}], while lower M_{BH} require very low L/L_{Edd} for the profiles to show a significant gravitational effect (Marziani 2023).

Blueshifted Component (BLUE) It is defined as the excess of emission on the blue side of the BC+VBC profile. The blueshifted component is usually not prominent at low Eddington ratios but can still affect the centroid and asymmetry index of both HILs and LILs. Due to its weakness, BLUE is always modelled by a shifted (symmetric) Gaussian.

Fig. 8.1 summarises the interpretation of the line profiles of CIV λ 1549 and H β assumed as prototypical HIL and LIL, respectively, for Population B, Population A, and extreme Population A. Since BLUE is barely resolved in Pop. B, no estimates of the metallicity Z will be attempted. For the object of extreme Population A an estimate has been carried out for BC and BLUE, while for Pop. B sources, for the BC and VBC. In the latter case, we expect that the metallicity is the same, but the physical conditions would reflect a gradient in ionisation (lower ionisation for the BC and higher for the VBC), and hence be different on average.

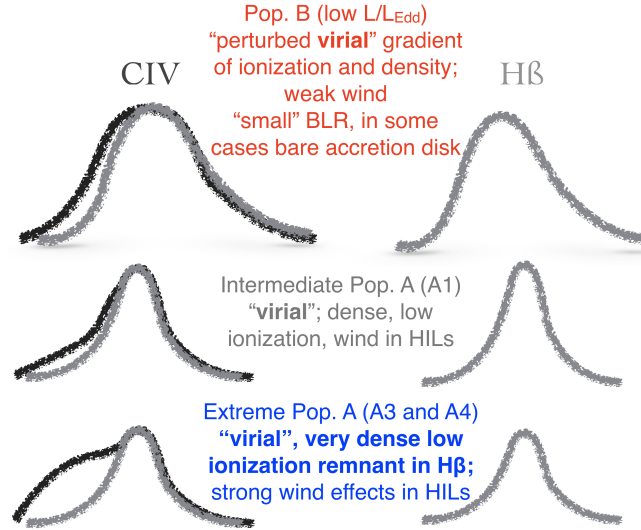


Fig. 8.1: Interpretation of the line profiles of low- and high-ionisation lines along the MS for isolating major spectroscopically resolved components.

8.3.2 Emission line ratios

Z indicator $C\text{IV}\lambda 1549/\text{SiIV}\lambda 1397 + \text{OIV}] \lambda 1402$ has been widely applied as metallicity indicator (e.g., Nagao et al. 2006b; Shin et al. 2013). In photoionisation equilibrium, the classical argument derived for HII regions that the electron temperature decreases with increasing metallicity (Pagel et al. 1979) works for the BLR as well. The intensity of the $C\text{IV}\lambda 1549$ line actually decreases as the metal abundance increases. However, the reason why the ratio $C\text{IV}\lambda 1549/\text{SiIV}\lambda 1397$ is a metallicity indicator resides in the "competition" of He^+ ions that have roughly the same creation potential of C^{++} . As a result, the Strömgen sphere of C^{+3} decreases much more strongly with increasing Z than for Si^{+3} : the ionisation potential of Si^{+2} is 2.46 Ryd, so the relatively unabsorbed continuum between 2.5 and 3.5 Ryd is available to maintain a proportionality with its abundance (Huang et al. 2023). This effect dominates over the lower electron temperature that affects the collisional excitation rates of both $\text{SiIV}\lambda 1397$ and $C\text{IV}\lambda 1549$, expected to be higher for $\text{SiIV}\lambda 1397$.

Z indicators $C\text{IV}\lambda 1549/\text{He II}\lambda 1640$ and $\text{SiIV}\lambda 1397/\text{He II}\lambda 1640$ When considering indicators like $C\text{IV}\lambda 1549/\text{He II}\lambda 1640$ and $\text{SiIV}\lambda 1397/\text{He II}\lambda 1640$, they should show sensitivity to the abundance of Carbon and Silicon, assuming that the ratio of Helium relative to Hydrogen remains constant. However, the dependence of $C\text{IV}\lambda 1549/\text{He II}\lambda 1640$ on Z is not monotonic: it increases for sub-solar metallicities and then declines steadily up to $200Z_{\odot}$, for specific conditions with $\log U \sim 0$ and $\log n_{\text{H}} \sim 9\text{cm}^{-3}$ (Śniegowska et al. 2021). For lower U values, the behaviour is monotonic (Garnica et al. 2022). This underscores the necessity for multiple intensity ratios that depend on Z and U .

Z indicators involving $\text{NV}\lambda 1240$, $\text{NV}\lambda 1240/C\text{IV}\lambda 1549$ and $\text{NV}\lambda 1240/\text{He II}\lambda 1640$ have also been extensively employed in previous studies (Hamann & Ferland 1993; Ferland et al. 1996; Nagao

et al. 2006b; Hamann et al. 2002; Shin et al. 2013). The strength of the NV λ 1240 line was unexpectedly high in a photoionisation scenario, possibly due to a selective enhancement of nitrogen (e.g., Osmer & Smith 1976; Shields 1976), resulting from secondary production of N by massive and intermediate-mass stars, and yielding $[N/H] \propto Z^2$ (Vila-Costas & Edmunds 1993; Izotov & Thuan 1999; Matsuoka et al. 2011). This process may be particularly significant in cases of abnormal star formation and evolution processes that are expected to occur within active nuclei. Contamination by narrow and semi-broad absorption features is often significant, and even with precise modelling of high-ionisation lines, it may be challenging to reconstruct the unabsorbed profile of the red wing of Ly α . In this analysis, we refrain from using ratios involving NV λ 1240 because they are not consistently measurable.

Density indicators The ratios Al III/Si III] and Si III]/C III] are responsive to density since they involve inter-combination lines with well-defined critical densities ($n_c \sim 10^{10} \text{ cm}^{-3}$ for C III] (Hamann et al. 2002) and $n_c \sim 10^{11} \text{ cm}^{-3}$ for Si III]).

Ionisation parameter Si III]/Si IV λ 1397, Si II λ 1816/Si III], and Si II λ 1816/Si IV λ 1397 are influenced by the ionisation parameter and remain insensitive to changes in Z since the lines are from different ionic states of the same element. Also, the ratio C III]/C IV λ 1549 is sensitive to the ionisation parameter but entails a strong dependence on the n_H as well. The ratio C IV λ 1549/H β is also a clear diagnostic, although it is also dependent on Z and, unfortunately, often made unreliable by the intrinsic variations of the quasar and by poor photometric accuracy if observations are not synoptic and dedicated.

Mixed diagnostics: Fe II/H β The ratio R_{FeII} deserves a particular attention. As with any other metal to Hydrogen ratio, it entails an obvious dependence on iron abundance and hence on metallicity. Nonetheless, R_{FeII} is dependent on density, ionisation parameter and column density of the line emitting gas, in the sense that large R_{FeII} ($\gtrsim 1$) seem possible only for relatively high n_H ($\gtrsim 10^{11} \text{ cm}^{-3}$), low ionisation and large N_c ($\gtrsim 10^{23} \text{ cm}^{-2}$) (Collin & Joly 2000; Matsuoka et al. 2008; Panda et al. 2019).

In the following, we will try to use the same ratios as much as possible for the three-line components. However, the BLUE components are often so weak to be undetectable in several LIL profiles. In this case, we consider upper or lower limits as appropriate. Table 8.1 provides an overview of the measured intensity ratios applied to the metallicity estimates of several of our targets.

8.3.3 Photoionisation simulations

Understanding the physical conditions within quasar environments involves estimating parameters like metallicity (Z), density (n_H), and ionisation state (ionisation parameter U). The three fundamental parameters can be estimated by comparing observed line ratios with model predictions obtained through computational models, such as CLOUDY, which simulate the interactions between radiation and gas in the environments of the broad line region Ferland et al. (2017). Input parameters for

Table 8.1: Diagnostic intensity ratios.

Component	$\text{SiIV+OIV}/\text{CIV}$	$\text{SiIV+OIV}/\text{He II}_{\text{UV}}$	$\text{CIV}/\text{He II}_{\text{UV}}$	$\text{CIV}/\text{CIII}]$	$\text{CIV}/\text{H}\beta$	AlIII/CIV	$\text{AlIII}/\text{He II}_{\text{UV}}$	$\text{AlIII}/\text{SiIII}]$	$\text{SiIII}]/\text{CIII}]$	R_{FeII}	$\text{HeII}_{\text{opt}}/\text{H}\beta$
BLUE [A]	○	○	○	—	>	<	<	—	—	<	—
BC	○	○	○	○	○	○	○	○	○	○	<
VBC [B]	○	○	○	○	○	○	—	<	<	○	○

○ measured ratio with associated uncertainty. < and >: upper and lower limit to intensity ratio, respectively. —: not available. He II_{UV} and $\text{He II}_{\text{opt}}$ are $\text{He II}\lambda 1640$ and $\text{He II}\lambda 4686$, respectively. Blue circles identify the ratios actually used for the new sources presented in this work; the use of the $\text{CIV}\lambda 1549/\text{H}\beta$ ratio has been considered only for Fairall 9, due to the non-contemporaneity of the rest-frame optical and UV data. Unavailable ratios involve two undetectable components.

photoionisation computations are the photoionising continuum spectral energy distribution (SED), the ionisation parameter (or an alternative, luminosity, and distance of the emitting region), gas hydrogen density, chemical composition, and a micro-turbulence parameter. There is evidence of trends for all of these parameters along the quasar main sequence, and in the case of Population B, there is evidence of a radial stratification of the properties within the BLR (Baldwin et al. 1995; Korista et al. 1997) that is heuristically modelled separating a BC and VBC (BLR and VBLR).

The arrays of simulations were therefore organised as follows: 5 different SEDs, one for each of the following cases: Pop. B RL, Pop. B RQ, with a dedicated SED for NGC 1275, an SED for Pop. A sources (Mathews & Ferland 1987) and one for extreme Pop. A (high Eddington ratio of Ref. Ferland et al. 2020). Metallicity (Z) was assumed to scale as solar (Z_{\odot}), with 12 values ranging between 0.01 and $1000 Z_{\odot}$ for Pop. A and 14 values between 0.001 and $20 Z_{\odot}$ for Pop. B. The micro-turbulence parameter was set to 0 km s^{-1} . This is relatively insignificant for resonance UV lines (Śniegowska et al. 2021), but is expected to lead to an under-prediction of Fe II emission (Sigut & Pradhan 1998, 2003; Śniegowska et al. 2021). For each metallicity value, we considered an array of simulations covering the n_{H} and U parameter plane in the range $7 \leq \log n_{\text{H}} \leq 14 \text{ cm}^{-3}$, $-4.5 \leq \log U \leq 1$ for Pop. A (667 simulations), and $7 \leq \log n_{\text{H}} \leq 13 \text{ cm}^{-3}$, $-3 \leq \log U \leq 1$ for Pop. B (425 simulations). For each source or composite spectra, the set of $\approx 8-9$ diagnostic ratios were compared with a set of ≈ 8000 and 6000 simulations covering the parameter space n_{H} , U , and Z , for Population A and B respectively. The computations were carried out independently for the three components identified in the emission lines, as they are thought to represent distinct regions in different physical conditions. The solution for the single zone model (i.e., a single point in the 3D space n_{H} , U , Z) was identified by the minimum χ^2 computed from the difference between the observed line ratios and the predicted line ratios over the entire 3D space (see, e.g., Śniegowska et al. 2021; Garnica et al. 2022).

Errors on measured line ratios were estimated assuming that the continuum placement was the dominant source of uncertainties and setting extreme continua as $\text{cont} \pm \text{rms}$, where cont is the best-fit continuum and rms is the noise measured over the continuum itself and propagated according to the “triangular distribution” (D’Agostini 2003). Limits at 1σ and 90% confidence were set by computing the ratio $F = \chi^2 / \chi^2_{\text{min}}$ between χ^2 of different models for $n_{\text{ratios}} - 3$ degrees of freedom.

There are several caveats in the method, related to both the quality of the data and the model assumption: (1) the non-simultaneity of the observations in the optical and UV. Often, optical and

UV observations are separated by years in the rest frame of the quasar. In addition, photometric inter-calibration between optical and UV data is problematic: while space-based observations are precise within a few percent, optical data are affected by uncontrolled light loss. As a result, the ratio $\text{C IV } \lambda 1549/\text{H}\beta$ was measured but ultimately removed from the computations in the new sources analysed in the present paper (Mark 335, Mark 478, PHL 1092) except for Fairall 9. In this case, simulations both with and without the ratio $\text{C IV } \lambda 1549/\text{H}\beta$ were run and gave consistent results. (2) A major assumption is that metallicity scales as solar. Albeit this is a time-honoured assumption (Nagao et al. 2006a; Maiolino & Mannucci 2019), it is not a reasonable one because major differences are expected for a disk star in a late-type spiral galaxy and the nuclear region of an active galaxy (Wang et al. 2023, and references therein). Actually, recent works discussed the evidence of pollution by supernova ejecta (Cantiello et al. 2021; Garnica et al. 2022). (3) Photoionisation computations are carried out under the assumption of single-zone emission. While this assumption seems a good one for extreme Population A, where density and ionisation tend toward limiting values (Panda et al. 2019), this might not be the case for Pop. B sources.

8.4 Case studies

Basic properties of the cases considered in this paper are reported in Table 8.2, and include the E1 optical parameter FWHM $\text{H}\beta$ and R_{FeII} , as well as the accretion parameters (luminosity, black hole mass M_{BH} , and Eddington ratio). The last columns provide the radio loudness parameter and some notes that list bibliographical sources of information or notable, recent work related to the specific object.

Composite RL - ST B1 — A RL composite spectrum was obtained from 20 RL sources, with redshift range $\approx 0.25 - 0.65$, absolute magnitudes between -23.5 and -26.5 and $\text{S/N} \approx 130$ and ≈ 55 for the visual and UV ranges. The Z estimates are used as provided by Marziani et al. (2023) since the method of analysis and measurement is basically the same.

NGC 1275 — NGC 1275 (Perseus A) is an elliptical galaxy, and the brightest cluster galaxy of the Perseus Cluster, one of the most massive galaxy clusters in the nearby Universe. NGC 1275 is associated with a cooling flow phenomenon, where gas in the cluster's intracluster medium is thought to cool and sink towards the central regions of the galaxy (Heckman et al. 1989; Lim et al. 2008), potentially fuelling its modest AGN activity. The photoionising continuum, which is crucial for understanding the ionisation state of the gas in NGC 1275, was defined ad hoc by observational constraints on the SED (see Punsly et al. 2018, for details). The estimated photoionising continuum had a spectral index $\alpha_{\nu} = 0.5$ in the far-UV range (500 to 800 Å) and a spectral break at 800 Å. Beyond this spectral break, the spectral index $\alpha_{\nu} = 2$ down to the soft X-ray band at 0.5 keV, with $\alpha_{\nu} = 1.0$ in the harder X-ray band. In summary, the SED of the far-UV shown by Punsly et al. (2018) indicates a broad line Seyfert-like AGN with a soft ionising continuum, a weak hard ionising continuum, and no Compton deflection hump.

The big blue bump associated with thermal emission from optically thick, geometrically thin accretion (Sun & Malkan 1989) is weaker than the ones of the SED templates appropriate for Population B quasars, see Fig. 5 of Punsly et al. (2018). The L/L_{Edd} is extremely low and, interestingly, the BLR is correspondingly weak, to the point that a careful, dedicated analysis was needed to disentangle the broad line profiles from the much stronger narrow line emission.

Composite RQ - ST B1 — A composite spectrum was constructed for a group of 16 RQ sources, all falling within the spectral bin B1, within the redshift range of approximately redshift range ≈ 0.002 – 0.5 . These sources span an absolute magnitude range -21 – -27 , which corresponds to a bolometric luminosity range $\log L \sim 45$ – 47 [erg s^{-1}]. To achieve comprehensive UV coverage from 1000 \AA to around 6000 \AA (including the spectral region from $\text{Ly}\alpha$ to $\text{H}\beta$), which is typically demanding and necessitates space-based observations, the UV data were obtained from HST/FOS observations as discussed in Sulentic et al. (2007a). Additionally, the optical spectra were sourced from Marziani et al. (2003b). The composite spectrum has a high signal-to-noise ratio (S/N) of approximately 90. The metallicities (Z values) for this composite and their corresponding uncertainties were adopted from Marziani et al. (2023).

Fairall 9 - ST B1 — Empirical parameters derived from the Main Sequence (MS) analysis indicate Fairall 9's spectral type as B1, a category well-populated among quasars along the MS. This classification consistently aligns with a low L/L_{Edd} ratio. Notably, Fairall 9 exhibits radio quietness, as it eluded detection in the Sydney University Molonglo Sky Survey (Mauch et al. 2003) with a detection limit of 6 mJy, implying a radio-to-optical specific flux ratio of $\lesssim 1.5$. We use $\log R_{\text{K}} \approx -0.04$ (Sikora et al. 2007).

The most recent assessment of the black hole mass includes estimates using the reverberation mapping technique that have converged on values ranging from $(1.5 - 2.5) \times 10^8 M_{\odot}$ (Peterson et al. 2004; Bentz & Katz 2015), contingent on the adopted virial factor, as well as a spectropolarimetric-derived M_{BH} that allowed for a virial factor estimate, yields $(1.5 \pm 0.5) \cdot 10^8 M_{\odot}$. A conventional estimate of Fairall 9's bolometric luminosity stands at $\log L_{\text{bol}} \approx 45.3 \text{ erg s}^{-1}$, with an Eddington ratio of $\log L/L_{\text{Edd}} \approx -2.0$, placing it toward the lower end within the distribution of Population B sources. The Spectral Energy Distribution (SED) also conforms to the characteristics of Population B objects, devoid of a prominent big-blue bump. More details are given in a recent paper by Jiang et al. (2021).

Mrk 335 - ST A1 — Markarian 335 is a population A Seyfert 1, spectral type A1. It is located in the nearby Universe with a redshift of 0.0256. This AGN exhibits characteristics typical of an RQ A1 AGN, with lower-than-average Fe II emissions, positioning it in the lower-left corner of the MS. Emission lines in the UV and optical ranges exhibit little to no blueshifts in their profiles. The only exception to this typical behaviour is the positive slope of its optical continuum, which is likely due to galactic extinction.

Mrk 478 - ST A2 — Markarian 478 is a Pop. A Seyfert 1, spectral type A2, borderline A3 from the measurements of the present analysis. It is located at a redshift of 0.077. Although classified as

Table 8.2: Object properties

Object name	ST	z	FWHM($H\beta$) [km s ⁻¹]	R_{FeII}	L_{bol} [erg s ⁻¹]	M_{BH} [M_{\odot}]	L/L_{Edd}	R_K	Notes
(1)	(2)	(3)	(4)	(5)	(6)	(7)	(8)	(9)	(10)
Composite RL	B1	$\approx 0.25-0.65$	7690	0.17	$8 \cdot 10^{44} - 8 \cdot 10^{45}$	$10^8 - 10^9$	0.01 - 0.1	≥ 80	Marziani et al. (2023)
NGC 1275	B1	0.017	4770	n.d. ^a , ≤ 0.2	1.2×10^{43}	8×10^8	$\leq 10^{-4}$	1744	L/L_{Edd} , M_{BH} , L_s : Punsly et al. (2018)
Composite RQ	B1	$\approx 0.002-0.5$	5530	0.34	$8 \cdot 10^{43} - 2 \cdot 10^{46}$	$4 \times 10^8 - 10^9$	0.01 - 0.04	≤ 10	Marziani et al. (2023)
Fairall 9	B1	0.04609	4550	0.43	2×10^{45}	$1.5 \cdot 10^8$	0.01	0.92	R_K : Sikora et al. (2007), M_{BH} : Jiang et al. (2021)
Mrk 335	A1	0.0256	2175	0.34	6.9×10^{44}	3.45×10^7	0.13	0.36	
Mrk 478	A2/A3	0.077	1322	1.04	4.4×10^{45}	2.90×10^7	1.02	0.85	Marshall et al. (1996); Hwang & Bowyer (1997); Yuan et al. (2004)
PHL 1092	A4	0.3965	2494	1.76	1.4×10^{46}	2.21×10^8	0.42	0.78	Radio-detected but RQ (Zacharias et al. 2005; Marinello et al. 2020b)
Composite	xA	2.1 - 2.5	3200 ^b	... ^b	$4 \times 10^{46} - 4 \times 10^{47}$	$10^9 - 10^{10}$	0.7 - 3	≤ 80	$<L/L_{Edd}> \approx 1$; Sniegowska et al. (2021); Garnica et al. (2022)

Notes. (1) Object common name. (2) Spectral type of the object. (3) Redshift. (4) Full Width at Half Maximum of $H\beta$ expressed in units of km s⁻¹. (5) Fe II prominence parameter, defined as the intensity ratio $R_{FeII} = FeII\lambda 4570/H\beta$. (6) Bolometric luminosity (L_{bol}) obtained by integrating the specific flux obtained from the NED database over all frequencies. (7) Mass of the supermassive black hole (M_{BH}) of the AGN, calculated using the scaling relation from Vestergaard & Peterson (2006). (8) Ratio between the bolometric luminosity of the object and the Eddington luminosity: $L/L_{Edd} = L_{bol}/[1.5 \times 10^{38}(M_{BH}/M_{\odot})]$. (9) Kellerman Ratio obtained from $\frac{f_{Radio}}{f_B}$ (Kellermann et al. 1989), where f_{Radio} is the specific flux at a wavelength of 6 cm (5 GHz) and f_B is the specific flux at 4400 Å (680 THz) in the B band. ^a: not detected, only a broad upper limit is estimated. ^b: $H\beta$ spectral range not covered; R_{FeII} not available. The FWHM refers to the best proximate of $H\beta$ in the UV, the Al III doublet.

A2, it exhibits characteristics that suggest it may be an extreme accretor. Table 8.2 shows that it has an Eddington ratio ≈ 1 . Additionally, it displays a strong Fe II emission and a pronounced outflowing component in its emission line profiles. Hence, it could be argued that Mrk 478 could be classified as an A3-type object.

PHL 1092 - ST A4 — Palomar Haro Luyten 1092 is a population A Seyfert 1, spectral type A4, located at a redshift of 0.3965. Its spectrum is characterised by strong UV emissions, with a notably sloped SED. PHL 1092 is considered an extremely accreting quasar, as it exhibits prime characteristics of one, including a strong outflowing component in its emission line profiles, particularly noticeable in C IV $\lambda 1549$ $\lambda 1549$ and Si IV $\lambda 1397$ +O IV] $\lambda 1402$, which casts a shadow on the virialised component. In the optical range, the $H\beta$ emission is overshadowed by the Fe II emission, mirroring the Fe II profile of I Zw 1, itself considered an extreme accretor.

Extreme Population A (A3, A4) — The intermediate redshift xA sample of Sniegowska et al. (2021) and Garnica et al. (2022) allowed for Z estimates from the UV spectral lines. The sample lacks the optical data providing the important information from the $H\beta$ spectral range, and the line width reported in Table 8.2 is the one of Al III. The sources were selected based on UV criteria that were found equivalent to the criterion $R_{FeII} \geq 1$ for the identification of extreme Population A sources, at least at a high degree of confidence (Buendia-Rios et al. 2023). Their luminosity is significantly higher than the luminosity of the other sources considered in this paper, although the Eddington ratio is consistent with the ones of Mark 478 and PHL 1092, $\sim O(1)$.

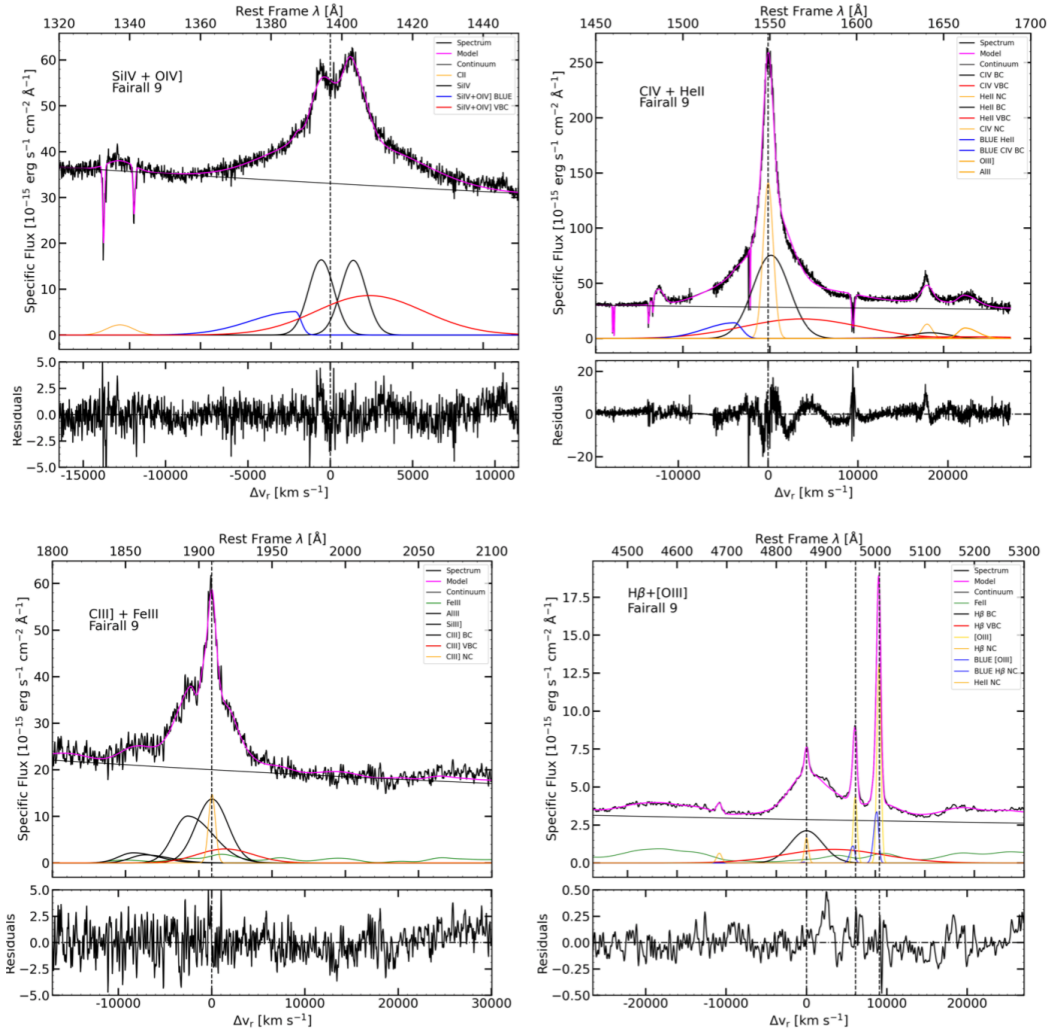


Fig. 8.2: Fits of the emission line spectrum of Fairall 9, the prototypical Population B source. From left to right, top row: 1400 Å blend; C IV λ 1549 + He II λ 1640 blend; bottom row: 1900 Å blend; H β + Fe II blend. The line profile of H β and the 1900 blend are accounted for by two components, BC (black lines) and VBC (red). The HILs in the rest-frame ultraviolet show an excess with respect to the BC+VBC extending on the blue side of the line, modelled with a skew Gaussian (Azzalini & Regoli 2012) and ascribed to emission from a spectroscopically resolved outflow that adds up to the virialised components. The magenta lines trace the full empirical model of the line profiles. The bottom panels show the (observed minus computed) residuals.

8.5 Results

8.5.1 Line profile analysis

The results of the line profile analysis are shown, as an example, for the case of Fairall 9 (Fig. 8.2). All the lines fit with the three components introduced in Section 8.3.1. He II λ 1640 and C IV λ 1549 are explained assuming that the components are present with consistent shifts and widths but changing their relative intensity ratios. This accounts for the flat He II λ 1640 profile that lacks the prominent

BC observed for CIV λ 1549, in turn implying CIV λ 1549/He II λ 1640 \gg 1 for the BC. The VBC CIV λ 1549/He II λ 1640 is much lower. A similar effect is visible for H β and HeII λ 4686 in the rightmost panel of Fig. 8.2. This has implications on the physical conditions derived for the VBLR and BLR, in turn motivating the model with two separate components, as discussed in several works (Popović et al. 2004; Snedden & Gaskell 2007; Bon et al. 2009). A second important implication is that the VBC of HeII λ 4686 and He II λ 1640 is much better defined than the BC, allowing for a more reliable estimate of the VBC ratios involving these lines.

Similar line profile decomposition has been carried out for quasar emission lines over a broad range of redshift (Leighly & Moore 2004; Vietri 2017; Yang et al. 2023), although the heuristic technique applied in this and some previous papers allows to consistently fit all quasars emission lines with only three components. The approach is equivalent to measuring profile intensity ratios (Shang et al. 2007; Garnica et al. 2022), with the advantage that the absorptions that are frequently found in high-redshift quasar spectra can be easily compensated. Intensity ratios for the three components are found consistent with the ones of previous work.

8.5.2 Estimation of Metallicity for the Virialised Emitting Region

Four of the case studies are new results on individual objects, and the metallicity values and the associated uncertainties at 1σ confidence level are reported in Table 8.3, along with estimates from previously published studies. Figs. 8.3 and 8.4 show the interval of confidence at 1σ level for the new cases in the planes Z vs. ionisation parameter and density n_{H} .

The case of Fairall 9 includes the best Z derived for the VLBR. The χ^2 is lower even if the number of degrees of freedom is lower, which allows for a much more restricted range in the parameter space than for the case of the BLR ratios. In this case, the parameters are rather loosely constrained, although the agreement between the minimum χ^2 derived for the BC and the one of the VBC, reinforces a metallicity estimate around $Z \approx 1 - 2Z_{\odot}$, as the two regions are expected to have the same Z . In the Fairall 9 case, the consideration of the ratio CIV λ 1549/H β (an important parameter connected, in addition to Z , also to U), confirms the estimate $Z \approx 1 - 2Z_{\odot}$, for both the BLR and VBLR.

Fig. 8.4 shows the planes Z vs. ionisation parameter and density n_{H} ordered along the sequence of increasing R_{FeII} within Pop. A. The Z values range from $\lesssim 0.1 Z_{\odot}$ to $50 Z_{\odot}$ from the B1 RL composite to PHL 1092. The Z value obtained for PHL 1092 confirms the high $Z \sim 100 Z_{\odot}$ obtained with UV intensity ratios only (Śniegowska et al. 2021; Garnica et al. 2022).

Fig. 8.5 shows the location of all case studies along the E1 main sequence. The Z values along the main sequence range from $0.1Z_{\odot}$ to $\sim 100 Z_{\odot}$, and the trend is one of a monotonic increase along the horizontal sequence of increasing R_{FeII} , from solar or slightly sub-solar, to highly super-solar, with Z at least a few tens the solar values. Spectral type B1 and A1 consistently show similar values around solar, with the weak but still significant Fe II emission.

An important result is the realisation that not all BLRs are made of gas with the same metal content. There is apparently a systematic gradient involving a range of more than a factor ~ 100 . No

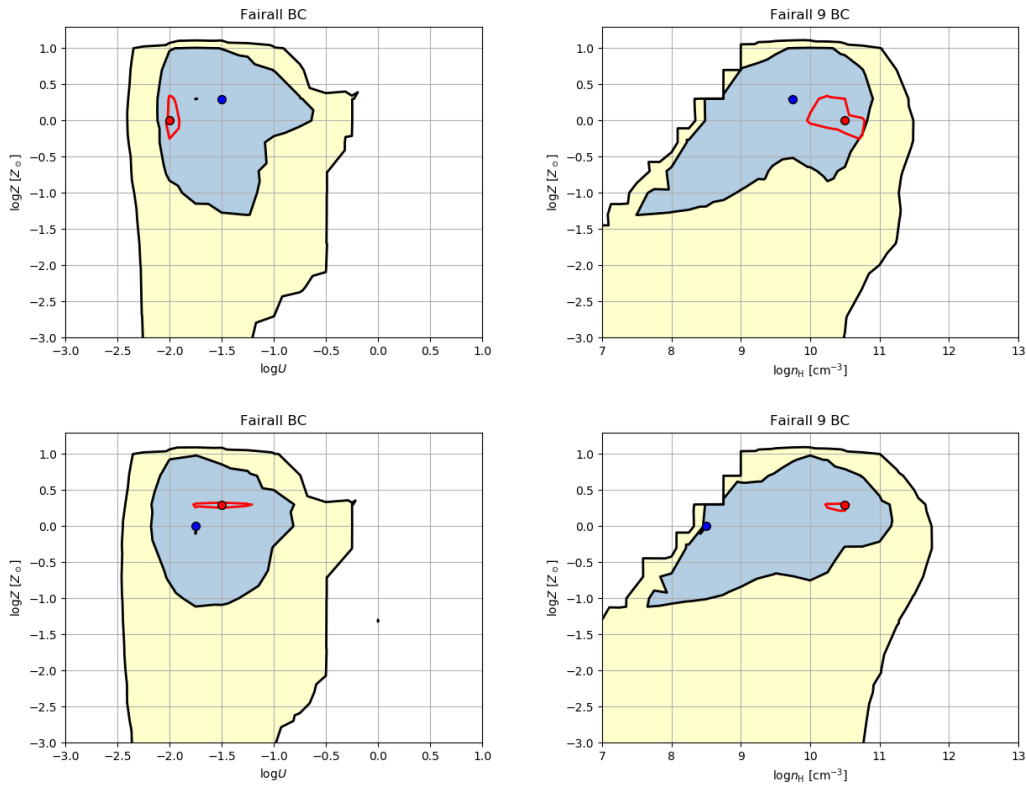


Fig. 8.3: Projections of the 3D parameter space (U , n_{H} , Z) onto the (U , Z) (left) and (n_{H} , Z) planes (right), for the prototypical Pop. B source Fairall 9. The top and bottom panels are for χ^2 computed with and without the $\text{C IV } \lambda 1549/\text{H}\beta$ ratio. The blue spot identifies the model yielding minimum χ^2 for the BC; the red one is the same for the VBC. Isophotal contours are a 1σ (pale blue) and 90% confidence level (yellow); the red line is the 1σ level for the VBC.

matter the exact values of the Z , especially at the extremes, the trend is substantiated by the trend in the most metal-sensitive ratios, $(\text{Si IV } \lambda 1397 + \text{O IV } \lambda 1402)/\text{C IV } \lambda 1549$, and $R_{\text{Fe II}}$, and ratios involving Al III. The range in Z can be compared with a recent systematic study for intermediate redshift quasars [Xu et al. \(2018\)](#). Highest values around $Z \sim 20Z_{\odot}$ are found for massive black holes ($\log M_{\text{BH}} \sim 9.7$ [M_{\odot}]), and are comparable with the value we obtain at low- z for high Eddington ratio sources.

At intermediate redshift, however, the BLR Z remains always highly super-solar, $\gtrsim 5Z_{\odot}$, much above the most metal-rich galaxies ($Z \sim 2Z_{\odot}$) [Maiolino & Mannucci \(2019\)](#). Quasars in the local Universe with modest masses ($\lesssim 10^8$ [M_{\odot}]) radiating at low L/L_{Edd} are not yet sampled in major surveys, and there is therefore no disagreement if low- Z sources are missing at intermediate redshift.

8.5.3 Outflows traced by the blueshifted components

Gas outflows appear to be a phenomenon shared by the vast majority of AGNs (e.g., [Feruglio et al. 2010](#); [Harrison et al. 2014](#); [Feruglio et al. 2015](#); [Woo et al. 2016](#); [Kovačević-Dojčinović et al. 2022](#)). Emission lines like $\text{C IV } \lambda 1549$ provide valuable information about massive, ionised outflows

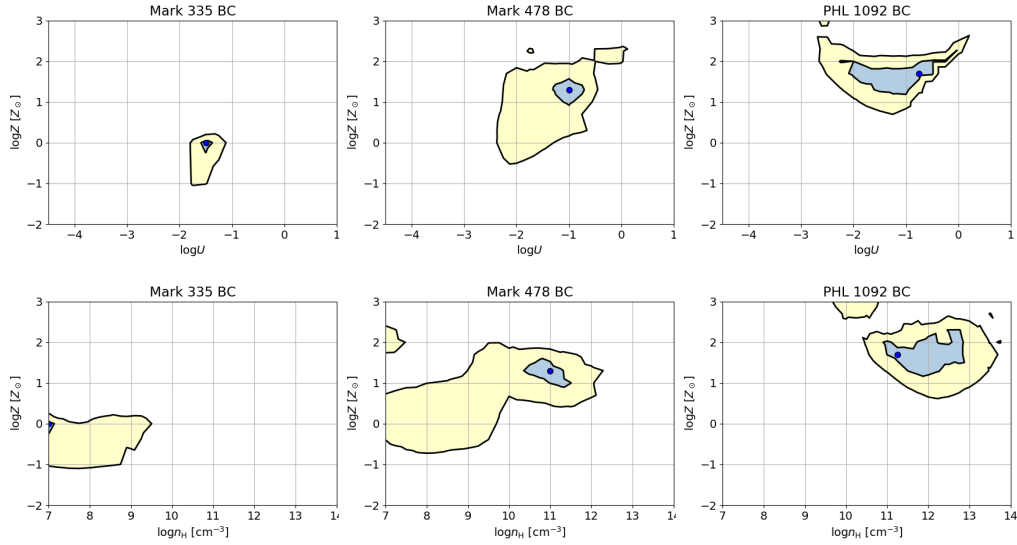


Fig. 8.4: Projections of the 3D parameter space (U , n_{H} , Z) onto the (U , Z) (top) and (n_{H} , Z) planes (bottom), for the Pop. A sources - Mark 335 (left), Mark 478 (middle), and PHL 1092 (right). The meaning of panels is the same as for the BC in Fig. 8.3.

Table 8.3: Metallicity estimates along the quasar MS

Identification (1)	Comp. (2)	$\log[Z/Z_{\odot}]$ (3)	1σ range (4)	Notes
Composite RL B1	BC	-1.7	-2 — -1	Marziani et al. (2023)
NGC 1275	BC	-0.3	-0.3 — 0	Punsly et al. (2018)
Composite RQ B1	BC	0.30	-0.70 — 1.00	Marziani et al. (2023)
Composite RQ B1	VBC	0.70	0.70 — 0.70	Marziani et al. (2023)
Fairall 9	BC	0.30	-1.30 — 1.00	This work; C IV $\lambda 1549/\text{H}\beta$ excluded
Fairall 9	VBC	0.00	0.00 — 0.30	This work; C IV $\lambda 1549/\text{H}\beta$ excluded
Fairall 9	BC	0.00	-1.00 — 0.70	This work
Fairall 9	VBC	0.30	0.30 — 0.30	This work
Mrk 335	BC	0.00	-1.00 — 0.00 ^a	This work
Mrk 478	BC	1.30	1.00 — 1.30	This work
PHL 1092	BC	1.70	1.30 — 2.30	This work
Composite $z \sim 2$	xA	1.70	1.30 — 2.00	Śniegowska et al. (2021); Garnica et al. (2022)

associated with the accretion disk, and in turn, contribute to understanding the dynamic processes within the BLR and its interplay with the accretion disk.

Selection of the lines most suitable for plasma diagnostics, including the metallicity, is much harder for the outflow component than for the virialised one, as the first appears spectroscopically resolved in high- and low-ionisation lines only for extreme Population A or at very high luminosity. We used four diagnostic ratios for estimating the physical properties of the blue, outflowing component: C IV $\lambda 1549/\text{He II} \lambda 1640$, C IV $\lambda 1549/(\text{OIV} \lambda 1402 + \text{SiIV} \lambda 1397)$, C IV $\lambda 1549/\text{H}\beta$ and $(\text{OIV} \lambda 1402 + \text{SiIV} \lambda 1397)/\text{He II} \lambda 1640$, along with constraints from upper limits for the ratios Al III/C IV $\lambda 1549$, Fe II/H β . The diagnostic ratios are consistent with the estimates of metallicity derived for the virialised components, for PHL 1092 ($Z \sim 50Z_{\odot}$, with a 1σ confidence range 20 – 50 Z_{\odot}). Median values of the BLUE components are $\sim 6Z_{\odot}$ for the xA intermediate z samples, somewhat lower and obtained only with three diagnostic ratios (H β was not measured). Note that this abundance estimate is obtained using ratios involving only α -elements. Other properties of the

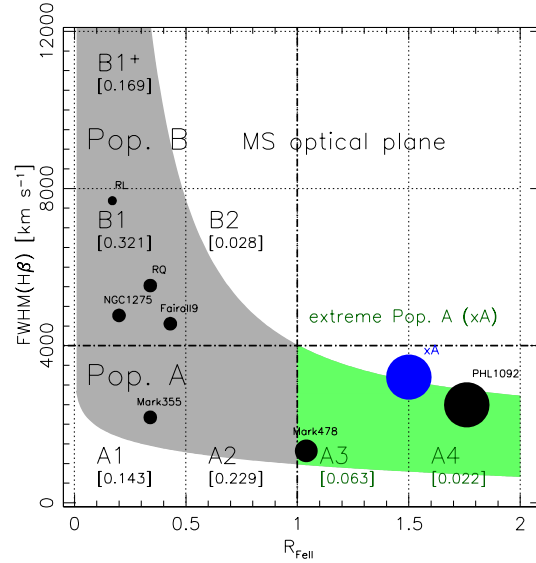


Fig. 8.5: Sketch of the quasar main sequence at low redshift, with circles of different sizes representing the metallicity estimates for different sources, composites, and samples presented in this paper and analysed in recent literature. The abscissa is Fe II prominence parameter R_{FeII} ; ordinate is the FWHM $\text{H}\beta$ in km s^{-1} . The numbers in square brackets report the prevalence of each spectral bin in an SDSS-based sample (Marziani et al. 2013a). The size of the circles depends on Z : smallest for $Z \lesssim 0.1Z_{\odot}$, intermediate for $0.5Z_{\odot} \lesssim Z \lesssim 2Z_{\odot}$, larger for $Z \sim 10Z_{\odot}$, and largest for $Z \sim 50Z_{\odot}$. The blue circle refers to the intermediate z sample of Garnica et al. (2022).

outflowing component are less well-constrained because of the limited number of diagnostics. A better precision might be achieved with higher S/N and additional diagnostic ratios. However, it is reasonable to assume that the outflowing gas from the high Eddington ratio sources might have $Z \sim 10Z_{\odot}$, a conservative estimate in agreement with other works (Xu et al. 2018, and references therein). If this is the case, the mass outflow rate is $\dot{M} \sim 10^3 L_{\text{CIV},45} n_{\text{H},9}^{-1}$, where $L_{\text{CIV},45} \text{ erg s}^{-1}$ is the C IV $\lambda 1549$ luminosity in units of $10^{45} \text{ erg s}^{-1}$ and $n_{\text{H},9}$ is the Hydrogen density in units of 10^9 cm^{-3} (Marziani et al. 2017a). Solar metallicity implies that 1.46% of the mass of the gas is due to metals. For a modest luminosity of $10^{44} \text{ erg s}^{-1}$, the implication is that about $\sim 15 M_{\odot}/\text{yr}$ of metals are returned to the interstellar medium (ISM). Over a high-accretion lifetime of $\sim 10^7 \text{ yr}$ (Collin et al. 2002; Li 2012), the metal mass expected to be returned to the ISM could be $\sim 10^8 M_{\odot}$. While this estimate is extremely coarse, and the actual effect will depend on how the outflow is dissipated within the host, it implies that there could be in principle a significant enrichment for a large stellar population and earlier for the ISM.

We have focused on low-luminosity quasars in the local Universe, characterised by relatively small black holes radiating near their Eddington limit. However, it's important to note that the outflow phenomena are most prominent in the highest luminosity quasars. These super luminous quasars exhibit a high prevalence of significant blueshifts in the blueshifts in the C IV $\lambda 1549$ and [O III] $\lambda \lambda 4959, 5007$ emission line profiles (Bischetti et al. 2017; Vietri et al. 2018; Deconto-Machado et al. 2023). The ionised gas mass, kinetic energy, and mechanical thrust in these cases are remarkably high, implying extensive feedback effects on the host galaxies of these exceptionally luminous quasars. These effects were particularly pronounced during cosmic epochs between 2 and 6 billion years after

the Big Bang, suggesting that these quasars might have played a substantial role in enriching the chemical composition of their host galaxies.

8.6 Discussion

8.6.1 A gradient in metal content and chemical feedback along the sequence

A cartoon depicting a global evolutionary scenario is shown in Fig. 8.6. At the one end of the sequence we encounter low mass, high Eddington ratio sources. They are accreting at a high rate, possibly following a merger and a burst of star formation. In the initial phases of the development of AGN and quasars, a series of events take place: wet mergers and strong interactions cause the accumulation of gas in the central regions of the galaxy. This accumulation triggers a burst of star formation (top of the inset, Sanders et al. 1988, 2009). Over time, mass loss from stellar winds and supernova explosions provide a source of accretion fuel for the massive black hole located at the centre of the galaxy. Subsequently, radiation force and mechanical energy can clear away the dust surrounding the black hole, particularly within a cone aligned with the axis of the accretion disk. This allows the radiative and mechanical energy to be released into the ISM of the host galaxy (bottom of the inset).

At a high accretion rate, a nuclear starburst can occur in the region where the disk becomes self-gravitating (Collin & Zahn 1999). As mentioned, the Z -values calculated for the BLR of quasars appear exceptionally high when compared to their host galaxies. For reference, the highest measured Z -value in a molecular cloud is approximately 5 times the solar metallicity (Maiolino & Mannucci 2019). However, it's important to note that the nuclear and circumnuclear environments of quasars may exhibit significant deviations from a typical interstellar setting. In these regions, stars traverse the disk, giving rise to the formation of accretion-modified objects that eventually attain substantial mass and, after a brief evolutionary phase, explode as core-collapse supernovae (Collin & Zahn 1999; Cheng & Wang 1999). Stars within the nuclear vicinity can rapidly become highly massive (with masses exceeding 100 times that of the Sun), leading to core-collapse events that contribute to enriching the disk with heavy elements via the substantial metal yields produced by supernova ejecta (Cantiello et al. 2021). Furthermore, the compact remnants of these stars may continue accreting material, resulting in recurrent supernova occurrences (Lin 1997). These accretion-modified star formation processes that enhance metallicity are projected to yield metal abundances approximately in the range of 10 to 20 times solar metallicity (Wang et al. 2011), which aligns with the values observed in the xA sources.

At the other end, we find very massive black holes, radiating at low Eddington ratios, in conditions that are proximate to "starvation" and in any case to the exhaustion of the reservoir of gas for accretion. Accretion material may come from evolved star winds that can sustain modelled accretion rates (Padovani & Matteucci 1993). Metallicity values might be in this case more conventional, around solar or sub-solar, such as the values ranging from ~ 0.1 to ≈ 2 times the solar metallicity found in the bulge of the Milky Way (Zoccali et al. 2003; Gonzalez & Gadotti 2016).

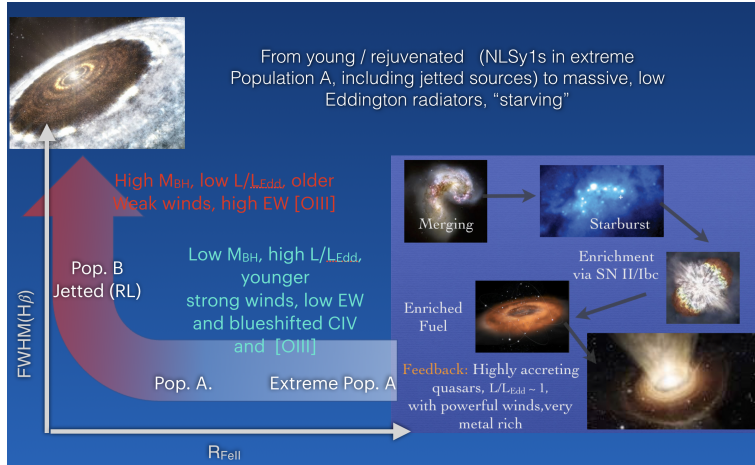


Fig. 8.6: Sketch depicting the evolutionary interpretation of the quasar main sequence. The inset on the right shows a possible evolutionary path leading to highly accreting quasar showing evidence of high metal enrichment in the BLR.

Pop. B sources have a slightly larger redshift than Pop. A ($\bar{z} \approx 0.33$ vs 0.07) in a large, SDSS-based, low- z sample (Zamfir et al. 2010) that might be easily explained by selection effects. However, a ten-fold increase in black hole mass from $10^8 M_{\odot}$ at moderate accretion rate can occur over a time $\sim 5 \cdot 10^8$ yr (Fraix-Burnet et al. 2017b). This timescale would correspond to a change in redshift $\delta z \approx 0.05$. Therefore, it is reasonable to assume that at least some Pop. B AGN evolved from Pop. A sources locally.

8.7 Conclusion

In conclusion, the main sequence concept in quasars reveals a gradient of metallicity across different quasar populations, shedding light on their evolutionary paths. The understanding of these populations and their associated characteristics contributes to a deeper comprehension of the processes driving quasar behaviour and their influence on their host galaxies. Expectations from accretion-modified stars within the active nuclei are consistent with highly super-solar metallicity.

GENERAL CONCLUSIONS OF THE THESIS

In this thesis, we presented for the first time, a dedicated analysis of radio-loudness and feedback effects on the quasar Main Sequence within a high-redshift context. We provide new spectroscopic observations for 32 high-redshift ($1.55 \lesssim z \lesssim 3.80$) and high-luminosity ($47.18 \lesssim \log L_{\text{bol}} \lesssim 48.36$ [erg s⁻¹]) quasars. The data was obtained using the ISAAC spectrograph at the VLT and cover the H β + [O III] $\lambda\lambda 4959, 5007$ spectral range, shifted to the near-infrared due to the redshift of the sources. Additionally, UV spectra from optical observations available in the SDSS archive and literature were used to analyse Si IV $\lambda 1397$ +O IV $\lambda 1402$, C IV $\lambda 1549$ +He II $\lambda 1640$, and the 1900Å blend. Emission lines in both optical and UV spectral ranges were characterised through quantitative parametrisation of the line profiles and decomposition using multicomponent fitting routines.

We incorporate previously published high- and low- z samples into our study, with available UV and optical spectra that have been analysed using the same approach for decomposing the emission line profiles. It consists of:

- 28 high- z sources from the Hamburg-ESO survey (HEMS), which are extremely luminous ($47.5 \lesssim \log L_{\text{bol}} \lesssim 48$ [erg s⁻¹]) and span a z range of $1.4 \lesssim z \lesssim 3.1$.
- 84 low- z sources from the FOS-HST, for which the C IV region has been reanalysed and the optical spectra (H β + [O III]) available in the recent literature were fitted for the first time.

The final samples considered in this thesis consists of a combination of 60 quasars from our ISAAC and the Hamburg-ESO surveys at high z and the 84 sources from FOS in the low- z range. Additional comparison samples were incorporated when relevant, such as a low- z SDSS sample, which includes 470 quasars with spectra covering the H β + [O III] range.

This thesis provides a comprehensive analysis of emission line properties across both the optical and UV spectral ranges, highlighting the main similarities and differences between both domains.

One of the main objectives is to investigate whether the trends observed in the quasar Main Sequence at low z are maintained at higher z ranges and to study the feedback mechanisms in both the BLR and NLR, using high-ionisation emission lines to understand how these mechanisms work at different redshifts. Another important focus of the thesis is the comparative study of spectral properties of RL and RQ quasars, with the aim of identify and characterise the physical differences between the two radio classifications and to evaluate how radio activity and accretion rate may influence the emission of these sources. Additionally, we also explore the suitability of high- and intermediate-ionisation lines as virial broadening estimators for black hole mass calculations and investigate a possible metallicity gradient across quasar populations, which may provide hints of their evolutionary paths. The main conclusions of this thesis are as follows:

The 4DE1 and its quasar Main Sequence persist at high z : our analysis confirms that the distinct characteristics in the H β profile between Pop. A and Pop. B quasars observed at low z

are preserved in the high z range. Pop. A broad profiles are generally well-represented by a single Lorentzian-like rest-frame broad component. In contrast, high- z Pop. B quasars are best modelled by a combination of two Gaussians: a broad component and a very broad redshifted component, which can reach FWHM of $\sim 10000 \text{ km s}^{-1}$ and account for nearly 50% of the entire $\text{H}\beta$ profile. In some extreme cases, both Pop. A (more frequently) and Pop. B of high z can exhibit a $\text{H}\beta$ blueshifted excess that we attribute to an outflowing component – a feature that is typically absent at low z .

This differentiation between Pop. A and Pop. B is also observed in other emission lines in both optical and UV spectral ranges. For instance, we found that the line widths of Al III and $\text{H}\beta$ are highly correlated and can be considered equivalent for most Population A quasars over five orders of magnitude in luminosity. In C IV , the Pop. B sources tend to exhibit slightly larger values of equivalent width than Pop. A (27\AA against 21\AA), although Pop. A tend to present greater FWHM, asymmetry, and centroid velocities in our complete high- z sample.

The dichotomy between these two populations can largely be attributed to differences in the physical properties of the emitting regions, ultimately related to accretion rates and black hole masses:

- As observed in low- z studies, the highest Eddington ratios at high- z are predominantly associated with Pop. A quasars. In our high- z sample (including ISAAC and HEMS data), the Eddington ratio vary in a range of $-0.83 \lesssim \log L/L_{\text{Edd}} \lesssim 0.47$, with Pop. A sources exhibiting a median $\log L/L_{\text{Edd}}$ of 0.03, while for Pop. B quasars this value is -0.26.
- The large FWHM values of $\text{H}\beta$ observed in Pop. B quasars, sometimes reaching several thousands of km s^{-1} , are indicative of the substantially larger black hole masses in these objects compared to Pop. A quasars. In our ISAAC sample, the median black hole mass of Pop. A is $10^{9.54} M_{\odot}$, while for Pop. B quasars it is $10^{9.75} M_{\odot}$.

Additionally, the ISAAC sample allowed for the reconfirmation of the displacement in the quasar MS towards broader $\text{H}\beta$ profiles and larger values of $R_{\text{Fe II}}$ at higher z compared to the low- z range. This trend could be partly attributed to an observational bias: at higher redshifts only the most massive and luminous quasars (those radiating close to the Eddington limit) are detected. Quasars with lower Eddington ratios and smaller black hole masses become increasingly difficult to observe due to the flux limit in high- z surveys. Consequently, the samples at high z are dominated by the most extreme quasars in terms of mass, for which a higher FWHM is expected if the low-ionisation BLR remains virialised.

Another trend in the MS that has been observed along this thesis involves the metallicity. At least at low- z , it increases from sub-solar levels in Pop. B sources to ~ 10 times solar in extreme Pop. A quasars, suggesting that if the high-metallicity gas is being expelled from the vicinity of the central black hole then these outflows might play a significant role in chemically enriching the host galaxy.

Our analysis indicates that quasars with very high luminosity across the Main Sequence are significantly influenced by powerful outflows spanning a wide range of spatial scales. Along this thesis, signatures of outflows due to the AGN activity were found in many emission lines from

both the optical and UV spectral regions. One of the main lines that traces the outflow contributions is the [O III], for which we found that:

1. In the ISAAC sample, the wide majority ($\sim 70\%$) of the [O III] profiles show significant outflows, with blueshifted velocities higher than 250 km s^{-1} , which is in contrast to what is observed at low- z case, in which very few sources present such strong outflows.
2. In many of our high- z sources, the blueshifted semi-broad component accounts for more than 50% of the total intensity of the [O III] profile, with the most pronounced ones observed in Pop. A sources ($\sim 64\%$).
3. Around 20% of the [O III] profiles that present detected outflows can be well-represented by only the blueshifted component.
4. In high- z quasars, sources with high Eddington ratios ($L/L_{\text{Edd}} \approx 1$) can often exhibit [O III] lines with FWHM values comparable to those of $H\beta$, indicating that the [O III] emitting gas in the NLR is moving much faster than expected, which could happen if the strong radiation coming from the quasar is accelerating the gas, potentially driving large-scale, powerful outflows.

Outflows are also found in $H\beta$. Eight sources from our ISAAC sample present a $H\beta$ outflowing component associated with [O III]. We have seen that if the blueshift or asymmetry is primarily localised at the peak of the $H\beta$ line, and if the $H\beta$ can be modelled similarly to [O III] $\lambda 5007$, indicating a “goiter” in the line profile, then the outflow evidence remains mostly within the NLR. However, the situation may change when the blueshift in the $H\beta$ line extends to lower fractional intensities, spreading out from the peak of the line. In such cases, the broader extent of the blueshift may imply that the outflow originates from the BLR, closer to the black hole.

Regarding the UV spectral region, clear outflows signatures were identified in Al III and, most frequently, in C IV. Al III outflows were detected in five Pop. A sources from the ISAAC sample, with an average blueshift of $\sim 1700 \text{ km s}^{-1}$ and accounting for $\sim 40\%$ of the full profile. For C IV at high z , the blueshifted component of C IV is the strongest component, contributing to $\sim 72\%$ and $\sim 51\%$ of the full C IV flux for Pop. A and Pop. B, respectively. In agreement with this, the largest blueshifts are found for the Pop. A sources, which can achieve $\sim 2600 \text{ km s}^{-1}$ (Pop. B in our ISAAC sample reached a maximum of $\sim 1900 \text{ km s}^{-1}$).

BLR and NLR are related. When we join the optical observations with those in the UV spectral range, particularly in high- z quasars, important results are found:

1. We found a good correlation between the blueshift and the FWHM of the [O III] emission line, with a Pearson c.c. of 0.86 (ρ -value of $\sim 10^{-7}$). This correlation, as well as the one between W and shift, closely mirror those seen in the C IV emission line. For C IV, we obtain a c.c. of ~ 0.90 between $c(1/2)$ and FWHM for high- z Pop. A sources. Both C IV FWHM and blueshift show a clear increase from spectral types A1 to A3, with the latter being the one with the highest blueshifts (median value of $\sim 4500 \text{ km s}^{-1}$) and the broadest FWHM (median value of

$\sim 9000 \text{ km s}^{-1}$). In the case of Pop. B C IV profiles, the average blueshift is $\sim 1681 \text{ km s}^{-1}$ and mean FWHM $\sim 5940 \text{ km s}^{-1}$, which is slightly smaller than for Pop. A.

2. The objects that present pronounced blueshifts in their [O III] emission lines will show similar blueshifts in the C IV line, however with larger outflow velocities, as well as stronger outflow parameters like kinetic power and thrust.
3. The correlations observed between the FWHM and shifts of the [O III] and C IV lines are strongly tied to the Eddington ratio and mass (or luminosity). For both [O III] and C IV, strong outflows (i.e., blueshifted velocities $\gtrsim 500 \text{ km s}^{-1}$ for [O III] and $\gtrsim 2000 \text{ km s}^{-1}$ for C IV) are found at Eddington ratios $\log L/L_{\text{Edd}} \gtrsim -0.8$ ($L/L_{\text{Edd}} \sim 0.2$).
4. While the bolometric luminosity and the black hole mass exhibit trends with the C IV blueshifts, the primary correlation is observed with the Eddington ratio, for which we obtained a Pearson c.c. of ~ 0.66 and a ρ -value for the null hypothesis $\sim 10^{-11}$. Similar results, albeit less significant, are observed for [O III].

These parallels suggest that there may be a physical connection between the outflows coming from the BLR and the NLR. Specifically, the outflows detected in C IV, which originate from regions within a few hundred gravitational radii, may be physically linked to the outflows observed in [O III], which originate from much further out, within the NLR, extending beyond 10^4 - 10^5 gravitational radii. This connection implies that the outflow mechanisms in quasars operate over a wide range of spatial scales, influencing both the BLR and the NLR, and are responsible for the observed line profile asymmetries and shifts in both the optical and UV spectral ranges.

Systematic differences between radio-loud and radio-quiet sources at low and high z were found. RL sources tend to present lower values of R_{FeII} than the RQ ones, never exceeding $R_{\text{FeII}} = 1$. However, the sources that present strong Fe II emission are found to also present very high Eddington ratios (usually $L/L_{\text{Edd}} \gtrsim 1$), which are more frequently found in RQ sources of Pop. A. Hence, this difference in R_{FeII} between RL and RQ sources may be linked to the accretion rate, which somehow can contribute to enhancing the Fe II emission in strong accretors.

We have seen that even though PKS2000-330 (a radio-loud) and Q1410+096 (a radio-quiet) share similar z and optical spectroscopic properties (both classified as A2 in the quasar Main Sequence), they present significant discrepancies in their UV data and in their [O III] outflow behaviour. While the RQ source presents a typical Pop. A UV spectrum, with similar intensities and shapes in both C IV $\lambda 1549$ and Si IV $\lambda 1392$ emission lines, the UV spectrum of the strong RL closely resembles that of a Pop. B quasar. This suggests that despite their classification within the same ST in the optical MS, the presence of strong radio emission in PKS2000-330 may have an influence on the physical conditions of the BLR.

Differences between RL and RQ are also found in the [O III] emission line when considering the complete high- and low- z samples:

- Within the same z range, the RL quasars tend to present a more symmetric and less intense blueshifted component, while the RQ usually show a highly skewed blueshifted component with a significant contribution to the full emission line profile.
- For both high- and low- z contexts, RQ sources present the largest outflows velocities compared to RL. Specifically, RQ sources reach peak velocities of $\sim 2000 \text{ km s}^{-1}$ at low z and around $\sim 2700 \text{ km s}^{-1}$ at high z . In contrast, RL sources display lower maximum velocities, with values of $\sim 500 \text{ km s}^{-1}$ at low z and $\sim 1000 \text{ km s}^{-1}$ at high z .

The fact that RQ sources present stronger outflows than RL ones is observed also in C IV, although at high z practically all C IV profiles (including that of both RL and RQ sources) present very significant outflow velocities (average $c(1/4)$ for RL is $\sim 1900 \text{ km s}^{-1}$). These results indicate that the radio-loudness may play a role in reducing the outflow velocities in both emission lines.

In order to perform an inter-comparison of the metallicity of RL and RQ sources of low- z ($z \lesssim 0.65$), we build composite spectra of ST B1 for both radio classifications. We have found that within the same ST of the optical MS, RL sources show definitely sub-solar chemical abundances, lower with respect to RQ. The difference is not marginal and is supported by several diagnostic indicators consistently observed to be lower in RL sources. This lower metallicity in RL quasars might be due to the fact that the jets observed in these sources can clear out gas from their surroundings, reducing star formation and chemical enrichment. On the other hand, RQ quasars (not presenting strong jets) allow more gas to stay in the galaxy, leading to more star formation and higher metallicities.

For higher redshifts, we examined a representative RL source (PKS 0226-038) from our ISAAC sample. Its optical and UV spectra differ notably from the low- z Population B composite, with weaker C III], stronger Fe II, and Al III nearly as strong as C IV. PKS 0226-038 exhibits significantly higher metallicity than typical low- z RL sources (~ 10 times solar).

While radio-loudness seem to modulate the outflow properties to some degree, the accretion rate stands out as the dominant factor affecting the observed outflows across different z regimes. The comparative study of RL and RQ quasars performed throughout this thesis shows that the relations observed between the [O III] and C IV emission lines do not appear to be affected by the radio emission properties of the quasars. However, RQ quasars exhibit stronger outflows in both lines, suggesting that radio activity may reduce feedback effects, at least to some extent.

For both the high- and low- z samples, the outflow parameters (mass-outflow rate, thrust, and kinetic power) of the [O III] and C IV emission lines were estimated. For the case of [O III], the outflow parameters were estimated following established methods from the literature; while for C IV we derived new scaling relations based on photoionisation predictions. We found that:

- For [O III], the median mass-outflow rate \dot{M}_{out} estimate is $\sim 22 M_{\odot} \text{ yr}^{-1}$ for the high- z sample (ISAAC and HEMS), and $\sim 1.67 M_{\odot} \text{ yr}^{-1}$ for the low- z data. In the case of C IV, these values are ~ 31 and $\sim 0.26 M_{\odot} \text{ yr}^{-1}$, respectively.

- There is a good correlation between bolometric luminosity L_{bol} with the kinetic power \dot{E}_{kin} and the thrust $\dot{M}_{\text{out}}v_o$ of [O III], with correlation coefficients of 0.66 and 0.74 (with ρ -value of $\sim 10^{-7}$ and $\sim 10^{-9}$, respectively), including sources spanning a wide range of redshift. Similar correlations were also found for C IV.

The results show that quasars at lower redshifts have substantially lower outflow parameters by one and two orders of magnitude (in [O III] and C IV, respectively) compared to high- z quasars. This z dependence likely reflects the more active phase of galaxies in the earlier universe, where higher accretion rates fuel more powerful outflows.

Our findings suggest that, while the [O III] outflowing gas at high z is likely driven by the AGN, its influence may be confined to the central kiloparsec regions due to their relatively low energetic efficiency. On the other hand, the C IV outflows at high z show a more significant impact. Around 38% of the sample exhibits kinetic powers \dot{E}_{kin} exceeding 0.5% of the bolometric luminosity L_{bol} , with the most extreme cases reaching $\sim 3\%$ of L_{bol} . These values approach the threshold required for effective feedback, where the outflows are powerful enough to influence the global properties of the host galaxy. In the case of C IV, the possibility of a significant feedback effect from the accretion disk wind seems to be valid for both RL and RQ sources, as the slightly lower velocities measured on the C IV profile of the RL are not enough to significantly affect the outflow dynamical parameters with respect to the RQ population.

We found that **the most powerful outflows in both [O III] and C IV are observed in quasars with the highest accretion rates, which suggests that the accretion rate plays a crucial role in driving these outflows.** Furthermore, we found that in the high- z range, not only RQ but also RL sources tend to radiate at high values of Eddington ratio (with $L/L_{\text{Edd}} \sim 1$, in some cases), while at lower z the most powerful RL quasars typically belong to Pop. B and radiate at more moderate Eddington ratios. This shift suggests an evolutionary change in how quasars drive feedback, with high- z sources being more radiatively efficient, while mechanical feedback via jets may be more relevant for low- z massive black holes.

FUTURE PERSPECTIVES

Throughout this thesis, we have examined the behaviour of the quasar MS correlations at high redshift and the effects of radio emission and AGN feedback on it. In this section, we summarise potential directions for future research that could further advance the study of the quasar Main Sequence.

Study the MS in big surveys: The MS exploration at high z has been made possible primarily due to the advent of infrared spectrographs capable of covering the $H\beta+[O\ III]$ spectral region, together with the optical instruments that cover the UV spectral region within this z range. One of my aims to the near future is to broaden the investigation of the MS, encompassing larger samples from both high- and low- z ranges. Particularly, surveys such as the SDSS provide a huge amount of data that allows to expand the MS studies to larger samples and would be key in the advance of the MS studies.

In addition, the analysis of a larger sample, especially of high- z quasars, covering all the spectral types within the MS, would be helpful to corroborate the findings presented in this thesis. By studying larger samples we can, for instance, provide an step further on the understanding of the relation between the BLR and NLR outflows. Additionally, we can investigate whether the observed signatures of outflow motion in different emission lines may represent variations on the physical processes driving these outflows, such as changes in accretion rates, feedback mechanisms, or even in the intrinsic properties of the AGN.

Investigate the extreme quasar outflows: Our research has highlighted the efficacy of the extreme Pop. A (xAs) quasars observed in a redshift range $z \sim 2-4$ as optimal candidates for studying AGN outflows. Outflows observed during later cosmic epochs exhibit some self-similarities with the xAs but are clearly less powerful compared them. In order to investigate feedback effects and its role on the galaxy evolution, it is important to look at sources showing the most extreme outflow parameters. In line with this, I plan to analyse a sample of xA quasars, for which data has been acquired via the VLT/X-Shooter spectrograph. This instrument is particularly well-suited for studying the 4DE1 in an optical and UV context, as it facilitates simultaneous spectral observations of both spectral regions.

The metallicity at high redshift: To further expand on the quasar MS research, I plan to study topics that require additional development within this context. One of the main topics that still require a dedicated analysis is the metallicity, especially at high redshifts. I plan to conduct a comprehensive analysis with the aim of validating the trends identified in these preliminary studies showed in the thesis that could shed light on the underlying mechanisms driving quasar evolution.

REFERENCES

- Abramowicz, M. A., Czerny, B., Lasota, J. P., & Szuszkiewicz, E. 1988, *ApJ*, 332, 646
- Adelman-McCarthy, J. K., Agüeros, M. A., Allam, S. S., et al. 2007, *ApJS*, 172, 634
- Ahumada, R., Prieto, C. A., Almeida, A., et al. 2020, *ApJS*, 249, 3
- Allen, J. T., Hewett, P. C., Maddox, N., Richards, G. T., & Belokurov, V. 2011, *MNRAS*, 410, 860
- Alonso-Herrero, A., Quillen, A. C., Rieke, G. H., Ivanov, V. D., & Efstathiou, A. 2003, *AJ*, 126, 81
- Antonucci, R. 1993, *ARA&Ap*, 31, 473
- Assef, R. J., Denney, K. D., Kochanek, C. S., et al. 2011, *ApJ*, 742, 93
- Axon, D. J., Capetti, A., Fanti, R., et al. 2000, *AJ*, 120, 2284
- Ayubinia, A., Woo, J.-H., Rakshit, S., & Son, D. 2023, *ApJ*, 954, 27
- Azzalini, A. & Regoli, G. 2012, *Ann. Inst. Statist. Math.*, 64, 857
- Bañados, E., Mazzucchelli, C., Momjian, E., et al. 2021, *ApJ*, 909, 80
- Bañados, E., Venemans, B. P., Mazzucchelli, C., et al. 2018, *Nat*, 553, 473
- Bachev, R., Marziani, P., Sulentic, J. W., et al. 2004, *ApJ*, 617, 171
- Baldwin, J., Ferland, G., Korista, K., & Verner, D. 1995, *ApJL*, 455, L119+
- Baldwin, J. A., Ferland, G. J., Korista, K. T., et al. 1996, *ApJ*, 461, 664
- Baldwin, J. A., Ferland, G. J., Korista, K. T., Hamann, F., & LaCluyzé, A. 2004, *ApJ*, 615, 610
- Barai, P., Gallerani, S., Pallottini, A., et al. 2018, *MNRAS*, 473, 4003
- Barthel, P. D. 1989, *ApJ*, 336, 606
- Barthel, P. D., Tytler, D. R., & Thomson, B. 1990, *AAPS*, 82, 339
- Becker, R. H., White, R. L., & Helfand, D. J. 1995, *ApJ*, 450, 559
- Bennert, N., Falcke, H., Schulz, H., Wilson, A. S., & Wills, B. J. 2002, *ApJL*, 574, L105
- Bennert, N., Jungwiert, B., Komossa, S., Haas, M., & Chini, R. 2006, *A&A*, 459, 55
- Bentz, M. C., Denney, K. D., Grier, C. J., et al. 2013, *ApJ*, 767, 149
- Bentz, M. C. & Katz, S. 2015, *Publications of the Astronomical Society of the Pacific*, 127, 67
- Berton, M., Foschini, L., Ciroi, S., et al. 2016, *A&A*, 591, A88
- Berton, M., Foschini, L., Ciroi, S., et al. 2015, *A&A*, 578, A28
- Berton, M. & Järvelä, E. 2021, *Universe*, 7, 188
- Best, P. N. & Heckman, T. M. 2012, *MNRAS*, 421, 1569

- Bian, W., Yuan, Q., & Zhao, Y. 2005, MNRAS, 364, 187
- Bianchi, S., Guainazzi, M., Matt, G., et al. 2005, A&A, 442, 185
- Bicknell, G. V. 2002, NAR, 46, 365
- Bischetti, M., Piconcelli, E., Vietri, G., et al. 2017, A&A, 598, A122
- Bisogni, S., Marconi, A., & Risaliti, G. 2017, MNRAS, 464, 385
- Blundell, K. M. & Beasley, A. J. 1998, MNRAS, 299, 165
- Boller, T., Brandt, W. N., & Fink, H. 1996, A&A, 305, 53
- Bon, E., Gavrilovic, N., La Mura, G., & Popovic, L. C. 2009, ArXiv e-prints [e-print[arXiv]0910.0991]
- Bon, N., Bon, E., Marziani, P., & Jovanović, P. 2015, ApSS, 360, 7
- Bon, N., Marziani, P., Bon, E., et al. 2020, A&A, 635, A151
- Bonzini, M., Mainieri, V., Padovani, P., et al. 2015, MNRAS, 453, 1079
- Boroson, T. A. 2002, ApJ, 565, 78
- Boroson, T. A. & Green, R. F. 1992, ApJS, 80, 109
- Breiding, P., Chiaberge, M., Lambrides, E., et al. 2023, arXiv e-prints, arXiv:2305.11804
- Brinkmann, W. & Siebert, J. 1995, A&A, 300, L33
- Brotherton, M. S., Runnoe, J. C., Shang, Z., & DiPompeo, M. A. 2015, MNRAS, 451, 1290
- Brotherton, M. S., Wills, B. J., Francis, P. J., & Steidel, C. C. 1994a, ApJ, 430, 495
- Brotherton, M. S., Wills, B. J., Steidel, C. C., & Sargent, W. L. W. 1994b, ApJ, 423, 131
- Bruhweiler, F. & Verner, E. 2008, ApJ, 675, 83
- Bruni, G., Piconcelli, E., Misawa, T., et al. 2019, A&A, 630, A111
- Brusa, M., Bongiorno, A., Cresci, G., et al. 2015, MNRAS, 446, 2394
- Buendia-Rios, T. M., Negrete, C. A., Marziani, P., & Dultzin, D. 2023, A&A, 669, A135
- Buttiglione, S., Capetti, A., Celotti, A., et al. 2010, A&A, 509, A6
- Caccianiga, A., Antón, S., Ballo, L., et al. 2015, MNRAS, 451, 1795
- Cano-Díaz, M., Maiolino, R., Marconi, A., et al. 2012, A&A, 537, L8
- Cantiello, M., Jermyn, A. S., & Lin, D. N. C. 2021, ApJ, 910, 94
- Capellupo, D. M., Netzer, H., Lira, P., Trakhtenbrot, B., & Mejía-Restrepo, J. 2015, MNRAS, 446, 3427
- Capetti, A., Axon, D. J., Macchetto, F., Sparks, W. B., & Boksenberg, A. 1996, ApJ, 469, 554
- Carniani, S., Marconi, A., Maiolino, R., et al. 2015, A&A, 580, A102
- Cavaliere, A. & Vittorini, V. 2000, ApJ, 543, 599

- Cheng, K. S. & Wang, J.-M. 1999, *ApJ*, 521, 502
- Chieffi, A. & Limongi, M. 2013, *ApJ*, 764, 21
- Choi, E., Somerville, R. S., Ostriker, J. P., Hirschmann, M., & Naab, T. 2024, *ApJ*, 964, 54
- Cicone, C., Maiolino, R., Sturm, E., et al. 2014, *A&A*, 562, A21
- Cielo, S., Bieri, R., Volonteri, M., Wagner, A. Y., & Dubois, Y. 2018, *Monthly Notices of the Royal Astronomical Society*, 477, 1336
- Coatman, L., Hewett, P. C., Banerji, M., & Richards, G. T. 2016, *MNRAS*, 461, 647
- Coatman, L., Hewett, P. C., Banerji, M., et al. 2017, *MNRAS*, 465, 2120
- Coatman, L., Hewett, P. C., Banerji, M., et al. 2019, *MNRAS*, 486, 5335
- Colbert, E. J. M., Baum, S. A., O’Dea, C. P., & Veilleux, S. 1998, *ApJ*, 496, 786
- Collin, S., Boisson, C., Mouchet, M., et al. 2002, *A&A*, 388, 771
- Collin, S. & Joly, M. 2000, *NAR*, 44, 531
- Collin, S., Kawaguchi, T., Peterson, B. M., & Vestergaard, M. 2006, *A&A*, 456, 75
- Collin, S. & Zahn, J.-P. 1999, *A&Ap*, 344, 433
- Collin-Souffrin, S., Dyson, J. E., McDowell, J. C., & Perry, J. J. 1988, *MNRAS*, 232, 539
- Collin-Souffrin, S. & Lasota, J.-P. 1988, *PASP*, 100, 1041
- Condon, J. J., Cotton, W. D., Greisen, E. W., et al. 1998, *AJ*, 115, 1693
- Condon, J. J., Kellermann, K. I., Kimball, A. E., Ivezić, Ž., & Perley, R. A. 2013, *ApJ*, 768, 37
- Corbin, M. R. 1993, *ApJL*, 403, L9
- Corbin, M. R. 1995, *ApJ*, 447, 496
- Corbin, M. R. & Boroson, T. A. 1996, *ApJS*, 107, 69
- Coziol, R., Andernach, H., Torres-Papaqui, J. P., Ortega-Minakata, R. A., & Moreno del Rio, F. 2017, *MNRAS*, 466, 921
- Cracco, V., Ciroi, S., Berton, M., et al. 2016, *MNRAS*, 462, 1256
- Cresci, G., Marconi, A., Zibetti, S., et al. 2015, *A&A*, 582, A63
- Croton, D. J., Springel, V., White, S. D. M., et al. 2006, *MNRAS*, 365, 11
- Dadina, M., Vignali, C., Cappi, M., et al. 2016, *A&A*, 592, A104
- D’Agostini, G. 2003, *Bayesian Reasoning in Data Analysis: A Critical Introduction* (Singapore: World Scientific)
- Decarli, R., Falomo, R., Treves, A., et al. 2010, *MNRAS*, 402, 2441
- Deconto-Machado, A., del Olmo, A., & Marziani, P. 2024, *arXiv e-prints*, arXiv:2408.06260

- Deconto-Machado, A., del Olmo, A., Marziani, P., Perea, J., & Stirpe, G. 2022a, *Astronomische Nachrichten*, 343, e210084
- Deconto-Machado, A., del Olmo Orozco, A., Marziani, P., Perea, J., & Stirpe, G. M. 2023, *A&A*, 669, A83
- Deconto-Machado, A., Riffel, R. A., Ilha, G. S., et al. 2022b, *A&A*, 659, A131
- del Olmo, A., Marziani, P., Ganci, V., et al. 2021, *Proceedings of the International Astronomical Union*, 356, 310
- Denney, K. D., Peterson, B. M., Pogge, R. W., et al. 2009, *ApJL*, 704, L80
- Di Matteo, T., Springel, V., & Hernquist, L. 2005, *Nat*, 433, 604
- Diamond-Stanic, A. M., Fan, X., Brandt, W. N., et al. 2009, *ApJ*, 699, 782
- Diana, A., Caccianiga, A., Ighina, L., et al. 2022, *Monthly Notices of the Royal Astronomical Society*, 511, 5436
- Dimitrijević, M. S., Kovačević, J., Popović, L. C., Dačić, M., & Ilić, D. 2007, *AIP Conference Proceedings*, 895, 313
- Dix, C., Shemmer, O., Brotherton, M. S., et al. 2020, *ApJ*, 893, 14
- Done, C., Davis, S. W., Jin, C., Blaes, O., & Ward, M. 2012, *MNRAS*, 420, 1848
- D’Onofrio, M. & Marziani, P. 2018, *Frontiers in Astronomy and Space Sciences*, 5, 31
- D’Onofrio, M., Marziani, P., & Chiosi, C. 2021, *arXiv e-prints*, arXiv:2109.06301
- Du, P., Brotherton, M. S., Wang, K., et al. 2018, *ApJ*, 869, 142
- Du, P., Lu, K.-X., Hu, C., et al. 2016a, *ApJ*, 820, 27
- Du, P. & Wang, J.-M. 2019, *ApJ*, 886, 42
- Du, P., Wang, J.-M., Hu, C., et al. 2016b, *ApJL*, 818, L14
- Du, P., Wang, J.-M., Hu, C., et al. 2014, *Monthly Notices of the Royal Astronomical Society*, 438, 2828
- Duras, F., Bongiorno, A., Piconcelli, E., et al. 2017, *A&A*, 604, A67
- Duras, F., Bongiorno, A., Ricci, F., et al. 2020, *A&A*, 636, A73
- Elvis, M. 2000, *ApJ*, 545, 63
- Elvis, M., Wilkes, B. J., McDowell, J. C., et al. 1994, *ApJS*, 95, 1
- Everett, J. E. 2007, *ApSS*, 311, 269
- Fabian, A. C. 2012, *ARA&Ap*, 50, 455
- Falcke, H., Sherwood, W., & Patnaik, A. R. 1996, *ApJ*, 471, 106
- Fanaroff, B. L. & Riley, J. M. 1974, *MNRAS*, 167, 31P
- Fath, E. A. 1909, *Lick Observatory Bulletin*, 149, 71

- Ferland, G. J., Baldwin, J. A., Korista, K. T., et al. 1996, *ApJ*, 461, 683
- Ferland, G. J., Chatzikos, M., Guzmán, F., et al. 2017, *RevMexA&Ap*, 53, 385
- Ferland, G. J., Done, C., Jin, C., Landt, H., & Ward, M. J. 2020, *MNRAS*, 494, 5917
- Ferland, G. J., Hu, C., Wang, J., et al. 2009, *ApJL*, 707, L82
- Feruglio, C., Fiore, F., Carniani, S., et al. 2015, *A&A*, 583, A99
- Feruglio, C., Maiolino, R., Piconcelli, E., et al. 2010, *A&A*, 518, L155
- Fian, C., Mediavilla, E., Jiménez-Vicente, J., et al. 2022, *A&A*, 667, A67
- Fine, S., Croom, S. M., Bland-Hawthorn, J., et al. 2010, *MNRAS*, 409, 591
- Fiore, F., Feruglio, C., Shankar, F., et al. 2017, *A&A*, 601, A143
- Fischer, T. C., Kraemer, S. B., Schmitt, H. R., et al. 2018, *ApJ*, 856, 102
- Fischer, T. C. o. 2013, *ApJS*, 209, 1
- Floris, A., Marziani, P., Panda, S., et al. 2024, arXiv e-prints, arXiv:2405.04456
- Fluetsch, A., Maiolino, R., Carniani, S., et al. 2021, *MNRAS*, 505, 5753
- Foschini, L., Berton, M., Caccianiga, A., et al. 2015, *A&A*, 575, A13
- Fraix-Burnet, D., D’Onofrio, M., & Marziani, P. 2017a, *Frontiers in Astronomy and Space Sciences*, 4, 20
- Fraix-Burnet, D., Marziani, P., D’Onofrio, M., & Dultzin, D. 2017b, *Frontiers in Astronomy and Space Sciences*, 4, 1
- Ganci, V., Marziani, P., D’Onofrio, M., et al. 2019, *A&A*, 630, A110
- Gardner, J. P., Mather, J. C., Clampin, M., et al. 2006, *Space Science Reviews*, 123, 485
- Garnica, K., Negrete, C. A., Marziani, P., et al. 2022, *A&A*, 667, A105
- Gaskell, C. M. 1982, *ApJ*, 263, 79
- Gaskell, C. M. 1985a, *Nat*, 315, 386
- Gaskell, C. M. 1985b, *ApJ*, 291, 112
- Gaskell, C. M. 1988, *ApJ*, 325, 114
- Gaskell, C. M. & Harrington, P. Z. 2018, *Monthly Notices of the Royal Astronomical Society*, 478, 1660
- Gavrilović, N., Popović, L. Č., & Kollatschny, W. 2007, in *IAU Symposium*, Vol. 238, *IAU Symposium*, ed. V. Karas & G. Matt, 369–370
- Giannuzzo, E. M. & Stirpe, G. M. 1996, *A&A*, 314, 419
- Gibson, R. R., Jiang, L., Brandt, W. N., et al. 2009, *ApJ*, 692, 758
- Gilmozzi, R. & Spyromilio, J. 2007, *The Messenger*, 127, 11

- Giustini, M. & Proga, D. 2019, *A&A*, 630, A94
- Gonzalez, O. A. & Gadotti, D. 2016, in *Astrophysics and Space Science Library*, Vol. 418, Galactic Bulges, ed. E. Laurikainen, R. Peletier, & D. Gadotti, 199
- González-Martín, O., Masegosa, J., Márquez, I., et al. 2015, *A&A*, 578, A74
- Graham, M. J., Clowes, R. G., & Campusano, L. E. 1996, *MNRAS*, 279, 1349
- Greenstein, J. L. 1963, *Nat*, 197, 1041
- Gregg, M. D., Becker, R. H., White, R. L., et al. 1996, *AJ*, 112, 407
- Grupe, D. 2004, *AJ*, 127, 1799
- Grupe, D., Beuermann, K., Thomas, H. C., Mannheim, K., & Fink, H. H. 1998, *A&A*, 330, 25
- Grupe, D., Komossa, S., Leighly, K. M., & Page, K. L. 2010, *ApJS*, 187, 64
- Guo, H., Shen, Y., He, Z., et al. 2020, *ApJ*, 888, 58
- Hamann, F. & Ferland, G. 1993, *ApJ*, 418, 11
- Hamann, F., Korista, K. T., Ferland, G. J., Warner, C., & Baldwin, J. 2002, *ApJ*, 564, 592
- Harrison, C. M. 2017, *Nature Astronomy*, 1, 0165
- Harrison, C. M., Alexander, D. M., Mullaney, J. R., & Swinbank, A. M. 2014, *MNRAS*, 441, 3306
- Harrison, C. M., Costa, T., Tadhunter, C. N., et al. 2018, *Nature Astronomy*, 2, 198
- Harrison, C. M. C. 2014, PhD thesis, Durham University, UK
- Hazard, C., Morton, D. C., Terlevich, R., & McMahon, R. 1984, *ApJ*, 282, 33
- Heckman, T. M. 1980, *A&A*, 87, 152
- Heckman, T. M., Baum, S. A., van Breugel, W. J. M., & McCarthy, P. 1989, *ApJ*, 338, 48
- Heckman, T. M. & Best, P. N. 2014, *ARA&Ap*, 52, 589
- Hopkins, P. F. & Elvis, M. 2010, *MNRAS*, 401, 7
- Hopkins, P. F., Hernquist, L., Cox, T. J., et al. 2006, *ApJS*, 163, 1
- Huang, J., Lin, D. N. C., & Shields, G. 2023, *MNRAS*[e-print[arXiv]2308.15761]
- Hubble, E. P. 1926, *ApJ*, 64, 321
- Hwang, C.-Y. & Bowyer, S. 1997, *ApJ*, 475, 552
- Ighina, L., Caccianiga, A., Moretti, A., et al. 2023, *MNRAS*, 519, 2060
- Izotov, Y. I. & Thuan, T. X. 1999, *ApJ*, 511, 639
- Jackson, C. A. & Wall, J. V. 1999, *MNRAS*, 304, 160
- Jarvis, M. E., Harrison, C. M., Thomson, A. P., et al. 2019, *MNRAS*, 485, 2710
- Jaunsen, A. O., Jablonski, M., Pettersen, B. R., & Stabell, R. 1995, *A&A*, 300, 323

- Jiang, B.-W., Marziani, P., Savić, Đ., et al. 2021, MNRAS[e-print[arXiv]2108.00983]
- Jin, C., Done, C., Ward, M., et al. 2023, MNRAS, 518, 6065
- Jones, D. H., Saunders, W., Colless, M., et al. 2004, MNRAS, 355, 747
- Juarez, Y., Maiolino, R., Mujica, R., et al. 2009, A&Ap, 494, L25
- Kaastra, J. S., Kriss, G. A., Cappi, M., et al. 2014, Science, 345, 64
- Kakkad, D., Mainieri, V., Vietri, G., et al. 2020, A&A, 642, A147
- Kaler, J. B. 1997, Stars and their Spectra, An Introduction to the Spectral Sequence (Cambridge University Press)
- Kaspi, S., Brandt, W. N., Maoz, D., et al. 2007, ApJ, 659, 997
- Kaspi, S., Brandt, W. N., Maoz, D., et al. 2021, arXiv e-prints, arXiv:2106.00691
- Kauffmann, G., Heckman, T. M., & Best, P. N. 2008, MNRAS, 384, 953
- Kellermann, K. I., Condon, J. J., Kimball, A. E., Perley, R. A., & Ivezić, Ž. 2016, ApJ, 831, 168
- Kellermann, K. I., Sramek, R., Schmidt, M., Shaffer, D. B., & Green, R. 1989, AJ, 98, 1195
- Khachikyan, É. Y. & Weedman, D. W. 1971, Astrophysics, 7, 231
- Kim, C., Woo, J.-H., Luo, R., et al. 2023, ApJ, 958, 145
- King, A. & Muldrew, S. I. 2016, MNRAS, 455, 1211
- King, A. & Pounds, K. 2015, ARA&Ap, 53, 115
- Kinney, A. L., Rivolo, A. R., & Koratkar, A. P. 1990, ApJ, 357, 338
- Kollatschny, W. & Zetzl, M. 2011, Nat, 470, 366
- Komossa, S., Voges, W., Xu, D., et al. 2006, AJ, 132, 531
- Komossa, S., Xu, D., Zhou, H., Storchi-Bergmann, T., & Binette, L. 2008, ApJ, 680, 926
- Komossa, S., Xu, D. W., & Wagner, A. Y. 2018, MNRAS, 477, 5115
- Korista, K., Baldwin, J., Ferland, G., & Verner, D. 1997, ApJS, 108, 401
- Kormendy, J. & Ho, L. C. 2013, Ann. Rev. Astron. Astroph., 51, 511
- Kormendy, J. & Richstone, D. 1995, ARA&Ap, 33, 581
- Kovačević, J., Popović, L. Č., & Dimitrijević, M. S. 2010, ApJS, 189, 15
- Kovačević-Dojčinović, J., Dojčinović, I., Lakićević, M., & Popović, L. Č. 2022, A&A, 659, A130
- Kovačević-Dojčinović, J. & Popović, L. Č. 2015, ApJS, 221, 35
- Krause, M. G. H., Shabala, S. S., Hardcastle, M. J., et al. 2019, MNRAS, 482, 240
- Krawczyk, C. M., Richards, G. T., Mehta, S. S., et al. 2013, ApJS, 206, 4
- Kriss, G. 1994, A.S.P. Conference Series, 61, 437

- Kriss, G. A. 2017, in American Astronomical Society Meeting Abstracts, Vol. 229, American Astronomical Society Meeting Abstracts #229, 209.01
- Kruczek, N. E., Richards, G. T., Gallagher, S. C., et al. 2011, *AJ*, 142, 130
- Kukreti, P., Morganti, R., Tadhunter, C., & Santoro, F. 2023, *A&A*, 674, A198
- Kundic, T., Hogg, D. W., Blandford, R. D., et al. 1997, *AJ*, 114, 2276
- Kuraszkiewicz, J., Wilkes, B. J., Czerny, B., & Mathur, S. 2000, *ApJ*, 542, 692
- La Franca, F., Gregorini, L., Cristiani, S., de Ruiter, H., & Owen, F. 1994, *AJ*, 108, 1548
- Lacy, M., Laurent-Muehleisen, S. A., Ridgway, S. E., Becker, R. H., & White, R. L. 2001, *ApJL*, 551, L17
- Laor, A. 2003, *ApJ*, 590, 86
- Laor, A. 2018, *Monthly Notices of the Royal Astronomical Society*
- Laor, A. & Brandt, W. N. 2002, *ApJ*, 569, 641
- Laor, A., Fiore, F., Elvis, M., Wilkes, B. J., & McDowell, J. C. 1994, *ApJ*, 435, 611
- Laor, A., Fiore, F., Elvis, M., Wilkes, B. J., & McDowell, J. C. 1997, *ApJ*, 477, 93
- Laurenti, M., Luminari, A., Tombesi, F., et al. 2021, *A&A*, 645, A118
- Lawrence, A., Elvis, M., Wilkes, B. J., McHardy, I., & Brandt, N. 1997, *MNRAS*, 285, 879
- Lawrence, C. R., Neugebauer, G., Weir, N., Matthews, K., & Patnaik, A. R. 1992, *MNRAS*, 259, 5P
- Lee, S.-S., Lobanov, A. P., Krichbaum, T. P., & Zensus, J. A. 2016, *The Astrophysical Journal*, 826, 135
- Leighly, K. M., Cooper, E., Grupe, D., Terndrup, D. M., & Komossa, S. 2015, *ApJL*, 809, L13
- Leighly, K. M. & Moore, J. R. 2004, *ApJ*, 611, 107
- Li, L.-X. 2012, *MNRAS*, 424, 1461
- Lim, J., Ao, Y., & Dinh-V-Trung. 2008, *ApJ*, 672, 252
- Lin, D. N. C. 1997, in *Astronomical Society of the Pacific Conference Series*, Vol. 113, *IAU Colloq. 159: Emission Lines in Active Galaxies: New Methods and Techniques*, ed. B. M. Peterson, F.-Z. Cheng, & A. S. Wilson, 64
- Lipari, S., Terlevich, R., & Macchetto, F. 1993, *ApJ*, 406, 451
- Lira, P., Kaspi, S., Netzer, H., et al. 2018, *ApJ*, 865, 56
- Lyke, B. W., Higley, A. N., McLane, J. N., et al. 2020, *ApJS*, 250, 8
- Maiolino, R. & Mannucci, F. 2019, *The Astronomy and Astrophysics Review*, 27, 3
- Malkan, M. A. 1983, *ApJ*, 268, 582
- Malkan, M. A. & Sargent, W. L. W. 1982, *ApJ*, 254, 22
- Marconi, A., Axon, D. J., Maiolino, R., et al. 2009, *ApJL*, 698, L103

- Marconi, A., Risaliti, G., Gilli, R., et al. 2004, *MNRAS*, 351, 169
- Marinello, M., Overzier, R. A., Röttgering, H. J. A., et al. 2020a, *MNRAS*, 492, 1991
- Marinello, M., Rodríguez-Ardila, A., Marziani, P., Sigut, A., & Pradhan, A. 2020b, *MNRAS*, 494, 4187
- Marshall, H. L., Carone, T. E., Shull, J. M., Malkan, M. A., & Elvis, M. 1996, *ApJ*, 457, 169
- Martínez-Aldama, M. L., Del Olmo, A., Marziani, P., et al. 2017, *Frontiers in Astronomy and Space Sciences*, 4, 29
- Martínez-Aldama, M. L., del Olmo, A., Marziani, P., et al. 2018, *A&A*, 618, A179
- Martínez-Aldama, M. L., Panda, S., Czerny, B., et al. 2021, *ApJ*, 918, 29
- Martini, P. & Weinberg, D. H. 2001, *ApJ*, 547, 12
- Marziani, P. 2023, *Symmetry*, 15
- Marziani, P., Berton, M., Panda, S., & Bon, E. 2021a, *Universe*, 7, 484
- Marziani, P., Bon, E., Bon, N., et al. 2022a, *Astronomische Nachrichten*, 343, e210082
- Marziani, P., Deconto-Machado, A., & Del Olmo, A. 2022b, *Galaxies*, 10, 54
- Marziani, P., del Olmo, A., Martínez-Carballo, M. A., et al. 2019, *A&A*, 627, A88
- Marziani, P., del Olmo, A., Perea, J., D’Onofrio, M., & Panda, S. 2020, *Atoms*, 8, 94
- Marziani, P., Dultzin, D., Sulentic, J. W., et al. 2018, *Frontiers in Astronomy and Space Sciences*, 5, 6
- Marziani, P., Dultzin-Hacyan, D., D’Onofrio, M., & Sulentic, J. W. 2003a, *AJ*, 125, 1897
- Marziani, P., Dultzin-Hacyan, D., & Sulentic, J. W. 2006, *Accretion onto Supermassive Black Holes in Quasars: Learning from Optical/UV Observations*, ed. P. V. Kreidler, 123
- Marziani, P., Martínez Carballo, M. A., Sulentic, J. W., et al. 2016a, *ApSS*, 361, 29
- Marziani, P., Negrete, C. A., Dultzin, D., et al. 2017a, *Frontiers in Astronomy and Space Sciences*, 4, 16
- Marziani, P., Negrete, C. A., Dultzin, D., et al. 2017b, in *IAU Symposium*, Vol. 324, *IAU Symposium*, 245–246
- Marziani, P., Olmo, A., Martínez-Aldama, M., et al. 2017c, *Atoms*, 5, 33
- Marziani, P., Olmo, A. d., Negrete, C. A., et al. 2022c, *ApJS*, 261, 30
- Marziani, P., Panda, S., Deconto Machado, A., & Del Olmo, A. 2023, *Galaxies*, 11, 52
- Marziani, P., Sniegowska, M., Panda, S., et al. 2021b, *Research Notes of the American Astronomical Society*, 5, 25
- Marziani, P. & Sulentic, J. W. 1993, *ApJ*, 409, 612
- Marziani, P. & Sulentic, J. W. 2012a, *NAREv*, 56, 49
- Marziani, P. & Sulentic, J. W. 2012b, *The Astronomical Review*, 7, 33

- Marziani, P. & Sulentic, J. W. 2014, *MNRAS*, 442, 1211
- Marziani, P., Sulentic, J. W., Dultzin-Hacyan, D., Calvani, M., & Moles, M. 1996, *ApJS*, 104, 37
- Marziani, P., Sulentic, J. W., Negrete, C. A., et al. 2015, *ApSS*, 356, 339
- Marziani, P., Sulentic, J. W., Negrete, C. A., et al. 2010, *MNRAS*, 409, 1033
- Marziani, P., Sulentic, J. W., Plauchu-Frayn, I., & del Olmo, A. 2013a, *A&A*, 555, A89
- Marziani, P., Sulentic, J. W., Plauchu-Frayn, I., & del Olmo, A. 2013b, *ApJ*, 764 [e-print[arXiv]1301.0520]
- Marziani, P., Sulentic, J. W., Stirpe, G. M., et al. 2016b, *ApSS*, 361, 3
- Marziani, P., Sulentic, J. W., Stirpe, G. M., Zamfir, S., & Calvani, M. 2009, *A&A*, 495, 83
- Marziani, P., Sulentic, J. W., Zamanov, R., et al. 2003b, *ApJS*, 145, 199
- Marziani, P., Sulentic, J. W., Zwitter, T., Dultzin-Hacyan, D., & Calvani, M. 2001, *ApJ*, 558, 553
- Marziani, P., Zamanov, R. K., Sulentic, J. W., & Calvani, M. 2003c, *MNRAS*, 345, 1133
- Massardi, M., Bonaldi, A., Bonavera, L., et al. 2016, *MNRAS*, 455, 3249
- Massaro, E., Giommi, P., Leto, C., et al. 2009, *A&A*, 495, 691
- Massaro, E., Maselli, A., Leto, C., et al. 2015, *ApSS*, 357, 75
- Massaro, F., Giroletti, M., D'Abrusco, R., et al. 2014, *ApJS*, 213, 3
- Mathews, W. G. & Ferland, G. J. 1987, *ApJ*, 323, 456
- Mathur, S. 2000, *MNRAS*, 314, L17
- Matsuoka, K., Nagao, T., Marconi, A., Maiolino, R., & Taniguchi, Y. 2011, *A&A*, 527, A100
- Matsuoka, Y., Kawara, K., & Oyabu, S. 2008, *ApJ*, 673, 62
- Matt, G., Guainazzi, M., & Maiolino, R. 2003, *Monthly Notices of the Royal Astronomical Society*, 342, 422
- Matteucci, F. 2012, *Chemical Evolution of Galaxies* (Springer Verlag)
- Matthee, J., Naidu, R. P., Brammer, G., et al. 2024, *Little Red Dots: an abundant population of faint AGN at z 5 revealed by the EIGER and FRESCO JWST surveys*
- Matthews, B. M., Shemmer, O., Dix, C., et al. 2021, *ApJS*, 252, 15
- Matthews, T. A. & Sandage, A. R. 1963, *ApJ*, 138, 30
- Mauch, T., Murphy, T., Buttery, H. J., et al. 2003, *MNRAS*, 342, 1117
- McIntosh, D. H., Rix, H. W., Rieke, M. J., & Foltz, C. B. 1999, *ApJL*, 517, L73
- McLure, R. J. & Dunlop, J. S. 2004, *MNRAS*, 352, 1390
- McLure, R. J. & Jarvis, M. J. 2002, *MNRAS*, 337, 109
- Mediavilla, E., Jiménez-Vicente, J., Fian, C., et al. 2018, *ApJ*, 862, 104

- Mejía-Restrepo, J. E., Lira, P., Netzer, H., Trakhtenbrot, B., & Capellupo, D. M. 2018a, *Nature Astronomy*, 2, 63
- Mejía-Restrepo, J. E., Trakhtenbrot, B., Lira, P., & Netzer, H. 2018b, *MNRAS*[e-print[arXiv]1805.00942]
- Mejía-Restrepo, J. E., Trakhtenbrot, B., Lira, P., Netzer, H., & Capellupo, D. M. 2016, *MNRAS*, 460, 187
- Mengistue, S. T., Del Olmo, A., Marziani, P., et al. 2023, *MNRAS*, 525, 4474
- Mineshige, S., Kawaguchi, T., Takeuchi, M., & Hayashida, K. 2000, *PASJ*, 52, 499
- Monari, G., Famaey, B., Carrillo, I., et al. 2018, *A&A*, 616, L9
- Morganti, R. 2017, *Frontiers in Astronomy and Space Sciences*, 4
- Morris, S. L. & Ward, M. J. 1989, *ApJ*, 340, 713
- Muñoz, J. A., Falco, E. E., Kochanek, C. S., Lehár, J., & Mediavilla, E. 2003, *ApJ*, 594, 684
- Mukherjee, D., Bicknell, G. V., Sutherland, R., & Wagner, A. 2016, *MNRAS*, 461, 967
- Mulcahey, C. R., Leslie, S. K., Jackson, T. M., et al. 2022, *A&A*, 665, A144
- Mullaney, J. R., Alexander, D. M., Fine, S., et al. 2013, *MNRAS*, 433, 622
- Murray, N. & Chiang, J. 1997, *ApJ*, 474, 91
- Murray, N., Chiang, J., Grossman, S. A., & Voit, G. M. 1995, *ApJ*, 451, 498
- Nagao, T., Maiolino, R., & Marconi, A. 2006a, *A&A*, 447, 863
- Nagao, T., Marconi, A., & Maiolino, R. 2006b, *A&Ap*, 447, 157
- Nardini, E., Lusso, E., Risaliti, G., et al. 2019, *A&A*, 632, A109
- Negrete, A., Dultzin, D., Marziani, P., & Sulentic, J. 2012, *ApJ*, 757, 62
- Negrete, C. A., Dultzin, D., Marziani, P., et al. 2018, *A&A*, 620, A118
- Negrete, C. A., Dultzin, D., Marziani, P., & Sulentic, J. W. 2013, *ApJ*, 771, 31
- Negrete, C. A., Dultzin, D., Marziani, P., & Sulentic, J. W. 2014, *ApJ*, 794, 95
- Nenkova, M., Sirocky, M. M., Nikutta, R., Ivezić, Ž., & Elitzur, M. 2008, *ApJ*, 685, 160
- Nesvadba, N. P. H., Drouart, G., De Breuck, C., et al. 2017, *A&A*, 600, A121
- Nesvadba, N. P. H., Lehnert, M. D., De Breuck, C., Gilbert, A., & van Breugel, W. 2007, *A&A*, 475, 145
- Netzer, H. 1977, *MNRAS*, 181, 89P
- Netzer, H. 1990, in *Active Galactic Nuclei*, ed. R. D. Blandford, H. Netzer, L. Woltjer, T. J.-L. Courvoisier, & M. Mayor, 57–160
- Netzer, H. 2013, *The Physics and Evolution of Active Galactic Nuclei*
- Netzer, H. 2015, *ARA&Ap*, 53, 365

- Netzer, H. 2019, MNRAS, 488, 5185
- Netzer, H., Lira, P., Trakhtenbrot, B., Shemmer, O., & Cury, I. 2007, ApJ, 671, 1256
- Netzer, H. & Marziani, P. 2010, ApJ, 724, 318
- Netzer, H., Shemmer, O., Maiolino, R., et al. 2004, ApJ, 614, 558
- O’Dea, C. P. 1998, PASP, 110, 493
- O’Dowd, M., Bate, N. F., Webster, R. L., et al. 2017, arXiv e-prints, arXiv:1708.07535
- Osmer, P. S. & Smith, M. G. 1976, ApJ, 210, 267
- Osterbrock, D. E. & Ferland, G. J. 2006, Astrophysics of gaseous nebulae and active galactic nuclei
- Osterbrock, D. E. & Mathews, W. G. 1986, ARA&Ap, 24, 171
- Osterbrock, D. E. & Shuder, J. M. 1982, ApJS, 49, 149
- Padovani, P. 2016, AApR, 24, 13
- Padovani, P. 2017, Nature Astronomy, 1, 0194
- Padovani, P., Alexander, D. M., Assef, R. J., et al. 2017, , 25, 2
- Padovani, P., Ghisellini, G., Fabian, A. C., & Celotti, A. 1993, MNRAS, 260, L21
- Padovani, P. & Matteucci, F. 1993, ApJ, 416, 26
- Pagel, B. E. J., Edmunds, M. G., Blackwell, D. E., Chun, M. S., & Smith, G. 1979, MNRAS, 189, 95
- Panda, S. 2021a, PhD thesis, Polish Academy of Sciences, Institute of Physics
- Panda, S. 2021b, A&A, 650, A154
- Panda, S., Czerny, B., Adhikari, T. P., et al. 2018, The Astrophysical Journal, 866, 115
- Panda, S., Martínez-Aldama, M. L., Marinello, M., et al. 2020, ApJ, 902, 76
- Panda, S., Marziani, P., & Czerny, B. 2019, ApJ, 882, 79
- Panessa, F., Baldi, R. D., Laor, A., et al. 2019, Nature Astronomy, 3, 387
- Panessa, F. & Bassani, L. 2002, A&A, 394, 435
- Patil, P., Whittle, M., Nyland, K., et al. 2022, ApJ, 934, 26
- Patnaik, A. R., Browne, I. W. A., Walsh, D., Chaffee, F. H., & Foltz, C. B. 1992, MNRAS, 259, 1P
- Perlman, E. S., Padovani, P., Giommi, P., et al. 1998, AJ, 115, 1253
- Peterson, B. M. 1997, An Introduction to Active Galactic Nuclei (Cambridge University Press)
- Peterson, B. M. 2014, SSR, 183, 253
- Peterson, B. M. & Ferland, G. J. 1986, Nat, 324, 345
- Peterson, B. M., Ferrarese, L., Gilbert, K. M., et al. 2004, ApJ, 613, 682

- Peterson, B. M. & Wandel, A. 1999, *ApJL*, 521, L95
- Peterson, B. M. & Wandel, A. 2000, *ApJL*, 540, L13
- Popović, L. Č., Kovačević-Dojčinović, J., & Marčeta-Mandić, S. 2019, *MNRAS*, 484, 3180
- Popović, L. Č., Mediavilla, E., Bon, E., & Ilić, D. 2004, *A&A*, 423, 909
- Popovic, L. C., Vince, I., Atanackovic-Vukmanovic, O., & Kubicela, A. 1995, *A&A*, 293, 309
- Press, W. H., Teukolsky, S. A., Vetterling, W. T., & Flannery, B. P. 1992, *Numerical recipes in FORTRAN. The art of scientific computing* (Cambridge University Press)
- Proga, D. 2007, in *Astronomical Society of the Pacific Conference Series, Vol. 373, The Central Engine of Active Galactic Nuclei*, ed. L. C. Ho & J.-W. Wang, 267
- Proga, D., Stone, J. M., & Drew, J. E. 1998, *MNRAS*, 295, 595
- Punsly, B. 2010, *ApJ*, 713, 232
- Punsly, B. 2013, *ApJL*, 762, L25
- Punsly, B., Marziani, P., Bennert, V. N., Nagai, H., & Gurwell, M. A. 2018, *ApJ*, 869, 143
- Punsly, B., Marziani, P., Berton, M., & Kharb, P. 2020, *ApJ*, 903, 44
- R Core Team. 2019, *R: A Language and Environment for Statistical Computing*, R Foundation for Statistical Computing, Vienna, Austria
- Ramos Almeida, C., Levenson, N. A., Alonso-Herrero, A., et al. 2011, *ApJ*, 731, 92
- Ramos Almeida, C. & Ricci, C. 2017, *Nature Astronomy*, 1, 679
- Rankine, A. L., Hewett, P. C., Banerji, M., & Richards, G. T. 2020, *MNRAS*, 492, 4553
- Rawlings, S. & Saunders, R. 1991, *Nat*, 349, 138
- Reynaldi, V. & Feinstein, C. 2013, *MNRAS*, 430, 2221
- Richards, G. T., Kruczek, N. E., Gallagher, S. C., et al. 2011, *AJ*, 141, 167
- Richards, G. T., McCaffrey, T. V., Kimball, A., et al. 2021, *AJ*, 162, 270
- Richards, G. T., Strauss, M. A., Fan, X., et al. 2006, *AJ*, 131, 2766
- Riffel, R. A., Nemmen, R. S., Ilha, G. S., et al. 2019, *MNRAS*, 485, 5590
- Risaliti, G. & Elvis, M. 2010, *A&A*, 516, A89
- Risaliti, G., Salvati, M., & Marconi, A. 2011, *MNRAS*, 411, 2223
- Rokaki, E., Lawrence, A., Economou, F., & Mastichiadis, A. 2003, *MNRAS*, 340, 1298
- Roy, N., Bundy, K., Cheung, E., & MaNGA Team. 2018, in *American Astronomical Society Meeting Abstracts, Vol. 231, American Astronomical Society Meeting Abstracts #231*, 250.46
- Sadowski, A. 2011, arXiv e-prints, arXiv:1108.0396
- Sameshima, H., Yoshii, Y., & Kawara, K. 2017, *ApJ*, 834, 203

- Sanders, D. B., Kartaltepe, J. S., Kewley, L. J., et al. 2009, in *Astronomical Society of the Pacific Conference Series*, Vol. 408, *The Starburst-AGN Connection*, ed. W. Wang, Z. Yang, Z. Luo, & Z. Chen, 3
- Sanders, D. B., Soifer, B. T., Elias, J. H., et al. 1988, *ApJ*, 325, 74
- Savage, A., Jauncey, D. L., White, G. L., et al. 1990, *Australian Journal of Physics*, 43, 241
- Scaringi, S., Cottis, C. E., Knigge, C., & Goad, M. R. 2009, *MNRAS*, 399, 2231
- Schlafly, E. F. & Finkbeiner, D. P. 2011, *ApJ*, 737, 103
- Schmidt, M. 1963, *Nat*, 197, 1040
- Schmidt, M. & Green, R. F. 1983, *ApJ*, 269, 352
- Seyfert, C. K. 1943, *ApJ*, 97, 28
- Shang, Z., Wills, B. J., Wills, D., & Brotherton, M. S. 2007, *AJ*, 134, 294
- Shankar, F., Dai, X., & Sivakoff, G. R. 2008, *ApJ*, 687, 859
- Shankar, F., Weinberg, D. H., & Miralda-Escudé, J. 2009, *ApJ*, 690, 20
- Shapovalova, A. I., Popović, L. Č., Burenkov, A. N., et al. 2012, *ApJS*, 202, 10
- Shemmer, O., Trakhtenbrot, B., Anderson, S. F., et al. 2010, *ApJL*, 722, L152
- Shen, Y. 2013, *Bulletin of the Astronomical Society of India*, 41, 61
- Shen, Y. & Ho, L. C. 2014, *Nat*, 513, 210
- Shen, Y. & Liu, X. 2012, *ApJ*, 753, 125
- Shen, Y., Richards, G. T., Strauss, M. A., et al. 2011, *ApJS*, 194, 45
- Shields, G. A. 1976, *ApJ*, 204, 330
- Shin, J., Woo, J.-H., Nagao, T., & Kim, S. C. 2013, *ApJ*, 763, 58
- Sigut, T. A. A. & Pradhan, A. K. 1998, *ApJL*, 499, L139
- Sigut, T. A. A. & Pradhan, A. K. 2003, *ApJS*, 145, 15
- Sigut, T. A. A., Pradhan, A. K., & Nahar, S. N. 2004, *ApJ*, 611, 81
- Sikora, M., Stawarz, Ł., & Lasota, J.-P. 2007, *ApJ*, 658, 815
- Singh, K. P., Garmire, G. P., & Nousek, J. 1985, *ApJ*, 297, 633
- Singha, M., Husemann, B., Urrutia, T., et al. 2022, *A&A*, 659, A123
- Skrutskie, M. F., Cutri, R. M., Stiening, R., et al. 2006, *AJ*, 131, 1163
- Slipher, V. M. 1917, *Lowell Observatory Bulletin*, 3, 59
- Sluse, D., Hutsemékers, D., Courbin, F., Meylan, G., & Wambsganss, J. 2012, *A&A*, 544, A62
- Small, T. A. & Blandford, R. D. 1992, *MNRAS*, 259, 725

- Smee, S. A., Gunn, J. E., Uomoto, A., et al. 2013, *AJ*, 146, 32
- Snedden, S. & Gaskell, C. 2004, in *Astronomical Society of the Pacific Conference Series*, Vol. 311, *AGN Physics with the Sloan Digital Sky Survey*, ed. G. T. Richards & P. B. Hall, 197
- Snedden, S. A. & Gaskell, C. M. 2007, *ApJ*, 669, 126
- Śniegowska, M., Kozłowski, S., Czerny, B., & Panda, S. 2018, arXiv e-prints, arXiv:1810.09363
- Śniegowska, M., Kozłowski, S., Czerny, B., Panda, S., & Hryniewicz, K. 2020, *ApJ*, 900, 64
- Śniegowska, M., Marziani, P., Czerny, B., et al. 2021, *ApJ*, 910, 115
- Somerville, R. S. & Davé, R. 2015, *ARA&Ap*, 53, 51
- Stickel, M., Kuehr, H., & Fried, J. W. 1993, *AAPS*, 97, 483
- Storchi-Bergmann, T., de Oliveira, B. D., Micchi, L. F. L., et al. 2018, *The Astrophysical Journal*, 868, 14
- Sulentic, J. & Marziani, P. 2015, *Frontiers in Astronomy and Space Sciences*, 2, 6
- Sulentic, J., Marziani, P., & Zamfir, S. 2011, *Baltic Astronomy*, 20, 427
- Sulentic, J. W. 1989, *ApJ*, 343, 54
- Sulentic, J. W., Bachev, R., Marziani, P., Negrete, C. A., & Dultzin, D. 2007a, *ApJ*, 666, 757
- Sulentic, J. W., Calvani, M., Marziani, P., & Zheng, W. 1990, *ApJL*, 355, L15
- Sulentic, J. W., del Olmo, A., Marziani, P., et al. 2017, *A&A*, 608, A122
- Sulentic, J. W., Dultzin-Hacyan, D., & Marziani, P. 2007b, in *Revista Mexicana de Astronomia y Astrofisica Conference Series*, Vol. 28, *Revista Mexicana de Astronomia y Astrofisica Conference Series*, ed. S. Kurtz, 83–88
- Sulentic, J. W., Dultzin-Hacyan, D., Marziani, P., et al. 2006a, *RevMexA&Ap*, 42, 23
- Sulentic, J. W., Martínez-Carballo, M. A., Marziani, P., et al. 2015, *MNRAS*, 450, 1916
- Sulentic, J. W. & Marziani, P. 1999, *ApJL*, 518, L9
- Sulentic, J. W., Marziani, P., del Olmo, A., et al. 2014a, *A&A*, 570, A96
- Sulentic, J. W., Marziani, P., Dultzin, D., D’Onofrio, M., & del Olmo, A. 2014b, in *Journal of Physics Conference Series*, Vol. 565, *Journal of Physics Conference Series (IOP)*, 012018
- Sulentic, J. W., Marziani, P., & Dultzin-Hacyan, D. 2000a, *ARA&Ap*, 38, 521
- Sulentic, J. W., Marziani, P., Dultzin-Hacyan, D., Calvani, M., & Moles, M. 1995, *ApJL*, 445, L85
- Sulentic, J. W., Marziani, P., Zamanov, R., et al. 2002, *ApJL*, 566, L71
- Sulentic, J. W., Marziani, P., Zwitter, T., Dultzin-Hacyan, D., & Calvani, M. 2000b, *ApJL*, 545, L15
- Sulentic, J. W., Repetto, P., Stirpe, G. M., et al. 2006b, *A&A*, 456, 929
- Sulentic, J. W., Stirpe, G. M., Marziani, P., et al. 2004, *A&A*, 423, 121

- Sulentic, J. W., Zamfir, S., Marziani, P., et al. 2003, *ApJL*, 597, L17
- Sulentic, J. W., Zwitter, T., Marziani, P., & Dultzin-Hacyan, D. 2000c, *ApJL*, 536, L5
- Sun, J. & Shen, Y. 2015, *ApJL*, 804, L15
- Sun, M., Xue, Y., Richards, G. T., et al. 2018, *ApJ*, 854, 128
- Sun, W.-H. & Malkan, M. A. 1989, *ApJ*, 346, 68
- Tadhunter, C., Rodríguez Zaurín, J., Rose, M., et al. 2018, *MNRAS*, 478, 1558
- Takahashi, R. & Inoue, K. T. 2014, *MNRAS*, 440, 870
- Temple, M. J., Ferland, G. J., Rankine, A. L., et al. 2020, *MNRAS*, 496, 2565
- Temple, M. J., Matthews, J. H., Hewett, P. C., et al. 2023, arXiv e-prints, arXiv:2301.02675
- Tonry, J. L. 1998, *AJ*, 115, 1
- Torrealba, J., Chavushyan, V., Cruz-González, I., et al. 2012, *RevMexA&Ap*, 48, 9
- Trakhtenbrot, B. & Netzer, H. 2012, *MNRAS*, 427, 3081
- Trakhtenbrot, B., Urry, C. M., Civano, F., et al. 2015, *Science*, 349, 168
- Tran, H. D. 2001, *ApJL*, 554, L19
- Tran, H. D. 2003, *ApJ*, 583, 632
- Trevese, D., Paris, D., Stirpe, G. M., Vagnetti, F., & Zitelli, V. 2007, *A&A*, 470, 491
- Trevese, D., Perna, M., Vagnetti, F., Saturni, F. G., & Dadina, M. 2014, *ApJ*, 795, 164
- Tytler, D. & Fan, X.-M. 1992, *ApJS*, 79, 1
- Tytler, D., O'Meara, J. M., Suzuki, N., et al. 2004, *AJ*, 128, 1058
- U, V., Barth, A. J., Vogler, H. A., et al. 2022, *ApJ*, 925, 52
- Ulvestad, J. S., Antonucci, R. R. J., & Barvainis, R. 2005, *ApJ*, 621, 123
- Urry, C. M. & Padovani, P. 1995, *PASP*, 107, 803
- Vanden Berk, D. E., Richards, G. T., Bauer, A., et al. 2001, *AJ*, 122, 549
- Vanden Berk, D. E., Wilhite, B. C., Kron, R. G., et al. 2004, *ApJ*, 601, 692
- Véron-Cetty, M. P. & Véron, P. 2010, *A&A*, 518, A10
- Véron-Cetty, M.-P., Véron, P., & Gonçalves, A. C. 2001, *AAp*, 372, 730
- Vestergaard, M. & Peterson, B. M. 2006, *ApJ*, 641, 689
- Vestergaard, M. & Wilkes, B. J. 2001, *ApJS*, 134, 1
- Vietri, G. 2017, in *American Astronomical Society Meeting Abstracts*, Vol. 229, American Astronomical Society Meeting Abstracts, 302.06
- Vietri, G., Mainieri, V., Kakkad, D., et al. 2020, *A&A*, 644, A175

- Vietri, G., Piconcelli, E., Bischetti, M., et al. 2018, *A&A*, 617, A81
- Vila-Costas, M. B. & Edmunds, M. G. 1993, *MNRAS*, 265, 199
- Villar-Martín, M., Arribas, S., Emonts, B., et al. 2016, *MNRAS*, 460, 130
- Villar Martín, M., Perna, M., Humphrey, A., et al. 2020, *A&A*, 634, A116
- Vogelsberger, M., Genel, S., Springel, V., et al. 2014, *MNRAS*, 444, 1518
- Voges, W. 1993, *Advances in Space Research*, 13, 391
- Volonteri, M., Haardt, F., & Madau, P. 2003, *ApJ*, 582, 559
- Walter, R. & Fink, H. H. 1993, *A&A*, 274, 105
- Wang, F., Yang, J., Fan, X., et al. 2019, *ApJ*, 884, 30
- Wang, H., Wang, T., Zhou, H., et al. 2011, *ApJ*, 738, 85
- Wang, J., Dong, X., Wang, T., et al. 2009, *ApJ*, 707, 1334
- Wang, J. & Li, Y. 2011, *The Astrophysical Journal*, 742, L12
- Wang, J., Wei, J. Y., & He, X. T. 2006, *ApJ*, 638, 106
- Wang, J., Xu, D. W., & Wei, J. Y. 2018, *ApJ*, 852, 26
- Wang, J.-M., Du, P., Brotherton, M. S., et al. 2017, *Nature Astronomy*, 1, 775
- Wang, J.-M., Du, P., Hu, C., et al. 2014, *ApJ*, 793, 108
- Wang, J.-M., Songsheng, Y.-Y., Li, Y.-R., & Du, P. 2023, *MNRAS*, 518, 3397
- Wang, S., Jiang, L., Shen, Y., et al. 2022, *ApJ*, 925, 121
- Wang, T., Brinkmann, W., & Bergeron, J. 1996, *A&A*, 309, 81
- Welling, C. A., Miller, B. P., Brandt, W. N., Capellupo, D. M., & Gibson, R. R. 2014, *MNRAS*, 440, 2474
- Whittle, M. 1985, *MNRAS*, 213, 33
- Wildy, C., Czerny, B., & Panda, S. 2019, *A&A*, 632, A41
- Wilkes, B. J., Elvis, M., & McHardy, I. 1987, *ApJL*, 321, L23
- Wilkes, B. J., Wright, A. E., Jauncey, D. L., & Peterson, B. A. 1983, *PASA*, 5, 2
- Wills, B. J. & Browne, I. W. A. 1986, *ApJ*, 302, 56
- Wills, B. J., Laor, A., Brotherton, M. S., et al. 1999, *ApJL*, 515, L53
- Wills, B. J., Thompson, K. L., Han, M., et al. 1995, *ApJ*, 447, 139
- Wilson, A. S. & Colbert, E. J. M. 1995, *ApJ*, 438, 62
- Wisotzki, L., Christlieb, N., Bade, N., et al. 2000, *A&A*, 358, 77
- Wolf, J., Salvato, M., Coffey, D., et al. 2020, *MNRAS*, 492, 3580

- Woo, J.-H., Bae, H.-J., Son, D., & Karouzos, M. 2016, *ApJ*, 817, 108
- Woo, J.-H. & Urry, C. M. 2002, *ApJL*, 581, L5
- Wu, J., Brandt, W. N., Anderson, S. F., et al. 2012, *ApJ*, 747, 10
- Xu, F., Bian, F., Shen, Y., et al. 2018, *MNRAS*, 480, 345
- Yang, J., Wang, F., Fan, X., et al. 2023, *ApJL*, 951, L5
- Yi, W., Zuo, W., Yang, J., et al. 2020, *ApJ*, 893, 95
- York, D. G., Adelman, J., Anderson, John E., J., et al. 2000, *AJ*, 120, 1579
- Yuan, M. J. & Wills, B. J. 2003, *ApJL*, 593, L11
- Yuan, Q., Brotherton, M., Green, R. F., & Kriss, G. A. 2004, in *Recycling Intergalactic and Interstellar Matter*, ed. P.-A. Duc, J. Braine, & E. Brinks, Vol. 217, 364
- Zacharias, N., Monet, D. G., Levine, S. E., et al. 2005, *VizieR Online Data Catalog*, 1297
- Zakamska, N. L., Hamann, F., Pâris, I., et al. 2016, *MNRAS*, 459, 3144
- Zamanov, R., Marziani, P., Sulentic, J. W., et al. 2002, *ApJL*, 576, L9
- Zamfir, S., Sulentic, J. W., & Marziani, P. 2008, *MNRAS*, 387, 856
- Zamfir, S., Sulentic, J. W., Marziani, P., & Dultzin, D. 2010, *MNRAS*, 403, 1759
- Zhang, K., Dong, X.-B., Wang, T.-G., & Gaskell, C. M. 2011, *ApJ*, 737, 71
- Zheng, W. 1988, *Astrophysical Letters and Communications*, 27, 275
- Zheng, W. & Keel, W. C. 1991, *ApJ*, 382, 121
- Zheng, W. & O'Brien, P. T. 1990, *ApJ*, 353, 433
- Zoccali, M., Renzini, A., Ortolani, S., et al. 2003, *A&A*, 399, 931

THE ISAAC SAMPLE – MULTICOMPONENT FITS AND INDIVIDUAL NOTES



In this appendix, we present the new VLT/ISAAC infrared spectra and the multicomponent fittings for the optical spectral range, including the fits of $H\beta + [O III]\lambda 5007$. An additional analysis of the UV spectra is also presented for the objects with available UV spectra, from the literature or from SDSS. The UV analysis includes fittings for $Si IV\lambda 1397 + OIV]\lambda 1402$, $C IV\lambda 1549 + He II\lambda 1640$ as well as for the 1900 Å blend. We also include notes for some of the individual objects.

A.1 ISAAC1

A.1.1 HE 0001-2340

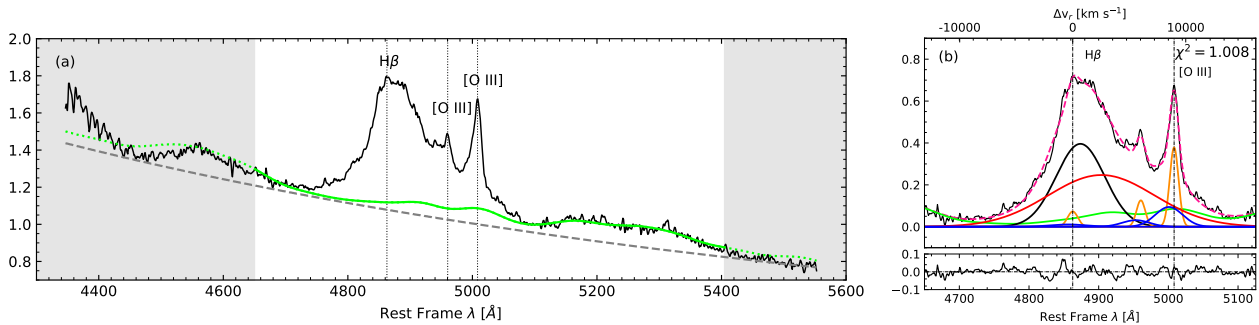


Fig. A.1.1: HE 0001-2340: (a) Rest-frame spectrum covering the $H\beta$ spectral range obtained with VLT/ISAAC. The spectrum is normalised by the continuum at 5100\AA (the flux values are available at Table 2.4). The grey dashed line traces a power law that defines the continuum level as obtained with the `SPECTFIT` multicomponent analysis. The green line shows the Fe II contribution. For this object Fe II was fitted only with the red Fe II blend due to the presence of atmospheric absorption in the blue. The vertical dotted lines indicate the rest-frame of the main emission lines in the $H\beta$ spectral range and the grey-shaded area indicate the regions that were not considered in the fittings. The white area indicates the region used to anchor both the continuum and the Fe II template. (b) Result of the fitting after continuum subtraction (upper panel) and the residuals (bottom panel) for the $H\beta$ region. Pink dashed line shows the final fit. Broad $H\beta$ component (BC) is represented by a black line meanwhile red line show the VBC. Orange lines represent narrow components and the blue ones correspond to the blueshifted components. The region in which the Fe II template was fitted is represented by the solid green line. Dotted green line indicate the expected Fe II contribution for the other parts of the spectra.

A.1.2 [HB89] 0029+073

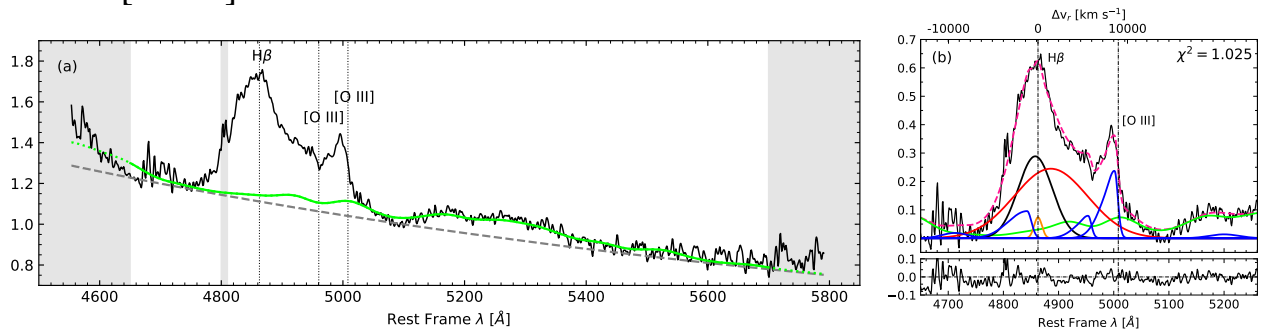


Fig. A.1.2: [HB89] 0029+073. Colours and lines as Figure A.1.1.

Jaunsen et al. (1995) listed this source as a gravitational lens candidate. [HB89] 0029+073 is another case in which the Fe II contribution was measured at $\lambda \geq 5000\text{Å}$ and then re-scaled to obtain the intensity of the Fe II λ 4570 blend.

A.1.3 CTQ 0408

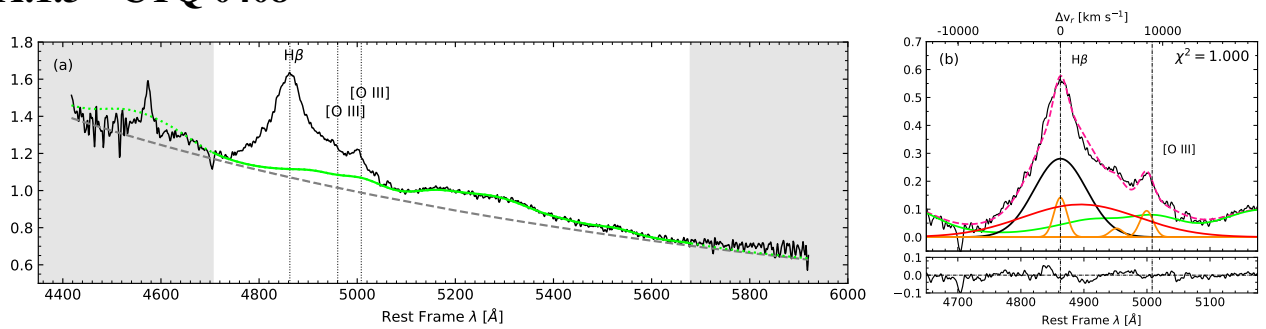


Fig. A.1.3: CTQ 0408. Details are the same as in Figure A.1.1.

As in the case of [HB89] 0029+073, the Fe II of CTQ 0408 was fit on the red side of H β with $\lambda \geq 5000\text{Å}$. Radio information about this source was found only in the SUMSS catalogue (Mauch et al. 2003). There is no radio map from NVSS nor FIRST for this object, because it is out of the respective survey fields.

A.1.4 SDSSJ005700.18+143737.7

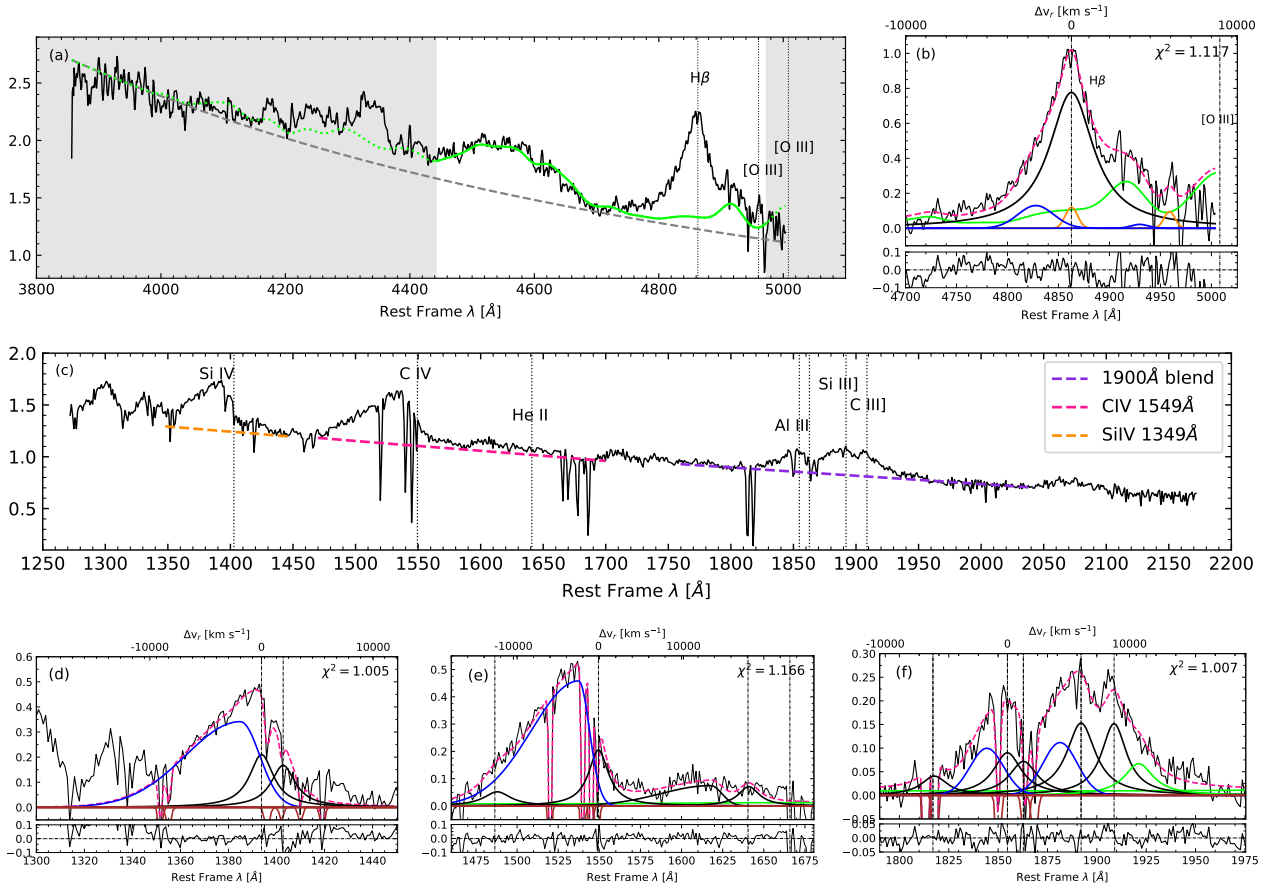


Fig. A.1.4: SDSSJ005700.18+143737.7. *Top panels:* Details are the same as in Fig. A.1.1. (c) Continuum-normalised UV spectrum from SDSS DR-16 with adopted continuum marked in colour. *Bottom panels:* Fits for (d) Si IV λ 1397+OIV λ 1402, (e) C IV λ 1549+He II λ 1640, and (f) the 1900 Å blend. Pink dashed lines show the final fitting. Broad components are represented by black lines, while blueshifted components are in blue. Green line represents the additional Fe III λ 1914 line in the red side of C III], observed in extreme Pop. A sources. Brown lines represent the absorptions seen in the spectrum and modelled as negative-flux Gaussians.

H β + [O III] λ 5007 falls at the red border of the observed spectrum. Consequently, the [O III] measurements should be treated as highly uncertain and special marks have been included in the corresponding tables in the chapter. The measurements and the analysis on the [O III] profile were performed with the [O III] λ 4959 instead of [O III] λ 5007. With respect to the UV spectrum, the object presents strong absorption lines likely associated with intervening absorbers throughout the three UV regions of interest. In the analysis we also included Gaussians profiles for the absorption lines in the fittings. It was necessary to include two blueshifted components for Al III and Si III] λ 1892, otherwise both Al III and Si III] λ 1892 BC are shifted by more than 1000 km s $^{-1}$.

A.1.5 H 0055-2659

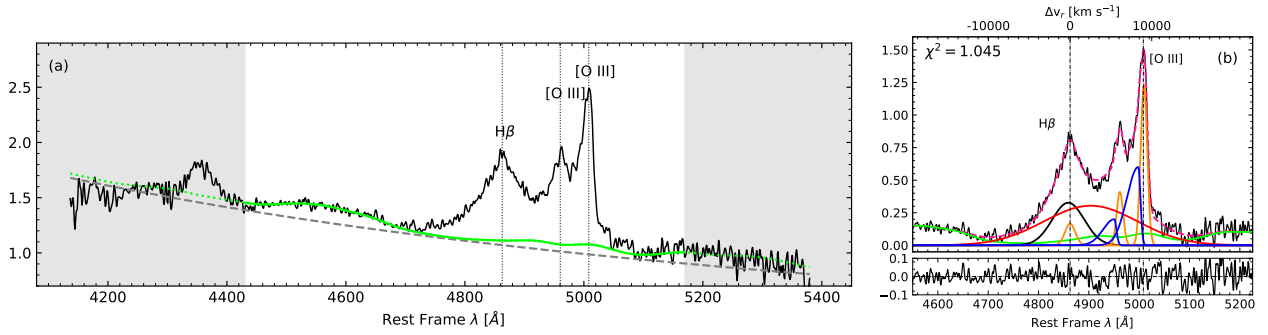


Fig. A.1.5: H 0055-2659. Details are the same as in Figure A.1.1.

The VLT rest-frame optical spectrum of H 0055-2659 presents a very flat profile and small Fe II multiplets contributions.

A.1.6 SDSSJ114358.52+052444.9

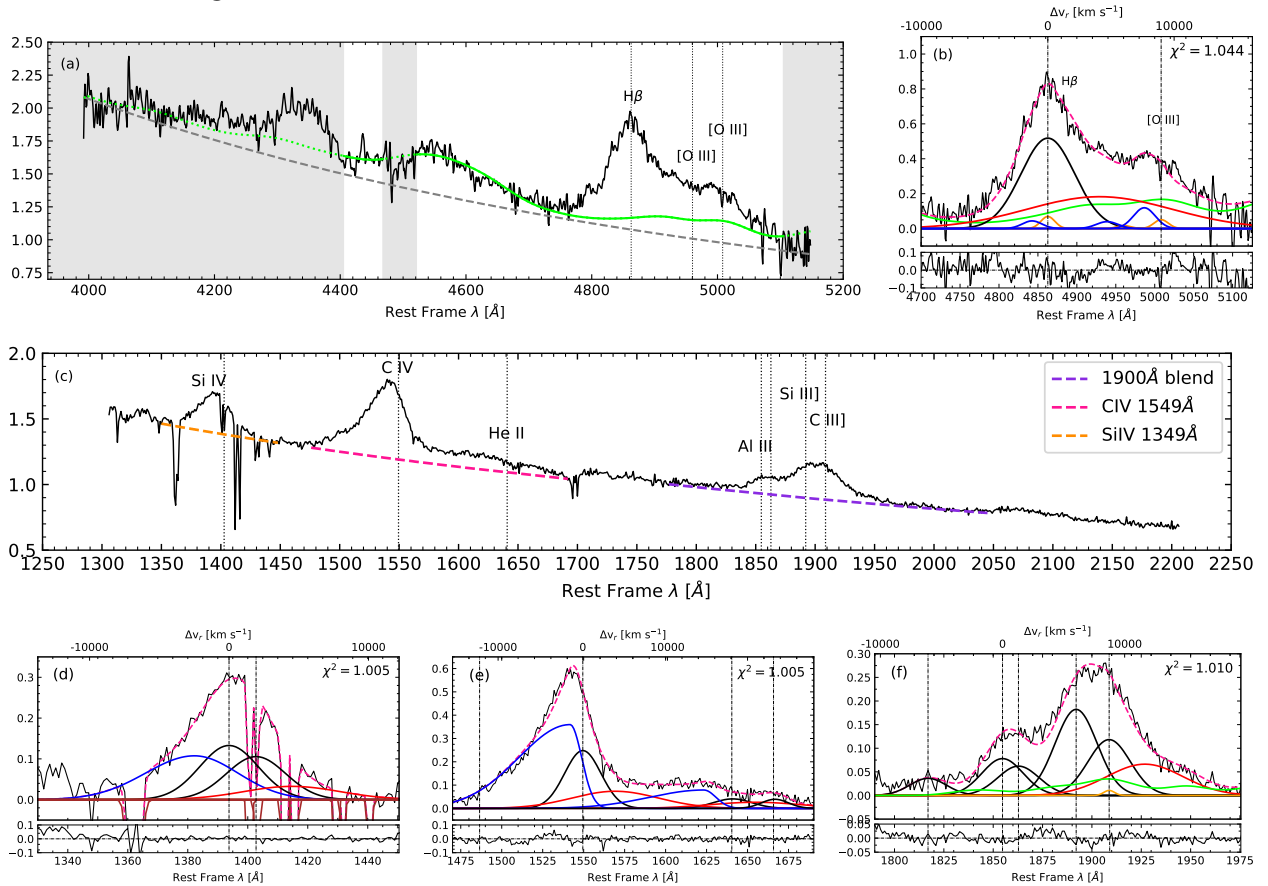


Fig. A.1.6: SDSSJ114358.52+052444.9. *Top panels:* Details are the same as in Fig. A.1.1 *Middle and bottom panels:* Same details as in Fig. A.1.4. Pink dashed lines show the final fitting. Broad components are represented by black lines, while blueshifted components are in blue. Brown lines represent the absorption lines seen in the spectrum.

A.1.7 SDSSJ115954.33+201921.1

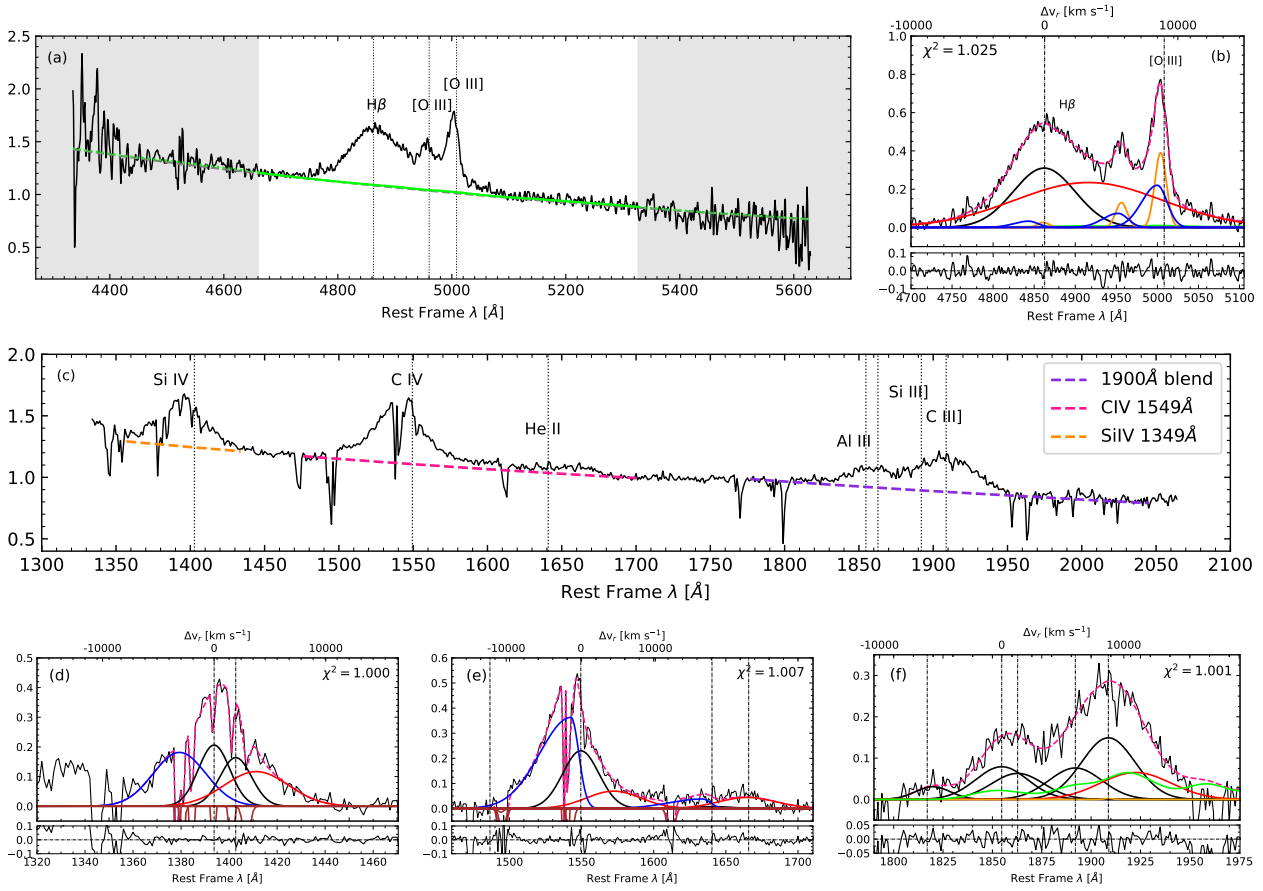


Fig. A.1.7: SDSSJ115954.33+201921.1. Same details as in Figure A.1.6.

In the optical range, this source presents a very flat spectrum and almost no Fe II contributions.

A.1.8 SDSSJ120147.90+120630.2

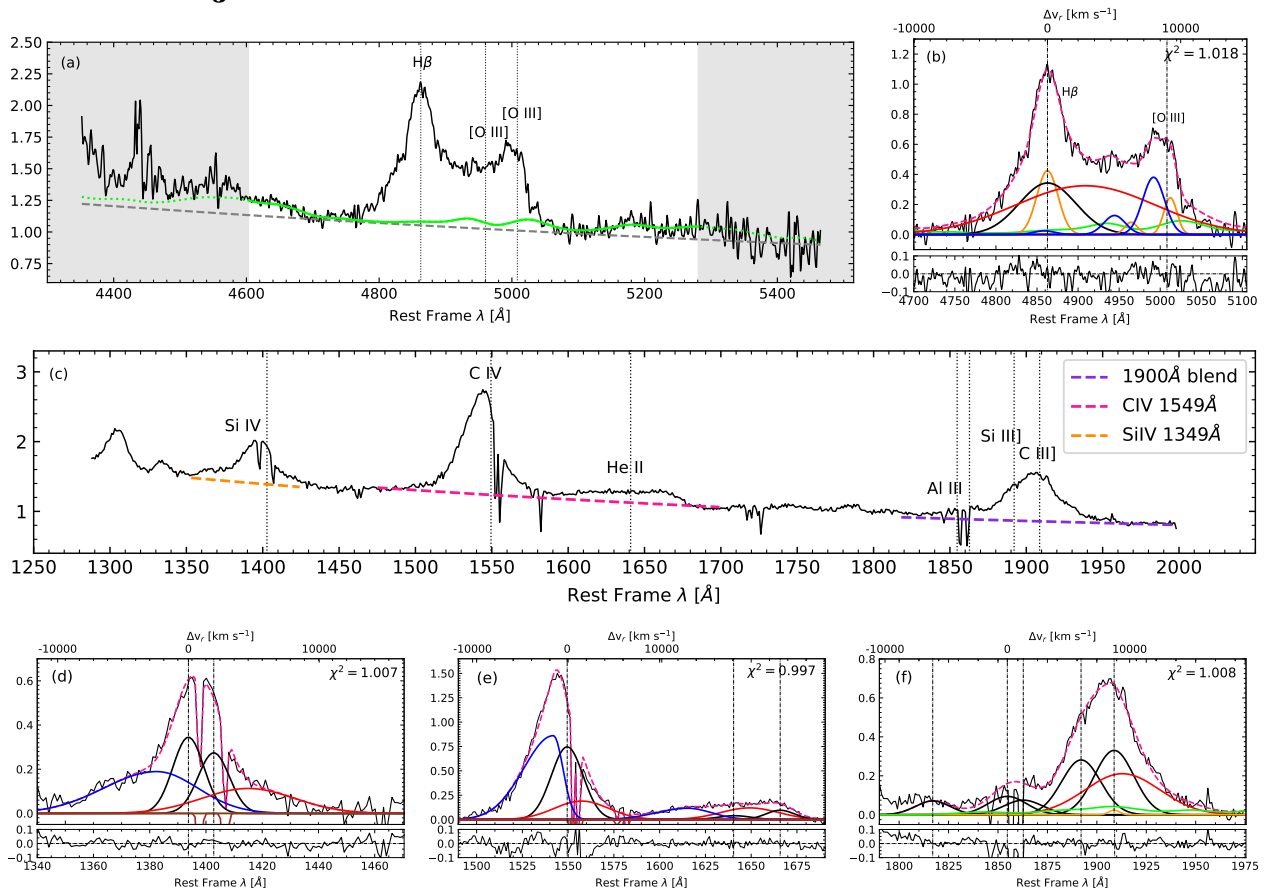


Fig. A.1.8: SDSSJ120147.90+120630.2. Same details as in Figure A.1.6.

This quasar has observations of the H β region at the Large Binocular Telescope (LBT), as reported in Bischetti et al. (2017). We stress that their spectrum is very similar to the one of ISAAC/VLT.

A.1.9 SDSSJ132012.33+142037.1

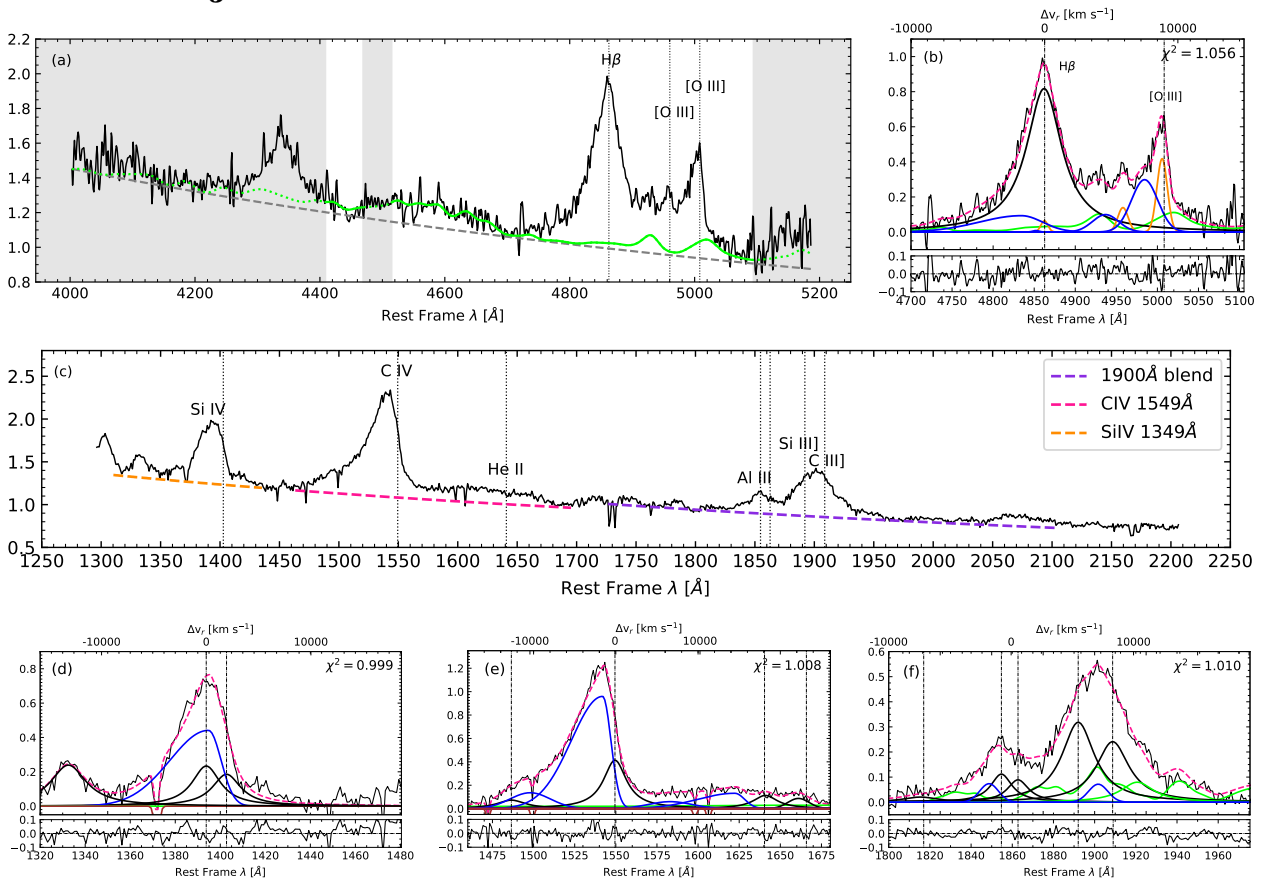


Fig. A.1.9: SDSSJ132012.33+142037.1. Same details as in Figure A.1.6.

A.1.10 SDSSJ135831.78+050522.8

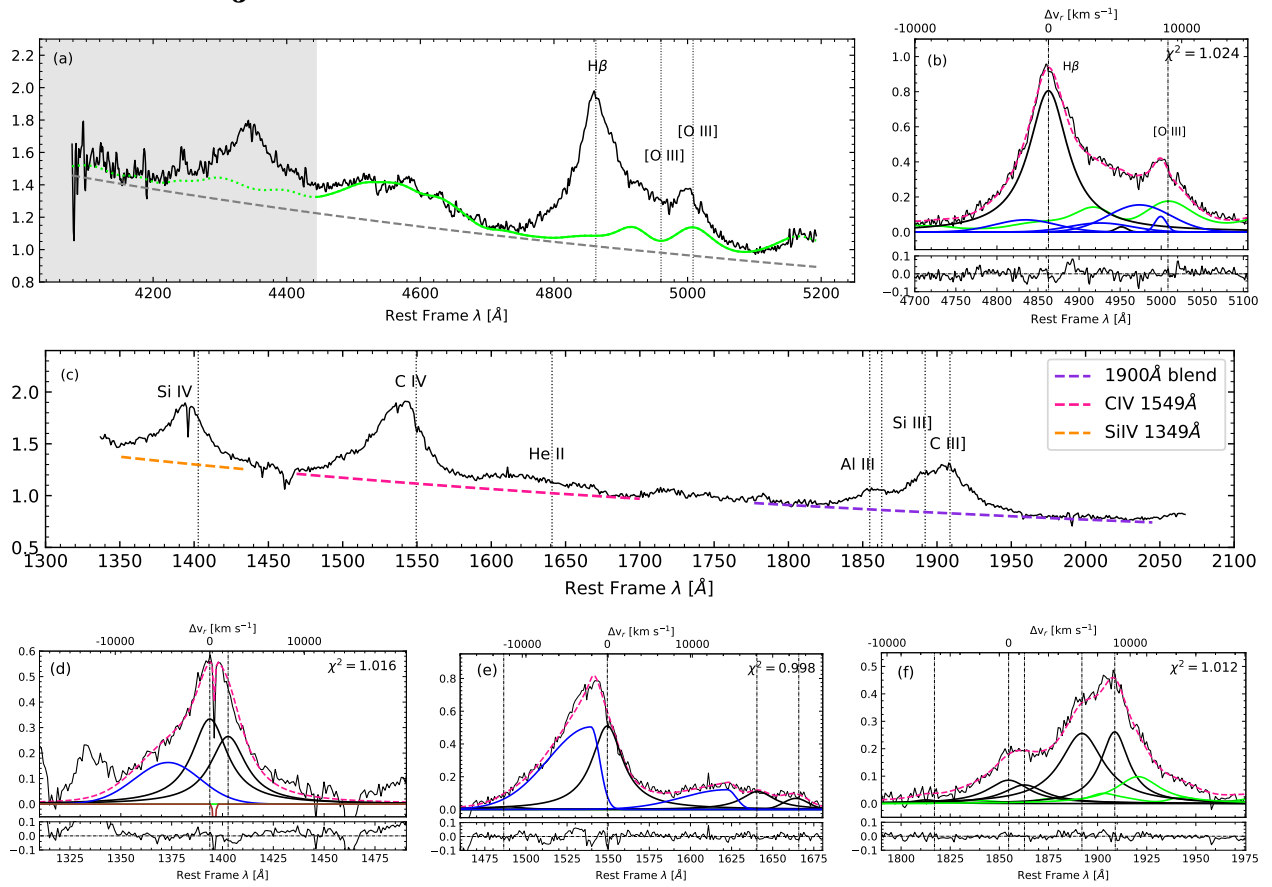


Fig. A.1.10: SDSSJ135831.78+050522.8. Same details as in Figure A.1.6.

A.1.11 Q 1410+096

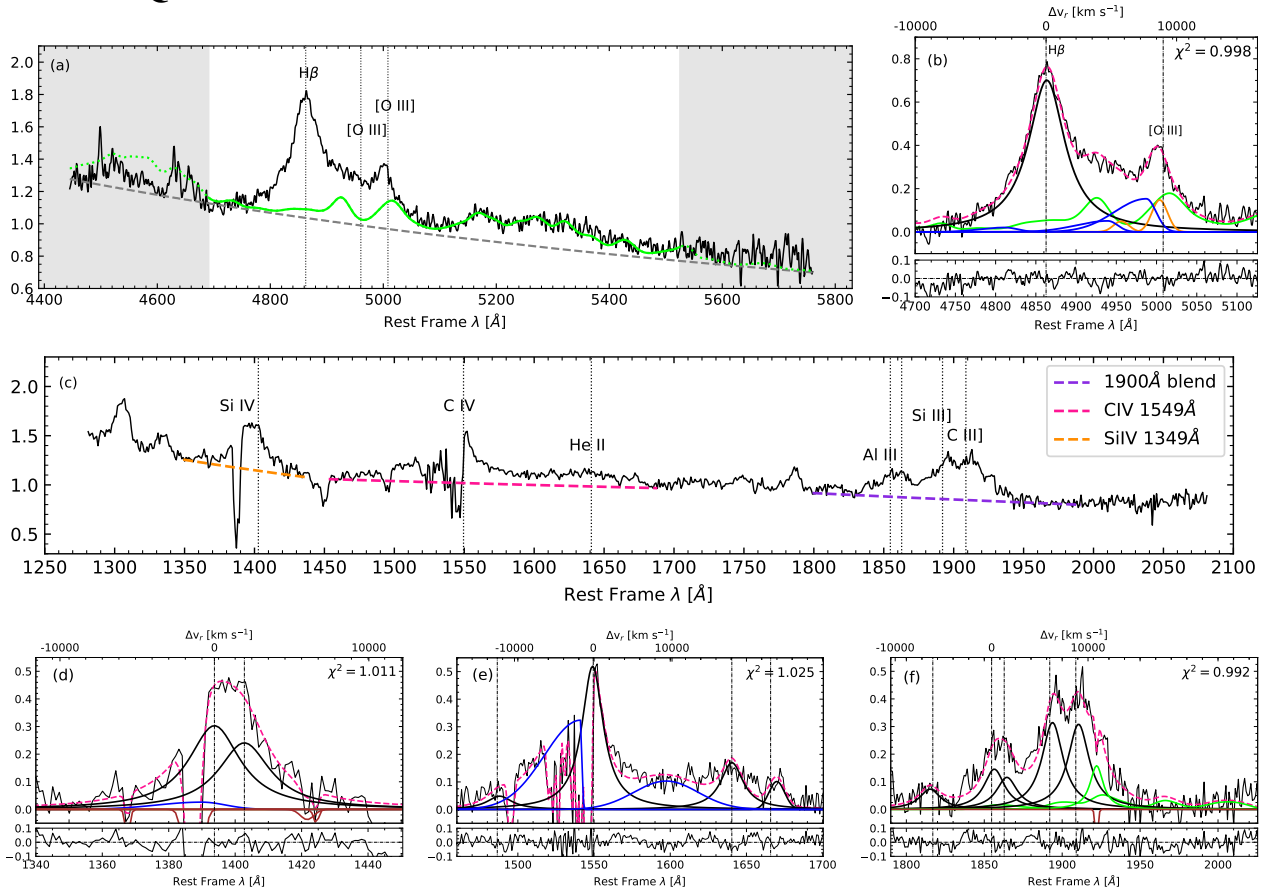


Fig. A.1.11: Q 1410+096. Same details as in Figure A.1.6.

This source has been identified as a BAL quasar by [Allen et al. \(2011\)](#) and the absorption lines are seen in the regions of the $\text{Si IV } \lambda 1397$ and $\text{C IV } \lambda 1549$ emission lines. In order to account for the multiplet contributions in the optical region, we performed a fitting of this Fe II emission on the red side of $\text{H}\beta$, since the blue part of the $\text{Fe II } \lambda 4570$ region is close to the border of the spectrum and evidently affected by background subtraction or telluric absorption correction.

For this quasar, we performed the fitting of the $\text{C IV } \lambda 1549$ line based on the $\text{He II } \lambda 1640$ profile. The Al III BC of 1410+096 is narrow when compared to $\text{H}\beta$, which may indicate that $\text{H}\beta$ might be affected by blueshifted emission. An excess (not included in the fit) is also visible on the blue side of Al III (bottom rightmost panel of Fig. A.1.11). This source has also been analysed in detail in [Deconto-Machado et al. \(2022a\)](#).

A.1.12 SDSSJ141546.24+112943.4

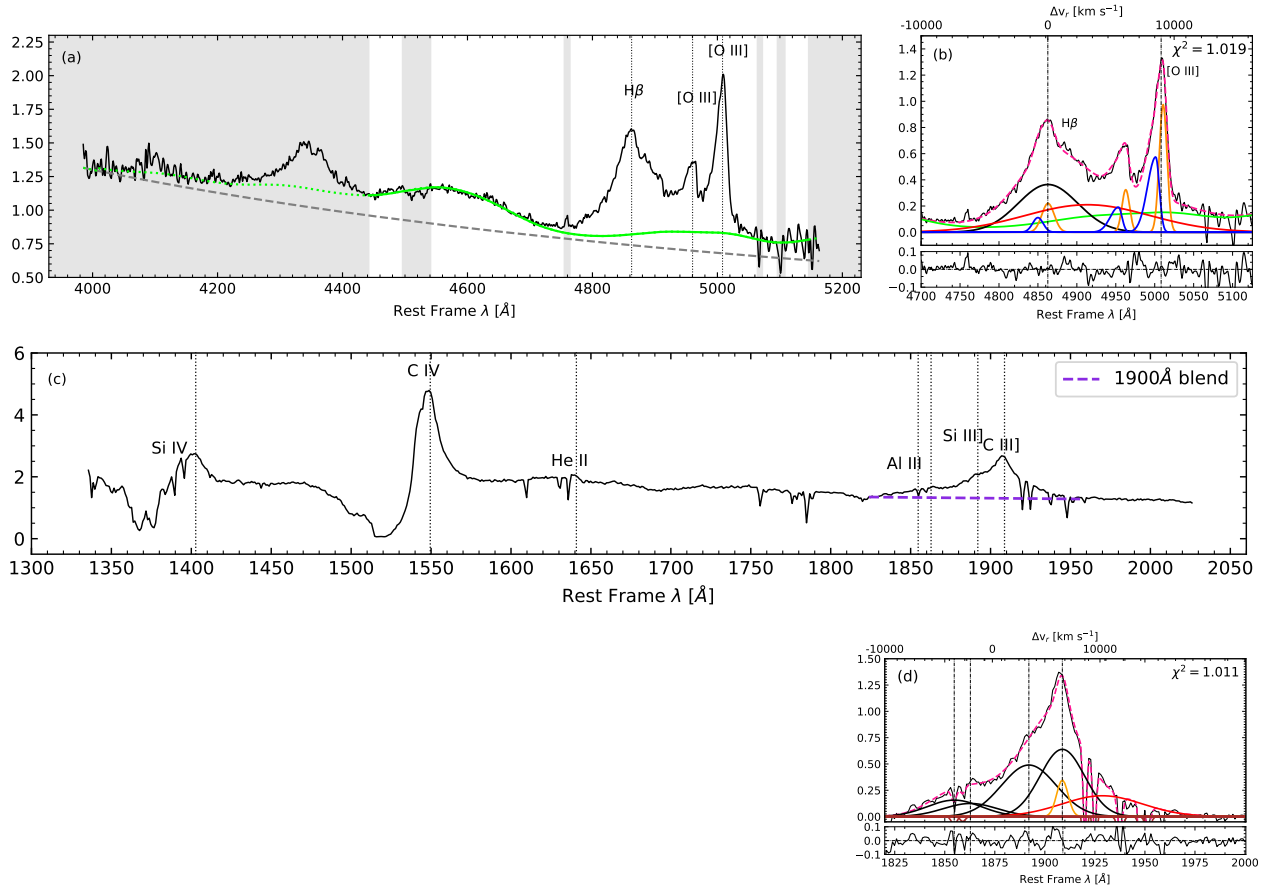


Fig. A.1.12: SDSSJ141546.24+112943.4. *Top panels:* Colours and lines are the same as in Fig. A.1.1. (c) UV spectrum. (d) Fits for the 1900 Å blend. Pink dashed lines show the final fitting. Broad components are represented by black lines, while narrow and very broad components are in orange and red, respectively. Brown lines represent the absorption seen in the spectrum.

This object is known as a weak microlensing candidate in the literature (Sluse et al. 2012; Takahashi & Inoue 2014). According to Welling et al. (2014), the quasar is a gravitationally lensed object split into four images separated by $\sim 1''$. SDSSJ141546.24+112943.4 is a modest core-dominated radio-loud source with a logarithmic radio loudness parameter of 1.09.

As can be seen in the UV spectra presented in Fig. A.1.12, the source is a BAL quasar, with broad absorption lines especially in the C IV $\lambda 1549$ and Si IV $\lambda 1397$ regions. Hazard et al. (1984) also report broad absorption lines in Al III that we can see on the blue side of the blend at $\lambda \approx 1820$ Å.

A.1.13 B1422+231

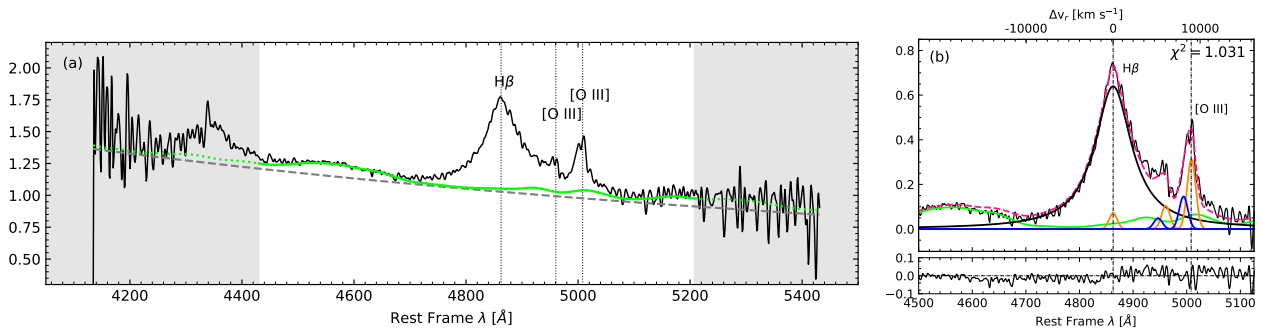


Fig. A.1.13: B1422+231. Colours and lines as the same as in Figure A.1.1.

The source was studied in detail for the first time by [Patnaik et al. \(1992\)](#). It consists of a gravitationally lensed system with a diameter of 1.3 arcsec and four non-resolved components from VLA observations. This quasar is lensed into four images by a galaxy with $z = 0.34$ ([Tonry 1998](#)). [Dadina et al. \(2016\)](#) used XMM-Newton to study the matter inflow at the centre of this source and found that its X-ray spectrum is quite similar to the one of a typical Seyfert galaxy. Several UV spectra were found in literature ([Tonry 1998](#); [Assef et al. 2011](#); [Kundic et al. 1997](#); [O’Dowd et al. 2017](#)), but are not available for public usage or do not correspond to the regions we want to analyse. No SDSS spectrum was found. It has also been analysed in the infrared by [Lawrence et al. \(1992\)](#) who conclude that the source presents similar structures in both radio and infrared. This is one of the radio-loud sources included in our sample.

A.1.14 SDSSJ153830.55+085517.0

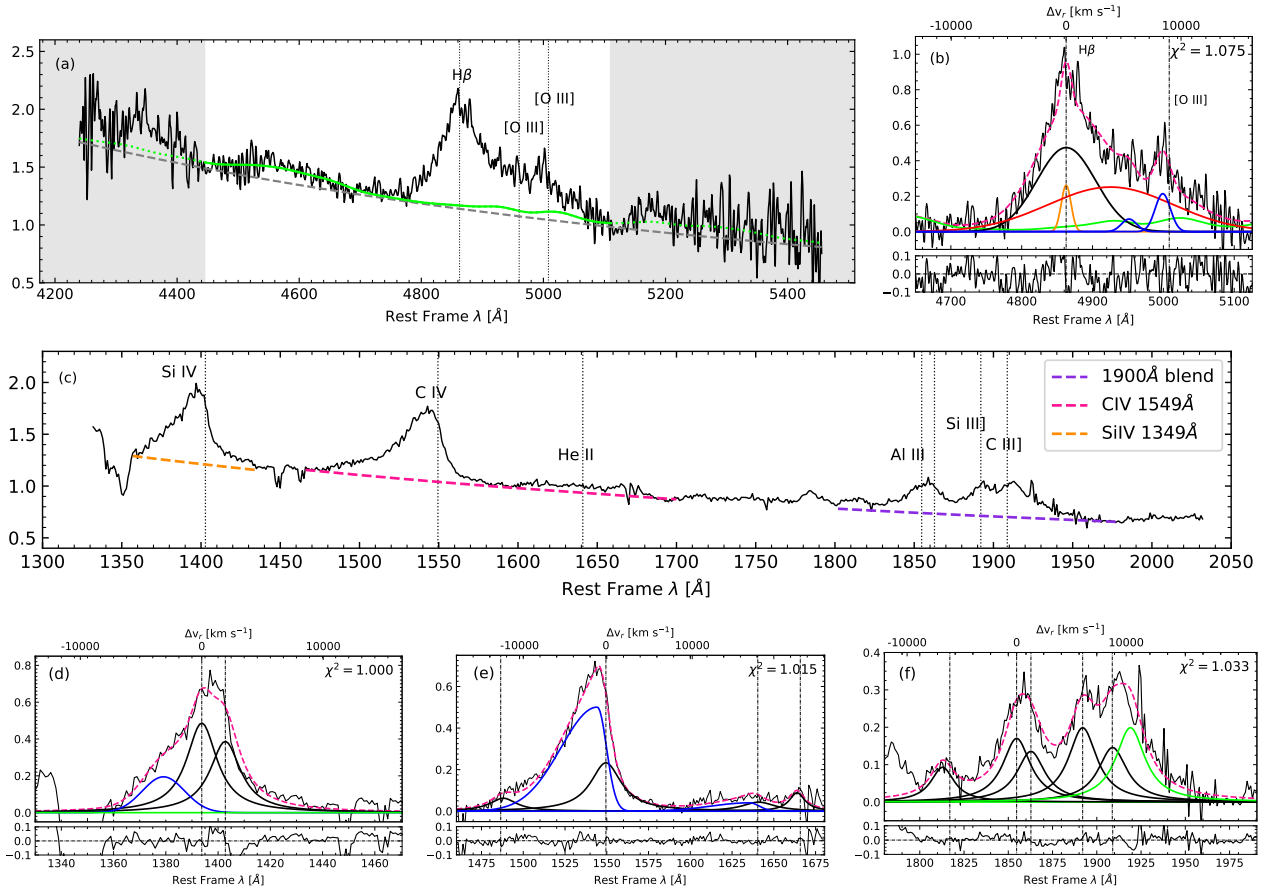


Fig. A.1.14: SDSSJ153830.55+085517.0. Same details as in Figure A.1.6.

When compared with the other sources of the sample, this source presents one of the spectra with lowest S/N. The low S/N might be due to the presence of a star that is located very close to the field of the quasar significantly increasing the background of the spectrum. This also may explain why the UV and the optical spectra of SDSSJ153830.55+085517.0 differ so much: while the optical spectrum shows a Pop. B-like profile, the UV is clearly the expected one for a Pop. A3 quasar. If this discrepancy is real, this would be the first case of discordant population classification from the UV and from the optical spectrum. SDSSJ153830.55+085517.0 had the 1900Å blend fit as Pop. A since it cannot reproduce any Pop. B model and its UV spectrum presents all the characteristics of a Pop. A quasar. SDSSJ153830.55+085517.0 has previous observations in the K -band at LBT (Vietri et al. 2018) and at UKIRT by Dix et al. (2020). In both cases, our NIR spectrum is compatible with those shown for the $H\beta$ region by these authors. As we remarked before, the UV spectrum obtained with BOSS shows a blend at 1900Å characteristic of the extreme end of Pop. A. An additional old UV SDSS spectrum exists, but it has no information on the 1900Å blend. A new UV spectrum would be necessary to disentangle its classification and possible peculiarity. Additionally, Bruni et al. (2019) has classified this source as a high-velocity BAL.

A.1.15 SDSSJ161458.33+144836.9

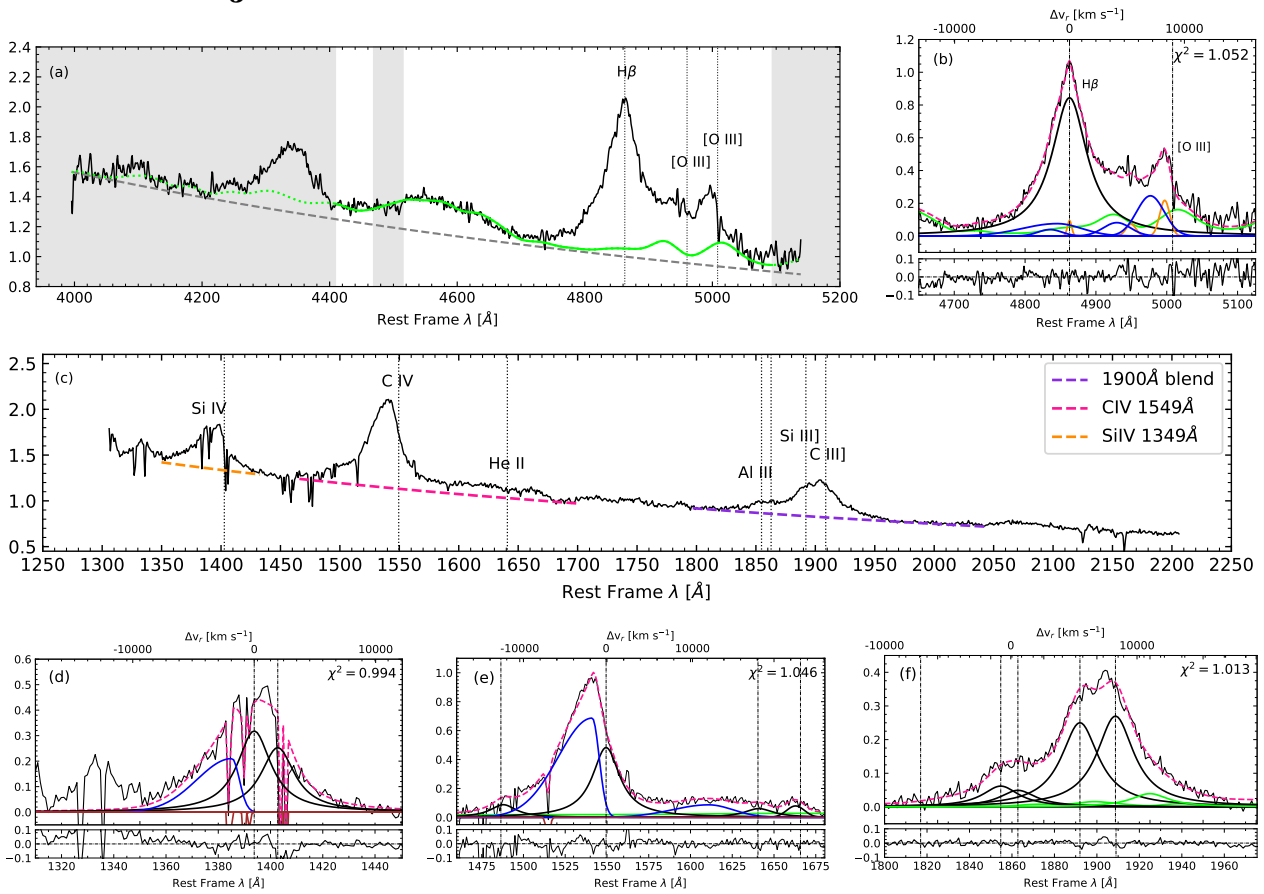


Fig. A.1.15: SDSSJ161458.33+144836.9. Same details as in Figure A.1.6.

A.1.16 PKS 1937-101

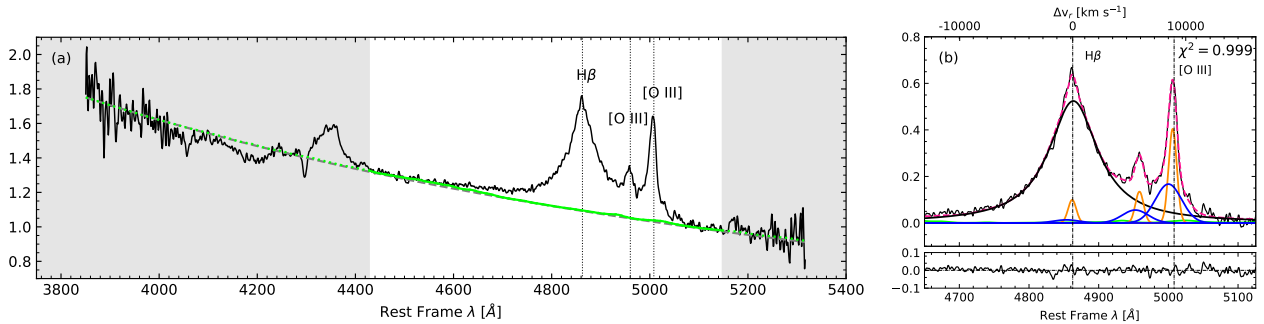


Fig. A.1.16: PKS 1937-101. Colours and lines as Figure A.1.1.

This object shows a very faint Fe II emission, as is typical of A1 spectra. A UV spectrum from the MOJAVE/2CM atlas for this source is presented in [Torrealba et al. \(2012\)](#). It is also one of the strongest radio-loud sources analysed in this work. Data from the Parkes 2.7 GHz Survey are shown in [Savage et al. \(1990\)](#). PKS 1937-101 is seen as a compact radio source after analysis of VLBI data ([Lee et al. 2016](#)). [Brinkmann & Siebert \(1995\)](#) has reported PKS 1937-101 as one of the most distant objects detected with the ROSAT survey ([Voges 1993](#)).

A.1.17 PKS 2000-330

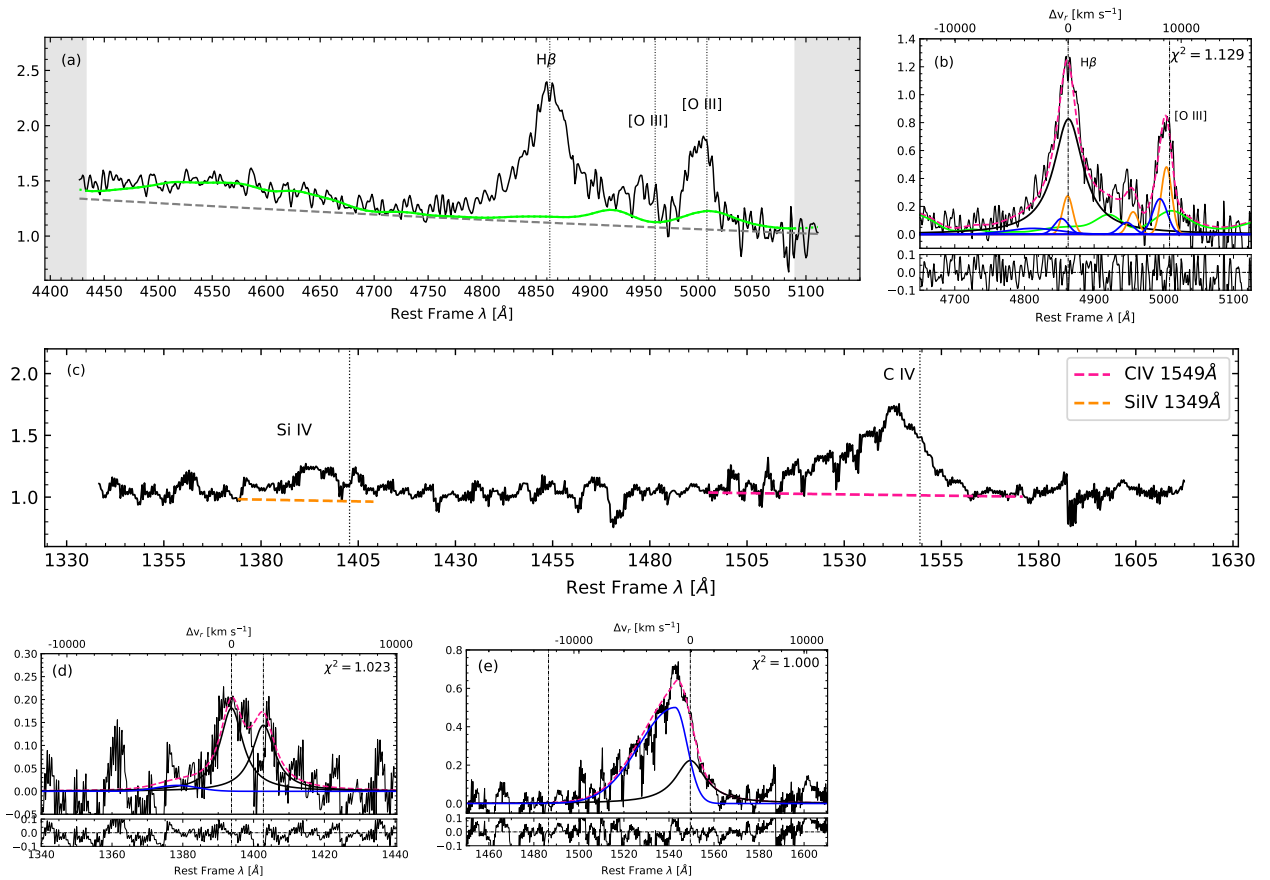


Fig. A.1.17: PKS 2000-330. *Top panels:* Same details as in Figure A.1.6. *(c)* UV spectrum. *Bottom panels:* Fits for (d) Si IV $\lambda 1397$ and (e) C IV $\lambda 1549$: The UV spectrum was digitised from [Barthel et al. \(1990\)](#).

The UV spectrum used in the fittings was obtained through the digitisation of the spectrum from [Barthel et al. \(1990\)](#). However, since this spectrum presents a small wavelength range that does not account either for the 1900 Å blend or for He II $\lambda 1640$, we analyse only the Si IV $\lambda 1397$ and C IV $\lambda 1549$ emission lines. A detailed comparison between this source and Q 1410+096 is performed in [Deconto-Machado et al. \(2022a\)](#).

This quasar is the strongest radio-loud source from the present sample ([Savage et al. 1990](#)). The position of this source is not within the area covered by the FIRST catalogue.

A.1.18 SDSSJ210524.49+000407.3

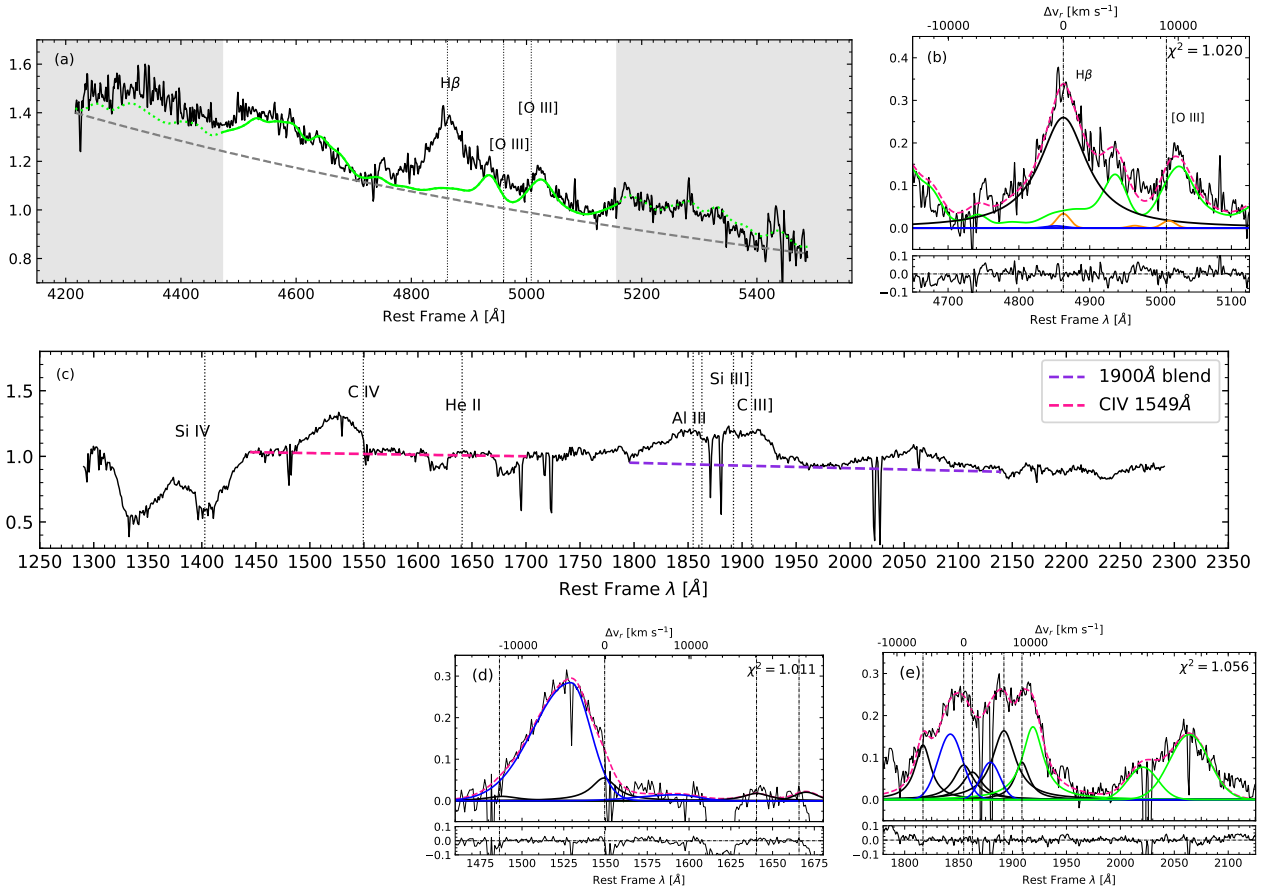


Fig. A.1.18: SDSSJ210524.49+000407.3. *Top panels:* Colours and lines as in Figure A.1.1. (c) SDSS UV spectrum. *Bottom panels:* Fits for (d) CIV λ 1549 and (e) the 1900 Å blend.

This source presents a $W([\text{O III}]) \approx 0.45 \text{ \AA}$. The low equivalent width makes it difficult to discern what corresponds to $[\text{O III}]\lambda 5007$ and to Fe II.

The UV region of this source is very unwieldy because of very broad absorption lines shortwards of CIV λ 1459. For the 1900 Å blend, we present two different fittings, one including blueshifted components for Al III and Si III λ 1892 and another without these lines. The motivation here is that if we do not include blueshifted components then the BC of the lines present a displacement of -1640 km s^{-1} , which can be seen as an indicative of some outflowing gas.

A.1.19 SDSSJ210831.56-063022.5

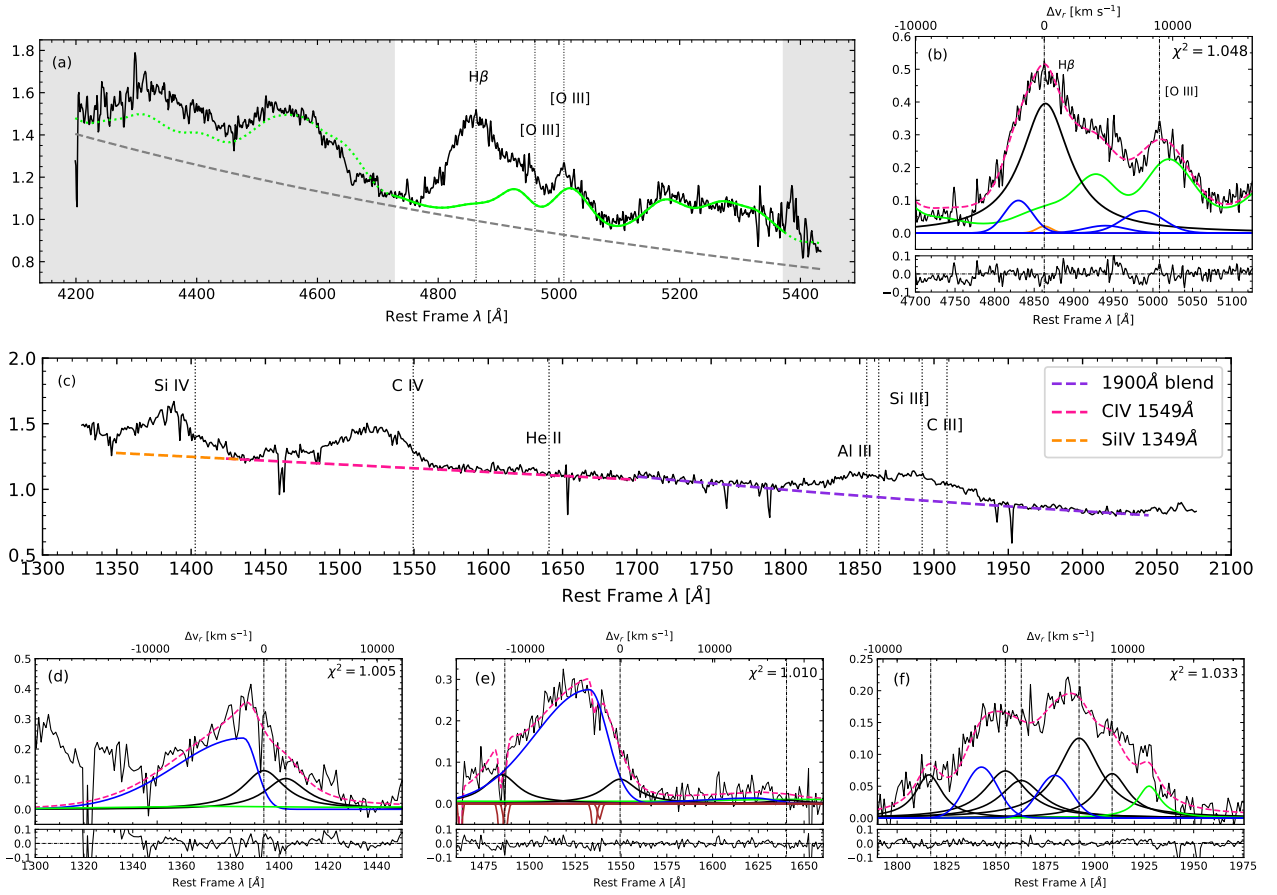


Fig. A.1.19: SDSSJ210831.56-063022.5. Same details as in Figure A.1.6.

This is another case in which the Fe II contribution is estimated through the red side of the spectrum. It is difficult to set the [O III] λ 5007 NC at rest-frame since the region close to these lines is dominated by the Fe II multiplets. Differently from the other Pop. A3 of the sample (SDSSJ005700.18+143737.7 and SDSSJ210524.49+000407.3), for this quasar it was not possible to reach a good χ^2 , without including blueshifted components for Al III and Si III] λ 1892. SDSSJ210831.56-063022.5 is a source that presents one of the widest H β BC of the sample. It could be that in this case the H β BLUE component has been underestimated, since we do find strong blueward asymmetries in the three fitted UV profiles.

A.1.20 SDSSJ212329.46-005052.9

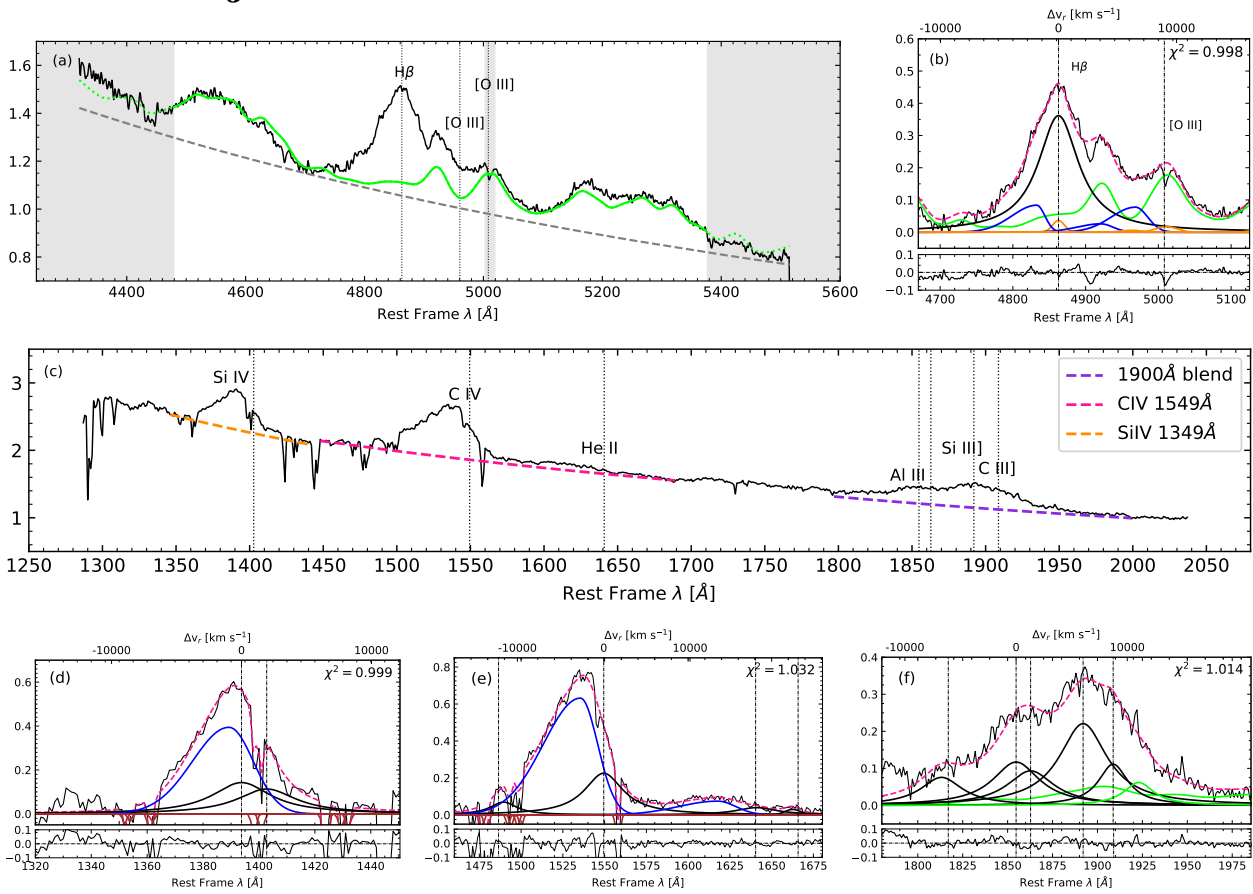


Fig. A.1.20: SDSSJ212329.46-005052.9. Same details as in Figure A.1.6.

A.1.21 PKS 2126-15

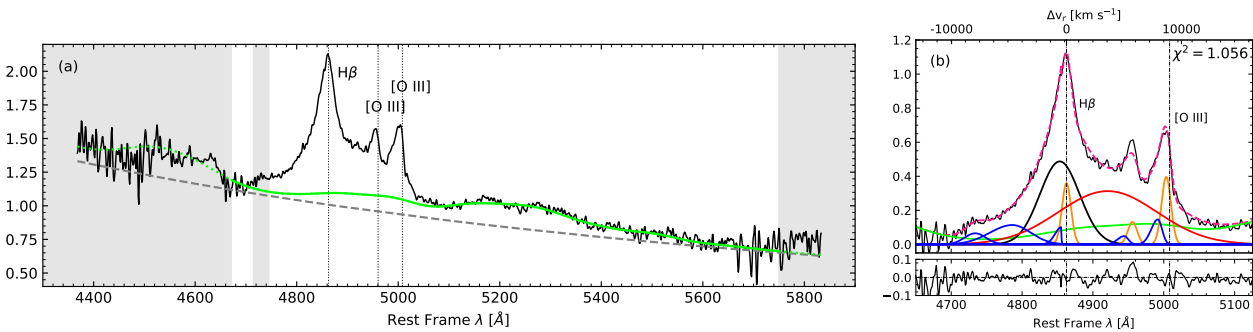


Fig. A.1.21: PKS 2126-15. Colours and lines are the same as in Figure A.1.1.

This object has been observed in the two runs. Since both observations can be used and present good S/N, we create a new spectrum by combining the two of them through the IRAF task `scombine`. The Fe II multiplets were fitted based on the shape seen in the red side of H β due to the fact that the blue side of H β is affected by noise and is almost at the border of the spectrum. In order to account for the [O III] λ 5007 contributions, it was necessary to include two blueshifted components, as can

be seen in Fig. A.1.21. Some UV spectra were found but they do not include the regions we are interested in. PKS 2126-15 is also one of the four radio-loud quasars from the sample.

A.1.22 SDSSJ235808.54+012507.2

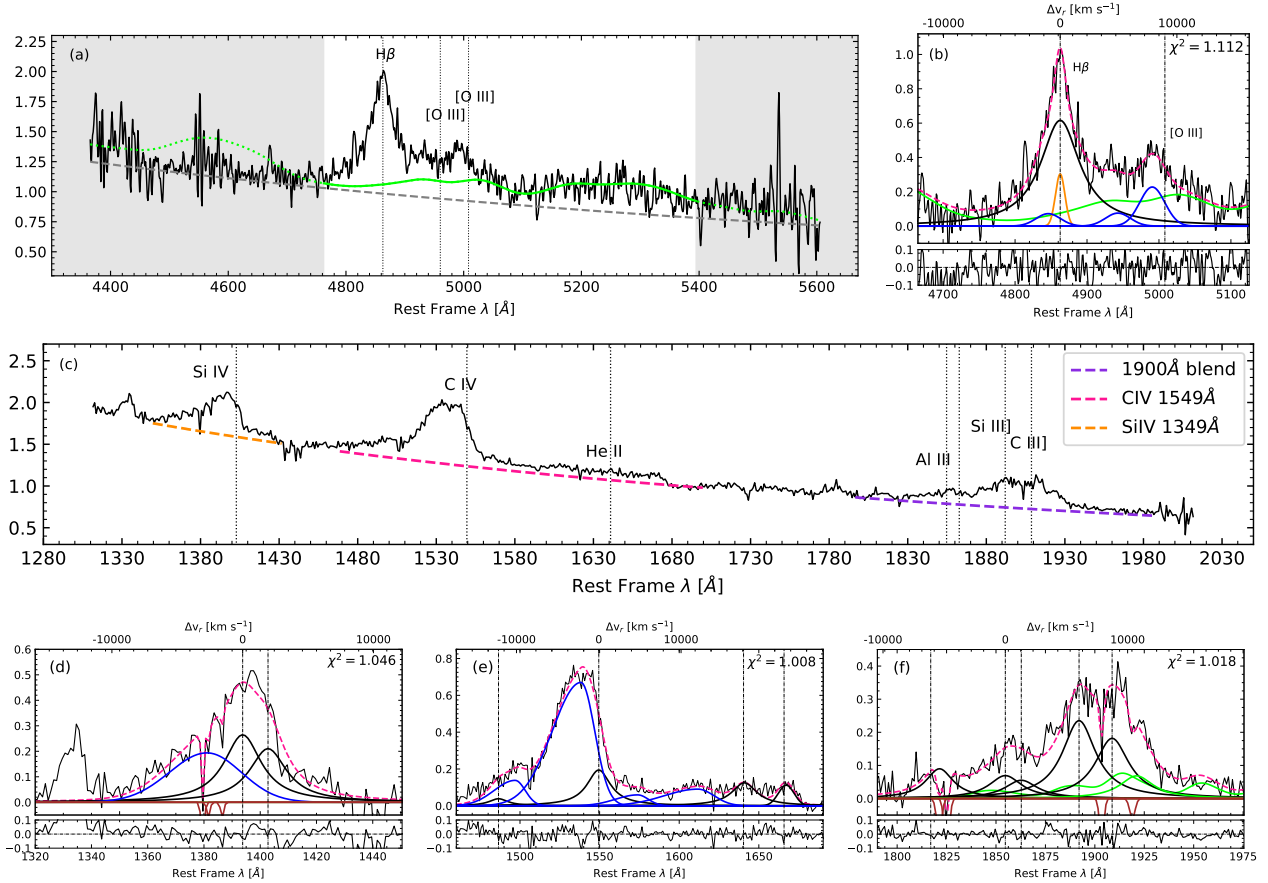


Fig. A.1.22: SDSSJ235808.54+012507.2. Same details as in Figure A.1.6.

The spectrum of this source is of low S/N when compared with the other sources of the sample, which makes it difficult to find the correct intensity of the continuum. As a consequence, caution should be taken when considering the location of the continuum and the Fe II contribution especially in the blue part of the spectrum.

A.2 ISAAC2

A.2.1 PKS0226-038

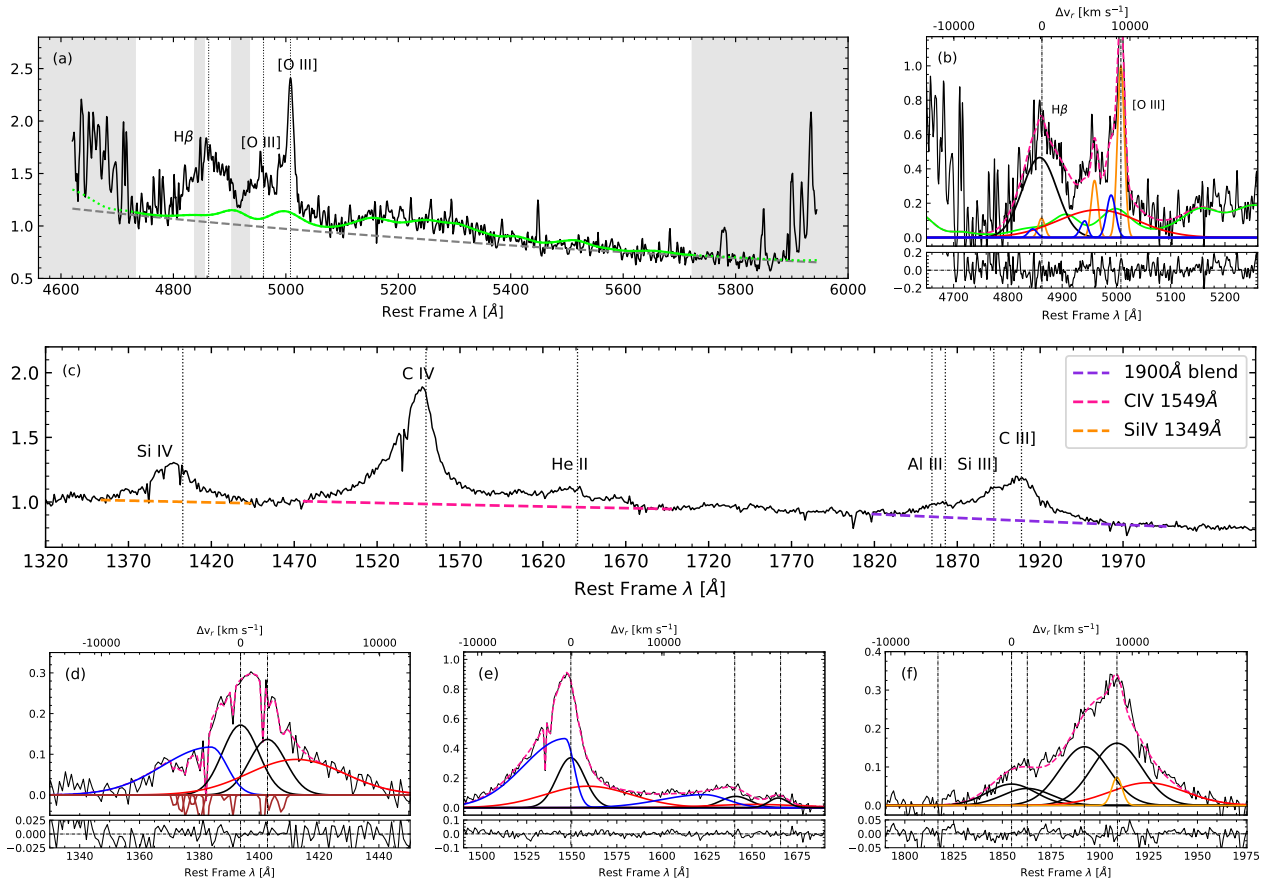


Fig. A.2.1: PKS0226-038. Colour and lines as Figure A.1.6.

A.2.2 PKS0237-23

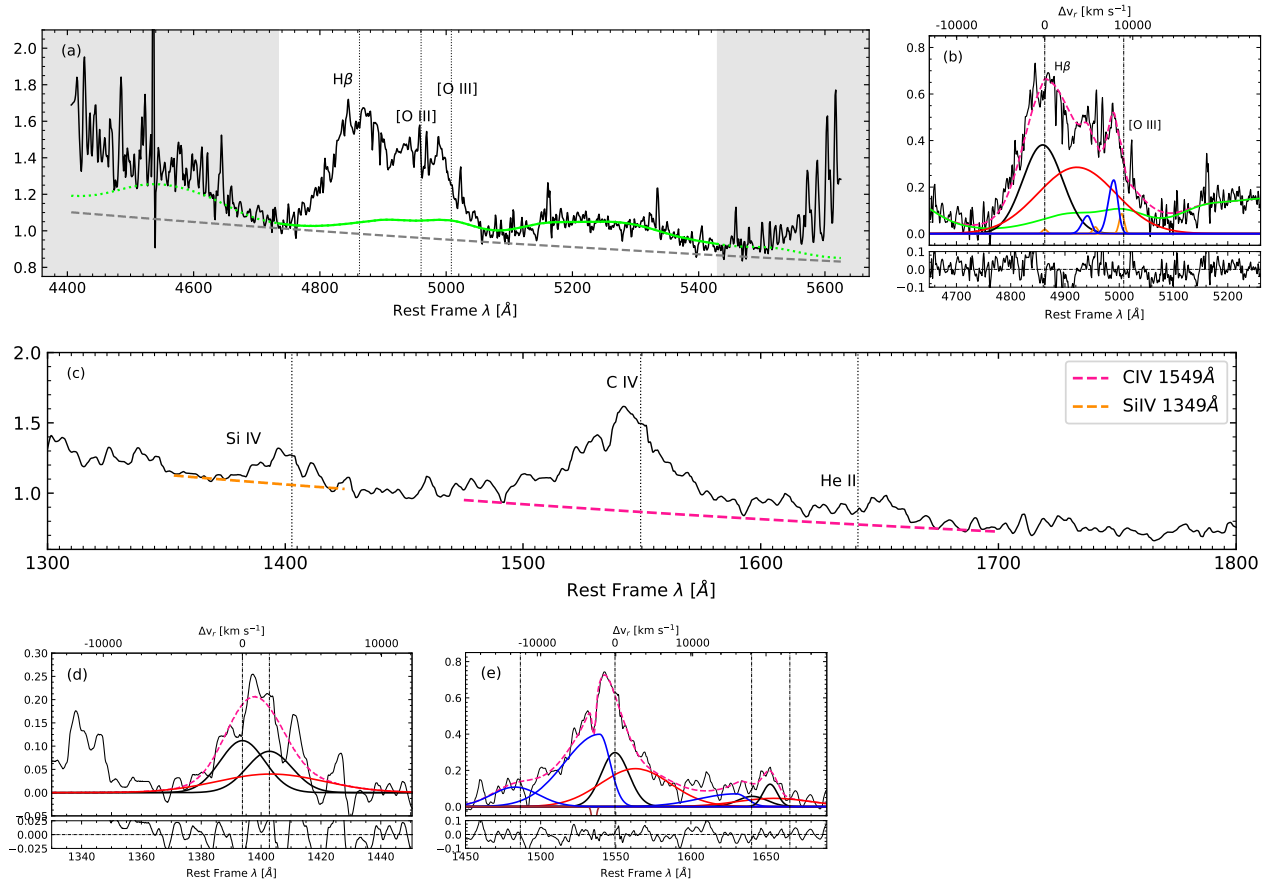


Fig. A.2.2: PKS0237-23. Colours and lines as Figure A.1.6.

A.2.3 BZQJ0544-2241

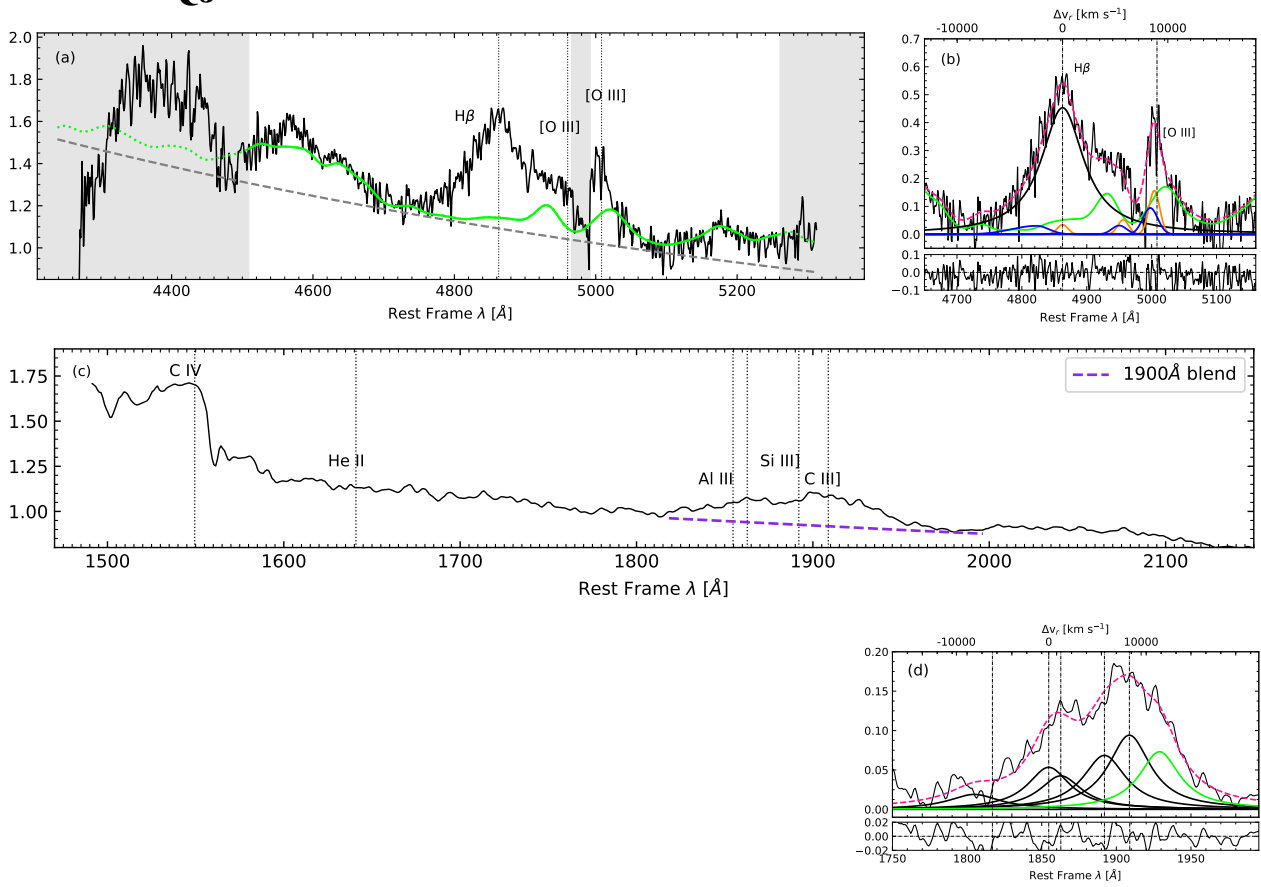


Fig. A.2.3: BZQJ0544-2241. Colours and lines as Figure A.1.6.

A.2.4 PKS0858-279

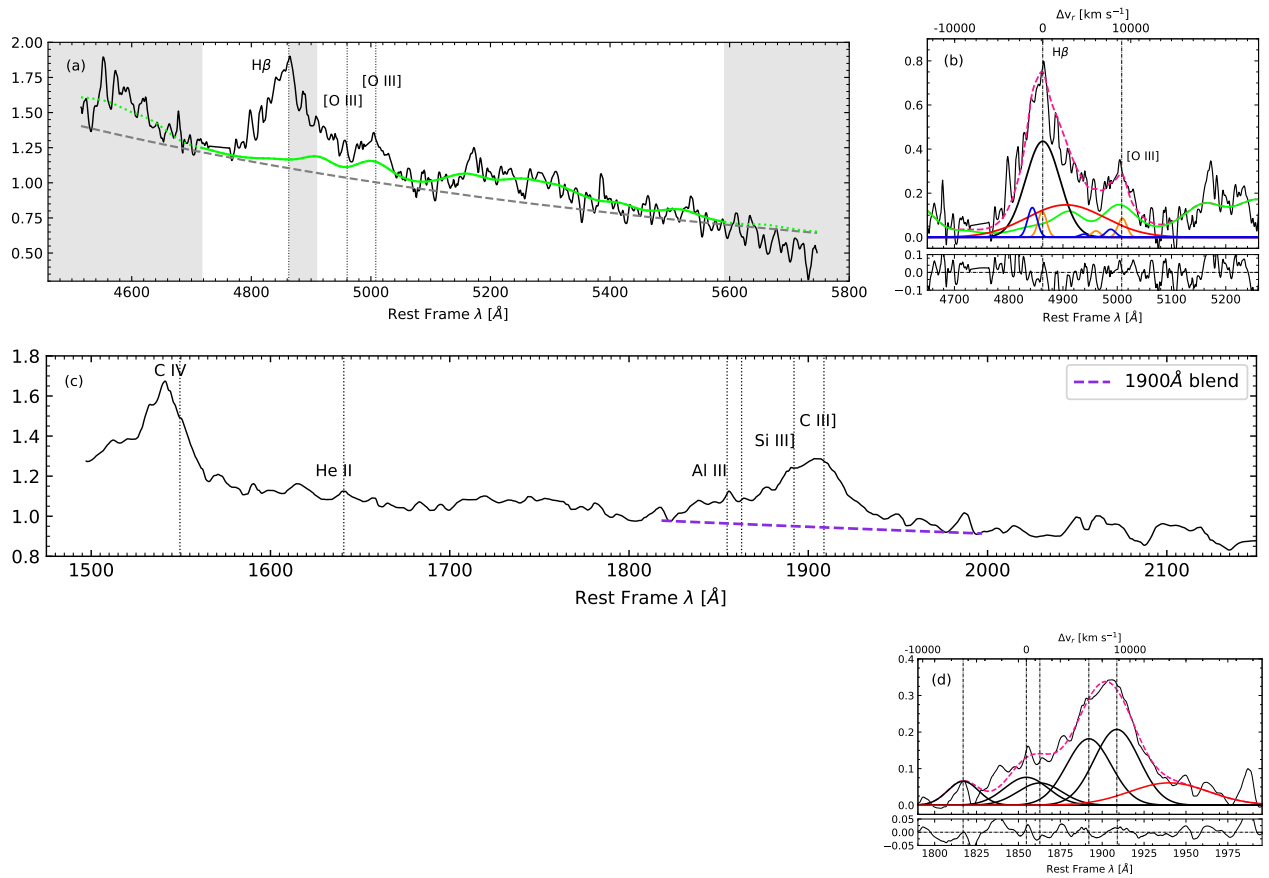


Fig. A.2.4: PKS0858-279. Colours and lines as Figure A.1.6.

A.2.5 CTSJ01.03

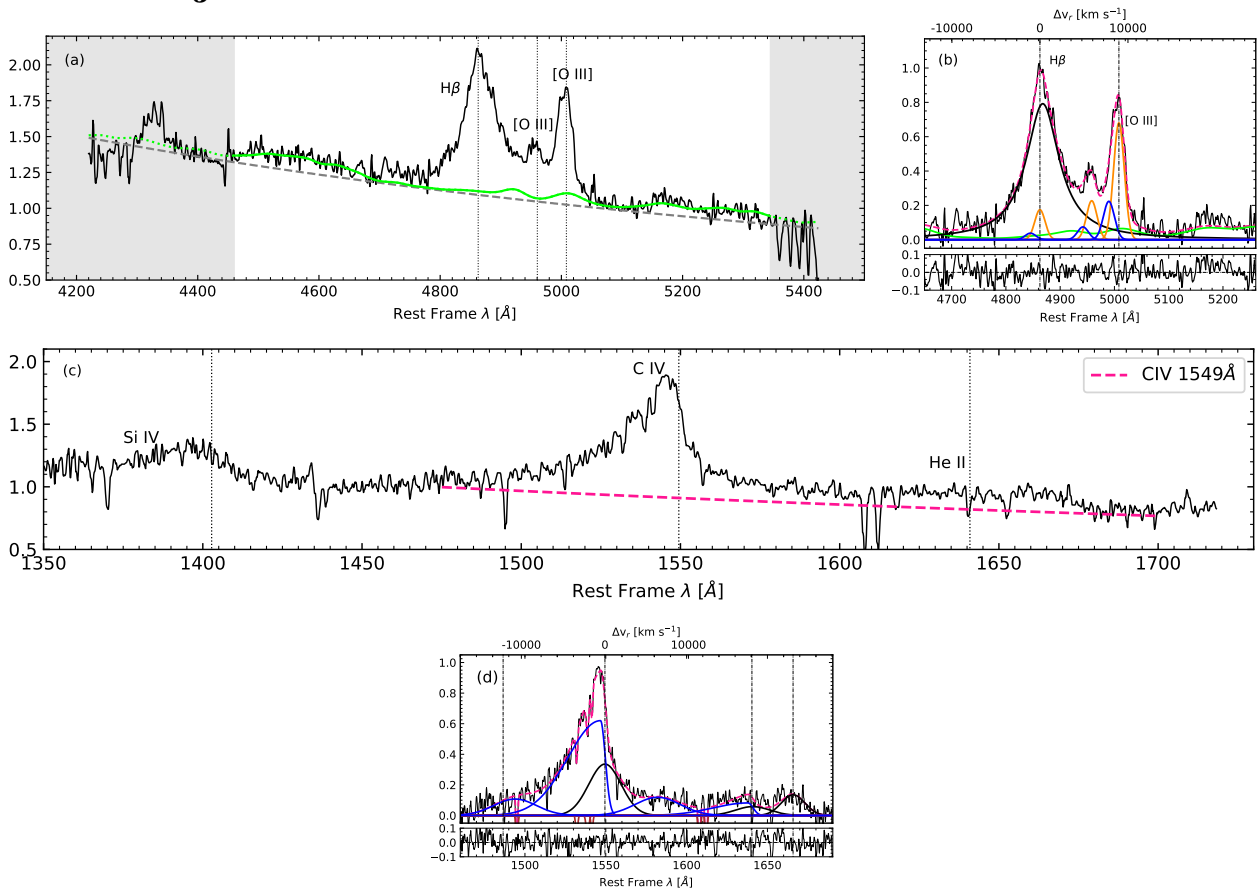


Fig. A.2.5: CTSJ01.03. Colours and lines as Figure A.1.6.

A.2.6 WB J0948+0855

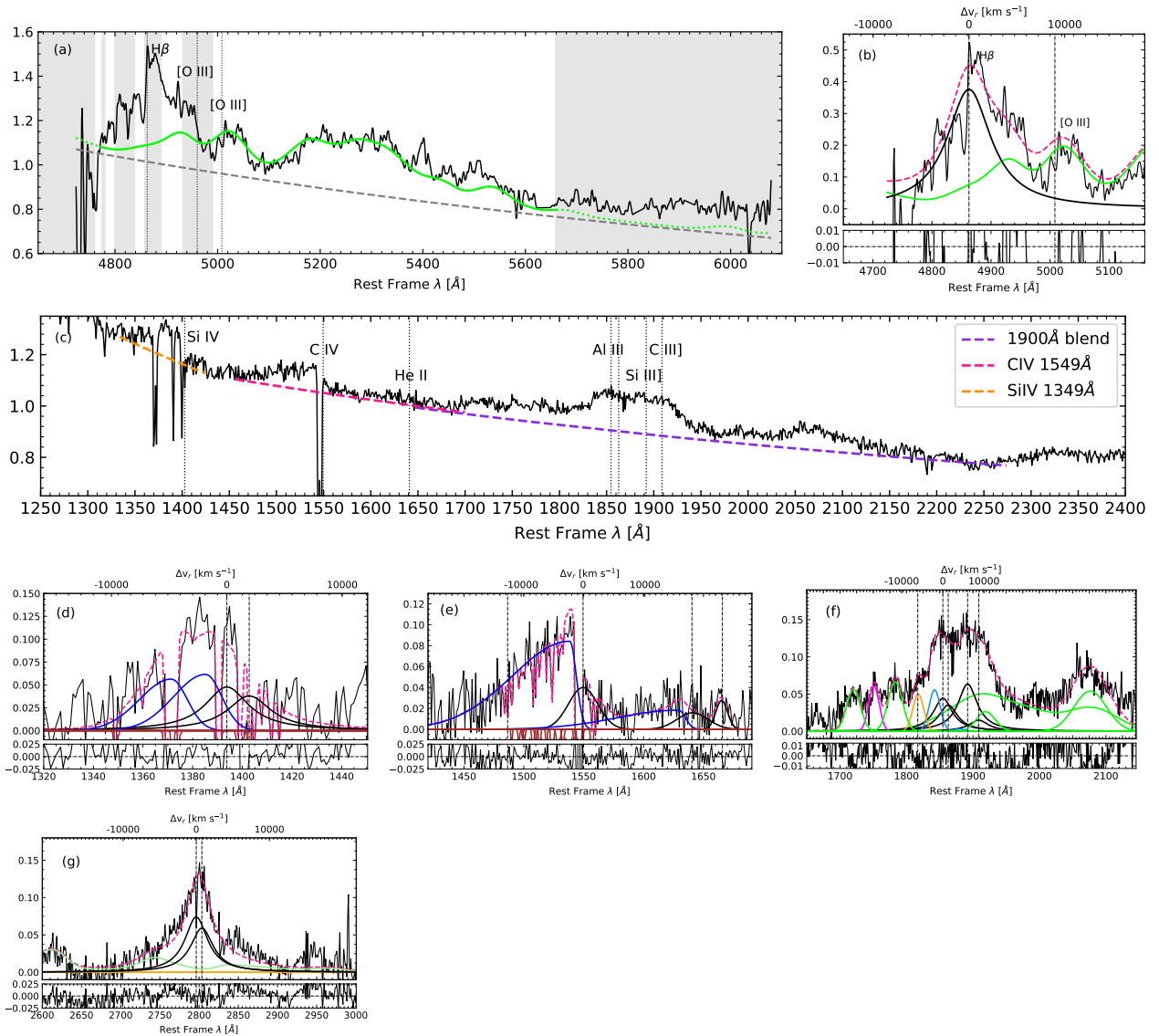


Fig. A.2.6: WB J0948+0855. Colours and lines as Figure A.2.1.

An H β BLUE component may be present, however we cannot detect it since the region is located exactly at the border of the spectrum. Due to the difficulty of isolating a narrow component in both H β and [O III] λ 5007 emission lines, the redshift of this source has been estimated based on the Mg II λ 2796,2803 doublet, since this line could be easily identified in the UV spectra (see panel (g) of Fig. A.2.6).

A.2.7 CTSJ03.14

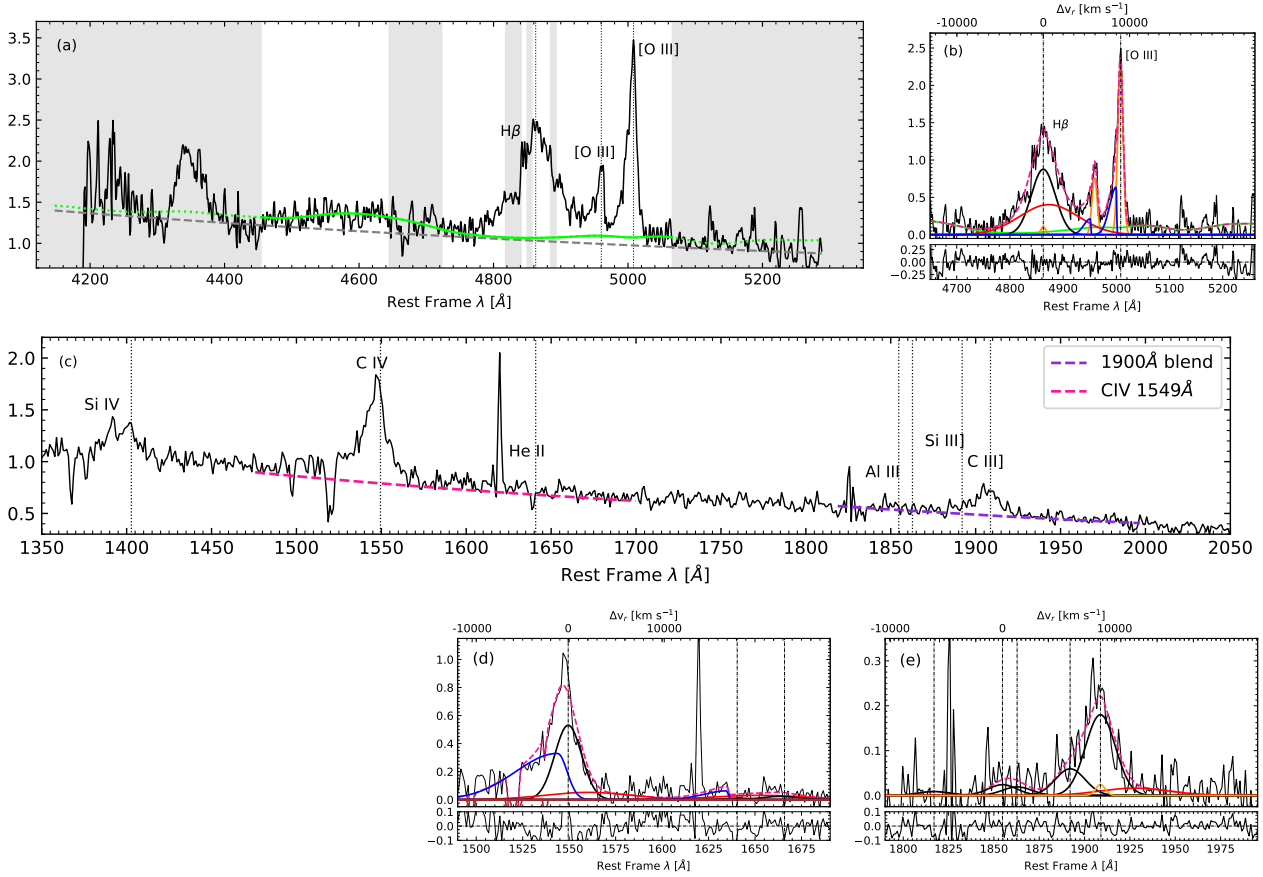


Fig. A.2.7: CTSJ03.14. Colours and lines as Figure A.1.6.

A.2.8 PKS1448-232

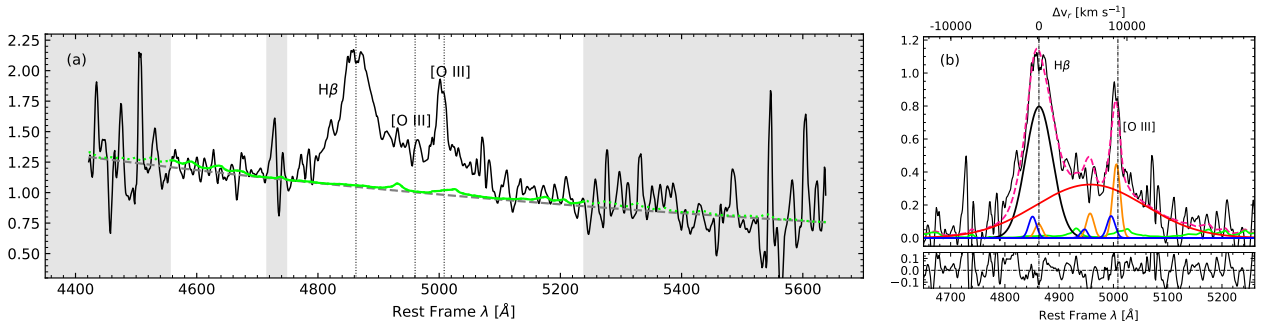


Fig. A.2.8: PKS1448-232. Colours and lines as Figure A.1.6.

A.2.9 [HB89]1559+088

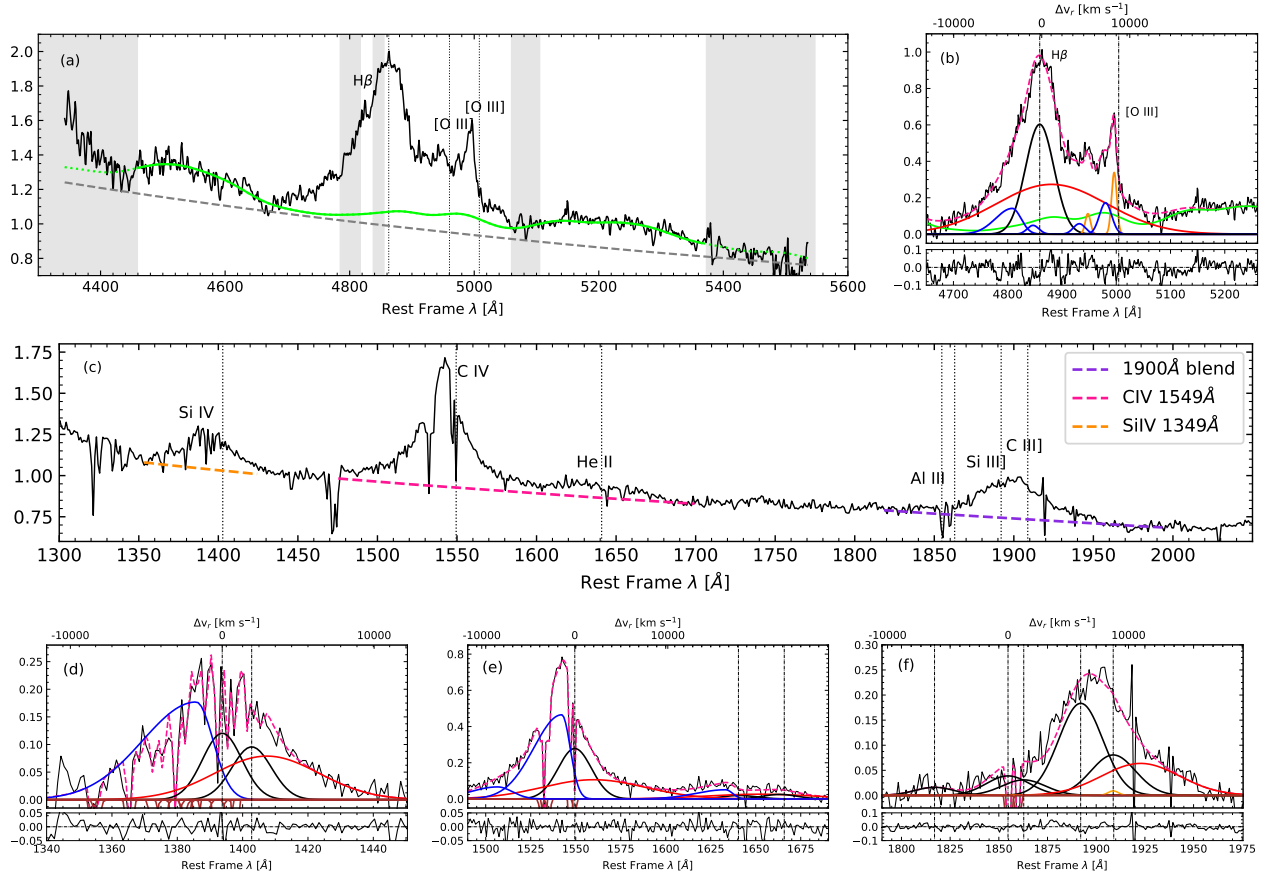


Fig. A.2.9: [HB89]1559+088. Colours and lines as Figure A.1.6.

A.2.10 FBQS J2149-0811

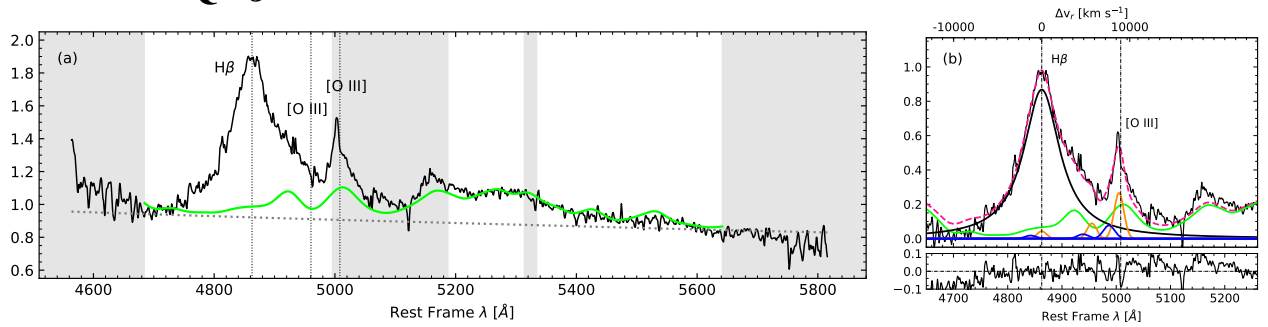


Fig. A.2.10: FBQS J2149-0811. Colours and lines as Figure A.1.6.

ADDITIONAL MATERIAL FROM CHAPTER 5

B

B.1 Radio properties of the samples

Table B.1: Identification and radio properties of HEMS and FOS samples.

Source (1)	RA (2)	DEC (3)	z (4)	$P_{1.4\text{GHz}}^{(a)}$ (5)	$\log(R_K)$ (6)	Radio Class. (7)
HEMS						
HE 0035-2853	00 38 06.5	-28 36 49	1.638	< 0.08	< 0.31	RQ
HE 0043-2300	00 45 39.5	-22 43 56	1.540	12.41	2.36	RL
HE 0058-3231	01 00 39.2	-32 14 57	1.582	< 0.07	< 0.35	RQ
HE 0109-3518	01 11 43.5	-35 03 01	2.406	< 0.17	< -0.09	RQ
HE 0122-3759	01 24 17.4	-37 44 23	2.200	< 0.14	< 0.23	RQ
HE 0203-4627	02 05 52.4	-46 13 30	1.438	15.45	2.07	RL
HE 0205-3756	02 07 27.2	-37 41 57	2.433	4.78	1.51	RQ
HE 0248-3628	02 50 55.3	-36 16 35	1.536	0.77	0.83	RQ
HE 0251-5550	02 52 40.1	-55 38 32	2.351	< 0.43	< 0.23	RQ
HE 0349-5249	03 50 59.3	-52 40 35	1.541	< 0.07	< -0.08	RQ
HE 0359-3959	04 01 14.0	-39 51 33	1.521	0.24	0.85	RQ
HE 0436-3709	04 38 37.3	-37 03 41	1.445	< 0.06	< 0.37	RQ
HE 0507-3236	05 09 17.8	-32 32 45	1.577	< 0.07	< 0.18	RQ
HE 0512-3329	05 14 10.8	-33 26 23	1.587	< 0.07	< 0.06	RQ
HE 0926-0201	09 29 13.5	-02 14 47	1.682	< 0.01	< -0.82	RQ
HE 0940-1050	09 42 53.5	-11 04 27	3.093	< 0.28	< 0.45	RQ
HE 1039-0724	10 42 19.3	-07 40 37	1.458	< 0.02	< 0.15	RQ
HE 1104-1805	11 06 33.5	-18 21 25	2.319	< 0.16	< 0.17	RQ
HE 1120+0154	11 23 20.7	01 37 48	1.472	< 0.02	< -0.53	RQ
HE 1347-2457	13 50 38.8	-25 12 16	2.599	< 0.20	< 0.19	RQ
HE 1349+0007	13 51 50.5	00 07 39	1.444	< 0.02	< -0.11	RQ
HE 1409+0101	14 12 21.7	00 47 19	1.650	0.43	0.65	RQ
HE 2147-3212	21 50 52.3	-31 58 26	1.543	< 0.07	< 0.33	RQ

Table B.1: Identification and radio properties of HEMS and FOS samples. (cont.)

Source (1)	RA (2)	DEC (3)	z (4)	$P_{1.4\text{GHz}}^{(a)}$ (5)	$\log(R_K)$ (6)	Radio Class. (7)
HE 2156-4020	21 59 54.7	-40 05 50	2.543	< 0.19	< 0.36	RQ
HE 2202-2557	22 05 29.8	-25 42 23	1.535	4.24	2.13	RL
HE 2349-3800	23 52 10.7	-37 43 22	1.604	4.66	2.07	RL
HE 2352-4010	23 55 34.5	-39 53 54	1.580	< 0.07	< 0.28	RQ
HE 2355-4621	23 58 09.2	-46 05 00	2.382	< 0.17	< 0.30	RQ
FOS						
ICRF J000559.2+160949	00 05 59.2	+16 09 49	0.450	4.71	2.99	RL
Mrk 335	00 06 19.5	+20 12 10	0.025	10^{-4}	0.31	RQ
LEDA 1790	00 29 13.7	+13 16 03	0.145	10^{-3}	0.67	RQ
87GB 004432.0+030343	00 47 05.9	+03 19 54	0.623	0.09	1.12	RQ
Mrk 1502	00 53 34.9	+12 41 35	0.061	10^{-4}	0.33	RQ
LBQS 0100+0205	01 03 12.9	+02 21 09	0.394	< 0.01	< 0.71	RQ
ICRF J020157.1-113233	02 01 57.1	-11 32 33	0.671	37.92	4.31	RL
3C 84	03 19 48.1	+41 30 42	0.018	0.17	3.65	RL
[HB89] 0403-132	04 05 34.0	-13 08 13	0.571	41.00	4.28	RL
LEDA 75249	04 52 30.0	-29 53 35	0.286	0.02	1.27	RQ
Mrk 1095	05 16 11.4	-00 08 59	0.032	10^{-4}	0.46	RQ
ICRF J074541.6+314256	07 45 41.6	+31 42 56	0.461	3.90	2.87	RL
ICRF J084047.5+131223	08 40 47.5	+13 12 23	0.680	37.05	5.27	RL
2MASS J08533423+4349023	08 53 34.2	+43 49 02	0.515	< 10^{-3}	< 0.07	RQ
LB 9308	09 06 31.8	+16 46 11	0.411	7.66	4.91	RL
ICRF J092703.0+390220	09 27 03.0	+39 02 20	0.695	42.84	4.19	RL
PG 0947+396	09 50 48.3	+39 26 50	0.207	< 10^{-4}	< 0.13	RQ
PG 0953+414	09 56 52.3	+41 15 22	0.235	< 10^{-4}	< -0.73	RQ
Ton 469	09 58 20.9	+32 24 02	0.530	10.34	3.21	RL
Ton 28	10 04 02.6	+28 55 35	0.330	< 10^{-3}	< -0.01	RQ
LEDA 29208	10 04 20.1	+05 13 00	0.161	< 10^{-4}	< -0.09	RQ
FBQS J101027.5+413238	10 10 27.5	+41 32 39	0.613	5.64	3.24	RL
NGC 3227	10 23 30.5	+19 51 54	0.004	10^{-5}	1.27	RQ
7C 1028+3118	10 30 59.0	+31 02 55	0.178	0.19	2.73	RL
PG 1049-005	10 51 51.4	-00 51 17	0.359	< 10^{-3}	< -0.13	RQ
2MASX J10523275+6125211	10 52 32.7	+61 25 20	0.421	5.01	3.67	RL
PG 1100+772	11 04 13.8	+76 58 58	0.312	6.25	3.26	RL
NGC 3516	11 06 47.4	+72 34 07	0.009	10^{-5}	1.31	RQ
ICRF J110715.0+162802	11 07 15.0	+16 28 02	0.632	10.51	3.60	RL
3C 254	11 14 38.7	+40 37 20	0.737	52.56	4.49	RL
PG 1114+445	11 17 06.3	+44 13 33	0.143	< 10^{-4}	< -0.34	RQ
LEDA 34570	11 18 30.2	+40 25 54	0.154	10^{-3}	0.60	RQ

Table B.1: Identification and radio properties of HEMS and FOS samples. (cont.)

Source (1)	RA (2)	DEC (3)	z (4)	$P_{1.4\text{GHz}}^{(a)}$ (5)	$\log(R_K)$ (6)	Radio Class. (7)
Ton 1388	11 19 08.6	+21 19 17	0.177	10^{-3}	0.42	RQ
2MASS J11243917+4201450	11 24 39.1	+42 01 45	0.225	$< 10^{-4}$	< -0.09	RQ
LBQS 1138+0204	11 41 21.7	+01 48 03	0.382	$< 10^{-3}$	< 0.09	RQ
LBQS 1144-0115	11 47 18.0	-01 32 07	0.383	$< 10^{-3}$	< -0.03	RQ
LB 2136	11 53 24.4	+49 31 08	0.334	4.86	4.04	RL
LEDA 38224	12 04 42.1	+27 54 11	0.165	$< 10^{-4}$	< -0.16	RQ
PB 3894	12 14 17.6	+14 03 13	0.081	10^{-4}	0.46	RQ
NGC 4253	12 18 26.5	+29 48 46	0.012	10^{-4}	1.28	RQ
PG 1216+069	12 19 20.9	+06 38 38	0.332	10^{-3}	0.25	RQ
3C 273	12 29 06.6	+02 03 08	0.158	23.86	3.45	RL
SBS 1250+568	12 52 26.3	+56 34 19	0.320	6.47	4.42	RL
LB 2522	13 01 12.9	+59 02 06	0.478	$< 10^{-3}$	< -0.35	RQ
ICRF J130533.0-103319	13 05 33.0	-10 33 19	0.278	1.50	2.71	RL
LEDA 45656	13 09 47.0	+08 19 48	0.155	$< 10^{-4}$	< -0.33	RQ
Ton 1565	13 12 17.7	+35 15 21	0.182	0.04	1.56	RQ
2XMM J135315.8+634546	13 53 15.8	+63 45 45	0.088	10^{-3}	1.22	RQ
PB 4142	13 54 35.6	+18 05 17	0.151	$< 10^{-4}$	< -0.15	RQ
[HB89] 1354+195	13 57 04.4	+19 19 07	0.720	41.34	3.87	RL
Ton 182	14 05 16.2	+25 55 34	0.163	10^{-4}	0.12	RQ
LEDA 50313	14 06 21.8	+22 23 46	0.097	10^{-4}	0.42	RQ
LEDA 51016	14 17 00.8	+44 56 06	0.115	10^{-4}	0.36	RQ
NGC 5548	14 17 59.5	+25 08 12	0.017	10^{-4}	0.88	RQ
Mrk 813	14 27 25.0	+19 49 52	0.111	10^{-4}	0.39	RQ
Ton 202	14 27 35.6	+26 32 14	0.363	0.40	2.40	RL
2MASS J14294306+4747262	14 29 43.0	+47 47 26	0.220	$< 10^{-4}$	< -0.05	RQ
Mrk 478	14 42 07.4	+35 26 22	0.077	10^{-4}	0.33	RQ
2MASS J14464593+4035057	14 46 45.9	+40 35 05	0.267	$< 10^{-4}$	< -0.32	RQ
ICRF J145427.4-374733	14 54 27.4	-37 47 33	0.314	2.56	3.59	RL
ICRF J151443.0+365050	15 14 43.0	+36 50 50	0.371	3.83	3.29	RL
PG 1538+477	15 39 34.8	+47 35 31	0.772	0.17	1.26	RQ
[HB89] 1543+489	15 45 30.2	+48 46 08	0.398	0.01	0.70	RQ
ICRF J154743.5+205216	15 47 43.5	+20 52 16	0.266	0.91	2.88	RL
Mrk 493	15 59 09.6	+35 01 47	0.031	10^{-4}	0.84	RQ
Ton 256	16 14 13.2	+26 04 16	0.131	10^{-3}	1.29	RQ
3C 334	16 20 21.8	+17 36 23	0.556	2.18	2.88	RL
SBS 1626+554	16 27 56.1	+55 22 31	0.133	$< 10^{-4}$	< -0.39	RQ
FBQS J163020.7+375656	16 30 20.7	+37 56 56	0.395	0.10	1.62	RQ
3C 345	16 42 58.8	+39 48 36	0.593	69.71	5.01	RL

Table B.1: Identification and radio properties of HEMS and FOS samples. (cont.)

Source (1)	RA (2)	DEC (3)	z (4)	$P_{1.4\text{GHz}}^{(a)}$ (5)	$\log(R_K)$ (6)	Radio Class. (7)
3C 351.0	17 04 41.3	+60 44 30	0.372	$< 10^{-3}$	< 0.34	RQ
4C 73.18	19 27 48.4	+73 58 01	0.302	9.89	3.79	RL
Mrk 509	20 44 09.7	-10 43 24	0.034	10^{-4}	0.44	RQ
2MASS J21145258+0607423	21 14 52.5	+06 07 42	0.461	0.01	0.27	RQ
[HB89] 2128-123	21 31 35.2	-12 07 04	0.500	12.94	3.22	RL
4C 31.63	22 03 14.9	+31 45 38	0.295	6.86	3.40	RL
UGC 12163	22 42 39.3	+29 43 31	0.025	10^{-4}	1.05	RQ
[HB89] 2243-123	22 46 18.2	-12 06 51	0.626	22.28	3.96	RL
MR 2251-178	22 54 05.8	-17 34 55	0.064	10^{-3}	0.53	RQ
4C 11.72	22 54 10.4	+11 36 38	0.326	4.21	3.18	RL
NGC 7469	23 03 15.6	+08 52 26	0.016	10^{-3}	0.87	RQ
4C 09.72	23 11 17.7	+10 08 15	0.434	4.21	3.16	RL
ICRF J234636.8+093045	23 46 36.8	+09 30 45	0.672	24.90	3.61	RL
4C -01.61	23 51 56.1	-01 09 13	0.174	1.26	3.50	RL

Notes. ^(a) In units of 10^{26} W Hz⁻¹.

B.2 Details on the estimations of the outflow parameters

B.2.1 [O III] λ 5007

The expressions for the [O III] λ 5007 outflow parameters were derived by [Marziani et al. \(2017a\)](#) assuming a bipolar outflow structure (c.f. [Kim et al. 2023](#), and references therein). All the [O III] λ 5007 outflow equations reported here are in accordance with the work of [Cano-Díaz et al. \(2012\)](#) and [Fiore et al. \(2017\)](#).

The [O III] λ 5007 luminosity can be related to the outflow mass by

$$M_{\text{ion}} = 1 \times 10^7 L_{[\text{OIII}],44}^{\text{out}} \left(\frac{Z}{5Z_{\odot}} \right)^{-1} n_{\text{H},3}^{-1} \text{ [M}_{\odot}], \quad (\text{B.1})$$

where $L_{[\text{OIII}],44}^{\text{out}}$ is the outflow-emitted luminosity of [O III] λ 5007 emission line in units of $10^{44} \text{ erg s}^{-1}$, the density (n_{H}) and the metallicity (Z) have been scaled to 10^3 cm^{-3} and 5 times solar, respectively.

If we assume that the outflow is confined to a solid angle Ω , then the mass outflow rate $\dot{M}_{\text{ion}}^{\text{out}}$ at a distance r can be written as:

$$\dot{M}_{\text{ion}} = 30 L_{[\text{OIII}],44}^{\text{out}} v_{\text{o},1000} r_{1\text{kpc}}^{-1} \left(\frac{Z}{5Z_{\odot}} \right)^{-1} n_{\text{H},3}^{-1}. \quad (\text{B.2})$$

Even if part of a nuclear outflow, the [O III] λ 5007 emitting gas is probably not being anymore accelerated by radiation pressure, and so we consider as maximum outflow velocity v_{o} the centroid at 1/2 intensity of the BLUE component. If we assume the [O III] λ 5007 outflow to be nuclear, we can then suppose a super-solar chemical composition $Z = 5Z_{\odot}$.

The thrust might be written as:

$$\dot{M}_{\text{ion}} v_{\text{o}} = 1.9 \times 10^{35} L_{[\text{OIII}],44}^{\text{out}} v_{\text{o},1000}^2 r_{1\text{kpc}}^{-1} \left(\frac{Z}{5Z_{\odot}} \right)^{-1} n_{\text{H},3}^{-1}. \quad (\text{B.3})$$

Similarly, the kinetic power \dot{E}_{out} is then given by $\dot{E}_{\text{out}} \sim \frac{1}{2} \dot{M}_{\text{out}} v_{\text{o}}^2$, which leads to

$$\dot{\epsilon}_{\text{kin}} = 9.6 \times 10^{42} L_{[\text{OIII}],44}^{\text{out}} v_{\text{o},1000}^3 r_{1\text{kpc}}^{-1} \left(\frac{Z}{5Z_{\odot}} \right)^{-1} n_{\text{H},3}^{-1}. \quad (\text{B.4})$$

B.2.2 CIV λ 1549

Both CIV λ 1549 and [O III] λ 5007 are predominantly produced by collisional excitation, for which the collisional excitation rate of Eq. 3.20 from Osterbrock & Ferland (2006) applies:

$$q_{12} = \frac{8.629 \cdot 10^{-6}}{T^{\frac{1}{2}}} \frac{\Upsilon}{g_1} \exp(-hv/kT) [\text{cm}^3 \text{s}^{-1}] \quad (\text{B.5})$$

where hv is the energy of the photon emitted in the transition (1.28×10^{-11} erg in the case of CIV λ 1549), and k is the Boltzmann's constant in erg K^{-1} . Υ is the collision strength and is almost independent from temperature (Osterbrock & Ferland (2006) yield $\Upsilon \approx 8.91$). The $g_1 = (2J + 1) = 2$, as the lower level of the transition is the ground state ($^2S_{\frac{1}{2}}$). The exponential argument is $hv/kT_{10000} \approx 9.28T_{10000}^{-1}$, and dominates over the factor $T^{-\frac{1}{2}}$.

The mass of ionised gas is given by

$$M_{\text{C}^{+3}} \sim \frac{L_{\text{CIV}}}{(hv)_{\text{CIV}} q_{12} n_{\text{H}} [\text{C}/\text{H}] X} \cdot \mu m_{\text{P}}. \quad (\text{B.6})$$

Here L_{CIV} is the CIV λ 1549 luminosity, $(hv)_{\text{CIV}}$ the CIV λ 1549 photon energy, $[\text{C}/\text{H}]$ the relative abundance of Carbon with respect to Hydrogen, in number: $8.43 \approx 12 + \log [\text{C}/\text{H}]$ for solar abundance, implying $[\text{C}/\text{H}] \approx 2.69 \cdot 10^{-4}$. The factor $X = [\text{C}^{+3}] / \sum_i [\text{C}^{+i}] \leq 1$ is the fraction of triply ionised Carbon, and μm_{P} is the molecular mass of the gas, with $\mu \approx 1.4$ (neglecting the mass of the metals), and m_{P} the proton mass.

The mass of the emitting gas strongly depends on temperature. A single value of the dynamical temperature could be assumed, in keeping with the simplest assumptions. However, the T value should be chosen carefully.

Observational constraints

To estimate a typical value of the dynamical temperature, we can apply two main observational constraints on the blueshifted emission due to the outflow:

- CIV λ 1549 equivalent width: in super-Eddington candidates, the equivalent width is typically very low $W \sim 10 \text{ \AA}$ and in Population A $W \lesssim 30 \text{ \AA}$ (Kinney et al. 1990; Sulentic et al. 2000c; Marziani et al. 2016a; Martínez-Aldama et al. 2018). The sources that are radiating at high Eddington ratio are the ones showing the lowest W along the E1 main sequence, with a large fraction of them being weak lined quasars (WLQs) (Shemmer et al. 2010; Wu et al. 2012; Marziani et al. 2016a; Martínez-Aldama et al. 2018; Jin et al. 2023). Even for the Pop. B sources of the HEMS and ISAAC samples $W_{\text{CIV}\lambda 1549}$ is usually below $\approx 50 \text{ \AA}$.
- CIV λ 1549/ $H\beta$ ratio: its value, due to the absence of a strong $H\beta$ blueshifted component, can be assumed to be $\text{CIV}\lambda 1549/H\beta \gtrsim 5 \sim 10$ for blueshifted components.

The decomposition of the C IV $\lambda 1549$ profile in two components reveals very different properties and physical conditions for the outflow and virial component. In the outflow case, the C IV $\lambda 1549$ equivalent width is in the range from the detectability limit of a few Å to a few tens Å. This observational constraint suggests that the outflow component of the C IV $\lambda 1549$ profile is not produced by gas in physical conditions optimised for its emission.

Photoionisation modelling

The diagrams of Fig. B.1 show the W of C IV $\lambda 1549$ (left panels) and the C IV/H β ratio (right panels) as a function of the ionisation parameter U , according to CLOUDY 17.02 (Ferland et al. 2017) computations, assuming two cases: (1) $M_{\text{BH}} = 10^9 M_{\odot}$, five times solar metallicity, and a standard AGN SED representative for low-redshift sources that have Eddington ratios $\gtrsim 0.1 - 0.2$ (Mathews & Ferland 1987) (upper panels); and (2) in bottom panels for $M_{\text{BH}} = 10^{9.5} M_{\odot}$, five times solar metallicity and the SED defined by Krawczyk et al. (2013), more appropriate for representing our high- z high luminosity sources (see more details below). Very low W is possible in conditions of Carbon under-ionisation and over-ionisation with respect to C $^{+3}$. For the blueshifted component, a high-ionisation solution has been found with typical values $\log U \sim -0.5 - 0$ (Śniegowska et al. 2021; Garnica et al. 2022).

The upper left panel of Fig. B.1 shows that the expected $W(\text{C IV } \lambda 1549)$ at $U \sim 1$ is several tens of Å, consistent with the observations if the covering factor is moderate ($\sim 0.2 - 0.5$), with a marginal dependence on density. The C IV $\lambda 1549$ /H β ratio is constrained to be $\gtrsim 5$, with C IV $\lambda 1549$ /H $\beta \sim 10$ for the density range $10^{9.5} - 10^{10} \text{ cm}^{-3}$.

The electron temperature associated with these conditions is high ($T \sim 20000 \text{ K}$), implying a very high efficiency for the collisional excitation. The point here is that, even if the collisional efficiency is high, the ionic fraction of C $^{+3}$ is very low (~ 0.01), yielding a $\tilde{q}X$ factor $\approx (3 - 4) \cdot 10^{-11} \text{ cm}^3 \text{ s}^{-1}$.

At high luminosity, however, the softening of the accretion disk emission due to large masses makes the SED significantly different from that of Mathews & Ferland (1987). The peak of the disk emission can be displaced toward lower frequency by a factor ~ 10 (Duras et al. 2017, 2020), reducing significantly the amount of ionising photons. We therefore considered a different SED, defined for intermediate redshift quasars with $W(\text{C IV}) \lesssim 30 \text{ Å}$ (Krawczyk et al. 2013). The simulations predict lower $W(\text{C IV})$ by a factor ≈ 5 (bottom panels on Fig. B.1) with respect to the Mathews & Ferland (1987) SED. The $W(\text{C IV})$ and the C IV/H β ratio provide some constraints over the ionisation parameter and density. The C IV/H β is $\gtrsim 10$ for the ISAAC sources where the BLUE of H β has been detected, and the $W \sim 10 \text{ Å}$. For $\log n_{\text{H}} \approx 9.5$, these conditions imply a $\log U$ between -0.7 and 0.3 . In this case, for $\log U \approx -0.2$, and computing a weighted average over r^2 , we obtain a much higher efficiency, $\overline{Xq(T)}$ to $\approx 1.22 \cdot 10^{-10} \text{ cm}^3 \text{ s}^{-1}$. Much lower efficiencies are possible if $\log U \rightarrow 0$ and $\log n_{\text{H}} \rightarrow 9$. In this case the predicted $W(\text{C IV})$ might be below 10 Å , as found for weak lined quasars (Diamond-Stanic et al. 2009; Shemmer et al. 2010; Marziani et al. 2016a).

Fig. B.2 shows the trends expected for the ionisation parameter and electron temperature as a function of radius, for the value of the density $\log n_{\text{H}} = 9.5 \text{ [cm}^{-3}\text{]}$. The intercepts between the

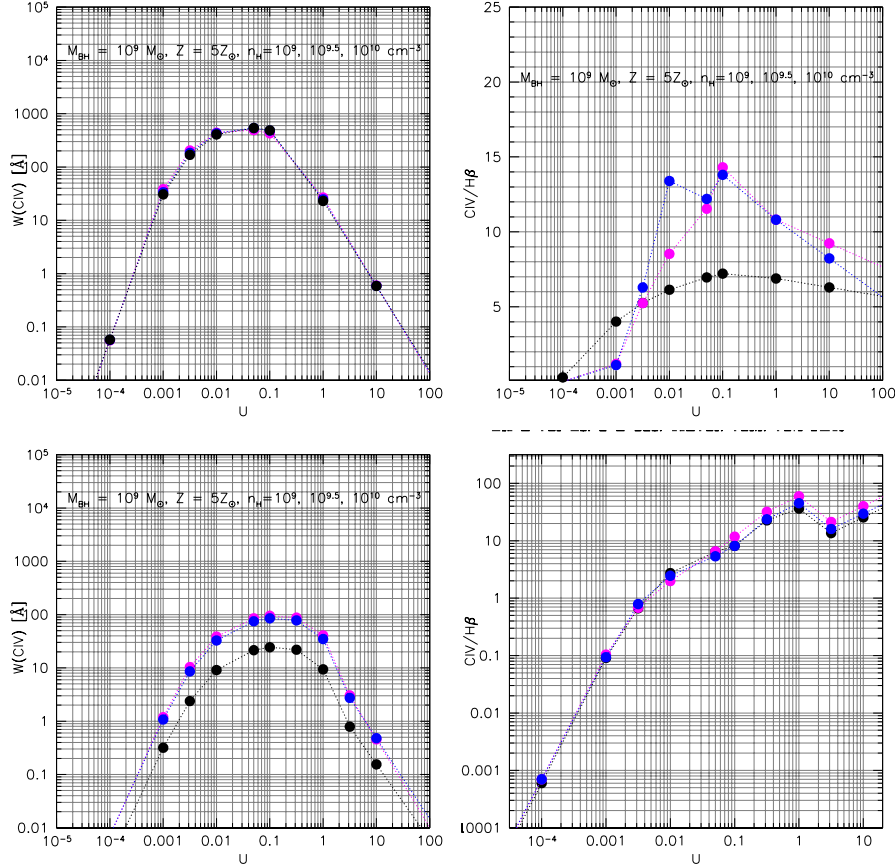


Fig. B.1: Relation between $W \text{ CIV } \lambda 1549$ (left panels) and intensity ratio $\text{C IV } \lambda 1549/\text{H}\beta$ (right panels) with the ionisation parameter U for three density values $\log n_{\text{H}} = 9, 9.5, 10$ [cm^{-3}] (black, blue, and magenta symbols, respectively), column density $N_{\text{c}} = 10^{22} \text{ cm}^{-2}$, 5 times solar metallicity. Top: For $\log M_{\text{BH}} = 10^9 [M_{\odot}]$, and a [Mathews & Ferland \(1987\)](#) SED. Bottom: $\log M_{\text{BH}} = 10^{9.5} [M_{\odot}]$, and a [Krawczyk et al. \(2013\)](#) SED.

expected range of ionisation parameter and radius does not fall in correspondence of the peak ionisation fraction (right panels of Fig. B.2). The lower limit assumed for $\log U \approx -0.5$ implies a condition of over-ionisation for the line emitting gas. Electron temperature is around $T_{\text{e}} \approx 20000 \text{ K}$.

The photoionisation computations predict an equivalent width more than an order of magnitude higher than the observed value if $\text{C IV } \lambda 1549$ emission is due to gas at $\log U \sim -1.3$ ([Vietri et al. 2020](#)). In addition, the distance expected for $\log U = -1.3$ and $\log n_{\text{H}} \approx 9.0$ is $\log r \approx 18.8$ [cm], more than one order of magnitude higher than the scaling radius of [Kaspi et al. \(2021\)](#), $\log r \approx 17.43$ [cm].

Taking into account previous considerations, we use for the ionised mass the following expression:

$$M_{\text{ion}} \approx 6.5 \cdot 10^2 L_{\text{CIV},45}^{\text{out}} n_{\text{H},9.5}^{-1} \left[\frac{Z}{5Z_{\odot}} \right]^{-1} M_{\odot} \quad (\text{B.7})$$

which incorporates the average over density in the range $10^{9.5} - 10^{10.5} \text{ cm}^{-3}$ of $Xq(T)$ for $\log U = 0$, $\overline{Xq(T)} \approx 3.3 \cdot 10^{-11} \text{ cm}^3 \text{ s}^{-1}$. Averaging over $\log U = -0.5, 0, +0.5$, would imply an increase of $\overline{Xq(T)}$ to $\approx 5.65 \cdot 10^{-11} \text{ cm}^3 \text{ s}^{-1}$, by a factor ≈ 1.7 . Such increase in the efficiency in C IV production would only reinforce the conclusion on the weakness of the outflows at low- z .

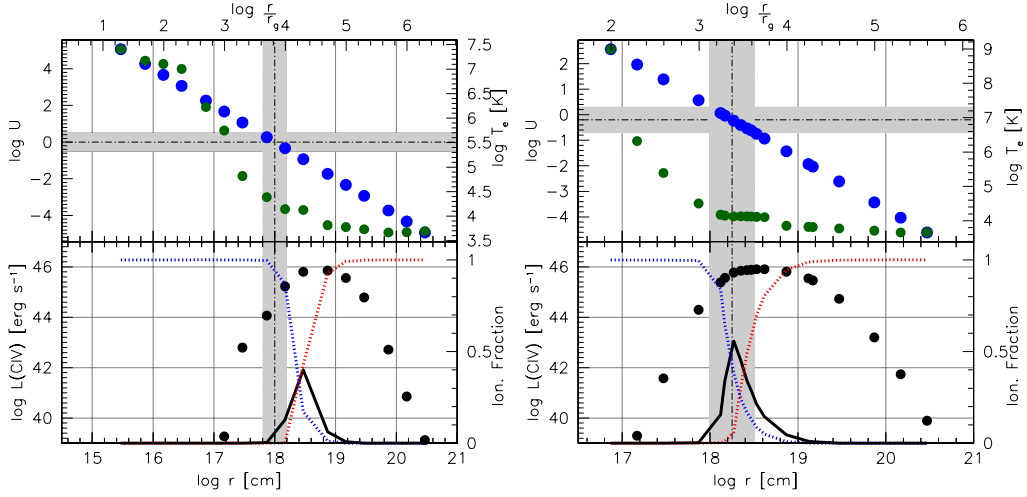


Fig. B.2: Behaviour of ionisation parameter, electron temperature, C IV $\lambda 1549$ luminosity, and ionic fraction as a function of radius for density value $\log n_{\text{H}} = 9.5$ [cm^{-3}], and for the two adopted SEDs for the low (top panels) and high z (bottom panels) samples. *Left, upper panel:* behaviour of the ionisation parameter (left axis scale, blue dots) and electron temperature (right axis scale, green dots) as a function of radius for a $M_{\text{BH}} = 10^9 M_{\odot}$ radiating at Eddington limit and illuminating a slab of gas. We assume column density $N_{\text{c}} = 10^{22} \text{ cm}^{-2}$, Mathews & Ferland (1987) SED, and the metallicity five times solar in all cases. *Left, lower panel:* logarithm of C IV $\lambda 1549$ luminosity (black dots) and ionic fraction as a function of radius. The blue and red line represent the ionic stages higher and lower than 3, respectively, and the dark green line ionic stage 3. *Right, upper and lower panels:* same as top panels, for $\log M_{\text{BH}} = 9.5$ [M_{\odot}], and SED from Krawczyk et al. (2013).

Wind dynamical parameters

To estimate the wind dynamical parameters we assume the same simple model utilised for [O III] $\lambda 5007$. The mass outflow rate is therefore given by:

$$\dot{M}_{\text{ion}} \approx 10 L_{45}^{\text{out}} v_{5000} r_{1\text{pc}}^{-1} n_{\text{H},9.5}^{-1} \left(\frac{Z}{5Z_{\odot}} \right)^{-1} M_{\odot} \text{yr}^{-1} \quad (\text{B.8})$$

where L_{45}^{out} is the luminosity of the blueshifted component in units of $10^{45} \text{ erg s}^{-1}$, the outflow velocity v_{5000} is scaled to 5000 km s^{-1} , the gas density is in units of $10^{9.5}$, and the radius is now in parsec units. For this paper, we assume that the C IV outflow is accelerated to a final, terminal velocity $v \approx c(1/2) + 2\sigma \approx c(1/2) + \text{FWHM}_{\text{BLUE}}/1.18$, where $c(1/2)$ corresponds to the centroid velocity at half intensity of the C IV BLUE component.

The thrust $\dot{M}_{\text{ion}}^{\text{out}} v$ and kinetic power can then be computed as:

$$\dot{M}_{\text{ion}} v \approx 3.15 \cdot 10^{35} L_{\text{CIV},45}^{\text{out}} v_{5000}^2 r_1^{-1} n_{\text{H},9.5}^{-1} \left(\frac{Z}{5Z_{\odot}} \right)^{-1} \text{ g cm s}^{-2} \quad (\text{B.9})$$

$$\dot{E}_{\text{kin}} = \frac{1}{2} \dot{M}_{\text{ion}} v^2 \approx 7.9 \cdot 10^{43} L_{\text{CIV},45}^{\text{out}} v_{5000}^3 r_1^{-1} n_{\text{H},9.5}^{-1} \left(\frac{Z}{5Z_{\odot}} \right)^{-1} \text{ erg s}^{-2} \quad (\text{B.10})$$

These expressions, used to calculate the dynamical parameters of the outflows for our low- z FOS sample, are quantitatively similar to the ones reported in earlier works (Marziani et al. 2016a, 2017a). Those authors assumed an ad hoc temperature to account for the low CIV λ 1549 radiative efficiency of the emitting gas suggested by the observed low equivalent width of CIV λ 1549.

At high luminosity, for the ISAAC and HEMS samples, and by considering the results from the CLOUDY computations by using the more appropriate SED from Krawczyk et al. (2013) and for an estimated $\log U \approx -0.2$, and an efficiency, $\overline{Xq(T)} \approx 1.22 \cdot 10^{-10} \text{ cm}^3 \text{ s}^{-1}$ (see section B.2.2), Eqs. B.7, B.8, B.9, and B.10 should be divided by a factor ≈ 3.63 . Eqs. B.7, once the constants are divided by the factor reported above yields estimates that are in basic agreement with those of Vietri et al. (2020): they differ by a factor ~ 2 -3 in M_{ion} , and the difference comes from the assumed efficiency of the CIV λ 1549 emission. Additional factors accounting for differences in the estimated values concern the geometry: a factor 3 from the assumption of a thin flat layer in place of a spherical surface element, and an additional factor of 2 for the unseen contribution of the receding cone enters in Eqs. B.7, B.8, B.9 and B.10.

ADDITIONAL MATERIAL FROM CHAPTER 6

C

C.1 Estimation of uncertainties

C.1.1 Bayesian estimates

Uncertainties were estimated following a Bayesian approach, considering the likelihood function

$$\log \mathcal{L} \propto - \sum_i \frac{(f_i - m_i(\Theta))^2}{2\sigma_i^2} \propto -\frac{1}{2} \log \chi^2, \quad (\text{C.1})$$

where f_i are the specific flux values as a function of wavelength (or of pixel number), σ_i the uncertainty in f_i (in practice from the S/N set constant over the spectrum), $m_i(\Theta)$ the expectation value for the multicomponent model Θ of the spectrum obtained via a `specfit` analysis. The Θ can be any set of free parameters employed in the fits: intensity, shift and width of each line, intensity, shift and width of each template. Priors were specified for several parameters in terms of a range of permitted values. The posteriors of the model parameters Θ (for instance, the distributions of FWHM H β and Al III given the data) were obtained by creating a random walk with a modified Metropolis-Hasting algorithm: a new candidate set of model parameters Θ was randomly generated, and screened by an acceptance parameter α . The set Θ included model parameters believed to significantly affect the line widths (in practice, most of the parameters included in the `specfit` analysis). For example, the [O III] $\lambda\lambda 4959, 5007$ lines were modelled with two components, a “core” component represented by a symmetric Gaussian, and a semi-broad component modelled by a skew Gaussian. The template Fe II emission was scaled, shifted and broadened as done in the `specfit` procedure. The dispersion of the posterior distribution of each spectral parameter was assumed to yield its uncertainty δ at 1σ confidence level.

C.1.2 The quality parameter Q

The next step was to connect the uncertainty in FWHM, shift and intensity to a quality parameter Q , which may turn useful in case very late samples of quasars are analysed. The quality parameter

$$Q = \log_{10} \frac{W}{\text{FWHM}} \cdot \frac{S}{N} \quad (\text{C.2})$$

Table C.1: Relation between fractional uncertainties and Q

Parameter	a	b	$\log Q$ domain
$H\beta$			
FWHM ^a	0.100	-0.125	$\approx -0.8 \dots 0.5$
F ^b	0.0666	-0.07022	
Shift ^c	66	-0.112	
Al III			
FWHM ^d	10.96	6.15	$\approx -1.6 \dots -0.6$
F ^b	0.061	-0.2277	
Shift ^c	180	-219.7	
CIII]			
FWHM ^a	0.160	-0.026	$\approx -2.5 \dots 0.0$
F ^b	-0.026	-0.292	
Fe II			
F ^b	-0.04755	0.07520	$\approx -0.8 \dots 0.5$

$$^a \delta\text{FWHM}/\text{FWHM} \sim a + b \log Q$$

$$^b \delta F/F \sim a + b \log Q$$

$$^c \delta s = a + b \log Q \text{ [km s}^{-1}\text{]}$$

$$^d \delta\text{FWHM}/\text{FWHM} \sim 1/(a + b \log Q)$$

defined as the product of the S/N times a line equivalent width W divided by its FWHM, increases with S/N and line prominence over the continuum and decreases with increasing line widths. The signal in each resolution element is proportional to the ratio W/FWHM , which is a measurement of the sharpness of the line, as obviously $Q \propto \log_{10} \frac{I_{\text{peak}} \cdot \text{FWHM}}{\text{FWHM} I_c} \cdot \frac{I_c}{N} \propto \frac{I_{\text{peak}}}{N}$. The quality parameter Q obviates to the inadequacy of the S/N measurement carried out on the continuum. By multiplying it by the ratio W/FWHM we compute a more apt average S/N for a line depending on its strength and width. The parameter Q is larger for sharp lines in spectra with high S/N in the continuum. The large differences in S/N, line width and line strength between Al III and $H\beta$ is reflected in the distribution of the Q parameter, shown in Fig. C.1.

To be of any practical use, the Q parameter needs to be anchored to estimates of the uncertainties. The posterior distributions of the spectral parameters were computed for about 30 sources. Fig. C.2 shows a well-defined trend between Q and the fractional uncertainty $\delta\text{FWHM}/\text{FWHM}$ for $H\beta$, Al III, and CIII] derived from the MCMC simulations. Especially for large Q values, the scatter is relatively modest, and the relation between the parameter FWHM, flux and shift and $\log Q$ can be written in a linear form, save for the fractional uncertainty of FWHM Al III that is best fit by $\delta\text{FWHM}/\text{FWHM} \approx 1/(a + b \log Q)$. Table C.1 provides the coefficients a and b of the best fits along with Q domain. The FWHM relations were obtained by a non-linear fit algorithm implemented in R (R Core Team 2019), and are shown as the thick lines in Fig. C.2.

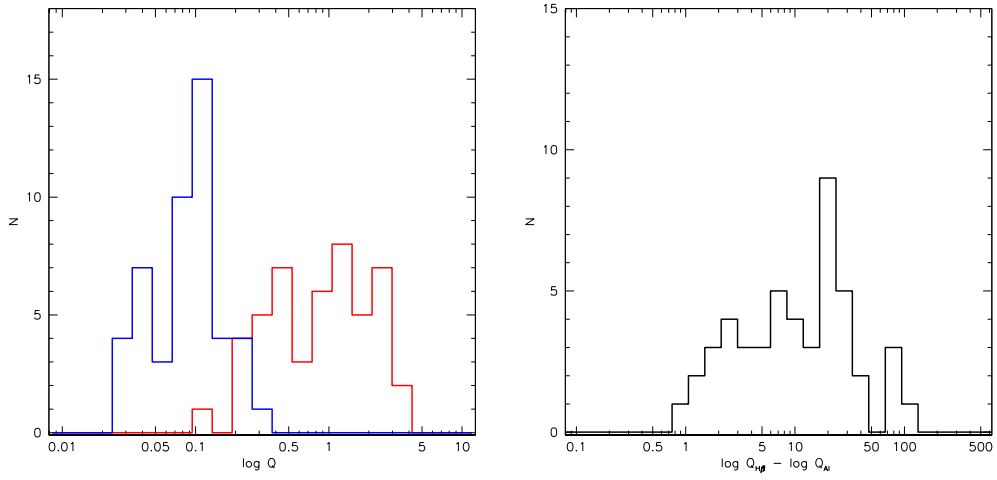


Fig. C.1: Left: distribution of the log of parameter Q parameter for Al III (blue) and H β (red) for the joint sample considered in this chapter. Right: distribution of $\log Q$ differences between H β and Al III.

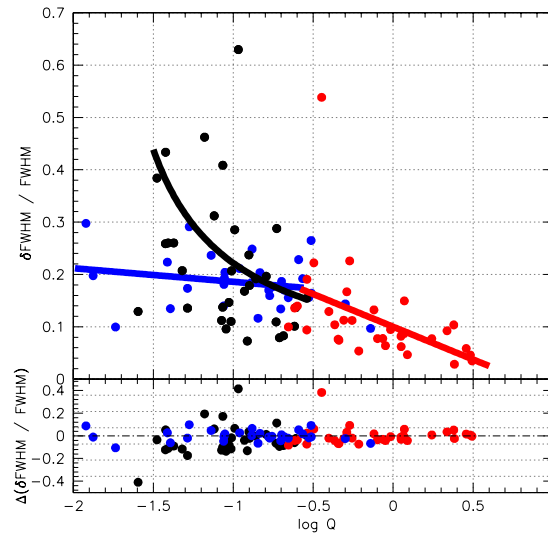


Fig. C.2: Relation between the fractional uncertainty $\delta FWHM / FWHM$ and the logarithm of parameter Q . Red spots are for H β , black for Al III, blue for CIII]. The thick lines trace the relations reported in Table C.1 for the FWHM of Al III (black) and CIII] (blue).

C.2 H β and 1900 blend paired comparison

The results of line profile fitting for the 1900 blend and H β are shown in the following figures: Fig. C.3 for the FOS sample, Fig. C.4 for the HE sample, Fig. C.5 for the FOS sample, and Fig. C.6 for the WISSH sample. All spectra have been continuum subtracted and normalised by the 5100 Å (H β) and 1700 Å (1900 blend) specific flux.

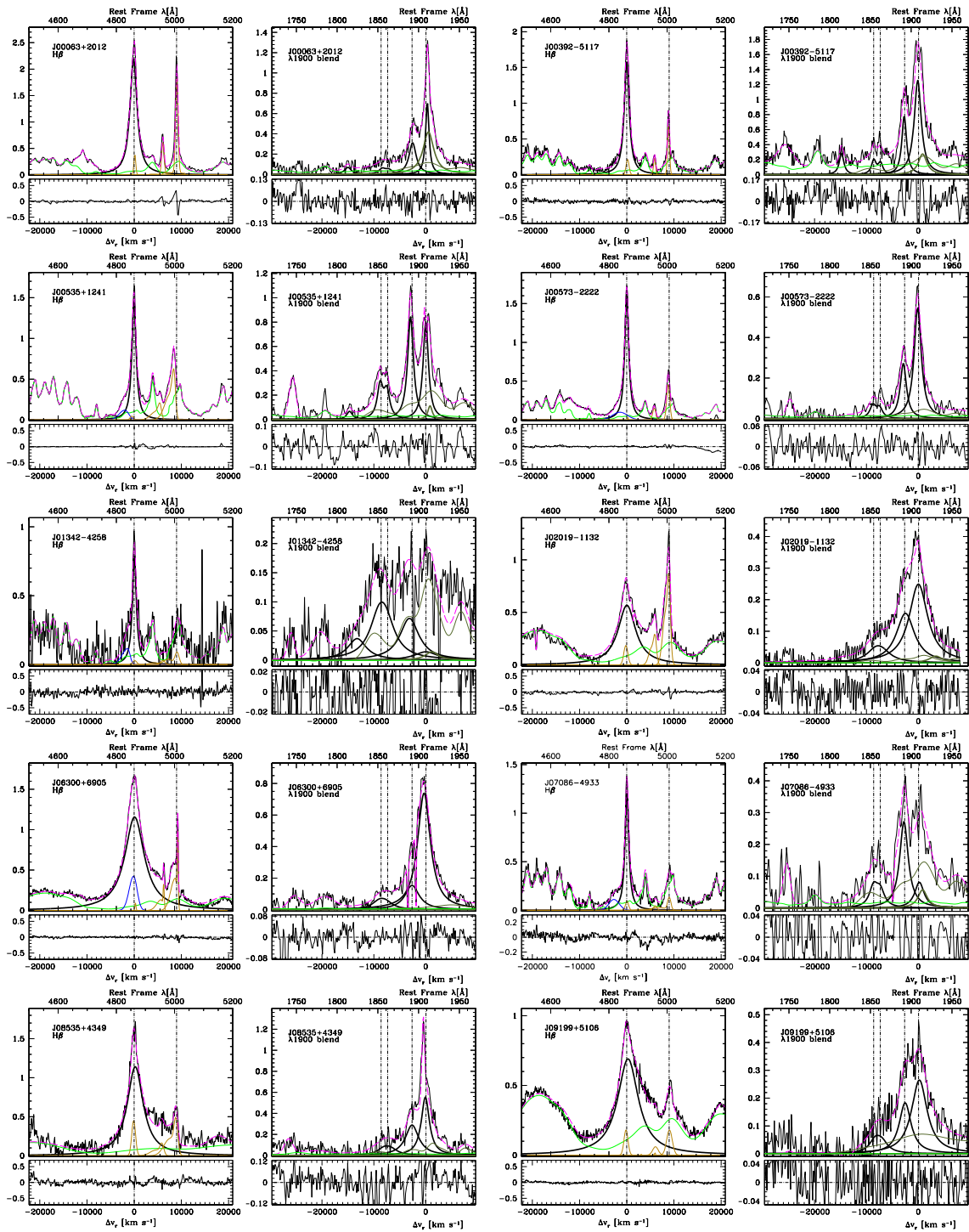


Fig. C.3: Analysis of the $H\beta$ spectral range (left) and of 1900 \AA blend (right), for the sources of the FOS^* subsample. Abscissa scales are rest-frame wavelength in \AA and radial velocity from rest-frame. Ordinate scale is normalised specific flux by the value at 5100 \AA and at 1700 \AA . The dashed magenta lines trace the sum of all emission components of the model. The black lines identify the $H\beta$ broad component $H\beta_{BC}$ (left), and $Al\ III$, $Si\ III$, and $C\ III$ (right). The blue line the blueshifted excess in the $H\beta$ profile. Green lines trace the adopted $Fe\ II$ (pale) and $Fe\ III$ (dark) templates. Golden lines trace narrow emission lines or line components.

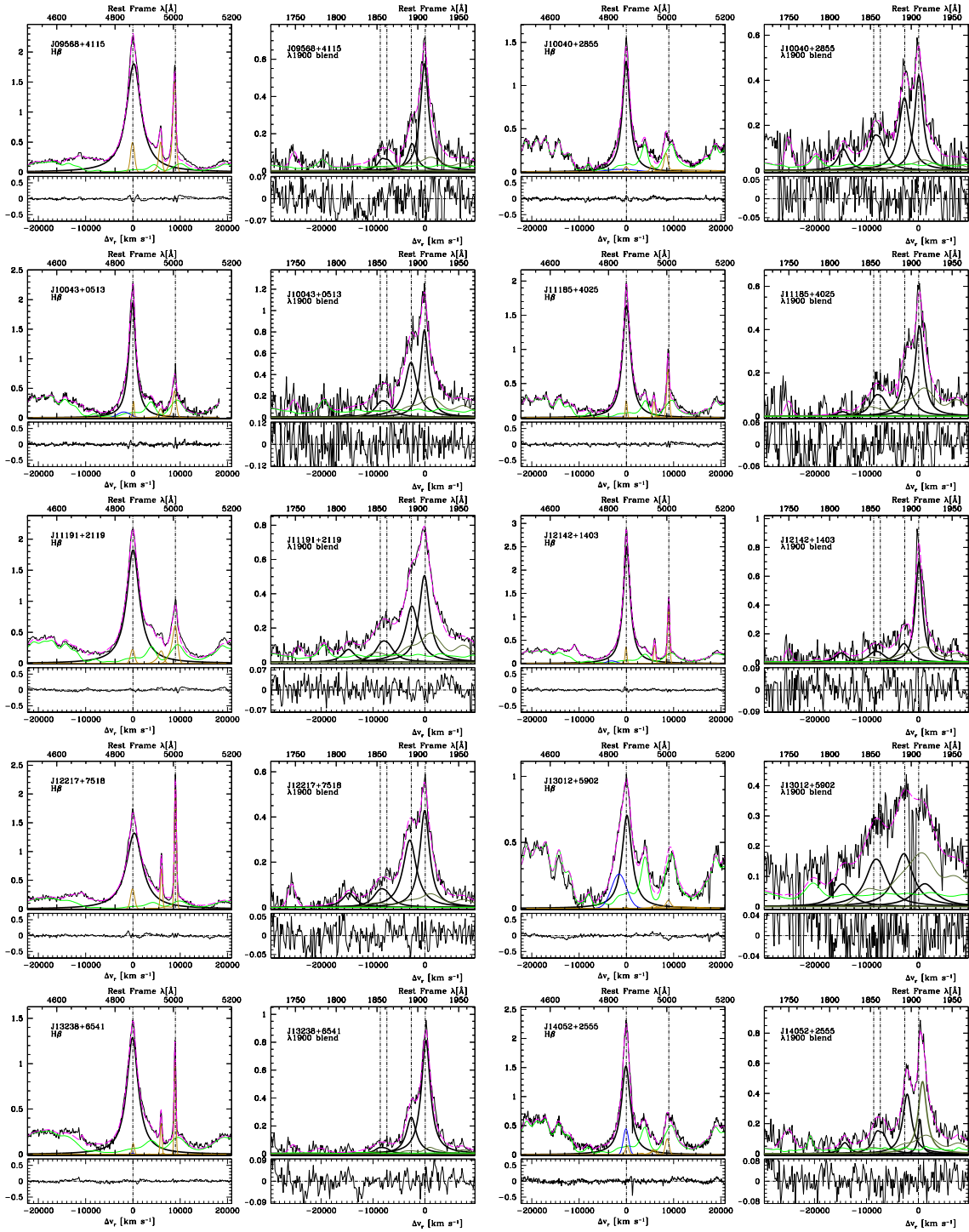


Fig. C.3: Analysis of H β and of the 1900 Å blend for the *FOS** subsample (cont.).

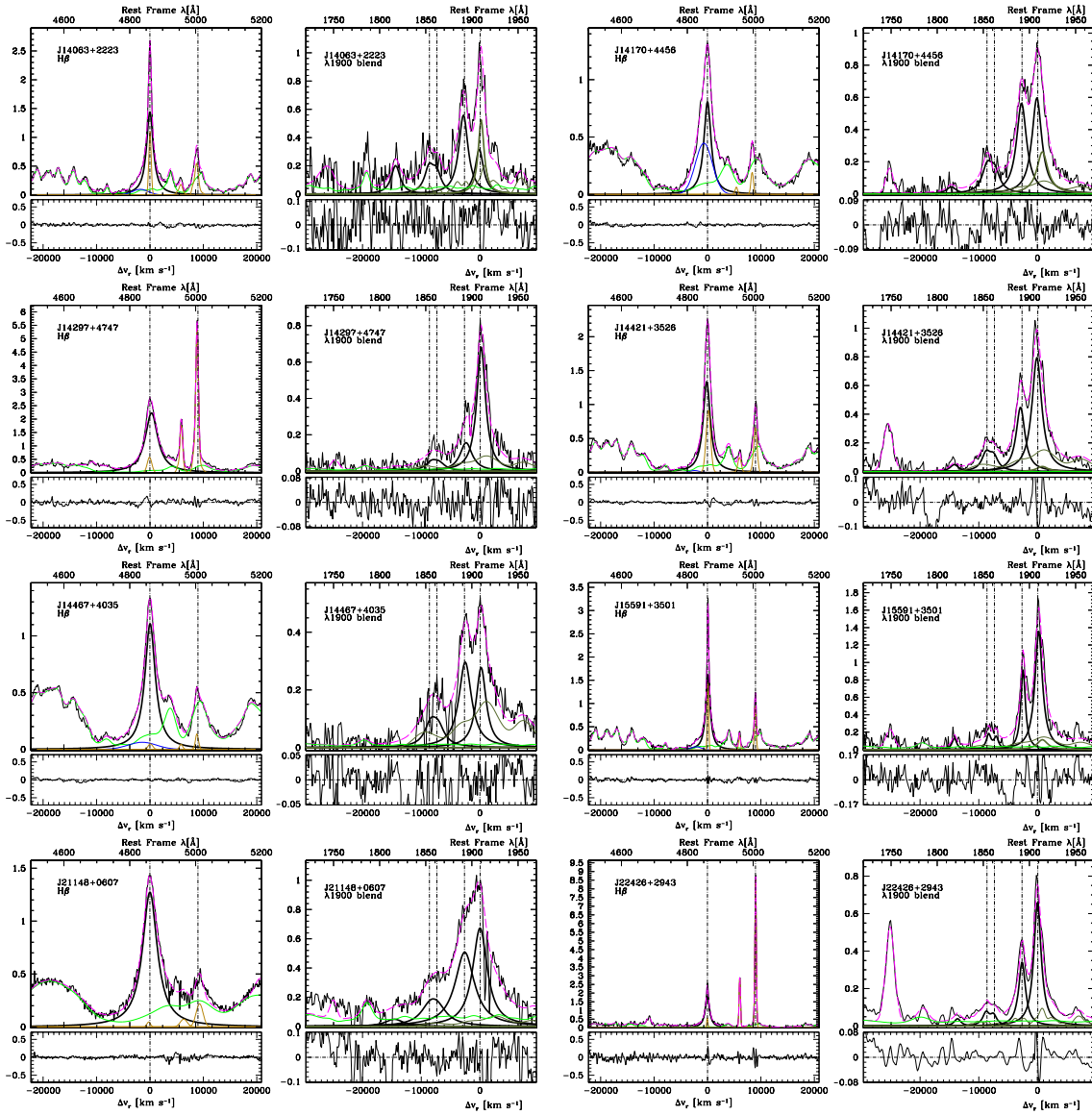


Fig. C.3: Analysis of H β and of the 1900 Å blend for the FOS^* subsample (cont.).

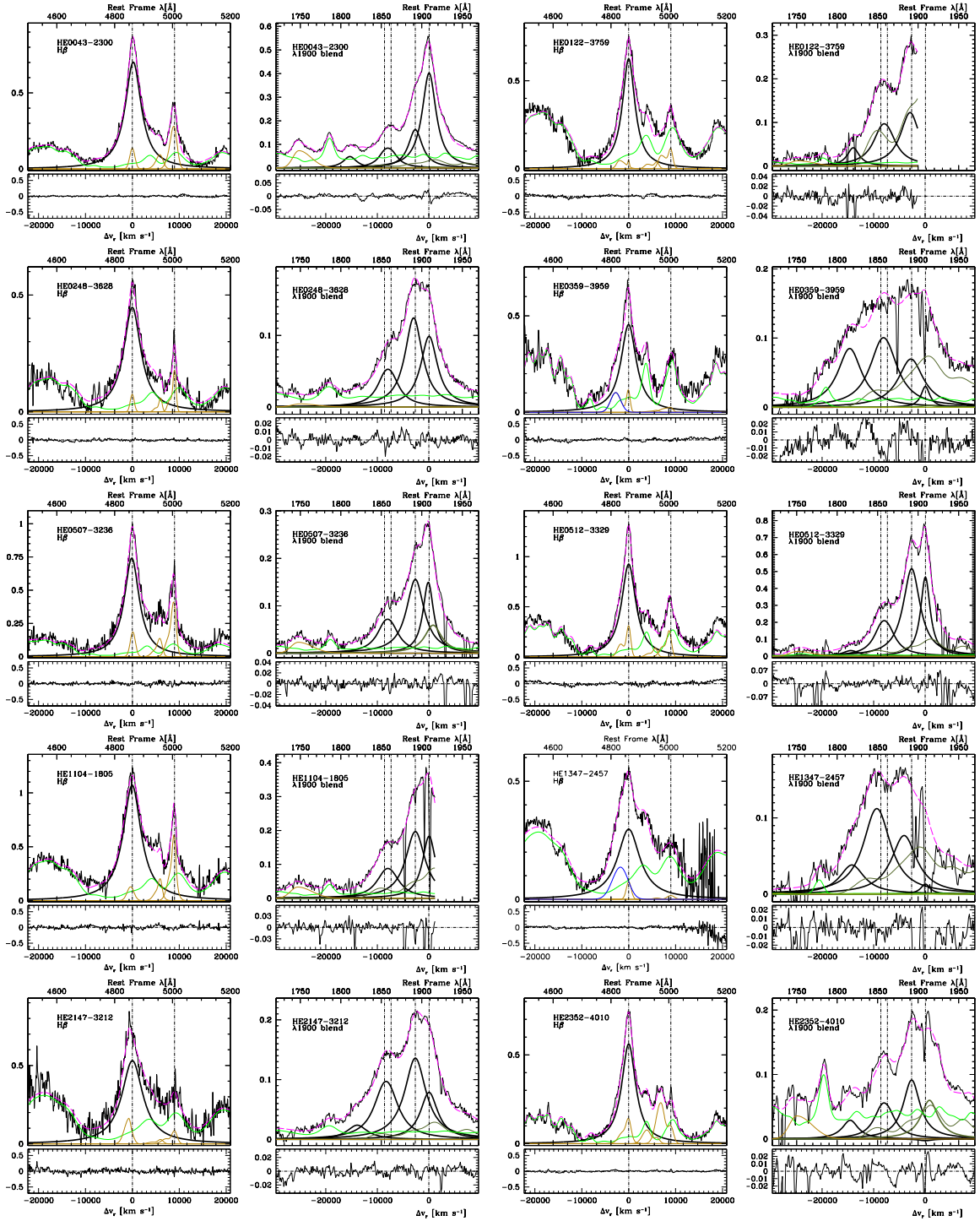


Fig. C.4: Analysis of the 1900 Å blend, for 10 Pop. A sources of the HE sub-sample. Meaning of colour coding is the same as in Fig. C.3.

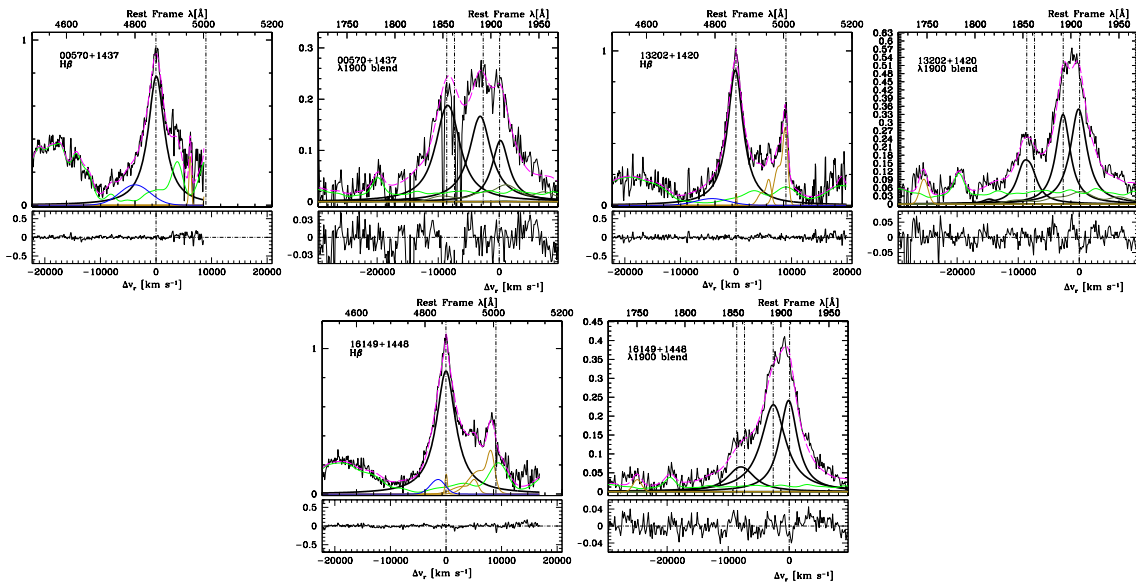


Fig. C.5: Analysis of H β and of the 1900 \AA blend for Pop. A sources of the ISAAC sample. Meaning of colour coding is the same of the previous Figures in the Appendix.

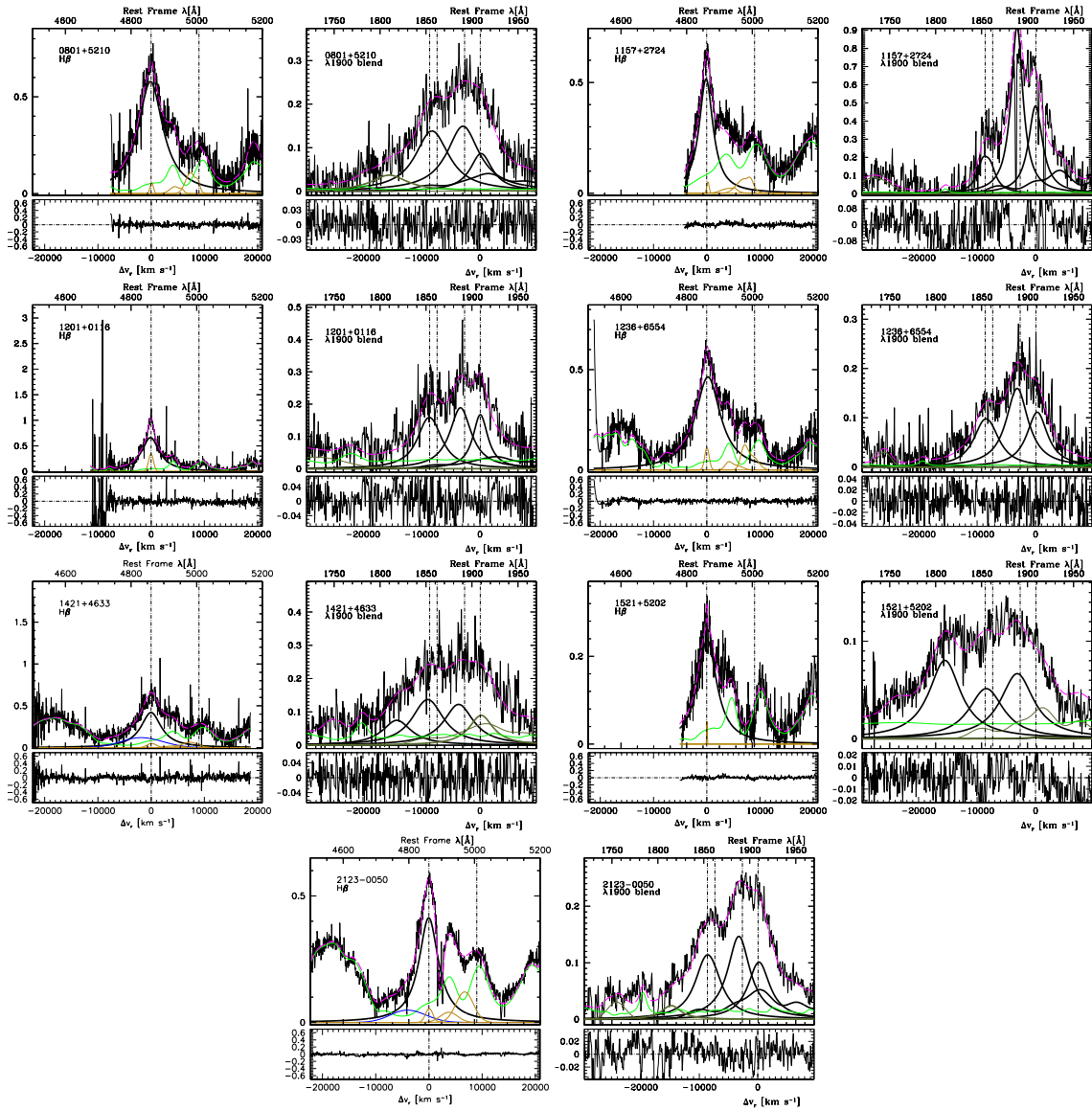


Fig. C.6: Analysis of H β and of the 1900 Å blend for Pop. A sources of the WISSH sample. Meaning of colour coding is the same of the previous Figures in the Appendix.

C.3 Notes on individual objects

J01342-4258 Extreme of extreme Population A. Strong feature at 2080 Å, extreme Fe III emission. In the UV spectrum a strong shelf of emission extends from the red end of the 1900 Å blend to beyond 1950 Å. Inverted radio spectrum not accounted for by the classical synchrotron scenario.

J02019-1132 The CSS source 3C 57 shows a spectrum of Pop. A in the optical range. Analysed by [Sulentic et al. \(2015\)](#).

HE 0248–3628 Candidate high-frequency peaking object which could be associated with an inverted or self-absorbed spectrum in 5 – 20 GHz frequency domain ([Massardi et al. 2016](#)). We speculate that HE 0248–3628 and J01342-4258 could be both objects whose radio emission is not due to a relativistic jet but to thermal sources ([Ganci et al. 2019](#)).

J09199+5153 Luminous quasar, considered with “unusually strong optical Fe II emission” ([Sulentic et al. 1990](#)). The $R_{\text{FeII}} \approx 0.8$ confirms that optical Fe II emission is prominent, but not extraordinarily so. The UV spectrum is definitely not xA, and is consistent with the A2 classification based on the optical spectrum.

J07086-4933 Bad spectrum contaminated by heavy absorptions; Al III lower limit.

HE 0043-2300 Apart from 3C 57, the only source truly “jetted” radio loud.

HE 0359-3959 High-luminosity analogous of J01342-4258; extreme C IV λ 1549 blueshift and extremely low ionisation in the virialised BLR ([Martínez-Aldama et al. 2017](#)).

J1157+2724 This WISSH source has a significant difference in the redshift estimated for the present work and the one published by [Vietri et al. \(2018\)](#) which is estimated from the narrow H β component, 2.2133 vs 2.2170. The difference is significant. The larger redshift of [Vietri et al. \(2018\)](#) would imply larger shifts of Al III.